NBS SPECIAL PUBLICATION 604

U.S. DEPARTMENT OF COMMERCE/National Bureau of Standards

Energy Dispersive X-Ray Spectrometry

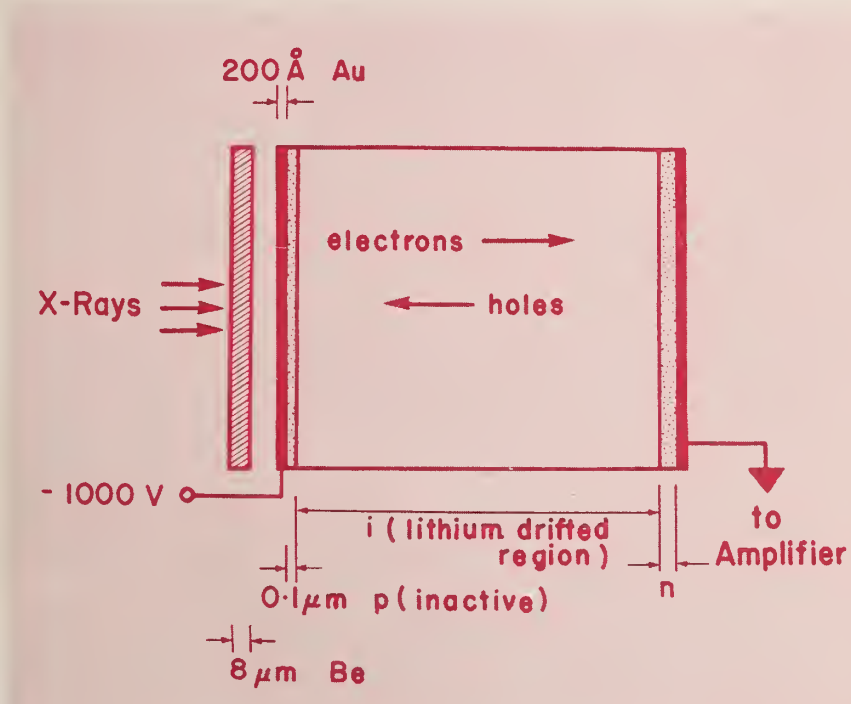

NATIONAL BUREAU OF STANDARDS

The National Bureau of Standards[1] was established by an act of Congress on March 3, 1901. The Bureau's overall goal is to strengthen and advance the Nation's science and technology and facilitate their effective application for public benefit. To this end, the Bureau conducts research and provides: (1) a basis for the Nation's physical measurement system, (2) scientific and technological services for industry and government, (3) a technical basis for equity in trade, and (4) technical services to promote public safety. The Bureau's technical work is performed by the National Measurement Laboratory, the National Engineering Laboratory, and the Institute for Computer Sciences and Technology.

THE NATIONAL MEASUREMENT LABORATORY provides the national system of physical and chemical and materials measurement; coordinates the system with measurement systems of other nations and furnishes essential services leading to accurate and uniform physical and chemical measurement throughout the Nation's scientific community, industry, and commerce; conducts materials research leading to improved methods of measurement, standards, and data on the properties of materials needed by industry, commerce, educational institutions, and Government; provides advisory and research services to other Government agencies; develops, produces, and distributes Standard Reference Materials; and provides calibration services. The Laboratory consists of the following centers:

Absolute Physical Quantities[2] — Radiation Research — Thermodynamics and Molecular Science — Analytical Chemistry — Materials Science.

THE NATIONAL ENGINEERING LABORATORY provides technology and technical services to the public and private sectors to address national needs and to solve national problems; conducts research in engineering and applied science in support of these efforts; builds and maintains competence in the necessary disciplines required to carry out this research and technical service; develops engineering data and measurement capabilities; provides engineering measurement traceability services; develops test methods and proposes engineering standards and code changes; develops and proposes new engineering practices; and develops and improves mechanisms to transfer results of its research to the ultimate user. The Laboratory consists of the following centers:

Applied Mathematics — Electronics and Electrical Engineering[2] — Mechanical Engineering and Process Technology[2] — Building Technology — Fire Research — Consumer Product Technology — Field Methods.

THE INSTITUTE FOR COMPUTER SCIENCES AND TECHNOLOGY conducts research and provides scientific and technical services to aid Federal agencies in the selection, acquisition, application, and use of computer technology to improve effectiveness and economy in Government operations in accordance with Public Law 89-306 (40 U.S.C. 759), relevant Executive Orders, and other directives; carries out this mission by managing the Federal Information Processing Standards Program, developing Federal ADP standards guidelines, and managing Federal participation in ADP voluntary standardization activities; provides scientific and technological advisory services and assistance to Federal agencies; and provides the technical foundation for computer-related policies of the Federal Government. The Institute consists of the following centers:

Programming Science and Technology — Computer Systems Engineering.

[1]Headquarters and Laboratories at Gaithersburg, MD, unless otherwise noted; mailing address Washington, DC 20234.
[2]Some divisions within the center are located at Boulder, CO 80303.

Energy Dispersive X-Ray Spectrometry

Proceedings of a Workshop on Energy Dispersive X-Ray Spectrometry
Held at the National Bureau of Standards, Gaithersburg, MD 20760
April 23-25, 1979

Editors:

K. F. J. Heinrich
D. E. Newbury
R. L. Myklebust

Center for Analytical Chemistry
National Measurement Laboratory
National Bureau of Standards
Washington, DC 20234

C. E. Fiori

Biomedical Engineering Instrumentation Branch
National Institutes of Health
Bethesda, MD 20205

U.S. DEPARTMENT OF COMMERCE, Malcolm Baldrige, Secretary
NATIONAL BUREAU OF STANDARDS, Ernest Ambler, Director

Issued June 1981

Library of Congress Catalog Card Number: 81-600047

National Bureau of Standards Special Publication 604
Nat. Bur. Stand. (U.S.), Spec. Publ. 604, 441 pages (June 1981)
CODEN: XNBSAV

U.S. GOVERNMENT PRINTING OFFICE
WASHINGTON: 1981

For sale by the Superintendent of Documents, U.S. Government Printing Office
Washington, D C 20402 - Price $9.

(Add 25 percent for other than U.S. mailing)

FOREWORD

The Center for Analytical Chemistry of the National Measurement Laboratory, National Bureau of Standards, seeks to develop new techniques of chemical analysis and to constantly improve existing analysis methods. Part of the mission of NBS is to disseminate knowledge in the scientific and technical community. To aid in achieving this objective, the Center for Analytical Chemistry has sponsored a series of workshops on various topics in analytical chemistry. The workshop topics are chosen to fulfill current needs for detailed discussions on well defined subjects in a wide variety of specialist areas of interest. The objective of these workshops is to bring together specialists from throughout the world to concentrate intensively on a particular subject in order to advance the state-of-the-art. It is often very difficult to achieve this goal at large international meetings where the size and diversity of topics presented often limit detailed discussion of specialist subjects. Past topics of these workshops and the published proceedings include: Quantitative Electron Probe Microanalysis (NBS Special Publication 298), Aerosol Measurements (NBS Special Publication 412), Secondary Ion Mass Spectrometry (NBS Special Publication 427), Use of Monte Carlo Calculations in Electron Probe Microanalysis and Scanning Electron Microscopy (NBS Special Publication 460), and Characterization of Particles (NBS Special Publication 533).These proceedings are available from the Superintendent of Documents, Government Printing Office, Washington, DC 20402. Further information on the workshops can be obtained by writing to the Center Office, Center for Analytical Chemistry, National Bureau of Standards, Washington, DC 20234.

This volume contains the proceedings of a Workshop on Energy Dispersive X-ray Spectrometry. The three-day meeting involved participants from the United States and Europe. The workshop format consisted of invited talks on each topic followed by contributed papers and extensive discussions.

The extensive development of electron beam instrumentation for microanalysis and microscopy has been greatly stimulated by the development of the energy dispersive x-ray spectrometer based on the silicon (lithium) detector. This publication provides a detailed view of the state-of-the-art of energy dispersive x-ray spectrometry, from the basics of the detection process to applications of the technique to quantitative x-ray microanalysis. The papers should be of wide interest to workers in many fields of science which utilize x-ray microanalysis.

John D. Hoffman, Director
National Measurement Laboratory

PREFACE

The scanning electron microscope, electron probe microanalyzer, and analytical transmission electron microscope have had great impact on the characterization of specimens in the physical and biological sciences as well as in the analysis of technological processes. A substantial part of this impact is derived from the capability of these instruments to provide quantitative elemental compositional analysis to complement the images obtained with the electron beam. Compositional analysis has been greatly stimulated by the development of energy dispersive x-ray spectrometry (EDS) based on the silicon (lithium) solid state x-ray detector and the simultaneous development of the laboratory minicomputer. The capability of the EDS system to provide a rapid qualitative analysis of a sample in seconds and a quantitative analysis in minutes in the laboratory has made it extremely attractive to a wide variety of workers. As a result, modern electron beam instruments are frequently equipped with a complete EDS system.

The purpose of this meeting was to bring together workers who are actively participating in the development of EDS detectors, signal processing systems, and multichannel analyzers and in the application of EDS systems to x-ray microanalysis and x-ray fluorescence analysis. We have witnessed a period of rapid development in EDS systems over the past five years. Recent advances in detector materials, and laboratory computer systems suggest that further advances can be expected in the near future. It thus seemed to be an appropriate time to review the current state of development in the EDS field. We hope that this report will serve the scientific community as a useful reference in this important area.

The editors gratefully acknowledge the excellent work of Joy Shoemaker and the members of the Text-Editing Facility of the Center for Analytical Chemistry in preparing this manuscript.

K. F. J. Heinrich
D. E. Newbury
R. L. Myklebust
Gas and Particulate Science Division
Center for Analytical Chemistry

C. E. Fiori
National Institutes of Health

Disclaimer

Certain commerical equipment, instruments, or materials are identified in this paper in order to adequately specify the experimental procedure. Such identification does not imply recommendation or endorsement by the National Bureau of Standards, nor does it imply that the materials or equipment identified are necessarily the best available for the purpose.

ABSTRACT

This book is the formal report of the Workshop on Energy Dispersive X-ray Spectrometry held at the National Bureau of Standards, April 23-25, 1979. The papers included in these proceedings cover a wide range of topics in the field: (1) Physics of detectors -- Properties of silicon (lithium), germanium (lithium), intrinsic germanium, and mercuric iodide detectors are described and compared. (2) Windowless x-ray detectors -- The application of windowless energy dispersive x-ray detectors to the measurement of soft x-rays below 1 keV is described, including special electronic techniques for processing pulses produced by low energy x-rays. (3) Electronics for energy dispersive x-ray spectrometry -- The signal processing chain is discussed with special emphasis on state-of-the-art multichannel analyzers. (4) Spectral processing and statistics -- Fundamental statistical considerations in spectral processing are described. A variety of curve fitting techniques is discussed, including sequential simplex and least squares fitting with a digital filter. (5) Artifacts in energy dispersive x-ray spectrometry in electron beam instruments -- Artifacts arising from the basic detection and amplification processes and instrument-related artifacts observed in electron beam instruments operating in the range 10 - 1000 keV are described. (6) Applications -- Applications of energy dispersive x-ray spectrometry are given in quantitative x-ray microanalysis and x-ray fluorescence analysis.

The papers include broad overviews of the subjects as well as specific applications and should be of interest to workers in the electron beam microanalysis and x-ray fluorescence analysis fields.

Key Words: Electron probe microanalysis; energy dispersive x-ray spectrometry; germanium (lithium) detector; scanning electron microscopy; silicon (lithium) detector; spectral deconvolution; x-ray analysis; x-ray fluorescence.

TABLE OF CONTENTS

Table of contents continued.

National Bureau of Standards Special Publication 604. Proceedings of the Workshop on Energy Dispersive X-Ray Spectrometry held at NBS, Gaithersburg, Maryland, April 23-25, 1979. (Issued March 1981)

THE DEVELOPMENT OF ENERGY-DISPERSIVE X-RAY ANALYSIS

Kurt F. J. Heinrich

National Bureau of Standards
Center for Analytical Chemistry
Washington, D.C. 20234

Abstract

Energy-dispersive x-ray analysis with gas proportional detectors has been used widely in x-ray spectrochemical analysis. It was particularly useful in the detection of low-energy x-ray emission, before the commercial availability of the Blodgett-Langmuir pseudo-crystals. With the development of solid-state x-ray detectors of high resolution, and improvement in associated electronics and computers, the interest in energy-dispersive x-ray analysis has increased enormously, to the point where it has replaced Bragg crystal diffraction spectrometry in many instances.

In the early years after the discovery of x-rays by W. C. Roentgen [1][1], x-rays of differing energy were distinguished according to their power of penetration through materials. After Haga and Wind demonstrated in 1899 that x-rays can be diffracted, and a practical method was proposed by W. H. Laue and W. L. Bragg obtained the first diffracting x-ray spectrum [2]. The x-ray spectra of many elements were obtained by Moseley [3], and from that time on x-ray lines were predominantly characterized in Bragg crystal spectrometers according to their wavelengths.

1. Spectrometers for X-ray Spectrochemical Analysis

In the fifties and early sixties, Geiger counters were preferred in x-ray spectrometric analysis, due to their simplicity and to the strong pulses emitted from these detectors. Geiger counters were later abandoned because of their slow speed, and of the fact that pulses generated by x-ray photons of different energy are indistinguishable. Therefore, they could not be used for spectrometric purposes except in conjunction with Bragg crystal spectrometers.

The subsequent widespread use of gas proportional detectors [4] generated interest in the analysis of x-rays according to their photon energies (pulse-height analysis). In these detectors, the energy of the x-ray photon is used to form pairs of electrons and negative ions. These are accelerated in the electrostatic field of the detector, and collisions of the electrons with other gas molecules produce an "internal amplification".

The total charge of the electron avalanche reaching the central anode wire determines the height of the resultant pulse, and the statistical dispersion of heights of pulses produced by photons of equal energy determines and limits the detector resolution. Several schemes were developed for the use of a single-channel analyzer to exclude high-order reflections of x-ray lines from wavelength spectra obtained with a Bragg spectrometer [5-7]. Birks et al., have advocated the use of proportional detectors for energy-dispersive analysis [8]. This approach was particularly useful for the separation of x-rays of long wavelength, such as OKα and CKα bands, and was followed by Dolby [9]. In principle, this

[1]Figures in brackets indicate the literature references at the end of this paper.

resolution can be predicted [10], and experimental results obtained with carefully designed and prepared detectors come close to the predicted values [11] for an argon-filled detector, it was found that

$$\sigma_V/\bar{V} = 0.15\ E^{-1/2}$$

in which the photon energy in keV is E, $\bar{V}$ is the mean height of the pulse distribution, and σ_V its standard deviation.

Dirt and irregularities on the surface of the detector wire as well as other sources of local electrostatic charges, considerably degrade this resolution. When the observation of x-rays of low (1-3 keV) photon energies rendered necessary the use of very thin windows made of organic films, further complications arose. To avoid electrostatic charges on these windows their metallization was required. Another problem arose from impurification of the detector gas, which had to be continually refilled in replacement of seepage through the window. Oxygen or residual impurities (which may accumulate when a gas cylinder is almost empty) cause a severe distortion of pulse height. Only when these difficulties were overcome, and practical solid-state electronic pulse height analyzers were developed, could pulse height selection and analysis be used to full advantage.

Energy dispersive analysis of γ-rays and very energetic x-rays by means of sodium iodide scintillators and photomultipliers was widely practiced in the measurement of radioactive materials, but these devices had little energy resolution to be useful in the domain of x-rays habitually used for spectrochemical analysis. Solid-state detectors became more interesting for this purpose with the advent of the lithium-drifted silicon detector [12]. Once the effectiveness of the Si(Li) detector as an ancillary tool in electron probe microanalyzers was demonstrated, it was soon tried in SEM's [13] and was shown to be of great value both in qualitative and quantitative analysis.

In general, the energy-dispersive mode of analysis is preferable where high effectiveness of the detector system is more important than high resolution. In fact, even at the present state-of-the-art in detector resolution (145 eV FWHM for Mn Kα), it is possible to find unsolvable interferences, such as a specimen having arsenic, sulfur, and lead (see figure 1). In practice, however, the occurrence of such situations is very infrequent. On the other hand, obtainable signal intensities (in terms of photons per primary electron) can be – depending on the respective systems – 10^2 to 10^3 times stronger with energy dispersive detection. For this reason, this mode has become prevalent in the analysis of thin films and small particles. A drawback of the Si(Li) device is the large volume of the Dewar flask used to store the liquid nitrogen required for cooling both the detector and the preamplifier. If solid-state detectors of adequate resolution were developed which will not require liquid-nitrogen cooling, this would considerably extend the useful range of solid-state x-ray detection.

2. Conclusions

In view of their complementary advantages, it is best, for general purposes, to provide instruments with both wavelength and energy dispersive spectrometers. In those analytical situations in which the x-ray intensities emitted from the specimen are weak, the energy-dispersive detector is mandatory. It can be used for quantitative applications and is attractive for simultaneous measurement of several x-ray lines. However, it is limited in resolution and, hence, background levels are comparatively high. Hence, in spite of the apparent simplicity of energy-dispersive spectra, a careful treatment and complex data handling routine are required for quantitative applications.

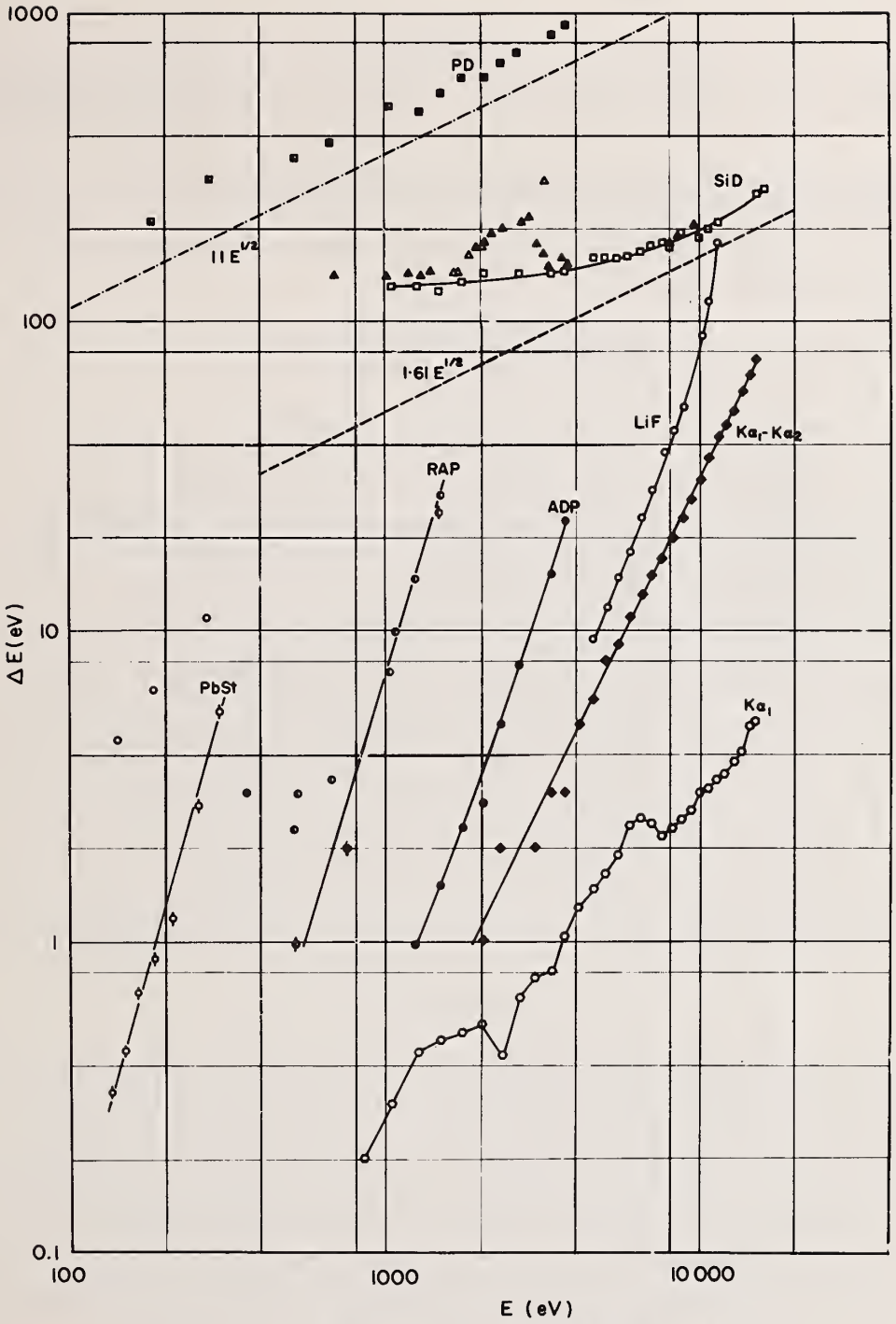

Figure 1. This log-log plot shows FWHM values for:

a) tabulated widths of the $K\alpha_1$ line
b) distances between $K\alpha_1$ and $K\alpha_2$
c) resolutions obtained in a conventional electron probe microanalyzer with curved crystals of lead stearate (PbSt), rubidium acid phthalate (RAP), $NH_4 \cdot H_2PO_4$ (ADP), and lithium fluoride (LiF)
d) the natural widths of bands from K emissions of elements of low atomic number (circles)
e) the theoretical (dashes) and practical resolution of a Si(Li) detector (SD), and
f) the theoretical (dashes and dots) and practical resolution of a Ar-CH_4 gas proportional detector. The high values marked with full triangles (for Si(Li) detector) are due to overlap of L lines. The bottom scale indicates photon energy.

3. References

[1] Roentgen, W. C., Ann. d. Physik, 64, 1 (1898); Science 3, 227 (1896), and 3, 726 (1896).

[2] Bragg, W. H. and Bragg, W. L., Proc. Roy Soc. (London)/A/88, 428 (1913).

[3] Moseley, H. G. J., Phys. Mag., 26, 1024 (1913); 27, 703 (1914).

[4] Fink, R. W., Chapter 5 of Atomic Inner-Shell Processes, Craseman, B., Ed., Vol. II, Academic Press, New York, 1975.

[5] Heinrich, K. F. J., Adv. X-ray Analysis, 4, 370 (1961).

[6] Riggs, F. B., Jr., Rev. Sci. Instr., 34, 912 (1963).

[7] Weber, K. and Marchal, J., J. Sci. Instr., 41, 15 (1964).

[8] Birks, L. S., Labrie, R. J., and Criss, J. W., Anal. Chem., 38, 701 (1965).

[9] Dolby, R. M., Proc. Phys. Soc., 73, 81 (1959); J. Sci. Instr., 40, 345 (1963).

[10] Campbell, A. J., Norelco Rept. 14, 103 (1967).

[11] Mulvey, T. and Campbell, A. J., Brit. J. Appl. Phys., 9, 406 (1958).

[12] Bowman, H. R., Hyde, E. K., Thompson, D. G., and Jared, R. C., Science, 151, 562 (1966).

[13] Russ, J. C., SEM-1971, Part 1, 65.

National Bureau of Standards Special Publication 604. Proceedings of the Workshop on Energy Dispersive X-Ray Spectrometry held at NBS, Gaithersburg, Maryland, April 23-25, 1979. (Issued March 1981)

PROPERTIES OF SILICON AND GERMANIUM SEMICONDUCTOR DETECTORS FOR X-RAY SPECTROMETRY[1]

R. W. Fink

School of Chemistry
Georgia Institute of Technology
Atlanta, Georgia 30332

Abstract

The characteristics of silicon and germanium semiconductor x-ray detectors of various designs (disk, top hat, grooved, and ion implanted types) are reviewed, including discussion of sensitive area and depth, metallic- and dead-layers. The effects of electronic operating conditions and timing requirements on spectral peak shapes (tailing), resolution, and efficiency in singles and in coincidence measurements are reported. The response to monoenergetic photons is discussed, including second-order x-ray spectral effects, such as the low-energy plateau, escape peaks, the continuum around the full-energy peak, summing and sum peaks, and effects of collimation. Various methods of measuring relative and absolute detector efficiencies for photons from about 200 eV to 140 keV in energy are summarized, and a useful table is presented of long-lived radioactive sources suitable for calibration of energy and efficiency curves of x-ray detectors, in which the current best values of halflife, photon energies, and the absolute number of photons emitted per 100 decays are tabulated. Finally, some recently reported advances in detectors, electronic systems, and a new method of unfolding partly-resolved doublets (e.g. $K\alpha_1$ and $K\alpha_2$ lines) in coincidence spectra are summarized.

1. Introduction

The purpose of this article is to update earlier studies and reviews [1-5][2] on the properties and characteristic response of silicon and germanium semiconductor detectors for x- and γ-ray spectrometry in the energy range below about 30 keV for silicon and 140 keV for germanium. Aside from some mention of efficiency and deadlayer determinations in silicon for K x-rays as low as 185 eV (boron), the scope of this review also is limited to the region of energies above about 3 keV, since there appears elsewhere in these proceedings a paper by Musket [6] dealing with essentially windowless Si(Li) x-ray detectors specializing in ultra-low-energy measurements from 2 keV to 185 eV. Excluded from the present review is any detailed discussion of fabrication techniques [7] or the fundamental physics of semiconductors. Moreover, detailed descriptions of electronic systems are not included, although some discussion of recent advances and performance considerations is given.

---

[1]Supported in part by the U.S. Department of Energy under Contract No. De-AS05-76-ERO-3346.

[2]Figures in brackets refer to the literature references at the end of this paper.

2. Characteristics of Various Detector Configurations

2.1 Resolution and Peak-to-Continuum Ratio

High resolution and a high peak-to-continuum ratio are of utmost importance. Resolution may be defined as the root-mean-square value of the electronic system line width, as determined with a randomized electronic pulser[3], and the intrinsic line width of the detector:

$$R = \sqrt{(\text{FWHM})^2_{(\text{pulser})} + (2.35F\varepsilon E)^2_{(\text{detector})}} \quad \text{eV} \qquad (1)$$

where R is the resolution in eV, expressed as the full-width at half-maximum, FWHM, of a single photon line, such as the 14.4 keV γ-ray from a ^{57}Co source or the 5.9 keV Kα x-ray doublet from a ^{55}Fe source; F is the well-known Fano factor, which accounts for deviations of the primary ionization from a Poisson statistical distribution, and is approximately 0.10 for Si and 0.1 to 0.129 for Ge; ε is the average energy to create an electron-hole pair and is about 3.58 ± 0.10 in Si and 2.94 ± 0.15 in Ge; and E is the photon energy in eV deposited in the sensitive volume.

A resolution of 146 eV FWHM at 5.9 keV at 1000 c/sec, for example, will resolve completely the K x-ray peaks of Si (1.74 keV) and Al (1.49 keV), whereas a resolution of 165 eV FWHM produces considerable overlapping of these two peaks. The best system resolution so far reported is 139 eV FWHM at 5.9 keV at 1000 c/sec for a 10 mm^2 x 3 mm Si(Li) detector. Values of resolution below 100 eV have been obtained at 1.49 keV (Al Kα). It is clear that for low energy x-ray experiments and for quantitative x-ray fluorescence analysis of low-Z adjacent elements, the highest possible resolution is crucial, consistent with a reasonable compromise on detector size in order to obtain sufficient solid angle, since one of the principal sources of experimental error arises from deconvolution of such partially-resolved peaks.

In addition to good resolution, the ratio of the full-energy peak to the continuum and the full-width at 1/10th maximum are important criteria of detector performance. Typically, the peak-to-continuum ratio should exceed about 1500:1 for Si(Li) at 5.9 keV, depending on detector size, quality, and collimation; and the full-width at tenth maximum should be less than about 1.85 the FWHM value. A low-energy "tail" extending from the full-energy peak, or a poor ratio of peak-to-continuum indicates a low quality or defective detector or an electronic system that is not properly tuned for optimum performance. The leading cause of such poor detector performance is trapping and recombination effects in the detector itself.

Charge trapping and recombination of electron-hole pairs, and variations in the depths of the traps, give rise to a wide distribution of lifetimes of trapping and a wide distribution of slow risetime pulses, which lie mainly in the low-energy continuum below the peak [3] owing to the incomplete collection of charge. For example, precipitated lithium in Si(Li) and Ge(Li) detectors constitutes a hole trap, whereas a lithium-deficient impurity site becomes an electron trap. The principal cause of asymmetric peak shapes ("tailing") is a non-uniform distribution of traps in the intrinsic (sensitive) volume. Other degrading effects which throw pulses into the tail include ohmic contact noise, microphonic problems, infrared (blackbody) radiation, and crystal lattice imperfections arising either from the original ingot or from radiation damage, e.g. from exposure to fast neutrons.

2.2 Detectors of Advanced Design

For photons in the energy range of interest, detectors range in size from 10 to as large as 750 mm^2 active area and from 2 to 5 mm in sensitive depth; generally, the highest resolution is achieved, the smaller the detector. To reach the best performance, it is necessary to have fast collection times, as well as the lowest possible detector capacitance, in order to reduce the incidence of slow-rising pulses due to deadlayers, dead edges, trapping, and recombination effects, since the largest proportion of slow pulses occurs in the low-energy tail [3]. Thus, the detectors should be operated at a very high reverse-bias voltage, from 1000 to 2000 volts, and to achieve such high electric fields without excessive

leakage currents ($<10^{-13}$ amp at 77 °K) and to reduce the detector capacitance, the simple disk-type planar detector configuration was soon replaced with other designs [8,9], such as those with concentric single- or double-grooves to form guard rings, or a top-hat design. Sophisticated designs have been reported [10] using double-grooved guard ring detectors, in which an anticoincidence signal is taken from the guard ring to reject events in the central detector that trigger both simultaneously. This effectively eliminates partial collection from escaping events in the peripheral regions of the central detector. A double guard ring [8,10] can even be used, the outer ring being grounded to reduce the edge leakage current while the inner ring serves as the anticoincidence signal discriminator to detect and reject even very small pulses.

The anticoincidence guard-ring detector can achieve very substantial improvement of peak-to-continuum ratios, as demonstrated by Landis, et al. [8]; for example, a 40-fold reduction in the continuum from Cd K x-rays (23 keV) is observed with no sacrifice in the resolution. The use of physical collimation is not at all as effective. Unfortunately, these sophisticated guard-ring detectors with reject circuitry are not routinely available commercially, although modern integrated NAND circuits could readily be incorporated into the preamplifier to provide rejection of small pulses from events escaping the center counter.

The properties of lithium-drifted Si(Li) and Ge(Li) detectors for low-energy photon and electron spectrometry have been thoroughly reviewed in the literature cited above. The production of ultra-high purity Si(HP) and Ge(HP) crystals (resistivities up to 10^5 ohm-cm) permits the fabrication of PN junction (rectifying) detectors which are free of drifted lithium with all of its problems. The first of such devices were known as "surface barrier" detectors because of their thin (200 Å, 40 μg/cm^2) gold metallic front window. These produce depletion layers under high reverse-bias voltage up to several mm in depth [11]. For example, N-type SI(HP) with a gold surface barrier and guarded N-type lithium-diffused (but not drifted) N+ contacts has been used to fabricate detectors with depletion layers 4 mm thick at 800 volts which can operate as high resolution x-ray spectrometers at liquid nitrogen temperature (77 °K) [12]. Similar results with gold surface-barrier Ge(HP) detectors have been achieved [13] and an extensive review has appeared [14]. A detailed investigation of the performance and efficiency of such a surface-barrier Ge(HP) x-ray detector has been published by Hansen, et al [15].

At the present time, it appears that such gold surface-barrier (Si(Au) and Ge(Au) detectors are being supplanted by much more rugged ion-implanted ultra-high purity detectors. These can be stored at room temperature indefinitely without deterioration and are far less sensitive to atmospheric leaks, moisture, and other impurities in the vacuum system, and which are not totally destroyed in the event of breakage of the beryllium window. They are also expected to have a longer useful life of laboratory use. For example, ion-implanted Si(HP) detectors with sensitive thicknesses from 20 μm to 5 mm are commercially available. Typically these may have a front contact of only 20 μg/cm^2 nickel or aluminum on an ion-implanted boron layer about 200 Å deep, and a rear contact of vacuum evaporated aluminum. The silicon deadlayer typically is in the range of 800 to 2000 Å. These Si(HP) detectors can be operated at room temperature for charged particle detection or may be cooled to 77 °K for low-energy electron, x-ray, or γ-ray spectrometry.

Single-crystal germanium with a residual active impurity concentration of $\leq 10^{10}$ atoms/cm^3 (1 part in 10^{12}) is currently used for ion implantation of boron (~200 Å thick) as a replacement for the evaporated metallic P-type front contact layer. This has two main advantages: (1) there is no fluorescent excitation of characteristic x-rays (e.g., gold, palladium) from the metallic layer, the Ge deadlayer being as thin or thinner than formerly, and (2) the ion-implanted device is more rugged and reliable, since the implanted atoms are embedded in the crystal lattice, rather than being deposited as a thin delicate surface layer. The rear N+ contact layer is made by diffusing lithium at a concentration of 10^{20-22} atoms/cm^3. The behavior of diffused lithium in a crystal should not be confused with that of drifted lithium. It is the latter that is unstable at room temperature. For example, lithium, being an interstitial impurity, can move about a mm a day in room temperature germanium, but only a few Ångstroms a day at 77 °K. Thus a lithium-drifted Ge(Li) detector can suffer serious deterioration if warmed to room temperature even for a few minutes. Moreover, the movement of drifted lithium in Ge(Li) and Si(Li) detectors, either through aging at 77 °K or by cycling to room temperature, can cause changes in the volume of the sensitive lithium-drifted region and thus changes in efficiency and deadlayer

thickness [16-17]. We have observed such efficiency changes in several Si(Li) and Ge(Li) x-ray detectors in our laboratory (e.g., see reference 15). We also observed a decline in efficiency of an early Ge(HP) gold surface-barrier detector with an N-type front layer, because of the fact that the depletion layer thickness in this type of detector is highly dependent on reverse-bias voltage (equation 2 below). Owing to increasing leakage current with age of this detector, the maximum bias voltage that could be used declined from over 100 volts to 25 volts, causing the efficiency that could be achieved to decline proportionately; i.e., the depletion depth is given by

$$W = (2\varepsilon V/qN)^{1/2} \qquad (2)$$

where ε is the dielectric constant, V is the applied voltage, q is the collected electron charge, and N is the concentration of doping impurities in the semiconductor material.

Figure 1, courtesy of ORTEC, Inc., compares the spectra in the energy range 60 to 87 keV produced by fluorescently exciting each of the two detectors with a ^{57}Co source, whose 122 and 136 keV γ-rays can excite gold K x-rays ($K\alpha^1$ 68.79 and $K\alpha^2$ 66.97 keV). The upper curve is for a Ge(Li) detector with a gold front layer [490 mm^2 x 7 mm depth, having resolution of 385 eV FWHM at 5.9 keV and 617 eV FWHM at 122 keV], and the lower curve is for an ion-implanted boron Ge(HP) detector [490 mm^2 x 10 mm depth, with resolution of 317 eV FWHM at 5.9 keV and 543 eV FWHM at 122 keV]. The lower continuum and complete absence of fluorescent gold x-rays makes it clear that ion implantation is superior.

The effect of risetime discrimination on resolution and especially on tailing and the peak-to-continuum ratio was investigated in 1969 by Freund, et al. [3] on Ge(Li) detectors, when it was found that an improvement in the peak-to-continuum ratio of a factor of about 3 could be attained by rejecting slow pulses of 1 to 2 μsec risetimes without affecting resolution of the 14.4 keV γ-ray peak from ^{57}Co. In contrast, our 1979 ion-implanted Ge(HP) detector shows less than five percent improvement with similar risetime discrimination, and its peak-to-continuum ratio is about seven times better than that of the 1969 Ge(Li) detectors. This can be attributed to the presence of considerable trapping effects in the older Ge(Li) detectors. The enormous decrease in trapping in the modern Ge(HP) detector means that it is no longer necessary to impose risetime discrimination in order to improve the performance of the detector.

It might be of interest to indicate the observed performance of our 1979 ion-implanted Ge(HP) detector. It is a 30 mm^2 x 3 mm depth, top-hat type, with physical collimation, as shown in figure 2. It was operated at 1000 volts reverse-bias and is fitted with an ORTEC dynamic charge restoration preamplifier and operated with a Canberra Model 1412 amplifier in the symmetric mode. After optimizing all electronic parameters, the observed resolutions are: 173 eV FWHM at 5.9 keV at 1000 c/sec with a 6 μsec shaping time constant, the FW at 1/10M being 1.95 the FWHM at 5.9 keV; 205 eV FWHM at 14.4 keV, and 475 eV FWHM at 122 keV, where the FW at 1/10M is 1.8 FWHM. The peak-to-continuum ratio and resolution of this detector exhibit an essentially flat response with bias voltage between 500 and 1000 volts, both of these characteristics deteriorating significantly below 500 volts. Typically, Ge(Li) and Si(Li) detectors have exhibited sloping performance of these two characteristics with changing bias voltage.

It is clear that the advent of ion-implanted Ge(HP) detectors, free of the problems of drifted lithium and of delicate metallic front contact layers, represents a major advance in the technology, both for the small detectors used in x-ray and electron spectrometry and for large volume Ge γ-ray spectrometers. It is quite likely that the coming years will see a complete phase-out of the lithium-drifted detector.

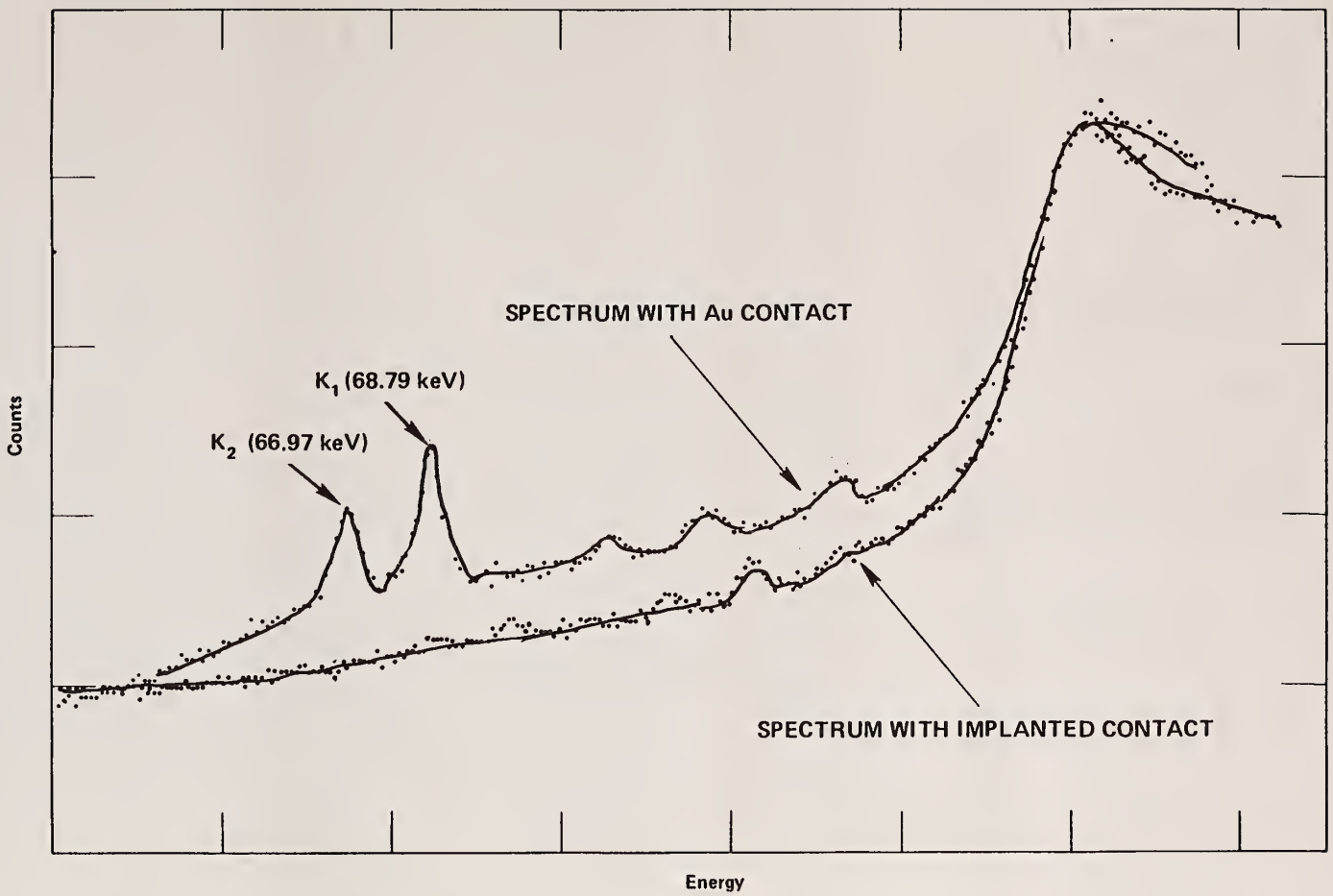

Figure 1. Comparison of the continuum excited by a 57Co source in Ge(HP) detectors with and without

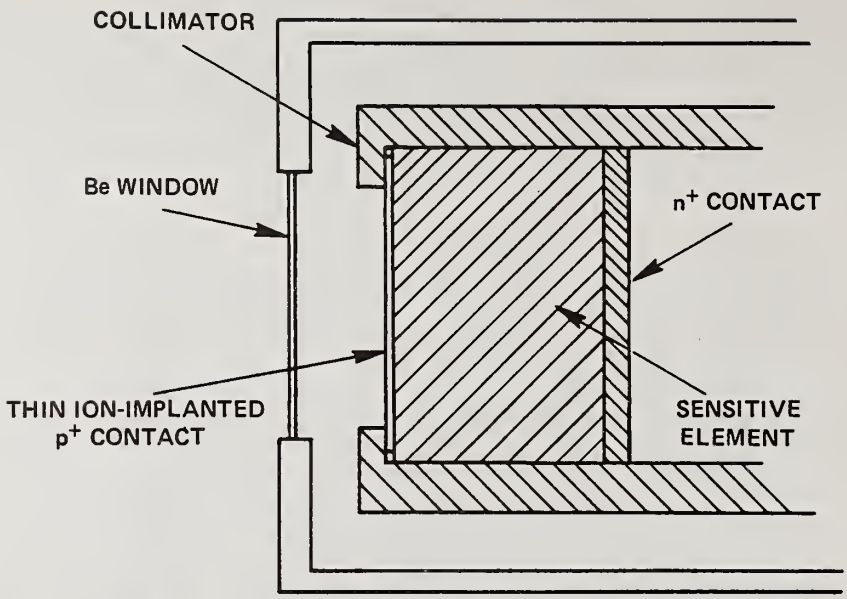

Figure 2. Cross sectional view of the mounting and internal collimator of typical ion-implanted Ge(HP) detectors (courtesy ORTEC, Inc.).

2.3 Measurement of Deadlayers

The presence of metallic and/or semiconductor entrance windows or deadlayers depends on the fabrication techniques used to produce the detector and are very undesirable, because they cause a cutoff of the lowest energy events, degrade the energy resolution, linearity, peak-to-tail ratios, and affect the detector efficiency at low energies. Typical entrance windows of most silicon and germanium detectors consist of 200 Å thick gold (40 μg/cm^2) and a relatively-insensitive "deadlayer" of the order of 0.01 to 0.5 μm in Si [18,19] and 0.1 to 0.3 μm in Ge [20,21]. Even worse, the deadlayer thickness varies with reverse-bias voltage [18]; e.g., the deadlayer of a Si(Li) detector was found to be 0.2 μm at 500 volts. The gold layer has been observed under the electron microscope [3] to have granular structure, with large ragged open regions, and surface roughness with whiskers of gold creating islands and bridges up to 2000 Å in size. Other metals, such as Al, Ni, or Pd, can be used instead of gold for the surface barrier, but it is possible that similar inhomogeneities occur with these as well. That the metallic layer is inhomogeneous in thickness as well as in a real distribution is demonstrated by the fact that carbon K x-rays (277 eV) can be detected, even though a 40 μg/cm^2 thickness of gold should absorb them completely. Owing to the higher Z and density, the deadlayer in Ge is much more serious than one in Si of similar thickness [66].

As pointed out above, the use of boron ion-implantation [22-24] to about 200 Å in depth in N-type material as a replacement for the metallic front surface barrier in Si(HP) and GE(HP) detectors results in deadlayers as thin or thinner than in Si(Li) and Ge(Li) detectors, and of course the fragile metallic layer with its inhomogeneities is eliminated. Another technique of solid-phase regrowth (recrystallization processing [25]) also has been used to construct thin P+ contacts, and a window thickness of about 0.2 μm was found.

Musket [6,26] has used grooved Si(Li) detectors to measure ultra-soft K x-rays of B, C, O, Al, and Lα+β x-rays of Cu (from 185 to 1487 eV). These x-rays were produced essentially free of bremsstrahlung by irradiating these elemental targets with 350 keV protons. The detector efficiency and fraction of the x-ray energy detected for carbon K x-rays (277 eV) all decreased with decreasing bias voltage, and this finding is consistent with an increasing silicon deadlayer as the bias voltage is reduced.

Approximate measurements of deadlayer thickness may be made by comparing the pulse heights obtained from irradiation of the detector surface with alpha-particles at 90° and at, say, 45° incident angles, or by comparing the pulse heights from alpha-particles at normal incidence and from collimated photons. Thicker deadlayers may be estimated purely with photons. However, even with low energy photons, such as 3 keV, the low value of the silicon K-shell fluorescence yield [28] ($\omega_K \approx 0.045$) does not permit convenient measurement of silicon deadlayers thinner than about 10,000 Å (1 μm), whereas typical deadlayers are currently less than 100 Å (0.01 μm) thick [27].

To determine the deadlayer thickness, for example, in Ge detectors a convenient source of γ-ray photons is used with energy above the 11.1 keV K-absorption edge of germanium (or if a gold layer is present, above the 11.92 keV gold L^3-absorption edge). Typically the 14.4 keV γ-ray from ^{57}Co, or Sr K x-rays from an ^{88}Y source, is used to measure deadlayers above about 3000 Å thick in Ge detectors. The deadlayer thickness X_{Ge} is then estimated from the formula

$$X_{Ge} = \frac{2}{\mu_K \omega_K} \left(\frac{C_K}{C_\gamma}\right)\left(\frac{\varepsilon_\gamma}{\varepsilon_K}\right) \qquad (3)$$

where (C_K/C_γ) is the observed ratio of Ge K x-rays and the exciting γ-rays, $(\varepsilon_\gamma/\varepsilon_K)$ is the ratio of intrinsic detector efficiencies for the exciting γ-ray and Ge K x-rays, μ_K is the mean K-shell attenuation coefficient in Ge for the exciting γ-rays, and $\omega_K = 0.55$ for germanium [28].

A new table of mass absorption coefficients for K and L x-rays in low-Z materials (carbon to arsenic) has appeared recently [29] which will be useful for estimating the absorption of x-rays in silicon, germanium, and other low-Z elements. For example, the absorption of 3 keV photons in a uniform 5000 A (0.5 μm) thickness of Ge or Si is 22 percent and 10 percent, respectively. Llacer, et al [66] found that Ge(HP) x-ray detectors have a relatively thick Ge entrance window that renders them practically useless below approximately 2.3 keV, and that this effect is due to a basic property of electron transport near a surface. We have also observed such a low-energy cutoff near 2 keV in our (1979) Ge(HP) detector.

2.4 Detector Mounting and Cryostats

Methods of mounting detectors within vacuum cryostats of various configurations, with and without beryllium windows, have been described in the literature [5-7,10,26]. Figure 2, courtesy of ORTEC, illustrates a typical mounting arrangement of a Ge(HP) detector. One should note that the low-Z collimator may be transparent to photons above a certain energy, e.g., 60 keV or so, so that the effective geometry (solid angle) is larger for higher energy photons than at low energies, and this can affect the shape of the efficiency curve in the energy region where transparency sets in. Very recently a mini-cryostat that is cooled by a miniature Joule-Thompson liquifier inserted into the cryostat and fed by compressed nitrogen gas at pressures above 100 atmos. has been developed [30]. This eliminates the large Dewar vessel and the need for liquid nitrogen. It produces a minimum available temperature of 77° K at the detector (same as liquid nitrogen). The cryostat is used with a Ge(HP) detector and thus can be stored normally at room temperature until used. About 10 min time is required to cool to operating temperature, and a 50 liter commercial tank of N_2 gas supplies the device for about 40 hours. The typical resolution of a 20 mm Ge(HP) detector in this cryostat is reported at several energies to be 221 eV FWHM at 5.9 keV (^{55}Fe), 297 eV at 17.74 keV (^{241}Am), and 544 eV at 122 keV (^{57}Co). Such a miniature x-ray detector can be used as a portable field instrument or on scanning electron microscopes, and it is clear that ion-implanted Si(HP) detectors could as well be used with such a cryostat.

3. Electronic Systems

The contribution of the electronic system noise to line broadening is shown in equation (1), Low-noise, DC-coupled, cooled, field-effect transistor (FET) preamplifiers have been discussed extensively in the literature [5,7,8]. To maintain the high resolution at higher counting rates (up to 20,000 c/sec) the use of pulsed-optical feedback preamplifiers was introduced in 1969 [2-33] and is available commercially in Kevex Corp. detectors. Unfortunately, reset pulses are introduced by this method which are very difficult to eliminate completely in electronic systems designed for x-ray coincidence spectrometry, and in addition, the shorter timing requirements of coincidence circuitry (typically, less than 2 μsec) do not take advantage of the improvement in resolution at higher counting rates produced by the use of pulsed-optical feedback preamplifiers with very long time constants (8 - 17 μsec) [8]. For these reasons, pulsed-optical systems should be avoided in coincidence spectrometry.

An alternate choice is the dynamic charge restoration preamplifier [34-36] which has continuous feedback and produces equivalent resolution with much shorter time constants (e.g., 6 μsec instead of 17 μsec at 10^4 c/sec) and without introducing the reset pulses which trouble coincidence circuitry.

Very recently, a pulsed drain feedback preamplifier has been introduced [37] which can reach 60,000 c/sec with only 10 percent noise degradation and a 4 percent deadtime without use of pulse pileup rejection.

Finally, a new pulse pileup rejection circuit has been reported [38] which gives good resolution performance at ultra-high counting rates (up to 260,000 c/sec) at 5.9 keV; without it, such counting rates completely obliterate the spectral resolution.

Since no two detector-preamplifier systems are identical, it is always necessary to optimize carefully the state-of-the-art main amplifier for such variables as time shaping constant, pole-zero adjustment, low-level threshold setting, and selection of a suitable mode of baseline restoration. It is often overlooked, but the input requirements of the amplitude-to-digital converter (ADC) of the multichannel analyzer may restrict the choice of amplifier time constant which may be used; for example, the use of an output amplifier pulse having a time constant appreciably longer (e.g., 8 μsec) than the length of the normally-closed linear gate input of the ADC (e.g., 2 μsec) results in failure to achieve optimum resolution. Therefore, the time length of the linear gate in the ADC should be adjusted to accommodate the amplifier output pulses, but not so long as to introduce unnecessary deadtime.

Goulding [70] has presented some lesser known but potentially important aspects of x-ray detectors and electronics, including deadlayer effects, time-dependent continuum and excess continuum, noise parameters of field-effect transistors, and time-variant pulse shaping.

4. Spectral Response to Monoenergetic Photons

For incident photon energies below 25 keV for silicon and below 60 keV for germanium, the interaction is primarily photoelectric, the ratio of photoelectric/scattering cross sections being greater than 10. For such low energies, the tailing arises primarily from slow charge collection due to trapping, and this was a serious problem in early detectors [3,5,7,15]. More recently, there have been dramatic improvements in quality for both Si and Ge detectors, and the tailing appears to have been reduced to a value not much larger than predicted by the ratio of photoelectric/Compton cross sections; e.g., the peak/tail counting-rate ratio in Si(Li) exceeds 1500/1 at an energy ratio of 5.9/1 keV; and in our recent ion-implanted Ge(HP) detector, it exceeds 90/1 at 5.9/2 keV.

With incident photons above about 25 keV in Si and above 60 keV in Ge, the ratio of photoelectric/Compton cross sections is less than 10, and thus Compton scattering becomes important and is manifested in two ways: (1) Compton scattering within the sensitive volume of the detector with escape of the scattered photon, and (2) Compton scattering outside of the detector with detection of the scattered photon. The former process appears as a rising tail at very low energies [3] or as a low-energy plateau [27], while the latter

effect appears as a bump or shoulder on the low-energy side of the full-energy peak [3]. The importance of Compton backscattering in giving rise to such a shoulder, or even a spurious "peak" below the full-energy peak in a tightly-collimated geometry [39] should not be overlooked. Calculation of the magnitude of the low-energy plateau from the first process has been published [27].

In addition to the above processes, Si and Ge K x-rays are generated in the detector from the primary interaction of the incident photons of energy above the K-absorption edge at 1.838 and 11.103 keV, respectively. A fraction of these K x-rays will escape the sensitive detector volume, removing 1.74-1.84 and 0.85-11.10 keV of Kα and Kβ energy from Si and Ge detectors, respectively, to give rise to escape peaks located below the full-energy peak by exactly these energies, respectively. These Si and Ge K-escape peaks are very similar in FWHM to the full-energy peak. The magnitude of the escape, expressed either as a ratio R of the escape/main peak heights, or as the fraction of K x-rays which escape the sensitive volume, corrected for the underlying continuum, as a function of incident photon energy, has been carefully studied [3,15,19,27,40,41,67,69]. At the K-edge, for example, the K x-ray escape probability can be as large as 12 percent in Ge and 3 percent in Si detectors, depending on size and configuration. For photons in the energy range 3 - 20 keV in Si detectors, experimental measurement [27] of the escape/main peak height ratio R was fitted by a formula $R = a(E + b)^{-c}$, where E is the incident photon energy in keV, and a, b, and c, are constants. The value of R is about 10^{-2} at 3.5 keV, decreasing with energy to a negligible value at 25 keV for a Si(Li) detector 50 mm^2 x 4 mm deep [27]. It is clear that the effect is much more serious for Ge than for Si detectors for photon energies above the Ge K edge (11.103 keV) and represents a serious complication, especially in multielement x-ray analysis, where the escape peaks can be mistaken for trace elements not really present, or can be hidden under peaks of other elements, the intensities of which have to be suitably corrected. A particular example in which an error could be introduced is in the calibration of detector efficiency with Np M x-rays from an ^{241}Am source. These M x-rays are spread from about 3 to 6.5 keV, but have their main intensity in a broad multiplet centered at 3.3 keV. Unfortunately, in Ge detectors, the Kα and Kβ x-ray escape peaks from the 13.9 keV Lα x-rays in ^{241}Am decay fall into the M x-ray region and must be taken into account in determining the Ge detection efficiency at 3.3 keV. This correction can easily be evaluated [15] by attenuating the M x-rays with a suitable absorber and observing the ratio of the escape/main (Lα) peak.

The low-energy continuum extending from the very low-energy Compton region to the full-energy peak is quite horizontal in both Si and Ge detectors. In a detailed investigation [27] of a Si(Li) detector of dimensions 50 mm^2 x 4 mm, this continuum region declined rapidly from about 1.5×10^{-5} to about 9×10^{-6} of the main peak intensity for photons from 3.5 to 12 keV, and then it increased to about 2×10^{-5} at 50 keV.

Sum peaks and the pulse pileup in the continuum lying above the full-energy peak can become serious problems, since they are dependent not only on counting rate, but also on the presence of more than one incident photon energy. For example, incident monoenergetic photons of two different energies entering the detector simultaneously can add to give three sum peaks, two of which are simple sums of the two incident radiations, and the third is a mixed sum peak caused by addition of two photons of different energies. Complex multipeak spectra can thus exhibit a multiplicity of both simple and mixed sum peaks, and in addition, the superimposed continuum between the peaks can give rise to a summed continuum as well. A detailed analysis of the statistical probability of summing has appeared [27], together with an analysis of the improvements which can be realized with the aid of a pulse pileup rejection circuit. The probability of a pileup pulse is approximately $I\tau$, where I is the rate of incidence of monoenergetic photons per sec and τ is the deadtime of the system. Provided the counting rate I is not so high as to give appreciable three-photon summing, the probability of summing of two incident photons is approximately $I^2\tau$, and relative to the incident counting rate of single pulses, the probability of summing increases linearly with counting rate.

includes the electronic pulse processing time, then varies, typically, from about 1.1 μsec at 2.5 keV to 0.1 μsec at 50 keV [27]. Recently, a spectacular new pulse pileup rejection circuit has been reported [38] which at 5.9 keV gives good resolution at ultrahigh counting rates up to 260,000 c/sec. The remaining sum peaks can be stripped from the spectra in the course of computer analysis of the spectral data [27].

The use of critical x-ray absorbers can also reduce summing of very strong peaks in spectra containing weaker peaks of other energies. For example, the 6.40 keV Kα and 7.06 keV Kβ x-ray peaks of iron, which are of overwhelming intensity in spectra of samples of steels, iron-ores, and whole blood, may be attenuated selectively by critical absorption in a thin foil of chromium, while affecting neighboring x-ray peaks only slightly.

5. Methods of Energy and Efficiency Calibration

5.1 Energy Calibration

The accuracy of energy determinations based on interpolation or extrapolation from peaks of accurately known energies depends on the overall system linearity and gain stability. An excellent discussion of this is given for larger volume germanium detectors used in γ-ray spectrometry [42], and similar principles apply as well to detectors used in the low-energy region below 140 keV. Experimentally determined non-linearities can be incorporated into computer programs (such as PEAKFIND, GAUSS, SAMPO, etc.) which search, locate, and fit peaks in a spectrum to determine their energies and intensities [43]. The correction for non-linearity is measured with radioactive sources of accurately known energy, such as those listed in Table 1. The computer program can then correct each peak position for non-linearity. This correction is of course more important in the analysis of low-energy γ-rays, because the latter are known from crystal spectrometry far more accurately than is required for identification in a semiconductor spectrum, since non-linearities of modern systems are too small to shift x-ray energies by amounts that would cause them to be mis-identified and assigned to the wrong element.

The linearity of Si(Li) and Ge(Li) detectors for low-energy photons has been studied in the range of 5 to 120 keV [44,45] and deviations below ±0.2 percent were found, the largest being at the lowest energies where the cause is ascribed to inefficient charge collection in the gold and detector deadlayers. With Si(Li) detectors having very thin deadlayers, better than 1 percent linearity was observed in the 500 eV to 2 keV region [18], and with a 30 mm^2 grooved Si(Li) detector [8] and using collimated beams of very low-energy x-rays excited by 350 keV protons [26] the linearity was found to be better than 1 percent in the region of carbon K to Al K x-rays (277 eV to 1.5 keV). The linearity of non-ion-implanted Ge(HP) gold surface-barrier detectors has been studied [54] and a maximum deviation of ±0.2 percent was found in the energy range 6.4 to 122 keV, and no abrupt change across the Ge K-edge at 11.1 keV was found, contrary to a previous report [44]. Equal or superior linearity should be exhibited by the new ion-implanted Ge(HP) and Si(HP) x-ray detectors at low energies, owing to the absence of a metallic front contact layer and deadlayers as thin or thinner as those of older types of detectors, but there are no published studies reported so far.

5.2 Efficiency Calibrations

Experience has shown that no two semiconductor detectors exhibit exactly the same spectral response or efficiency, even though they may have identical nominal specifications as to active area, depth, resolution, and peak-to-continuum ratio. A theoretical model [15] can, however, describe the detection efficiency with an accuracy comparable to that of the experimental measurements in the region from 5 - 60 keV, provided that all of the parameters are carefully measured for each detector (e.g., source-to-detector distance; thicknesses of the Be window, gold contact layer, if any, deadlayer, and sensitive depth; determination of the sensitive area and collimation, if any, by photon scanning [15,52]; and charge collection efficiency. The theoretical calculation [15], once these detector parameters are determined, requires a knowledge of the photoelectric and Compton absorption and attenuation coefficients [29] as a function of photon energy for the absorbing media between the source and detector sensitive volume, as well as the escape peak probability vs. photon energy.

The full-energy peak detection efficiency ε_E for photons of energy E can be written as

$$\varepsilon_E = \varepsilon_R \, G_{(E)} \tag{4}$$

where $G_{(E)}$ is the fraction of the 4π solid angle subtended ($\Omega/4\pi$) by a plane parallel to the detector surface and located at a mean interaction depth $Z_{(E)}$ for photons of energy E. The relative detector efficiency ε_R is the product of the intrinsic detector efficiency ε_a and several correction factors

$$\varepsilon_R = \varepsilon_a \, f_a \, f_{Au} \, f_d \, f_e \, f_c \varepsilon_s \tag{5}$$

where f_a, f_{Au}, and f_d correct for the attenuation in materials in front of the sensitive volume, such as air and Be window, gold layer if present, and the deadlayer, respectively; f_e and f_c correct for the escape of Ge (or Si) K x-rays from the sensitive volume and for the effects of collimation, if any, respectively; and ε_s is the efficiency of charge collection for the full-energy peak. The details of evaluating these factors are given in reference 15. The results of scanning the detector with highly collimated photon beams, in order to probe the sensitive area and depth, are reported [10,15,19,41,52]; again, the efficacy of guard rings [10] in minimizing the dependence of the sensitive volume on photon energy should be noted. The evaluation of deadlayer thickness and uniformity has been discussed above (section 2.3) and the problem of escaping Ge (or Si) K x-rays is treated in section 4.0 above.

An alternate, and much easier, procedure is to fit an analytical expression to the experimentally measured efficiency points [19,46,47], in order to facilitate interpolation without graph-reading error. This method depends entirely on the absolute calibration of the radioactive standard sources and does not offer a check based on calculations from the theoretical model.

Experimental calibration of detection efficiency with radioactive sources has been extensively discussed [3,15,19-21,41,45-50]. Recently, however, Campbell, et al. [46] demonstrated that the use of the usual drop-evaporated standard radioactive sources in the energy region 5 to 40 keV can result in values of efficiency points from sources of ^{54}Mn, ^{57}Co, ^{65}Zn, and ^{241}Am that are low by amounts varying from 3 to 16 percent, when compared with vacuum-evaporated sources. This is a very serious situation when one is attempting to establish an efficiency curve to 1 - 2 percent. Unfortunately, the metrology laboratories which supply absolutely calibrated low-energy photon sources normally do not offer vacuum-evaporated sources, but in view of this finding, they should.

The accuracy which can be reached with this method, using vacuum-evaporated standardized radioactive sources, can reach about 1 percent from 6.4 to 18 keV, increasing to about 2 percent at 30 keV in Si(Li) detectors [46]; with drop-evaporated sources, checked by calculations of a theoretical model, accuracies of about three percent in the region five to 60 keV were obtained [15], and at higher energies, the accuracy decreases to as low as seven percent.

In addition to errors caused by self-absorption in crystallites in drop-evaporated sources described above [46,47], there are two other principal causes of error in efficiency determinations with radioactive sources. The rather long amplifier time-constant used to achieve the best energy resolution gives rise to pulse pileup at higher counting rates, and correction for the deadtime is required. This means that the efficiency calibration for the detector should be performed at the same counting rate that the detector will observe in experiments for which the calibration is being done; otherwise, the errors involved in determining an accurate deadtime correction will enter. The second cause of error is produced by small variations in source position, not only in distance from the detector, but also in lateral deviation from the axial center [65]. The latter may be caused by poor centering of the detector itself inside the vacuum shield. A 5 percent error in a 2 cm source-to-detector distance for a 20 mm dia x 3 thick detector causes an

efficiency shift by about 8 percent [5], and a 2 mm shift off-center causes a 1.5 percent drop in efficiency at the same distance. The longer the source-to-detector distance, the smaller are these kinds of errors.

Table 1 gives a compilation of long-lived radioactive nuclides suitable for energy and efficiency calibration of low-energy photon detectors. Only a few nuclides from this long list are presently available as absolutely calibrated photon emission standards in the x-ray region from the National Bureau of Standards [51], the Physikalisch-Technische Bundesanstalt, Braunschweig, West Germany, or the Laboratoire de Métrologie des Rayonnements Ionisants, Gif-sur-Yvette, France, but is is likely that more will become available in the future.

Changes in detector response characteristics (resolution, peak/tail ratio) and in the efficiency have been observed to occur with age [15,53]. Rather substantial efficiency changes in Si(Li) detectors (up to 20 percent increase) were observed on recycling to 77 °K after warmup to room temperature, and slowly decreasing efficiency with time for Ge(Li) detectors [15] and Si(Li) detectors [47] is regularly found. The ion-implanted Ge(HP) and Si(HP) detectors in principle should have constant efficiency at constant bias-voltage, but no long-term observations have so far been reported. We have noted that a Ge(HP) gold surface-barrier detector purchased in 1970 exhibited a decline in efficiency with age, because of the lower and lower bias voltage that could be imposed due to the increasing leakage current with age. Thus, it is clear that the need to repeat the efficiency calibration exists in long experiments, and one should routinely recalibrate the detectors at regular time intervals.

Typical efficiency curves for Si(Li) and Ge detectors are shown in figures 3 - 5, determined with calibrated radioactive sources.

Campbell, et al. [46] have pointed out that new intensity data around 45 keV are desirable, as are better values of the x-ray/γ-ray intensity ratios in the 20 - 25 keV region. From Table 1 it can be seen that the radioactive nuclides ^{145}Pm, ^{109}Cd, ^{113}Sn, and ^{119m}Sn would be suitable sources for these energy regions, should they be made available from the meteorology laboratories as point-source (preferably vacuum-evaporated) absolute photon emission-rate standards.

An accurate method for determining detection efficiency with uncalibrated radioactive sources is based on measurements of K-conversion electrons-K x-ray coincidences [15,55], known as the "CEX" technique. The detection efficiency $\varepsilon_K(E)$ for K x-rays of given energy E is given by

$$\varepsilon_K(E) = \frac{C_{K(e_K)}}{C_{e_K}\,\omega_K\,\varepsilon_c} \qquad (6)$$

where $C_{K(e_K)}$ is the number of coincidence counts of K x-rays gated by K-conversion electrons from the same γ-ray transition, C_{e_K} is the number of counts in the K-conversion electron gate, corrected for underlying continuum and L-conversion electron tailing [15,55], ω_K is the K-shell x-ray fluorescence yield [28] of the K x-rays of energy E, and ε_c is the coincidence efficiency, which should be adjusted to unity by using a sufficiently wide time-gate in the time-to-amplitude (TAC) unit of the coincidence system.

The CEX method has been used with sources of ^{113}Sn (E_γ = 393 keV), ^{137}Cs (662 keV), ^{203}Hg (279 keV), ^{243}Am (277.6 keV transition in ^{239}Pu), and ^{249}Cf (388 keV transition in ^{245}Cm). With either a Si(Li) or Ge detector for K x-rays, depending on energy, and a Si(Li) detector for conversion electrons having energy sufficient to pass through the Be window, a coincidence resolving time of 2τ = 1.0 μsec was sufficient to give a 100 percent coincidence efficiency (ε_c = 1.0) [15]. Since values of ω_K are known [28] to accuracies of 1 to 2 percent, depending on the region of Z involved, the detection efficiency can be

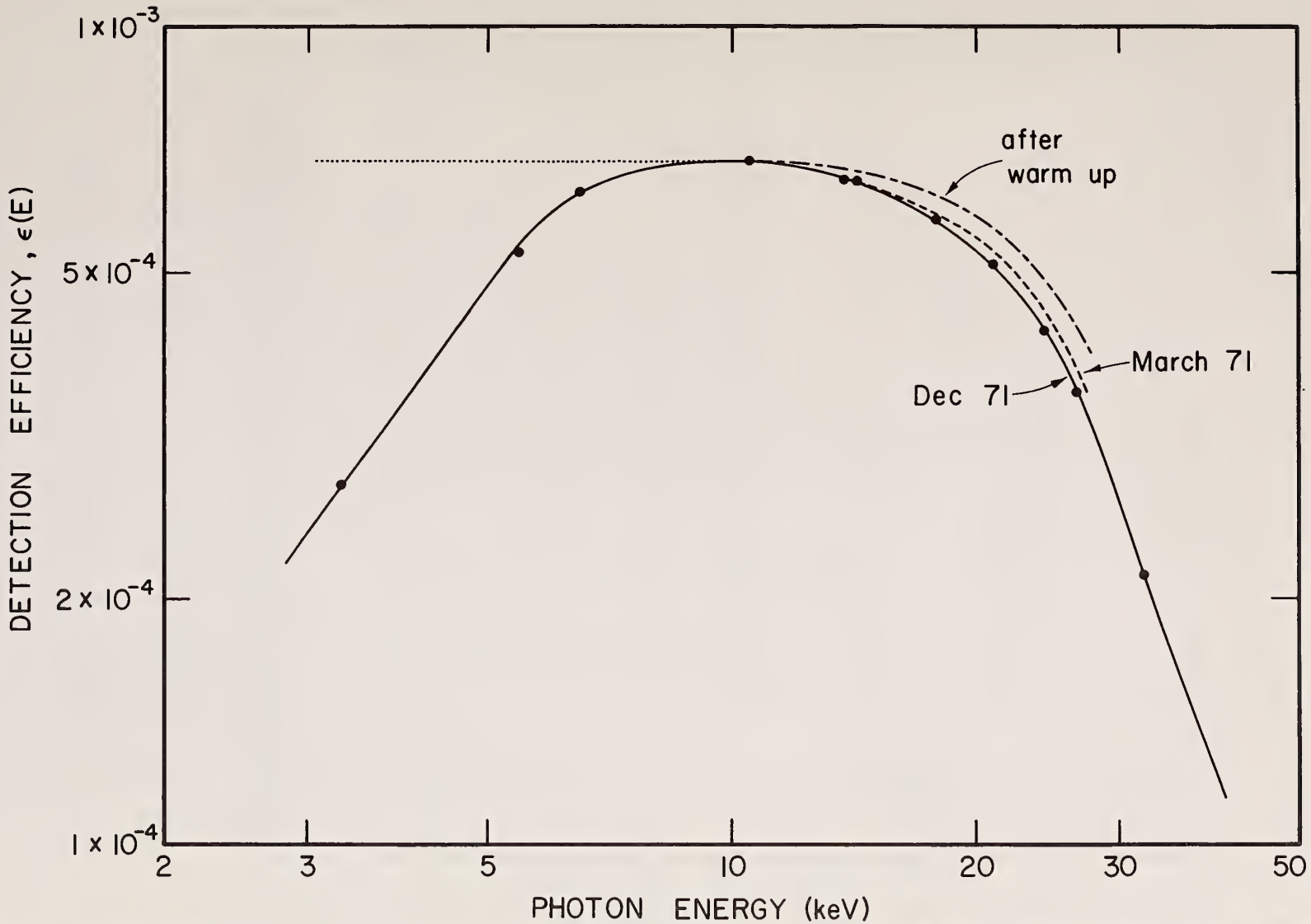

- Figure 3. Experimental detection efficiency on a log-log plot of a Si(Li) detector showing effects of aging and a one-hour warmup. Over a period of 9 months (March-December, 1971) prior to the warmup, the efficiency at 14.4 keV was constant to about 1%, but decreased by about 6% at 26.4 keV. Immediately following the warmup, the full-energy peak efficiency at 26.4 keV increased by 17% and the tailing at 24.2 keV decreased from 36 to 21%, while the efficiency at 14.4 keV remained unchanged within 1%, and no change in resolution was observed (figure and data from ref. 15).

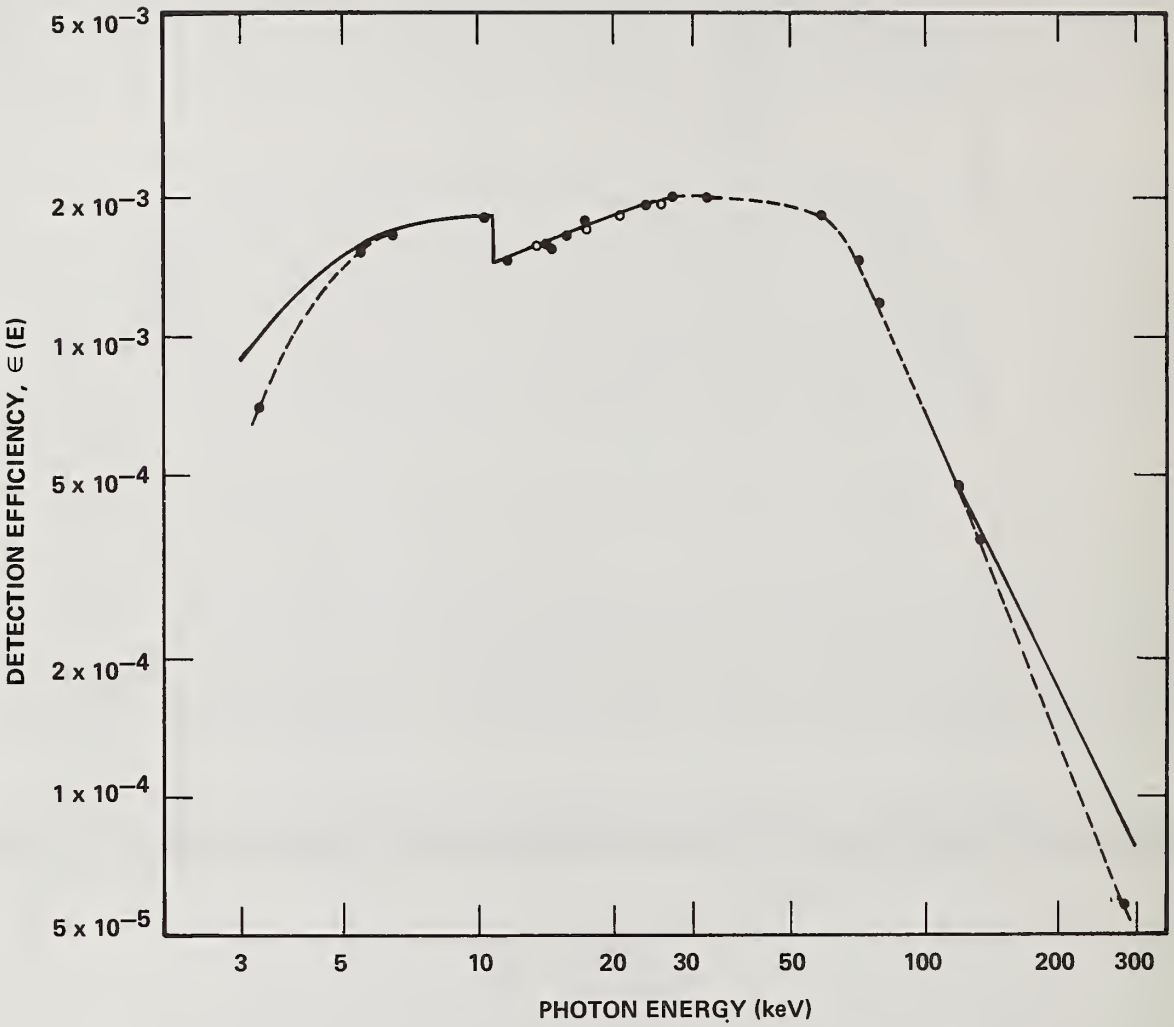

Figure 4. Detection efficiency on a log-log plot of an N-type gold surface-barrier Ge(HP) detector, ca. 1970. The solid line is a prediction from the theoretical model of ref. 15, and the dashed curve is drawn through the experimental points. (Figure from ref. 15.)

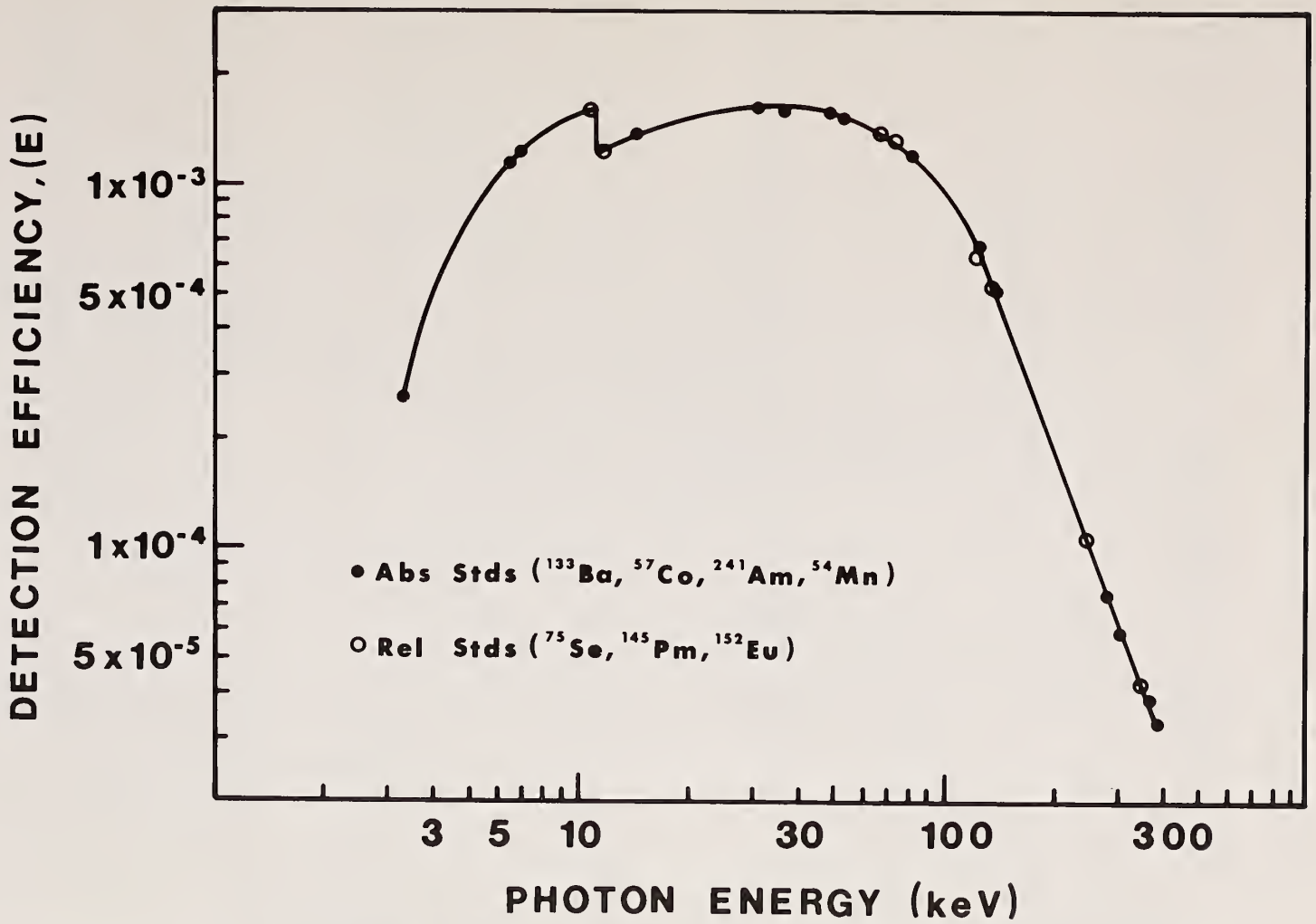

Figure 5. Detection efficiency of a 1979 ion-implanted P-type Ge(HP) detector measured in April, 1979. (Courtesy of B. E. Gnade, School of Chemistry, Georgia Tech.)

determined to about 1.5 to 3 percent accuracy (2σ) [15]. The efficiency found at 32.0 keV in a 50 mm^2 x 3 mm (Ge(Li) detector by the CEX method was 2 percent higher than that from drop-evaporated IAEA calibration standards, and at 24.1 keV, 3.6 percent higher [55]. This seems to confirm the results quoted above [46,47] that efficiencies determined from drop-evaporated radioactive calibration standards are several percent lower than those from vacuum-evaporated sources.

The principal advantages of the CEX technique are that it does not depend on absolute calibration of radioactive sources by someone else, nor is it dependent on knowledge of such radioactive decay parameters as halflife, conversion coefficients, or branching fractions. Moreover, having determined the detection efficiency in this way, the K x-ray singles counting rates from the sources of ^{113}Sn, ^{137}Cs, ^{203}Hg, ^{243}Am, ^{249}Cf, etc. used in the CEX method then give the absolute K x-ray emission rates from these sources, so that they can be used in turn to calibrate other detectors in the singles mode.

Another method for calibrating radioactive sources in the low-energy region, relative to a primary standard source, over a wide range of energies not exceeding about 50 keV, has been reported by Chew, et al. [56]. The source to be calibrated is placed external to the Be window of a large-volume, wall-less multiwire proportional counter, the gas detection efficiency of which can be varied by changing the gas pressure. A maximum occurs in the gas counting efficiency with variation of the pressure. Thus, if the counting rates of low-energy photons from different sources are maximized by changing the pressure, then the detection efficiency of the center counter is the same, and its absolute value depends only on the ratio of the two geometrical distances defining the center- and ring-counters, as shown in figure 6. Because the true effective geometry is not identical with that based on the actual dimensions, this method can be used only relative to a primary standard source and not as an absolute standardization method [56]. With this method, several different sources may be standardized to better than about 3.5 percent (2σ + linear addition of systematic errors) against one or more primary x-ray standards [56].

An accurate determination of the K-edge discontinuity at 11.103 keV in Ge efficiency curves (and at 1.838 keV in Si) is of interest, because the magnitude of this K-jump is strongly dependent both on the deadlayer thickness and on the probability of K x-ray escape. Detailed experimental studies of the Ge K-edge discontinuity have appeared [57, 58]. These are based on comparisons of the detected ratios either of $L\alpha/L\beta$ or $K\alpha/K\beta$ x-ray intensities with known theoretical or experimental values from elements with emitted x-ray energies near and above the K-edge, or which straddle it (e.g. $K\alpha$ and $K\beta$ peaks from arsenic). The $L\alpha,\beta$ x-rays may be excited in foils of heavy elements of Ta, W, Ir, Pt, Au, Hg, Tl, Pb, and Bi (covering the energy range 8.088 to 13.021 keV) either by low-energy protons or by an ^{241}Am source, which excites few, if any, K x-rays in these elements [57]. The $K\alpha$ and $K\beta$ x-rays can be excited by an ^{241}Am source in thin samples of Ga, Ge, As, Se, Br, and Rb (covering the region 9.252 to 14.951 keV) [58]. These methods cover the region of the Ge K-edge in fine steps each smaller than 500 eV. A convenient fast way, however, to estimate the depth of the K-jump is with a radioactive source of ^{75}Se, whose $K\alpha$ and $K\beta$ x-rays of arsenic straddle the Ge K-edge [15,21].

The efficiency of Ge(Li) and Si(Li) detectors in the energy range of 1 to 5 keV can be determined by a simple method [59,60] in which an element or a chemical compound, such as $CaCl_2$, is fluorescently excited by ^{55}Fe (e.g. a 100 mCi annular source). From the ratio of Ca and Cl fluorescent K x-ray peak intensities at 3.69 and 2.62 keV, respectively, the deadlayer thickness may be determined [59]. The deadlayer is the major factor in the drop of efficiency in the region below 5 keV, other than the beryllium window. The energy region of 3-4 keV, which usually is calibrated with Np M x-rays from ^{241}Am decay [15], has a high continuum coming from the strong 59.6 keV γ-ray in the decay of ^{241}Am, but fluorescent excitation with ^{55}Fe leaves a clean background all the way down to noise level (<185 eV). Targets of elemental Mg, Al, Si, S, and compounds CaF_2 and KCl have been used for this region [59,60]. The accuracy in this region in the absolute detection efficiency curve is better than about 5 percent.

A convenient and simple method [61] for obtaining the efficiency curve of a Si(Li) (or Ge) detector up to about 50 keV utilizes a comparison of its response with that of a small NaI(Tl) scintillation detector (e.g. 13 mm thick x 38 mm dia) fitted with a 5-mil (0.125 mm) Be window. The intrinsic efficiency of the NaI(Tl) detector is 100 percent

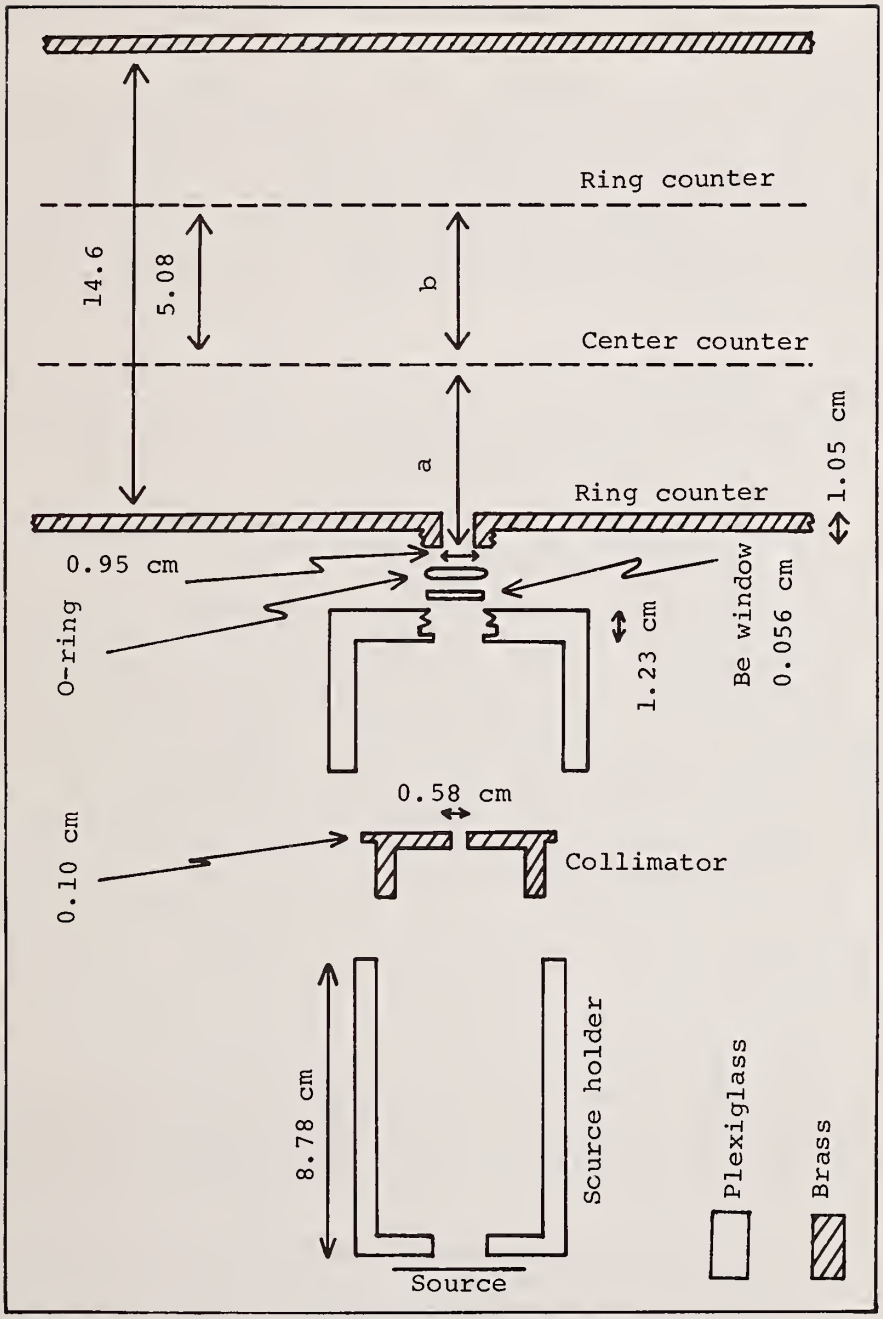

Figure 6. Experimental arrangement for the calibration of radioactive low-energy photon sources, relative to a primary standard source, with a wall-less multiwire gas proportional counter (after Chew et al., ref. 56).

from 60 to 12 keV, below which a correction for attenuation in the Be window is necessary. An ^{241}Am source (100 mCi) is used to excite K x-rays from 6.40 to 48.8 keV in targets ranging from iron to erbium [61]. Since the NaI(Tl) detector does not resolve the Kα and Kβ peaks, a correction must be applied for known Kβ/Kα ratios to obtain the net Kα x-ray intensity for a comparison with that from the semiconductor detector. Also, the iodine K and L x-ray escape peaks must be included in the K-peak intensity from the NaI(Tl) scintillator, although the latter correction is small in the case of L x-ray escape. The overall uncertainty is estimated to ±3 percent from 5 to 30 keV, and increases to a maximum of ±10 percent at 50 keV.

The absolute sensitivity of a ruggedized Si(HP) surface-barrier type detector having a 50 ± 2 μg/cm^2 aluminum front electrode (25 mm^2 active area x 500 μm depletion depth) was investigated in the DC (current) mode in the energy range from 185 to 932 eV [62]. Protons were used to excite K x-rays from boron (185 eV) and carbon (277 eV) and L x-rays from titanium (452 eV), chromium (574 eV), iron (704 eV), and copper (932 eV). These collimated x-rays were intensity-calibrated with a gas proportional counter. A small discontinuity in the sensitivity between 452 and 574 eV was observed, which was tentatively ascribed to oxygen. It would be desirable to have further detailed x-ray studies of ion-implated Si(HP) detectors with depletion layers 3 to 5 mm deep, as these become available commercially.

Finally, a detailed study of the performance of a 50 mm^2 x 4 mm thick Si(Li) detector having a 150 Å gold front contact layer and fitted with a 1-mil (0.025 mm) Be window has been reported by Keith and Loomis [63]. This detector was found by them to have a deadlayer no thicker than 100 A, and to exhibit resolutions of 327 eV FWHM at 5.4 keV, decreasing to 490 eV FWHM at 46 keV, using a relatively short pulse-shaping time constant of one μsec and a deadtime of about 10 percent at 10^4 c/sec. The efficiency of this detector was calibrated in the range 2.5 to 50 keV with a claimed accuracy of ±0.1 percent (1σ) by comparison with a flow-gas proportional counter in the range 2.6 - 11.2 keV and with a NaI(Tl) scintillation counter in the range 5.9 - 50.4 keV, using monoenergetic x-rays generated by a copper-anode x-ray tube and selected by a crystal monochromator operating in a helium atmosphere. The quoted accuracy of the efficiency values, however, is not realistic. The geometry of the solid angle of the x-ray beam passing through a defined, but not accurately measured, collimator introduces much larger uncertainties than quoted; it must be obtained from accurate physical dimensions and checked with an independently-calibrated radioactive source, the continuum from which also introduces appreciable uncertainties. For example, the use of proportional and NaI(Tl) counters with defined solid angle geometry to calibrate radioactive sources at low energies at the National Bureau of Standards [51] results in an overall accuracy that is of the order of ±1 percent [64] (1σ). Thus, the overall accuracy of the efficiency determination of Keith and Loomis is in fact of the same order of accuracy as other measurements of efficiency reported on the usual basis of 2σ statistical error plus linear addition of systematic error, or a similar method of combining statistical and systematic error, such as the student-t distribution.

6. Considerations in the Choice of Ge or Si Detectors

We have already pointed out that there are strong reasons to prefer ion-implanted high-purity Ge and Si detectors over the lithium-drifted types, and that in the future the lithium-drifted Ge detector, and perhaps even the Si(Li) detector as well, will disappear. As to the choice between Ge and Si detectors, the following considerations should be reviewed.

For photons above 3 keV, the Ge detector has an order-of-magnitude greater peak-to-continuum response than Si, owing to its higher-Z; in addition, because the mean energy to create and electron-hole pair in Si is about 26 percent larger than in Ge, the intrinsic resolution which can be achieved is, in principle, better in Ge detectors. On the other hand, the smaller bandgap in Ge increases the detector noise problems, and this, together with the Ge deadlayer, severely degrades the performance of Ge detectors below 3 keV.

With photons of energies above about 30 keV, however, the efficiency of Si detectors, even with depletion depths as thick as 5 mm, falls off drastically, and the Ge detector becomes the one of choice from 30 to 140 keV. Unfortunately, the presence of such higher energy photons in a Ge detector being used to investigate lower energies not only gives rise to a continuum which rises steeply (e.g. at 45°) with decreasing energy, but also can cause amplifier overload by the largest pulses, whereas a Si detector will have a relatively lower and more horizontal continuum, being as it is much less sensitive to the higher energy photons.

Generally, for photons below about 25 keV, the Si detector clearly is the superior choice, because its thinner and less opaque deadlayer is a major consideration at the very lowest energies (<3 keV). Moreover, in the region above the 11.10 keV Ge K-edge, the Si detector is free of the fairly intense Ge K x-ray escape peaks, which cause spectral complexity, especially when investigating weak peaks, as in the analysis of a mixture of elements, some of which are at trace levels while others are at minor or major concentrations. For this reason, many workers prefer to analyze the L x-rays of heavy elements with Si detectors, in spite of the more complex nature of the L x-ray spectrum and the lower x-ray fluorescence yield [28] of the L-shell compared with the K-shell. The escape peaks from Si detectors are resolved only at very low energies (<2 keV) and are in any case much smaller than those from Ge.

There are cases, however, in which K x-rays or γ-rays need to be detected at energies above about 30 keV, as in the K x-ray – L x-ray coincidence experiments indicated in the following section, and for these, the use of a Ge detector is indicated.

7. Coincidence Spectrometry

The requirements of a long amplifier pulse-shaping time constant ($\geq$8 μsec) for the best detector resolution and of a short logic gate-width ($\approx$2 μsec) in the coincidence circuitry requires a compromise; namely, in order to achieve the maximum ratio of true/chance coincidences, the ultimate resolution is not utilized because the amplifier time constant is reduced approximately to the same duration as the gate-width. The choice of 2 μsec for this gate-width is determined by a reasonable compromise between having a high ratio of true/chance coincidence events while maintaining a reasonable counting rate, and it also matches the requirement of the ADC units in our Nuclear Data ND-4420 multiparameter analyzer that all input signals (analog and logic) arrive within an interval of 2 μsec, in order to be recognized and stored as coincidence events. In our current coincidence system [68] with a Ge(HP) and a Si(Li) x-ray detectors, the typical coincidence resolving time is 70 to 110 nsec, and the true/chance ratio is typically about 99/1 for singles counting rates of the order of 1200 c/sec. Under these conditions the resolutions of our detectors are approximately 90 percent of their ultimate capabilities.

In experiments involving x-ray coincidences with semiconductor detectors, it is frequently necessary to resolve an x-ray multiplet, such as the $K\alpha_1$ and $K\alpha_2$ doublet, in partly-resolved spectra. Previously, the singles shape of a calibration γ-ray in the same energy region has been normalized to the higher energy member of the multiplet, e.g., the $K\alpha_1$ peak, in order to subtract its tail contribution from the lower energy members, e.g., the $K\alpha_2$ peak. However, in recent work from our laboratory [68], it was observed that the low-energy tail of a photon line in a singles spectrum is somewhat broader than it is in a coincidence spectrum; and even more importantly, in a coincidence gate set, for example, on a $K\alpha_2$ peak, the $K\alpha_2$ events originate from the $K\alpha_2$ peak, whereas the $K\alpha_1$ events arise from the tail of the $K\alpha_1$ peak. Since the tail contains a larger proportion of slow-rising pulses [3] than the full-energy peak, this implies that the tailing correction depends on the coincidence timing. Therefore, we developed a new method [68] for the evaluation of the net intensity of each component of a partially-resolved multiplet in a low-energy coincidence spectrum. The method requires only that all members of the multiplet have the same peak shape which need not be known and does not require any additional measurements other than the coincidence runs and is independent of timing problems.

The author thanks Dr. R. A. Braga, of the School of Chemistry, Georgia Tech, for making available the results of his measurements on the performance characteristics of the new (1979) Ge(HP) ORTEC x-ray detector and of the somewhat older Kevex Si(li) x-ray detectors used in coincidence x-ray studies, as well for helpful discussions. He also thanks Mr. Rex Trammell of ORTEC, Inc., Dr. R. G. Musket of Kevex Corp., and Nuclear Semiconductor Corp. for technical information on their latest detectors.

References

[1] The first high resolution silicon x-ray spectrometer was reported by E. Elad and M. Nakamura, Nucl. Instr. Meth. 41, 161 (1966) with subsequent improvements in resolution and performance reported by J. M. Jaklevic and F. S. Goulding, IEEE Trans. Nucl. Sci. NS-18, 187 (1971).

[2] Muggleton, A. H. F., Nucl. Instr. Meth. 101, 113 (1972).

[3] Freund, H. U., Hansen, J. S., Karttunen, E., and Fink, R. W., proceedings of the 1969 conference, Radioactivity in Nuclear Spectroscopy, Vol. 2, (Hamilton, J. H. and Manthuruthil, J. C., eds.) Gordon & Breach Science Publishers, New York, 1972, pp. 623-649.

[4] Woldseth, R., X-ray Energy Spectrometry (Kevex Corp., 1973).

[5] Bertolini, G. and Restelli, G., in Atomic Inner-Shell Processes, Vol. 2, (Crasemann, B., ed.) Academic Press, Inc., New York, 1975, pp. 123-167.

[6] Musket, R. G., This Volume (1980), pp. 97-126.

[7] A comprehensive review of fabrication techniques and basic properties of Si and Ge crystals, etc. is contained in Proc. 2nd Symposium on Semiconductor Detectors for Nuclear Radiation (Siegbahn, K., ed.) Nucl. Instr. Meth., 101, North-Holland Publishing Co., Amsterdam, 1972, specific papers in this volume of interest in this review are cited separately.

[8] Landis, D. A., Goulding, F. S., and Jarrett, B. V., Nucl. Instr. Meth. 101, 127 1972).

[9] Trammell, R. C., IEEE Trans. Nucl. Sci. NS-25, 910 (1978).

[10] Jaklevic, J. M. and Goulding, F. S., IEEE Trans. Nucl. Sci. NS-19, 384 (1972).

[11] Fox, R. J. and Borkowski, C. J., IEEE Trans. Nucl. Sci. NS-9, 213 (1962) and Rev. Sci. Instr. 33, 757 (1962); Meyer, O. and Langmann, H. J., Nucl. Instr. Meth. 39, 119 (1966).

[12] Tavendale, A. J., private comm. (quoted in reference 5).

[13] Pehl, R. M., Cordi, R. C., and Goulding, F. S., IEEE Trans. Nucl. Sci. NS-19, 265 (1972).

[14] Bertolini, G., Cappellani, F., and Restelli, G., Nucl. Instr. Meth. 112, 219 (1973).

[15] Hansen, J. S., McGeorge, J. C., Nix, D., Schmidt-Ott, W. D., Unus, I., and Fink, R. W., Nucl. Instr. Meth. 106, 365 (1973); 112, 239 (1973).

[16] Wagner, S., Trammell, R., and Walter, F. J., Proc. Scintillation and Semiconductor Symposium, Washington, D. C. (March, 1972), pp. 1-4.

[17] Cappellani, F., Ostidich, A., and Restelli, G., Nucl. Instr. Meth. 79, 170 (1970).

[18] Jaklevic, J. M. and Goulding, F. S., IEEE Trans. Nucl, Sci. NS-18, 187 (1971).

[19] Wood, R. E., Rao, P. V., Puckett, O. H., and Palms, J. M., Nucl. Instr. Meth. 94, 245 (1971).

[20] Campbell, J. L., Goble, R. J., and Smith, H. J., Nucl. Instr. Meth. 82, 183 (1970).

[21] Forcinal, G., Nucl. Instr. Meth. 107, 125 (1973).

[22] Baertsch, R. D., IEEE Trans. Nucl. Sci. NS-18, 166 (1971).

[23] Herzer, H. S., Kalbitzer, S., Ponpon, J., Stuck, R., and Siffert, P., Nucl. Instr. Meth. 101, 31 (1972).

[24] Trammell, R., ORTEC, Inc. (1978).

[25] Ottaviani, G., Marrello, V., Mayer, J. W., Nicolet, M. A., and Caywood, J. M., Appl. Phys. Lett. 20, 323 (1972).

[26] Musket, R. G. and Bauer, W., Nucl. Instr. Meth. 117, 385 (1974); 109, 449 (1973); 109, 593 (1973).

[27] Keith, H. D. and Loomis, T. C., X-ray Spectrom., 5, 93 (1976).

[28] Bambynek, W., Crasemann, B., Fink, R. W., Freund, H. U., Mark, H., Swift, C. D., Price, R. E., and Rao, P. V., Rev. Modern Phys. 44, 716 (1972).

[29] Montenegro, E. C., Baptista, G. B., and Duarte, P. W. E. P., Atomic-Nuclear Data Tables 22, No. 2, 131 (1978).

[30] Alberti, G., Clerici, R., and Zambra, Z., Nucl. Instr. Meth. 158, 425 (1979).

[31] Kandiah, K. and Stirling, A., in Semiconductor Nuclear Particle Detectors and Circuits (National Academy of Sciences-National Research Council, 1969), p. 495.

[32] Landis, D. A., Goulding, F. S., and Jaklevic, J. M., Nucl. Instr. Meth. 87, 211 (1970).

[33] Landis, D. A., Goulding, F. S., Pehl, R. H., and Walton, J. I., IEEE Trans. Nucl. Sci. NS-18, 115 (1971).

[34] Gedke, D. A., Elad, E., and Dyer, G. R., in Proc. 6th Int. Conf. on Electron Microprobe Anal. (Electron Probe Anal. Soc., New York, 1971), p. 5a.

[35] Gedke, D. A., Elad, E., in Proc. 6th Int. Conf. Opt. Microanal. (Univ. of Tokyo Press, 1972), p. 253.

[36] Gedke, D. A., X-ray Spectrom. 1, 129 (1972).

[37] Bussolati, C., Manfredi, P. F., Maroli, D., and Krakowski, R., Nucl. Instr. Meth. 156, 553 (1978).

[38] Goulding, F. S. and Landis, D. A., IEEE Trans. Nucl. Sci. NS-25, 895 (1978).

[39] Fink, R. W. and Robinson, B. L., Rev. Sci. Instr. 27, 712 (1956).

[40] Pehl, R. M., Cordi, R. C., and Goulding, F. S., IEEE Trans. Nucl. Sci. NS-19, 265 (1972).

[41] Campbell, J. L. and McNelles, L. A., Nucl. Instr. Meth. 101, 153 (1972); 98, 433 (1972); 125, 205 (1975).

[42] Helmer, R. G. , Cline, J. E., and Greenwood, R. C., in The Electromagnetic Interaction in Nuclear Spectroscopy, (Hamilton, W. D., ed.) North-Holland Publishing Co., Amsterdam, 1975, p. 775.

[43] Greenwood, R. C., Helmer, R. G., and Gehke, R. J., Nucl. Instr. Meth. 77, 141 (1970).

[44] Zullinger, H. R. and Aitken, D. W., IEEE Trans. Nucl. Sci. NS-14, 563 (1967); NS-15, 466 (1968); NS-16 47 (1969).

[45] Palms, J. M., Rao, P. V., and Wood, R. E., IEEE Trans. Nucl. Sci. NS-16, 36 (1969).

[46] Campbell, J. L., Jorch, H. H., and Thompson, J. A., Nucl. Instr. Meth. 140, 167 (1977); 143, 551 (1977).

[47] Gallagher, W. J. and Cipolla, S. J., Nucl. Instr. Meth. 122, 405 (1974); and Cipolla, S. J. and Hewitt, M. J., Nucl. Instr. Meth. 136, 347 (1976).

[48] Notea, A. and Segal, Y., Adv. in X-ray Anal. 14, 92 (1971).

[49] Gehrke, R. J. and Lokken, R. A., Nucl. Instr. Meth. 97, 219 (1971).

[50] Fink, R. W., Nucl. Instr. Meth. 112, 243 (1973).

[51] Hutchinson, J. M. R., Mann, W. B., and Mullen, P. A., "Development of the NBS Low-Energy Photon Emission-Rate Radioactivity Standards," in ERDA Symposium on Low-Energy X-ray and γ-ray Spectrometry (Univ. of Michigan, Ann Arbor, 1976).

[52] Campbell, J. L., Smith, H. J., and MacKenzie, I. K., Nucl. Instr. Meth. 92, 237 (1971).

[53] Slapa, L., Nucl. Instr. Meth. 118, 237 (1974).

[54] Drummond, W. E., IEEE Trans. Nucl. Sci. NS-18, 91 (1971).

[55] Schmidt-Ott, W. D. and Fink, R. W., Z. Physik 249, 286 (1972); and Hansen, J. S., McGeorge, J. C., Fink, R. W., Wood, R. E., Rao, P. V., and Palms, J. M., Z. Physik 249, 373 (1972).

[56] Chew, W. M., McGeorge, J. C., and Fink, R. W., Nucl. Instr. Meth. 106, 499 (1973).

[57] Rosner, B. and Gur, D., Nucl. Instr. Meth. 111, 577 (1973); 116, 171 (1974).

[58] Scott, R. D., Nucl. Instr. Meth. 116, 173 (1974).

[59] Rosner, B., Gur, D., and Shabason, L., Nucl. Instr. Meth. 131, 81 (1975); and Maor, D. and Rosner, B., J. Phys. (London) E11, 1141 (1978).

[60] Habricht, G., Knaf, B., Pressen, G., and Stähler, J., Nucl. Instr. Meth. 144, 359 (1977).

[61] Johnson, G. A., Manson, E. L., Jr., and O'Foghludha, F., Nucl. Instr. Meth. 151, 217 (1978).

[62] Gaines, J. L., Kuckuck, R. W., and Ernst, R. D., Proc. 4th Ann. Conf. on the Use of Small Accelerators (Institute of Electrical & Electronic Engineers, New York, 1976), p. 234; and ERDA Symposium on X- and γ-ray Sources and Appl. (Univ. of Michigan, Ann Arbor, 1976), p. 6.

[63] Keith, H. D. and Loomis, T. C., X-ray Spectrom. 5, 93 (1976); Appl. Spectros. 29, 316 (1975).

[64] Hutchinson, J. M. R., private communication (1976).

[65] Alfassi, Z. B. and Nothman, R., Nucl. Instr. Meth. 143, 57 (1977).

[66] Llacer, J., Haller, E. E., and Cordi, R. C., IEEE Trans. Nucl. Sci. NS-24, 53 (1976).

[67] Dyson, N. A., Nucl. Instr. Meth. 114, 131 (1973).

[68] Gnade, B. E., Braga, R. A., Western, W. R., Wood, J. L., and Fink, R. W., Nucl. Instr. Meth. (in press, 1979).

[69] Reed, S. J. B. and Ware, N. G., J. Phys. (London) E5, 582 (1972) and Statham, P. J., J. Phys. (London) E91023 (1976).

[70] Goulding, F. S., Nucl. Instr. Meth. 142, 213 (1977).

Table 1. Long-lived radioactive ources suitable for energy and efficiency calibration of x-ray detectors.[a]

Nuclide	Halflife	Photon Energy (keV)	Absolute No. of Photons emitted per 100 decays
^{44}Ti	47.3 ± 1.4 y	4.0861 ($K\alpha_2$)	5.8 ± 0.6
		4.0906 ($K\alpha_1$)	11.7 ± 1.1
		4.46 ($K\beta$)	2.26 ± 0.21
		67.85 ± 0.03 (γ)	87.7 ± 1.5
		78.40 ± 0.06 (γ)	94.7 ± 1.5
^{49}V	330 ± 20 d	4.5049 ($K\alpha_2$)	7.36 ± 0.2
		4.5108 ($K\alpha_1$)	14.6 ± 0.3
		5.00 ($K\beta$)	2.60 ± 0.10
^{54}Mn	312.6 ± 0.8 d	5.4055 ($K\alpha_2$)	7.43 ± 0.21
		5.4147 ($K\alpha_1$)	14.7 ± 0.4
		6.00 ($K\beta$)	2.94 ± 0.10
		834.83 ± 0.01 (γ)	99.9760 ± 0.0002
^{55}Fe	2.72 ± 0.03 y	5.88765 ($K\alpha_2$)	8.2 ± 0.7
		5.8975 ($K\alpha_1$)	16.3 ± 0.12
		6.49 ($K\beta$)	3.3 ± 0.3
^{57}Co	271.23 ± 0.63 d	6.3908 ($K\alpha_2$)	16.5 ± 0.5
		6.4038 ($K\alpha_1$)	32.5 ± 0.8
		7.06 ($K\beta$)	6.56 ± 0.20
		14.4147 ± 0.0025 (γ)	9.54 ± 0.13
		122.063 ± 0.003 (γ)	85.59 ± 0.19[b]
		136.476 ± 0.003 (γ)	10.61 ± 0.18
^{65}Zn	244.52 ± 0.07 d	8.0278 ($K\alpha_2$)	11.5 ± 0.3
		8.0478 ($K\alpha_1$)	22.6 ± 0.5
		8.94 ($K\beta$)	4.61 ± 0.13
		1115.52 ± 0.3 (γ)	50.75 ± 0.10

continued

Table 1 continued.

Nuclide	Halflife	Photon Energy (keV)	Absolute No. of Photons Emitted per 100 Decays
^{73}As	80.30 ± 0.6 d	9.8553 ($K\alpha_2$)	30.5 ± 1.6
		9.8864 ($K\alpha_1$)	60 ± 3
		11.0 ($K\beta$)	13.3 ± 0.7
		53.437 ± 0.009 (γ)	10.5 ± 0.3
^{75}Se	120 ± 1 d	10.5080 ($K\alpha_2$)	16.3 ± 1.0
		10.5437 ($K\alpha_1$)	31.7 ± 1.8
		11.79 ($K\beta$)	7.3 ± 0.5
		66.05 ± 0.01 (γ)	1.011 ± 0.024
		96.733 ± 0.002 (γ)	3.20 ± 0.06
		121.115 ± 0.003 (γ)	16.72 ± 0.19
		136.000 ± 0.005 (γ)	56.8 ± 0.7
^{85}Sr	64.68 ± 0.23 d	13.3358 ($K\alpha_2$)	17.1 ± 0.4
		13.3953 ($K\alpha_1$)	33.0 ± 0.7
		15.0 ($K\alpha_1$)	8.67 ± 0.24
		513.990 ± 0.010 (γ)	98.0 ± 1.0
^{88}Y	107.2 ± 0.7 d	14.0979 ($K\alpha_2$)	17.6 ± 0.8
		14.16500 ($K\alpha_1$)	33.9 ± 1.4
		15.9 ($K\beta$)	9.1 ± 0.4
		898.020 ± 0.020 (γ)	93.4 ± 0.7
		1836.040 ± 0.020 (γ)	99.35 ± 0.03
^{109}Cd	453 ± 2 d	2.98 ($L\alpha$), 3.24 ($L\beta$)	11 ± 4
		21.9903 ($K\alpha_2$)	29.1 ± 1.0
		22.1629 ($K\alpha_1$)	55.1 ± 1.8
		25.0 (K_β)	17.8 ± 0.7
		88.037 ± 0.005 (γ)	3.72 ± 0.11

continued

Table 1 continued.

Nuclide	Halflife	Photon Energy (keV)	Absolute No. of Photons Emitted per 100 Decays
^{113}Sn	115.1 ± 0.3 d	3.28 (Lα), 3.6 (Lβ)	6.7 ± 2.3
		24.0020 ($K\alpha_2$)	20.7 ± 0.8
		24.2097 ($K\alpha_1$)	39.0 ± 0.14
		27.67 (Kβ)	13.0 ± 0.5
		255.115 ± 0.015 (γ)	2.12 ± 0.07
^{119m}Sn	293.0 ± 1.3 d	3.44 (Lα), 3.77 (Lβ)	12 ± 4
		23.875 ± 0.101 (γ)	16.2 ± 0.4
		25.0440 ($K\alpha_2$)	7.8 ± 0.4
		25.2713 ($K\alpha_1$)	14.7 ± 0.6
		28.8 (Kβ)	4.96 ± 0.21
^{125}I	60.14 ± 0.11 d	3.77 (Lα), 4.16 (Lβ)	15 ± 6
		27.2017 ($K\alpha_2$)	39.8 ± 1.4
		27.4723 ($K\alpha_1$)	74.2 ± 2.5
		31.3 (Kβ)	25.8 ± 1.0
		35.46 ± 0.03 (γ)	6.67 ± 0.22
^{129}I	(1.97 ± 0.14) x 10^7 y	4.105 (Lα), 4.57 (Lβ)	8.2 ± 2.5
		29.4580 ($K\alpha_2$)	20.0 ± 0.6
		29.7790 ($K\alpha_1$)	37.1 ± 0.9
		34.0 (Kβ)	13.2 ± 0.4
		39.58 ± 0.03 (γ)	7.5 ± 0.20

continued

Table 1 continued.

Nuclide	Halflife	Photon Energy (keV)	Absolute No. of Photons Emitted per 100 Decays	
^{133}Ba	10.74 ± 0.10 y	4.28 (Lα) 4.48 (Lβ)	17	± 5
		30.625 ($K\alpha_2$)	33.4	± 1.1[c]
		30.973 ($K\alpha_1$)	61.7	± 1.8[c]
		35.4 (Kβ)	22.9	± 0.6[c]
		53.155 ± 0.016 (γ)	2.18	± 0.04[c]
		79.621 ± 0.011 (γ)	2.67	± 0.07[c]
		80.997 ± 0.005 (γ)	34.7	± 0.8[c]
^{137}Cs	30.02 ± 0.15 y	4.46 (Lα) 4.99 (Lβ)	1.1	± 0.3
		31.8171 ($K\alpha_2$)	2.11	± 0.07
		32.1936 (α_1)	3.90	± 0.12
		36.4 ($K\beta_1$)	1.13	± 0.10
		37.3 ($K\beta_2$)	0.29	± 0.03
		661.661 ± 0.003 (γ)	85.3	± 0.4
^{139}Ce	137.66 ± 0.05 d	4.64 (Lα) 5.21 (Lβ)	13	± 4
		33.033 ($K\alpha_2$)	23.7	± 0.8
		33.4413 ($K\alpha_1$)	43.7	± 1.4
		37.80 ($K\beta_1$) 38.73 ($K\beta_2$)	16.0	± 0.6
^{145}Pm	17.7 ± 0.4 y	0.98 (M)	--	
		5.22 (Lα) 5.9 (Lβ)	14.4	± 2.0
		36.8474 ($K\alpha_2$)	21.1	± 0.7
		37.3610 ($K\alpha_1$)	38.6	± 1.2
		42.269 ($K\beta_1$) 43.298 ($K\beta_2$)	14.7	± 0.5
		67.20 ± 0.10 (γ)	0.65	± 0.03
		72.40 ± 0.10 (γ)	2.18	± 0.15

continued

Table 1. continued.

Nuclide	Halflife	Photon Energy (keV)	Absolute No. of Photons Emitted per 100 Decays
^{181}W	120.95 ± 0.02 d	1.71 ($M\alpha_1$)	--
		1.77 ($M\beta$)	--
		6.21 ± 0.03 (γ)	0.97 ± 0.22
		8.12 ($L\alpha$) 9.5 ($L\beta$)	22 ± 3
		56.2770 ($K\alpha_2$)	19.0 ± 2.0
		57.5320 ($K\alpha_1$)	33 ± 4
		65.210 ($K\beta_1$) 66.999 ($K\beta_2$)	14.0 ± 1.5
^{203}Hg	46.59 ± 0.5 d (note d)	2.71 ($M\alpha_1$)	--
		2.362 ($M\beta_2$)	--
		10.22 ($L\alpha$) 12.24 ($L\beta$)	5.9 ± 0.7
		70.8319 ($K\alpha_2$)	3.73 ± 0.12
		72.8715 ($K\alpha_1$)	6.32 ± 0.19
		82.558 ($K\beta_1$)	2.1 ± 0.1
		84.904 ($K\beta_2$)	0.63 ± 0.05
		279.188 ± 0.006 (γ)	81.55 ± 0.80
^{207}Bi	33.4 ± 0.8 y	2.346 ($M\alpha_1$)	--
		2.443 ($M\beta_2$)	--
		10.5 ($L\alpha$) 12.62 ($L\beta$) 14.76 ($L\gamma_1$)	. . . 35.0 ± 2.0 $L\ell:L\alpha:L\beta:L\gamma$ = 5.5:43.5:42.4:8.6
		72.8042 ($K\alpha_2$)	22.8 ± 0.5
		74.9694 ($K\alpha_1$)	38.6 ± 0.7
		84.922 ($K\beta_2$) 87.343 ($K\beta_2$)	17.1 ± 0.4
		569.670 ± 0.020 (γ)	97.8 ± 0.5
		1063.620 ± 0.020 (γ)	74 ± 3
		1442 ± 10 (γ)	0.147 ± 0.020
		1770.22 ± 0.04 (γ)	7.3 ± 0.4

continued

Table 1. continued.

Nuclide	Halflife	Photon Energy (keV)	Absolute No. of Photons Emitted per 100 Decays
^{241}Am	431 ± 4 y	3.30 (Mα)[e]	6.35 ± 0.60[f]
		13.945 ($L\alpha_1$) / 13.758 ($L\alpha_2$)	13.3 ± 0.4
		16.837 ($L\beta_2$) / 17.740 ($L\beta_1$)	19.3 ± 0.7
		20.77 ($L\gamma_1$)	4.93 ± 0.21
		59.536 ± 0.001 (γ)	35.5 ± 0.3

[a]The data represent current "best values" assembled from the following sources:

Martin, M. J., Nuclear Decay Data for Selected Radionuclides (Nuclear Data Project), Oak Ridge National Laboratory Report ORNL-5114 (1976).

Nuclear Data Sheets, current issues (Academic Press, Inc., New York).

Lederer, C. M. and Shirley, V. S., Table of Isotopes, 7th Edition (Wiley-Interscience, Inc., New York, 1978).

Fink, R. W., current isotope files, based on current literature.

[b]Calculated using data from Freund, H. U. and McGeorge, J. C., Z. Physik, 238, 6 (1970).

[c]Values are those from the Physikalisch-Technische Bundesanstalt, Braunschweig, West Germany, from which absolutely calibrated sources of ^{133}Ba may be purchased.

[d]Some chemical or photochemical instability with age of ^{203}Hg sources has been observed. Owing to this and the relatively shorter halflife, the use of ^{203}Hg sources as absolute calibration standards is not especially recommended.

[e]M x-rays from ^{241}Am decay are spread over a range of about 3 to 6.5 keV. Special caution should be exercised with Ge detectors, since the Kα and Kβ x-ray escape peaks from the 13.945 keV Lα x-ray fall in the region 2.65 to 6.64 keV which is within the M x-ray region.

[f]Value from Karttunen, E. I., Freund, H. U., and Fink, R. W., Phys. Rev. A4, 1695 (1971).

Remarks concerning Table 1.

Not all of the sources listed in Table 1 are available commercially, and only a few of them at present can be obtained as absolutely calibrated photon emission standards from the National Bureau of Standards, the Physikalisch-Technische Bundesanstalt of Braunschweig, West Germany, or the Laboratoire de Métrologie des Rayonnements Ionisants, Gif-sur-Yvette, France. Some additional calibrated low-energy photon emission sources may become available from these metrology laboratories in the future.

Other long-lived radioactive nuclides which could become suitable standards for energy and efficiency calibration of x-ray intensities are 391.1 ± 1.2 d ^{235}Np (which exhibits approximately 2.95 K x-rays per 100 EC decays and 49 L x-rays per 100 EC decays [1], (1.03 ± 0.04) x 10^5 y ^{41}Ca, 1 x 10^5 y ^{59}Ni [2], ion-implanted 2.1 x 10^5 y ^{81g}Kr [3], 16.4 ± 0.4 y ^{93m}Nb, 3000 y ^{93g}Mo, 3.0 ± 0.4 y ^{101g}Rh, 90 y ^{151}Sm, 234 d ^{153}Gd, 144 d ^{159}Dy [4], 33 y ^{163g}Ho, which might be suitable as a very low energy calibration standard, since it emits essentially only 1.3 keV M x-rays, 588 ± 10 d ^{179}Ta, 115 d ^{182}Ta, which is a good relative photon intensity standard for γ-rays from 84.68 to 264.1 keV, but which needs absolute K and L x-ray photon emission intensity measurements, and 50 y ^{193g}Pt, which emits only M and L x-rays at 2.0 and 9.1 – 10.8 keV, respectively. The calibration and use of 7370 y ^{243}Am [5] and of 350.6 ± 2.1 y ^{249}Cf [6] for x-rays and γ-rays might be useful for some laboratories.

---

[1] McGeorge, J. C., Nix, D. W., Fink, R. W., and Landrum, J. H., Z. Physik, 255, 335 (1972).

[2] Chew, W. M., Xenoulis, A. C., and Fink, R. W., Nucl. Phys. A218, 372 (1974).

[3] Chew, W. M., Xenoulis, A. C., Fink, R. W., Schima, F. I., and Mann, W. B., Nucl. Phys. A229, 79 (1974).

[4] Rao, P. V., Z. Physik, A260, 47 (1973); McGeorge, J. C., Freund, H. U., and Fink, R. W., Nucl. Phys., A154, 526 (1970).

[5] Pate, J. C., Baker, K. R., Fink, R. W., McClure, D. A., and Kendrick, Jr., N. S., Z. Physik, A272, 169 (1975).

[6] Schmidt-Ott, W. D., Fink, R. W., and Rao, P. B., Z. Physik, 245, 191 (1971).

National Bureau of Standards Special Publication 604. Proceedings of the Workshop on Energy Dispersive X-Ray Spectrometry held at NBS, Gaithersburg, Maryland, April 23-25, 1979. (Issued March 1981)

A COMPARISON OF SILICON AND GERMANIUM X-RAY DETECTORS

N. C. Barbi and D. B. Lister

Princeton Gamma-Tech
Princeton, New Jersey 08540

Abstract

In recent years, semiconductor detectors (germanium and silicon) have become widely used in the analysis of x-rays. Si(Li) detectors have been applied predominantly in the analytical range of 1 to 30 keV, while Ge(Li) and intrinsic germanium (IG) detectors have been applied in the analysis of higher energy photons. This devision of detector application with x-ray energy is a consequence of the inherent characteristics of the two materials.

Germanium, due to its lower band gap energy, can theoretically exhibit superior resolution compared to silicon. For example, resolution at 5.9 keV for a commercially available IG detector with an active area of 25 mm^2 would be comparable to a Si(Li) detector with half the active area. However, the resolution advantage in germanium detectors is often countered by other material characteristics, and is therefore not realized throughout the spectrum. In particular, for photon energies less than 3 keV, peaks from the germanium detector exhibit severe tailing, due to incomplete charge collection, rendering the germanium detectors of little use in the analysis of Na through S.

As the photon energy increases from 3 to $\cong$ 20 keV, the IG performance becomes comparable to that of the Si(Li) detector, with the exception of the more complex escape peak effects in germanium. Above $\cong$ 30 keV, the IG detector has the advantage of better detection efficiency than the Si(Li).

The choice of detector for a particular application should be based on resolution and efficiency parameters for the analytical range of interest. A secondary, but practical, consideration is that IG detectors can be stored indefinitely at room temperature without degradation. Practical applications of the IG detector in x-ray analysis will be discussed and a comparison of the detector performance to that of Si(Li) for these applications will be presented.

1. Introduction

In recent years, semiconductor detectors (silicon and germanium) have become widely used in x-ray spectroscopy. Si(Li) detectors have been applied predominantly in the analytical range of 1 to 30 keV, while Ge(Li) and intrinsic germanium (IG) detectors have been applied to the analysis of higher energy photons. This selection of detector type based on x-ray energy is a consequence of the inherent characteristics of the two materials.

An empirical comparison of the performance of IG and Si(Li) detectors in the x-ray region is presented below. Ge(Li) detectors are not explicitly discussed since they have been essentially supplanted by IG detectors for this application, although the general description of the characteristics of IG detectors will also apply to Ge(Li) detectors. Before presenting the results, a brief description of the two main detector parameters, resolution and efficiency, is given in the light of the germanium and silicon comparison.

1.1 Detector Resolution

The resolution of a semiconductor x-ray detector is taken as the measured FWHM of a MnKα peak (emitted from a Fe-55 radioactive source). Modern IG and Si(Li) detectors exhibit comparable resolution on this basis, although germanium has an advantage at medium and high energies due to its lower band-gap energy. At lower x-ray energies (<3 keV), the inherent superior resolution of germanium is completely overcome by a broadening of the low energy side of the peak due to incomplete charge collection. This degradation in peak shape, called tailing, is severe for x-rays in the 1.2 to 2 keV range in germanium detectors.

1.2 Detector Efficiency

The beryllium window through which x-rays must pass to reach the detector in the cryostat is the dominant factor in determining the efficiency of a Si(Li) spectrometer for low energy x-rays. A typical spectrometer may be nearly 100 percent efficient for a CaKα x-ray (3.69 keV), but only 40 percent efficient for a NaKα x-ray (1.04 keV). This loss of efficiency is due primarily to the relatively high absorption of Na x-rays in the beryllium window itself. Although the beryllium window presents an identical problem in germanium detectors, the usefulness of the IG detector in the low energy region is limited first by poor resolution due to incomplete charge collection, as discussed above. Peak tailing severely limits the use of these detectors below 3 keV, where window absorption is just beginning to significantly degrade detector efficiency. A conventional Si(Li) spectrometer, which is generally useful down to 1 keV is therefore superior in performance, from a resolution standpoint, to a Ge detector in this low energy region.

In the high energy region (>30 keV), however, the IG detector is clearly superior. Because germanium is a higher atomic number material than silicon, it is inherently a stronger x-ray absorber. X-rays which might pass right through a silicon crystal may still be absorbed (and, therefore, detected) in germanium.

Figure 1 shows the efficiency for photoelectric absorption of 5 mm thick Si(Li) and germanium detectors, emphasizing the medium and high energy region. The dotted line in the germanium curve represents the loss in efficiency due to the rather significant escape peak interaction for medium energy photons. At ≅30 keV, the efficiency of germanium becomes superior to that of a Si(Li) detector of equal thickness, with its advantage becoming more pronounced as x-ray energy increases beyond that value.

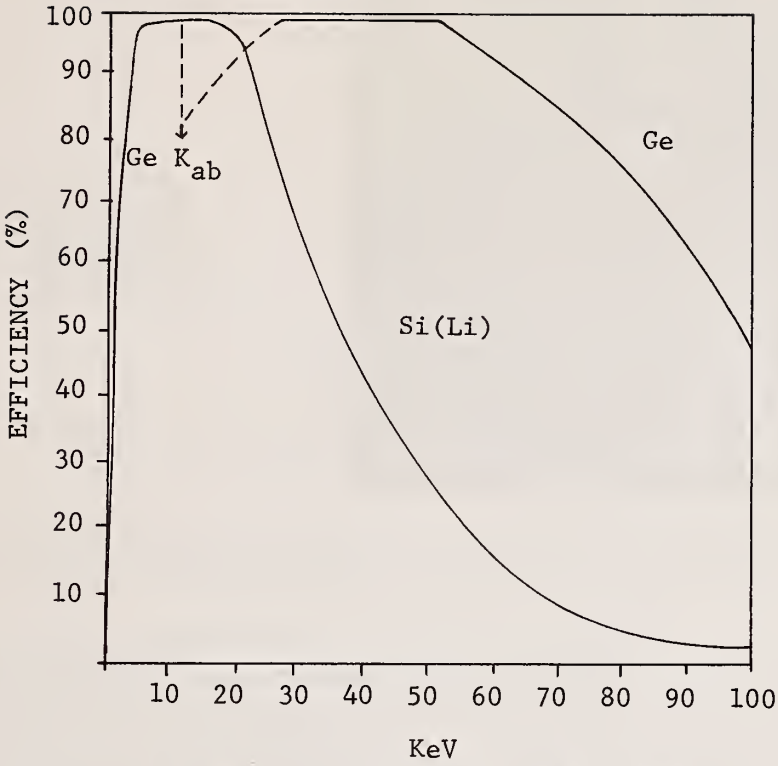

Figure 1. Photoelectric efficiency (5 mm thick detector).

2. Experimental Procedure

For purposes of collecting low energy x-ray spectra, a 5 mm thick IG and a 3 mm thick Si(Li) detector of ≅160 eV resolution were interfaced to a scanning electron microscope. The accelerating voltage was either 28 or 18 kV, as noted on the individual spectra.

To compare high energy performance, 5 mm thick detectors were used to analyze radiation emitted from, or fluoresced by, radioactive sources.

3. Results

3.1 Low Energy Performance

Figure 2 shows a comparison of the two detectors used for low energy spectra at MnKα. Note that tailing is already becoming apparent in the spectrum (in dots) collected using the germanium detector.

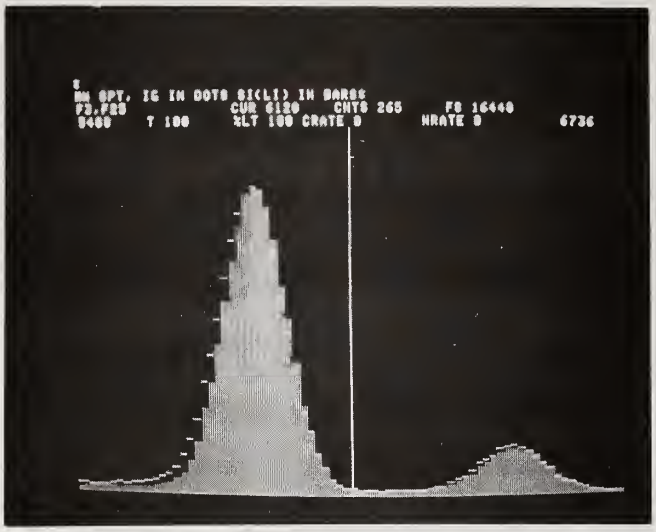

Figure 2. MnKα (5.9 keV) and Kβ (6.3 keV) collected using the IG detector (dots) and Si(Li) detector (bars) interfaced to the SEM for this study.

Figure 3 illustrates a stainless steel spectrum acquired at 18 keV using the IG detector. Its appearance is essentially identical to that expected from a Si(Li) spectrometer.

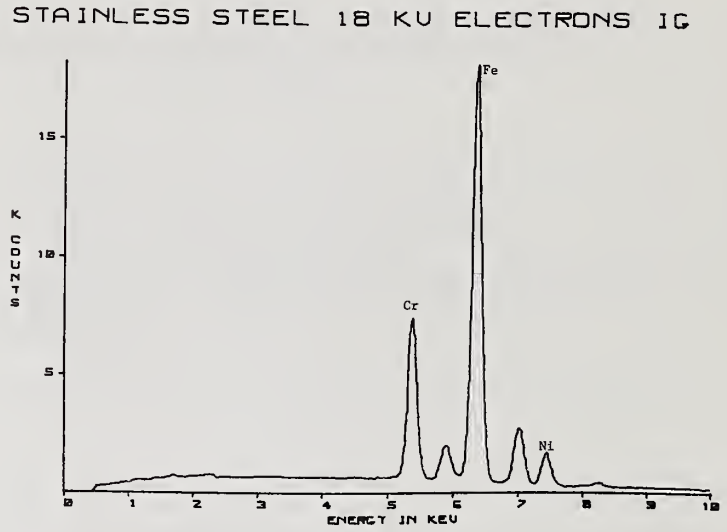

Figure 3. Stainless steel spectrum collected using IG Detector on SEM.

Performance differences between the detectors become significant only in the regions below 3 keV or above 30 keV. Figure 4, however, shows a spectrum from pure molybdenum, illustrating two of the more subtle characteristics exhibited in the germanium detectors in the medium energy region: prominent escape peaks and a clearly defined efficiency jump at the germanium K-absorption edge.

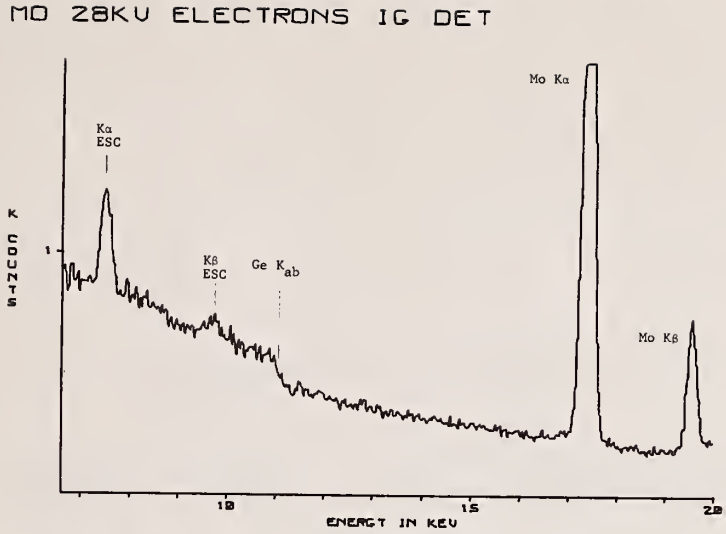

Figure 4. Mo Spectrum, collected using IG Detector on SEM, showing escape peaks and K absorption edge.

Figures 5a and 5b illustrate the effects on peak shape of the incomplete charge collection in germanium when low energy x-rays are absorbed. Figure 5a shows MoLα at 2.29 keV, SiKα at 1.74 keV, and GeLα at 1.19 keV, as analyzed with a germanium detector. The tailing is apparent for the molybdenum peak, and becomes more pronounced as the energy decreases to the SiKα energy. It will continue to worsen until the L absorption edge for germanium is reached (≅1.2 keV). Below this energy, peak shape is partially restored, as seen for the germanium L line. For K lines of light elements, this means that the peak shape will be the poorest for a MgKα line (1.25 keV), but will be at least partially restored for the NaKα line (1.04 keV). Figure 5b compares silicon peaks analyzed using the Si(Li) and IG detectors, showing the magnitude of the peak shape degradation in germanium.

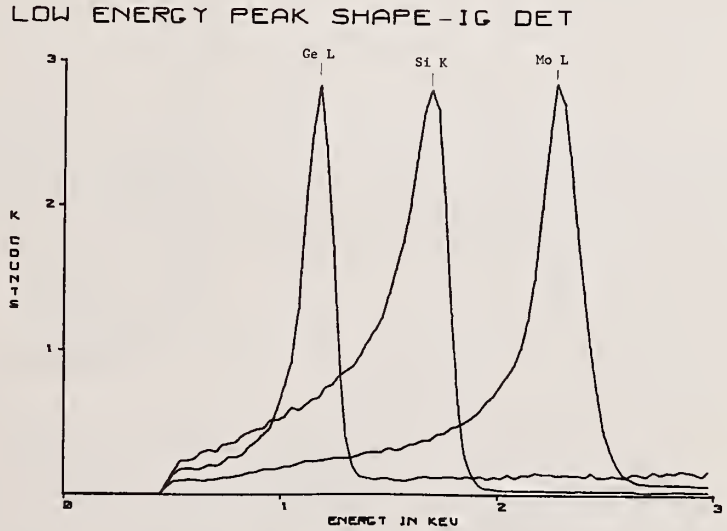

Figure 5a. Low energy peak shape degradation due to incomplete charge collection in the IG detector.

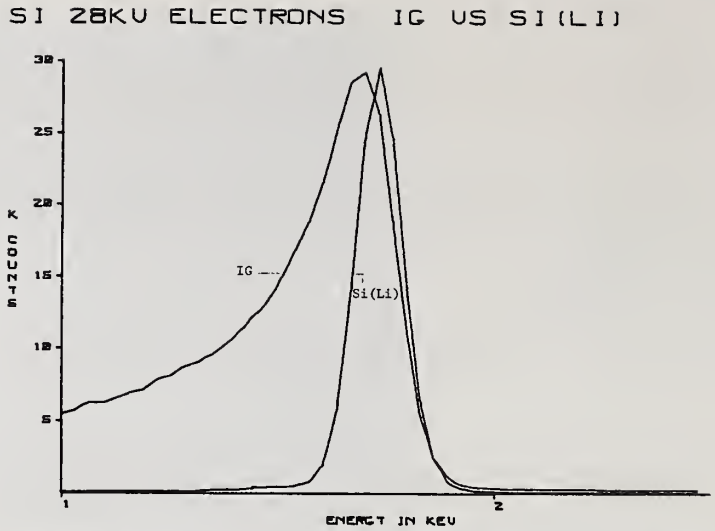

Figure 5b. Comparison of Si peak from IG and Si(Li) Detectors.

To illustrate the effects of the tailing problem exhibited at low energies in germanium detectors, several materials containing light elements were analyzed. Figure 6a is an iron-3 percent silicon material, analyzed with the IG detector (the iron peaks are off-scale). Although this spectrum by itself does not look particularly unusual, the degradation in peak-to-background ratio for the silicon peak (and therefore sensitivity for silicon) in the IG spectrum becomes apparent when compared to the Si(Li) spectrum of the same material, shown in figure 6b. The difference in silicon P/B between the two spectra is nearly an order-of-magnitude.

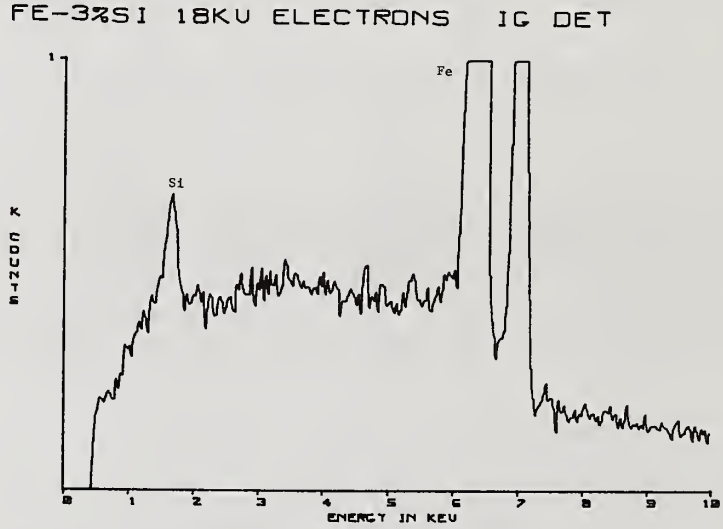

Figure 6a. Fe-3 percent Si spectrum collected using IG Detector on SEM.

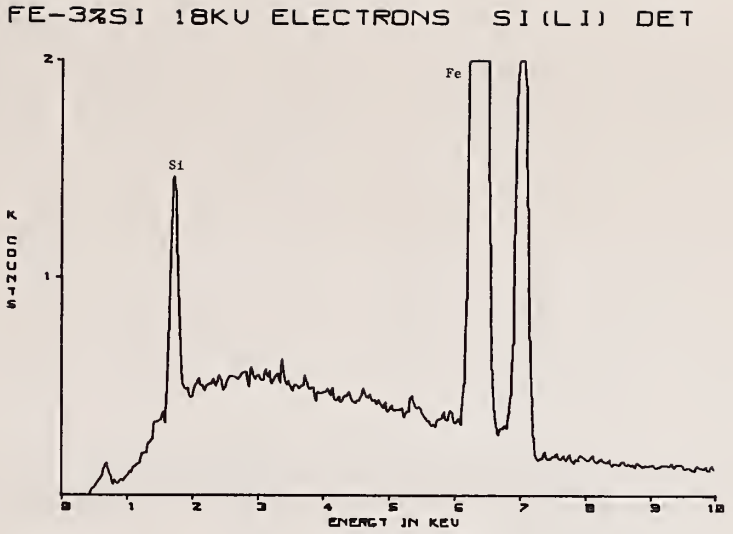

Figure 6b. Fe-3 percent Si spectrum collected using Si(Li) Detector on SEM.

Figures 7a and 7b compare spectra from anorthite (≅16% Al, 24% Si, 10% Ca, 0.4% Fe, remainder oxygen) using the two detectors. Not only is the separation between the aluminum and silicon peaks severely degraded in the IG spectrum, but the small Na peak is lost completely in the aluminum and silicon tails.

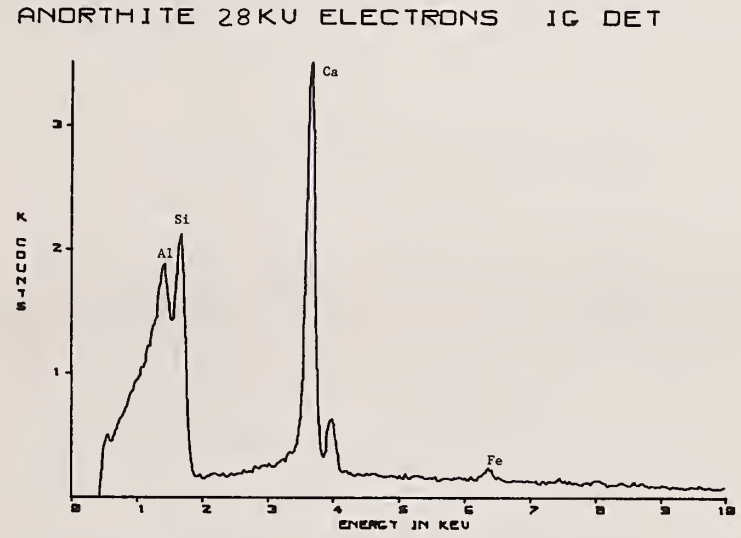

Figure 7a. Anorthite spectrum collected using IG Detector on SEM.

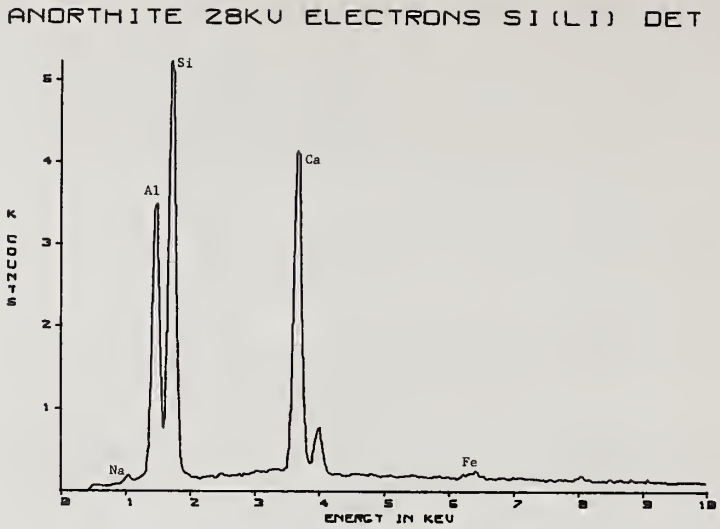

Figure 7b. Anorthite spectrum collected using Si(Li) Detector on SEM.

3.2 High Energy Performance

High Energy Performance

Figure 8a illustrates a high energy spectrum using an IG detector. The spectrum is the Pb K-series, excited by a Co-57 radioactive source. Figure 8b is a comparison of the Pb K spectra obtained using the IG and Si(Li) detectors. The spectra were normalized at the PbLα line (10.6 keV), at which energy the efficiency of the two detectors is about equal. The superiority of the IG detector in the higher energy region is clearly demonstrated.

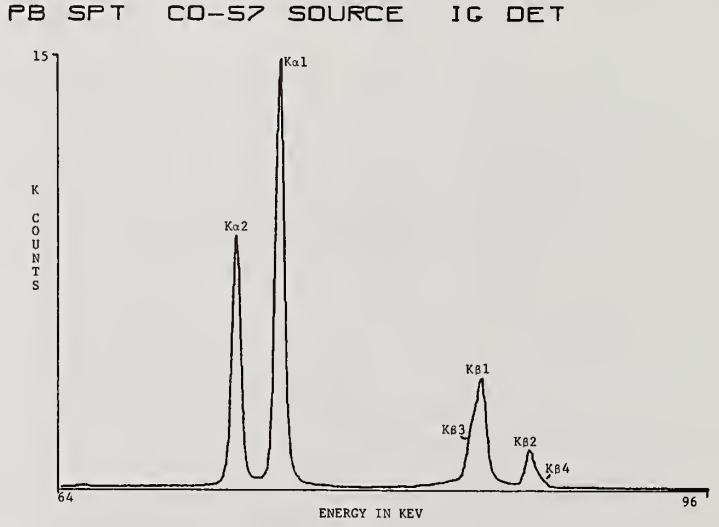

Figure 8a. Pb K spectrum excited by Co-57, collected using IG and Si(Li) Detectors.

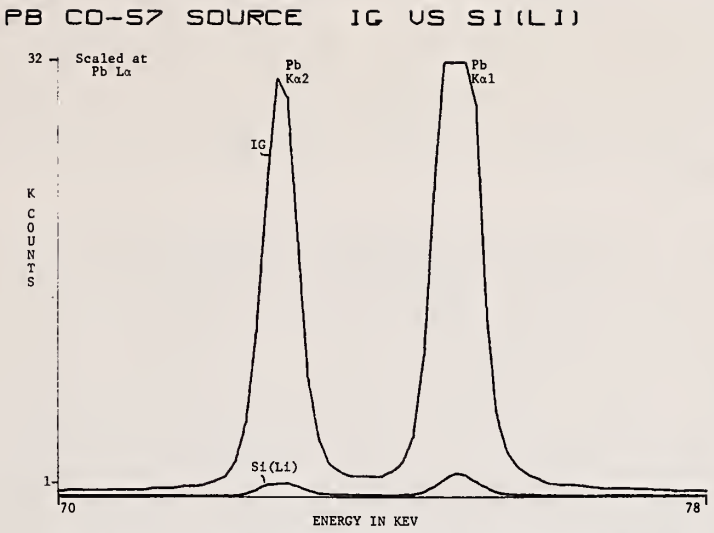

Figure 8b. Comparison of Pb K spectra collected using IG and Si(Li) Detectors.

Figure 9 compares Si(Li) and IG spectra from Eu K x-rays (40-50 keV), emitted from a GD-153 radioactive source. Note that not only is the efficiency better for the IG detector, but the resolution (quality of peak separation) at the $K\alpha_1$-$K\alpha_2$ lines is also superior.

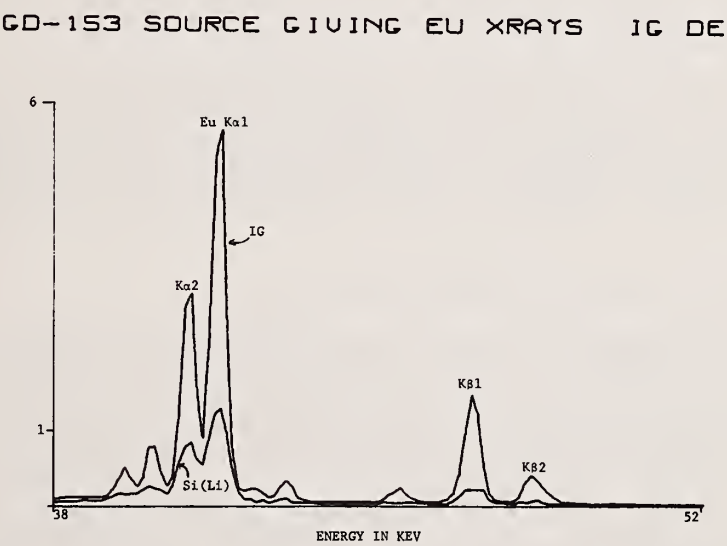

Figure 9. Comparison of Eu K spectra emitted from Gd-153 source, collected using IG and Si(Li) Detectors.

4. Discussion and Conclusions

The reasons governing the application of Si(Li) detectors to low energy x-ray spectroscopy (<30 keV) and germanium detectors to high energy x-ray spectroscopy have been illustrated. The limitation on using germanium detectors for low energy spectra is placed by the resolution degradation due to incomplete charge collection for x-rays less than 3 keV in energy. The limitation on using Si(Li) detectors for high energy spectra is placed by poor efficiency.

The phenomenon of incomplete charge collection is discussed in detail by Llacer et al., [1][1]. X-rays absorbed near the surface of the germanium detector (and to some extent in silicon as well) produce charge which is not always fully collected. At about 3 keV in germanium, the resulting peak tailing becomes significant, and continues to worsen as x-ray energy (and therefore penetration into the detector) decreases. As the x-ray energy decreases below the germanium L absorption edge, the mass absorption coefficient drops significantly, penetration increases, and peak shape is at least partially restored. With further decrease in energy, one would expect tailing to increase again.

Incomplete charge collection is therefore responsible for poor resolution at low energies in germanium detectors. However, at medium and high energies, germanium detectors exhibit better resolution than Si(Li) detectors due to the lower band-gap energy for germanium compared to silicon. For the higher energy region, therefore, germanium will exhibit better resolution than a Si(Li) detector for a given detector area, or for a given detector resolution, a germanium detector of larger size can be applied. For example, a premium Si(Li) detector of 145 eV resolution will typically have an active area of 10 mm^2. A premium germanium detector of the same resolution will typically have a 25 mm^2 active area. In fact, IG detectors with resolutions better than 185 eV and an active area of 100 mm^2 are routinely fabricated.

One practical advantage of IG detectors is their ability to be stored indefinitely at room temperature. Although the detector must be used at cryogenic temperature to limit thermal and electronic noise, the liquid nitrogen level in the cryostat need not be maintained when the detector is not in use.

On the other hand, it is generally recommended that the Li-drifted detectors be stored at cryogenic temperature at all times in order to limit the possibility of Li redistribution in the crystal. The IG detector is high purity germanium, and does not require lithium-drifting; therefore, room temperature storage is normal procedure. For some industrial or remote process monitoring applications, this feature may be a significant advantage.

In summary, the following conclusions can be stated:

1. The Si(Li) detector outperforms germanium for low energy x-ray analysis based on superior resolution for x-rays <3 keV.

2. The germanium detector outperforms Si(Li) for higher energy x-ray analysis, based on superior efficiency for x-rays >30 keV.

3. The IG detector can be stored at room temperature, whereas it is generally recommended that Si(Li) detectors be maintained at cryogenic temperature at all times.

4. IG detectors typically exhibit better resolution for medium and high energy x-rays than Si(Li) detectors with equal active area.

Reference

[1] Llacer, J., Haller, E. E., and Cordi, R. C., "Entrance Windows in Germanium Low-Energy X-Ray Detectors", IEEE Trans on Nuclear Sci., NS-24, 53-60 Feb. 1977.

[1]The figure in the bracket indicates the literature reference at the bottom of this page.

National Bureau of Standards Special Publication 604. Proceedings of the Workshop on Energy Dispersive X-Ray Spectrometry held at NBS, Gaithersburg, Maryland, April 23-25, 1979. (Issued March 1981)

ROOM TEMPERATURE ENERGY DISPERSIVE X-RAY SPECTROMETRY WITH MERCURIC IODIDE DETECTORS

A. J. Dabrowski[1], M. Singh, G. C. Huth, and J. S. Iwanczyk[1]

University of Southern California
Medical Imaging Science Group
4676 Admiralty Way, Suite 932
Marina del Rey, California 90291

Abstract

The compound semiinsulator mercuric iodide is under development as a detector for room temperature operable, energy dispersive x-ray spectrometry. Energy resolution values approaching those characteristic of cryogenically cooled semiconductor detectors have been achieved. A miniature spectrometer consisting of an HgI_2 detector and preamplifier and having a total volume of 300 cm^3, has been fabricated. This does not even closely approach reduction in spectrometer size that is possible and much smaller designs are possible in the near-term future. Portable x-ray spectrometers are currently being designed for on-site, extra-laboratory applications such as detection of uranium in mines, or for microanalysis in space. An energy resolution of 420 eV is currently obtained with a 7 mm^2 HgI_2 detector for the 5.9 keV x-rays of Fe-55. An improvement in resolution by 50-100 eV is expected in the near future.

The various sources which contribute to noise and background in the x-ray spectra have been studied and compared to corresponding features of cooled Si(Li) and germanium detectors. X-ray spectra of many targets have been measured with mercuric iodide detectors. These spectra were generated either by charged-particle excitation of the sample, or by the method of x-ray fluorescence. Several potential applications have been outlined which are particularly suited to mercuric iodide x-ray spectroscopy.

1. Introduction

The success of silicon and germanium in fabrication of nuclear detectors for a wide range of applications has stimulated consideration of other materials that might offer special advantages in specific applications. In particular the development of high energy resolution, ambient temperature solid state x-ray detectors has been highly desirable. Because of the high level of noise associated with leakage current at room temperature, high bandgap materials had to be taken into consideration for this purpose.

Numerous solid state crystals have been exploited for this purpose. The most work has been done with three compounds: gallium arsenide [1,2][2], cadmium telluride [3,4], and mercuric iodide [5,6]. A comparison of some properties of these materials is shown in Table 1. Gallium arsenide and cadmium telluride are semi-insulators with a bandgap of 1.4 eV and 1.5 eV respectively, which leads to a room temperature leakage current in the order of nanoamperes or higher.

---

[1]On leave from the Institute of Nuclear Research, Swierk, Poland.

[2]Figures in brackets indicate the literature references at the end of this paper.

Table 1. Comparison of some physical and electrical properties of three solid state compounds.

Compound		Band-Gap (eV)	Leakage Current	$(\mu\tau)_e$ (cm^2/V)	$(\mu\tau)_h$ (cm^2/V)
GaAs	Semi-Insulator	1.4	Nanoamperes	$\leq 10^{-3}$	$\leq 5\times10^{-5}$
CdTe	Semi-Insulator	1.5	Nanoamperes	$\leq 5\times10^{-2}$	$\leq 5\times10^{-4}$
HgI_2	Insulator	2.1	Picoamperes	$\leq 10^{-3}$	$\leq 10^{-5}$

As we have shown elsewhere [7], a leakage current of nanoamperes produces noise levels which limit the energy resolution to >1 keV (FWHM). Mercuric iodide has a bandgap of 2.1 eV which leads to the leakage current at room temperature in the region of picoamperes. Because of that, electronic noise of the HgI_2 spectrometer could be reduced to the values close to those obtained by cryogenically cooled systems. This feature combined with exceptionally good charge carrier transport properties (for insulators), makes HgI_2 a particularly attractive material for room temperature low energy x-ray spectroscopy.

2. Crystals and Detectors

Some physical properties of mercuric iodide are presented in Table 2. α-mercuric iodide is a bright red tetragonal crystal which above 127 °C undergoes a phase transformation into the yellow colored orthorhombic β-HgI_2. The low-temperature tetragonal crystalline structure is the basic form of mercuric iodide used for nuclear detector fabrication. This is a lamellar crystal cleaving easily along the iodine-iodine planes.

The raw α-HgI_2 has such impurities like carbon, silicon, iron, aluminum, potassium, and boron. It is purified by zone refining, extraction from solvent or repeated sublimation. Crystals are grown using initially purified raw materials by either a static or dynamic pulling vapor-growth or solution-growth method. Large crystals weighing as much as 100 grams are common with the growth period being of several weeks duration [8,9].

Taking advantage of the lamellar nature of the crystal, "plates" are carefully cleaved to be used in the fabrication of x-ray detectors [7]. These plates can be up to a centimeter in diameter. Subsequent x-ray detector fabrication is exceptionally simple. The detector plate is first etched to the required thickness (200-500 μm). The actual detector area is then defined by painting on contacts of emulsified carbon ("aquadag") to both sides of the crystal. Evaporation of thin metal films, usually Pd, is also used. Contact wires are embedded in the carbon contacts for remote attachment. Finally, the crystal is sprayed with a common commercial electronic encapsulant ("humiseal"). This effectively eliminates moisture or vacuum interaction with the HgI_2 surface and possible degradation of detector leakage current and noise behavior. These detectors perform equally well under high vacuum (10^{-6} torr) or ambient pressure. In use, the detectors are biased in the 50-500V range, depending on the thickness of the plate and transport properties of the crystal. Leakage current less than 5 pA is common and is required for high energy resolution.

Table 2. Physical properties of mercuric iodide.

Atomic Numbers	53, 80
Crystal Structure	Tetragonal (low T.) Orthorhombic (high T.)
Lattice Parameters	a = 4.368 Å c = 12.435 Å
Molecular Weight	454.45 g/mole
Atomic Density	2.54×10^{22} at/cm^3
Melting Point	259 °C
Phase Transition	127 °C
Density	6.3 g/cm^3
Dielectric Constant	$\varepsilon \cong 8.3$
Index of Reflection	n = 2.89
Band Gap	2.13 eV
Band Gap Change with Temperature	-7×10^{-4} eV/K range (100K - 300K)
Resistivity	$\sim 10^{13}$ Ωcm at 300K
Atoms/Cell	6
Electron Mobility	~ 100 cm^2/Vs at 300K ~ 250 cm^2/Vs at 100K
Hole Mobility	~ 10 cm^2/Vs at 300K ~ 30 cm^2/Vs at 100K
$(\mu\tau)_e$	$\leq 10^3$ cm^2/V
$(\mu\tau)_h$	$\leq 10^5$ cm^2/V
Energy per Electron-hole	4.15 eV at 300K

3. Energy Resolution

Various factors which have led to the presently available level of energy resolution of mercuric iodide detectors, will be discussed here.

In the solid state energy dispersive x-ray spectrometers the energy resolution is mainly affected by the first two stages of the system: detector and preamplifier (we do not consider here high counting rate).

To discuss the energy resolution of the solid state spectrometers it is convenient to distinguish three values of this parameter.

1. Electronic noise (in FWHM) of the electronic system without the detector – this gives the lower possible limit of the energy resolution of the spectroscopic system.

2. Electronic noise (in FWHM) of the spectrometer (detector and electronic system) measured as the width of the line of a pulser (injection of a definite amount of charge by an external pulser through a small capacitor into the input stage of the system).

3. Energy resolution (in FWHM) of the observed x-ray line – usually it is referred to the Mn K x-rays at 5.9 keV.

Energy resolution values obtained by different systems with HgI_2 detectors are summarized in Table 3.

The upper line of Table 3 shows the first published spectrum of low energy x-rays obtained using a HgI_2 detector in 1974 [5]. The detector was 4.2 mm^2 x 210 μm. The energy resolution of the Fe 55 peak was 850 eV (FWHM) and for the pulser 760 eV (FWHM). By selection of components of the input stage of the electronics, it was possible to improve the electronic noise level and consequently the energy resolution of the detector, as is shown in the second and third line of Table 3 [6,7]. To further reduce the noise level of the preamplifier, the input FET was cooled using a small thermoelectric Peltier cooler [10,11] (fourth row of Table 3).

In all hitherto applications, commercially available components have been used in the input stage of the preamplifier. As it is known, the package of the commercially available FET's cause additional degradation of their noise characteristics. Consequently the next step in the evolution of the input stage of the low noise room temperature preamplifier was taking the FET chip out of the "noisy" case and mounting it on a low noise ceramic substrate.

The results are shown along the fifth row in Table 3 and in figure 1. These results, presented for the first time here, show an energy resolution of 380 eV (FWHM) for Fe 55 peak, and 300 eV (FWHM) for the pulser. The electronic noise of the system without detector is 240 eV (FWHM) for HgI_2 (which corresponds to a value of 205 eV (FWHM) for silicon). This value was obtained when both HgI_2 detector and preamplifier were at room temperature.

For comparison, at the bottom of Table 3 the results for the best cryogenically cooled Si(Li) systems are shown. It is worth saying that the results both for proportional and scintillation counters for Fe 55 line, would be situated outside the right border of this Table.

Referring to Table 3, further improvement of the spectrometer means that the value of the electronic noise of the system without the detector, E, has to be further diminished, and the distances between E and P as well as P and X on this diagram have to be possibly small.

Table 3. Energy Resolution of X-ray Spectrometers with HgI_2 Detectors

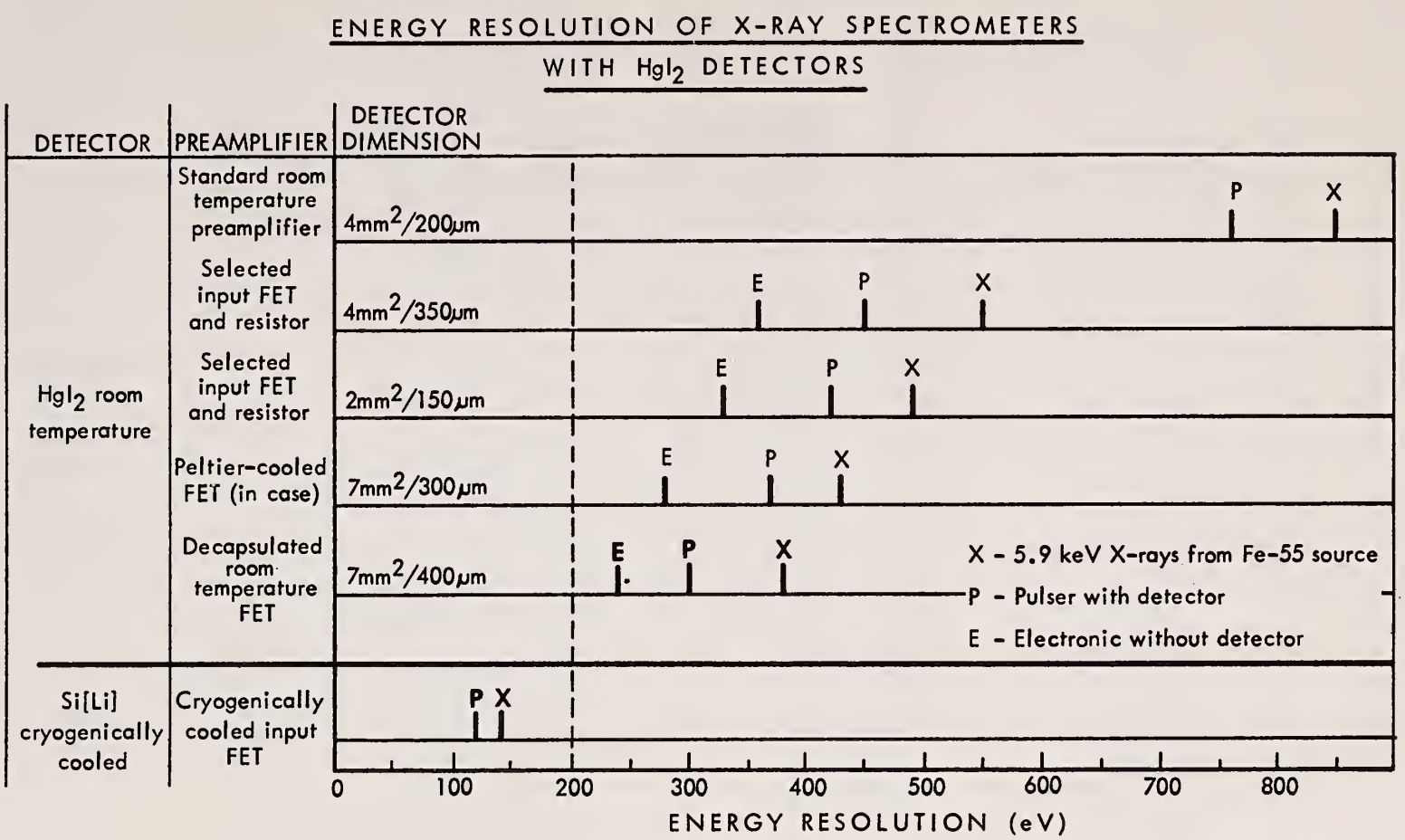

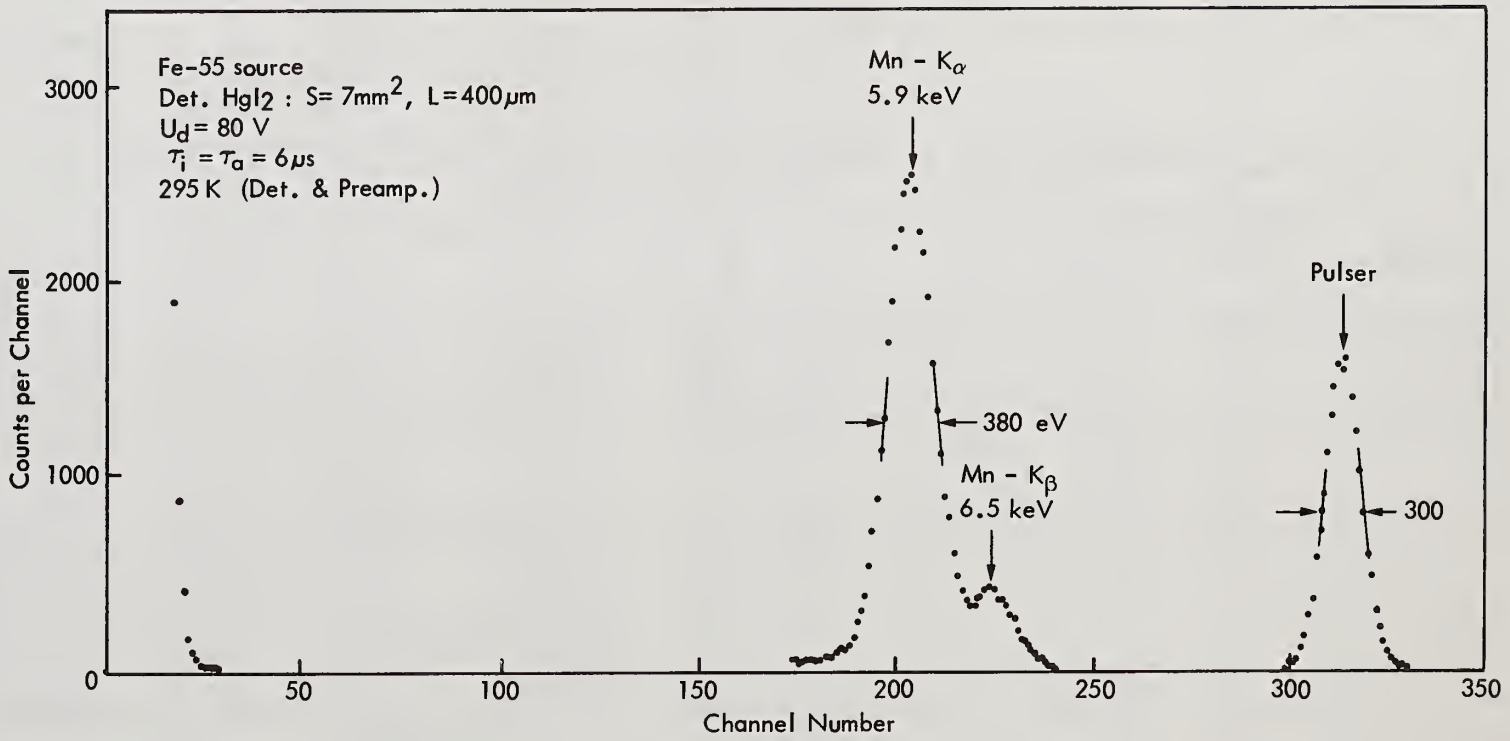

Figure 1. Fe 55 spectrum measured by HgI_2 room temperature spectrometer.

Further improvement of the electronic noise of the system, E, is expected, when better selection of the input FET will be made. Also the FET chips on the ceramic substrate will be cooled down to about -50 °C using small thermoelectrical Peltier coolers. Reduction of the value of E to below 200 eV (FWHM) for HgI_2 is expected after these procedures.

To shorten the distance between E and P on the discussed diagram, the smallest values of the leakage current and the capacity of the HgI_2 detector should be achieved. Improvement in fabrication of HgI_2 detectors, to achieve these goals, is in progress.

Factors which contribute to the spread between E and X in the diagram of Table 3 are mainly transport properties of the charge carriers in the HgI_2 cyrstal (trapping), statistical effects in the charge generation process, nonuniformity of the crystal, which causes dispersion of trapping parameters and distortions of the electric field through the active volume of the detector, and detector edge and window effects. Additional effort in fabrication of mercuric iodide crystals and designing of the detectors which could mainly improve the energy resolution for x-rays and bring it closer to the pulser line width, is now under investigation.

4. Low Energy X-Ray Spectra

The behavior of mercuric iodide spectrometers for detecting very low energy x-rays from different targets has been studied using as an excitation source, an alpha particle beam obtained from a Van de Graaff accelerator at the California Institute of Technology [10]. A 7 mm^2 x 310 μm HgI_2 detector masked down to an exposed entrance window of 3 mm^2 has been used for this experiment. Characteristic lines below 10 keV of different elements (such as sodium, magnesium, aluminum, silicon, iron, nickel, copper) have been measured. The energy resolution of the spectrometer at 5.9 keV was 450 eV (FWHM). The input FET (in its original case) was thermoelectrically cooled.

The spectrum obtained from a magnesium target using a 6.0 meV α-excitation beam is shown in figure 2. The K line at 1.25 keV has a FWHM of 390 eV and is well separated from the noise.

The low-energy x-ray peaks obtained by HgI_2 detector exhibit excellent symmetry as demonstrated by the Mg peak on figure 2. This is in contrast to the behavior of cooled high-purity germanium (HPGe) detectors for energies below about 2.3 keV, where a large asymmetry in the form of a tail on the low-energy side of the peak is observed. This behavior of HPGe has been studied by Llacer et al. [12]. During the experiment in Caltech mentioned above we have also observed such asymmetrical low-energy x-ray peaks with a cryogenically cooled HPGe detector. As an example of this effect the x-ray line from a Si- target measured by HgI_2 spectrometer (450 eV FWHM for Fe 55) and a cryogenically cooled HPGe spectrometer (175 eV FWHM for Fe 55) under exactly the same experimental conditions, is shown in figures 3 and 4.

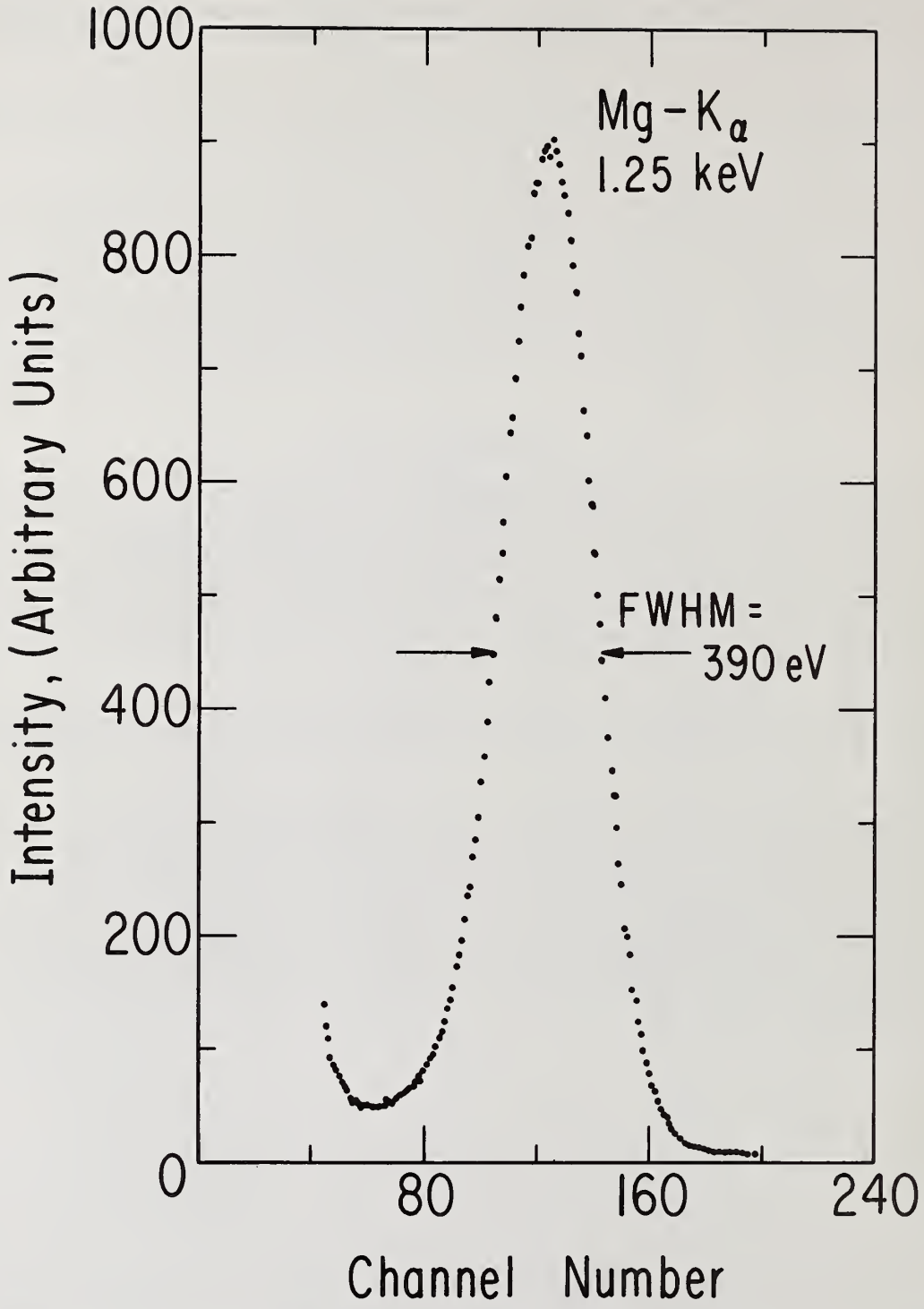

Figure 2. K x-ray line from a magnesium target using 6.0 MeV α-excitation beam.

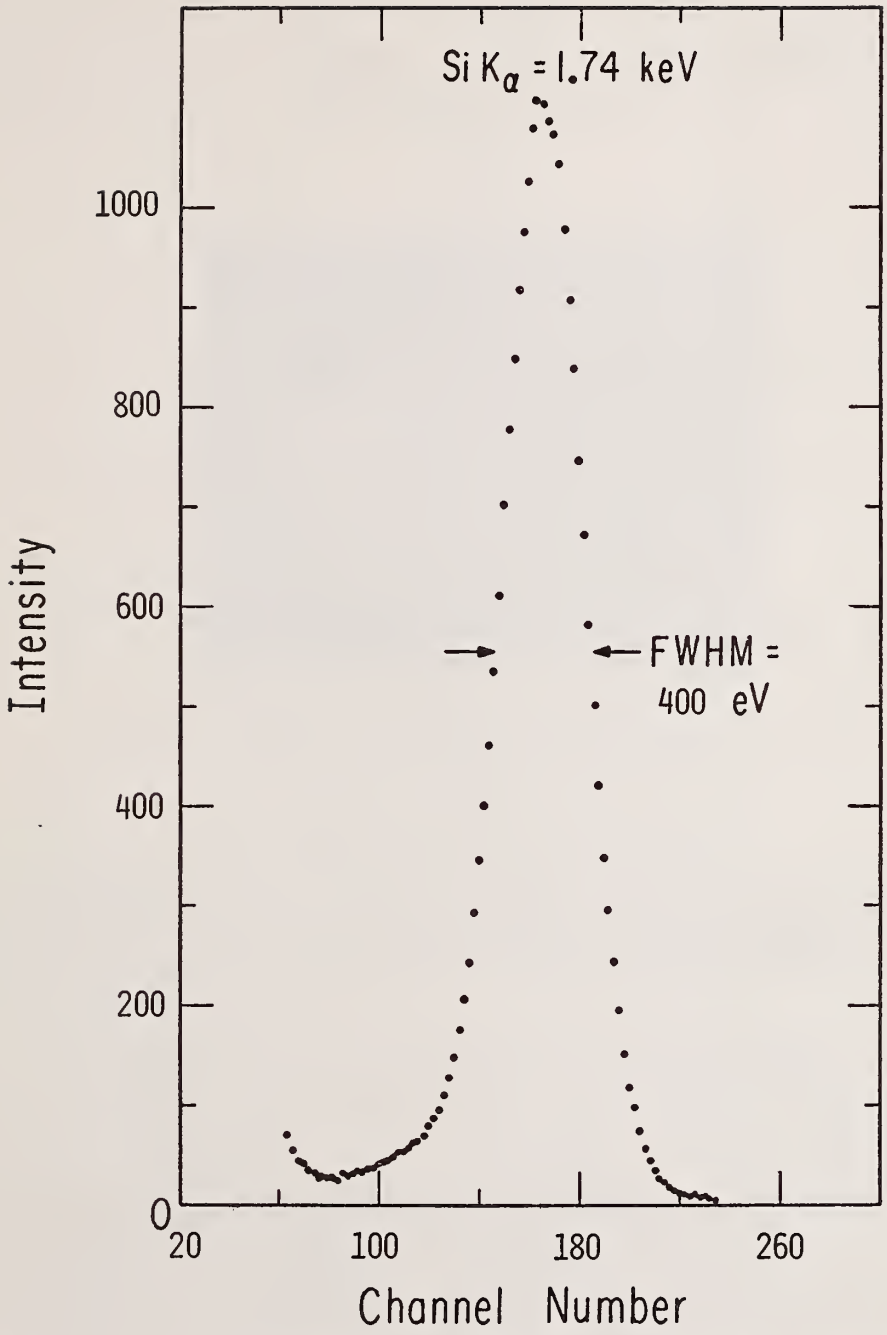

Figure 3. K x-ray line from a silicon target measured by HgI_2 spectrometer.

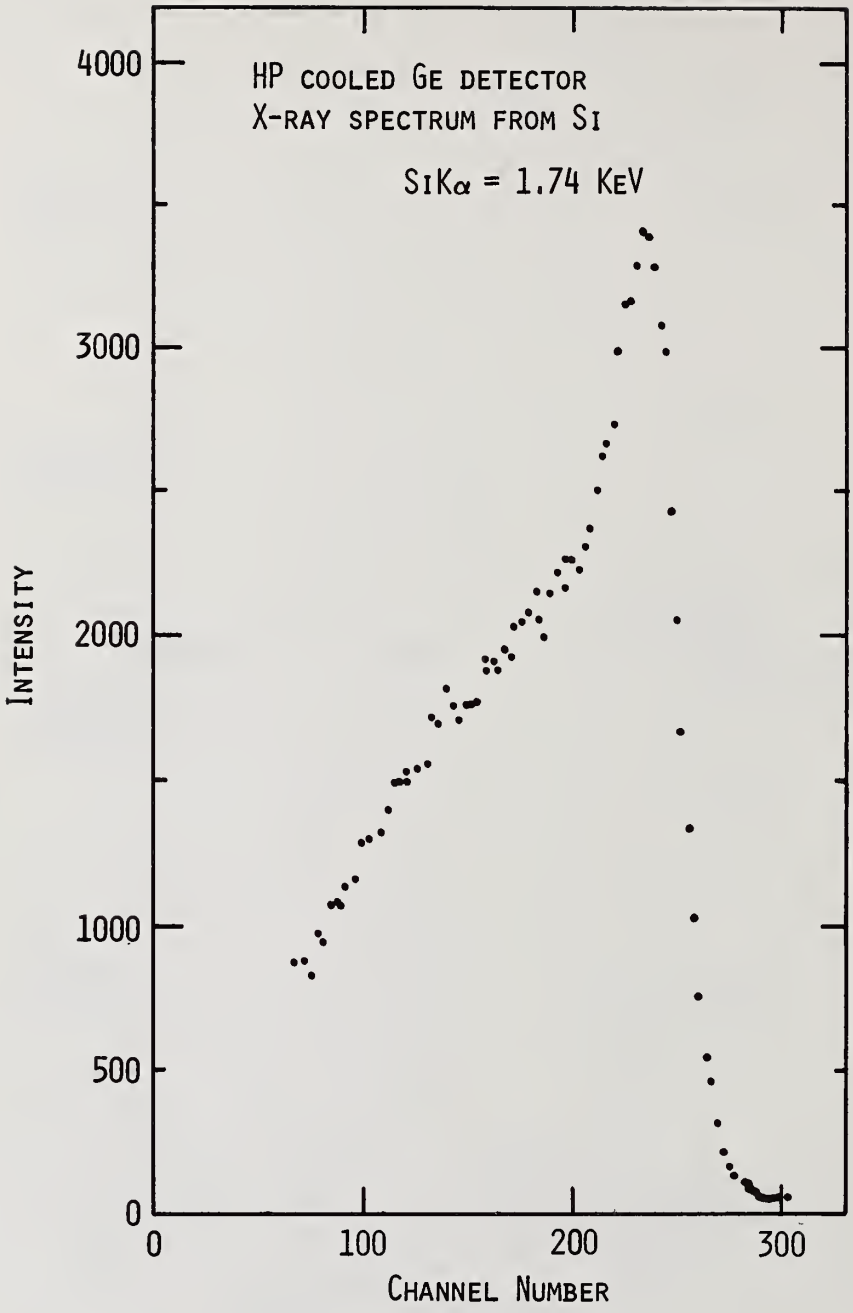

Figure 4. K x-ray line from a silicon target measured by a cryogenically cooled HPGe spectrometer.

5. Portable Spectrometer

We have fabricated a prototype of room temperature mercuric iodide x-ray spectrometer (figure 5). The spectrometer is based on a Tennelec Model 161D preamplifier, which has been modified to improve room temperature noise level. The HgI_2 detector is incorporated over the first stage of preamplification for optimum coupling. The preamplifier case has been modified to achieve a light-tight environment for the HgI_2 detector. Total volume of the spectrometer is 300 cm^3. An energy resolution of 380 eV (FWHM) has been obtained with 7 mm^2 HgI_2 detector for 5.9 keV x-rays from FE 55.

Figure 5. Front end of a prototype portable x-ray mercuric iodide room temperature spectrometer.

6. Analysis by X-Ray Fluorescence (XRF)

One of the major applications of energy-dispersive mercuric iodide spectrometry lies in room temperature XRF analysis. The detector-preamplifier combination and the excitation source can all be contained within a small package, thereby producing a portable and convenient high energy resolution XRF system without requiring the cumbersome paraphernalia associated with cryogenic cooling.

In typical XRF applications, the excitation source (a radioisotope or an x-ray tube) is chosen to produce characteristic x-rays under 30 keV from the sample. Although this energy region is usually sufficient to identify a large number of elements from their characteristic K or L emissions, it is sometimes desirable to record higher energy x-rays from some samples. A typical HgI_2 detector approaches 100 percent detection efficiency below 30 keV, and, because of its high Z, it can also be used to record higher energy x-rays with ~80 percent efficiency for energies up to 100 keV. Although room temperature energy resolution of HgI_2 detectors is still poorer than for cryogenically cooled silicon and germanium detectors, it has potential possibilities to be used both for low and high energy x-ray measurements. This provides an advantage over silicon detectors which are not suitable for energies above about 20 keV, and over germanium detectors which show a large "tailing" effect below 2.3 keV [12].

In addition to the characteristic x-rays, a typical XRF spectrum recorded with a HgI_2 detector consists of several peaks ("scatter" peaks, "escape" peaks) and a continuum background. The "scatter" peaks produced by a coherent or incoherent scattering event between the exciting radiation and the sample matrix, are quite large, and are usually responsible for producing most of the background in an XRF spectrum. The "escape" peaks in HgI_2 arise from production and subsequent escape of characteristic x-rays of mercury and iodine from

the detector material. The continuum background can be produced by several mechanisms such as escape of Compton scatter photons, escape of photoelectrons, incomplete charge collection, etc. Similar background effects are seen with all energy-dispersive semiconductor detectors. We have computed the probabilities for "escape peak" production and "continuum background" generation in a HgI_2 detector. Details of these calculations and experimental verification will be published in a separate report [13].

XRF spectra from several standard and unknown samples have been obtained using Fe 55 or Cd 109 as the excitation source [13]. A few typical results will be mentioned here.

A Cd 109 source was used to excite L x-rays of uranium, and XRF spectra were obtained from uranium ores containing different concentrations of uranium. The HgI_2 detector used was about 500 μm thick and had an active area of ~9 mm^2 which was then masked down to about 3.4 mm^2 to avoid edge effects. An angle of 110° was formed between the exciting source radiation and the line-of-sight of the detector. The detector to sample distance was about 1 cm, and the source to sample distance about 2 cm. The Cd 109 source was ~10 mci.

A series of spectra obtained from ores containing different concentrations of uranium is shown in figure 6. The characteristic L x-rays of uranium observed are the Lα peak at 13.6 keV, $L\beta_1$ and $L\beta_2$ at 17.22 and 16.4 keV, and $L\gamma_1$ at 20.16 keV. Also seen are the coherent "scatter" peaks at 24.94 and 22.16 keV (silver x-rays from the Cd 109 source), and the incoherent scatter peaks corresponding to an angle of 110° at 23.4 and 20.9 keV. These peaks can be easily separated in the spectrum recorded from a 4 percent uranium sample (see figure 6a). For a lower concentration of uranium, the Lγ peak becomes obscured by the scattered source radiation. However, the Lα and Lβ peaks remain visible down to 0.01 percent uranium as shown in figure 6d. The energy resolution obtained for the 13.6 keV Lα peak was about 850 eV (FWHM) in this measurement.

In applications involving Cd 109 excitation, the escape peaks mainly arise from the escape of mercury Lα and Lβ x-rays (9.98 keV and 11.85 keV) from the "scatter" peaks, and have an intensity of about 1-2 percent of the parent peak (see figure 6). They are best seen in figures 6c and 6d on the left of the 13.6 keV uranium peak.

Another example of XRF analysis is shown in figure 7. Figure 7a is from a sample containing 50 percent Fe and 50 percent Ni, while figure 7b is from a sample which had 90 percent Fe and 10 percent Ni. A Cd 109 source was used. As seen from these spectra, although the Kβ peak of iron is obscured by the Kα peak from nickel, the Kα peak of iron (6.4 keV) and the Kα and Kβ peaks of nickel at 7.47 and 8.27 keV are well separated. By using peak stripping techniques, it should be possible to subtract the contribution of iron Kβ peak from the nickel Kα line. An accurate analysis of iron-nickel ores is therefore possible with a HgI_2 system.

Room temperature mercuric iodide spectrometry has several other potential applications, some of which are listed below.

- In mining, to determine the amount of specific elements in ores.
- In industrial production and manufacturing, to check on levels of some key elements (on-line).
- In electron microscopy, where a gain of about two orders of magnitude in geometrical detection efficiency due to the small size of the detector housing could be achieved relative to other detectors.
- In space applications, to determine the chemical composition of planetary bodies on space missions.

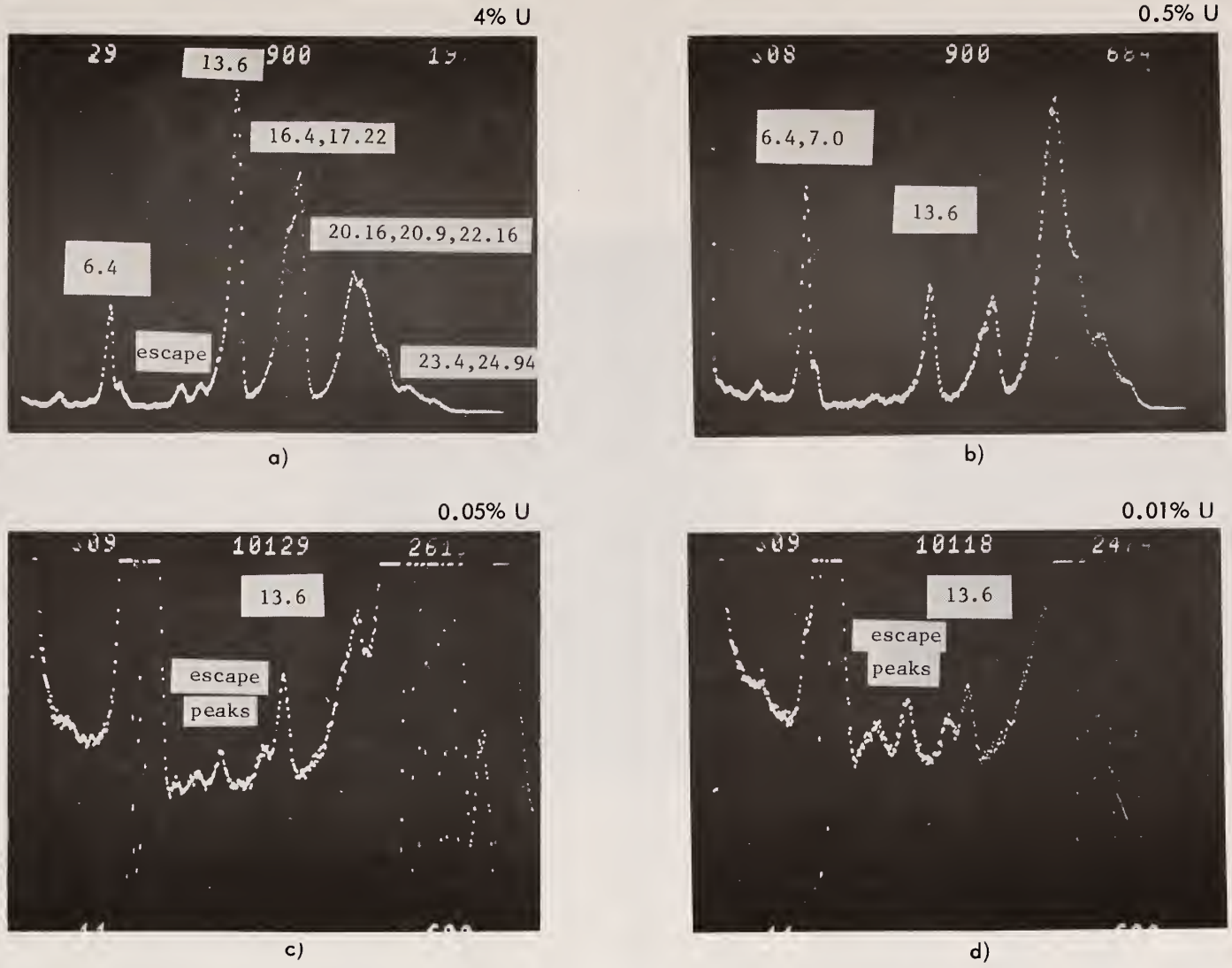

Figure 6. Analysis of uranium ores by x-ray fluorescence using Cd 109 source and mercuric iodide detector.

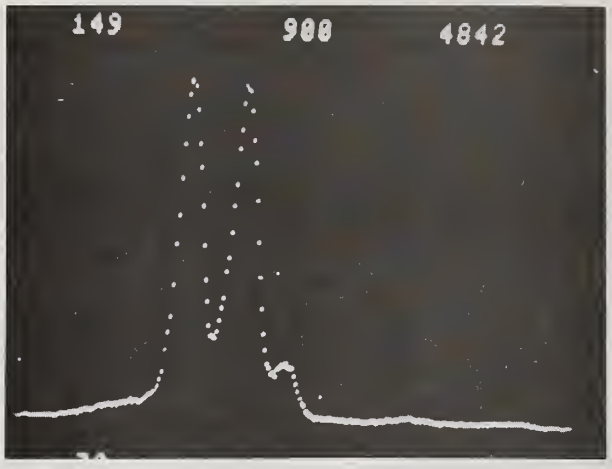

a)

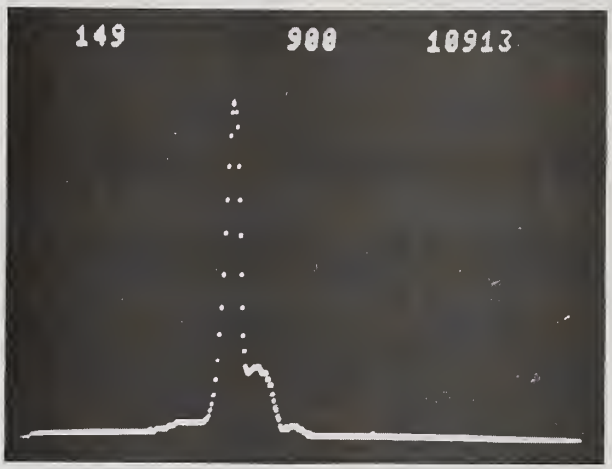

b)

Figure 7. Fluorescence x-ray analysis of a sample containing a) 50% Fe and 50% Ni; b) 90% Fe and 10% Ni, measured by HgI_2 detector.

7. Conclusions

A portable, room temperature x-ray spectrometer has been developed consisting of a "single crystal" mercuric iodide detector coupled to a low-noise room temperature preamplifier. An energy resolution of 380 eV (FWHM) for 5.9 keV x-rays has been obtained. Further improvement in energy resolution and reduction of the peak to background ratio is expected upon development of guard-ring structure mercuric iodide detectors as well as thermoelectric cooling of the input FET chip of the preamplifier. A hybrid low noise preamplifier is being designed to achieve microminiaturization of the spectrometer.

References

[1] Eberhardt, J. E., Ryan, R. D., and Tavendale, A. J., "Evaluation of Epitaxial n-GaAs for Nuclear Radiation Detectors", Nucl. Instr. Meth., 94, 463 (1971).

[2] Kobayashi, T., Kuru, I., Hojo, A., and Sugita, T., "Fe-Doped High Purity GaAs as a Room Temperature Gamma-Ray Spectrometric Detector", IEEE Transactions on Nuclear Science, NS-23, No. 7, 97 (1976).

[3] Iwanczyk, J. and Dabrowski, A. J., "The Effect of Charge Trapping on the Spectrometric Performance of n-Type CdTe Surface-Barrier Detectors", Nucl. Instr. Meth., 134, 505 (1976).

[4] Dabrowski, A. J., Iwanczyk, J., Szymczyk, W. M., Kokoschinegg, P., Stelzhammer, J., and Triboulet, R., "Advantages and Limitations of n-Type Low Resistivity Cadmium Telluride Nuclear Radiation Detectors", Nucl. Instr. Meth., 150, 25 (1978).

[5] Swierkowski, S. P., Armantrout, G. A., and Wichner, R., "Recent Advances with HgI_2 X-ray Detectors", IEEE Transactions on Nuclear Science, NS 21, No. 1, 302 (1974).

[6] Slapa, M., Huth, G. C., Seibt, M., Schieber, M., and Randtke, P. T., "Capabilities of Mercuric Iodide as a Room Temperature X-ray Detector", IEEE Transactions on Nuclear Science, NS-23, No. 1, 101 (1976).

[7] Dabrowski, A. J. and Huth, G. C., "Toward the Energy Resolution Limit of Mercuric Iodide in Room Temperature Low Energy X-ray Spectrometry", IEEE Transactions on Nuclear Science, NS-25, No. 1, 205 (1978).

[8] Schieber, M., Schnepple, W. F., and Van Den Berg, L., "Vapor Growth of HgI_2 by Periodic Source or Crystal Temperature Oscillation", Journal of Crystal Growth, 33, 125 (1976).

[9] Van Den Berg, L. and Whited, R. C., "Recent Improvements in HgI_2 Detectors", IEEE Transactions on Nuclear Science, NS-25, No. 1, 395 (1978).

[10] Dabrowski, A. J., Huth, G. C., Singh, M., Economu, T. E., and Turkevich, A. L., "Characteristic X-ray Spectra of Sodium and Magnesium Measured at Room Temperature Using Mercuric Iodide Detectors", Appl. Phys. Lett., 33 (2), 211 (1978).

[11] Huth, G. C., Dabrowski, A. J., Singh, M., Economu, T. E., and Turkevich, A. L., "A new X-ray Spectroscopy Concept – Room Temperature Mercuric Iodide with Peltier-Cooled Preamplification", Proceedings of the 27th Annual Conference on Applications of X-ray Analysis held in Denver, August 1-4, 1978.

[12] Llacer, T., Haller, E. E., and Cordi, R. C., "Entrance Windown in Germanium Low-Energy X-ray Detectors", IEEE Transactions on Nuclear Science, NS-24, No. 1, 53 (1977).

[13] Singh, M., Dabrowski, A. J., Huth, G. C., Iwanczyk, J. S., and Clark, B. C., "X-ray Fluorescence Analysis at Toom Temeprature with an Energy dispersive Mercuric Iodide Spectrometer", Proceedings of the 28th Annual Conference on Application of X-ray Analysis held in Denver, July 30-August 3, 1979, p. 249, in Vol. 23, Advances in X-ray Analysis.

National Bureau of Standards Special Publication 604. Proceedings of the Workshop on Energy Dispersive X-Ray Spectrometry held at NBS, Gaithersburg, Maryland, April 23-25, 1979. (Issued March 1981)

STANDARD TECHNIQUES FOR MEASURING WINDOW ABSORPTION AND OTHER EFFICIENCY LOSSES IN SEMICONDUCTOR X-RAY ENERGY SPECTROMETERS

F. J. Walter and R. Stone

EG&G Ortec
100 Midland Road
Oak Ridge, Tennessee 37830

and

D. H. Blackburn and P. A. Pella

National Bureau of Standards
Washington, D. C. 20234

Abstract

A conceptual technique for measuring the relative window and dead-layer thickness on semiconductor x-ray energy spectrometers by monitoring the transmitted intensity of a series of lines from a standard target has been described previously. This technique, which utilizes secondary x-rays fluoresced from a standard glass by the Mn x-rays from decay of Fe-55, was never incorporated in a measurements standard because there was no suitably stable glass target whose composition was traceable and certifiable. Recently, the National Bureau of Standards has developed a glass, SRM-477, specifically for this application.

Results of tests on the sensitivity, repeatability, and reliability of the technique will be presented. The various contributions to dead and partially dead layers will be discussed. Other techniques used to verify the efficiency of semiconductor x-ray detectors which are also proposed for the new IEEE/ANSI/IEC standard will also be described.

1. Introduction

The efficiency of any semiconductor detector depends on many physical parameters. For x-ray measurements, especially below 5 keV, window thickness is one of the most significant factors affecting detector efficiency. The window transmission losses may include a metal (e.g., beryllium) window in the vacuum enclosure, a possible dead-layer of semiconductor material and any other material which might be present between the source of the x-rays and the active region of the semiconductor detector. Because of the importance of window absorption, a standard measuring technique is needed to characterize this parameter. The purpose of this work is to describe measurements used in the development of such a standard technique and to describe the standard as it appears in the latest working draft of "Standard Test Procedures – Semiconductor X-Ray Energy Spectrometers" which was prepared by the Nuclear Instruments and Detectors Committee of the IEEE Nuclear Science Group.

There are several characteristics which are desirable for a window attenuation standard. Window transmission loss characteristics should be specifiable and measurable without detailed knowledge of the internal structure of the spectrometer. This allows ready comparison of spectrometers made to different designs or by different manufacturers. It should also allow a user in his own laboratory to verify the window transmission losses of his detector independently of specific data provided by the detector manufacturer. In addition, it is desirable to be able to specify window attenuation at any of several energies

appropriate to the type of detector and its intended use. Finally, it is advantageous to have a standard technique which does not require complex and expensive equipment.

These desirable characteristics are realized by basing window attenuation measurements on the relative transmitted intensities of x-rays fluoresced from a standard glass. The National Bureau of Standards has provided several samples of a glass (designated SRM-477) which was designed specifically for this purpose. We have made measurements to demonstrate the applicability of this technique and to determine any needed constraints (such as limitations on geometry) which should be incorporated into a standard technique.

Methodology The construction of the apparatus used in making the evaluation measurements is shown in figure 1. The glass target, a disk 25 mm in diameter and 3 mm thick, is held in a plastic lid which covers the top of the chamber. An annular ^{55}Fe source irradiates the glass with 5.9 and 6.4 keV Mn Kα and Kβ x-rays. Fluorescent x-rays from the glass then pass through the hole in the source and are incident on the detector. Mn x-rays from the ^{55}Fe, which are coherently backscattered from the glass target, are also incident on the detector. Several spacers are used to vary the geometry, and an adapter is provided to fit the detector endcap. Additional thicknesses of beryllium may be inserted over the detector to test the sensitivity of the technique. The chamber is evacuated to prevent x-ray absorption by air.

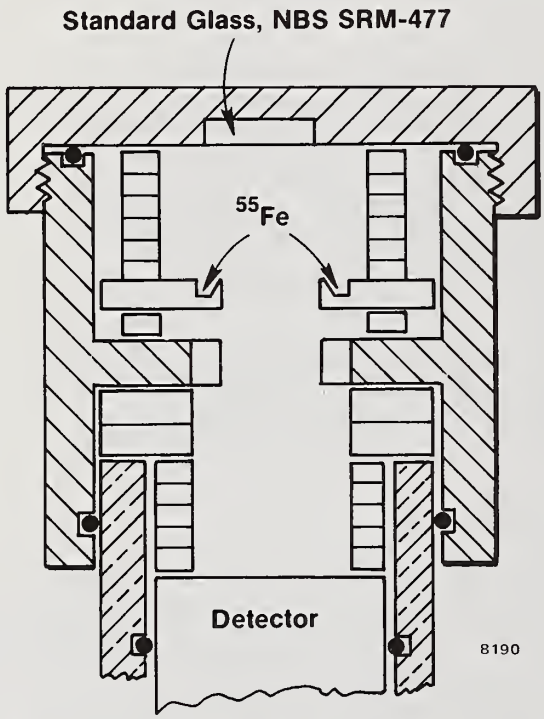

Figure 1. Apparatus for window thickness measurements with a glass fluorescent source.

The construction of the annular ^{55}Fe source is shown in figure 2. It is necessary that this same geometry be used to make measurements under this standard. Source to glass target distances are measured from the glass surface to the Be window of the source. The source strength used was 22 mCi. Although the standard is independent of source strength, an activity much below 20 mCi may result in inconveniently long counting times needed to achieve suitable statistics.

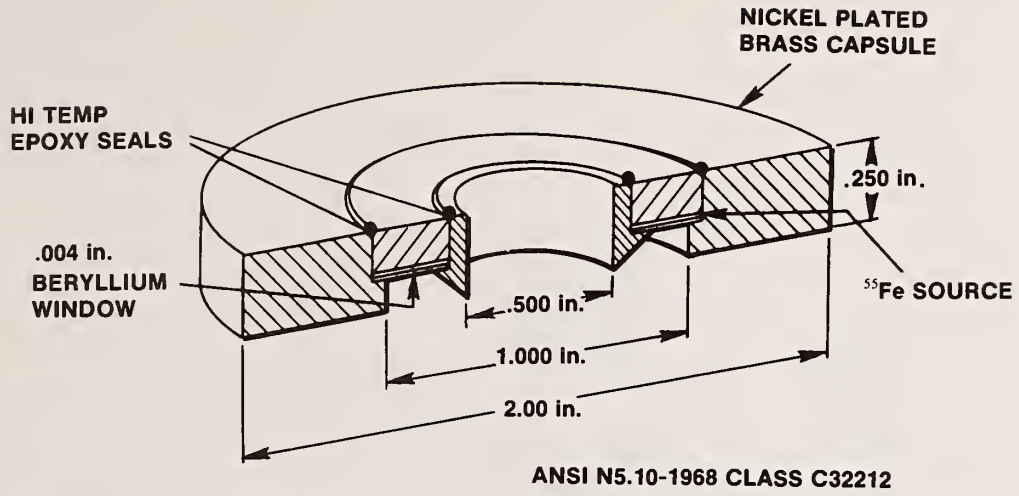

Figure 2. New England nuclear ^{55}Fe annular source registered with the NRC as Model NER-461A.

It is proposed that window attenuation characteristics be specified by a window attenuation index. This index is the ratio of the area of a specific fluorescent peak to the area of the backscattered 5.9 keV Mn peak as measured by this method. It was decided not to express this index in terms of a Ge, Si, or Be thickness equivalent in order to keep the standard simple and equally meaningful for all detector and window materials.

Measurement of this index does not involve a detailed knowledge of the system's structure and may be made independently with simple equipment. It may be made at any of several available energies and does not rely on elaborate calibration and correction. Despite the apparent simplicity of this technique, limitations on the geometry used for the standard measurement are necessary, largely as a result of self-absorption in the glass target.

Experimental Results A characteristic spectrum obtained with this technique is displayed in figure 3 on a relative intensity log scale. A Si(Li) detector 6 mm in diameter and 5 mm thick with a resolution of 165 eV FWHM at 5.9 keV was used for this measurement. The glass target is composed of the oxides of Si, Ba, Ca, Li, Mg, Zn, and B. The energies of the peaks range from 1.0 to 6.4 keV. For this spectrum, the front contact of the detector itself and 8 μm of Be are the only materials between the active region of the detector and the glass. Especially prominent are the coherently backscattered Mn lines, L lines of Ba, Kα, and Kβ lines of Ca, and Kα lines of Si, and Mg. The window attenuation index may be measured at the energy of any of the fluorescent lines.

The spectrum in figure 4 was taken under the same conditions as figure 3, except that an extra layer of 130 μm of Be was inserted over the detector. Comparing this with the previous spectrum, the much greater attenuation of the lower energy lines is evident, illustrating the basis of this technique. The counting statistics here are not the same as for the previous spectrum, but the relative size of the lower energy peaks with respect to the 5.9 keV peak is obviously much less.

Table 1 quantitatively illustrates the effect of increasing window thickness on the window attenaution indices. This measurement and those which follow were made with a Si(Li) detector 4 mm in diameter and 4 mm thick with a resolution of 160 eV FWHM at 5.9 keV. Even small changes in Be window thickness produce quite measurable effects in the normalized intensities of the 1.25 keV Mg or 1.74 keV Si lines. The Mg line or the 1.0 keV Zn line (not shown) would probably be useful in characterizing so-called windowless systems. However, with increasing window thickness, the Mg and Zn lines soon lose their usefulness because of the rapid decrease in count-rate.

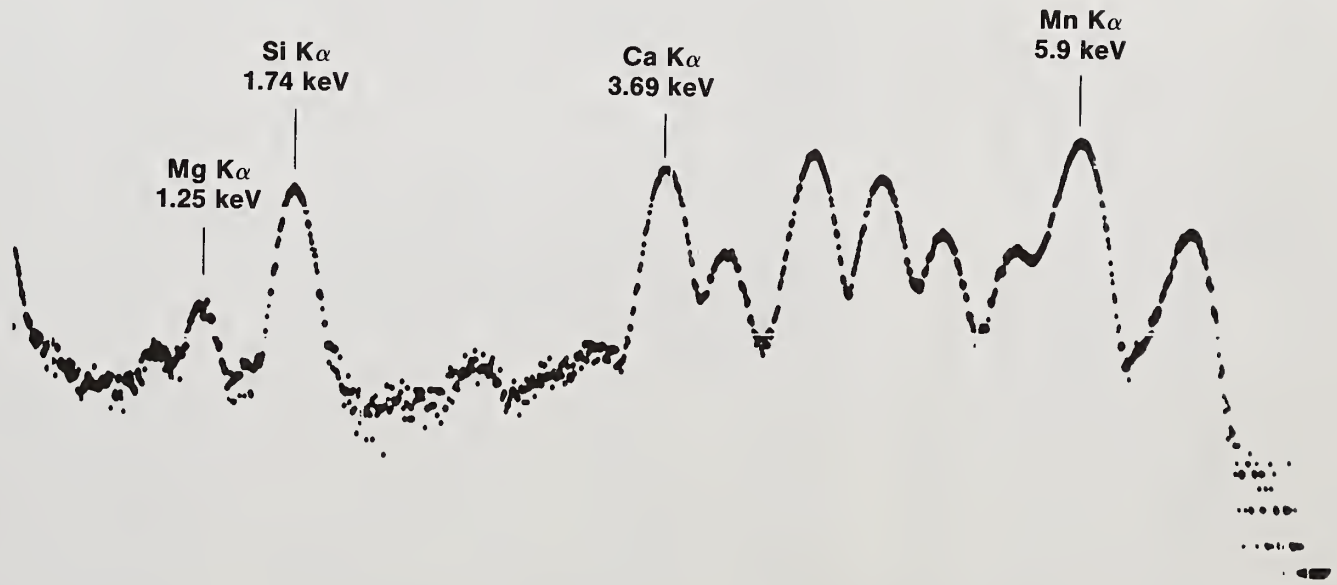

Figure 3. A characteristic spectrum obtained with an 8 μm beryllium window.

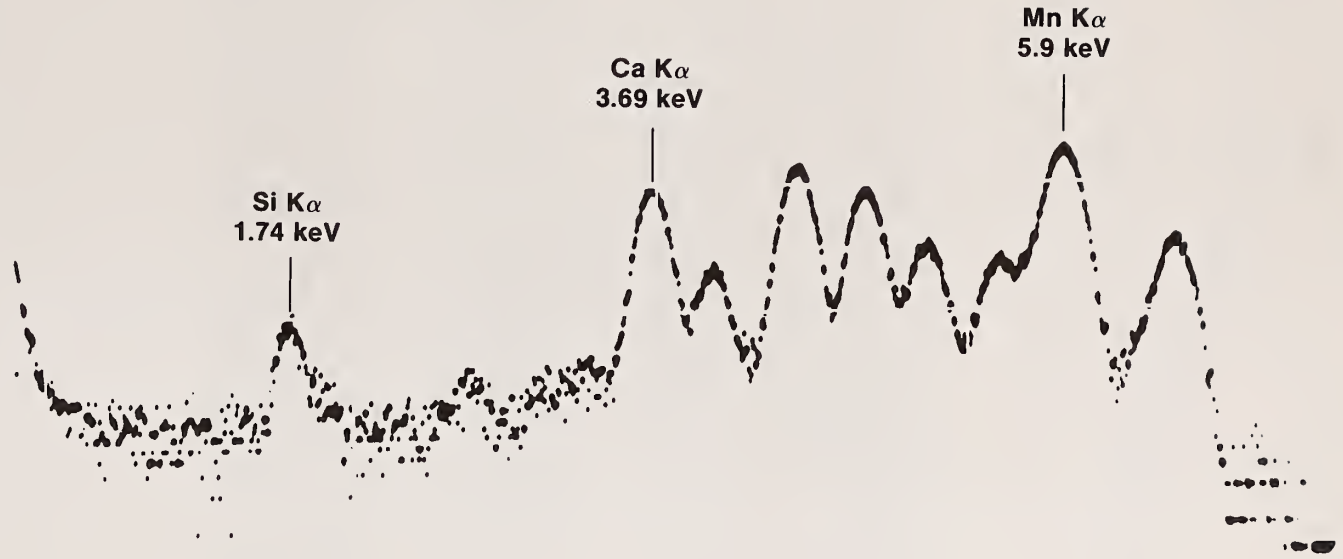

Figure 4. A characteristic spectrum obtained with a 132 μm beryllium window.

Table 1. The effect of window thickness on relative peak intensity normalized to the 5.9 keV Mn Kα peak.

Be Window Thickness (μm)	Mg Kα (1.25 keV) (I_{Mg}/I_{Mn}) X 100	Si Kα (1.74 keV) (I_{Si}/I_{Mn}) X 100	Ca Kα (3.69 keV) (I_{Ca}/I_{Mn}) X 100
13	1.80	28.8	51.5
25	.97	22.2	51.3
64	.18	12.1	49.4
140		2.35	44.4
190		.90	41.1
270			35.1

In order to determine the sensitivity of this technique to the source-target-detector geometry, relative intensity measurements were made at several different source to glass target distances and several different source-to-glass target distances and several different target to detector distances. Maximizing count-rate is useful because runs of several hours are needed to produce accurate results. This may obviously be accomplished by moving the ^{55}Fe source or the detector closer to the glass target.

The effect of source to target distance on count-rate is shown by curve b in figures 5, 6, and 7. Count rate increases as this distance decreases until a maximum is reached at 7 mm. As the distance decreases beyond this point, the rate drops rapidly because of the source structure which begins to block the radiation path.

The effect of source to target distance on the intensity of the Ca, Si, and Mg Kα lines as normalized to the Mn Kα line is shown by curve a in figures 5, 6, and 7. This value, of course, is the actual window attenuation index times 100. Since the index is sensitive to the source to target distance, this distance needs to be specified in the standard, and a value of 8 mm has been proposed. Nevertheless, the rate of change of the index with this distance is not so great that small errors in source position would appreciably affect the results.

The effect of changing the glass to detector distance is shown in Table 2. Within the range of distances used, there is very little effect on the normalized intensities of the various peaks. Of course some effect here is actually expected, but if the solid angle which the detector makes with the glass source is kept smaller than it is for any case shown in Table 2 (where the detector diameter is 4 mm), no significant effect on the measured window attenuation index is evident. An appropriate limitation is a specification that the glass to detector distance be at least 10 times the active diameter of the detector.

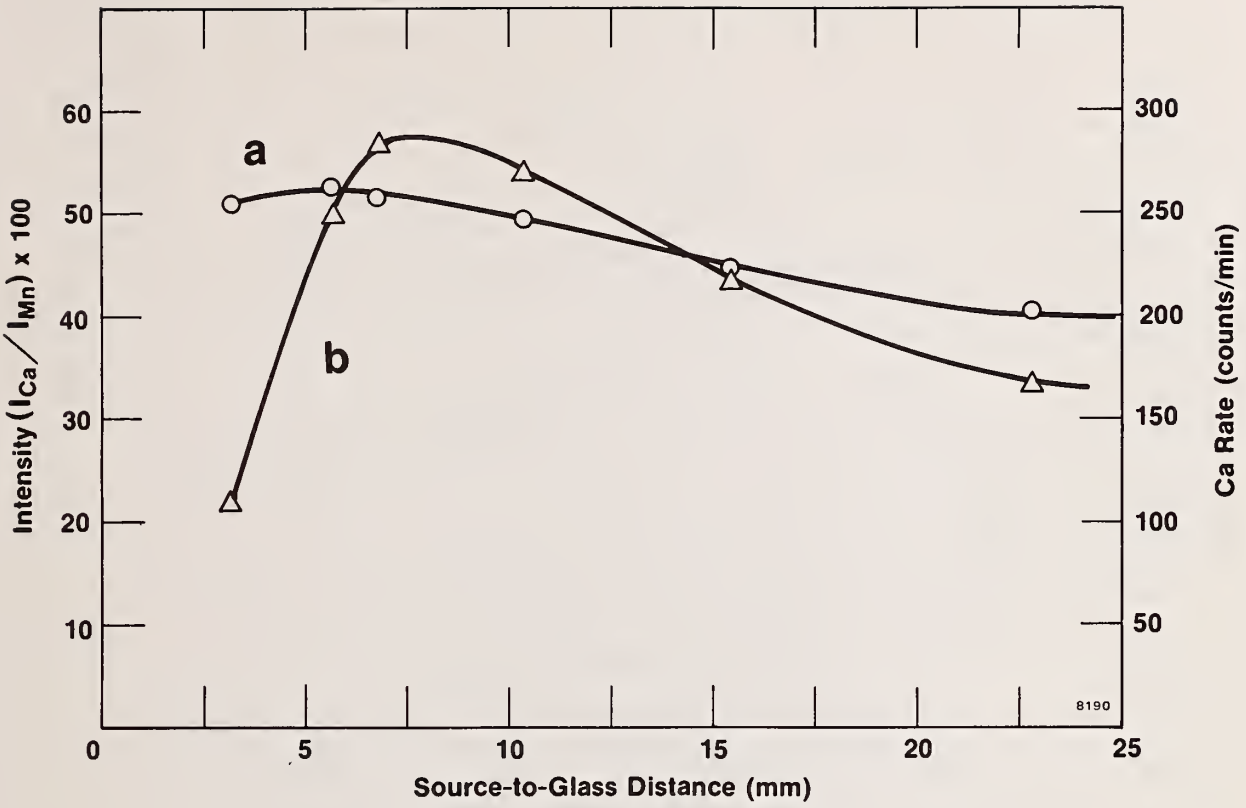

Figure 5.

a) **Intensity of Ca Kα Line as Normalized to the Mn Line and Plotted as a Function of Source-to-Glass Distance.**

b) **Count Rate of Ca Kα Line as a Function of Source-to-Glass Distance.**

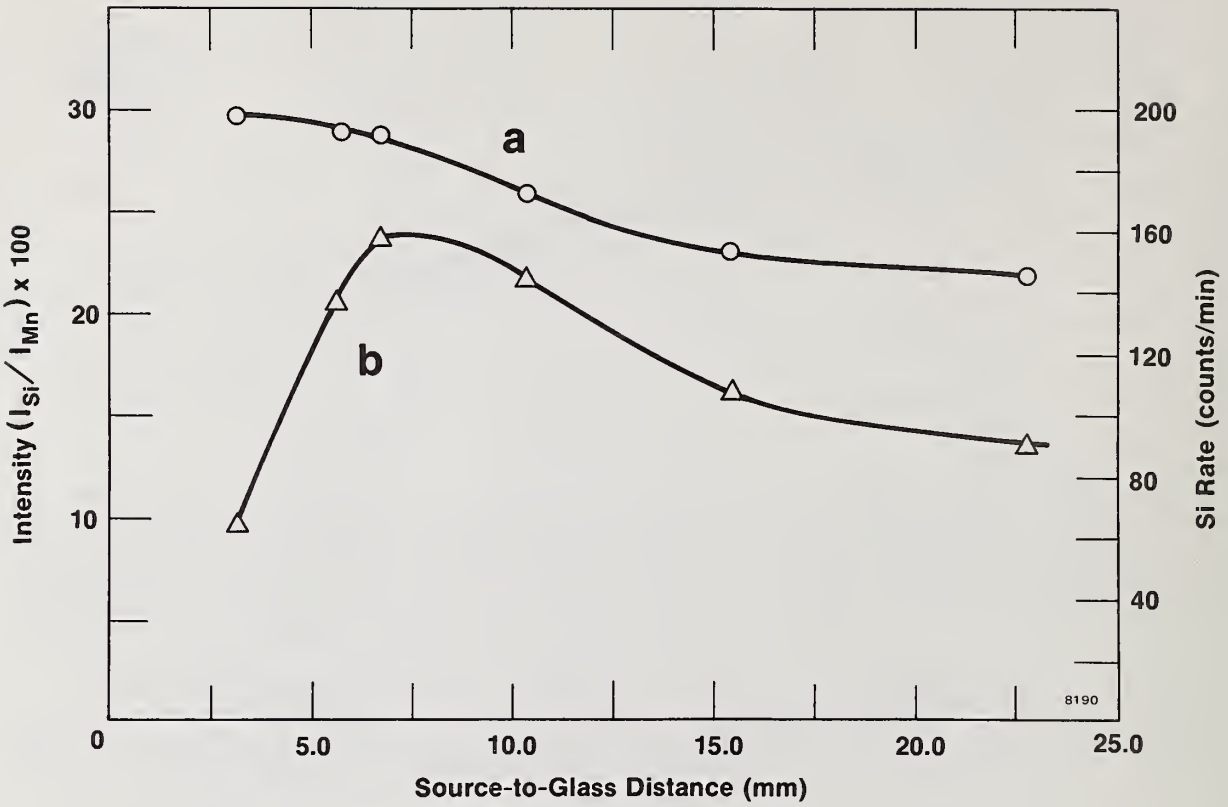

Figure 6.

a) **Intensity of Si Kα Line as Normalized to the Mn Line and Plotted as a Function of Source-to-Glass Distance.**

b) **Count Rate of Si Kα Line as a Function of Source-to-Glass Distance.**

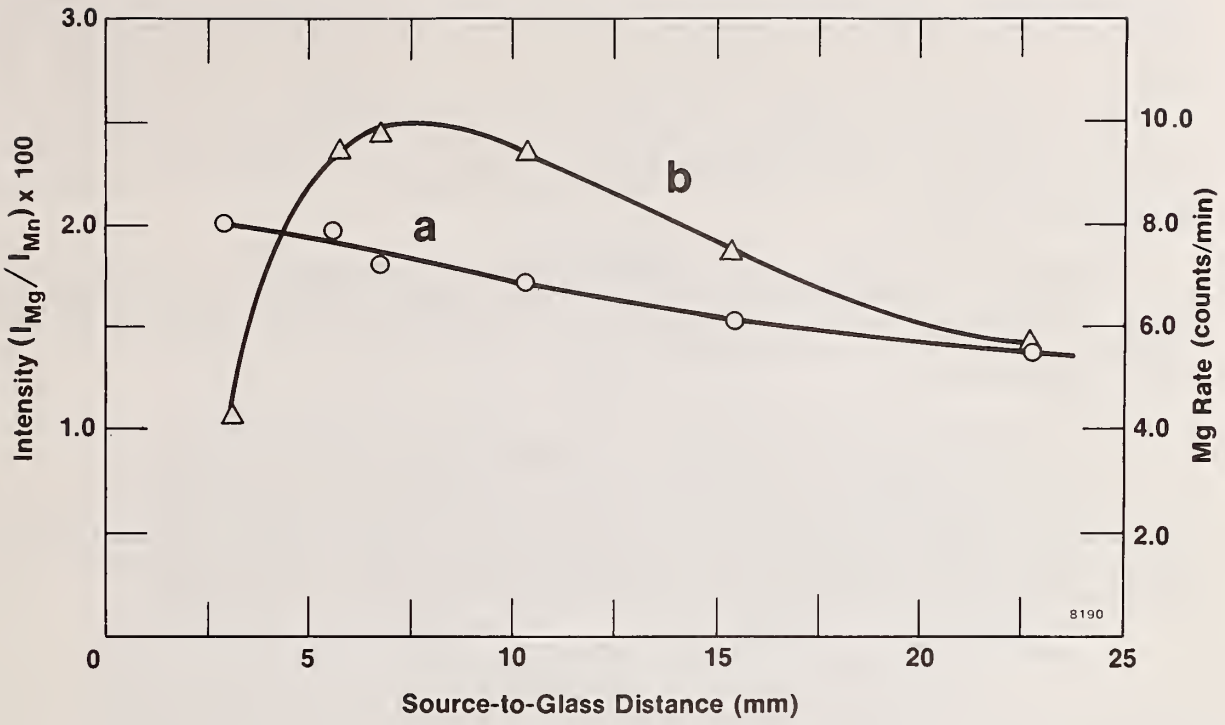

Figure 7.

a) Intensity of Mg Kα Line as Normalized to the Mn Line and Plotted as a Function of Source-to-Glass Distance.

b) Count Rate of Mg Kα Line as a Function of Source-to-Glass Distance.

Table 2. The effect of glass to detector distance on relative peak intensity normalized to the 5.9 keV Mn Kα peak.

Glass to detector Window Distance (mm)	Mg Kα (1.25 keV) (I_{Mg}/I_{Mn}) X 100	Si Kα (1.74 keV) (I_{Si}/I_{Mn}) X 100	Ca Kα (1.69 keV) (I_{Ca}/I_{Mn}) X 100
60.2	1.80	28.8	51.5
52.8	1.81	27.9	52.0
46.3	1.93	28.8	52.9
39.8	1.89	28.5	52.8
33.1	1.89	29.1	51.9
Probable Error	±.20	±.4	±.5

Conclusions A "window attenuation index" based on the relative detected intensities of x-rays from NBS SRM 477 fluoresced by an annular ^{55}Fe source is a sensitive, cost-effective, reliable and simple method for characterizing the low energy efficiency roll-off from window attenuation in semiconductor x-ray energy spectrometers. This technique does not require detailed knowledge of the interior of the spectrometer and does not require corrective calculations for source age (i.e., it is independent of the activity level and age of the source), internal absorptions, etc. Because of the straightforward nature of the measurement, there should be relatively little debate about how the results should be interpreted or compared.

Although this technique is in principle sensitive to the geometry of the measurement, the cylindrically symmetrical configuration and relatively small solid angles employed result in a configuration that is satisfactorily insensitive to small errors in geometry. The SRM 477 glass target is very uniform, very chemically stable in normal ambients, and highly reproducible.

2. Summary

A standard technique for measuring window absorption and other efficiency losses in semiconductor x-ray spectrometers is described. This technique has been proposed as an IEEE and IEC standard. Measurements are reported which have been used to establish limits on the geometry of the technique and to establish the effectiveness of the method.

This study was made possible through the continued support of L. Costrell and K. F. J. Heinrich of the National Bureau of Standards in the development of SRM-477.

The authors would like to thank T. Raudorf and M. Martini for their assistance with this manuscript.

National Bureau of Standards Special Publication 604. Proceedings of the Workshop on Energy Dispersive X-Ray Spectrometry held at NBS, Gaithersburg, Maryland, April 23-25, 1979. (Issued March 1981)

USE OF WINDOWLESS DETECTORS FOR ENERGY DISPERSIVE LIGHT ELEMENT X-RAY ANALYSIS

J. C. Russ and A. O. Sandborg

EDAX Laboratories
P. O. Box 135
Prairie View, Illinois 60069

Abstract

Energy-dispersive Si(Li) detectors can be used to efficiently detect soft x-rays in the 0.2 – 1.5 keV (C K – Al K) range by removing the Be window normally used to isolate the detector from the microscope vacuum. This requires some hardware changes to protect the detector from contamination, electrons, and light. Normal high energy performance of the same detector is nor compromised in most cases. Analysis of elements in this range in concentrations from about 0.5 percent up is practical for many samples; examples and exceptions are noted. The spectrum appearance in this range is not easily handled by the techniques routinely employed at higher energies, and in any case conventional quantitative (ZAF) methods are nor readily used for these elements.

1. Introduction

The energy-dispersive method of x-ray analysis on the electron microscope has generally been limited in three aspects, in comparison with the wavelength-dispersive electron microprobe: resolution, count rate, and ability to analyze the light elements. The resolution of energy dispersive detectors has been gradually improved, but will never challenge the diffracting crystal; fortunately computer stripping methods have become widely used and in many cases give satisfactory separation of peaks not resolved by the detector itself. Similarly, improvements have been made in count rate handling capability, particularly in the prevention of spectral distortion at high rates; the continuing use of smaller beams and thin sections has shifted much of the emphasis from the ability to handle high count rates, to the use of very large detector solid angles to get acceptable results in inherently low count rate situations.

At the same time, work has progressed in the detection of the light elements: carbon, nitrogen, oxygen, and fluorine. First, detection was demonstrated with a windowless detector [1][1]. Then a commercially available detector was offered that could be used to detect and even analyze these elements semiquantitatively [2,3]. Further progress has now refined the detector design so that good routine operation is possible with minimum sacrifices in other desirable features, while at the same time a body of experience has been accumulated that can be used to assess the practical capabilities that such a detector provides.

2. Mechanical Design

After some evolution, the design of current detectors (see figures 1-4) is compact, positive in operation, and interlocked for safety. The windows are carried on an outer cylinder, concentric with the vacuum cylinder housing the detector and FET preamplifier. The outer tube is rotated to one of three detent positions to align the standard beryllium window, an aluminum-coated Formvar window, or an open hole, into place in front of the detector. When the beryllium window is in place, it is sealed by an O-ring around its edge, by retracting the outer tube about 1 mm. The mechanism to rotate or seal the windows

[1]Figures in brackets indicate the literature references at the end of this paper.

is external to the vacuum and positive in operation. When a positive seal is made, it is locked to prevent accidental leaks. Only then does the remote indicator (normally mounted next to the microscope vacuum system controls and/or electrically connected to them) show that it is safe to vent the chamber.

Because the unit is compact in size, the mounting flange can be adapted to many SEM's (minimum port size 5 cm). The mounting bracket is extensible (figure 2) so that the front end can be moved close to the sample. The magnetic electron trap and cryo-trap against detector contamination take up some space in front of the detector, placing the front surface of the silicon 24 mm behind the outer end of the tube. For a 10 mm^2 detector, this gives a solid angle of 0.00824 steradians, for a sample 3 mm from the end cap. The internal hardware is designed to assure excellent collimation and eliminates stray radiation from the pole pieces, the specimen stage, etc.

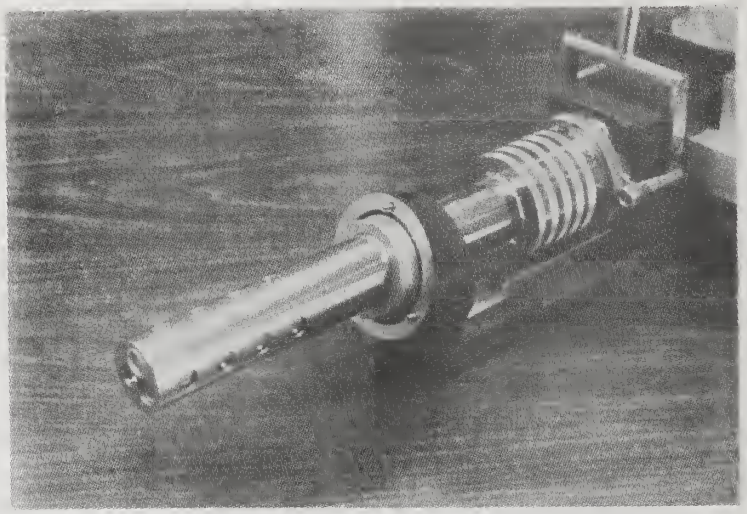

Figure 1. Rotating outer barrel holds windows, and is moveable from outside the vacuum chamber.

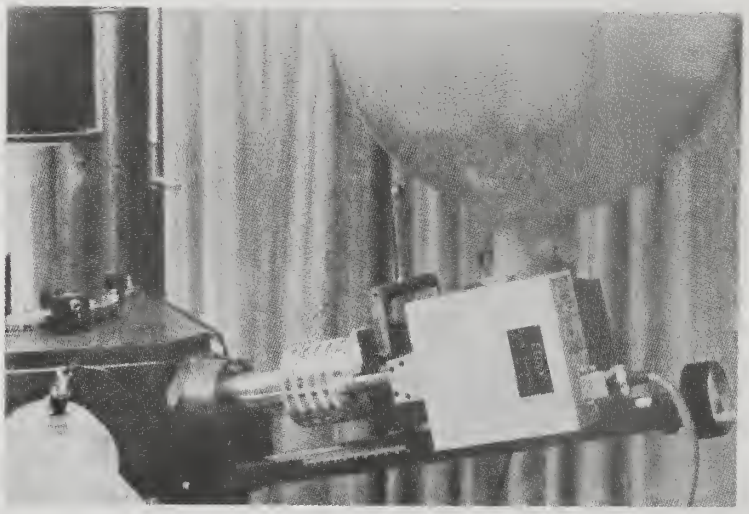

Figure 2. Extensible mounting provides close specimen-to-detector positioning. Window controls are readily accessible.

Figure 3. Organic window mounted on an aluminum ring, held in place with an easily removed c-clip.

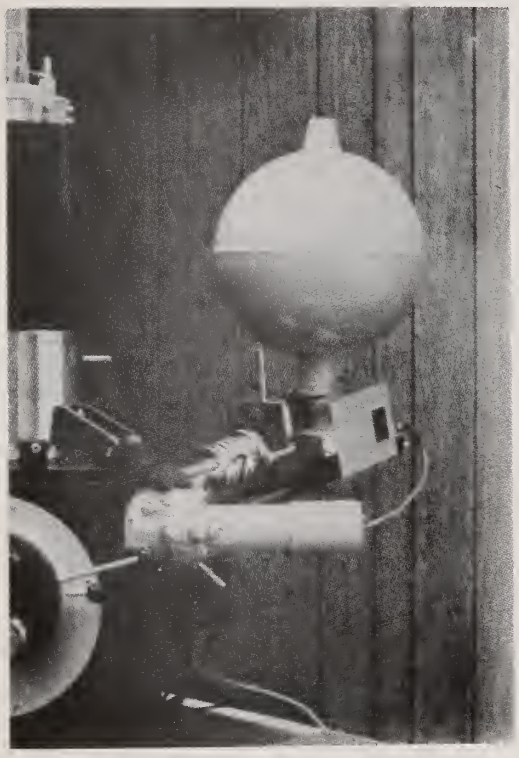

Figure 4. Complete detecting unit, with 10 liter Dewar and unitized amplifier.

The aluminized Formvar window is easily replaced by the user, while the cryostat remains sealed by the standard beryllium window. Depending on the particular SEM design and the access to the chamber, in many cases window replacement is possible without removing the detecting unit from the microscope. The window is mounted on an aluminum ring, held in place by a "C" clip (figure 3). The user can replace the window either to use a different organic polymer (to minimize absorption for a particular light element, or minimize permeability when samples outgas water heavily) or to use different coating thicknesses (as dictated by the cathodoluminescence of samples). In any case these organic windows age in vacuum and should be replaceable by the user whenever needed. The organic window will not withstand a one-atmosphere pressure differential.

3. Low Energy Efficiency

Removing the beryllium window from the front of the detector eliminates a major absorber of low energy x-rays, but not all the absorption. Figure 5 shows the efficiency of the detector as a function of energy, for the standard 7 μm beryllium window and without a window. The gold contact of the surface, and the inactive silicon near the surface, still produce a drop at low energies. An additional loss in detection efficiency at very low energy that limits the sensitivity for light elements is due to absorption of the x-rays within the sample itself. Accordingly, this absorption should be minimized by the use of as high an x-ray takeoff angle as practical. By comparing spectra measured with the window removed, with the aluminized Formvar, and the beryllium window in place, we can directly compare the improvement in light element sensitivity. Figures 6 and 7 show spectra measured on cryolite (predominantly Na_3AlF_6, with a small amount of SiO_2). The increase in sensitivity for the lower-energy peaks is apparent; it can be more readily compared in terms of the estimated minimum detection limit. Neglecting the effects of matrix absorption or peak interferences, we can express this as,

$$C_{MDL} = 3\sqrt{B}\ C_{STD}/P$$

where P and B are the net peak intensity and background intensity, C_{STD} is the concentration of the element in the sample and the 3 indicates that a peak three times greater than the standard deviation of the background is required for detection. These values are not always good guides to actual detection limits in a given sample, but show the relative variation due to the window removal. Using data measured on the cryolite sample for 200 seconds at 6 kV, a 30 degree surface tilt, and 57 degree takeoff angle, the following calculated results were obtained. The beam current gave 700 c/s in the total spectrum with the beryllium window in place; this rose to 2600 c/s with the window removed. (Figure 8.)

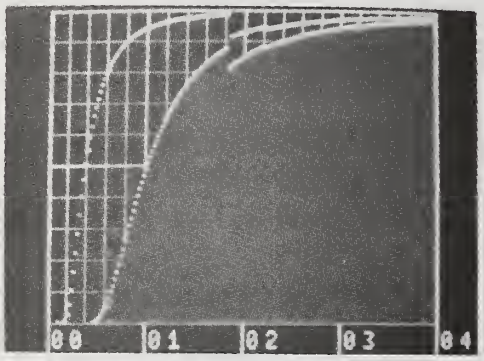

Figure 5. Low energy efficiency (100% full scale) for standard 7 μm beryllium window and windowless detecting units.

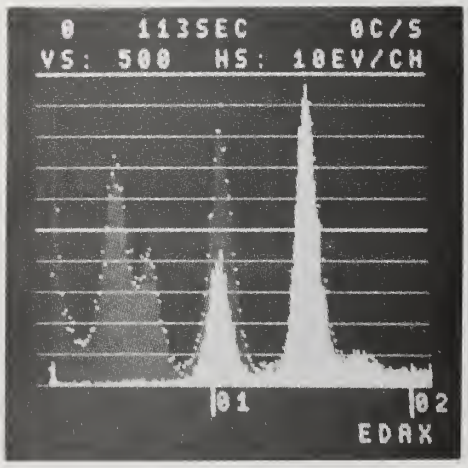

Figure 6. Cryolite with standard beryllium window (solid) and no window (dots).

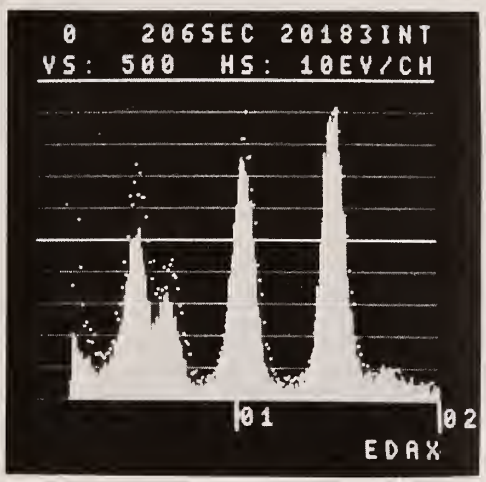

Figure 7. Cryolite with no window (dots) and aluminized Formvar window (solid).

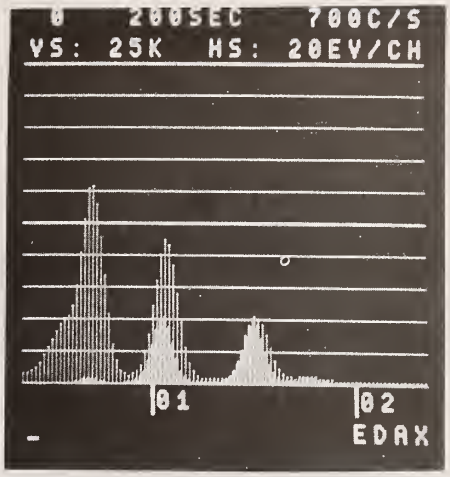

Figure 8. Spectra used for M.D.L. calculation (see text).

	Be Window	Formvar	No Window
Al	0.10%	0.08%	0.08%
Na	0.18%	0.13%	0.11%
F	2.50%	0.18%	0.15%

For the 1.5 keV Al K x-rays, the removal of the window does little to increase sensitivity, while for the 0.67 keV F K x-rays, more than an order of magnitude improvement is observed.

For the light elements O, N, and C, detection limits can be calculated in the same way from samples such as minerals, metals, carbides, or other stoichiometric compounds. Generally these numbers are not very accurate when extrapolated to low concentrations, but serve as a rough guide to practical expectation and illustrate the effect of the Formvar window.

	Formvar	No Window
O	0.2%	0.2%
N	0.5%	0.5%
C	0.6%	0.5%

4. Problems of Peak Identification

The energy-dispersive x-ray peaks at these low energies present a few problems for routine identification that are not normally encountered at higher energies. Line identification is complicated by the presence of interfering peaks from other elements. Figure 9 shows a spectrum from an alloy steel, with the window in place and open. The large Cr L and Fe L peaks are evident (.57 keV and .71 keV, respectively) and the cursor marks the smaller Ni L peak (.85 keV). It is likely that this particular sample is partly oxidized on its surface, but no oxygen K peak (.53 keV) can be seen as it is completely obscured by

the other peaks. The shape of these peaks is too complex for practical stripping, both because the detector response for these low energies is not perfectly Gaussian due to incomplete charge collection (the low energy incident x-rays are absorbed very near the detector surface, where imperfect lithium compensation of the silicon produces an inactive, or partially inactive layer of material), and due to the presence of many overlapped individual lines.

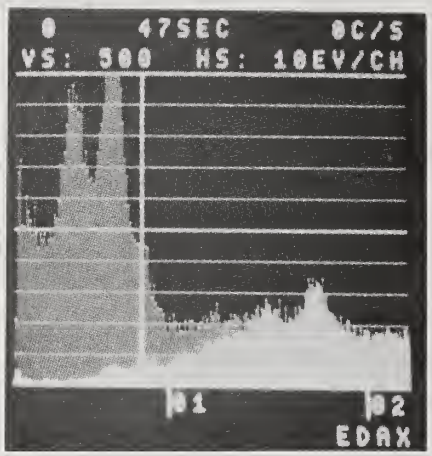

Figure 9. Stainless steel (see text) with beryllium window (solid) and without window (dots).

An additional complication in the low energy spectrum is the presence of escape peaks from other, higher energy x-rays. Escape peaks result from the removal of energy from the detector in the form of a silicon K x-ray. The probability of exciting the silicon x-ray near the surface, where it can escape, is greatest for incident x-rays with energy just greater than the silicon K edge [4]. This produces an escape peak (energy equal to the incident energy minus the 1.74 keV silicon K energy) in the .2 - 1.5 keV range we are interested in. For example, figure 10 shows the escape peak from the analysis of pure sulfur (2.32 keV - 1.74 keV = 0.58 keV). The peak is easily mistaken for oxygen K, suggesting that some of the sulfur might be an oxide, but this spectrum was measured with the window closed! With the window open (figure 11) the background shape changes, but no additional peaks are seen. The small silicon peak (marker) is due to fluorescence of the inactive surface layer of silicon on the detector [5].

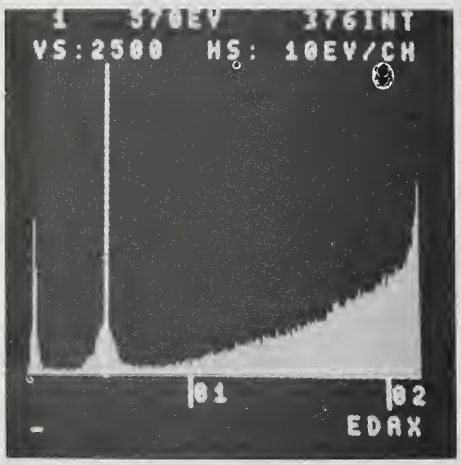

Figure 10. Escape peak from sulfur K x-rays (Be window in place).

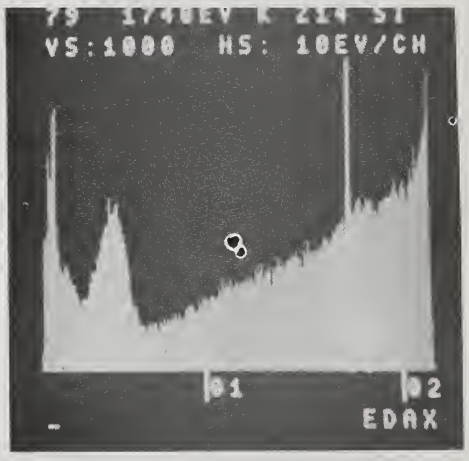

Figure 11. Sulfur "escape peak" and fluoresced silicon peak – window open.

Another artifact peak that can cause confusion can arise from pulse pile-up. If two x-rays enter the detector close together in time, their pulses add together in the amplifier producing a single pulse with a height that is the sum of the individual pulses. This produces a sum, or pileup peak in the spectrum. At higher energies these pileup peaks are suppressed by a special circuit in the amplifier that senses pulses and rejects ones that occur so close in time that they cannot be individually measured. The rejection circuit uses a very "fast" (short time constant) amplifier, which therefore has poor energy discrimination and misses the pulses from these ultra-low energy x-rays. Consequently, at all but the lowest count rates, pileup will occur at energies below 1 keV.

This is illustrated in figures 12 and 13 for the carbon peak. The two spectra shown in comparison were stored at total count rates of 200 and 1500 cps, to the same height of the K peak. The pileup peak (0.5 keV) is evident in both spectra, but is 2.5 times larger at the higher count rate. Figure 14 shows the same effect for the copper L lines (0.93 keV) at count rates of 200 and 1500 cps. The table below summarizes data for carbon (0.28 keV), oxygen (0.53 keV), and copper (0.93 keV) as a function of count rate, and emphasizes the need to keep total count rates quite low when the best low energy results are required.

Ratio-sum peak to main peak

	200 cps	600 cps	1500 cps
C K	1.4%	1.9%	3.4%
O K	1.0%	1.4%	2.6%
Cu L	0.6%	1.0%	1.7%

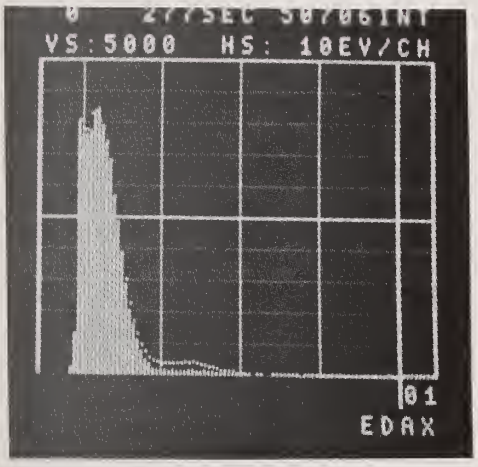

Figure 12. Carbon peak from pure graphite. Spectra recorded at different rates to same peak height.

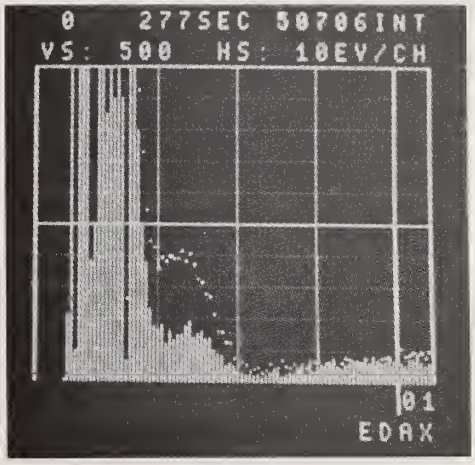

Figure 13. Size of carbon sum depends on count rate (see text).

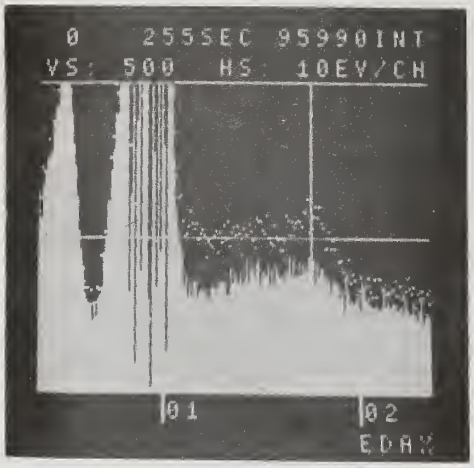

Figure 14. Pileup peak for copper L lines at 200 (solid) and 1500 (dots) cps. (same height main peak).

5. Sample Contamination

Another problem that may be encountered in trying to analyze light elements in samples is their presence as surface contaminants. These can be present before the sample is put into the microscope, or build up during analyses. For example, most metals have a thin layer of oxide that will give a significant peak. Some, like magnesium, oxidize so rapidly it is nearly impossible to prevent it from forming. Figure 15 shows the spectrum from freshly polished pure magnesium – the oxygen peak is evident.

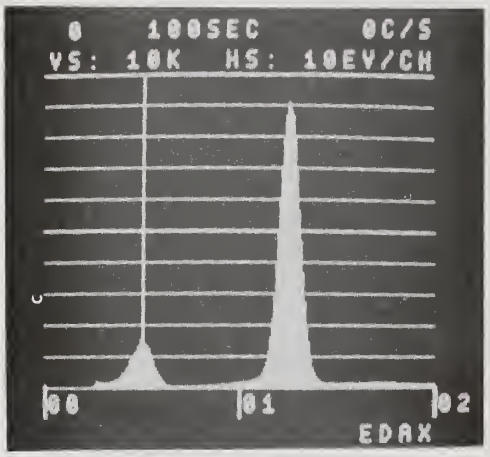

Figure 15. Oxygen peak from surface oxide on pure magnesium.

The polishing of samples itself can cause contamination as well. Figures 16 and 17 show pure copper. The small Si and C peaks are from the silicon carbide polishing compound used to remove oxide or other surface contaminants. The sample was cleaned before analysis in an ultrasonic cleaner, but some Si C particles remained. Similar problems with oil, fingerprints, bits of adhesive, etc., become far more evident when light element analysis is attempted.

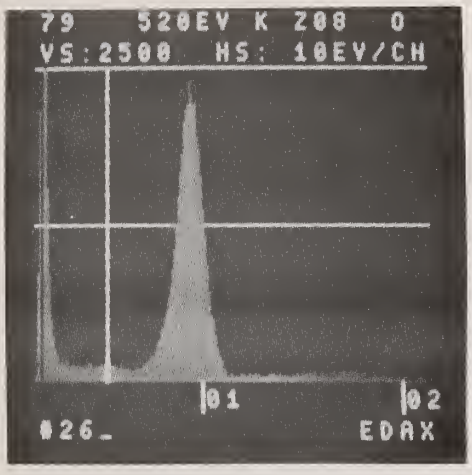

Figure 16. Trace oxygen is very small on freshly polished copper.

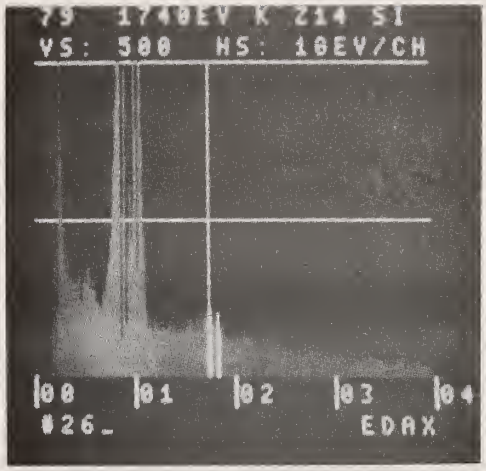

Figure 17. Silicon and carbon peaks on freshly polished pure copper, due to polishing compound.

Even assuming the sample makes it into the microscope "clean", contamination can build up with time under the electron beam. This is partly a function of the microscope vacuum system – the degree of trapping to prevent oil backstreaming from pump, etc. But a more significant effect is usually sample-related – the outgassing or volatilization of the specimen produces contaminant molecules near the surface that are readily deposited on it and largely independent of the SEM vacuum system. In its simplest case, this type of contamination is usually carbon rich. Figure 18 shows two spectra measured on a pure aluminum stub, one when it was first introduced and the second after the beam had been on it, scanning in a small raster, for 15 minutes. The buildup in C is apparent. Other types of complex samples, or the adhesives used to attach them, can produce exotic combinations of contaminant elements.

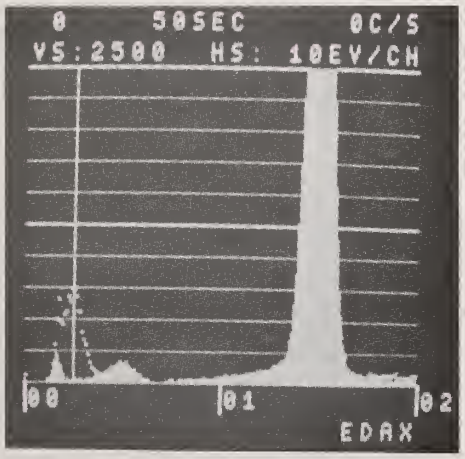

Figure 18. Carbon contamination peak on pure aluminum after exposure (compared to original spectrum).

6. Removing Background at Low Energies

A critical step in any quantitative analysis or trace element analysis is accurately subtracting the spectrum background. In conventional spectra the high energy region, above about 3 keV, is generally simple, while the region from 1-3 keV where the background varies more rapidly presents greater problems. Since the use of a windowless detector "straightens out" this region so that it continues to rise, this might be expected to simplify things. Two questions need to be answered, 1) is there any change in the use of background

subtraction methods in the 1-3 keV range? and 2) do these methods also work at energies below 1 keV (where the background is partly from Bremsstrahlung generated in the sample and partly electronic noise)?

Figures 19-20 show spectra measured on a graphite stub containing a small amount of sulfur (and traces of Si, P, and V). With the window closed, standard spectra were obtained with the characteristic sharp drop in background. Good results in fitting background, detecting the trace peaks, and getting the net peak areas, are provided by calculation methods (figure 19) [6,7].

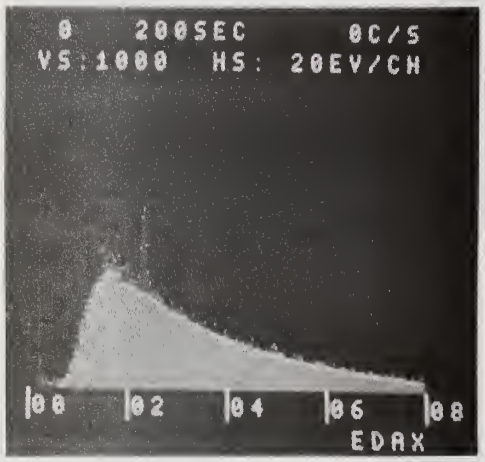

Figure 19. Calculated background, normal window.

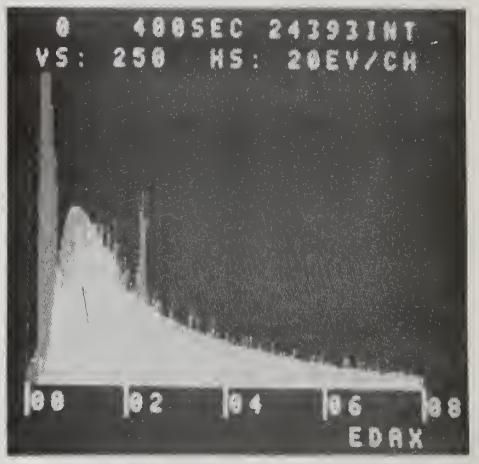

Figure 20. Calculated background, no window.

When the detector window is removed the shape of the background changes, continuing to rise to below 1 keV and then dropping. The calculation method (figure 20) ignores the electronic noise under the carbon peak and errs on the continuum in the 0.5 - 1 keV region. This is probably due to inadequacies in the present models for continuum generation, particularly at these very low energies. (The models assume the absorption of continuum x-rays is the same as for characteristic x-rays, or in other words that their depth of generation is the same. For very low energies this is clearly not the case since the continuum x-rays are generated deeper in the sample, toward the end of the electron path and are therefore subject to more absorption.)

Since the calculation method is widely used for handling general quantitative calculations, it is important to see how well it works for light element peaks. Figure 21 shows spectra measured on the cryolite sample used previously for illustration. Figures 22 and 23 show the calculated backgrounds, illustrating the large absorption edges that become increasingly significant at low energies. Figures 24 and 25 show that the calculated backgrounds fit quite well to the spectra and give far more accurate net peaks (figures 26 and 27) than any interpolation or fitting method can achieve. Examples of quantitative results for oxygen using this approach will be shown below. For carbon, a separate fitting and subtraction of the zero-energy noise peak should be made first, or other more empirical background fitting methods employed.

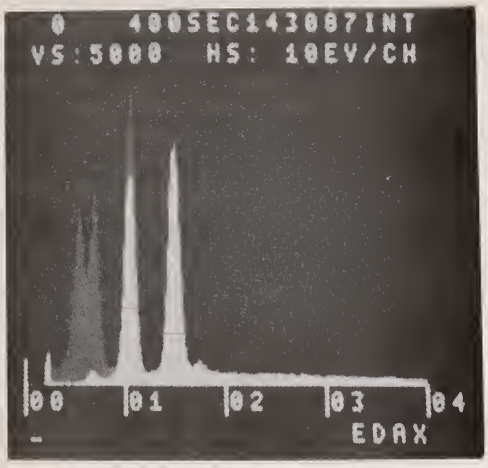

Figure 21. Cryolite spectra, with standard window (solid) and without window (gray).

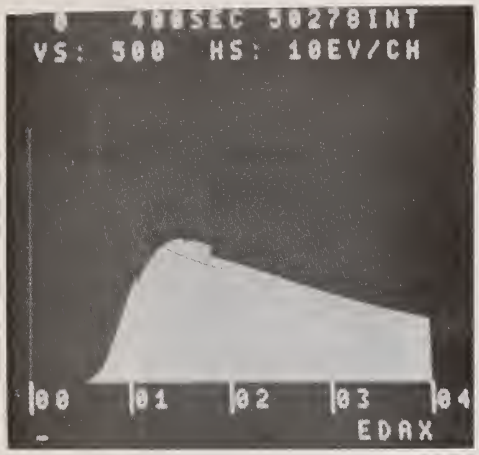

Figure 22. Calculated background with standard window.

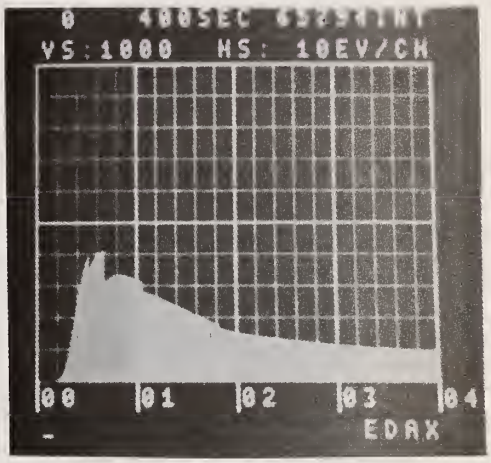

Figure 23. Calculated background for windowless detector.

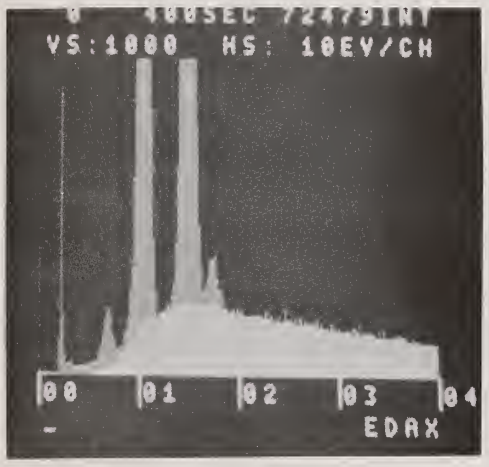

Figure 24. Comparison of spectrum and background.

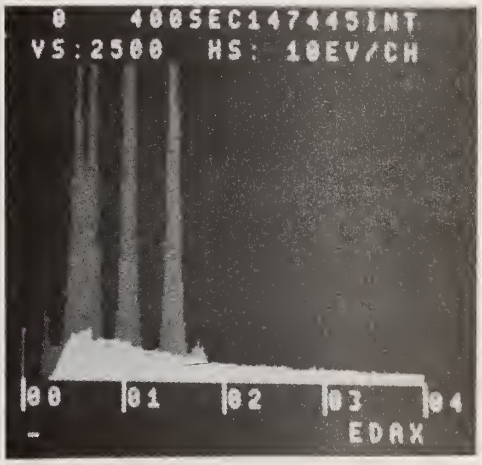

Figure 25. Comparison of spectrum and background.

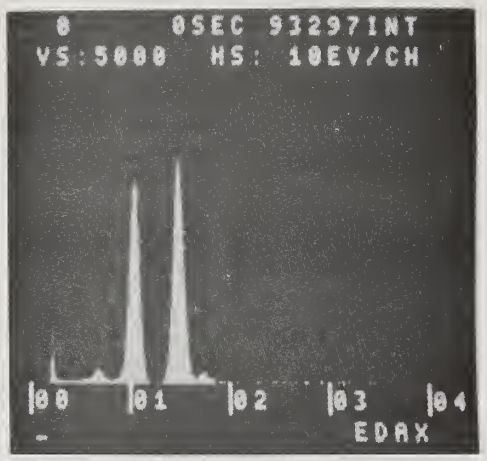

Figure 26. Net peaks for standard window.

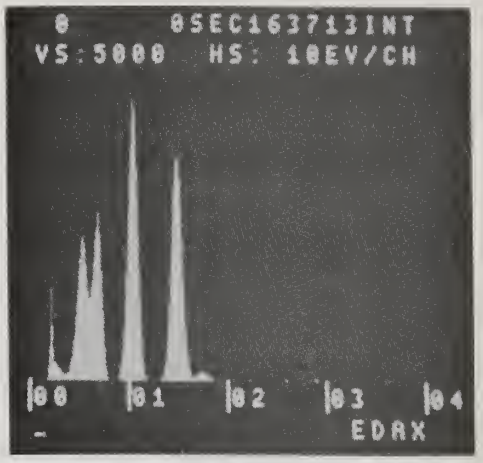

Figure 27. Net peaks for windowless detector.

7. Background from High Energy Electrons

In a conventional system, the beryllium window serves to stop electrons and light photons from reaching the detector. A standard 7 μm window can stop electrons up to about 25-30 keV. Higher-energy electrons still can penetrate to the detector, and cause high background in the spectrum at high energies [8]. This is usually prevented in the TEM by the magnetic field around the sample that prevents the scattered electrons from passing in a straight line through the collimator to the detector. In the SEM the sample is in field-free space and no such protection is available, but high voltages are rarely used with bulk material.

When the window is removed, we substitute a magnetic field as an electron trap, to deflect scattered electrons so they cannot reach the detector. This trap is also useful at high voltages even with the normal Be window in place, since some high energy electrons may not be completely stopped by 7-8 μm of Be. Figure 28 shows the effect of the trap in reducing electron background.

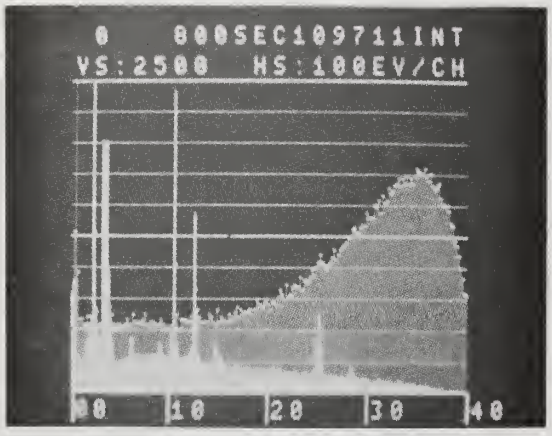

Figure 28a. Spectrum from solder (Pb-Sn alloy) at 50 kV. Dot spectrum shows electrons penetrating window, solid spectrum shows effect of magnetic electron trap.

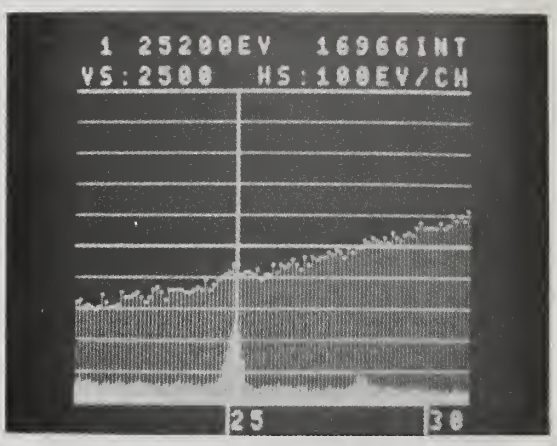

Figure 28b. Expansion of 30a around tin Kα line.

As a side note, it is interesting to use Si(Li) detectors as electron energy spectrometers as well as for normal x-ray work. By removing the magnet, the spectrum of x-rays plus electrons is recorded. When the trap is in place, the x-rays only are detected. The difference gives the energy distribution of the backscattered electrons. Figure 29 shows superimposed, the spectra (for a copper target) of x-rays plus electrons (upper curve) and x-rays only (lower curve), the latter obtained with the use of a magnetic electron trap in front of the detector. Subtraction then gives backscattered electron spectra as shown in figures 30a-30f. In each spectrum the caption shows the atomic numbers of the elements. In all cases the higher curve corresponds to the higher atomic number. The shape of the curves is in good qualitative agreement with the various published curves of predicted backscattered electron intensity.

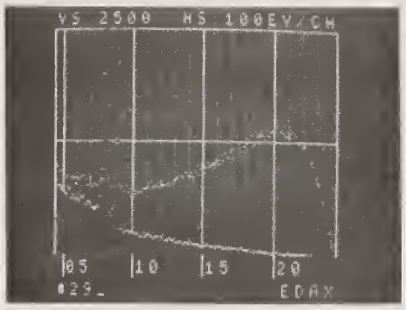

Figure 29. Copper spectra; top, electrons + x-rays: bottom, x-rays only.

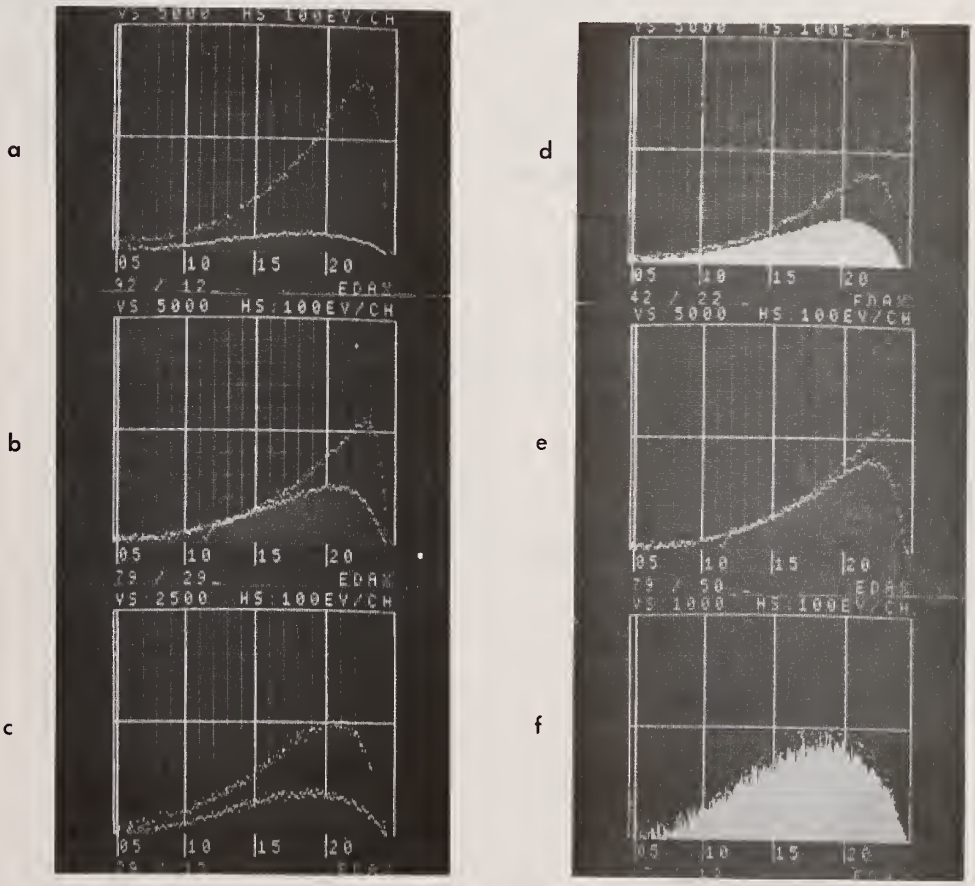

Figure 30. Backscattered spectra from: a) uranium, magnesium; b) gold, copper; c) copper, aluminum; d) molybdenum, titanium; e) gold, tin; and f) aluminum, magnesium.

From the figures, it is evident that there is the expected trend of increasing total backscattering (total area under the curve) with increasing atomic number. This can be discerned even for a difference of one Z number, as shown for magnesium and aluminum in figure 30f. The peak energy of the curve also rises with Z, since higher Z materials can turn electrons back through the surface with fewer scattering events, a shorter total path and less energy loss. Figure 31 summarizes the data for these measurements. The peak energy was determined from a polynomial fit to each spectrum. Both curves have the general trend expected from theory; that is, they rise with increasing atomic number.

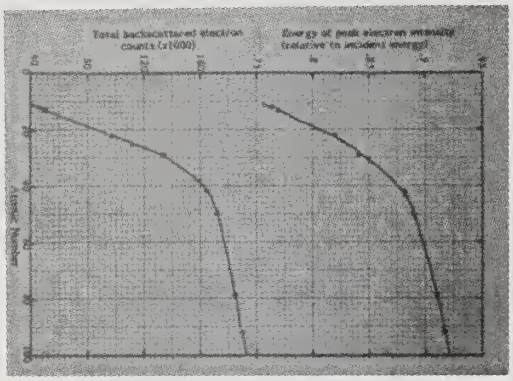

Figure 31. Total B.S.E. intensity (bottom) and peak energy (top).

These curves were measured with 24.8 keV electrons incident on a sample inclined at 20 degrees, and the detector at an angle 20 degrees above the horizontal (a total takeoff angle of 40 degrees). To study the effect of orientation, a copper target inclined at an angle of 45 degrees was rotated so that the detector was in the direction of tilt and 65 degrees from that direction. The backscattered electron spectra (figure 32a) show that the total backscattering is less at the 65 degree angle but the peak energy is higher. A similar effect is seen with perpendicular electron incidence on the copper target and changing takeoff angle (by raising and lowering the SEM stage). At a takeoff angle of 45 degrees there is more total backscattering than at 10 degrees, but at 10 degrees the peak energy is higher (figure 32b).

a

b

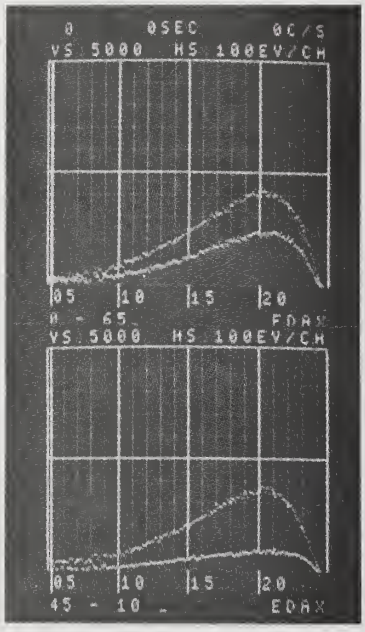

Figure 32. B.S.E. spectra from copper geometries described in text. (a) lateral angles (b) vertical angles.

Studies with other geometries, targets, and electron energies will be useful to supplement existing data on backscattered electron energies, and to confirm Monte Carlo models for electron scattering [9-11], as well as to develop optimized geometrical arrangements for backscattered electron detectors.

9. Cathodoluminescence

The detector must also be protected from light photons. Figure 33 shows what happens when light can reach the detector – the electronic noise in the preamplifier causes resolution to get worse, and peaks to shift. The sample is BeO, and the light is emitted under the electron beam. To keep these cathodoluminescence photons from reaching the detector, the aluminized Formvar window is moved into place. This window can also be kept in place to reduce the rate of contamination molecules entering the detecting unit when samples are being examined that may outgas.

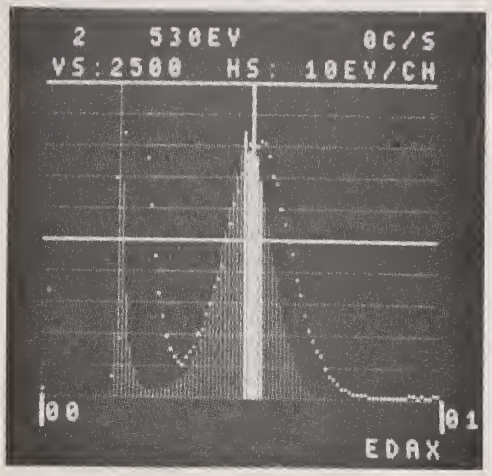

Figure 33. Spectrum from BeO with window open (dots) and with aluminized Formvar window (bars).

10. Analytical Results

Ultra-low energy peaks can be used in the same way as other peaks for x-ray mapping on the SEM. Figure 34 shows an example, maps for carbon and oxygen on an area of grey cast iron ingot mold. The oxygen around the graphite flake resulted from internal oxidation during service. The requirements for adequate peak/background ratios and numbers of dots must still be met for acceptable pictures.

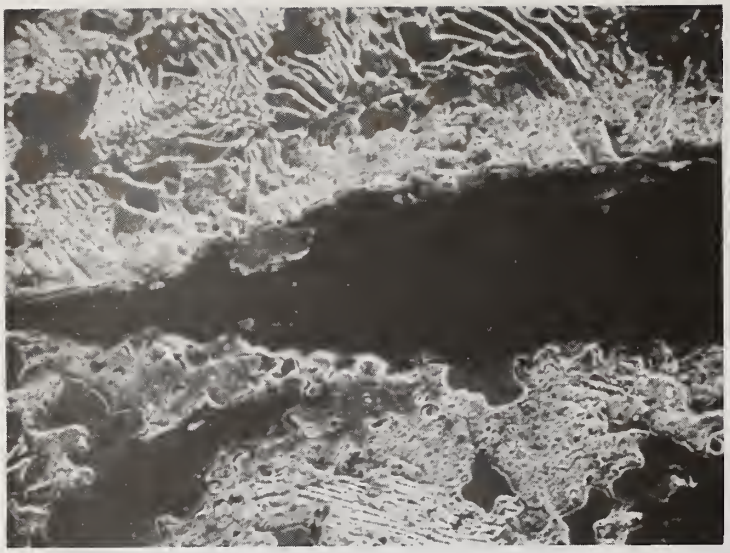

Figure 34a. Secondary electron image.

Figure 34b. Carbon Kα x-ray image.

Figure 34c. Oxygen x-ray map.

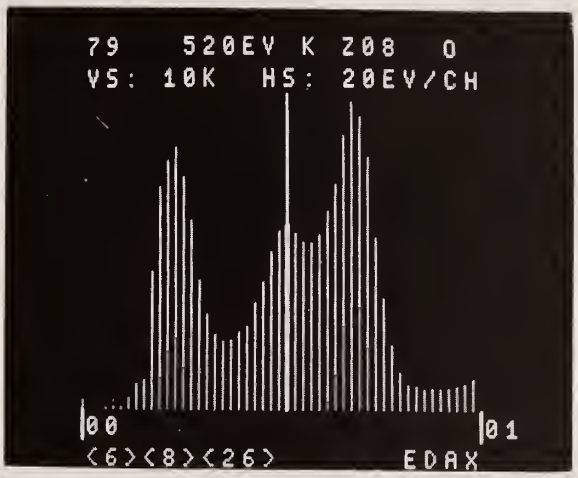

Figure 34d. Spectrum taken from scanned area on page 1.

A practical application for semiquantitative oxygen analysis is the measurement of oxide coating thicknesses (for instance, oxygen on semiconductors). The use of the intensity ratio of oxygen to silicon normalizes minor variations in surface finish or orientation, and gives a sensitive calibration curve as shown in figure 35. Ten percent accuracy is readily achieved using this simple approach [3].

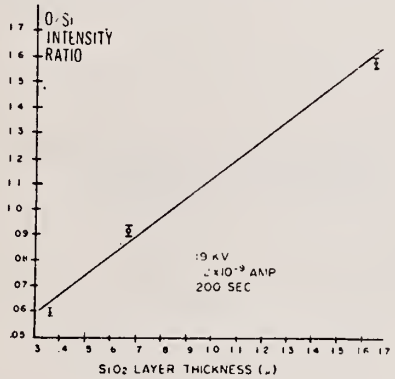

Figure 35. Calibration curve for oxide layer thickness.

11. Examples of Application

Another example of comparative analysis is the oxygen content of man-made Courtelle fibers [12,13]. Areas 2.5 μm square in the shell and core regions of 10 sections of fibers gave spectra such as shown in figure 36. The background was subtracted by fitting a Gaussian noise peak plus a constant. The ratio of net peak intensity to background under the peak was used as a measure of concentration. This ratio was 2.66 ± 0.52 in the shell regions, and 1.88 ± 0.25 in the core of the fibers. A similar measurement on a fiber with a uniform structure, independently analyzed as having an 8.4 percent oxygen content, gave a P/B ratio of 2.50. Using this as a standard gives a calculated concentration of 6.3 ± 0.8 percent in the core and 8.9 ± 1.7 percent in the shell.

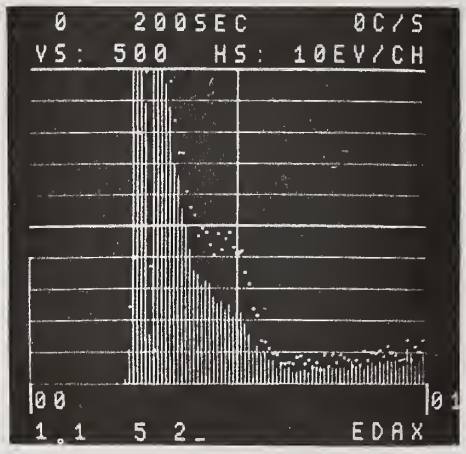

Figure 36. Comparison to show difference in oxygen between core (bars) and shell (dots) of Courtelle fibers (series A).

Another example of oxide analysis, showing ability to accurately discriminate different oxide forms, was carried out with oxides Fe_2O_3 and Fe_3O_4 (see table below). By analyzing the iron L and oxygen K lines, the two oxides can be distinguished (figure 37). The ratio of the two peaks, shown in the table, agrees closely with the calculated values using a full ZAF calculation [14]. The net intensities were obtained using the calculated background method (figures 38 and 39).

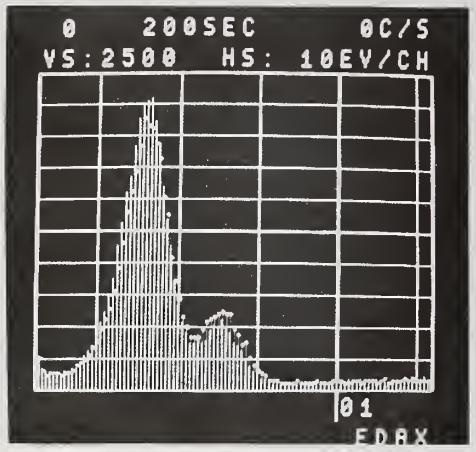

Figure 37. Comparison of spectra from Fe_2O_3 (bars) and Fe_3O_4 (dots).

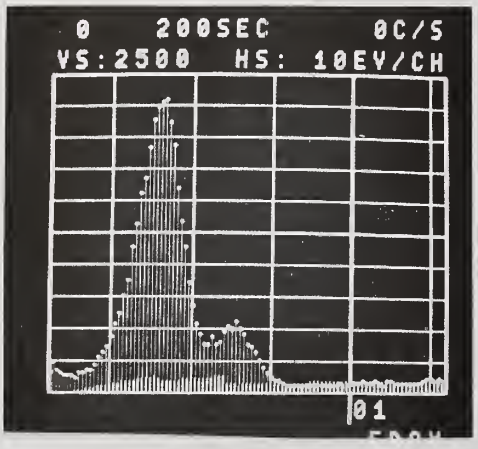

Figure 38. Spectrum and calculated background for Fe_2O_3.

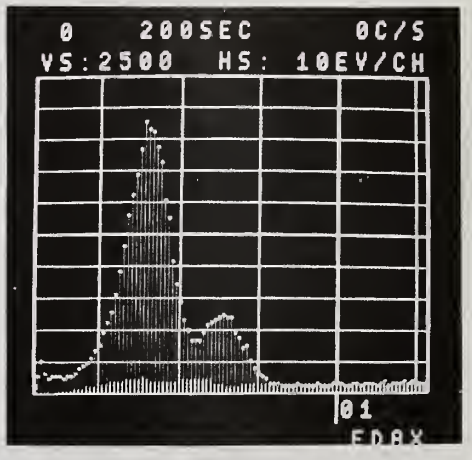

Figure 39. Spectrum and calculated background for Fe_3O_4.

Iron Oxide Analysis

Oxide	Element	Conc.	Intensity		
			Total	B.G. (calc.)	Net
Fe_2O_3	Fe	69.94	8324	1984	6340
	O	30.06	28581	2858	25723
Fe_3O_4	Fe	72.36	8073	2136	5937
	O	27.64	29427	2888	26539

Intensity Ratio Fe_2O_3/Fe_3O_4

Element	Measured	Theoretical
Fe	1.068	1.063
O	0.969	0.970

A fully quantitative oxide analysis was performed on a complex oxide containing SiO_2 and spinel ($MgO \cdot Al_2O_3$). The spectrum (figures 40 and 41) shows the peaks to be clearly resolved. Again, the background was calculated (figure 42) as part of the iterative quantitative analysis routine, simultaneously with the ZAF factors. The intensities are listed below.

Intensities on Oxide Specimen

Element	Actual Conc.	Intensity (400 sec.)		
		Total	B.G. (calc.)	Net
Mg	15.07	19723	2782	16941
Al	33.43	37083	2395	34688
Si	10.16	10063	2024	8039
O	41.34	48044	2349	45695

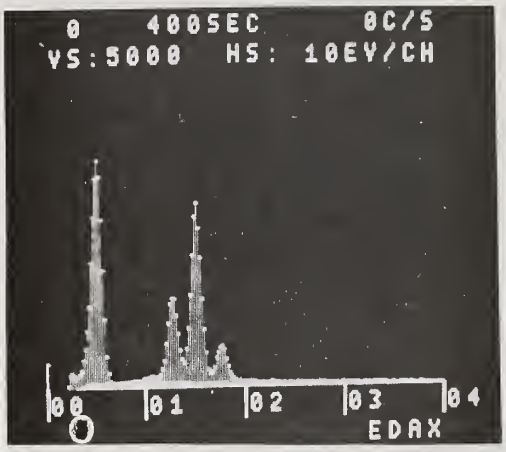

Figure 40. Complex oxide (silica and spinel) used for quantitative analysis.

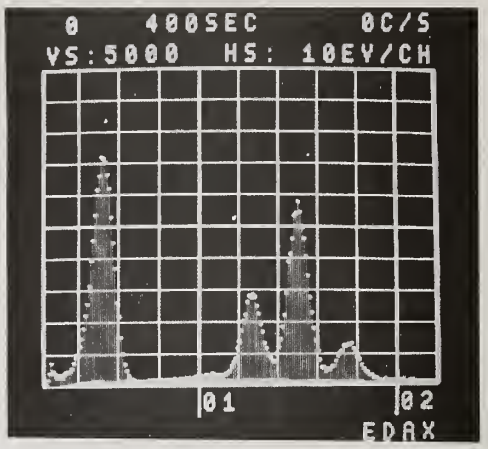

Figure 41. Oxygen, magnesium, aluminum, and silicon peaks.

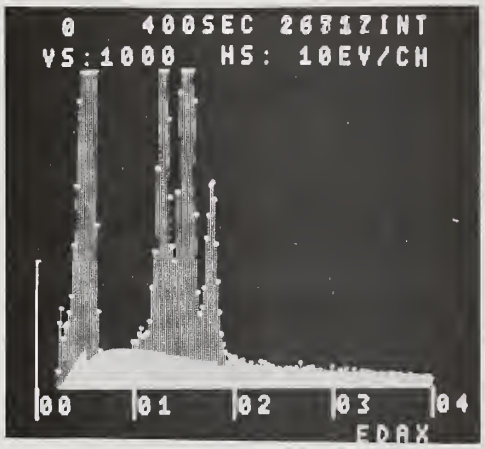

Figure 42. Calculated background for quantitative analysis.

As a standard for the analysis, pure SiO_2 was used. In this case the background was calculated directly since the concentrations were known. Then the ZAF factors were computed (again using the known concentrations) and used to calculate the pure intensities that would be obtained from theoretical pure element standards of silicon and oxygen.

Intensities on SiO_2 Standards

		Intensity (400 sec.)			
Element	Conc.	Total	B.G. (calc.)	Net	Calculated Pure Int.
Si	46.72	44934	2078	42856	97560
O	53.28	55057	2417	52640	73453

Then the theoretical pure intensities (P) of aluminum and magnesium were calculated using the expression

$$P\alpha\ (U-1)^{5/3}\ R(W\ L)\ T\ F/A$$

where
- U = overvoltage
- R = backscatter factor
- (WL) = fluorescence yield and line intensity
- T = spectrometer efficiency
- F = self absorption correction
- A = atomic weight

Using simple algorithms for these terms (which are in fact also needed in the calculation of the ZAF factors), and for the analysis conditions used (6 kV accelerating voltage, sample surface inclination 30 degrees, x-ray takeoff angle 40 degrees) we obtain the ratios,

$$P_{Al}/P_{Si} = 1.1263$$
$$P_{Mg}/P_{Si} = 1.3206$$

which gives us theoretical pure intensities for aluminum and magnesium (109876 and 128828 respectively).

Dividing these pure intensities into the net intensities gives K-ratios that are used in a conventional ZAF calculation, giving the results shown below. The estimated error shown for each element is based on the total statistical error introduced by background subtraction on both unknown and standard. Normalizing the total concentration to 100 percent further improves the results. Each of these various steps, shown here separately for clarity, are in fact carried out automatically by the program.

Quantitative Results

		Concentration-Percent		
Element	K-Ratio	Calculated	Normalized	Actual
Mg	0.1315	13.83 ±.24	14.06 ± .25	15.07
Al	0.3157	35.25 ± .50	35.83 ± .51	33.43
Si	0.0824	9.24 ± .17	9.57 ± .17	10.15
O	0.6221	39.89 ± .32	40.54 ± .33	41.34

Other examples of quantitative oxygen analysis with oxide standards have also been published. In all these cases of ZAF calculations for light elements, special care is needed to assure that the program used has models, particularly for energies, which extrapolate well to low energies. In the ultimate case, it may be necessary to directly enter from tables the best available parameters for mass absorption coefficient, etc., for the light elements.

A good example of this is the analysis of carbon in Fe_3C, measured in a spheroidized steel. The spectrum, shown in figure 43 (dots) had well defined Fe L and C K peaks, but there was also a small oxygen peak, due to oxidation of the polished steel by the metallographic etchant. This peak was removed by stripping away a manually generated oxygen peak (figure 44 bars).

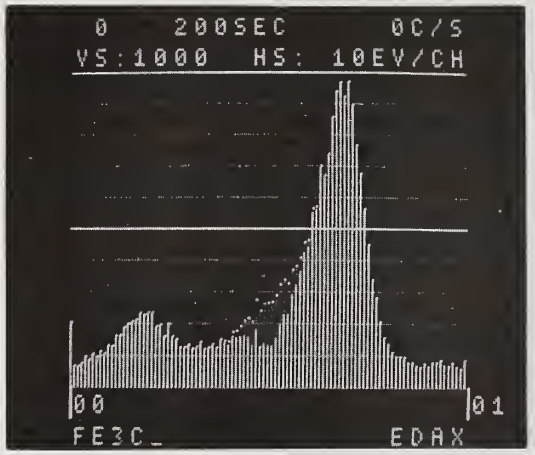

Figure 43. Removal of oxygen peak by stripping.

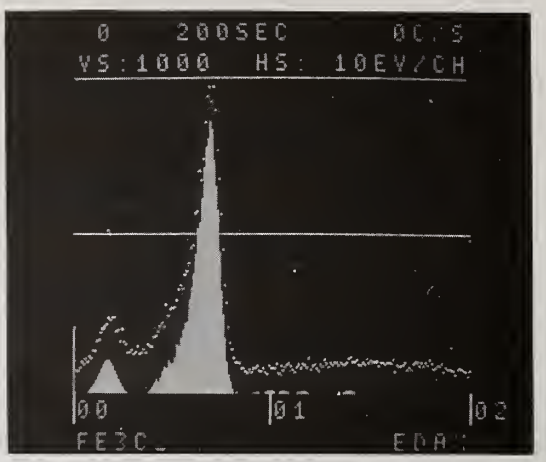

Figure 44. Subtraction of background from spectrum.

To obtain good net intensity values, a peak-generating routine was used to construct peaks for the iron and carbon (figure 45) which matched the measured peaks as closely as possible. It should be noted that these peaks may not lie at exactly the precise energies indicated by charts nor are they symmetrically shaped, and the generated peaks should be adjusted to fit the actual data, as judged by the remains after subtraction (figure 46). The net intensities are then taken as the areas of the generated peaks. The values, with statistical (one sigma) uncertainties, are:

Fe: 10272 ± 163

C: 1307 ± 75

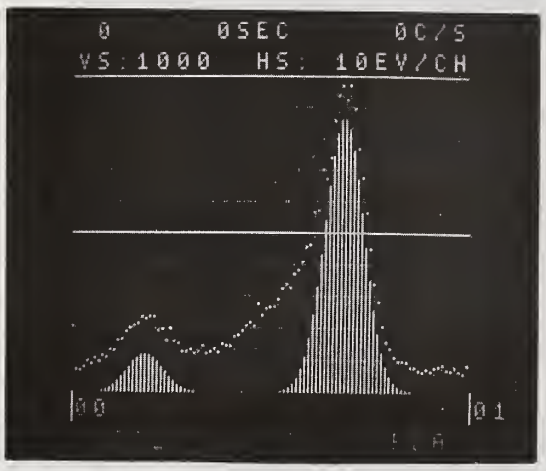

Figure 45. Constructed Fe and C peaks.

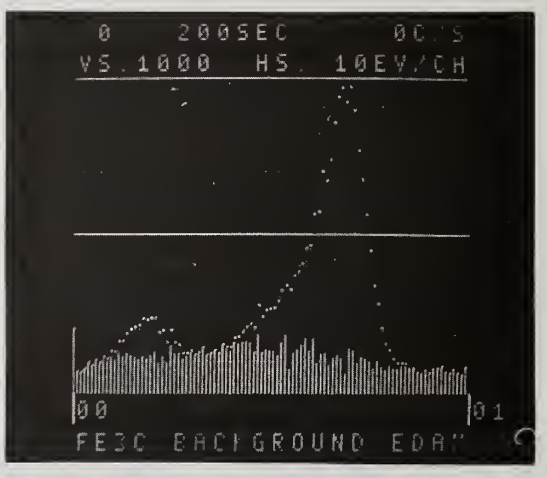

Figure 46. Background left after peak removal.

Standards consisting of pure electrolytic iron and a small diamond were analyzed under identical conditions (in fact they were mounted in the same holder and the stage controls used to bring them into view and into focus with no readjustment of the electron gun or lens settings). The standard spectra (figure 47) were used to obtain net intensities in exactly the same way, by generating peaks for iron (figure 48) and carbon (figure 49) that matched the measured peak, and then taking the total area of the generated peak. Again with statistical uncertainty, these standard intensities are:

Fe: 10454 ± 159

C: 13621 ± 184

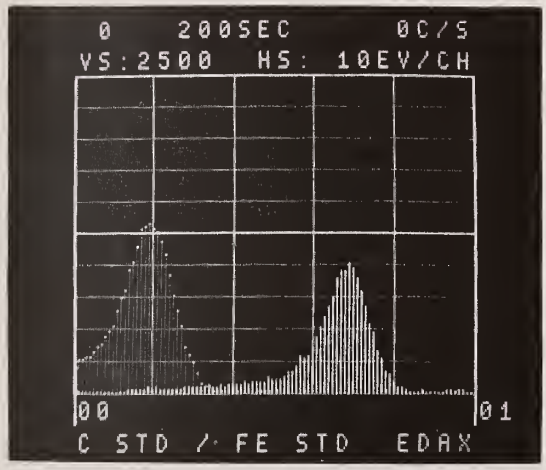

Figure 47. Carbon and iron standard spectra.

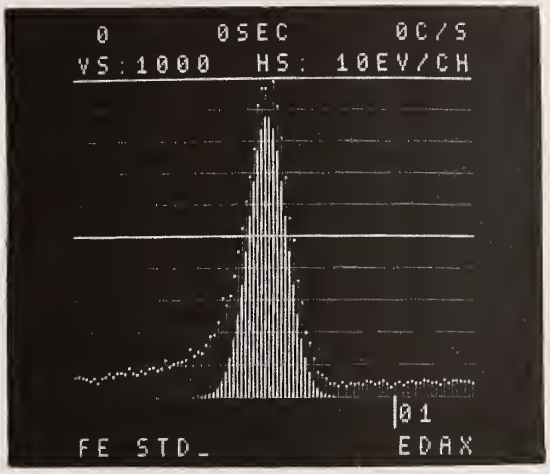

Figure 48. Fe standard spectrum with net pure Fe peak.

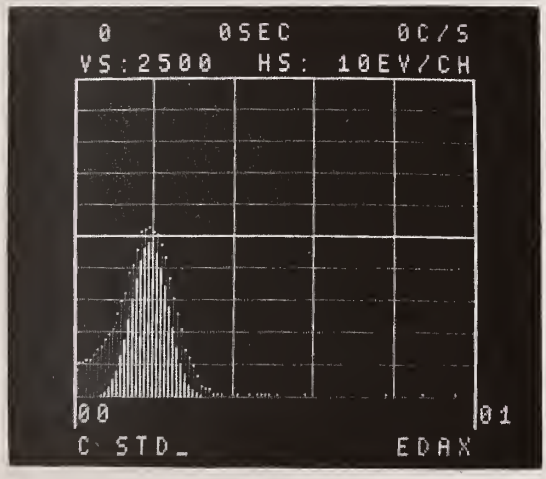

Figure 49. C standard spectrum with net pure C peak.

This gives K ratios, uncertainties, and relative errors for iron and carbon:

Fe: 0.98259 ± 0.02160 (2.2%)

C: 0.0959 ± 0.00566 (5.9%)

A modified ZAF program with tables of parameters for ultra light elements gives:

```
RUN
KV=? 6   S=? 16    T=? 20
ELEM(Z)            LINE            K-RATIO
? FE/ 26           ? L/ 2          ? 0.99259
? C /  6           ? K/ 1          ? 0.09574
? 0
ELEM(Z)            Z-CORR.         A-CORR.          F-CORR
26                 0.976144        1.07194          1.00592
6                  1.27816         1.15084          1.00058

ELEM(Z)            %
26                 93.0295
6                   6.50372
*READY
```

These answers, with the uncertainty due to the statistical errors above, are 93.0 ± 2.04 percent Fe, 6.5 ± 0.38 percent C which are quite close to the actual composition of Fe_2C (93.3% Fe, 6.7% C). This is partly due to choosing analyzing conditions which keep the Z, A, and F factors relatively near to 1.0.

12. Conclusion

The second-generation design of this removable-window detector assures reliable routine operation, and minimizes operating limitations by providing protection against electron, light photons and contamination molecules entering the detecting unit. The extensible design allows practical optimization of detector position.

The inherent limitations of ultra-low energy x-ray analysis must be understood by the user. They include problems of peak identification and sample preparation, but can be dealt with by intelligent operation and data interpretation. Count rate in the low energy region must be limited to avoid pile-up effects.

Practical analytical results, both qualitative and quantitative, can be obtained. Calculated backgrounds, possibly supplemented with an "instrumental noise" background, and either synthesized or measured and stored peak shapes can be used to deconvolute a spectrum provided severe overlaps are avoided. ZAF methods using appropriate standards and parameter values can yield good results.

References

[1] Jaklevic, J. M. and Goulding, F. S., "Detection of Low Energy X-rays with Si(Li) Detectors", Trans. Nucl. Soc., 187-191 (Feb. 1971).

[2] Barbi, N. C., Sandborg, A. O., Russ, J. C., and Soderquist, C. C., "Light Element Analysis on the Scanning Electron Microscope using a Windowless Energy-Dispersive X-ray Spectrometer", Proc. 7th SEM Symposium, 151-158 (1974).

[3] Barbi, N. C. and Russ, J. C., "Analysis of Oxygen on a SEM using a Windowless Energy-dispersive X-ray Spectrometer", Proc. 8th SEM Symposium, 85-91 (1975).

[4] Reed, S. J. B. and Ware, N. G., "Escape Peaks and Internal Fluorescence in X-ray Spectra Recorded with Lithium-drifted Silicon Detectors", J. Phys. E: Sci. Inst., 5, 582-584 (1972).

[5] Russ, J. C., "Erroneous Peaks in Energy Dispersive X-ray Spectra", 24th Annual EPASA (1972).

[6] Ware, N. G. and Reed, S. J. B., "Background Corrections for Quantitative Electron Microprobe Analysis Using a Lithium-Drifted Silicon X-ray Detector", J. Phys. E: Sci. Inst., 6, 286-288 (1973).

[7] Fiori, C. E., Myklebust, R. L., and Heinrich, K. F. J., "Prediction of Continuum Intensity in Energy-Dispersive X-ray Microanalysis", Anal. Chem., 48, 172-176 (1976).

[8] Russ, J. C., "X-ray Microanalysis at High beam Voltages", Proc. 9th Annual SEM Symposium (ed. by O. Johari), 134-140 (1976).

[9] Darlington, E. M., Ph.D. Thesis, Univ. Cambridge, 1971, cited in [10].

[10] Love, G., Cox, M. G. C., and Scott, V. D., J. Phys. D., Appl. Phys., 10, 7-23 (1977).

[11] Heinrich, K. F. J., Newbury, D. E., and Yakowitz, H. (ed.), Use of Monte-Carlo Calculations in Electron Probe Analysis and Scanning Electron Microscopy, NBS Special Publication 460, Dec. 1976.

[12] Love, G., Cox, M., and Scott, V., "Electron Probe Microanalysis of Oxygen in Heat-treated Orlon Fibres", Mat. Res. Bull., 10, 815-818 (1975).

[13] Specimens courtesy of Dr. G. Love, University of Bath, School of Materials Science, Bath, U.S.

[14] Yakowitz, H., Myklebust, R. L., and Heinrich, K. F. J., "FRAME-an on-line Correction Procedure for Quantitative Electron Probe Microanalysis", NBS Technical Note 796, 1973.

National Bureau of Standards Special Publication 604. Proceedings of the Workshop on Energy Dispersive X-Ray Spectrometry held at NBS, Gaithersburg, Maryland, April 23-25, 1979. (Issued March 1981)

PROPERTIES AND APPLICATIONS OF WINDOWLESS Si(Li) DETECTORS

R. G. Musket

Kevex Corporation
Foster City, California 94404

Abstract

Windowless and ultra-thin-windowed Si(Li) detectors are useful for the energy-dispersive spectrometry of x-rays with energies E_x above approximately 200 eV. Properties of such detectors are discussed with regard to the limits they impose on performance. In particular, considerations of detection efficiency, output linearity, energy resolution, peak shapes, vacuum conditions, and general requirements are presented. Recent developments have greatly increased the actual and potential applications of these detectors. Examples of applications to bulk, thin film, and surface-layer analyses using ion and electron excitation will serve to demonstrate the advantages and limitations of these detectors in contrast to beryllium-windowed detectors.

1. Introduction

The development and applications of windowless (WL) Si(Li) detectors have been progressing steadily since the first documented results in the early 1970's [1,2][1]. Such detectors are useful for the spectrometry of x-rays with energies greater than about 200 eV. In contrast, Si(Li) detectors with beryllium windows have a useful x-ray analysis range above 1 keV. This low-energy limit applies, even for the thinnest commercially available window of approximately 8 μm, because of strong absorption in the beryllium of the x-rays with energies below 1 keV. Recently ultra-thin-windowed (UTW) Si(Li) detectors have been employed successfully in applications where the sample chamber vacuum has not been adequate for WL operation. Since the UTW has reasonable x-ray transmission and an integral light barrier, a UTW Si(Li) detector can often provide performance superior to a pure WL detector.

The main purpose of this document is to discuss several properties of WL and UTW Si(Li) detectors with regard to the limits they impose on performance and applications. Considerations of detection efficiency, output linearity, energy resolution, peak shapes, vacuum conditions, and general requirements permit definition of the limits. This will be accomplished by (a) describing the above properties and procedures for their determination and (b) presenting results of applications to bulk, thin film and surface-layer analyses using ion and electron excitation. Although much of the material discussed here has been previously published, it is reviewed and combined with some new results to yield a more complete understanding of WL and UTW detectors and their applications.

2. Properties

2.1 Detection efficiency

Detection efficiency will be defined as the probability of detecting an x-ray incident upon the outer surface of the Si(Li) crystal. A Si(Li) crystal consists of a 2 - 3 mm thick sensitive region with an x-ray entrance surface consisting of layers due to contamination, the gold contact for application of bias (i.e., an electric field) and silicon characterized by incomplete charge collection (i.e., the dead-layer). Assuming the detection efficiency

[1]Figures in brackets indicate the literature references at the end of this paper.

is 1.0 for all x-rays that penetrate these three layers and interact in the sensitive region, the efficiency $\eta(E)$ of a WL detector for x-rays of energy E can be expressed as

$$\eta(E) = \exp(-\mu_C(E)m - \mu_{Au}(E)\ell - \mu_{Si}(E)t) \quad , \tag{1}$$

where $\mu_C(E)$, $\mu_{Au}(E)$, and $\mu_{Si}(E)$ are the mass absorption coefficients, in cm^2/g, for x-rays of energy E and m, ℓ, and t are the thicknesses, in g/cm^2, of the contamination, gold, and dead layers.

Although the exact nature of the layers is complex and probably indeterminate, an assumption of discrete and uniform layers with appropriate "effective" thicknesses permits assessment of the efficiency for various layer combinations and conversely, the layer thicknesses from measure efficiencies.

For a WL detector with a negligible amount of contamination the efficiency can be expressed as [3,4]

$$\eta(E) = \exp(-\mu_{Au}(E)\ell - \mu_{Si}(E)t) . \tag{2}$$

Thus, if the efficiency is experimentally determined for two x-ray energies E_a and E_b, ℓ and t can be evaluated from simultaneous solution of the following two equations:

$$\eta(E_a) = \exp(-\mu_{Au}(E_a)\ell - \mu_{Si}(E_a)t) \tag{3a}$$

and

$$\eta(E_b) = \exp(-\mu_{Au}(E_b)\ell - \mu_{Si}(E_b)t) \quad . \tag{3b}$$

The x-ray energies E_a and E_b best suited for this purpose are those for which $\eta(E_a)$ and $\eta(E_b)$ are strongly dependent on ℓ and t through large values of μ_{Au} and μ_{Si}, as tabulated in appropriate tables [5].

This approach has been applied to C(K) and O(K) x-rays excited by protons to yield effective layers ℓ = 42 $\mu g/cm^2$ and t = 21 $\mu g/cm^2$, which translate to thicknesses of 220 A Au and 0.09 μm Si for bulk densities of 19.3 and 2.33 g/cm^3, respectively [4]. The experimentally measured efficiencies for C(K) and O(K) were 0.26 and 0.52. Figure 1 is a plot of Equation (2) using the above gold layer and silicon dead-layer thicknesses and tabulated values for $\mu_{Au}(E)$ and $\mu_{Si}(E)$. From this energy dependence of the detector efficiency η, the detector efficiency for B(K) x-rays should be 0.14, which is quite significant. In fact, the detection of proton-induced B(K) x-rays has been demonstrated (figure 2) [4]. The minimum at approximately 130 eV in the $\eta(E)$ function of figure 1 is a consequence of the maxima in the energy dependencies of the μ_{Au} and μ_{Si}.

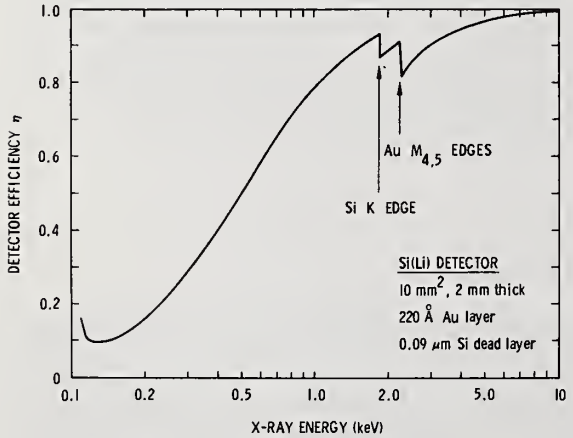

Figure 1. Energy dependence of windowless Si(Li) efficiency for indicated gold layer and silicon dead layer thicknesses using tabulated mass absorption coefficients [4].

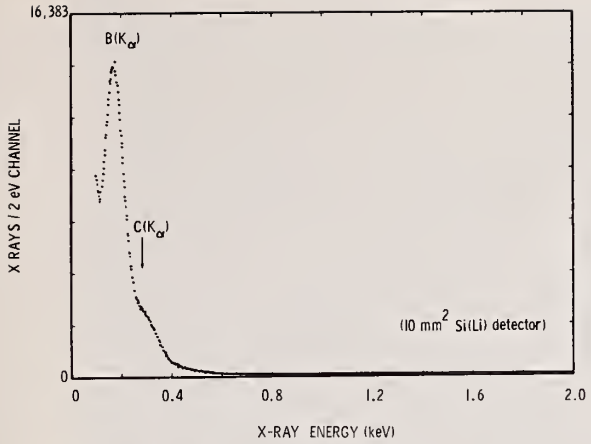

Figure 2. Proton-induced x-ray spectrum from polished boron [4]. Proton energy was 350 keV with an analysis time of 200 seconds at approximately 50% dead time.

Since the effective silicon dead-layer is a function of the applied bias [1], the relative efficiency for any x-ray energy will depend on the bias. This dependence for C(K) x-rays in two different 3 mm thick Si(Li) detectors is presented in figure 3 [6]. The absolute efficiencies at 1000 V bias were 0.010 and 0.0079 for the 14 mm^2 and 30 mm^2 detectors, respectively [6].

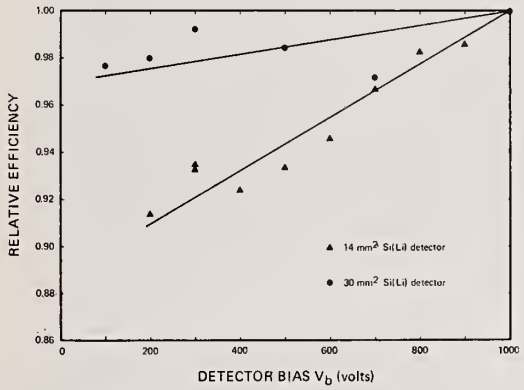

Figure 3. Relative Si(Li) detector efficiencies for C(K) x-rays [6].

Although exact values of $\eta(E)$ are required in Equation (3) to determine ℓ and t for a given detector, only the efficiency ratio $\eta_m(E)/\eta_o(E)$ for contaminated and clean crystals is required to evaluate m, the effective thickness of the contamination layer. This may be expressed as

$$\eta_m(E)/\eta_o(E) = \exp(-\mu(E)m) \tag{4}$$

Unfortunately even less is known about the exact nature of the contamination layer than was known about the gold contact and silicon dead layers, for which the essential elemental composition is known. Evaluation of $\mu_c(E)$ in Equation (4) requires knowledge of the composition of the layer. This knowledge may be obtained from a variety of sources including (a) the partial pressures and sticking coefficients of gases impinging on the crystal, (b) identification of the K-shell binding energies corresponding to a discontinuity in the x-ray spectrum from a bremsstrahlung source, and (c) testing assumed layer compositions for several x-ray energies until self-consistent results are obtained.

All three ways were employed to assess the type and amount of removable contamination present on a detector used almost daily for one year at pressures usually less than 2×10^{-7} torr. The relative efficiency of the detector for C(K) and F(K) x-rays was determined using the ALPHA-X [7] spectrum from Teflon. Since water vapor was the major gas present during the year of operation, it was reasonable to assume that there was an ice layer on the crystal. Figure 4 compares the Teflon spectrum obtained after the year of

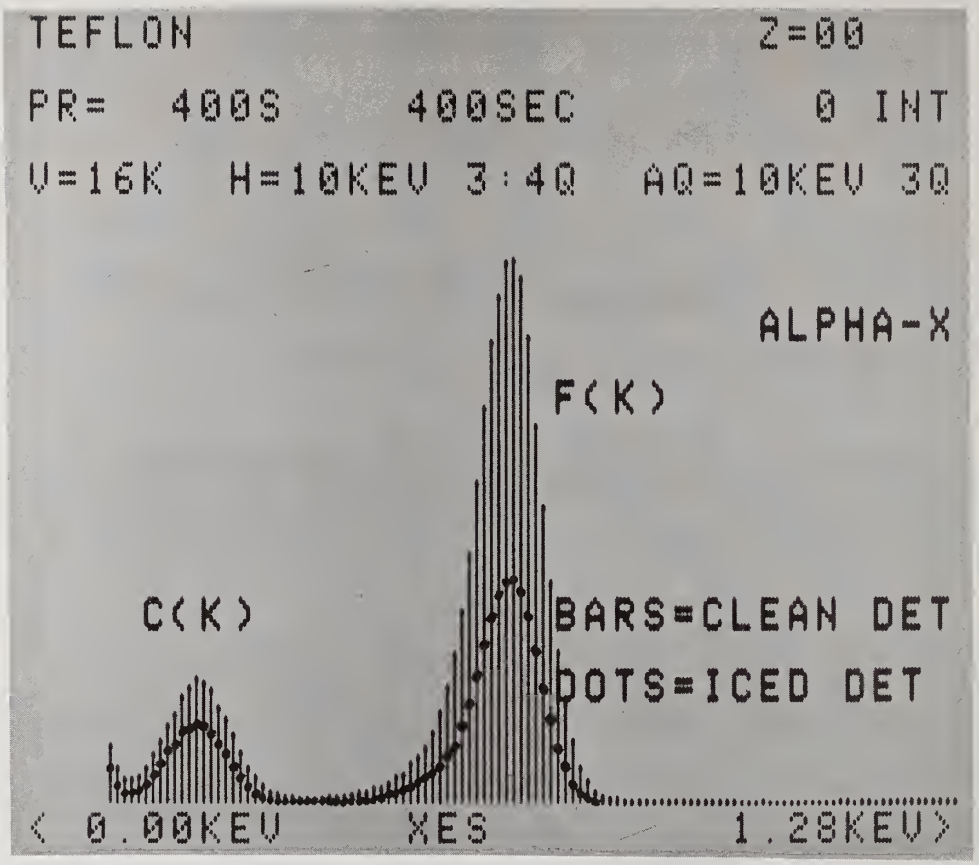

Figure 4. Comparison of the ALPHA-X spectrum of Teflon for a Si(Li) detector iced and clean.

operation (i.e., iced detector) to one subsequently obtained following a temperature-cycle, in an oil-free vacuum, to room temperature and back to normal operating temperature. The relative increase in sensitivity for F(K) is greater than that for C(K). This would be consistent with the removal of oxygen atoms from the surface of the crystal because oxygen absorbs F(K) x-rays more strongly than C(K) x-rays. Assuming the removable contamination was purely ice (i.e., H_2O) and using tabulated mass absorption coefficients [5], Equation (4) yielded the effective values of m: 82 μg H_2O/cm^2 and 62 μg H_2O/cm^2 from the relative efficiencies of F(K) and C(K), respectively. The average value of 72 μg H_2O/cm^2 is equivalent to 0.72 μm of ice (assumed density of 1 g/cm^3).

Of course, such a thick ice layer should also be manifested as a large discontinuity in a bremsstrahlung x-ray spectrum at the O(K) edge. For the crystal conditions corresponding to those of figure 4, the beta-induced x-ray spectra obtained from an erbium film hydrided with deuterium and tritium to form ErDT on a molybdenum disk are shown in figure 5. Although the ALPHA-X instrument was used to obtain the spectra of figure 5, the alpha-induced contribution to the spectra was negligible compared to that from the beta particles emitted by the decay of tritium in the film. The discontinuity due to absorption at the O(K) edge is the only strong discontinuity present. Even the clean detector shows some evidence for the O(K) edge, presumably from ice formed as a consequence of the partial pressure of water vapor present when the crystal was initially cooled or an oxide on the silicon crystal. Using Equation (4) for x-rays with 0.58 keV, corresponding to the large dip just above the edge, and the measured relative intensities, the removable oxygen contamination was calculated to be 57 μg O/cm^2, which is equivalent to 65 μg H_2O/cm^2 or 0.65 μm of ice. Even though this procedure is less precise than that employing the efficiency for characteristic x-rays, the effective thickness of the ice layer is within about ten percent of that determined using characteristic x-rays.

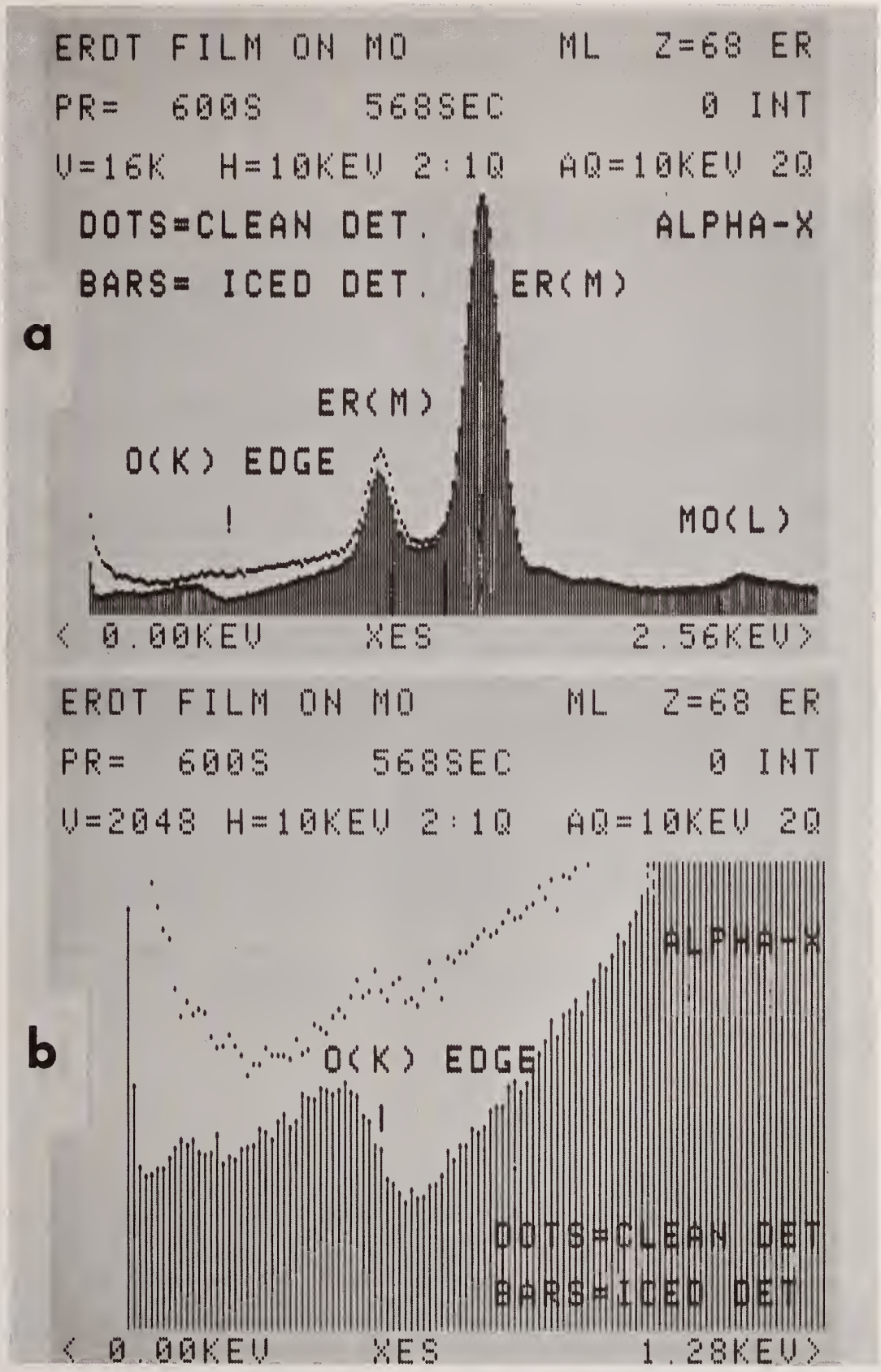

Figure 5. Comparison of the beta-induced x-ray spectrum of a ErDT film on molybdenum for a Si(Li) detector iced and clean. The spectra were normalized at the large Er(M) peak. (a) 0 - 2.56 keV and (b) 0 - 1.28 keV.

Although the properties of the surface layers on Si(Li) crystals cannot be specified exactly, these studies have shown that the efficiency of a WL Si(Li) detector can be characterized and understood in terms of the "effective" layers on the surface of the sensitive volume of the crystal.

2.2 Detector linearity

For the present discussion, a detector with good linearity can be defined as one exhibiting a nearly linear relationship between x-ray energy and the output pulse amplitude. In a practical sense, the entire system consisting of (a) the Si(Li) crystal, (b) the field-effect-transistor (FET) with pulsed optical feedback, (c) the preamplifier, (d) the pulse processor (i.e., linear amplifier, pulse pileup rejector, and live time corrector), and (e) the energy-to-digital converter must be considered in any linearity discussion. Linearity of complete commercial systems is quite good for x-rays with energies above 1.5 keV, but documented results for energies less than 1.5 keV have suggested quite different linearity curves [1,4,6].

Jaklevic and Goulding [1] reported that the C(K) and N(K) peaks had system pulse heights of 0.7 and 0.9 of the values expected from extrapolation of the linear relationship from higher x-ray energies. Since pulser measurements of the linearity of their system electronics did not exhibit any non-linearity, they attributed the non-linearity to charge collection effects in the 20 mm^2 Si(Li) crystal. However, they did not resolve the C(K) and N(K) peaks from the steep low-energy background and, hence, the peaks only appeared to have a much lower pulse-height than expected. Measurements of proton-induced x-rays with a 30 mm^2 detector collimated down to the center 17.7 mm^2 coupled with computerized fits to the digital data provided the pulse height for the resolved C(K) Gaussian peak [6]. This latter study yielded an x-ray vs. pulse-height relationship within two percent of linear for C(K), O(K), Cu(L), and Al(K) x-rays. Subsequent measurements with a 10 mm^2 detector extended this linearity relationship down to an energy of 183 eV using B(K) x-rays resolved from the steep noise tail (figure 6) [4]. These latter studies have shown that Si(Li) detector systems can be linear for x-rays with energies greater than 183 eV. Typically, complete commercial detector systems have resolved C(K) and O(K) pulse heights of about 0.9 and 0.97 of the values expected from linearity considerations. Although these deviations are not desirable, unambiguous identification of the x-ray peaks can still be made.

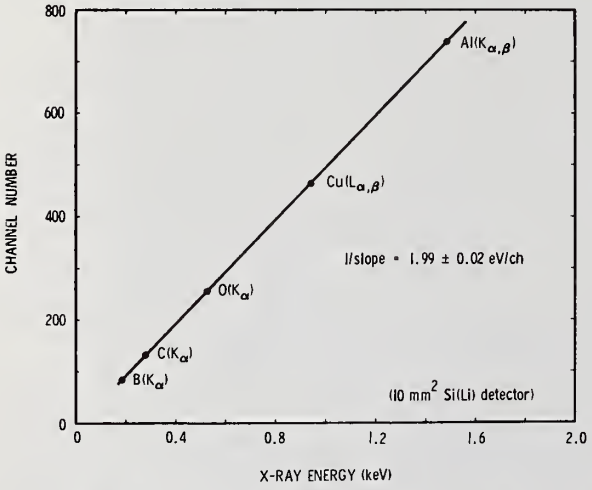

Figure 6. Relationship between detected pulse height (i.e., channel number) and x-ray energy for a Si(Li) detector [4].

Isolation of the component causing the non-linearity is quite difficult because of problems associated with accurately simulating the pulses, including noise, for such low energy x-rays. However, the bias applied across the Si(Li) crystal is one parameter that can be changed without affecting the remainder of the system. This approach has yielded spectra such as that presented in figure 7. The detector was a 30 mm^2 Si(Li) crystal (3 mm thick) collimated down to the center 10 mm^2. A study of the dependence of the relative, resolved pulse-heights on detector bias provided the data displayed in figure 8 [6]. The 14 mm^2 and 30 mm^2 detectors were collimated down to the center 12.5 mm^2 and 17.7 mm^2. The pulse height is a measure of the ability of the detector to collect the energy deposited into electron-hole pairs and, as normalized, can be considered to be the fraction of the

x-ray energy that was detected. Normalization was made with respect to the values at V_b= 1000 V because this bias yielded a C(K) pulse height that fitted the linearity relationship. Note the asymptotic nature of the curves indicates that the C(K) pulse height would not be increased significantly for bias values exceeding 1000 V (i.e., electric fields of 333 V/mm). Determination of the proper operating bias to obtain the best linearity from each Si(Li) crystal and collimation arrangement must be made on an individual basis.

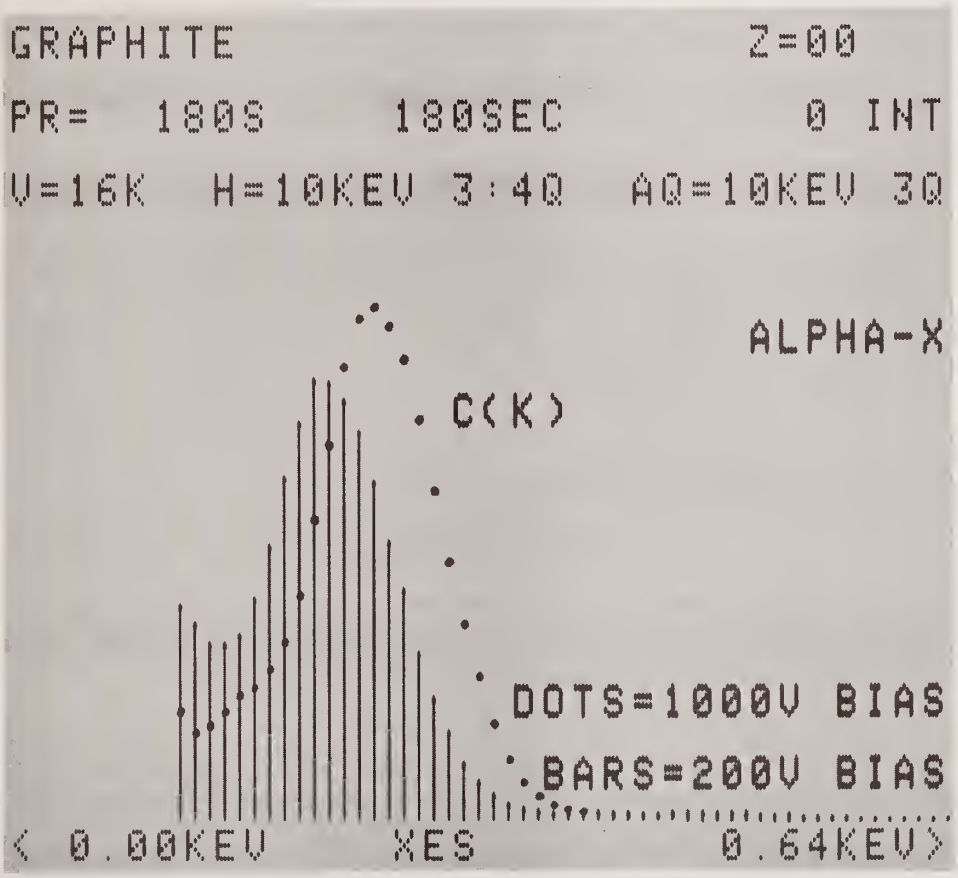

Figure 7. Effect of applied bias on the pulse amplitude of C(K) x-rays detected by a Si(Li) detector.

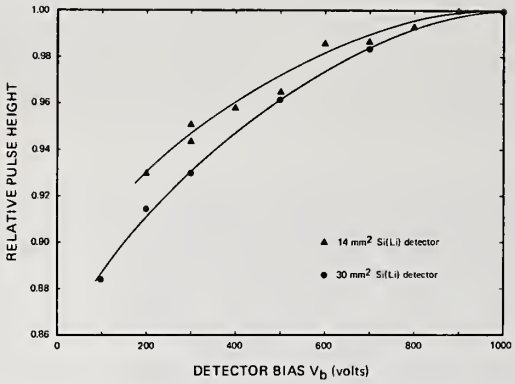

Figure 8. Relative pulse heights for C(K) x-rays in 3 mm thick Si(Li) detectors [6].

2.3 Energy resolution

Energy resolution is a measure of the capability to distinguish clearly x-ray peaks with similar energies. For energy dispersive x-ray spectrometry the resolution is normally expressed as the full-width at half-maximum (FWHM) for the Mn(Kα) x-ray peak, with lower FWHM values corresponding to better resolution. A good approximation is to assume that isolated x-ray peaks are Gaussian-shaped with a standard deviation σ, yielding FWHM = 2.355σ.

Contributions to the FWHM can be estimated from [8]

$$(\text{FWHM})^2 = \Delta_{el}^2 + \Delta_d^2 \quad , \tag{5}$$

where Δ_{el} is the width associated with the electronic noise including leakage currents and microphonics and Δ_d is the width intrinsic to the detector and includes pair creation statistics. If pair-creation effects dominate Δ_d, then Δ_d is given by

$$\Delta_d^2 = (2.355)^2 F\varepsilon E \quad , \tag{6}$$

where F is the Fano factor (i.e., the fraction of the total photon energy detected in the pulse of electron-hole pairs), ε = 3.81 eV [9] is the energy required to form an electron-hole pair in silicon near liquid nitrogen temperature, and E is the total photon energy in eV. Combining Equations (5) and (6),

$$\Delta_{el}^2 = (\text{FWHM})^2 - (2.355)^2 F\varepsilon E \quad . \tag{7}$$

Determination of the FWHM for two appropriate characteristic x-rays with the same detector system (i.e., same Δ_{el} and F) permits evaluation of Δ_{el} and F. This has been demonstrated using resolved C(K) and Al(K) x-rays to yield F = 0.11 ± 0.04 [4], where the uncertainty reflects the uncertainties in the FWHM's. This range of 0.07 - 0.15 for F contains all of the tabulated experimental F values for Si(Li) detectors [1,8], but does not include the theoretically projected value of F = 0.05 [8,9]. It is important to note that not every Si(Li) detecto` system satisfies Equation (7) over a wide energy range. However, figure 9 displays the energy dependence of the resolution calculated from Equation (7) for detectors having Mn(Kα) resolutions of 146, 155, and 165 eV. This plot shows that a 9 eV difference in Mn(Kα) resolution leads to a 13 eV difference in C(K) resolution. Such considerations combined with the fact that the K x-rays are more closely spaced for low-atomic number Z elements emphasizes the importance of using the highest resolution detectors for low energy x-ray spectroscopy.

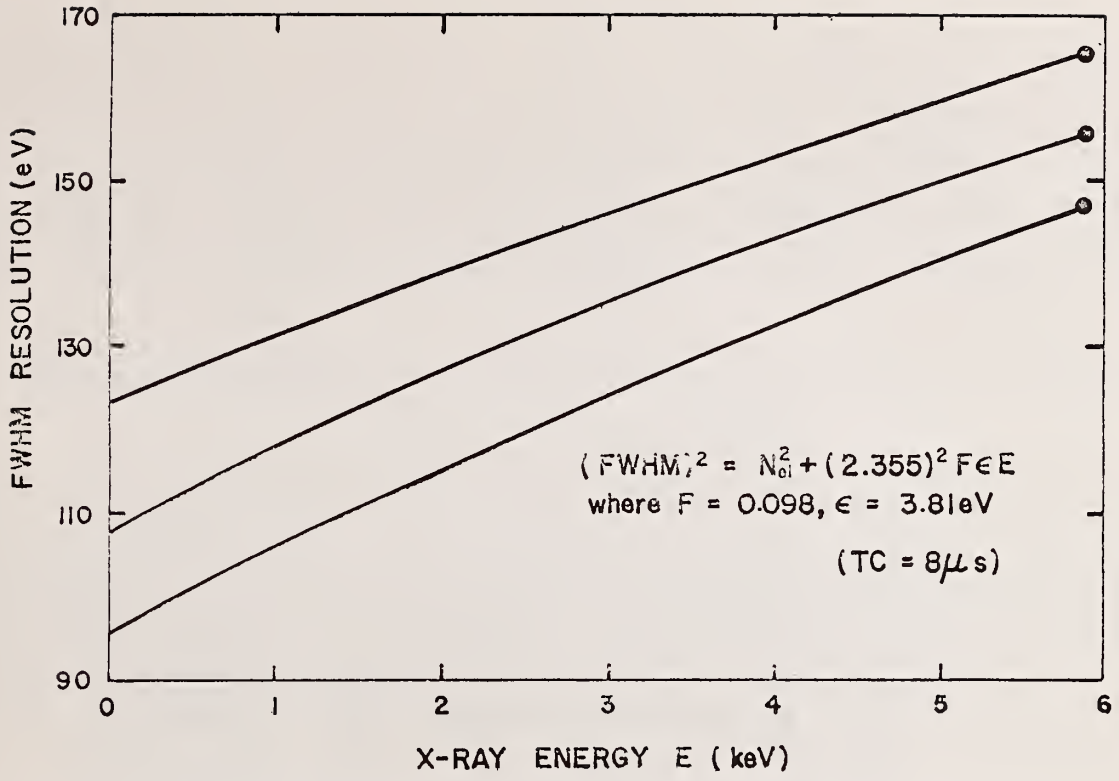

Figure 9. Calculated energy dependence of the resolution of Si(Li) detectors with specified Mn(Kα) resolutions of 146, 155, and 165 eV.

Although increasing the shaping time constant of the pulse processing electronics above 8 μs does not significantly change the resolution of x-ray energies above 5.9 keV (Mn(Kα)), such increases have a marked effect on the resolution for the low energy x-rays because the electronic noise term of Equation (5) becomes dominant at the lower energies. These points are illustrated by the data of figure 10. Thus, for low count rates the use of higher time constants can significantly improve the resolution for low energy x-rays. The reduced electronic noise corresponding to higher time constants will also be reflected in the reduced noise tailing observed in the spectrum. This noise tailing is due to a large peak located at essentially zero energy. If the noise tail is minimized then the interference between the tail and low-energy x-rays (e.g., C(K)) would be minimized and elemental detection limits would be improved. Typically, Δ_{el} = 95 eV corresponds to an electronic noise cutoff energy of $\leq$ 200 eV. Analysis of x-rays with energies less than 200 eV can only be performed under special conditions (i.e., low-energy x-ray count rate comparable to noise count rate at the energy of interest).

The major sources of noise are (a) various forms of electronic noise intrinsic to the crystal and design of the detector system, (b) microphonics due to the environment of the application, (c) leakage currents due to surface contamination on the crystal, and (d) photoconductivity induced in the crystal by visible and ultraviolet (UV) light. Although source (a) is not within the control of the user of the WL detector system, sources (b) - (d) can be minimized by appropriate attention to vibration, proper vacuum procedures (see Section E below), and exclusion of light from the detector region. Sources (c) and (d) are not significant in a beryllium-windowed detector/cryostat because the beryllium window insures both the quality and light tightness of the detector vacuum environment. Since proper low-energy x-ray spectrometry imposes much greater resolution and noise tail constraints on a detector system than does that for higher energy x-rays, the importance of minimizing the noise sources must be emphasized.

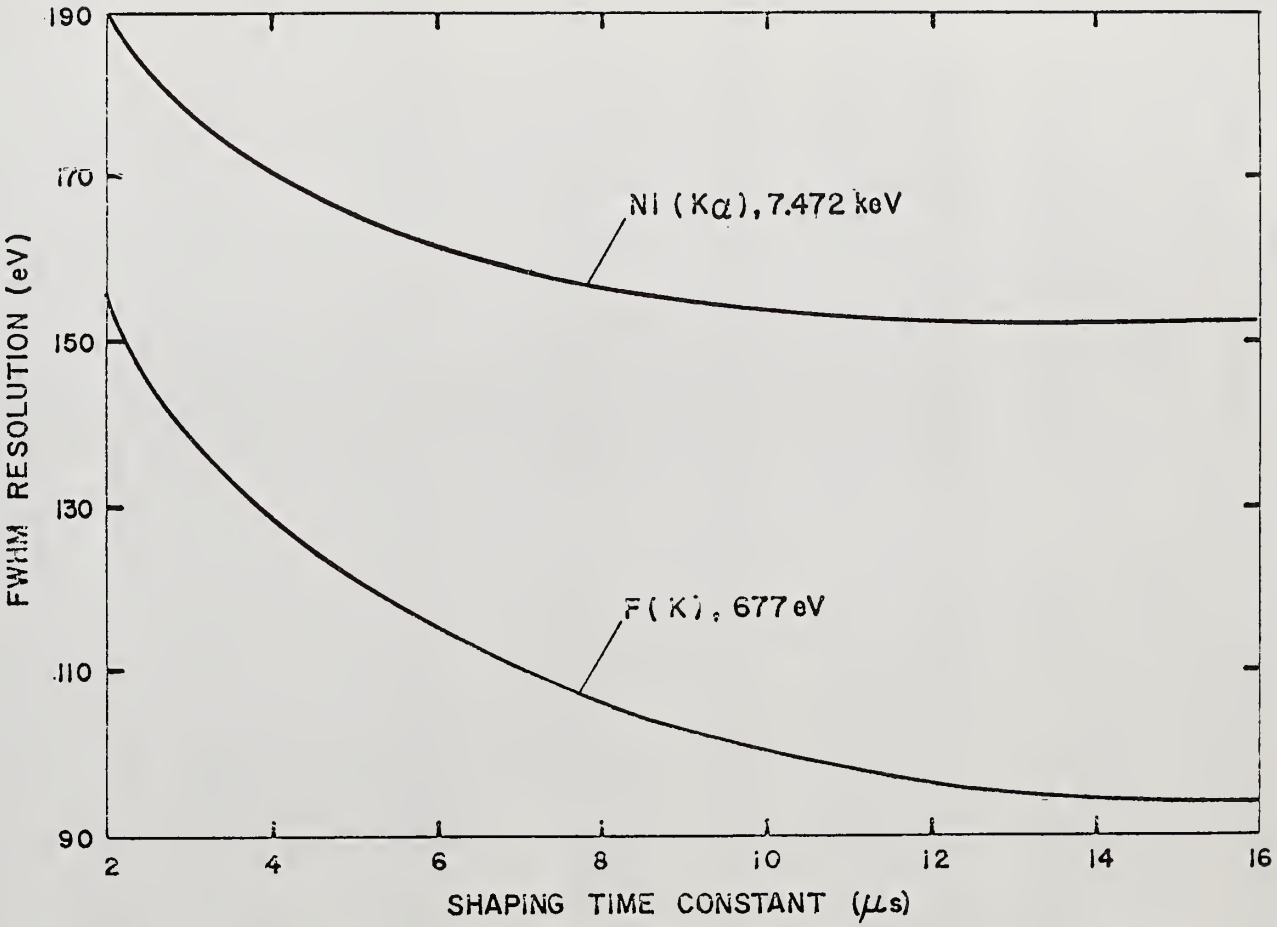

Figure 10. Measured dependence of the resolution of Ni(Kα) and F(K) x-rays on the shaping time constant.

2.4 Peak shapes

Although single x-ray peaks in energy dispersive x-ray spectra have shapes that are essentially Gaussian for x-ray energies above 1.5 keV, the observed shapes for peaks at lower x-ray energies have been varied. Jaklevic and Goulding [1] found increased peak tailing (on the low-energy side of the peak) at lower energies from measurements of the full-width at 1/10 maximum and at low bias voltages. They interpreted these results as dead-layer related charge collection problems. Unfortunately they obtained the results from peaks that were not resolved from the background and adjacent peaks. From the nature of their spectra they must have drawn most of the results from the somewhat clean O(K) and F(K) peaks. The F(K) spectrum was obtained from electron-excitation of Teflon, which is hydroscopic, and was not corrected for either the background or the O(K) peak due to water in the Teflon.

Musket and Bauer [2,10] found that the resolved O(K) x-ray peak could be approximated by a Gaussian shape of the form

$$G(E, E_o) = H \exp(-((E - E_o)^2/2\sigma^2)) \quad , \tag{8}$$

where the energy E_o is the Gaussian centroid, σ is the standard deviation width, and H is the peak height. Subsequently, Musket and Bauer [3,4,6] presented data that clearly showed C(K) peaks that were quite symmetric and, by least-squares curve-fitting, Gaussian. However, they observed that the resolved O(K) peak, although approximately Gaussian, did not fit a Gaussian form as well as the C(K) peaks. The O(K) peaks had a longer tail on the low energy side of the peak. In one study [11], the shape of the resolved O(K) peak was found to be well-fit by a modified Gaussian G_m of the form

$$G_m(E, E_o) = H \exp(-((E - E_o)^2/2\sigma^2)), \; E \geq E_o - E_c \tag{9a}$$

$$G_m(E, E_o) = H \exp(-(E_c/\sigma^2)(E_o - E - 0.5E_c)), \; E \leq E_o - E_c \tag{9b}$$

where E_c is the energy (below the centroid) at which the function G_m changes from Gaussian to exponential. This modified Gaussian is similar to the β-ray response function of scintillators [12]. Musket and Bauer [11] thought this type of function would provide some physical basis for describing the effects of photoelectrons from x-rays absorbed near the "boundary" between the sensitive and volume and the dead layer of the Si(Li) crystal.

Figure 11 shows the symmetrical (and Gaussian) shape of a C(K) peak when the influence of the low-energy noise tail is negligible. The spectrum in figure 12 clearly shows the apparent inconsistency of tailing on the O(K) peak and no tailing on the C(K) peak. Refer to figure 4 and note that the F(K) peak from thin Teflon tape is more symmetric than an O(K) peak. ALPHA-X spectra of thick Teflon always show an O(K) peak on the low-energy side of the F(K) peak due, presumably, to the presence of water vapor in the Teflon.

Although no detailed study of the low-energy peak shapes has been reported, a plausible explanation, to account for the apparent inconsistencies in the detected shapes can be based on the influence of solid state effects on the true x-ray spectrum. Since the resolution for these low energy x-rays is about 100 eV, such solid state effects in the sample (width of 10 - 20 eV) may influence the shape and width of the resultant peak. The most direct way to test this hypothesis is to eliminate solid state effects by determining the x-ray spectrum from gaseous oxygen. Indirectly the hypothesis may be tested by adding, in quadrature, contributions from electronic noise, charge-collection statistics, and true C(K), O(K), and F(K) spectra. The resultant peaks would then be compared to resolved peaks obtained from appropriate samples. If the results were in agreement, then the explanation would seem plausible. Ultimately this approach could be used to determine some solid state properties by removing the contributions of electronic noise and charge collection statistics from the peak shape. In any case, low-energy x-ray peak shapes remain a topic for future investigations.

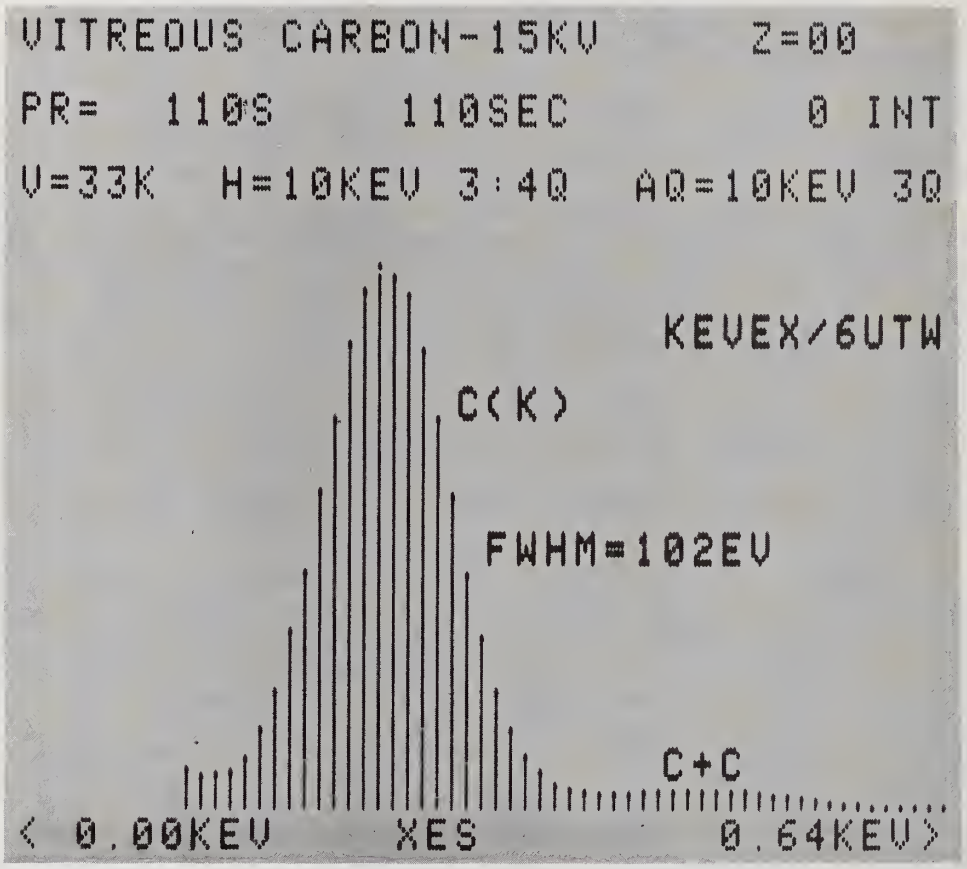

Figure 11. Electron-excited x-ray spectrum from vitreous carbon.

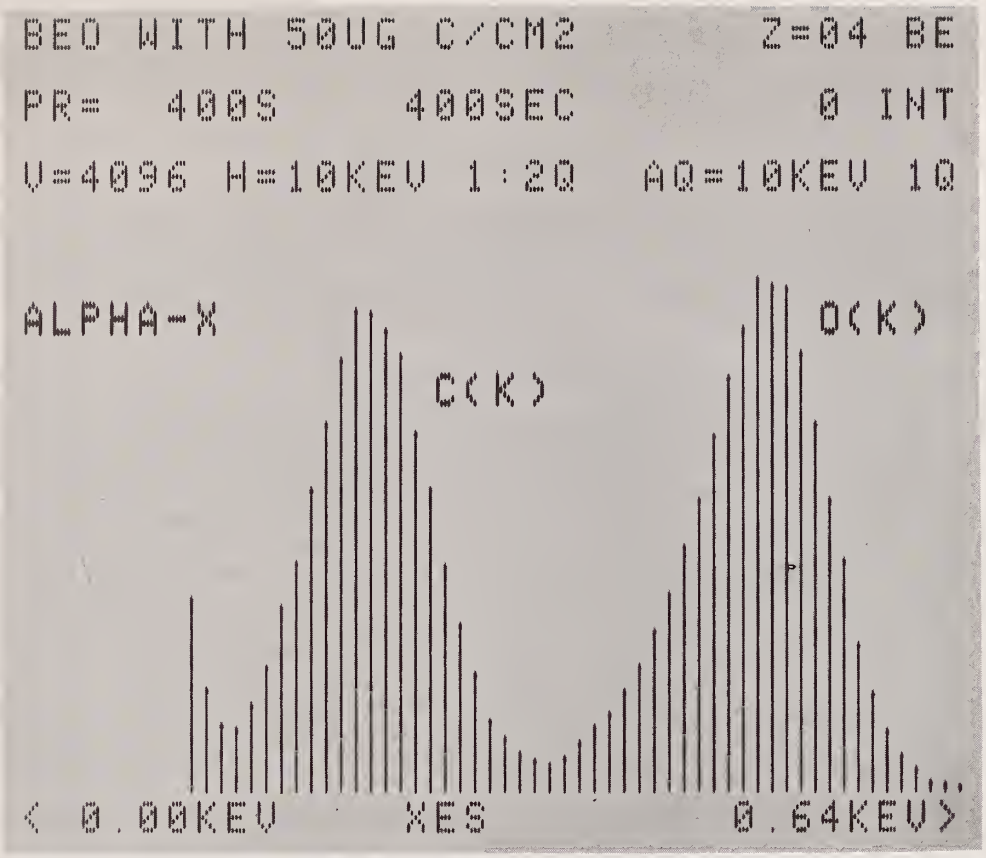

Figure 12. ALPHA-X spectrum of a BeO crystal covered with a carbon film (50 μg/cm^2).

2.5 Vacuum considerations

The essential requirement for operation of a WL Si(Li) detector is that the vacuum environment be clean and oil-free. Such an environment can be achieved by combining proper vacuum design and materials with sputter-ion and cryogenic pumping. Ideally both these pumping capabilities would be integral components of the detector/cryostat to insure the proper vacuum environment even when the detector is not in use. Initial evacuation of the detector with the detector at room temperature must be to the lowest possible pressure to minimize the formation of layers on the crystal after the liquid nitrogen is added (pressures below 1×10^{-6} torr are acceptable). Since the major condensable gas in such vacuum systems is usually water vapor, the discussion on ice layer formation and removal in Section A above is applicable. For long-term, high efficiency operation of detectors, the maximum recommended operational pressure in a clean, oil-free system is 1×10^{-7} torr. The time required to form an ice layer of a certain thickness will be longer for lower operational pressures. In contrast, oil-vapor contamination generally cannot be removed by simply warming the crystal to room temperature under a good vacuum, and the oil may actually render the crystal unusable for high resolution purposes. These constraints place extreme restrictions on the sample and sample chamber environment for application of a WL detector and excludes use of WL detectors on diffusion-pumped sample chambers.

An attractive alternative to the WL detector is the UTW detector, which employs an UTW mounted with an o-ring to make a vacuum seal and completely isolate the detector vacuum from the sample chamber vacuum. The UTW is an ultra-thin parylene-N film (i.e., C_8H_8) coated with a similarly thin aluminum coating of about 2000 Å. Typical transmission probabilities are 0.2 and 0.5 for C(K) and O(K), respectively. Since the UTW cannot support pressures exceeding about 10^{-3} torr, the UTW detector must be treated as though it was a WL detector (i.e., it must be retracted and its gate valve closed before venting the sample chamber).

The restrictions on the sample chamber vacuum for UTW operation are (a) clean, oil-free sample chambers with pressures less than 10^{-3} torr and (b) only diffusion-pumped systems with liquid nitrogen traps and operational pressures less than 5×10^{-6} torr. Restriction (a) insures that the UTW doesn't rupture and restriction (b) minimizes contamination of the UTW by oil vapor from the diffusion pump.

2.6 General considerations

In addition to the vacuum requirements outlined above, there are several other considerations to observe for proper energy-dispersive measurements of low-energy x-rays. Included are (a) exclusion of light (visible and UV), electrons, and other energetic particles from impinging on the Si(Li), (b) collimation using apertures not tubes, and (c) pulse pileup of low energy x-rays.

Light photons can be eliminated using a light barier (LB) such as the window material described above for the UTW detector. A pinhole-free aluminum coating of 1000 - 2000 Å is more than adequate to reduce the light photon flux to an acceptable level. The difference between the LB and UTW versions of such windows is that UTW versions provide vacuum isolation as well as "dark" detector environments. If electrons are not prevented from bombarding the Si(Li) crystal then an anomalously high bremsstrahlung background will be observed due to the interaction of the electrons with the crystal. Even the thinnest beryllium window (8 μm) will stop electrons with energies below 25 keV and preclude their bombardment of the crystal. Thus elimination of electrons from a beryllium-windowed detector needs only to be considered if the application includes scattered electrons with energies above 25 keV. However for a WL, LB, or UTW detector system an integral magnetic trap in front of the window and crystal can serve to remove the backscattered electrons from the x-ray axis. Other energetic particles can also give rise to peaks and background not associated with the true x-ray spectrum and their flux should be reduced to an acceptable level by procedures appropriate to the nature of the particles.

For beryllium-windowed detectors, collimation is usually accomplished using an aluminum collimator with a carbon-coated tubular aperture. Al(K) x-rays generated by x-rays, electrons or other particles bombarding the collimator are absorbed in the carbon coating and C(K) x-rays are absorbed by the beryllium window. Consequently, there is no evidence of the collimator in the detected x-ray spectrum. For detector/cryostat systems capable of detecting C(K) x-rays, such a tubular collimator approach is not acceptable. Replacing the carbon coating with a beryllium coating is plausible but the thickness of beryllium required to absorb an appropriate fraction of the Al(K) x-rays is quite large and the potential health hazards associated with beryllium coatings are great. However, collimation using a series of knife-edged apertures has proven to provide the needed collimation without introducing extraneous x-rays into the detected spectrum.

Although commercially available pulse-pileup rejection systems perform quite well for pulses from x-rays with energies above about 1 keV, performance decreases with decreasing x-ray energy. Thus, pileup or sum peaks are not uncommon in spectra containing low energy x-rays. Figure 11 shows the main and sum C(K) peaks for electron excitation of graphite. The total C(K) count rate was about 900 cts/sec. In some cases a sum peak due to a low-energy x-ray peak and a higher energy x-ray peak can be obtained (e.g., O(K) + Al(K) from Al_2O_3). In the absence of appropriate pulse-pileup rejection circuitry true low energy spectra can only be obtained at count rates low enough to assure negligible sum peaks. Note that this restriction on count rates is consistent with using longer time constants for optimum resolution. Thus, in general, the most correct low-energy x-ray spectra will be obtained using low count rates and long shaping time constants.

3. Applications

Examples of applications of WL and UTW detectors to bulk, thin film, and surface-layer analyses using ion and electron excitation will illustrate several detector capabilities. For most analyses using energy-dispersive x-ray spectroscopy, the penetration of the ion or electron defines the maximum depth of analysis. However, in analyses for the light elements, the escape of the low energy x-rays limits the depth probed. This effect is shown in figure 13 where the x-ray yield for a layer of thickness L has been normalized to that for an infinitely thick layer under the assumption of uniform ionization of the atoms in the

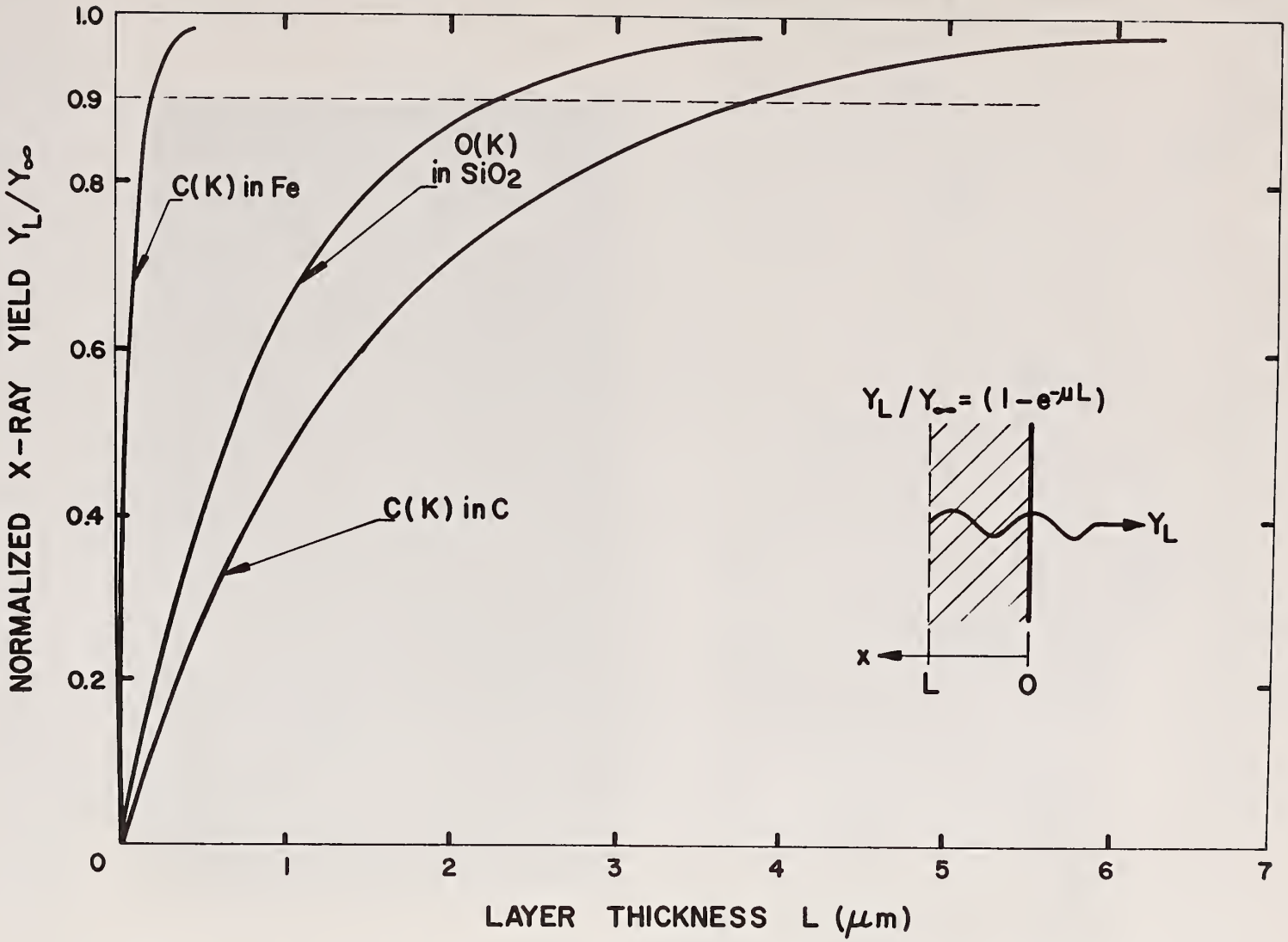

Figure 13. X-ray yield from layer of thickness L normalized to that from an infinitely thick layer for uniform x-ray production and a 90 ° takeoff angle.

layers and a 90 ° takeoff angle. A reasonable measure of the thickness probed is the layer thickness giving a normalized x-ray yield of 0.9 that of the infinitely thick layer. The ninety percent thicknesses for C(K) in Fe, O(K) in SiO_2, and C(K) in C are 2000 Å, 2.2 μm, and 3.8 μm, respectively. Of course the ninety percent thicknesses would be reduced considerably for smaller takeoff angles due to increased x-ray absorption. Such considerations serve to highlight the critical importance of a high takeoff angle for the analysis of low-Z elements. The applications discussed below were undertaken with either a 90° takeoff angle (ion excitation) or a 45° takeoff angle (electron excitation).

3.1 Ion excitation (ALPHA-X)

The ALPHA-X version of the alpha-induced x-ray emission technique is shown schematically in figure 14 [7]. Detailed description of the physical concepts have been previously published [7,14]; however, a brief outline is given here to provide a basis for interpretation of the results to be presented. The ALPHA-X technique consists of the detection and analysis of x-rays emanating from a specimen irradiated with 5.8 MeV alpha particles (i.e., doubly ionized helium) from a radioactive Cm-244 source. As shown in figure 15, the ALPHA-X probe is a compact combination of a specially designed alpha source attached to a unique source holder and electron-trap/collimator assembly which is installed in the end of the tubular housing of a high-efficiency WL Si(Li) detector. Although a WL detector can usually be employed for analysis of alpha-induced x-rays (provided extraneous light is eliminated), alpha-induced light can be a source of noise in the case of some samples (e.g., thick insulators such as alumina, boron nitride, beryllia). Of course, either a LB or UTW detector could be used as a component of ALPHA-X. Figure 16 shows a typical installation of the ALPHA-X instrument. The exterior dimensions and features are the same as those of a WL detector. Since the alpha-particles are continuously emitted, analysis with ALPHA-X consists of (a) evacuating the sample chamber to $<10^{-7}$ torr (for WL detector), (b) opening the gate valve to ALPHA-X, (c) moving the probe near the sample, and (d) turning on the detector electronics.

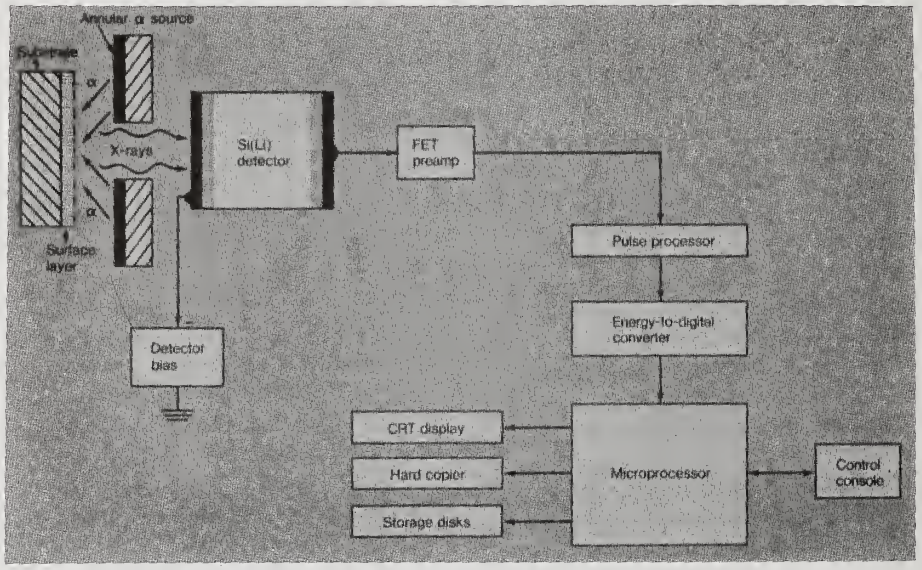

Figure 14. Schematic of components of ALPHA-X technique [7].

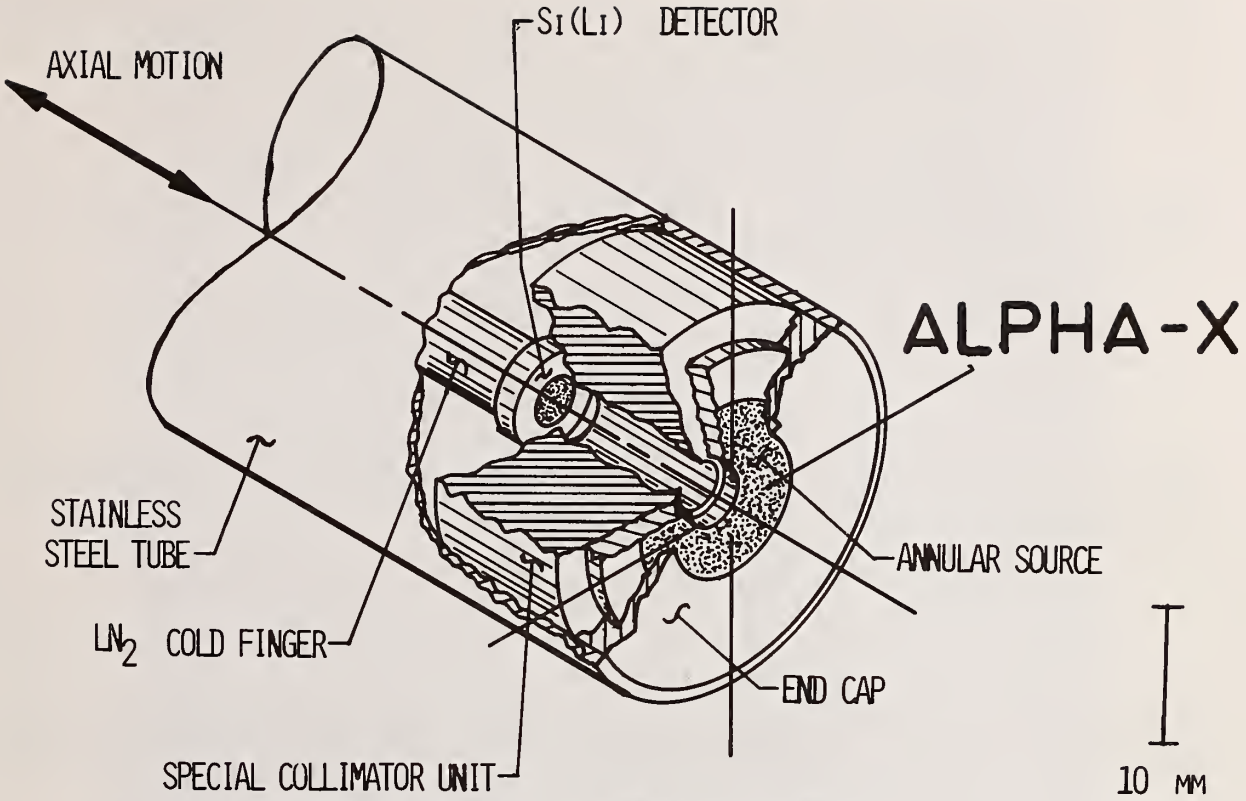

Figure 15. Geometry of the ALPHA-X probe [13].

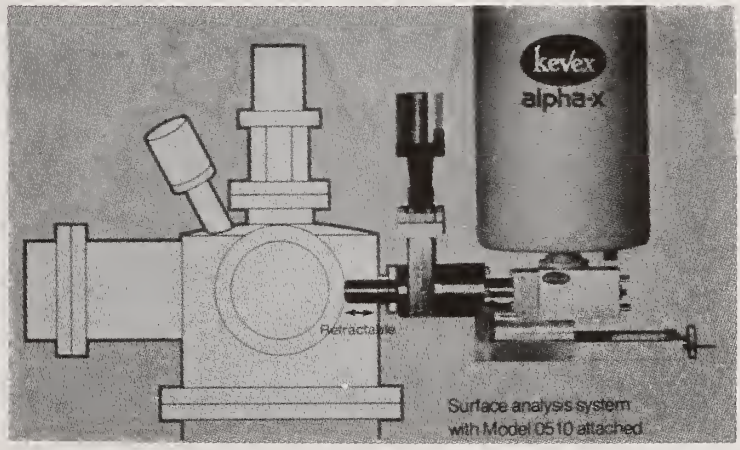

Figure 16. Typical installation of the ALPHA-X instrument.

Three types of studies will demonstrate the usefulness of ALPHA-X for analyses of low-Z elements on various substrates. These studies are determination of oxygen surface densities (i.e., oxide thicknesses), carbon on and in steels, and low-Z elements in aerosol samples. The value of ALPHA-X for assessment of detector performance has been illustrated in the section on properties.

Oxide thickness determination

Using previously published procedures and principles for oxide thickness determination from ion-induced oxygen x-rays [2], the ALPHA-X oxygen x-ray yield I_u (x-rays/sec) from an

unknown sample can be compared to that I_s from a standard with known oxygen surface density L_s (g O/cm^2) to permit evaluation of the unknown oxygen surface density L_u using

$$L_u = -\frac{1}{\mu_u} \ln\left(1 - \frac{C_s I_u \mu_u}{I_s}\right) \tag{10}$$

where $C_s \equiv (1/\mu_s)(1 - \exp(-\mu_s L_s))$ and μ_u and μ_s the oxygen x-ray absorption coefficients (cm^2/g O) for the unknown and standard oxides.

In general, the composition of the unknown oxide is required to evaluate μ_u; however, if $C_u I_u \mu_u / I_s \ll 1$ (i.e., for very thin oxides), then

$$L_u \cong C_s I_u / I_s \ , \tag{11}$$

and the exact composition of the oxide is not needed. However, determination of the thickness T_u of the unknown oxide requires knowledge of both the oxide density ρ_u (g/cm^3) and the weight fraction of oxygen in the oxide W for use in

$$T_u \cong L_u / \rho_u W \ . \tag{12}$$

The net O(K) yield from the oxidized silicon standard (figure 17) provided the value for I_s in Equation (10). Then the oxygen surface density represented by the net O(K) yield of figure 18 was determined to be 20.2 μg O/cm^2, which corresponds to about 1280 Å of Ta_2O_5 (bulk density = 8.74 g oxide/cm^3). Of course the same formalism applies to the thickness determination of layers other than oxides.

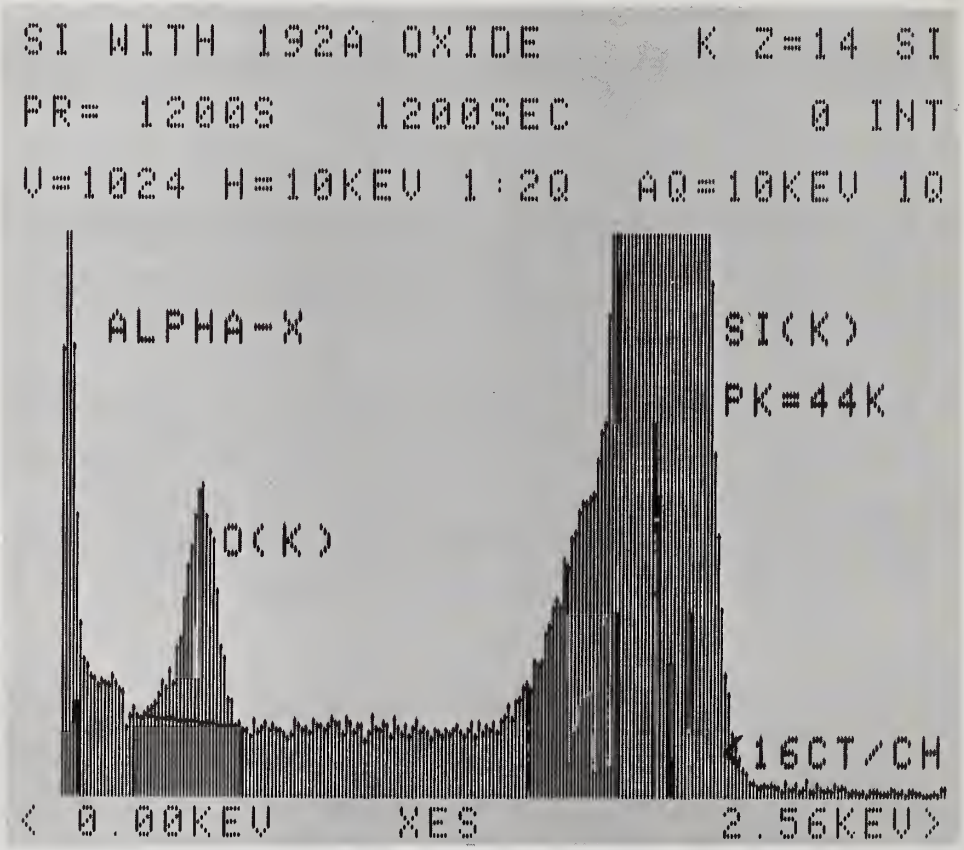

Figure 17. ALPHA-X spectrum of high purity silicon with 2.37 μg oxygen/cm^2 (i.e., 192 A SiO_2).

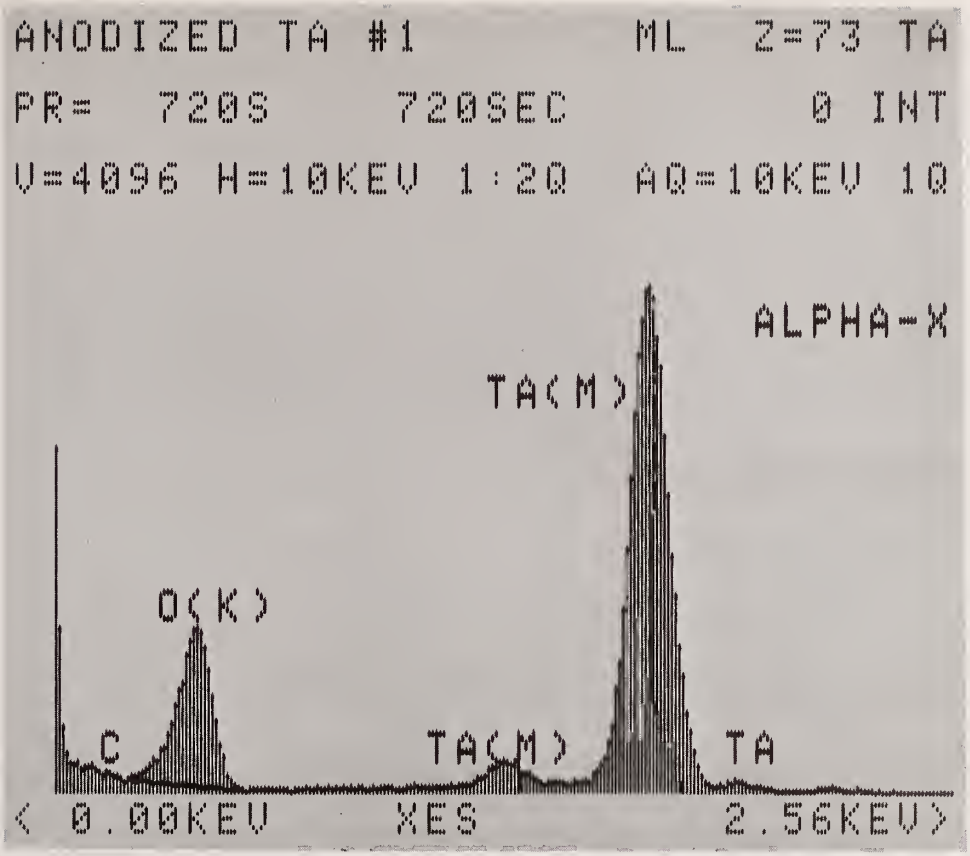

Figure 18. ALPHA-X spectrum of anodized tantalum.

Analysis for carbon on and in Steels

ALPHA-X studies have provided quantitative, non-destructive determinations of the carbon content in surface layers and in the bulk [13]. For thin carbon layers, a version of Equation (11) was applied to determine the carbon surface densities from the ratio of the carbon x-ray count-rate for the unknown layers to that for standard free-standing carbon films. Figure 19 compares the low-energy part of the spectrum from Steel "L" with a low level of carbon contamination to that from Steel "H" with a higher level of carbon contamination. The levels of carbon contamination represented by these spectra were found to be 0.25 and 0.88 μg carbon/cm^2, respectively. Equivalent carbon thicknesses were 11 and 39 Å, assuming a bulk carbon density of 2.26 g/cm^3. The three-sigma minimum detection limits for twenty minute analyses were 0.1 μg carbon/cm^2 (equivalent to approximately 5 Å). Argon-ion sputtering was used to completely remove the contamination from the surface of the steel. Subsequent ALPHA-X measurements showed no evidence for C(K) x-rays, indicating that the bulk carbon of 0.05 weight-percent was not detectable.

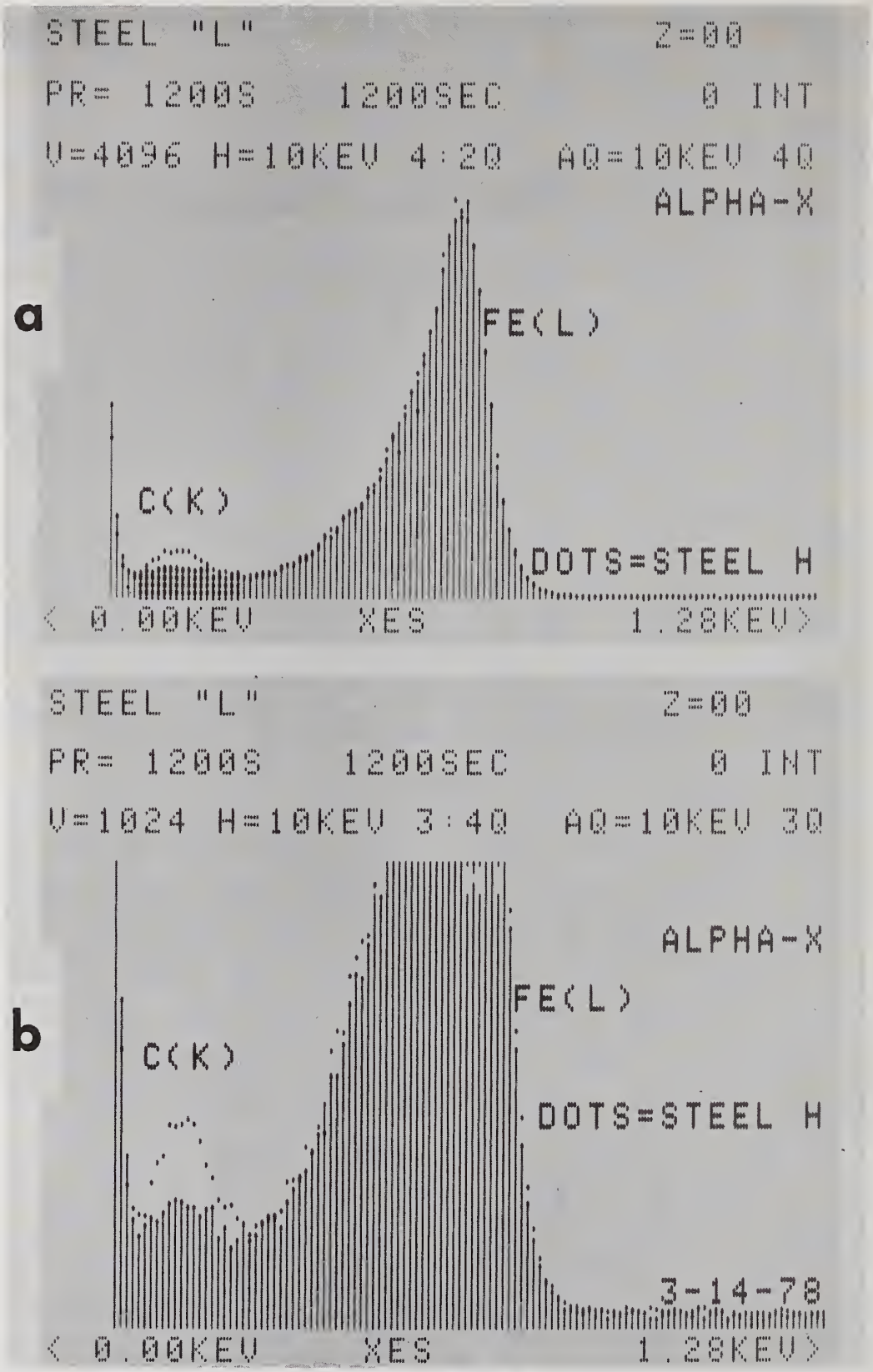

Figure 19. Comparison of ALPHA-X spectra from Steel "L" and Steel "H": (a) 4096 CFS and (b) 1024 CFS [13].

Evaluation of the detection limit for carbon in steel was made using British Chemical Standard Steel 407 with 0.5 weight percent carbon. Figure 20 gives the low-energy spectra of this steel before and after sputter-cleaning to remove the surface carbon. Note the small-but-distinguishable differences at the energies of the C(K) and O(K) x-rays. These reductions are attributable to sputter removal of a thin oxide and light carbon contamination from the freshly polished sample. The minimum detection limit was 0.1 weight percent carbon for a twenty minute analysis. This result verified the inability of ALPHA-X to detect the 0.05 weight percent carbon in sputter-cleaned Steel "L".

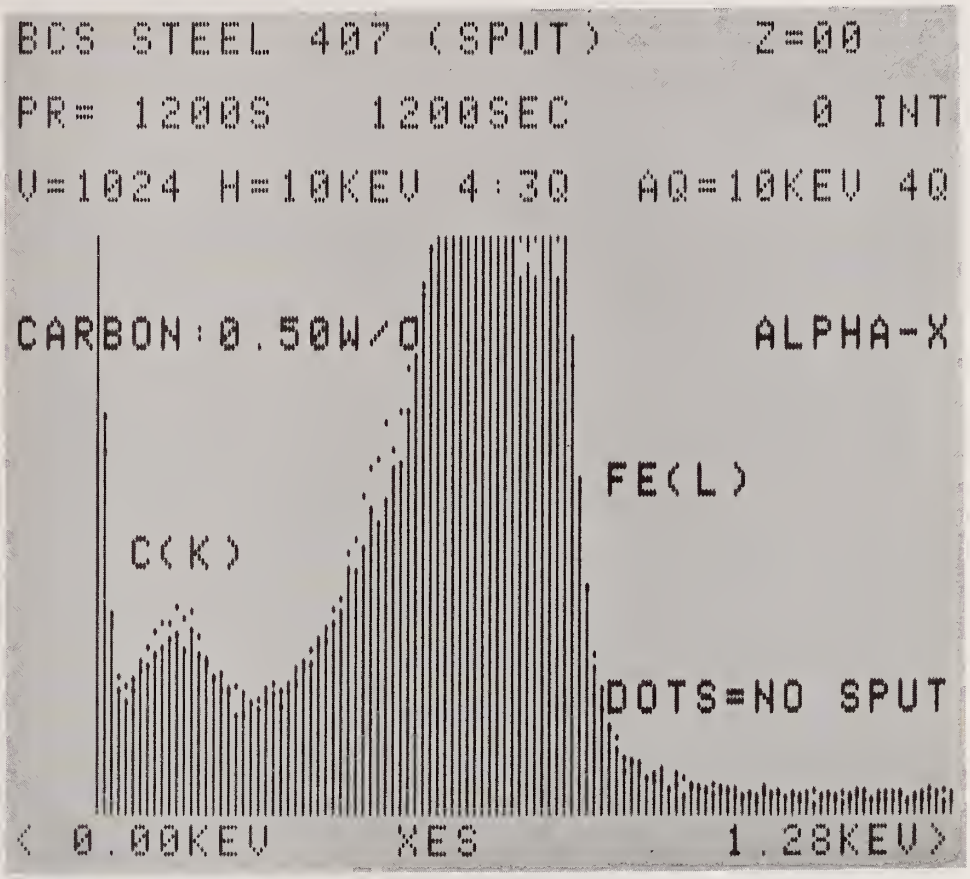

Figure 20. Comparison of the low-energy spectrum of BCS Steel 407 before and after sputter-cleaning [13].

Low-Z analysis of aerosol samples

The analysis of low-Z elements in aerosol samples collected on plain and nickel-coated porous silver filters is important for a proper evaluation of particulate material in air pollution studies. ALPHA-X has provided such analyses with a minimum detection limit of less than 1 μg carbon/cm^2 on a nickel-coated silver-filter in a 300 second analysis. Assessment of the total carbon in aerosol samples collected on silver filters is not a straight-forward procedure due to the contribution from the Ag(M) x-ray peak (figure 21). However, a coating of 1.1 μm nickel on the silver filter is more than adequate for absorption of the Ag(M) x-rays and such a filter is an excellent substrate for direct analysis of carbon (figure 22). The Ni(L) peak does not interfere with any other peaks in the aerosol sample; however, care must be taken to minimize the oxide on the evaporated Ni coating.

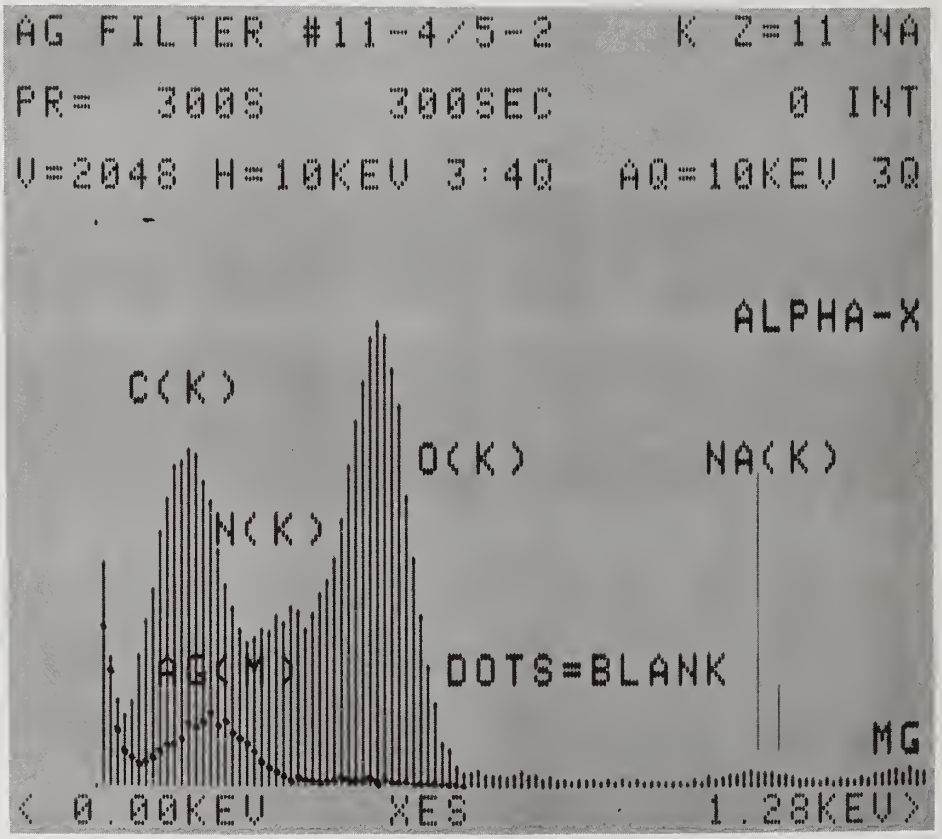

Figure 21. Comparison of ALPHA-X spectrum of aerosol sample collected on plain silver filter with that of blank filter.

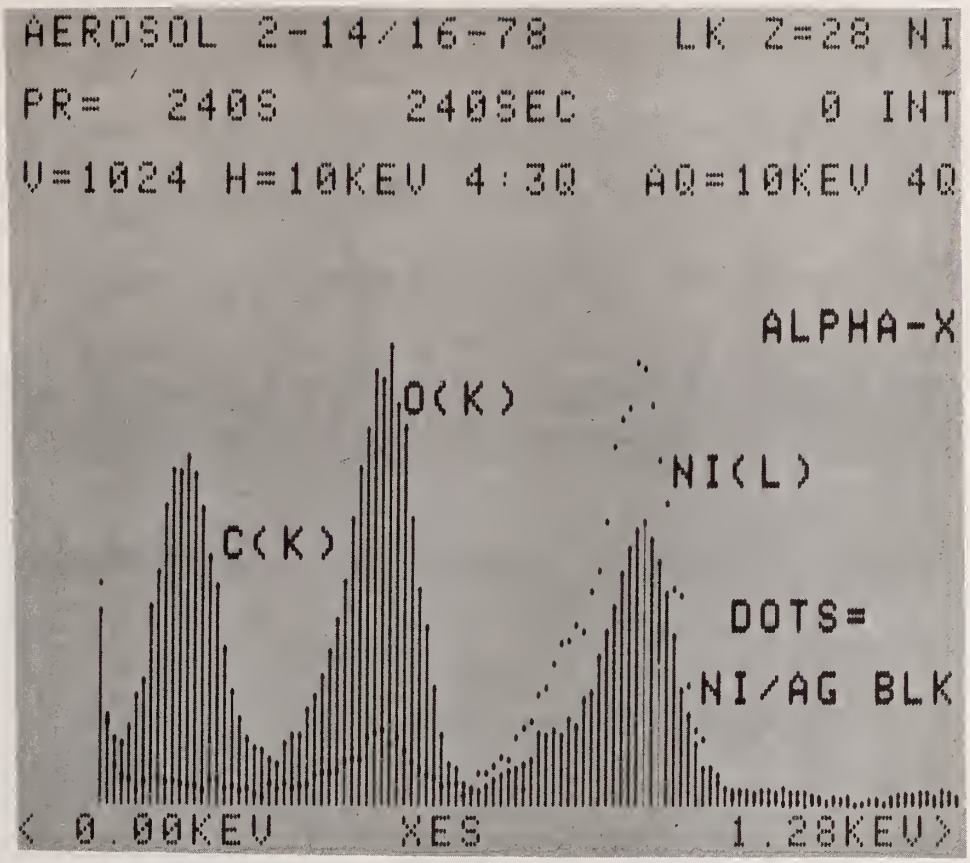

Figure 22. Comparison of ALPHA-X spectrum of aerosol sample collected on nickel-coated silver filter with that of blank nickel-coated filter.

3.2 Electron excitation

As discussed in the section on detector properties, low-energy dispersive x-ray spectrometry on a diffusion-pumped scanning electron microscope (SEM) can be readily accomplished by an UTW detector with an integral electron trap. Spectra have been obtained using such a detector that subtended 10^{-4} steradians from the SEM sample under bombardment by a true electron current of 10 to 15 nA. The pulse processor time constant was 8 μs.

Figure 23 shows the spectrum from solid SiO_2 for 15 keV electrons. Note the O + Si pileup peak. Figure 24 resulted from the bombardment of salt by 10 keV electrons. The small Ni(L) peak seems to be a system peak characteristic of the SEM and appears in many of the spectra. For Fe_2O_3 the low energy portion of the electron-excited spectrum is displayed in figure 25. 15 keV electrons were used to generate the spectrum of x-rays from calcium carbonate (figure 26).

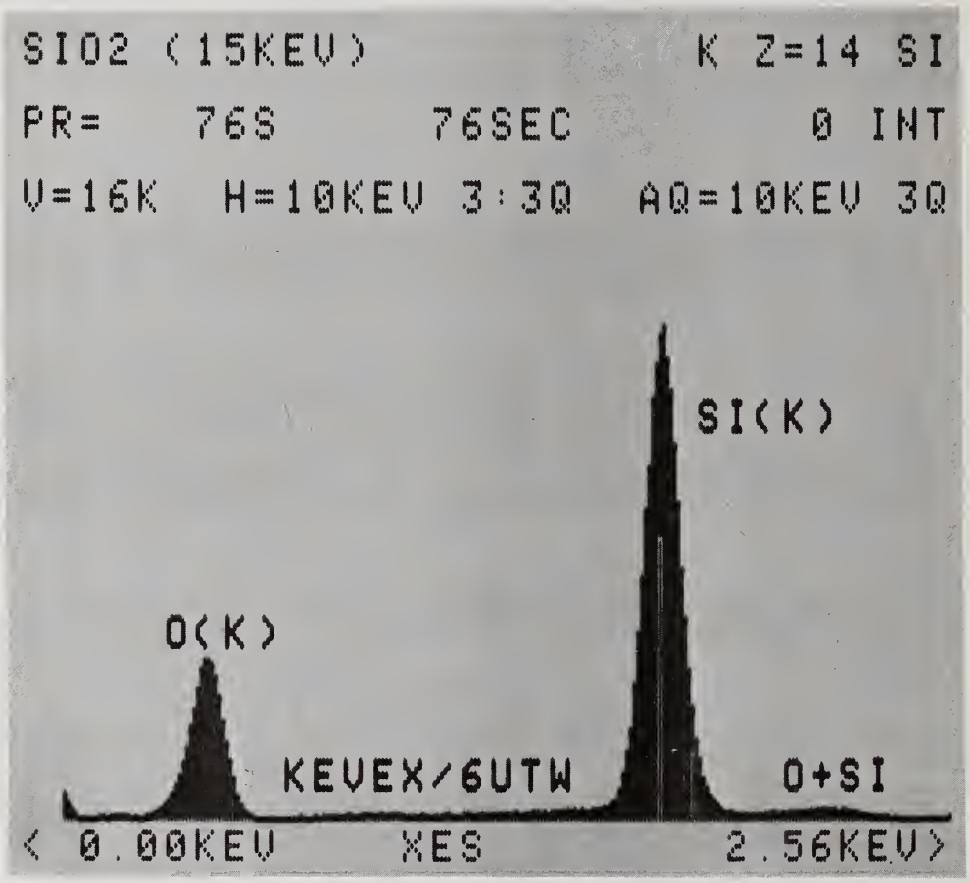

Figure 23. Electron-excited spectrum from solid SiO_2 (Electron energy = 15 keV).

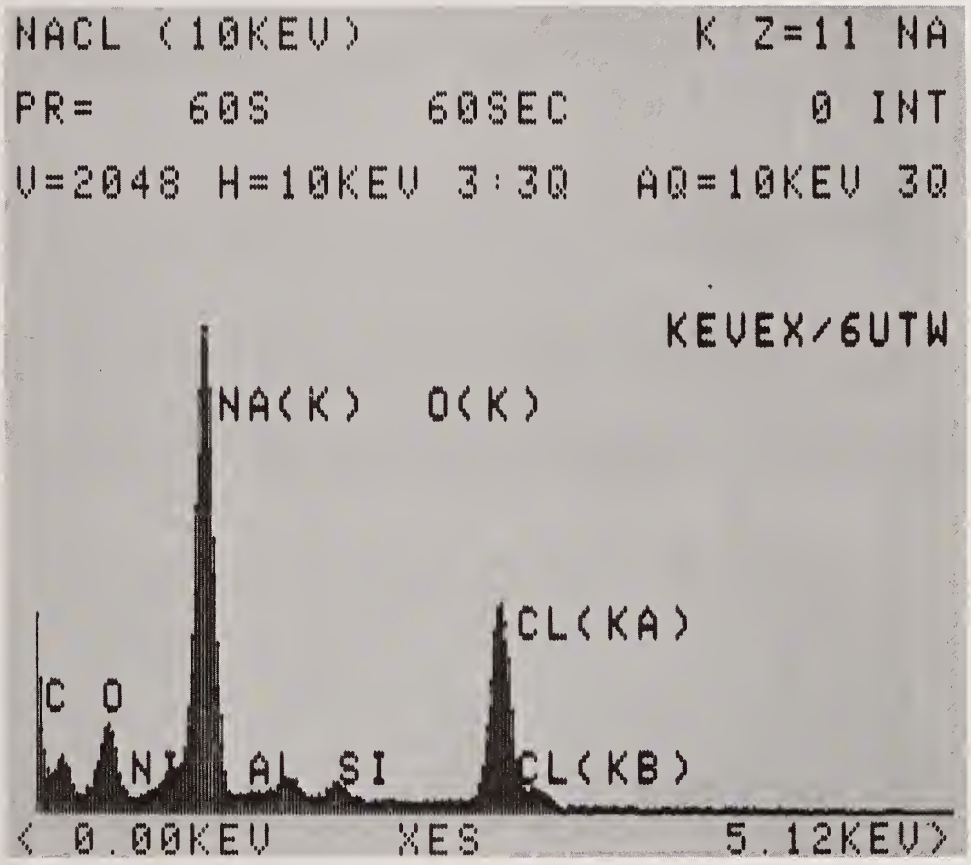

Figure 24. Electron-excited spectrum from sodium chloride (Electron energy = 10 keV).

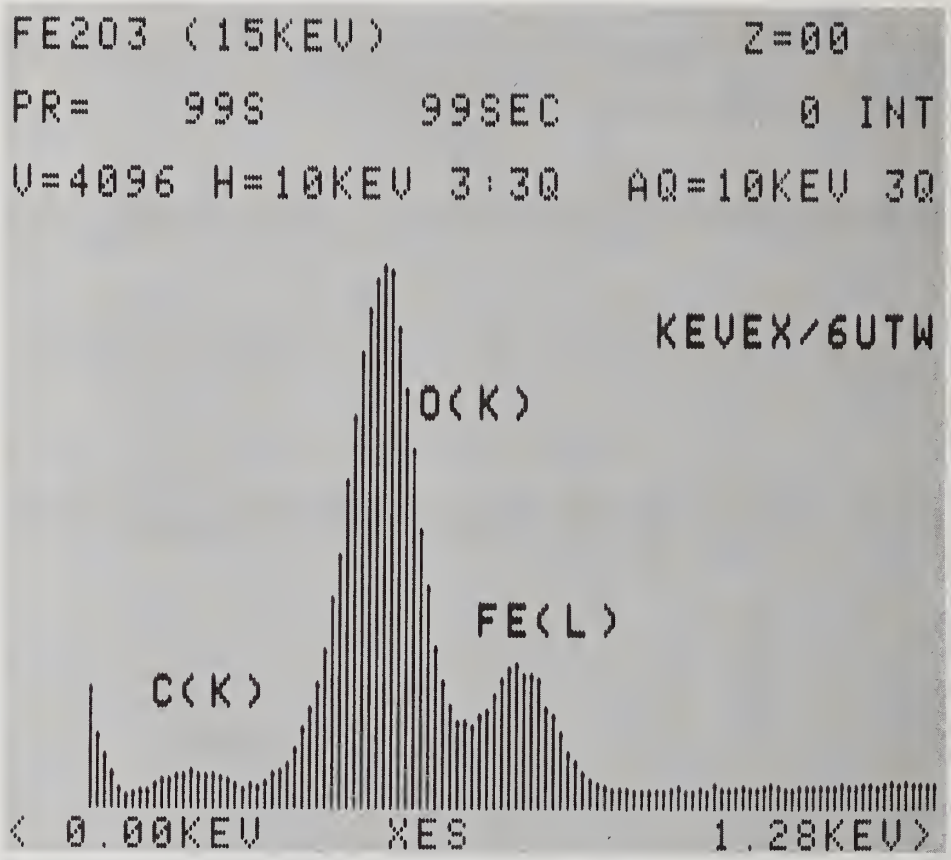

Figure 25. Low-energy portion of electron-excited spectrum from solid Fe_2O_3 (Electron energy = 15 keV).

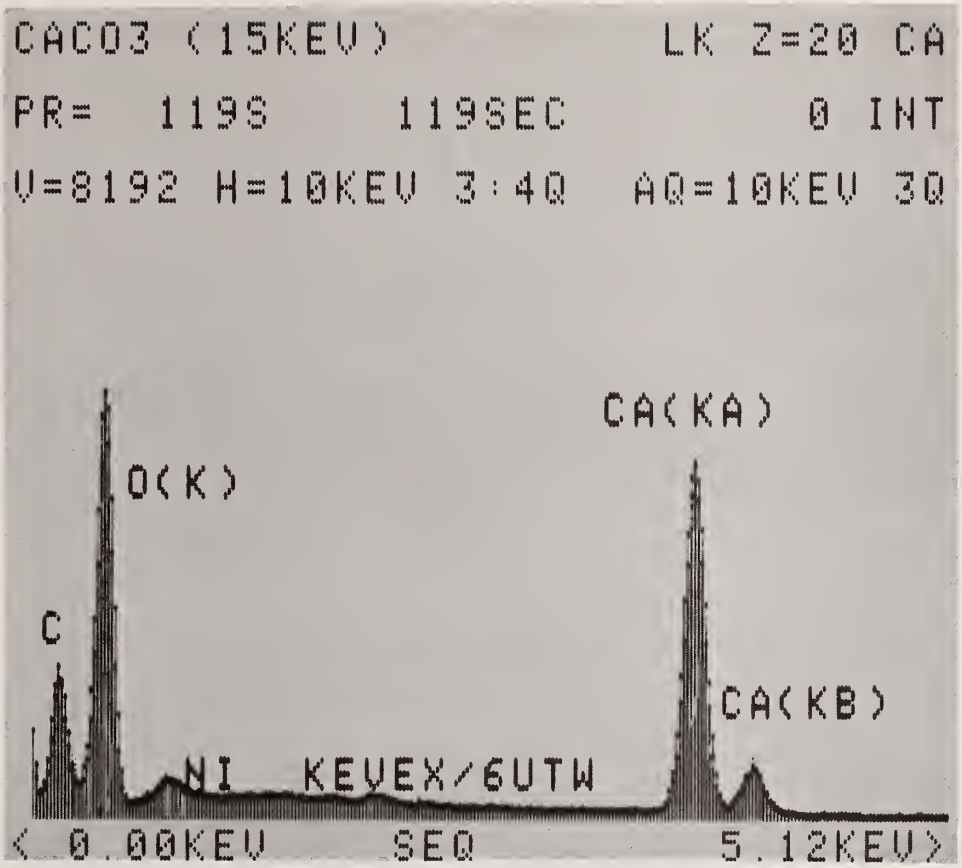

Figure 26. Electron-excited spectrum from calcium carbonate (Electron energy = 15 keV).

Although the UTW detector with an electron trap permits energy-dispersive x-ray spectrometry of low-energy x-rays in the mediocre vacuum normally found with a SEM, proper interpretation of the acquired spectra requires consideration of the processes occurring on or in the electron-bombarded sample. Buildup of contaminants on an irradiated sample can be particularly difficult to eliminate unless the vacuum system is better than average. A comparison of spectra obtained from fresh (i.e., previously unirradiated) MgO to that obtained after the electron beam was rastered over the analysis region for ten minutes is presented in figure 27. Both spectra were obtained in 22 seconds of live time. The large increase in the C(K) intensity and the small increase in O(K) intensity presumably resulted from molecular dissociation of background gases that impinge on the surface of the sample. This presumption is consistent with the linearly increasing C(K) intensity with time (figure 28). For a liquid-nitrogen-trapped, diffusion-pumped system operating at less than 5×10^{-6} torr (as required for use of an UTW detector), this type of sample contamination can be reduced considerably.

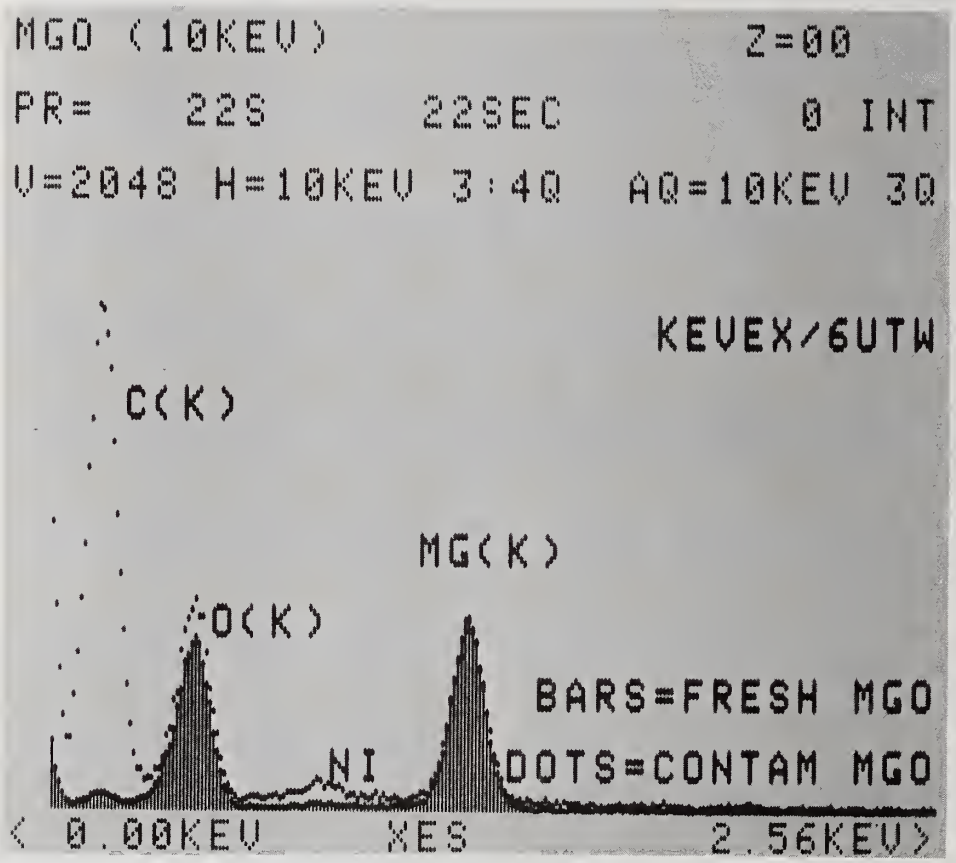

Figure 27. Comparison of electron-excited spectra from MgO at the beginning of electron irradiation and after ten minutes of irradiation (Electron energy = 10 keV).

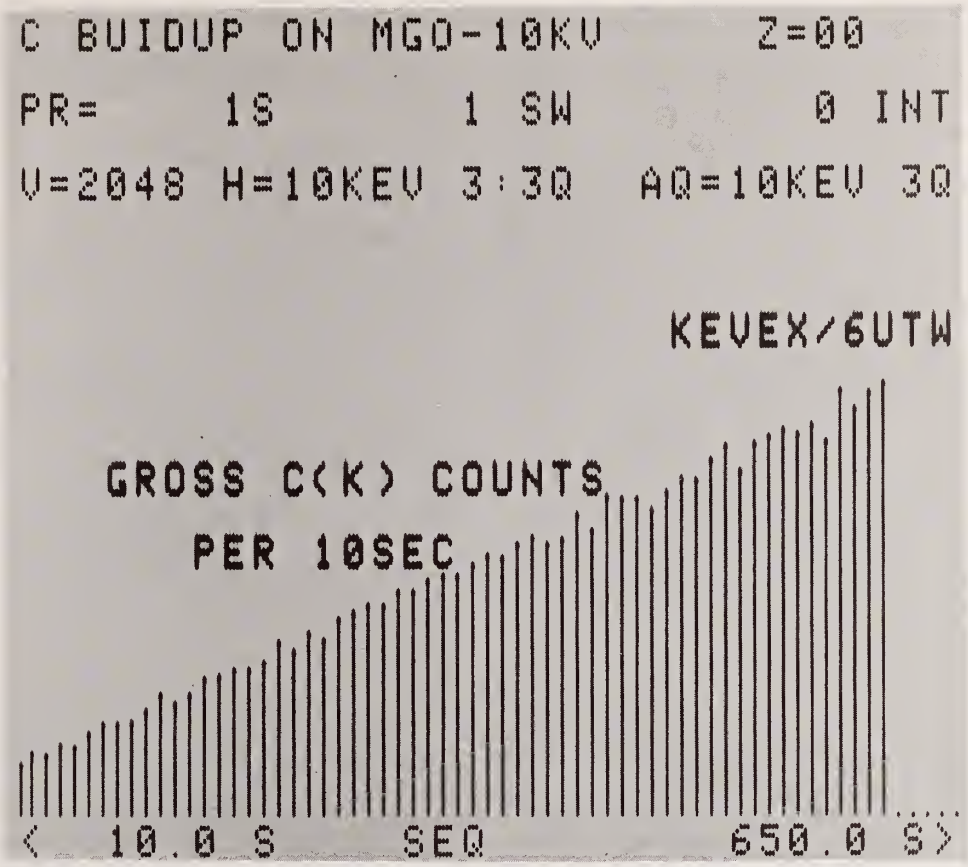

Figure 28. Time dependence of the carbon buildup on MgO for a SEM environment (Electron energy = 10 keV).

4. Conclusions

Windowless (WL), light-barrier (LB), and ultra-thin windowed (UTW) Si(Li) detectors have been shown to be useful for the energy-dispersive spectrometry of x-rays with energies above 200 eV. Efficiencies of 0.05 to 0.25 for C(K) x-rays and 0.10 to 0.50 for O(K) x-rays may be expected for UTW (or LB) and WL detectors, respectively. These detectors have an output linearity more than adequate to permit unambiguous identification of the basically Gaussian peaks with an energy resolution of about 102 eV for C(K) when that for Mn(K) is 146 eV. The availability of detectors appropriate for a variety of vacuum environments permits low-energy x-ray spectroscopy in a wide range of analysis systems, including SEM's, TEM's, Auger systems, and ESCA systems. These detectors should play an increasingly important role in the total analysis (i.e., surface and bulk) of materials.

References

[1] Jaklevic, J. M. and Goulding, F. S., IEEE Trans. Nucl. Sci., NS-18, 187 (1971).

[2] Musket, R. G. and Bauer, W., J. Appl. Phys., 43, 4786 (1972).

[3] Musket, R. G. and Bauer, W., Nucl. Instr. and Meth., 109, 593 (1973).

[4] Musket, R. G., Nucl. Instr. and Meth., 117, 385 (1974).

[5] Veigele, W. J., Atomic Data, 5, 51 (1973).

[6] Musket, R. G., and Bauer, W., Nucl. Instr. and Meth., 109, 449 (1973).

[7] Musket, R. G., Research/Development, 28 (10), 26 (1977).

[8] Zulliger, H. R. and Aitken, D. W., IEEE Trans. Nucl. Sci., NS-17, 187 (1970).

[9] Zulliger, H. R., J. Appl. Phys., 42, 5570 (1971).

[10] Bauer, W. and Musket, R. G., J. Appl. Phys., 44, 2606 (1973).

[11] Musket, R. G. and Bauer, W., J. Appl. Phys., 47, 353 (1976).

[12] Wohn, F. K., Clifford, J. R., Carlson, G. H., and Talbert, W. L., Jr., Nucl. Instr. and Meth., 101, 343 (1972).

[13] Musket, R. G., in, Advances in X-ray Analysis, Vol. 22, G. J. McCarthy et al., eds., (Plenum, New York, 1979), p. 401.

National Bureau of Standards Special Publication 604. Proceedings of the Workshop on Energy Dispersive X-Ray Spectrometry held at NBS, Gaithersburg, Maryland, April 23-25, 1979. (Issued March 1981)

THE EFFICIENCY OF Si(Li) DETECTORS AT VERY LOW PHOTON ENERGIES

P. J. Statham

Link Systems Ltd.
Halifax Road, High Wycombe
Bucks. HP12 3SE England

Abstract

The efficiency of a Si(Li) detector for low x-ray energies is an important parameter in determining both the shape of the observed continuum and the sensitivity factors for "standardless" techniques such as the analysis of thin samples by the intensity ratio technique. This paper considers the factors which determine the efficiency and examines the possibilities for measurement and their limitations.

1. Introduction

To date, detailed studies of detection efficiency seem to concentrate on the x-ray energy region above about 2.5 keV primarily because of the absence of "doublet" standards with peaks at suitable energies. However, the tacit assumption is often made that the efficiency for energies below 2.5 keV can be predicted satisfactorily using physical formulae based on quoted thicknesses for materials constituting the detector entrance window. There is already enough evidence in the literature to suggest that such an assumption is not always justified and this paper attempts to gather together such evidence and present new information to demonstrate the errors which could result.

Knowledge of detection efficiency is important in a number of techniques such as measurement of absolute x-ray yields [1][1], prediction of the continuum (bremsstrahlung) shape for background correction and measurement [2-6], determining efficiency factors for the "ratio" technique for thin film quantitation [7] and for "standardless" analysis [8]. Whereas the Si(Li) spectrometer behaves in an almost ideal fashion in the energy range 5-10 keV, the elements Na, Mg, Al, Si are often of interest and fall in an energy region where the efficiency is determined by several unrelated factors. In "windowless" systems some of the uncertainty is removed by elimination of the Be vacuum window, but new experimental problems are introduced which detract from this apparent advantage.

If we assume that the detector is well collimated so that off-axis efficiency variations [9] are not significant, then the geometric efficiency can be determined [1] and the remaining fall-off in efficiency is due to absorption in the Be window, gold conductive coating and silicon "dead layer", charge collection effects within the detector, and to the efficiency of pulse detection by the electronics.

1.1 Beryllium window

The manufacturers of beryllium foil recommend that it be stored and used in a dry atmosphere (< 50% RH) to maintain the vacuum integrity of the foil which is extremely sensitive to all oxidizing agents. Although detector manufacturers take great care to obey these guidelines, the user is not always aware of them and windows are sometimes quite innocently exposed to water vapor and even caustic gases.

[1]Figures in brackets indicate the literature references at the end of this paper.

Although the crystal and cold finger are suspended in a vacuum, there is invariably a small amount of heat transfer to the cryostat wall with the result that the window is normally one of the coldest surfaces in the specimen chamber. Furthermore, the problem is worse when space requirements force the detector snout to be very narrow. As a consequence, oil and water vapor condense preferentially on the window and cause an increase in effective window thickness and thus a drop in efficiency. The problem is somewhat alleviated by the presence of a cold finger, as would be used to reduce specimen contamination for example, and some success has been achieved by using the heat from a miniature electric light bulb to slightly raise the snout temperature (D. Smith, University of Alberta, private communication).

Eight μm or "1/3 mil" is the most common thickness used for x-ray work, and aluminum foils of this thickness exhibit roll-marks and occasional pin-holes (P. Morris, Alcan Laboratories, private communication). The SEM micrograph in figure 1 shows that surface defects are also visible on a typical beryllium foil and furthermore the side view in figure 2 indicates that the thickness is irregular on a microscopic scale. In practice, the average thickness may vary by about 30 percent from the nominal value of 8 μm and there may be some inaccuracy in values for mass absorption coefficients [10] so, even if irregularities are ignored, direct calculation of x-ray absorption is prone to error. Since foil thickness is usually determined indirectly by weighing a specific area of material, in effect it is the average mass thickness which is being measured so it seems fair to assume that an average mass thickness could be used in a formula for absorption. However, absorption is a non-linear effect and the use of an average thickness tends to produce an underestimate of transmission efficiency. This is demonstrated in Table 1 where the transmission efficiency has been calculated for a composite foil where half of the foil area has a thickness of 5 μm and the remainder is 10 μm thick. The mean thickness of the foil is 7.5 μm and the calculated transmission efficiencies agree quite well down to 1.5 keV. However, at low energies, when the efficiency falls below 50 percent, the composite foil transmits a disproportionate fraction of the radiation through the thin areas and at 0.5 keV, the transmission is almost a factor of three greater than predicted for a 7.5 μm foil of uniform thickness.

Figure 1. SEM micrograph in plan view showing the surface of a 1/3 mil. Be foil originally used for a detector window.

Figure 2. SEM micrograph as for figure 1 but viewed from the side and slightly above the foil. Some blobs of epoxy resin, originally used to secure the window, are visible on the surface.

Table 1. Calculated transmission efficiency for a 7.5 μm Be foil compared with that for a composite foil with equal areas of 5 μm and 10 μm thickness.

Energy keV	Percent 7.5 μm	Transmission Composite
0.5	0.8	2.1
0.6	5.8	8.6
0.7	15.9	19.0
0.8	28.6	31.1
0.9	40.9	42.7
1.0	51.6	52.9
1.5	81.3	81.5
2.0	91.3	91.4
2.5	95.3	95.3

1.2 Gold layer

A gold film is used to establish the electrical contact at the front surface of the detector and usually has a nominal thickness of 200 Å. There is evidence to suggest that such films are extremely non-uniform in thickness. Jaklevic and Goulding [11] point out that the resistance of the evaporated layer shows an abrupt decrease when the thickness exceeds 80 Å and suggest this is due to the growth of islands which eventually coalesce to form a filamentary net. Films of similar thickness are used when coating specimens for electron microscopy and do exhibit this filamentary structure [12] and large open areas may still be present in 200 Å films [11].

When calculating absorption within this layer, it has been suggested [11] that conventional theory becomes inappropriate for radiations such as C Kα (λ = 44 Å) where the wavelength approaches the film thickness. However, as pointed out at this meeting (R. Musket, Kevex Corporation), if the film is indeed segregated, the regions responsible for absorption will be thicker than the average value of 200 Å so normal absorption calculations should be valid. Nevertheless, the situation is still not trivial and, as shown in Table 1, a film of non-uniform thickness transmits more radiation than a uniform film with the same average thickness. It has been suggested [11] that if the film were uniform, then the consequent attenuation produced by 200 Å of gold would seriously affect the usefulness for detecting low energy x-rays from carbon and oxygen.

One way of measuring the effective gold layer is to observe the absorption steps present in the bremsstrahlung background. However, if the gold layer thickness is included as a variable parameter in a least squares fitting routine used to determine all the window thickness parameters, the predicted gold thickness often turns out to be much less than 200 Å or sometimes even negative. For this reason, the gold layer is often ignored but Au absorption steps can usually be seen in a spectrum of carbon with good counting statistics (at least 10K counts per channel). Brombach [13] has suggested that the gold edges are less visible than one would expect because the largest discontinuities (Au $M_{IV,\ V}$) actually involve a smooth transition in the mass absorption coefficient value. The author provides a theoretical argument which is substantiated by the experimental findings of Steele [14] and shows that experimental spectra can be accurately fitted in the 1.5 to 2.5 keV energy range by using a modified formula for absorption coefficients, and assuming a gold layer thickness of 200 Å and a 25 percent gold free area. The main absorption step occurs in the region of 2.2 keV and typically corresponds to a change of 5 percent in efficiency. There is little to differentiate between the absorption effects of beryllium and gold below 2 keV, so when window thickness parameters are determined indirectly, by least squares fitting to bremsstrahlung spectrum, the predicted gold thickness is often misleading. A 5 percent step in the background is undetectable in typical electron-excited spectra with roughly 200 counts per channel, so omission of the gold layer

term does not have any serious consequences for background corrections. However, observed characteristic peak intensities for elements such as P, Cl, S will be influenced by the gold which therefore should not be ignored for accurate work.

1.3 Silicon dead layer

The silicon "dead" layer is a region near the surface of the detector where charge collection is poor and not a passive zone of silicon on the front surface of the detector. When an x-ray photon of energy E is absorbed close to the surface, some of the charge may be lost in the energy-to-charge conversion process. As a consequence a count appears in the spectrum at an energy less than E and is "lost" by virtue of not appearing in the correct channel. The proportion of photo-electric events which occur close enough to the surface to exhibit such behavior is determined by the absorption coefficient for radiation of energy E in silicon, so counts are "lost" from a spectral peak just as if photons were absorbed in a thin layer of passive silicon. Therefore, for some applications, it is convenient to calculate the absorption due to a silicon "dead" layer which would remove counts completely from the spectrum, rather than attempt to correct the spectrum for incomplete charge collection which displaces counts from a peak into a low-energy tail.

The "escape" effect [15] also results in counts being displaced (by 1.74 keV) from their true position in the spectrum. SiKα photons are only produced in the detector by incident photons with energy greater than 1.84 keV. Therefore, a step of about 2 percent appears at the SiK_{ab} energy because there is approximately a 2 percent chance of SiKα escape for photons with energy greater than the silicon absorption edge whereas no SiKα escape is possible below this energy. The size of this step is consistent with a passive layer of silicon roughly 0.03 μm in thickness.

Since the "dead" layer is a consequence of poor charge collection, the thickness is influenced by both the magnitude of the H.T. bias voltage and the state of the surface. Jaklevic and Goulding [11] measured a variation from 0.4 μm to 0.2 μm as the H.T. bias was raised from 100 V to 1000V. In a more recent paper, Llacer et al. [16], suggest that the window effect is due to a fundamental transport limitation of electrons which is only slightly affected by the applied external field and cite the example of a high purity Ge detector where the observed peak tailing was only slightly dependent on bias in the region 300-1000V in a 4 mm detector that was fully depleted at 20V. Although the theory [16] leads to a larger window than is observed, the general form of peak tailing is predicted quite well and the authors [16] propose that the hot-electron transport mechanism represents a physical limit to window thickness (0.4 μm in Ge) which is not likely to be overcome because of the very high field that would be required to do so. However, they point out that the surface potential could depend on surface treatment and metal work function, so different detector fabrication techniques may lead to slightly different window thicknesses.

The effect of the Si dead layer is most evident for x-rays with energy just above the silicon absorption edge so the peak shape for phosphorus shows a marked low-energy tail which, in the example shown in figure 3, reaches a maximum of roughly 7 percent of the peak height. X-rays with energy just below the edge have a much greater range so very few get absorbed in the window region and no tailing is apparent on a SiKα peak for example. When the bremsstrahlung spectrum is observed in this energy region (figure 4), the step in the vicinity of the Si absorption edge is enhanced because degraded events from just above the edge are "dumped" in a region just below the edge. The phosphorus example in figure 3 suggests that this enhances the step height by roughly 7 percent and distorts the background shape in a region extending roughly 0.5 keV below the absorption edge. (The distortion of the background shape is very clearly demonstrated in a spectrum of carbon presented by Fiori and Newbury [17].) This effect has rather serious implications in the context of efficiency since it implies that if the apparent Si dead layer is determined by observation of the step in the background, the thickness will be overestimated by more than 0.1 μm. In terms of modeling the background shape, the significant problem is the distortion below the edge but the real danger arises if one attempts to use such a "fitted" dead layer thickness when predicting overall efficiency.

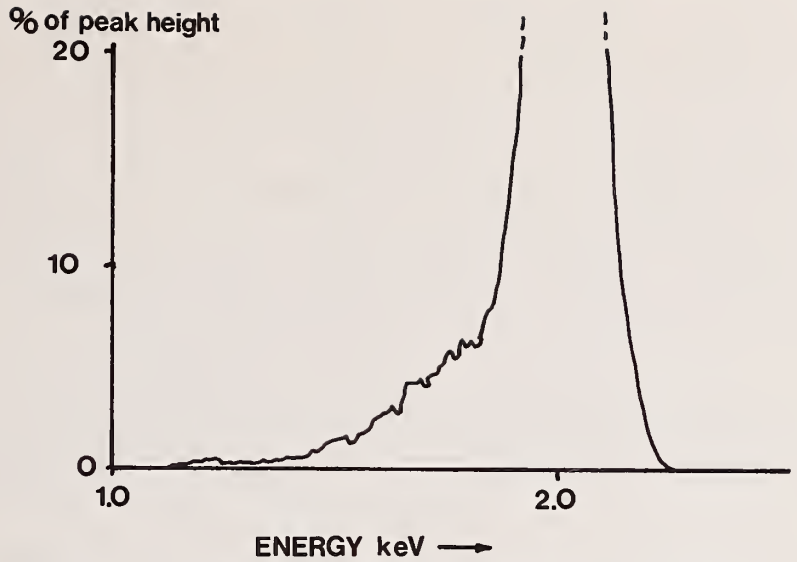

Figure 3. Low-energy tailing on the side of a phosphorus peak.

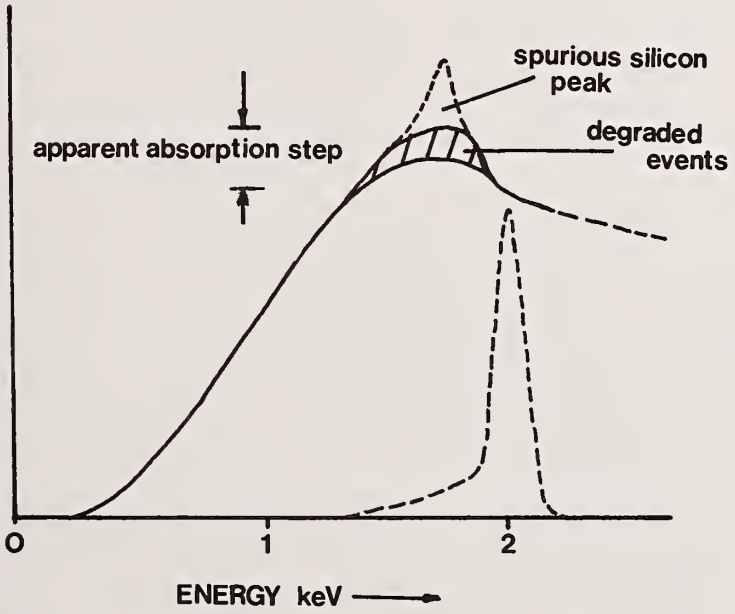

Figure 4. The shape of the bremsstrahlung spectrum in the vicinity of the silicon K absorption edge. The dashed curve shows the shape of a phosphorus peak with associated tail due to poor charge collection.

If counts that appear in the low-energy tail are included when calculating characteristic peak areas, then charge-collection defects will have no effect on the apparent efficiency and there will be no "dead" layer to consider. In other words, if the spectrum were corrected for charge-collection, then there would be no discontinuity in efficiency at the silicon edge. This statement requires some qualification since it only applies to a detector which has been prepared in such a way that there is no inactive silicon left on the front surface. If the lithium drifting, or subsequent surface preparation, is imperfect, there may indeed be truly dead areas of silicon. In this case, x-rays absorbed

in such regions may give rise to fluorescent SiKα x-rays which travel towards the active region of the detector and produce an "internal silicon fluorescence" peak [15]. In Figure 4, I have labeled such a peak as "spurious" since, as a purely empirical phenomenon, it cannot be predicted from physical theory. If the peak is present it is often greater in size than is predicted by calculations which assume a totally-dead layer of 0.1 μm of silicon [15]. Furthermore, the spurious Si peak can be much larger if electrons are actually transmitted through the BE window [18]. Thus, although there is evidence to suggest that the "classic" silicon dead layer is a result of charge-collection processes which may vary only slightly from detector to detector and could in principle be calculated, there may be an amount of dead silicon on the surface which is a function of the method of fabrication used and is essentially indeterminate. Detectors which have been prepared by the same procedure still exhibit spurious Si peaks which vary in size and this observation was corroborated at this meeting (J. Russ, Edax Laboratories).

As a final note in this section, it seems worth pointing out that layers containing silicon do not necessarily have to be connected with the detector itself. Vacuum oils and greases and proprietary vacuum-sealant sprays often contain silicon, so spurious silicon peaks and "dead layer" effects may be in part due to contamination of the entrance window.

1.4 Pulse detection efficiency

Because electrical noise is present, there is always a chance that a pulse may be "missed" by the measurement electronics. This is easiest to understand and to quantify if we look at the behavior of an amplifier which produces unipolar output pulses which are detected if they exceed a threshold voltage [19]. If noise is present, there is a chance that a pulse may arrive at the same time as a negative-going noise excursion so that the resultant voltage waveform fails to exceed the threshold. The smaller the pulse, the more likely this is to occur so the pulse-detection efficiency decreases at low energies. The effect on the overall spectrometer efficiency depends on the noise performance of the channel which is effectively being used to detect the pulse. In many systems it is the discriminator on the output of the main processing channel which open the ADC gate and effectively decides whether a pulse is detected or not. In this case, the noise typically corresponds to 100 eV f.w.h.m. so the efficiency would begin to decrease below an energy of 250 eV if the threshold were set just into the noise distribution [19]. At this meeting, Ron Musket (Kevex Corporation) pointed out that the carbon peak obtained with a "windowless" detector does not show the same low-energy tail as does the oxygen peak. It is possible that the rapid fall-off in pulse-detection efficiency below 250 eV is responsible for this phenomenon since it would in effect attenuate the lower energy pulses preferentially and tend to correct the asymmetry caused by incomplete charge collection. The asymmetry would also be affected by non-linearity in the vicinity of the threshold associated with "peak-detect" pulse measurement. With systems having a beryllium window, the ADC threshold can be raised to exclude low-energy pulses. In this case, the pulse detection efficiency goes through the transition from 100 percent to 0 percent in an energy region extending from roughly 130 eV above to 130 eV below the effective threshold energy.

In some electronic processors, the detection of a pulse is determined by an auxiliary inspection channel which can also be used for pile-up rejection. Since shorter time constants are involved the noise is much greater than in the measurement channel so the roll-off in efficiency occurs at a much higher energy. With a 1 μs shaper, the efficiency typically begins to fall below about 800 eV when the discriminator is set close to noise [19]. However, if the discriminator thereshold is set well above noise, or if shorter time constants are used, the roll-off will occur at higher energies and will affect the overall efficiency in roughly the same way as would be observed with a thicker Be window.

1.5 Efficiency calculations

While engaged in my Ph.D. research [20], I had the opportunity to study two detector systems because the first detector with a 1 mil Be window was replaced with an improved version with a 1/3 mil window. Since the overall efficiency of both systems appeared to be stable with time, the Kα peak intensities for all the electron microprobe standards were compared with the intensity for CoKα from a pure cobalt specimen and standard factors were stored on disk so that subsequently only the CoKα intensity was required to determine all standard intensities. Now the intensity for a given Kα line is given by

$$I_{K\alpha} \propto C \frac{N}{A} \left(\int_{E_c}^{E_o} \frac{Q}{S} dE \right) \omega_K \left[\frac{K\alpha}{K\alpha + K\beta} \right] R\, f(\chi)\, F\, f_{esc}\, \varepsilon \qquad (1)$$

where
- C = element concentration by weight
- N = Avogadros number
- A = atomic weight
- Q = ionization cross section
- E_o = incident beam energy
- E_c = critical excitation potential
- S = stopping power
- E = electron energy
- ω_K = fluorescence yield
- $\frac{K\alpha}{K\alpha + K\beta}$ = fraction of K intensity within Kα peak
- R = backscatter correction
- $f(\chi)$ = absorption correction
- F = fluorescence correction
- f_{esc} = correction for escape effect
- ε = spectrometer efficiency

so by calculating all the unknown terms, the ratio of efficiencies, $\varepsilon_{elmt}/\varepsilon_{cobalt}$, could be determined from the individual standard factors, $I_{elmt\ K\alpha}/I_{CoK\alpha}$. Different calculations were made using the data from one system. The same formulae were used for most of the terms [20] with exception of the generation integral involving Q where two different methods were employed. In one, the integral was evaluated numerically using the Green/Cosslett [21] expression for Q and the Bethe stopping power law [22] and the other used the approximate formula $(U-1)^{1.67}$, with $U = E_o/E_c$, which was suggested by Green and Cosslett [21] and has also been used in a standardless approach by Russ [8]. Thus, from a single set of standard factors, two sets of apparent relative efficiency values were calculated. The realtive efficiencies, $\varepsilon_{elmt}/\varepsilon_{cobalt}$, were then fitted by a least squares technique to the formula

$$k \exp\left(-1.82 \left(\frac{\mu}{\rho_{Be}} \right) \chi_{Be} - 2.33 \left(\frac{\mu}{\rho_{Si}} \right) \chi_{Si} \right) \qquad (2)$$

where both the scaling constant k and the thickness parameters χ_{Be} and χ_{Si} were to be determined. Heinrich's tables [23] were used for mass absorption coefficients, (μ/ρ). The purpose of the original study was to see whether a formula, as in equation (2), could be used to parameterize the efficiency term in equation (1) so that standard factors could be predicted from theory. As seen in Figures 5 and 6, equation (2) fits the derived efficiency ratios to within about 5 percent relative error, irrespective of the formula used for the generation term in equation (1). However, note that those window thickness parameters which are necessary to ensure such a good fit are very different in the two cases. In other words, differences in the theoretical formulae for x-ray generation are compensated by using different values for the Be and Si window thicknesses. It is not surprising that the efficiency calculated by an indirect method should give results which

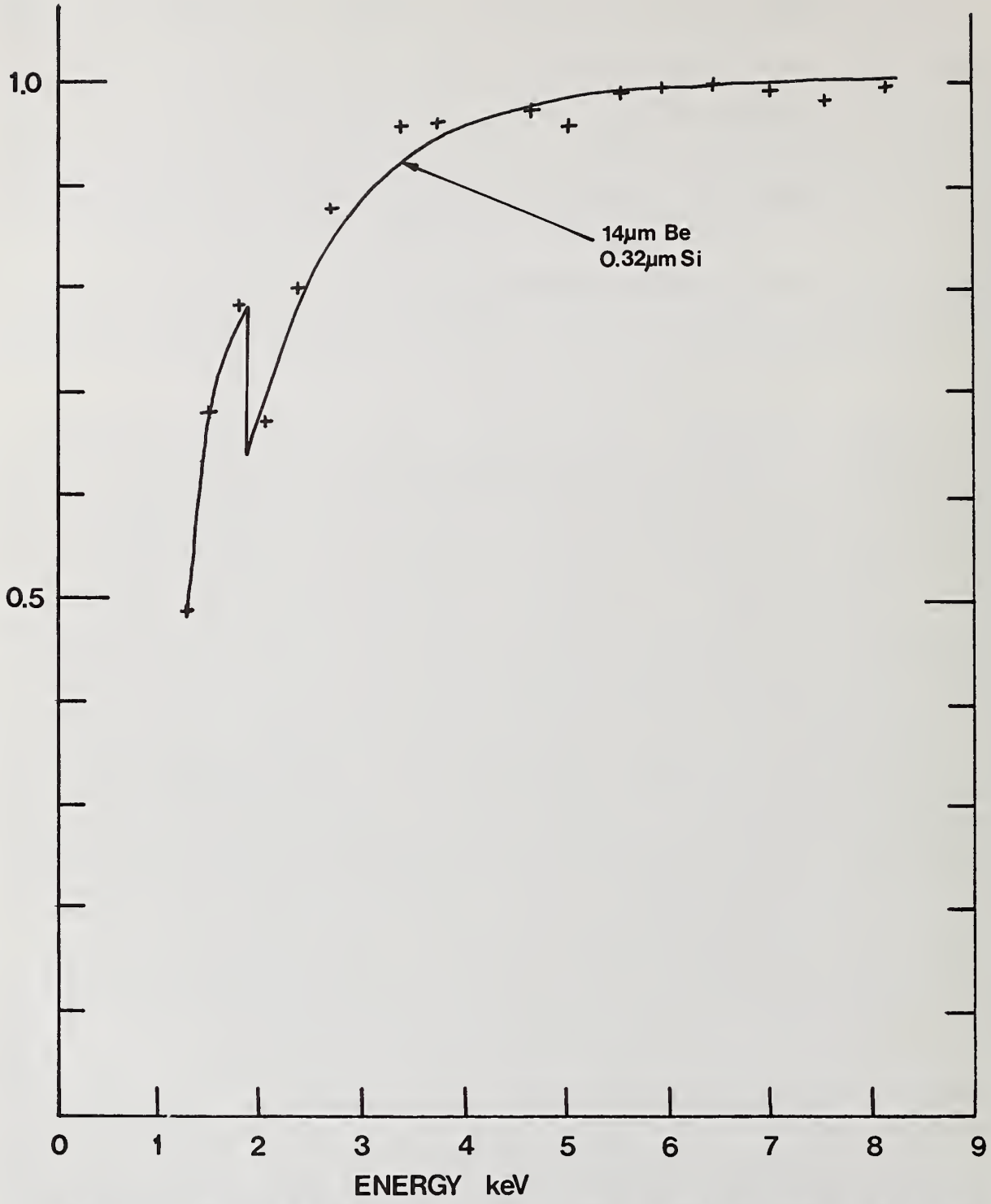

Figure 5. Efficiency relative to that for CoKα, calculated from intensity data from system 2. The intensity integral was evaluated explicitly in equation (1) and the solid curve shows the fit obtained for equation (2).

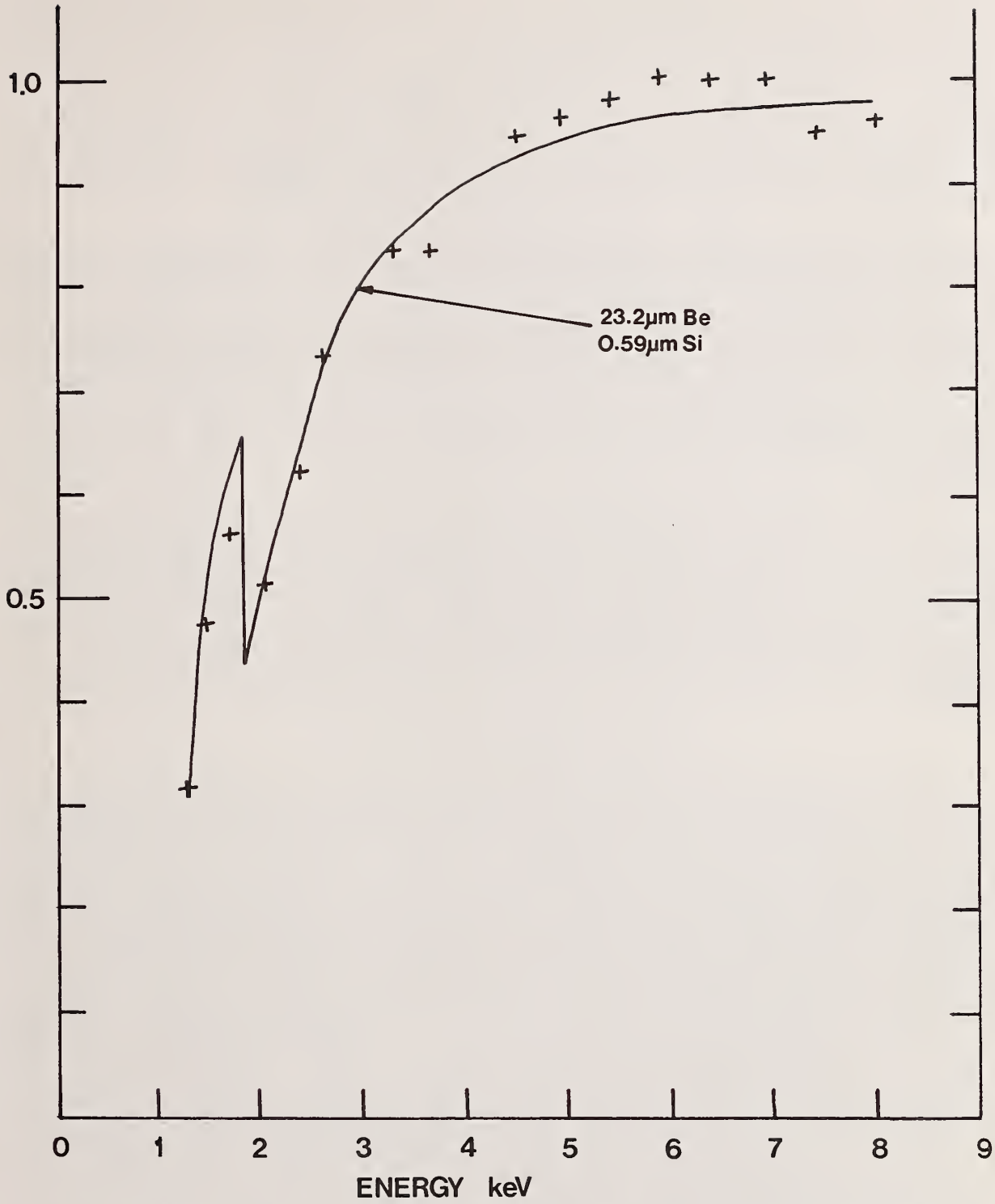

Figure 6. Efficiency relative to that for CoKα, calculated from intensity data from system 2. The approximation $(U-1)^{1.67}$ was used in equation (1) and the solid curve shows the fit obtained for equation (2).

depend on the accuracy of the theories involved and there is a danger of attaching too much significance to the predicted values without appreciating the sources of error. The examples shown clearly demonstrate the folly of assuming that fitted window thickness parameters accurately describe the detector structure; although the manufacturer's nominal specifications for χ_{Be} and χ_{Si} were 8 μm and 0.1 μm respectively, the fitting method predicted 14 μm, 0.3 μm and 23 μm, 0.6 μm as alternative descriptions derived from the same set of experimental data. The formalism described by equations (1) and (2) is obviously useful in that it correctly describes the overall trends in generated x-ray intensity and therefore can be used to interpolate between experimental values. However, it is safer to treat the formulae as a convenient way to mathematically parameterize a system rather than as a route to determining fundamental constants.

Similar arguments apply to the fitting of the bremsstrahlung background. Although one set of window thicknesses may produce a good fit when used in a theoretical expression for the background spectrum obtained under a specific set of experimental conditions, there is no guarantee that the same set of thickness parameters will result in an equally good fit when the experimental conditions (such as kV, take-off angle, specimen composition) are changed. Again, this is because the window absorption term tends to compensate for inaccuracies in the theory, which are likely to vary as conditions are changed. In general, fitting to the background and fitting to characteristic line data yield different results for the optimum set of window thickness parameters, both because of inaccuracies in theoretical expressions and because of fundamental considerations such as the silicon "dead" layer, which, as described above has a different effect on characteristic lines and the continuum.

The gold coating was not considered in equation (2) because of its relatively small effect and in any case, the scatter of the data suggest that a 5 percent step due to a gold layer could not be determined with any confidence. The effects of both the gold layer and silicon dead layer should cancel to some extent when one considers the ratio of efficiencies for two systems and the plot in Figure 7 shows the results of fitting just a beryllium window term to the ratio of intensities obtained for the two systems. The quality of the fit suggests that assumption of a uniform thickness layer and use of fitted absorption coefficients is satisfactory for Be windows approximately 1 mil (25 μm) in thickness.

1.6 Advantages of poor efficiency

Although it is obvious that good efficiency is required at low energies if one is to observe the light elements C, O, N, it is not often realized that this will compromise the high-energy performance. As mentioned above, the detection efficiency for the electronics is very poor below 1 keV when shaping times are shorter than about 1 μs so pile-up rejection is virtually non-existent for x-rays in this region. Therefore, it is desirable to absorb unwanted low-energy x-rays with a thicker window to avoid the peak shift and broadening which results from undetected pile-up [24]. A further problem concerns the transmission of electrons through the window. Transmitted electrons usually appear in the spectrum as a broad hump superimposed on the background [17] and those of low-energy will go undetected by the pile-up inspector and thereby induce peak shift and broadening. Although an 8 μm Be window should stop 20 kV electrons effectively, experiments indicate that enough 20 kV electrons can penetrate a nominal 8 μm window to generate a significant silicon peak from dead zones of silicon and at 30 kV, roughly half the observed continuum is due to transmitted backscattered electrons [18] (in a SEM). The ideal solution is to install an electron trap but this can involve the generation of fields which upset the electron optics of the microscope and may be impossible because of space restrictions. If this is the case, then again it is desirable to use a thicker window, at the expense of low-energy x-ray efficiency, to absorb the troublesome electrons. For voltages up to 30 kV, a 4 μm mylar film provides an effective barrier to electrons when placed in front of a nominal 8 μm Be window [18].

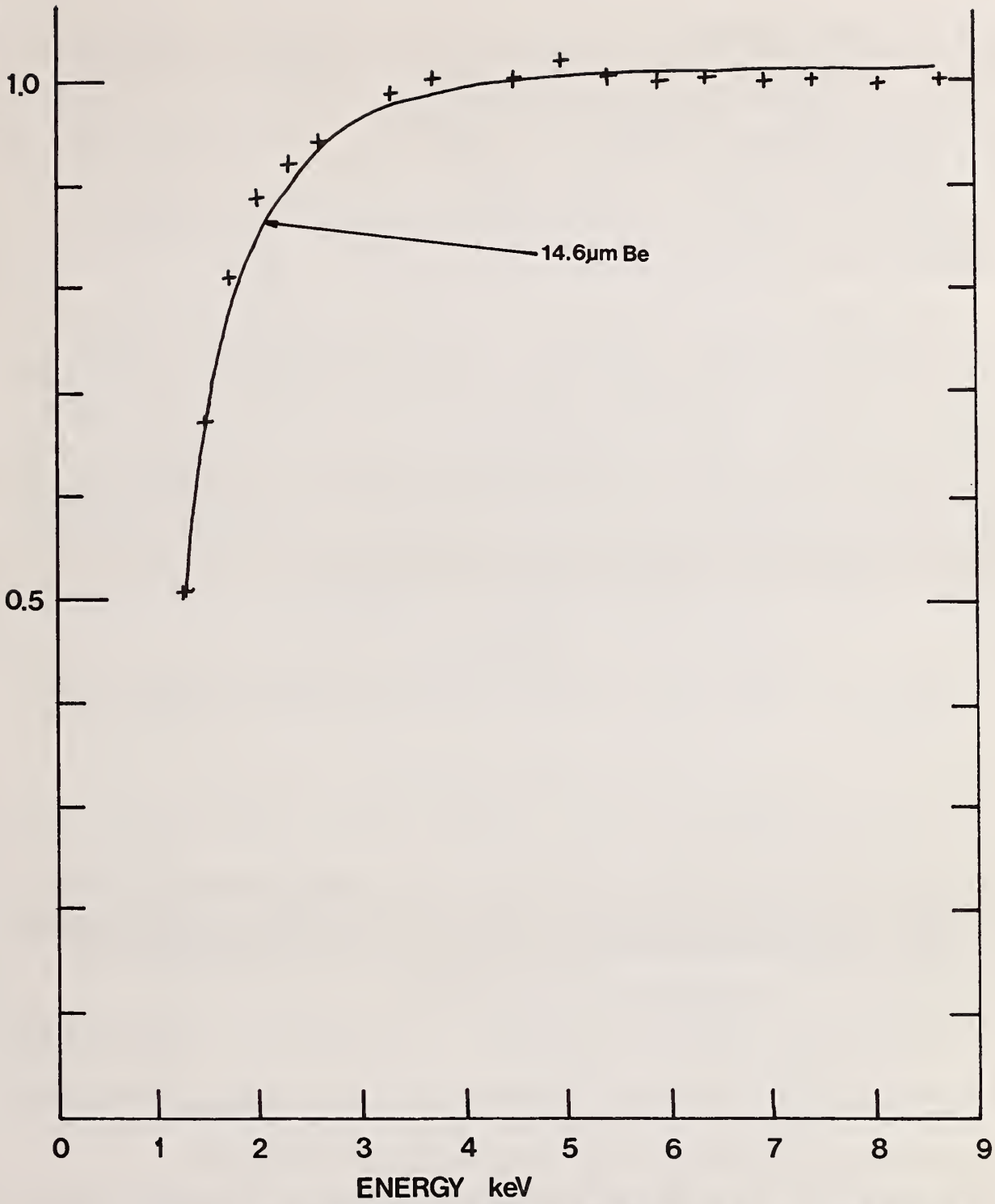

Figure 7. Ratio of efficiencies for system 1 and system 2. The solid line shows the fit obtained for equation (2). System 1: 1 mil Be, System 2: 1/3 mil Be (nominal thicknesses).

2. Conclusions

The nominal thicknesses quoted by a manufacturer for the layers constituting the detector entrance window are only a guide to overall performance and are subject to wide tolerance even when some method of physical measurement is possible. (In the case of the Be window, this tolerance typically corresponds to a variation of 15 percent in the efficiency at 1 keV). Furthermore, the individual layers are non-uniform in thickness so conventional absorption calculations may be inappropriate. Indirect methods of measuring efficiency are limited by the accuracy of fundamental parameters in theoretical expressions and formulae such as equation (2) should really be treated merely as convenient functions for parameterizing performance. The silicon "dead" layer is primarily a charge-collection phenomenon so its effect on efficiency is really a question of definition and the overall efficiency may vary with time because of contamination build-up on either the Be window or the detector surface.

This summary paints a bleak picture but is intended to emphasize why characterization of spectrometer performance is non-trivial at low-energies. At present, probably the only way to determine efficiency accurately is to use a flow proportional counter as a "transmission cell" and calibrate the spectrometer using the method described by Loomis and Keith [25]. Such a calibrated spectrometer could in principle be used to categorize a suitable portable secondary standard, such as a well-characterized material excited by an electron beam or x-rays of known energy. It is perhaps worth mentioning that the action of comparing peak intensity from an unknown with that from a standard cancels out the efficiency term, which is only of importance for fundamental measurements or standardless analysis. Although use of thinner entrance windows effectively removes some of the uncertainty in the efficiency term, low energy x-rays and electrons have a detrimental effect on spectrometer performance because of undetected pile-up so, in practice, it is desirable to use as thick a window as the experiment will tolerate.

References

[1] Lifshin, E., Ciccarelli, M. F., and Bolon, R. B., Proc. 12th Ann. M.A.S. Conf., Boston, Mass., U.S.A., (1977), paper 104 and Proc. 8th Int. Conf. X-Ray Optics and Microanalysis (in press).

[2] Ware, N. G. and Reed, S. J. B., J. Phys. E.: Sci. Instr., 6, 286 (1973).

[3] Lifshin, E., Proc. 9th Ann. Conf. Microbeam Analysis Society (M.A.S.), Ottawa, Canada, paper 53 (1974).

[4] Fiori, C. E., Myklebust, R. L., and Heinrich, K. F. J., Anal. Chem., 48, 172-176 (1976).

[5] Small, J., Heinrich, K., Fiori, C., Newbury, D., and Myklebust, R., Proc. 13th Ann. Conf. Microbeam Analysis Society (M.A.S.), Ann Arbor, MI, U.S.A., paper 56, (1978).

[6] Statham, P. J., X-Ray Spectrom., 5, 154-168 (1976).

[7] Goldstein, J. I., Costley, J. L., Lorimer, G. W., and Reed, S. J. B., Proc. Scanning Electron Microscopy, Vol, I, 315-323 (1977).

[8] Russ, J. C., Proc. 9th Ann. Conf. Microbeam Analysis Society (M.A.S.), Ottawa, Canada, paper 22 (1974).

[9] Alfassi, Z. B. and Nothman, R., Nucl. Instr. & Meth., 143, 57-60 (1977).

[10] Heinrich, K. F. J., in The Electron Microprobe (McKinley, T. D., Heinrich, K. F. J., and Wittry, D. B., eds.) Wiley, N. Y., 1966, pp. 296-377.

[11] Jaklevic, J. M. and Goulding, F. S., IEEE Trans. Nucl. Sci., NS-18 (1), 187-191 (1971).

[12] Echlin, P., Scanning Electron Microscopy, Vol. I, 109-132 (1978) (SEM Inc. AMF O'Hare, Il 60666, U.S.A.) (1978).

[13] Brombach, J. D., X-Ray Spectrometry, 7, 81-91 (1978).

[14] Steele, W. J., Proc. 9th Ann. Conf. on Electron Microprobe Analysis, Microbeam Analysis Society, Ottawa, Canada, paper 19 (1974).

[15] Reed, S. J. B. and Ware, N. G., J. Phys. E.: Sci. Instr., 5, 582-584 (1972).

[16] Llacer, J., Haller, E. E., and Cordi, R. C., IEEE Trans. Nucl. Sci., NS-24 (1), 53-60 (1977).

[17] Fiori, C. E. and Newbury, D. E., Scanning Electron Microscopy, Vol. I, 401-422 (1978) (SEM Inc., AMF O'Hare, Il 60666, U.S.A.) (1978).

[18] Statham, P. J., 14th Ann. Microbeam Analysis Society Conference, San Antonio, Texas, U.S.A., 247-253 (1979).

[19] Statham, P. J., X-Ray Spectrom., 6, 94-103 (1977).

[20] Statham, P. J., Ph.D. Thesis, University of Cambridge, England (1975).

[21] Green, M. and Cosslett, V. E., Proc. Phys. Soc., 78, 1206 (1961).

[22] Bethe, H. A. and Ashkin, J., in Experimental Nuclear Physics, 1, Wiley, N. Y., 1953, pp. 166-357.

[23] Yakowitz, H., Myklebust, R. L., and Heinrich, K. F. J., NBS Tech. Note 796, (1973) on "FRAME" Program.

[24] Kandiah, K., in Physical Aspects of Electron Microscopy and Microbeam Analysis, Chapter 24 (Siegel, B. and Beaman, D. R., eds.) Wiley & Sons, 1975.

[25] Loomis, T. C. and Keith, H. D., Appl. Spectroscopy, 29, 316-322 (1975).

National Bureau of Standards Special Publication 604. Proceedings of the Workshop on Energy Dispersive X-Ray Spectrometry held at NBS, Gaithersburg, Maryland, April 23-25, 1979. (Issued March 1981)

ELECTRONIC TECHNIQUES FOR PULSE-PROCESSING WITH SOLID-STATE X-RAY DETECTORS

P. J. Statham

Link Systems, Ltd.
Halifax Road, High Wycombe
Bucks. HP12 3SE
England

Abstract

This paper reviews the methods which have been proposed for quantifying the output of a solid-state detector and summarise the state-of-the-art with regard to noise and count rate performance for x-ray systems. Ancillary techniques which improve the performance of the basic pulse-processor such as pulsed excitation, pile-up rejection and spectrum stabilisation will also be discussed and the fundamental limitations will be analyzed.

1. Introduction

To a large extent, detailed knowledge of the operation of pulse processing electronics is no longer a pre-requisite for successful x-ray energy spectrometry because sophisticated design techniques have gone a long way to reducing the apparent complexity to that of a simple amplifier with just input, output and power supply connections. Indeed, with the astonishing technological advancement in the field of digital electronics and consequent trend towards automation, there has been a tendency to de-emphasize the importance of analogue electronics and to concentrate on the more prestigious aspects of a computer based system such as interactive colour graphic monitors with a variety of display modes, multi-port data acquisition memories and automation packages for microscopes and XRF equipment. Certainly, the early problems of amplifier lock-up, drift, excessive pile-up and count-rate-dependent peak shift have been solved to the extent that if incident x-rays are limited to an energy range from 1 keV to 20 keV and to count rates less than 10 kcps, then characteristic peaks will appear within one channel of their expected position in a 1000-channel spectrum and qualitative analysis can be performed without difficulty. However, comparatively new fields, such as light element analysis with particle excitation and analytical electron microscopy, involve x-rays with energies extending far outside the 1 keV to 20 keV range and an understanding of the limitations of pulse processing electronics is essential to the correct interpretation of spectra. Even with a restricted range of energies, second-order defects within the electronics can have disastrous consequences for quantitative analysis when severely-overlapping peaks have to be resolved and an appreciation of the fundamentals can help in deciding whether or not a given pulse amplifier will be adequate for a particular application. This paper will cover the salient features of various electronic techniques without paying attention to the details of implementation (which are really the reserve of a design engineer) and thus attempt to give the reader enough insight to predict situations where performance of a given system is likely to suffer.

2. Head Amplifier

When a detector, appropriately biased, is exposed to a beam of x-rays, each detected photon is converted to a packet of charge which is collected at the electrodes to give a voltage proportional to energy and inversely proportional to the effective capacitance of the reverse-biased junction. Since this capacity changes with voltage, a charge-sensitive amplifier configuration is normally employed as the first stage in the electronic chain

(figure 1). A field effect transistor (FET) is now exclusively used at the signal input because of its low noise properties which are improved by cooling to about 100 °K. The gate is connected directly to the detector to avoid the noise component and risk of damage due to breakdown which would be present if a coupling capacitor were used. The detector and FET leakage currents and the mean current due to arrival of photons at the detector will cause the output to drift in such a dc-coupled system so some method of stabilisation is required. The charge produced by a low-energy x-ray photon is of the same order as that produced by a current of 0.1 nA flowing for 1 μs so the feedback current has to be very small and could be achieved by connecting a very-high-valued resistor as shown in figure 1. However, such high-valued resistors have reactive components, may change resistance at low temperatures, involve extra noise due to added capacitance and generate extraneous noise [1][1] so that resistive feedback offers a rather poor compromise between noise performance and stabilisation for x-ray work. Several alternative feedback techniques have been suggested but the one that really revolutionised the field was opto-electronic charge neutralisation.

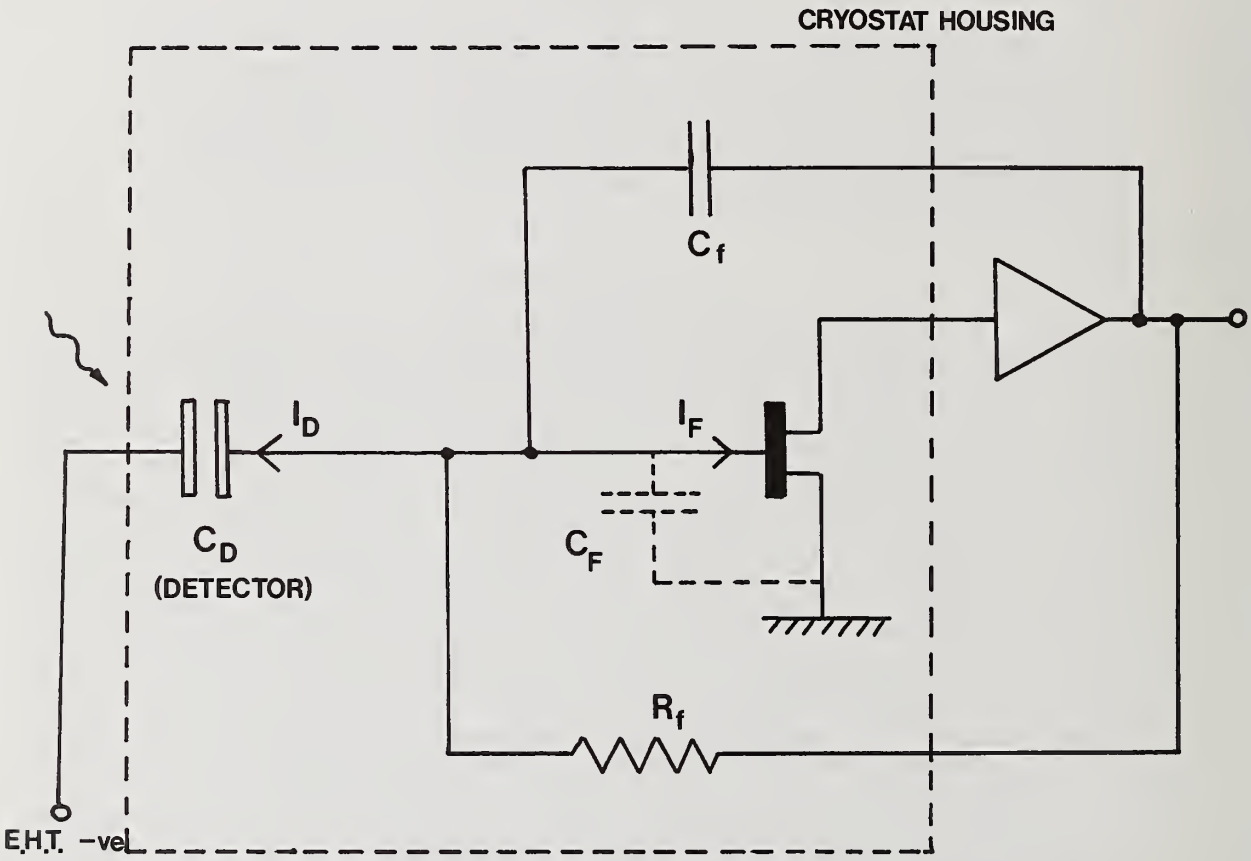

Figure 1. Schematic of head amplifier. The feedback capacitor, C_f, is connected to make the amplifier charge-sensitive. In modern systems, the feedback resistor, R_f, is usually replaced by more effective electronic schemes (see text). Components within the cryostat housing (dashed line) are kept cool by liquid nitrogen.

2.1 Opto-electronic charge neutralisation

In 1966, Kandiah [2] suggested the use of photodiodes for charge restoration at the head amplifier input. Two GaAs lamps were placed near two small silicon photodiodes so that pulses from control logic could drive the input in either positive or negative directions (figure 2(a)). When the output of the head amplifier drifted outside limits defined by threshold discriminators, suitable control signals were generated to restore the input to zero volts thus providing "pulsed restoration". In 1968, this system was improved by modifying the control to neutralise the head after every event. This technique of "pulse-by-pulse restoration" avoided the massive restore pulses which were required to neutralise the head after several events and by restricting the dynamic swing, also avoided the need to maintain high linearity in the amplifier over a range many times greater than that covered by individual pulses.

Unlike the high-valued resistor, the opto-electronic link behaves as an almost perfect linear attenuator with good high frequency response and in 1969 Goulding et al., [4] decided to use such a link in the continuous feedback mode (figure 2(b)). Although this was a significant improvement over resistive feedback, the feedback current still had to increase with count rate to balance the mean detector current, with a consequent increase in noise, and the LED/photodiode combination was still found to exhibit non-linearity which had a detrimental effect on high count rate performance of the system. Perhaps the most significant development described in the paper [4] was the use of the drain-gate junction of the FET itself as the photodiode (figure 2(b)), thus avoiding the added capacity (and noise) due to an extra discrete component. The advantages of this modification were only fully realised when it was used in the pulsed restoration mode. In 1970, Landis et al., [5] described a system which neutralised the FET input after several events, as in Kandiah's original scheme [2], and in 1975, Kandiah et al., [6] described a spectrometer using pulse-by-pulse restoration, specifically designed for x-ray work, where they acknowledged the improvement afforded by use of the FET as the restoring photodiode. Thus, systems in current use are mostly based on the arrangement shown in figure 2(c).

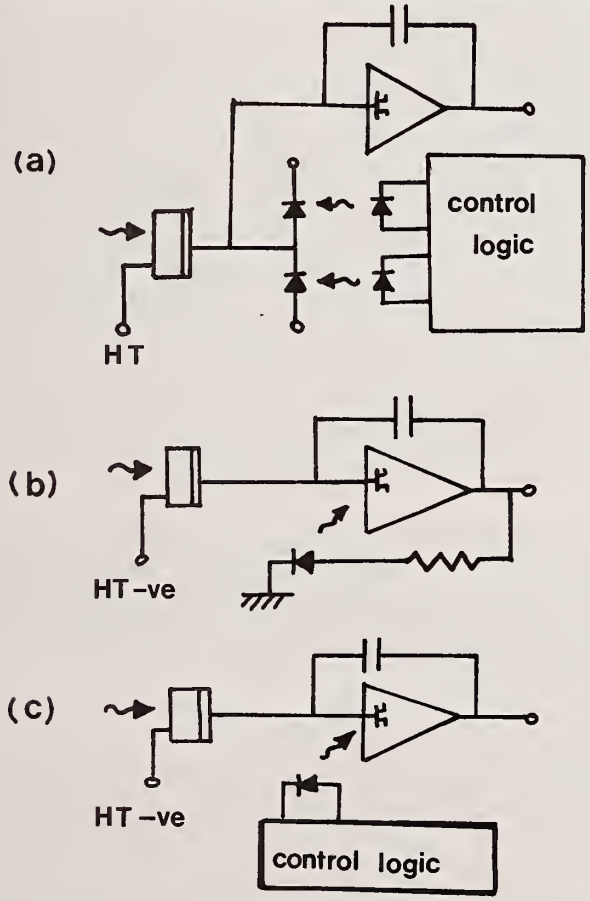

Figure 2. Opto-electronic charge neutralisation schemes:

(a) Pulsed feedback and pulse-by-pulse restoration using silicon photodiodes (Kandiah 1966; Kandiah et al., 1968).

(b) Continuous feedback using FET junction (Goulding et al., 1969).

(c) Modern schemes using FET junction. (Pulsed feedback, Landis et al., 1970, pulse-by-pulse restoration, Kandiah et al., 1975).

The historical development is interesting because it shows the trend to remove non-essential components in order to reduce the noise component due to stray capacitance. In particular, note that only a single photodiode is shown in figure 2(c) because if the detector leakage current is greater than the FET leakage current, then, with or without x-rays, the amplifier output will always drift in the same direction. Unfortunately, the leakage current in modern detectors is often smaller than the FET leakage so, that in the absence of x-rays, or even at very low count rates (< 100 cps), the amplifier may drift in a direction where it cannot be restored by a single photodiode; so the amplifier "drops out" or stops "ramping" and the spectrometer becomes inoperative. Although a burst of x-rays will bring the system back to life, this situation is obviously unsatisfactory. One solution is to enhance the detector leakage by raising the EHT voltage, but this involves the risk of breakdown and should not be done without consulting the manufacturer first. However, it may transpire that the only realistic solution is to include a second photodiode, as in Kandiah's original system [2], and to accept the slight noise penalty.

2.2 Systems in current use

A comprehensive review of pulsed feedback techniques is given by Landis et al., [7] but, for a variety of reasons, there are no serious competitors for opto-electronic restoration in the field of low-energy x-ray spectrometry. However, there is another continuous feedback technique called "drain feedback" which is used in some commercial x-ray systems. This method, introduced by Elad [8], involves regulating the FET drain voltage according to the input energy times count-rate product whereupon a component of gate current produced by impact ionisation provides sufficient charge to neutralise the detector. Apart from avoiding the complication of mounting extra components near the detector, drain feedback apparently does not suffer from the potential problems caused by long-lived surface states which are excited when light shines on the FET and there is no dead-time penalty associated with resetting of the head amplifier. However, at high count rates, drain feedback, as with any continuous feedback approach, suffers the disadvantages of enhanced noise owing to the increase in gate current necessary to balance the x-ray-induced detector current.

Opto-electronic feedback is most commonly implemented in pulsed mode whereby the charge due to several events is neutralised when the amplifier output exceeds a given threshold level. The main amplifier has to be gated to inhibit the effects of the large restore transient and some time is lost while the electronics recover but the dead time penalty is normally only significant at count rates in excess of 10 kcps. A potentially more serious problem is that of the after-effects of light pulsing. Charge stored in surface states can sometimes take a long time to leak away and leads to degraded resolution at high count rates. This effect has been noted in photodiodes [2] and FETs [5] but is most severe in the detector [5] so it is very important to prevent stray light from reaching the detector surface. It should be emphasised that this is a potential problem and with a good system, the high-count-rate performance is better than with drain feedback. As mentioned above, pulse-by-pulse opto-electronic restoration has the advantage that the head amplifier output is kept within a small dynamic range and the restore transient is about the same size as the original signal. In a time-variant processor, the reset recovery time can be incorporated as part of the pulse processing interval so there is no dead time penalty [6] and, because the restore signal is smaller, there may be less of a problem due to after-effects of light pulsing, although this depends on the exact nature of the problem.

To summarise, whereas there is no theoretical argument to suggest that drain feedback or either of the pulsed opto-electronic techniques is substantially better than the others for low-energy x-ray spectrometry at low count rates, the pulsed systems do perform better when the energy times count-rate product gets large and the pulse-by-pulse opto-electronic system, though difficult to implement, will handle the greatest dynamic range without any compromise to the low-energy, low-count-rate performance.

3. Pulse Processing

The output of the head amplifier is a series of steps with heights proportional to the energy of the x-ray photons involved and the primary aim of the pulse processor is to obtain an accurate measurement of the height of each step. Each measurement will be affected by the history of the system before the event and electrical noise, and these factors dictate the essential features of pulse shaping:

(1) High frequency noise must be suppressed. "Integration" is therfore involved which smooths out the front edge of the step.

(2) The amplifier must be restored to its quiescent state as fast as possible after the event so that succeeding events will be unaffected. This involves "differentiation" which shapes the step into a pulse of a finite length.

(3) The height of the pulse must be measured and the result must be proportional to the original step height. This is facilitated if the pulse has a fairly flat top.

Before considering the relative merits of various processing schemes, it is instructive to consider some of the fundamental problems which face the designer of such a system. In order to reduce the effect of dc drift and slow variations at the input, ac coupling can be used, which also frees the designer from the problems of matching dc operating points of the various stages in the amplifier. Thus, the pulse is subject to one or more "secondary" time-constants, due to interstage couplings and "decoupling" capacitors, which are equivalent to CR-differentiator stages with long time-constants. In figure 3(a), the effect of passing a unipolar pulse through a differentiating stage is demonstrated with reference to an idealised rectangular pulse shape. After reaching a peak, the output pulse decays exponentially according to the time-constant $\tau_s = CR_s$ and therefore "droops" below the input waveform. When the negative-going edge arrives, the output undershoot decays with time-constant, τ_s. Since the stage cannot transmit a dc level, the positive and negative areas must be equal. If τ_s is made bigger to reduce the "droop", the undershoot is smaller but lasts longer so that there is no easy way of avoiding the effect on a subsequent pulse which is shown as a baseline movement in figure 3(a). In figure 3(b), the effect on a bipolar pulse is considered. In this case, the droop on the first lobe of the pulse almost cancels the overshoot for the second lobe so the decaying residual voltage is proportional to $(T/\tau_s)^2$. Thus, the residual effect on a subsequent pulse is considerably smaller and bipolar shaping gives excellent baseline stability at high count rates. Unfortunately, the poor signal-to-noise ratio precludes the use of bipolar shaping for low-energy x-ray work, although it can still be useful for pile-up rejection and event recognition for time-variant processors [3,6].

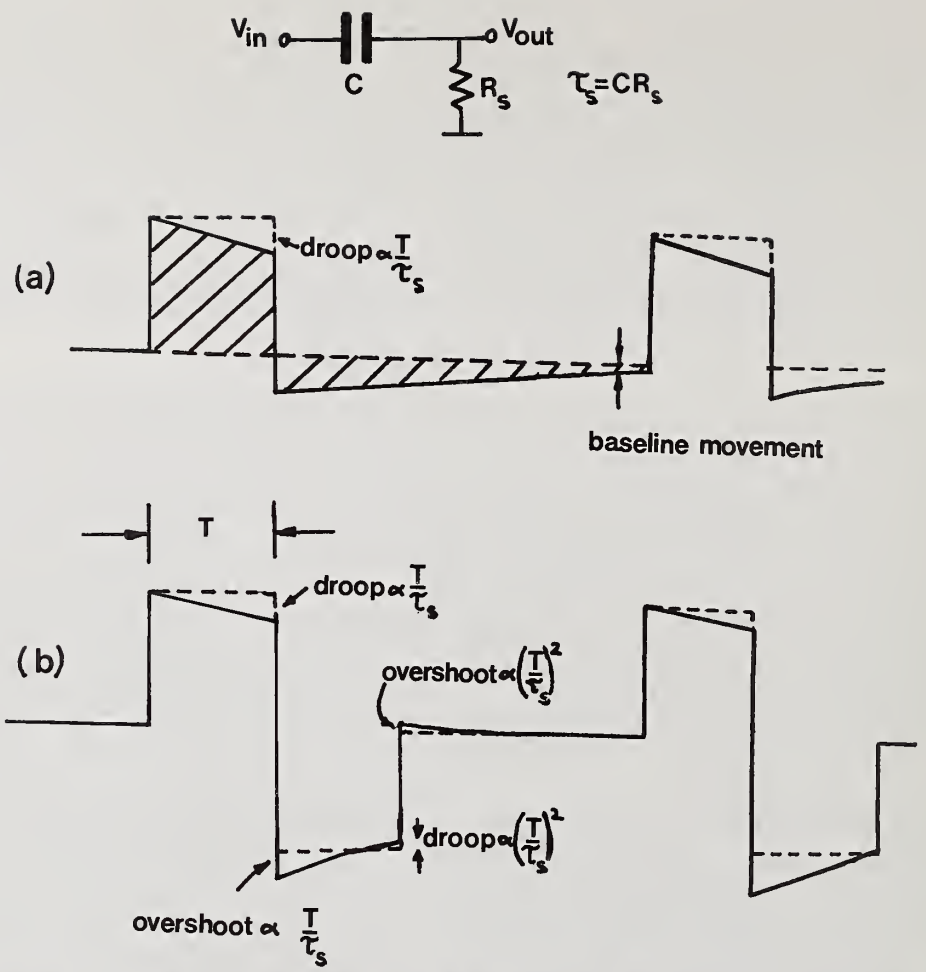

Figure 3. Effect of secondary differentiating time constant on a pulse.

(a) Unipolar rectangular pulse of width $T \ll \tau_s$.

(b) Bipolar rectangular pulse. A second pulse is shown to illustrate how residual voltage affects subsequent pulse measurements.

3.1 Pole-zero cancellation

Although the undershoot problem for unipolar pulses cannot be cured by a simple change of time-constant, the technique of pole-zero cancellation [9] can be used. If a step waveform is passed through a single stage of differentiation, a unipolar pulse will be produced. As shown in figure 3(a), if the unipolar pulse is passed through a secondary stage of differentiation, an undershoot is produced. In the present context, the effect of a secondary differentiating time-constant, τ_s is easier to understand if we assume that the input step has passed through such a stage and is decaying to zero with time constant τ_s before it reaches the main shaping differentiator (see figure 4(a)). The output from the shaper would decay to zero, were it presented with a flat-topped step, but undershoots because of the decay introduced by τ_s. The undershoot decays with time-constant τ_s ($\tau_s \gg \tau$) and the technique of pole-zero cancellation involves feeding some of the input waveform through to the output to cancel the undershoot (figure 4(b)). By choosing the shunt resistor, R_s, so that $CR_s = \tau_s$, the output waveform no longer undershoots and decays

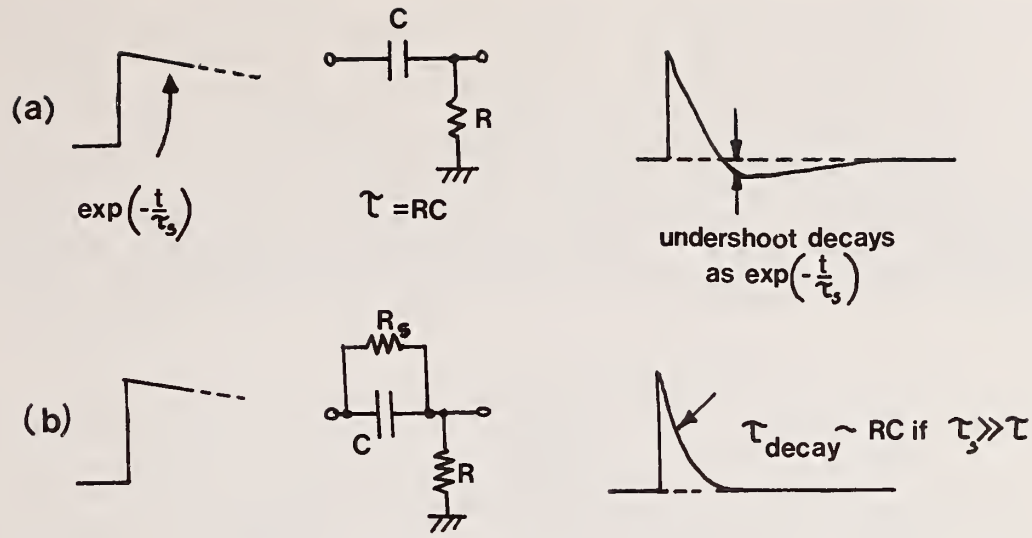

Figure 4. Pole-zero cancellation.

to zero with time-constant governed by the main shaper. One instance where pole-zero cancellation is particularly relevant is with continuous feedback (e.g., drain feedback) where the steps at the head amplifier output decay with a time-constant which is usually much greater than that of the main pulse shaper. The technique can be applied more than once to cancel the effect of other secondary time-constants, if these are present, but note that the modified stage in figure 4(b) involves dc coupling between input and output and this may not be permissible in some instances.

The term "pole-zero" stems from the theory of linear circuits and cancellation of a "zero" by a "pole" is only totally effective if all circuits are linear. Non-linearity can appear in an amplifier which is driven close to saturation or in feedback components such as high-valued resistors [4] and results in decays which are not purely exponential. In this case the pole-zero cancellation circuits have to be adjusted to provide the best compromise in performance for a particular application. When pole-zero circuits have not been adjusted properly, peaks exhibit distortion which may appear as low-energy tailing [10]. Non-linearities and any pecularities in detector response combine to make the adjustment sensitive to both count rate and spectral content. This brings out the important point that the performance of the pulse processor depends on the detector and head amplifier and cannot always be treated in isolation.

3.2 Baseline restorers

Although pole-zero cancellation goes some way to solving the problem, baseline fluctuations are invariably present because of residual pulse tails and undershoots due to uncancelled secondary time-constants. Therefore, some form of keeping the quiescent baseline level close to zero volts is required; the circuit used is called a baseline restorer (BLR). Various schemes have been suggested and are reviewed by Fairstein [11] and Karlovac [12]. Figure 5 summarises the basic features of each method and shows how the unit behaves when presented with an idealised rectangular pulse and with a similar pulse with an undershoot represented by a negative lobe. The symmetric restorer [13] (figure 5(a)) affects both positive and negative excursions equally. When presented with a positive pulse, the left diode is switched off and the current, I, discharges the capacitor and produces a droop on the output pulse. When the back edge of the input pulse drives the output negative, both diodes become conducting and a net current, 2I-I = I, charges the capacitor and rapidly restores the small undershoot to zero. When the input pulse has an undershoot, or negative lobe, the restorer operates just as effectively and attempts to neutralise both the main pulse and undershoot with equal force. At high count rates, there is greater chance for a pulse to arrive before the effect of the previous pulse has been neutralised and symmetric restorers cease to become effective at count rates >0.5/T, where T is the pulse width at the baseline. If unipolar pulses are involved, an asymmetric restorer

(figure 5(b)) can permit operation at higher count rates. In this case, the rate of restoration for positive excursions is less than thatfor negative excursions; so there is less droop in a positive pulse and the correspondingly-smaller undershoot is more rapidly restored to zero. Unfortunately, if the input pulse has a negative undershoot, the capacitor stores charge during the undershoot period and an after-pulse is generated which being positive, is only neutralised slowly (lower waveform, figure 5(b)). The resultant output pulse has a greater positive dc component than the input pulse; this demonstrates the rectifying property of an asymmetric restorer which will also rectify noise to give a baseline offset proportional to the noise level. These problems are removed if the restoring currents are switched off during the pulse. Such a gated, or time-variant, BLR is shown in figure 5(c). There is no droop on a pulse because the gate signal keeps the switch open and any undershoot is restored symmetrically, without generating any long-lived after-pulses.

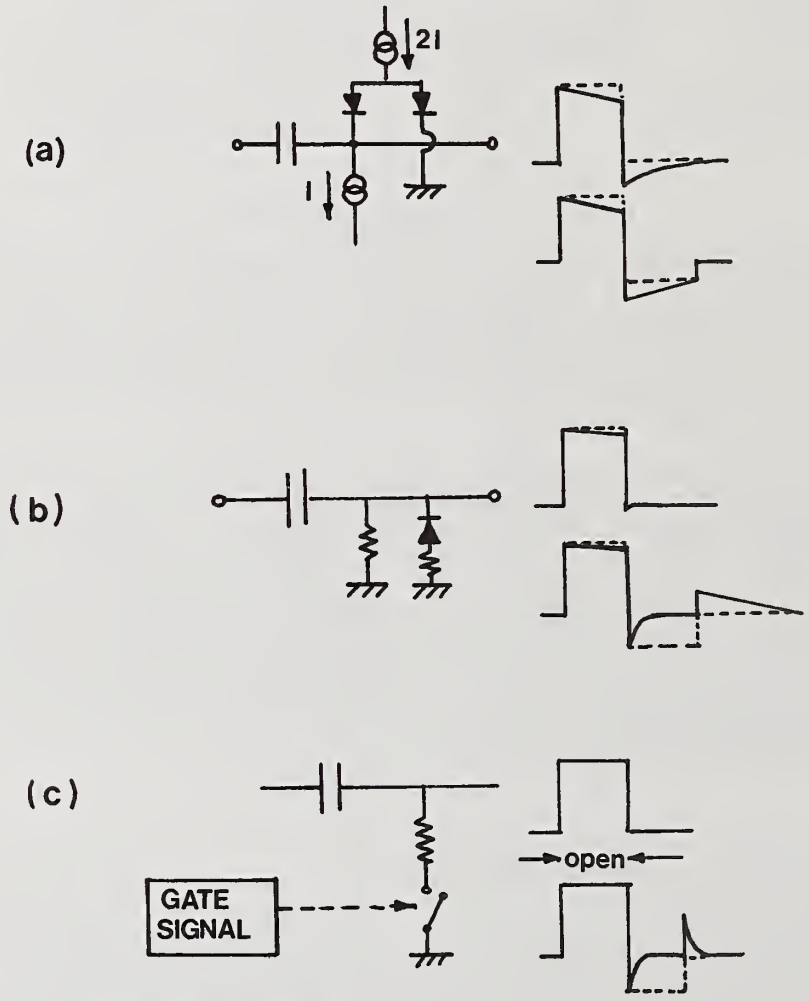

Figure 5. Baseline restorers.

(a) Symmetric.

(b) Asymmetric.

(c) "Time-variant" or "gated". Each circuit is an idealised representation of one implementation of each type of BLR. Tye top waveform in each case shows the response to a unipolar rectangular pulse and the lower waveform shows the response to a pulse with undershoot, approximated by a bipolar rectangular pulse.

The main function of the BLR is to remove baseline fluctuations which could be considered as low-frequency "noise" but this involves a compromise with respect to the response to high-frequency noise. The noise "introduced" by a BLR has been calculated by Radeka [14] but crudely speaking, the noise increases as the restoring currents are increased. In practice, this limits the effective restoring time-constant to be more than 10 x the pulse duration [12]. On earlier amplifiers a switch was usually available to enable the amount of restoration to be matched to the count rate but nowadays it is more common for x-ray systems to be provided with a fixed restorer which is only optimised for low-count-rate work with low-energy x-rays. This may mean that special modification will be necessary for the system to be useful if it is to operate at high rates, as can occur with pulsed excitation, or with high-energy x-rays that are produced in a transmission microscope, for example. If the BLR setting is not optimised, count-rate-dependent peak shift and broadening are apparent [10].

The gated BLR offers the best compromise between good baseline stability and noise performance but, since the stabiliser is only switched on in the interval between pulses, the characteristics are a function of count rate. Thus, suppression of low-frequency fluctuations is less effective and noise is greater at high rates. Nevertheless, the high-count-rate performance is usually considerably better than with "passive" restorers [12]. At this stage, it is worth mentioning that figure 6 is only intended to point out the essential features and practical circuits are considerably more sophisticated than is suggested by the circuit diagrams.

4. The Kandiah/Harwell Processor

So far, the pulse-processing techniques that have been described represent a "piece meal" approach to the various problems and most systems are arranged as in figure 6 with a shaping unit, including pole-zero cancellation, followed by a baseline restorer and finally the analogue-to-digital converter (ADC). However, Kandiah [2,3,6] took an entirely different approach and redesigned the system to try and eliminate the source of many of the problems. The operation of the whole system is co-ordinated by control logic which also issues the signal to restore the head amplifier (figure 7). DC coupling is used throughout which immediately improves high-count-rate performance and time-constants are switched by the control logic to minimise the effective "memory" of previous events.

A simplistic view of the processing of a single pulse is shown in figure 8(a). The main processing channel is effectively grounded until the arrival of a pulse is detected by the fast recognition channel. At this time, the time constants are switched to change the amplifier characteristics and the pulse is integrated for a precise interval. The charge on the integrating capacitor is held long enough to allow the ADC to record and hence measure the voltage and then the time constants are switched again to rapidly restore the system to its quiescent condition. In the pulse-by-pulse restoration mode, the head amplifier is also neutralised at this stage so that, in effect, all memory of the event is removed. The "protect" interval which follows is necessary to allow the enhanced noise [15], which results from the switching, to die away so that when the system is ready to accept another pulse; subsequent measurements will not be significantly affected by such noise. The signal-to-noise ratio primarily depends on the effective time taken for the measurement; so it is fair to compare the pulse duration with that for a typical "passive" shaper which has a peaking time equal to the integration time for the Kandiah system (figure 8(b)). Clearly, for similar noise performance, the dead time associated with the time-variant filter is much less than for the passive shaper, despite the protect interval, so that much higher throughput rates can be achieved.

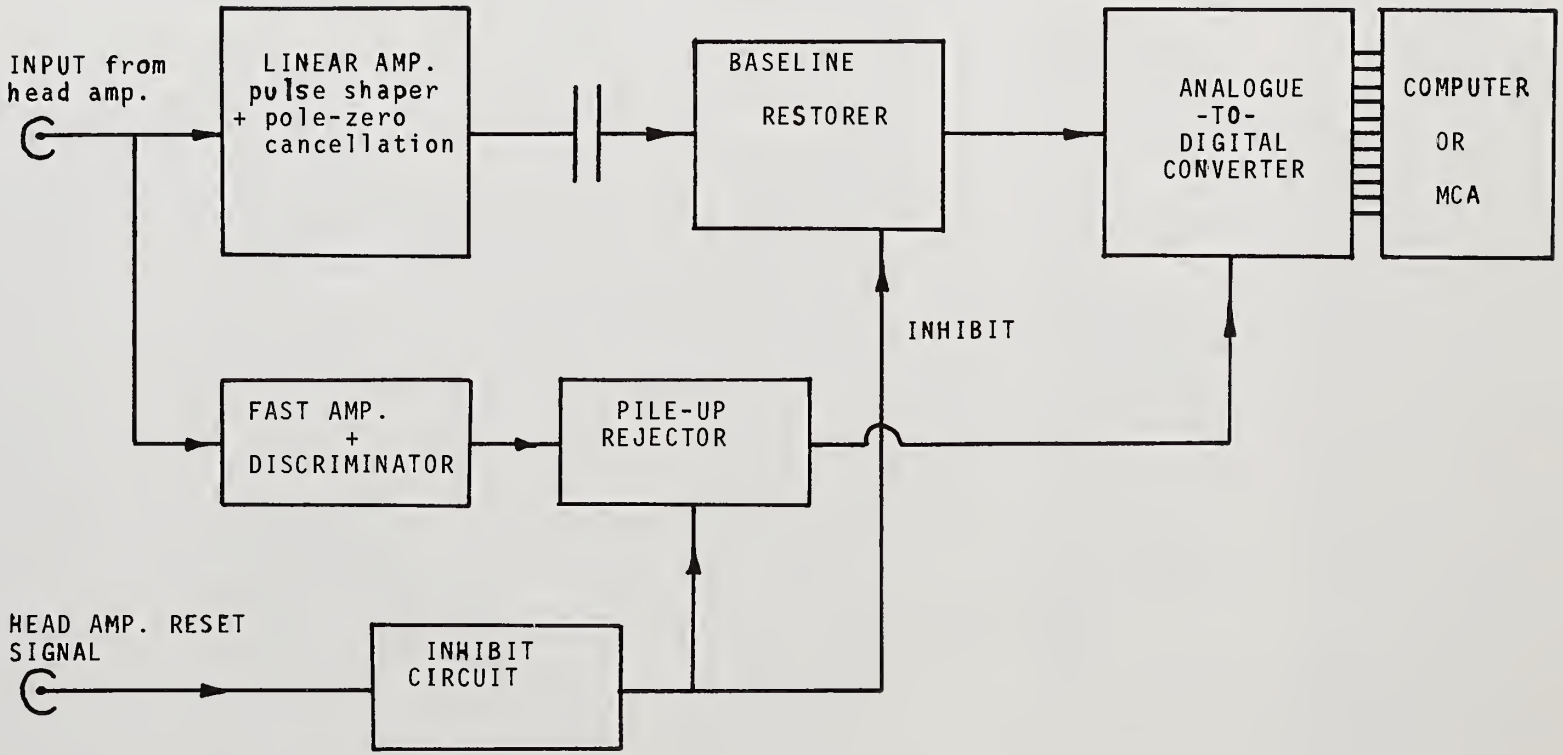

Figure 6. Block diagram of typical pulse-processor.

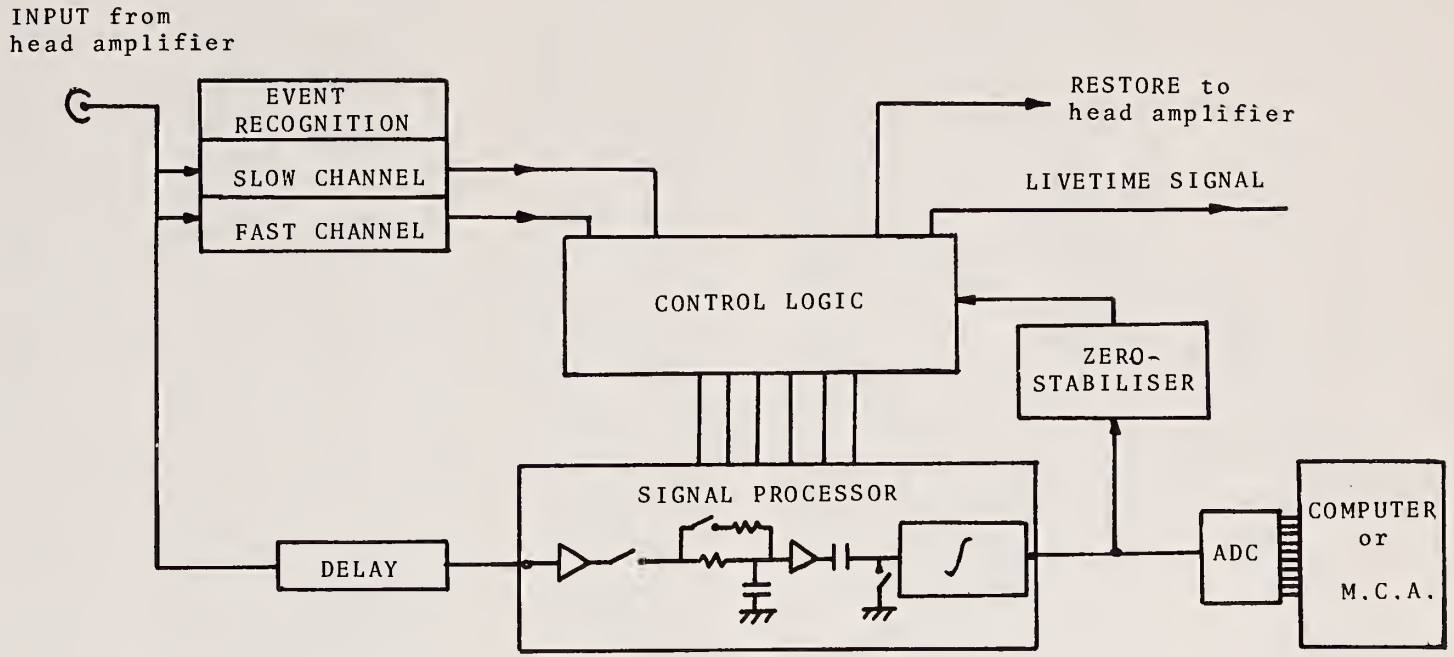

Figure 7. Block diagram for x-ray pulse-processor designed by Kandiah et al.

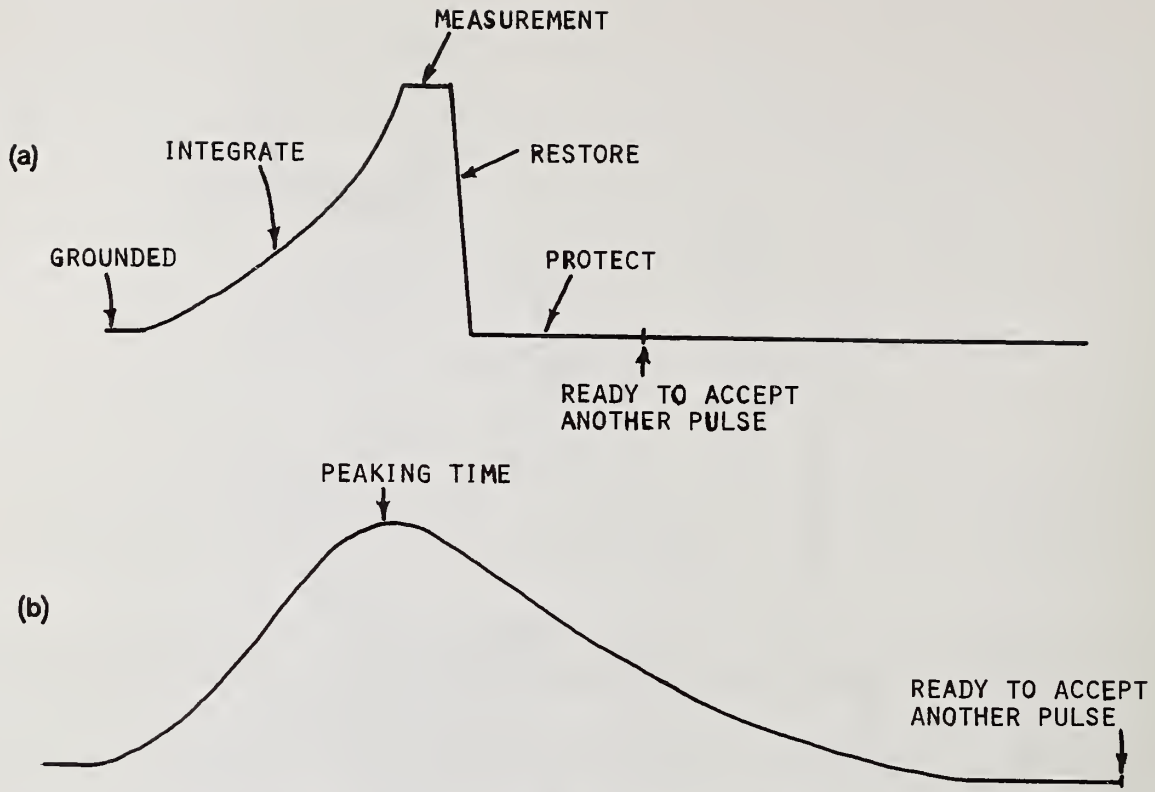

Figure 8. (a) Waveform showing various stages in the shaping of a pulse in the time-variant Kandiah scheme.

(b) Typical waveform for a non-time-variant or "passive" pulse shaper.

4.1 Throughput rate

Deighton [16] has compared the theoretical performance of a time-variant processor with that of an amplifier using "semi-Gaussian" shaping (one differentiating CR, four integrating CR's). Besides the reduced residual voltage at the end of each pulse and removal of baseline fluctuations, Deighton demonstrates the improved counting efficiency. With the semi-Gaussian shaper, a time-to-peak of 20 μs is typical for x-ray work and after 80 μs, the residual voltage is 0.16 percent of the pulse height. If an amplifier is designed to reject a pulse unless a preceding interval of 80 μs and following interval of 20 μs are free from other pulses, then the maximum throughput rate that can be achieved is approximately 3.7 kcps. On the other hand, the switched time-constant, gated integrator shaper can be designed with a time-to-peak of 20 μs, measurement and restore time of 7 μs and protect time of 13 μs so that the maximum throughput rate is approximately 7.3 kcps.

4.2 Baseline stability

In practice, the Kandiah processor can still be used at input count rates of 100 kcps with marginal peak shift but, of course, it is pointless to work under these conditions when greater throughputs can be obtained at much lower rates. To put this into perspective, time-variant or gated BLR's can provide similar baseline stability up to 30 kcps, which is adequate for x-ray work, but a conventional BLR becomes ineffective at relatively low count rates and peak centroid shifts greater than 10 eV (0.29% at MnKα) are typically observed at 10 kcps input rate. This comparison again assumes that a pulse peaking time of about 20 μs is involved (with four CR-integrators, peaking time = 4 x time constant).

4.3 Zero stabiliser

With the problems of baseline fluctuation essentially solved, the added refinement in the Kandiah system is a zero stabiliser. At regular intervals, and provided a pulse is not already being measured, the control logic is triggered to perform a pulse measurement in the usual way and thus monitors the baseline level. The resulting measurements are added to the spectrum and constitute a "strobed zero peak" whose shape faithfully reflects the electronic contribution to any peak in the spectrum. The zero stabiliser works by comparing the result of each strobed-zero measurement with a fixed level and using the result to modify the dc offset within the processor. The principles of "spectrum stabilisation" are described in detail by Dudley and Scarpatetti [17].

4.4 Overload recovery

Another feature of the system is the ability to restore the electronics at any time to their quiescent condition, within a period not much greater than the "protect time" (figure 8(a)). Thus, a "restore" can be issued to quickly remove a pulse rejected by the pile-up inspector but, perhaps even more important, large pulses which would normally overload the amplifier and cause peak broadening can be nullified as soon as they are detected, thus also saving much of the processing time and possibly paralysis time which would otherwise be wasted. This rapid recovery from overload is very important for spectrometers attached to high voltage electron microscopes because a 100 kV (or a 1 MeV!) photon can severely overload a system optimised for x-rays in the 1 to 10 keV energy range. Walter [10] shows one example where the overload due to 122 keV γ-rays from a Co[57] source degraded the resolution of an FeKα peak by 10 eV. Even in XRF systems operating at much lower energies, the fast reject facility is useful in saving some of the dead time normally spent in processing the dominant large-amplitude backscatter pulses, and trace element x-rays can therefore be recorded at higher rates.

In reviewing the field of analogue signal processing in 1976, Goulding [18] suggested that the unit described by Kandiah et al., [6] designed as an integral processing package with convenient operator controls, might well become the basis for the design of future x-ray spectrometers. In fact, a prototype system was evaluated for use in microprobe analysis in 1973 [19] and a commercial system has now been on the market for almost three years [20]. Once the complexity of circuit design has been mastered, the advantages of the time-variant, dc-coupled approach are readily apparent so it is indeed likely that other systems based on these ideas will appear in the future.

5. Noise Performance

The electronic noise contribution to line width becomes progressively more important at low energies and is the major factor in determining the resolution, and thus peak-to-background ratio, at the NaKα position for example. The standard method of calculating the signal-to-noise ratio involves integration of the noise power spectrum in the frequency domain (see, for example, Tsukada [21]). However, Deighton [22] developed a time-domain method for noise calcuations which is much more suitable for time-variant systems where the effect of a noise pulse depends upon its time of arrival relative to that of a signal pulse. Goulding [23] summarises this technique and introduces the concepts of "step" noise and "delta" noise (previously termed "parallel" and "series" noise): Charge due to electron flow in the input circuit is effectively in parallel with the signal current and is integrated by the input circuit capacitance to appear as tiny voltage steps. Flow of current through the input and subsequent amplifying elements is effectively added in series with the signal and the discrete nature of the charge can be represented by a delta-function voltage generator in series with the input circuit. The response of the processor to such signals involves straightforward calculations but there are other noise sources, described by terms such as "generation-recombination", "dielectric", "trapping", "surface", "excess resistor" and "flicker" or "1/f" noise, which are not so easy to analyse. However, "1/f" noise has been discussed, for example by Koeman [24], and Llacer [25] analyses the performance of various filters in the presence of "step", "delta" and "1/f" noise.

Despite the apparent complexity of noise calculations, the general features can be appreciated by the simplified representation shown in figure 9. If the $(fwhm)^2$ of the noise distribution is plotted against the time constant, τ, or alternatively the peaking time for a given shaping circuit, the noise calculations can be separated as follows:

$$\text{noise } (fwhm)^2 = k_s \frac{C^2}{g_m} \frac{1}{\tau} + k_p . I \tau + k_{1/f} \qquad (1)$$

where k_s, k_p and $k_{1/f}$ are constants which depend on the design of the shaper and are associated with "series" ("delta"), "parallel" ("step") and "1/f" noise respectively. C is the total effective capacitance at the input composed of the sum of detector, FET and feedback capacities, I is the sum of detector and FET leakage currents and an equivalent feedback current and g_m is the mutual conductance of the FET in mA/V. When the three components are added, the total noise passes through a minimum at a particular time constant value. In figure 10, the optimum noise fwhm is shown for several different shaping schemes on the assumption that there is no "1/f" noise. The exponential cusp (figure 10(a)) is the theoretical optimum step response and all fwhm values are shown relative to that obtained with such a filter. In practice, such a cusp can only be approximated and it is considerably easier to implement the shapers shown in figure 10(b) - 10(d). The semi-Gaussian shaper (figure 10(c)) gives an optimum noise performance 16 percent worse than the cusp but if more CR-integrators are included, or some other technique is used to make the pulse shape more symmetrical [26], then the noise can be reduced by a further four percent (figure 10(b)). The simple shaper with only a single stage of differentiation and integration (figure 10(d)) is rarely used, because of its poor noise performance and long tail, and other shapers, such as the triangle or trapezoid, are presumably not used because of expense of implementation, even though the noise performance is very close to that of the cusp. The Kandiah-type shaper (figure 10(e)) with a switched integrating time-constant and gated integrator gives a theoretical performance only two percent worse than the cusp [22] which might suggest that the noise performance is 10 - 14 percent better than that of the commonly-used passive shapers, 10(b) and 10(c). However, this comparison is unfair because it only considers the minimum noise that can be achieved and this might occur at such a large value of time-constant to be physically impractical (figure 9). Furthermore, "1/f" and other noise sources have been ignored in this treatment.

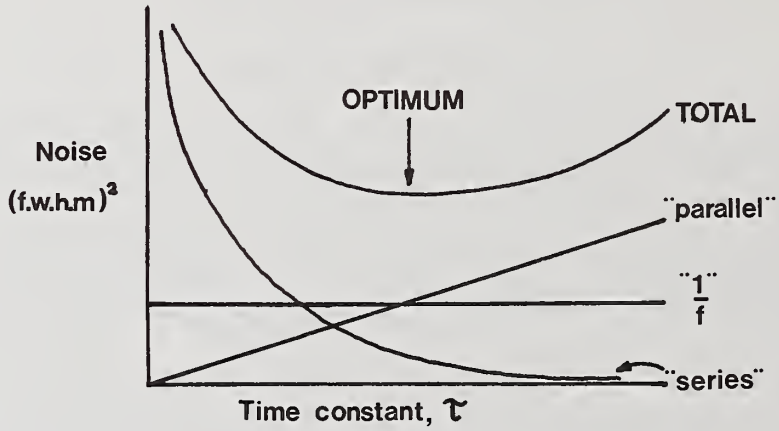

Figure 9. Electronic noise as a function of time constant used in a given pulse shaper. The various contributions are explained in the text and are given by equation (1).

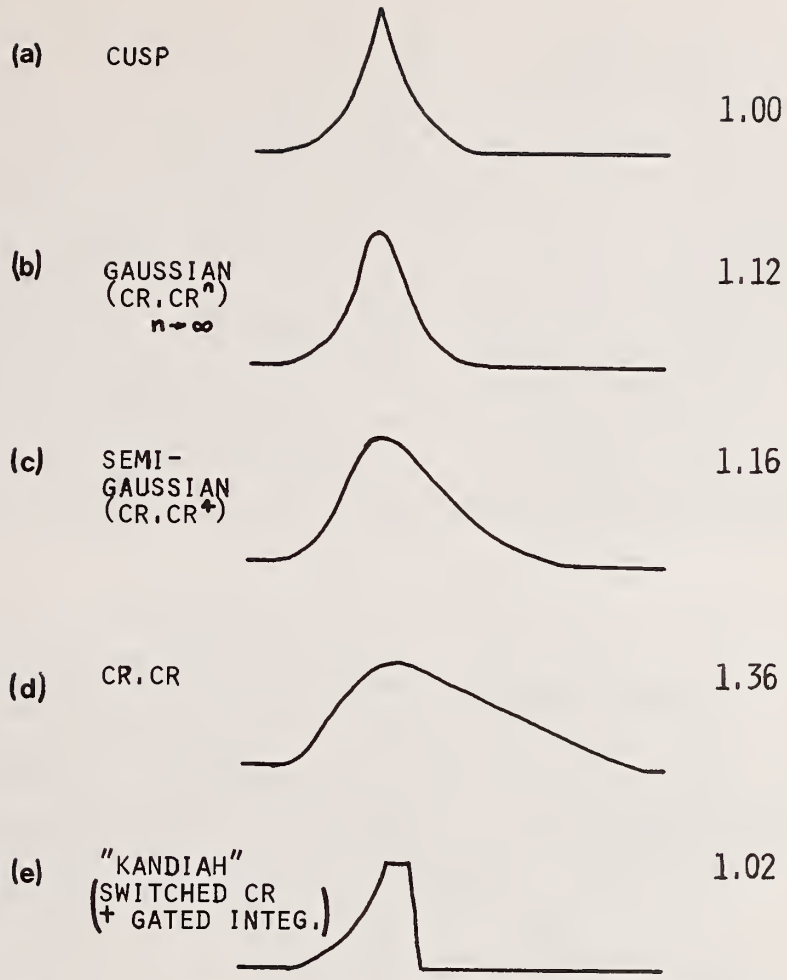

Figure 10. Optimum noise performance for different pulse-shaping schemes. The numbers on the right indicate relative fwhm values. Calculations only account for "series" and "parallel" noise contributions.

In spectrometers using pulsed opto-electronic restoration, there is effectively no noise-inducing feedback so that the "parallel" noise, which increases with time constant, is relatively small. Llacer [25] suggests that, with the long measurement times used for x-ray work, "1/f" noise is a dominant contribution so the filter should be optimised with respect to this noise. His analysis suggests that a tailored cusp shape would improve the noise fwhm by typically 8-10 eV over that for a 7th order Gaussian. Unfortunately, the cusp is difficult to implement but Llacer [25] observed that the step response for Kandiah's time-variant shaper (figure 9(d)) shows marked similarities to that for the cusp (a point also noted by Deighton [22]) and in fact a complete analysis of a particular example suggested that the Kandiah filter would perform even better than the cusp, giving a fwhm of 75 eV, as compared to 82.5 eV for the cusp and 90.5 eV for the 7th order Gaussian (at a peaking time of 32 μs). In a more recent paper, Llacer and Meier [27] followed up this theory by comparing the performance of a conventional 7th order pseudo-Gaussian filter with that of a commercial processor using the Kandiah design [20]. They found that the theoretical findings were borne out in practice and the improved performance of the Kandiah design for both "series" and "1/f" noise resulted in as much as 15 eV reduction out of 90 eV fwhm at long time constants. In particular, at a peaking time of 20 μs, the Kandiah system gave about 95 eV fwhm as compared to 110 eV fwhm for the pseudo-Gaussian amplifier.

The "resolution-race" has traditionally been concerned with improvements in the fwhm for the MnKα peak (at 5.9 keV) obtained with an Fe-55 radioactive source. Although this is a reasonable way of summarising overall improvements in both detector fabrication techniques and electronic noise, the graph with time [28] shows signs of an asymptotic approach to a fwhm only slightly below 140 eV which might suggest that significant improvements in spectrometer performance are unlikely. At 5.9 keV, the separation of Kα peaks is roughly 500 eV (figure 11) so indeed, there is little to be gained by improving the resolution at 5.9 keV (unless, of course, it could be reduced sufficiently to allow Kβ/Kα overlaps to be resolved). However, down at 1 keV, the Kα separation is only 200 eV and in addition there is a significant problem with overlaps from L and M-series peaks so it is highly desirable to improve the resolution. Two curves have been calculated to illustrate how a reduction in electronic noise from 100 eV to 50 eV would improve the overall resolution for a spectrometer where the Fano-factor for the detector is 0.1 (figure 11). Although halving the noise gives only about 25 eV improvement in the fwhm at 5.9 keV, the full effect of the noise reduction is seen at 1 keV and below. Thus, reduction in electronic noise is of vital significance in the field of x-ray spectrometry, and improvement is most likely to arise from advances in FET design. Development of FET's with large g_m and small capacitance would obviously help to reduce the "series" noise, as indicted by equation (1), but of equal importance is the reduction of "1/f" and other "extraneous" noise contributions which dominate the behaviour at long time constants.

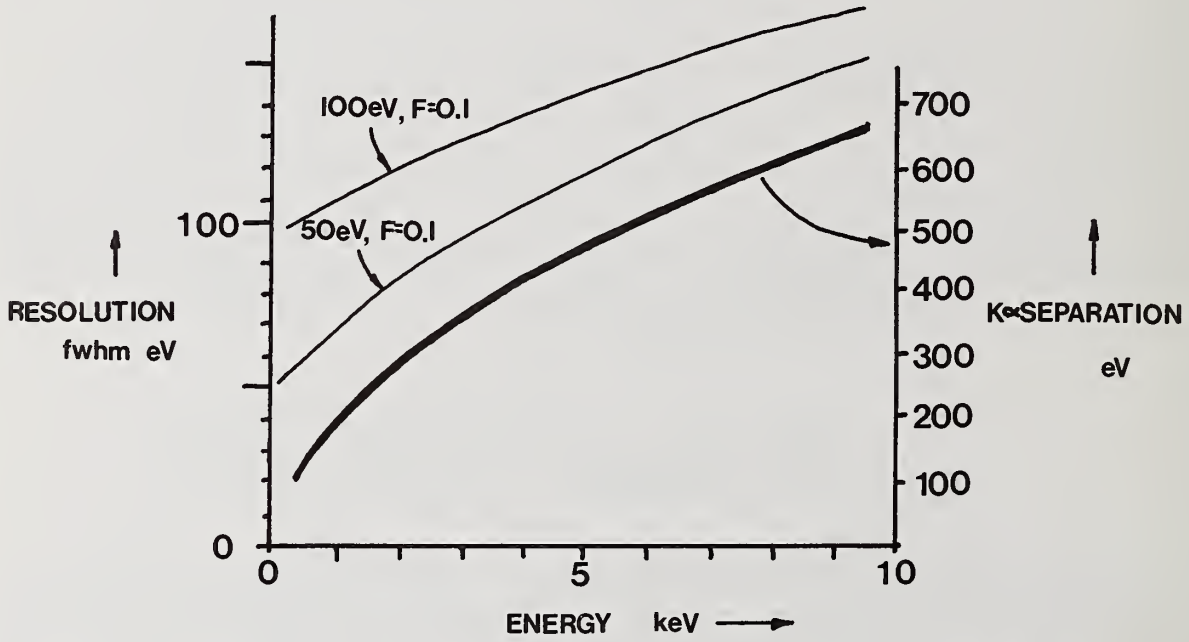

Figure 11. Resolution as a function of energy calculated for two systems, one with a noise contribution of 100 eV fwhm and the other 50 eV fwhm, both with a detector Fano-factor of 0.1. The thick curve shows the separation of Kα peaks for adjacent atomic number elements (right hand scale) as a function of energy.

6. Pile-up Rejection

A full discussion on pile-up rejection appears elsewhere [29]; so here I will only attempt to summarise the features which are of major interest in x-ray spectrometry. The idealised diagram in figure 12 illustrates the most common method of pile-up rejection which involves use of an auxiliary channel, with short time-constants, to separate pulses which overlap in the main measurement channel because of the long time-constants involved. Correct adjustment of the fast channel discriminator is essential if low-energy x-rays (< 2 keV) are present in the spectrum; if the level is too high, small pulses due to these x-rays will be missed and pile-up rejection will be ineffective, while if the level is too low, the amplifier will be saturated by the high rate of triggering of the discriminator by noise. A reasonable compromise is to set the discriminator to give a triggering rate of about 500 cps in the absence of x-rays. If the time constants are reduced to improve the pulse-pair resolution time, the noise is effectively increased and the efficiency of detection is worse for low-energy x-rays, even with the discriminator correctly adjusted. Although these considerations are of little consequence when the pile-up is studied on a spectrum from Fe-55, they have serious implications for behaviour of the spectrometer when presented for example, with a spectrum of aluminum excited by electron bombardment. If the discriminator level is too high, or the pulse-pair resolution is much less than 1 μs, a continuum caused by unresolved pile-up, and excessive peak shift will be observed even at count rates as low as 5 kcps.

6.1 Correcting the spectrum for pile-up

Even when the pile-up inspector is working properly, sum peaks can be troublesome when they overlap with elements of interest (e.g., CaKα + SiKα $\tilde{\sim}$ CrKα) or when they fall in a region which is to be used for fitting a background curve. Automatic correction for sum peaks would be a simple matter if the pulse-pair resolution time were constant but unfortunately it usually depends on the relative heights of the pulses involved. A full correction of the spectrum could take longer than the original recording time [29] and would therefore be no more effective than the solution of using a lower count rate with a larger recording interval. When high count rates are unavoidable, individual sum peaks can be corrected for by including suitably-shaped profiles to represent these peaks in a least-squares fit to the spectrum but this is less satisfactory at low-energies because sum peaks become distorted and merge into the pile-up continuum.

6.2 Electronic limitations

If no correction is to be applied to the spectrum it is advantageous to use two inspection channels, one with longer time-constants, optimised for low-energy x-rays and the other with much shorter time-constants to give a good resolving time for high-energy x-rays [6] (figure 7). The present state of the art in noise performance dictates that 1 μs is about the best resolving time that can be achieved for 1 keV pulses so in microprobe analysis, where Na, Mg, Al, and Si peaks and bremsstrahlung continuum are present, the count rate has to be kept below 5 kcps in order to avoid significant pile-up. Of course, with a windowless detector, the problems are much worse and shaping times of the order of 10 μs are required to detect x-rays down to 250 eV in energy which limits the count rate to well below one kcps if pile-up is to be avoided.

6.3 Future developments

Pulse pile-up is perhaps the most serious limitation for low-energy x-ray spectrometry if it limits the usable count rate to well below that which produces maximum throughput rate. Reduction of electronic noise is therefore again of prime importance in the development of improved spectrometers. One technique, which could, in principle, reduce the effective resolving time significantly, involves "beam switching" [30]. In this case, since the source of x-rays is switched off as soon as a pulse is detected, the effective resolving time is the time taken for a pulse to first exceed the threshold rather than the time for the pulse to reach a peak and return below the threshold [29].

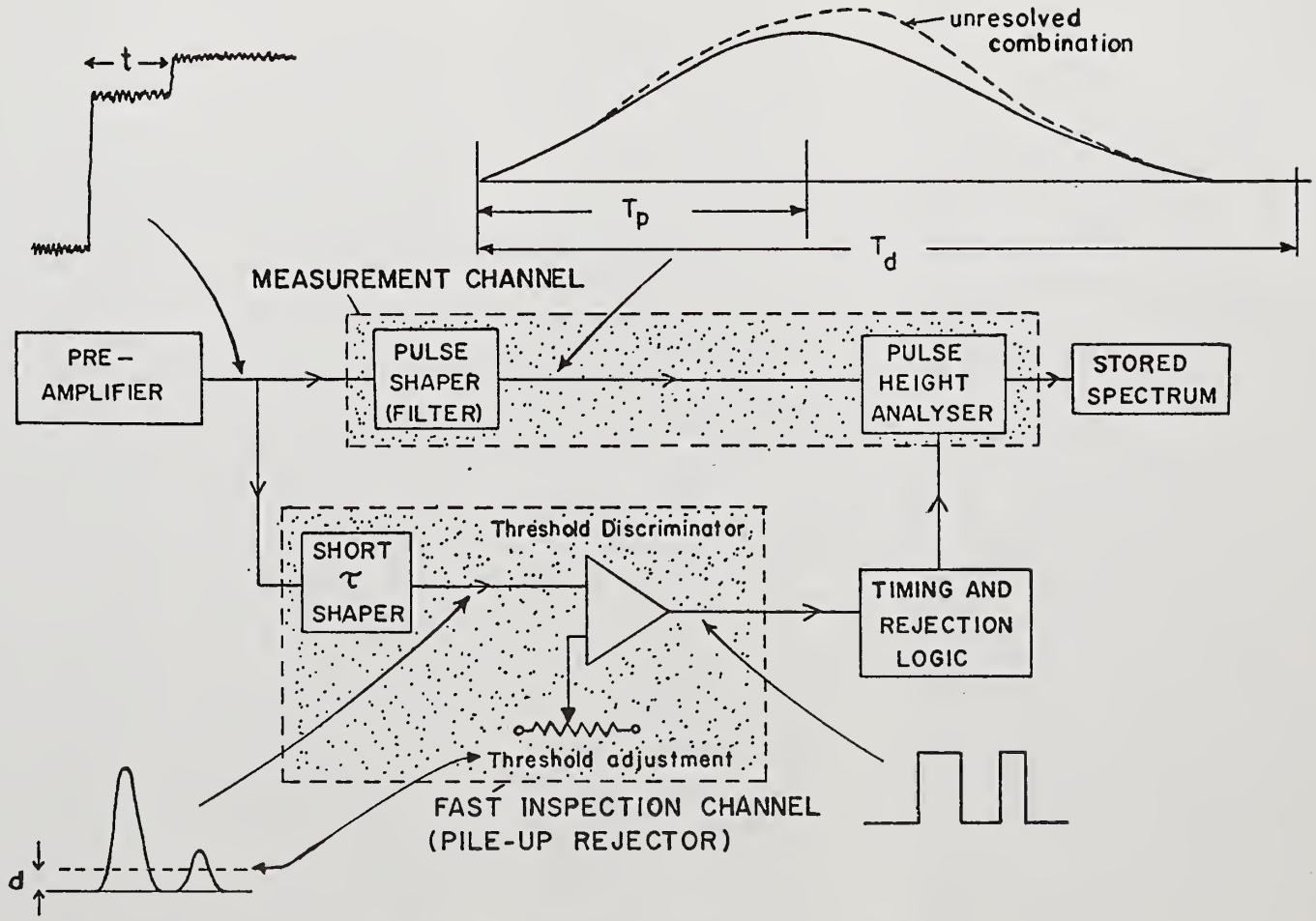

Figure 12. Schematic diagram of a pulse-processor to illustrate pile-up rejection. T_d is typically 4 x T_p though it can be as low as 2 x T_p in a time-variant system. The pulses in the inspection channel are usually less than 1 μs in duration which is considerably less than a typical value, 20μs, for T_p.

6.4 Guard-ring rejection

A refinement in detector design involves use of a double guard ring to define the outer boundary of the sensitive volume of the detector [31]. The inner ring is connected to a fast amplifier and discriminator so that if a charge cloud is collected via the peripheral region, a signal will be detected from the ring. If such signals are used to reject subsequent processing of the main pulse, the system effectively provides electronic collimation and thus eliminates many of the events that would otherwise suffer charge loss in the peripheral region and would therefore add to the background shelf on the low-energy side of a peak. The method is mentioned here because essentially the same principles are involved as for pile-up rejection. The inspection channel connected to the inner guard ring has a pulse detection efficiency governed by both electronic noise and the discriminator level setting. If the ring only intercepts a small fraction of the main charge cloud, the pulse will be correspondingly smaller and may be missed by the inspector. Therefore it is to be expected that the system would be ineffective at detecting both pulses which have only been slightly degraded, and pulses which are severely degraded where only a small fraction of the total charge is collected by central area and guard ring alike. Thus, effects of poor charge collection would appear as counts just below the main peak energy and also at very low energies. As the authors point out [31], it is important to reduce noise so that small signals can be detected and the system does indeed work better for higher energy x-rays, presumably because of the larger signals involved. As in the case of pile-up rejection, the use of long-time-constant shaping should improve the detection efficiency (unless of course, the guard ring channel is subject to excessive low-frequency noise) and will give a greater signal if charge collection is slow due to weak fields at the periphery.

7. Pulsed Excitation

The pulsed excitation method operates in the following manner: as soon as an x-ray photon is detected, the source of x-rays is switched off until the electronics has finished processing the pulse. This ingenious idea was originally suggested in a paper by Jaklevic *et al.*, [32]. These authors used a grid-modulated x-ray tube to pulse the exciting beam in x-ray fluorescence equipment, effectively derandomising the arrival of pulses and hence raising the efficiency and output rate that could be achieved. Basically, this a technique for avoiding pile-up and has already been mentioned above in the context of pile-up rejection. By eliminating the time normally wasted on rejected pulses, the maximum throughput rate can be increased by a factor of three or more over that attainable with continuous excitation. In practice, this higher throughput rate cannot always be fully exploited because of the time taken to switch off the source x-rays. When an x-ray photon arrives at the detector, there is a delay before it is detected (which is dependent on both photon energy and shaping time-constants used), a propogation delay while the signal is transmitted to the grid control, and a decay while the field which deflects the electrons is established. During this time, a second x-ray can arrive and "pile up" with the first, so the count rate emitted when the x-ray source is on cannot be too high or else significant sum peaks will appear in the spectrum.

Additional problems arise when pulsed excitation is implemented on an electron microprobe [19,30] because x-rays are emitted from regions outside the probe spot while the electron beam is being switched. The spectrum cannot be corrected for pile-up involving such x-rays because they are emitted from areas of unknown composition. This problem is minimised by switching the beam off very fast; with a voltage applied to parallel plates this can be achieved in 30 ns [30] and probably less with modern electronic components. Contamination of the spectrum with spurious x-rays can be avoided by modifying the electronics to reject all pulses which arrive before the beam has switched on and stabilised at the original probe position [30]. With these precautions, quantitative analysis can be achieved at accummulation rates around 12 kcps [30].

Because of pile-up, the high-count-rate capability is not always easy to exploit for low-energy x-ray work. However, there are still a number of advantages to be had with pulsed excitation. Since the input rate is always less than with continuous excitation for a given output rate, count-rate-induced effects such as peak shift and

broadening are reduced [33]. Furthermore, the same output rate can be obtained with a smaller average beam current so specimen damage due to electron bombardment may be less with pulsed excitation.

7.1 X-ray mapping

The technique has particular advantages to offer for x-ray mapping. Since the output rate increases monotonically with input rate, there is no danger of contrast inversion; this can occur with a continuous beam because the output rate on a region of high intensity can actually be less than that from a region of low intensity. When mapping at TV rates, the input count rate, and hence probability of pile-up rejection, varies with time so the resulting map is subject to intensity distortion. For example, the horizontal bars on a copper grid appear darker than the vertical bars when a map is made using a conventional raster scan [33]. With a switched beam, vertical striations can appear near an edge due to the more periodic arrival of pulses at high rates. A theoretical analysis of these anomalies [33] indicates that with a switched beam, higher rates can still be used without incurring significant distortion and in a particular example, x-ray maps could be obtained at 8 kcps accumulation rate as opposed to 3 kcps with a continuous beam.

8. ADC

The operation of the Wilkinson run-down analogue-to-digital converter (ADC) is discussed by Gedcke [34] and will not be described here. For low-energy x-ray spectrometry at relatively low count rates, such a converter is perfectly adequate; with a clock rate of 100 MHz, 1000 channel precision can be obtained with a maximum conversion time of 10 μs which is still significantly less than a typical processing time for a pulse. It is impractical to improve the speed much further if conventional circuitry is to be used because the response time of logic elements and discriminators is of the order of 10 ns. In the future, with improved noise performance, smaller time constants and use of pulsed-excitation techniques, the successive approximation ADC (as described, for example by Kandiah et al., [3]) will come into its own because much shorter conversion times can be achieved without the problems of a high speed clock.

8.1 Low-energy considerations

The sequence of operations in a run-down ADC is usually initiated by the pulse exceeding a threshold level, so the efficiency of detection rolls off in the vicinity of this threshold. With a noise fwhm of 100 eV, the efficiency would begin to decrease for photon energies below about 250 eV if the threshold were set just into the noise distribution [29]. Furthermore, the "peak detect and stretch" scheme, when used in conjunction with a passive (non time-variant) pulse shaper, introduces non-linearities in pulse height measurement for small pulses [35] basically because a positive-going noise fluctuation can cause the maximum of the resultant waveform to occur either before or after the signal pulse itself has reached a peak. These defects in behaviour are only significant for low-energy work with a windowless detector.

8.2 Differential linearity

With conventional spectrometers, it is differential linearity which is of prime importance to the analyst. Differential linearity reflects the relative widths of adjacent channels in the spectrum. The standard deviation of channel-to-channel fluctuations due to Poisson counting statistics is $N^{1/2}$ for a channel with N counts. If an electron-excited spectrum of, say, carbon is recorded for a long time, the bremsstrahlung background exhibits channel-to-channel variations due to both differential non-linearities and counting statistics. Thus, if each channel contains 10,000 counts, a differential non-linearity of 1 percent or better will not be visible. However, if a channel contains 10^6 counts, differential non-linearities of the order 1 percent will account for most of the observed channel-to-channel variation and will therefore affect the accuracy of spectrum processing procedures.

9. Livetime Correction

ADC conversion time, computing overheads, pile-up rejection and head amplifier restoration all affect the throughput rate and because the method of implementation varies from system to system, it is desirable for the electronics to automatically correct for dead-time losses since no mathematical formula is universally applicable. Briefly, the purpose of livetime correction is to produce a clock so that if one accumulates a spectrum for T_L "live" seconds on this clock and N counts are recorded within a given energy window, then the true input counting rate for x-rays in this energy range is N/T_L.

In terms of pile-up rejection, there are two situations which have to be accounted for. In "trailing edge" pile-up (figure 13(a)), the first pulse is measured successfully but the second pulse is rejected. In the Covell [36] technique, the clock is kept off until the processor is ready to accept another pulse (i.e., the dead time is "extended") so that the clock is effectively only running when the processor is "live and and waiting" (as would be the case in a perfect processor which took zero time to make a measurement). In "leading edge" pile-up (figure 13(b)), the measurement of the first pulse is corrupted by the second so the measurement is "lost". One way of compensating for this "lost" measurement is to simply add a count to the spectrum and distribute such counts statistically among the channels according to the form of the spectrum (figure 13(c)(ii)). This is basically the "Harms" method [37] which suffers from the drawback that statistical errors cannot be calculated directly from the spectrum. An alternative solution is to keep the clock off until the next successful measurement [38]. Thus, the interval preceding the first pulse (figure 13(c)(i)), during which the clock was counting, is not wasted and still is associated with a single measurement. This technique works very well provided that the intensity of the x-ray source is not fluctuating on a time scale comparable to the processing time. If this is the case, then the "Harms" method is to be preferred.

Livetime correction becomes important when the spectrometer is being used to measure absolute x-ray yields, or when the peak intensities on a specimen and an unknown are being compared. Ideally, the correction should be tested by recording spectra of the same material at known levels of excitation (e.g., beam current) for the same total livetime and checking that the number of recorded counts are proportional to excitation.

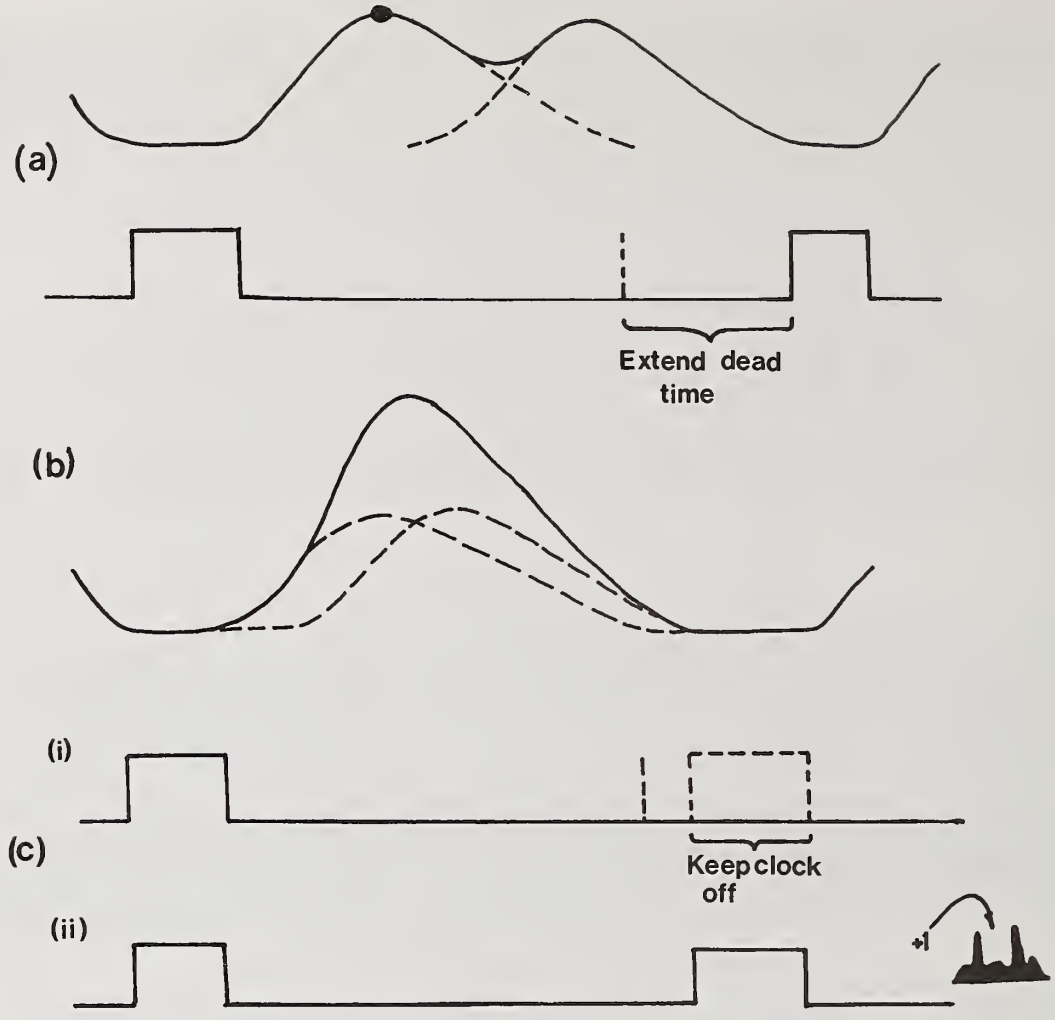

Figure 13. Livetime correction techniques. The rectangular waveforms refer to the livetime clock.

(a) Trailing-edge pile-up.

(b) Leading-edge pile-up

(c) Methods for correcting for a "lost" measurement.

10. Summary

Pulsed opto-electronic feedback is still the most popular method for neutralising charge at the detector. Although "drain" feedback is also used on commercial spectrometers, performance is about the same for low-count-rate, low-energy spectrometry while both resolution and dynamic range are improved by pulsed opto-electronic techniques and in particular pulse-by-pulse restoration. Whatever technique is employed, it is important to prevent light from reaching the detector; otherwise the electronic performance can suffer. This is just one example where the input to the pulse processor is modified and illustrates the general point that the detector and electronics cannot be treated in isolation. If the head amplifier does not produce a perfect step for each x-ray photon then peak shift and resolution degradation will be exaggerated at high count rates. Thus, non-linearity, leakage and low-frequency noise sources such as ground loops and microphony can all seriously affect the performance of even a well-designed pulse-processor.

Over the last few years there has been an increasing emphasis towards the use of time-variant pulse processing techniques. One example is the time-variant, or "gated" baseline restorer but such methods have been most extensively used in the processor designed by Kandiah. In Kandiah's system, count-rate-dependent baseline shift is virtually eliminated and noise performance is in some cases better than what was originally thought to be the theoretical optimum. Furthermore, a zero-stabiliser is incorporated and the electronic noise peak is monitored so that each spectrum can be accurately corrected for any resolution variations.

To date, developments have concentrated on optimising performance for low-energy (1 - 20 keV), spectrometry but in the relatively new field of analytical electron microscopy, very-high-energy photons are generated which can overload and sometimes completely paralyse a processor which has been set up to observe the spectrum below 20 kV. This situation can be avoided by vetoing such high-energy events in a time-variant processor such as that designed by Kandiah.

For low-energy spectrometry, particularly with windowless detectors, electronic noise is the most important parameter affecting system performance. Resolution, and thus peak-to-background ratio, is almost directly proportional to noise (fwhm) and pile-up rejection is only effective for pulses which are significantly above the noise level. In the future, improvements in FET design will therefore be of greater significance for low-energy work than will the Fano-factor for detectors.

References

[1] Goulding, F. S., Walton, J. T., and Malone, D. F., Nucl. Instr. and Methods, 71, 273 (1969).

[2] Kandiah, K., Proc. Conf. on Radiation Measurements in Nuclear Power, Inst. of Physics and the Physical Society, London, 420, 1966.

[3] Kandiah, K., Stirling, A., Trotman, D. L., and White, G., International Symposium on Nuclear Electronics, Versailles, 1, 69-71, 1968; also A.E.R.E. Harwell Report R5852, 1968.

[4] Goulding, F. S., Walton, J. T., and Malone, D. F., Nucl. Instr. and Methods, 71, 273 (1969).

[5] Landis, D. A., Goulding, F. S., and Jaklevic, J. M., Nucl. Instr. and Methods, 87, 211 (1970).

[6] Kandiah, K., Smith, A. J., and White, G., Proc. 2nd ISPRA Nuclear Electronics Symposium, Stresa, Italy, 153, 1975; also IEEE Trans. Nucl. Sci., Oct. 1975 (1975).

[7] Landis, D. A., Goulding, F. S., Pehl, R. H., and Walton, J. T., IEEE Trans. Nucl. Sci., NS-18, 115 (1971).

[8] Elad, E., IEEE Trans. Nucl. Sci., NS-19, 403 (1972).

[9] Nowlin, C. H., Blankenship, C. L., and Blalock, T. V., Rev. Sci. Instrum., 38, 1063 (1965).

[10] Walter, F. J., "Characterisation of Semiconductor X-ray Energy Spectrometers", Energy Dispersion X-ray Analysis, ASTM STP 485, American Society for Testing and Materials, 82-112, 1971.

[11] Fairstein, E., IEEE Trans. Nucl. Sci., NS-22, 463 (1975).

[12] Karlovac, N., ibid., 457 (1975).

[13] Robinson, L. B., Rev. Sci. Inst., 32, 1057 (1961).

[14] Radeka, V., Rev. Sci. Inst., 38, 1397 (1967).

[15] Deighton, M. O., Nucl. Instr. and Methods, 58, 201 (1968).

[16] Deighton, M. O., Nucl. Instr. and Methods, 103, 1 (1972).

[17] Dudley, R. A. and Scarpatetti, R., Nucl. Inst. and Methods, 25, 297 (1964).

[18] Goulding, F. S., Lawrence Berkeley Laboratories, Report LBL-5368, presented at Int. Conf. Particle Induced X-ray Emission and Its Analytical Applications, Lund, Sweden, 1976.

[19] Long, J. V. P., Proc. Scanning Electron Microscopy: Systems and Applications, Newcastle, U.K., 1973, Conf. Series 18, Institute of Physics, London and Bristol, 228 (1973).

[20] Link Systems, Ltd., Model 2010 pulse processor manufactured under license from U.K.A.E.A., Harwell, England.

[21] Tsukada, M., Nucl. Instr. and Methods, 14, 241 (1961).

[22] Deighton, M. O., Nucl. Instr. and Methods, 58, 201 (1968).

[23] Goulding, F. S., Nucl. Instr. and Methods, 100, 493 (1972).

[24] Koeman, H., Nucl. Instr. and Methods, 123, 161 (1975).

[25] Llacer, J., Nucl. Instr. and Methods, 130, 565 (1975).

[26] Mosher, C. H., IEEE Trans. Nucl. Sci., NS-23, 226 (1976).

[27] Llacer, J. and Meier, D. F., Nucl. Instr. and Methods, 142, 597 (1977).

[28] Woldseth, R., Proc. 11th Annual Conf. Microbeam Analysis Society, Miami, Florida, USA, 1976, paper 1, 1976.

[29] Statham, P. J., X-ray Spectrometry, 6, 94 (1977).

[30] Statham, P. J., Long, J. V. P., White, G., and Kandiah, K., X-ray Spectrom., 3, 153 (1974).

[31] Goulding, F. S., Jaklevic, J. M., Jarrett, B. V., and Landis, D. A., Adv. in X-ray Analysis, 15, 470 (1971).

[32] Jaklevic, J. M., Goulding, F. S., and Landis, D. A., IEEE Trans. Nucl. Sci., 3, 392 (1972).

[33] Pawley, J., Statham, P. J., and Menzel, T., Scanning Electron Microscopy/1977, 1, 297 (1977).

[34] Gedcke, D. A., X-ray Spectrom., 1, 129 (1972).

[35] De Lotto, I. and Gatti, E., Int. Symposium on Nucl. Electronics, Versailles, 1968, paper 64, 1968.

[36] Covell, D. F., Sandomine, M. M., and Eichen, M. S., Anal. Chem., 32, 1086 (1960).

[37] Harms, J., Nucl. Instr. and Methods, 53, 192 (1967).

[38] Bartosek, J., Masek, J., Adams, F. A., and Hoste, J., Nucl. Instr. and Methods, 104, 221 (1972).

National Bureau of Standards Special Publication 604. Proceedings of the Workshop on Energy Dispersive X-Ray Spectrometry held at NBS, Gaithersburg, Maryland, April 23-25, 1979. (Issued March 1981)

UNDERSTANDING MULTICHANNEL ANALYZERS

Eric Lifshin and Steven R. Hayashi

General Electric Company
Corporate Research and Development
Schenectady, New York 12301

Abstract

The multichannel analyzer (MCA) is a basic component of any solid state detector system. It is responsible for the sorting of pulses from the main amplifier, the storage and retrieval of spectra and, in most modern computer-based systems, the various states of data reduction required for both qualitative and quantitative analyses. Over the past few years, the need for a detailed understanding of the inner workings of MCA's has diminished through the development of more user oriented systems where tedious tasks like counting dots, calculating energies from channel numbers and looking up peak positions in tables have been replaced by "push button controls". While on the surface this clearly leads to improved operator productivity, it is important to periodically examine the inner workings of such systems both from the point of view of obtaining a general understanding of what's going on as well as to assure oneself that the various compromises which have been made are really compatible with special purpose user needs. The intent of this paper is to provide a general overview of what's behind the buttons.

1. Introduction

The multichannel analyzer (MCA) is a basic component of any solid state detector system. It is responsible for the sorting of pulses from the main amplifier, the storage and retrieval of spectra and, in most modern computer-based systems, the various stages of data reduction required for both qualitative and quantitative analyses. Over the past few years, the need for a detailed understanding of the inner workings of MCA's has diminished through the development of more user oriented systems where tedious tasks like counting dots, calculating energies from channel numbers and looking up peak positions in tables have been replaced by "push button controls". While on the surface this clearly leads to improved operator productivity, it is important to periodically examine the inner workings of such systems both from the point of view of obtaining general understanding of what's going on, as well as to assure oneself that the various compromises which have been made are really compatible with special purpose user needs. To date the most detailed descriptions of MCA operation are found in the manufacturer's operating manuals which often tend to be highly specific. The number of published papers on the general use of such systems for x-ray analysis is also quite limited, with the last review article published in 1971 [1][1]. Therefore, the intent of this paper is to provide a general overview of what's behind the buttons.

2. Basic Components

Figure 1 is a photograph of a modern multichannel analyzer, the principal components of which are illustrated schematically in figure 2. They include an analog to digital converter (ADC), a memory unit and various output devices. Each voltage pulse from the main

[1]The figure in the bracket indicates the literature reference at the end of this paper.

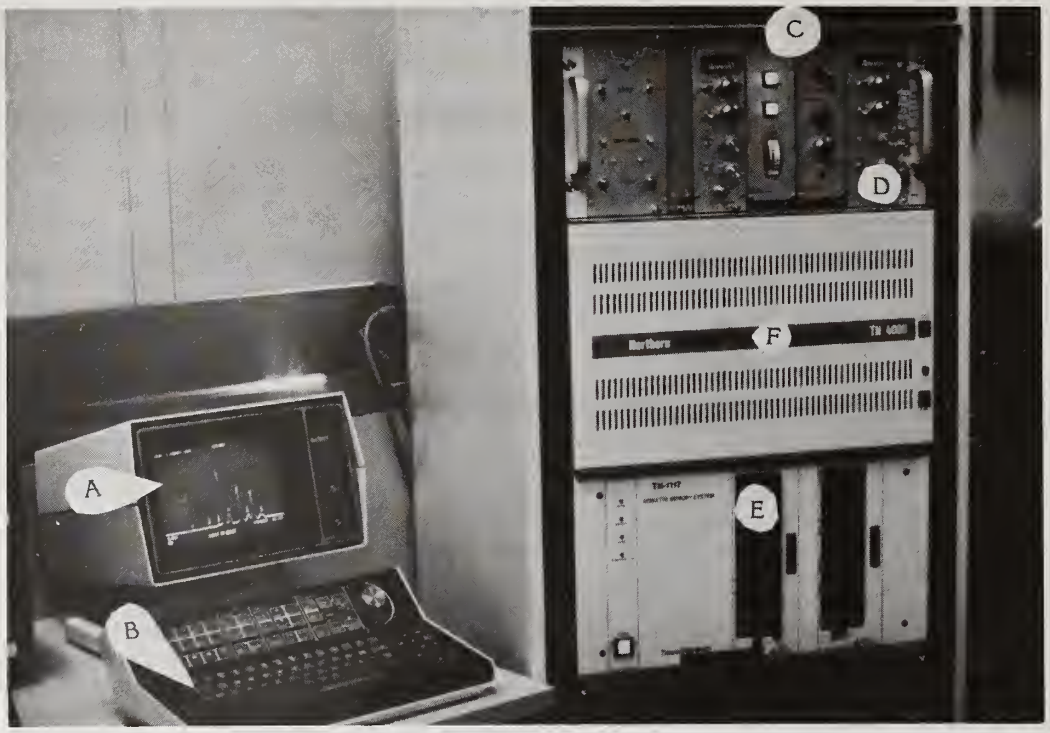

Figure 1. Modern commercial multichannel analyzer.

A. CRT Display
B. Keyboard Entry
C. Detector Electronics
D. Analog to Digital Converter
E. Floppy Disc Storage
F. Computer

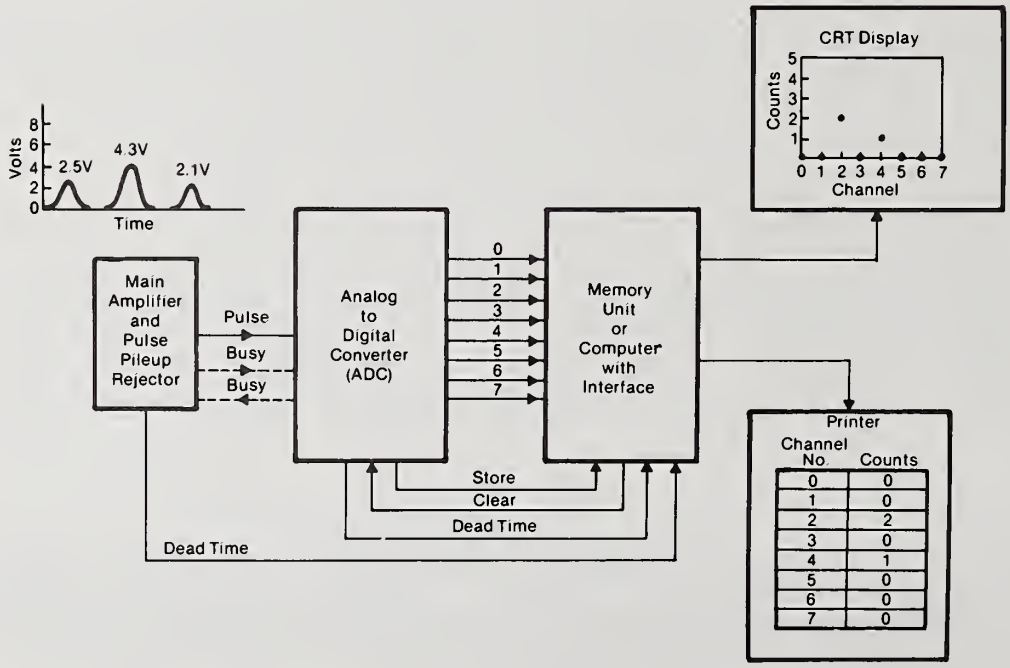

Figure 2. Simplified schematic of multichannel analyzer.

amplifier is transformed into a digital signal by the ADC. The output of the ADC then becomes the address of a channel in the memory unit where one count is to be added. In effect, the memory unit acts as a set of independent scalers counting pulses in preselected voltage increments. In the example shown, channel 0 corresponds to pulses from 0 to 1 volt, channel 1 to pulses from 1 to 2 volts and so on up to channel 7 which counts pulses from 7 to 8 volts. In actual operation the memory is initially cleared, then the first pulse (2.5V) is counted in channel 2, the second (4.3V) in channel 4, and the third (2.1V) is also counted in channel 2. Upon completion of a preselected data collection time (clock or live) the contents of the MCA memory can be printed out directly, displayed on a CRT or further processed by the computer. In the CRT mode the electron beam of the display tube is scanned across the x-axis in such a way as to generate a series of dots through the use of appropriate gating circuitry. The number of dots corresponds to the number of channels selected and the horizontal displacement of each one is made directly proportional to the channel number. Vertical deflection is then used to indicate the number of counts per channel. This is accomplished by converting the digital signal stored in memory back to a proportional analog voltage. The proportionality constant and, therefore, the counts "full scale" is set by the operator using a multiposition range switch on the instrument panel. Since many instruments use 16 bit memories, the maximum number of counts per channel is typically 65,535 although software or hardware options for greater storage capacity are often available. Analog horizontal and vertical scale displacement and expansion controls as well as a logarithmic display mode are also usually provided.

3. The ADC

A block diagram of a typical ADC is presented in figure 3 along with a corresponding waveform diagram given in figure 4. Pulses from the main amplifier are first tracked by a voltage follower required to ensure compatability with the next stage of electronics. The output (point A) is inspected by both upper and lower discriminators set by the operator. Unacceptable pulses are blocked by a gate. Each accepted pulse, however, simultaneously triggers an SCA output pulse, is examined by peak detection circuitry, and also charges the peak stretcher capacitor to the maximum pulse voltage (point B). When the pulse voltage exceeds the analog zero level value ZL (also set by the operator) an appropriate logic signal (point D) combined with the peak detected pulse (point C) activates the pulse stretcher busy (PSB) and ADC busy circuits.

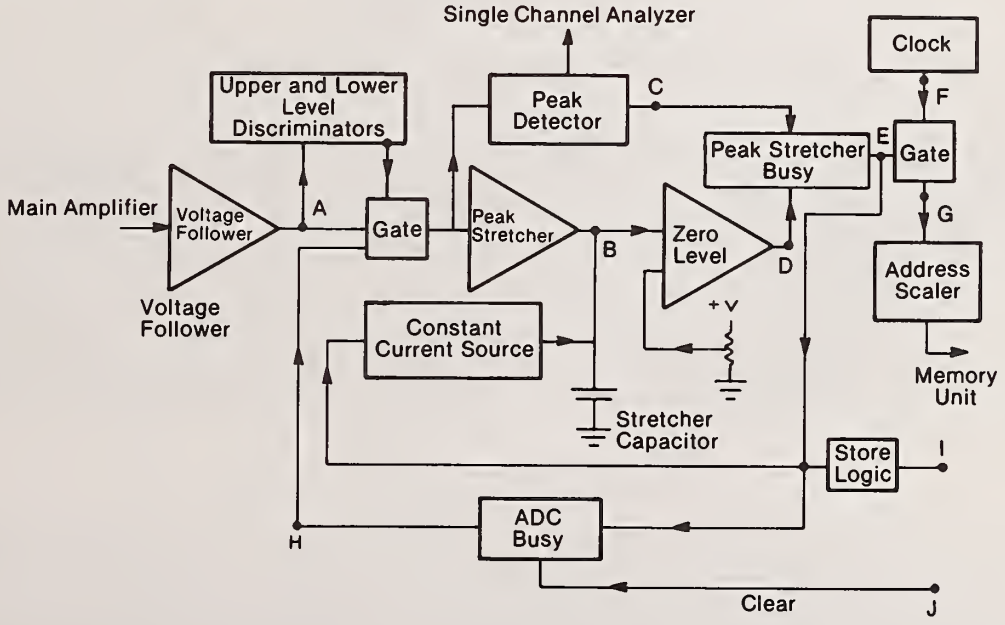

Figure 3. Analog to digital converter block diagram.

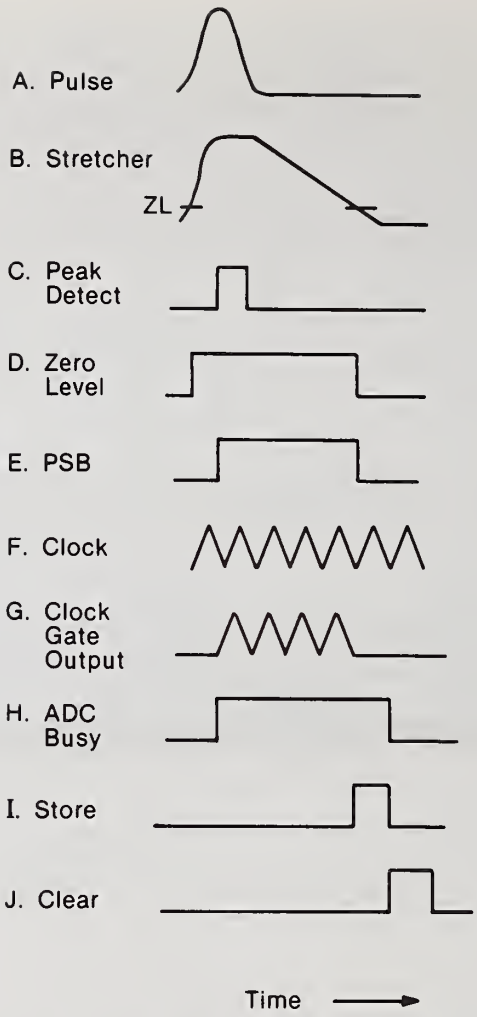

Figure 4. Waveforms from selected points in figure 3.

The PSB signal (point E) causes a gate to open which allows pulses from a clock to be counted by a scaler. In addition it causes a constant current source to linearly discharge the stretcher capacitor. When the zero level is again crossed the PSB signal is lifted closing the gate to the clock (points F & G) thereby, leaving the address scaler containing a count of clock pulses directly proportional to the original pulse voltage. Lifting of the PSB signal combined with other test conditions not shown in figure 3 results in the output of a store pulse (point I) which causes the address to be transferred to the memory unit (see figure 2). The ADC busy signal (point H) which has been clocking all incoming pulses is then reset by a clear pulse (point J) from the memory unit making it possible to accept new pulses and the entire process can then be repeated until the predetermined data collection time is reached.

4. Definition of Terms

Examination of figures 3 and 4 should now make it possible to understand a number of terms used in conjunction with MCA's. For example:

The conversion gain of an ADC refers to the total number of increments (addresses) used to characterize a measured pulse distribution. Switch selectable values typically range from 32 to 8192 in multiples of two. In effect the conversion gain determines the

ADC resolution (volts/channel) by controlling the discharge rate of the stretcher capacitor. This determines the number of clock pulses to be counted for a main amplifier pulse of a given size. In terms of figure 4, waveform B, the slope and therefore the time required to reach zero level (ZL) are determined by the switch setting. For a maximum acceptable main amplifier pulse of 8 volts, a conversion gain of 1024 means that at least 1024 pulses must be counted to achieve an ADC resolution of (8/1024) = .0078 volts. Use of a 100 megahertz ADC implies that the clock frequency is 100 million cycles per second. For the example just given the time required to convert an 8 volt pulse to a digital signal will, therefore, be 1024 x 10^{-8} sec.=10 μseconds. It is reasonable to ask if the conversion time ever becomes the rate limiting factor in the overall spectrum collection process. This question can be answered with the aid of figure 5, which shows three pulse shapes corresponding to 1, 6, and 10 μsecond main amplifier time constants. As described elsewhere, long time constants are required for high energy resolution at the cost of increased pulse pileup rejection (high dead time) while short values are associated with lower energy resolution and increased pulse throughput. In the upper part of the figure the ADC conversion time is plotted as a function of pulse height for a series of ADC speeds ranging from 25 to 200 megahertz and conversion gains of 1024. Thus, for example, as shown with line C an 8 volt pulse would take 20 μseconds to convert following the sensing of the peak maximum while a 4 volt pulse would take only 10 microseconds. Note also that although the pulse amplitudes shown are for 4 volts, the horizontal scale for the pulse shape curves will be independent of the pulse height. Therefore, in some cases the ADC sorting time may be rate limiting while in others the main amplifier time to base line will dominate pulse throughput. This, of course, assumes that a pileup rejector is used to block all incoming pulses until the peak effectively returns to the baseline. For a 4 volt pulse and a 100 megahertz ADC, line A, it can be seen that pulse processing in the main amplifier is the slow step for all of the pulses shown. It should also be mentioned that in addition to the ADC conversion time which varies with pulse height, a fixed time increment is required for the storage of each pulse in memory. This increment can be anywhere from a few μseconds to more than 10 depending on whether the operation is done by hardware or software.

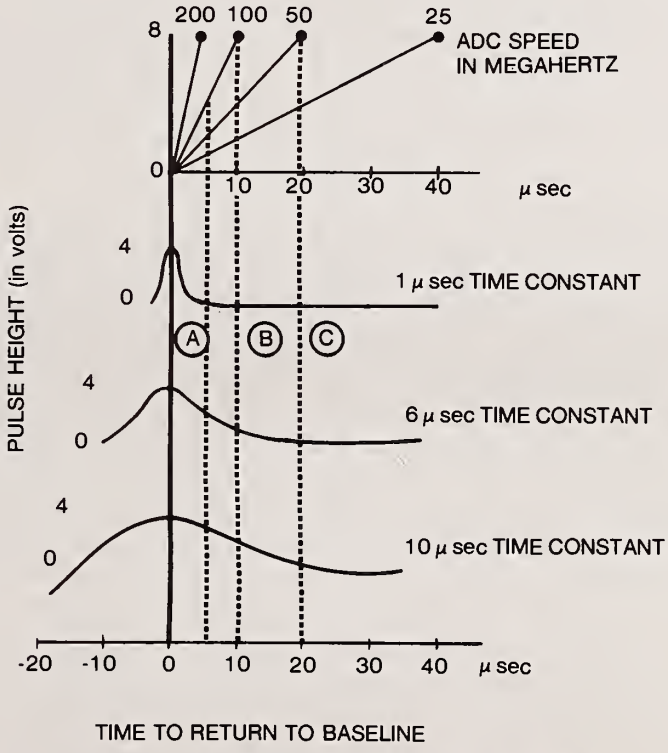

Figure 5. Relationship between pulse to baseline and analog to digital conversion times, conversion gain 1024.

Memory group size refers to how large a section of the memory is actually used for spectral storage. In the simple example presented in figure 2, eight lines, each corresponding to a single address, were shown connected, one for one, to an eight channel memory. In reality separate lines are not needed to each channel since the address can be binary coded. Sixteen lines are sufficient to carry any address from 0 to 65,535 (2^{16}-1). In the earliest MCA's coupled to EDS systems, hard wired magnetic memory units were used which could be divided by the operator into specific groups. Consider, for example a system with a total of 2048 channels. Switch selectable memory groupings include:

Switch Setting	Memory Size
1/1 full memory	2048 channels each
1/2, 2/2 first and second halves	1024 channels each
1/4, 2/4, 3/4, 4/4 four quarters	512 channels each

If the conversion gain is set equal to the memory size then, for the example given, either one, two, or four complete spectra can be stored in memory depending on the resolution required. Computer based systems allow for more dynamic allocation of memory, while the newest systems have returned to dedicated memories which are readily accessible to other parts of the system.

For practical purposes the user is interested in pulse energy rather than channel number. This is often accomplished by specifying a number of eV/channel, typically ranging from 5 to 40, and information is then displayed as energy. Consider first a calibrated system in which the zero level has been adjusted to remove any DC offsets. Then, for example, if a value of 20 eV/channel is used, and 512 is selected for both the memory group size and the conversion gain, then the recorded spectra will cover x-ray energies of from 0 to 10.24 keV. Under these conditions copper Kα (8.048 keV) will give rise to a pulse distribution centered around channel 402. Almost all of the peak will be contained within a band defined by plus or minus one FWHM. Therefore, for a 160 eV detector measured at CuKα the entire peak will contain about 16 channels, which is a reasonable number for most applications. Needless to say if one wishes to accurately measure detector resolution to better than 20 eV it is definitely desirable to use less eV/channel.

The analog zero offset controls the value of ZL as shown in waveform B of figure 4. By varying the point where the clock gate output pulse is lowered, it provides a way of either adding or subtracting a constant number of clock pulses to the conversion of all main amplifier pulses being processed. This, of course, shifts all of the addresses in memory by a fixed amount. From the point of view of the MCA CRT display, varying ZL produces a linear displacement of the entire spectrum on the viewing screen (see figure 6a). In the example just mentioned, a ZL value of two volts would result in a displacement of the spectrum by 25 percent. The display would cover a region of from 2.56 eV to 12.80 keV and the copper Kα would have the same width but appear centered around channel 402-256=146. In practice the analog zero adjust is usually restricted to removing unwanted DC levels for calibration purposes. Shifts of the type just described are normally performed by using digital offset switches (see figure 6b) which subtract fixed numbers from the ADC scaler addresses. Their use makes it possible to use memory group sizes smaller than the conversion gain. High ADC resolution can then be combined with limited memory capacity for the examination of selected regions of a spectrum. This feature is particulary useful in accurately measuring detector resolution to a few eV by going, for example, to a combination of a conversion gain of 8192 with 512 channels of memory and then using digital offset to bracket the peak position. Recognize, however, that digital offset leads to more ADC time than the analog approach since the subtraction occurs after the stretcher capacitor rundown.

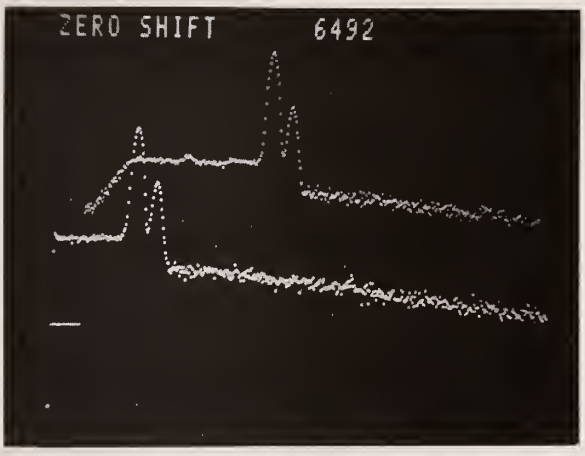

Figure 6a. Effect of analog offset.

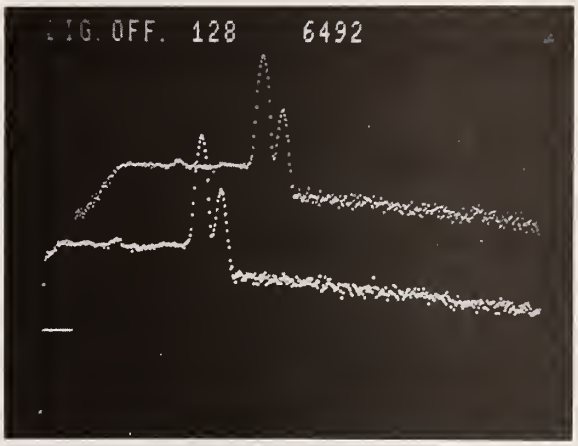

Figure 6b. Example of digital offset.

5. Calibration Procedures

The relationship between channel number and energy requires consideration of the role played by the various components in the detection chain illustrated in figure 7. Each x-ray photon absorbed in the active area of a lithium drifted silicon detector results in the ejection of a photoelectron which in turn creates a number of electron-hole pairs. The total charge is then converted to a voltage pulse by a charge sensitive preamplifier whose output is essentially a step pulse. The first stage of the main amplifier then converts this pulse to a near gaussian form by a combination of differentiations and integrations. The corresponding waveform at this point (A) in the circuitry is shown in the figure. The pulse amplitude is given by:

$$V_p = \frac{EeG_p}{\varepsilon C} + Z_1 \qquad (1)$$

where E is the pulse energy, e the charge per electron, G_ρ the preamplifier gain, ε the average number of eV required to produce an electron hole pair, C the preamplifier feedback capacitance and Z_1 any DC offset that might be present (Z_1 and Z_2 are exaggerated for the figure). The main amplifier output Point (B) is then given by

$$V_a = G_a V_p + Z_2 \qquad (2)$$

where G_a is the user controllable gain and Z_2 is any DC offset at its output. Combining equations (1) and (2) gives

$$V_a = (G_a G_p \frac{e}{\varepsilon C})E + G_a Z_1 + Z_2 \qquad (3)$$

where the total DC offset Z_o is given by

$$Z_o = G_a Z_1 + Z_2 \qquad (4)$$

or

$$V_a = (G_a G_p \frac{e}{\varepsilon C})E + Z_o \qquad (5)$$

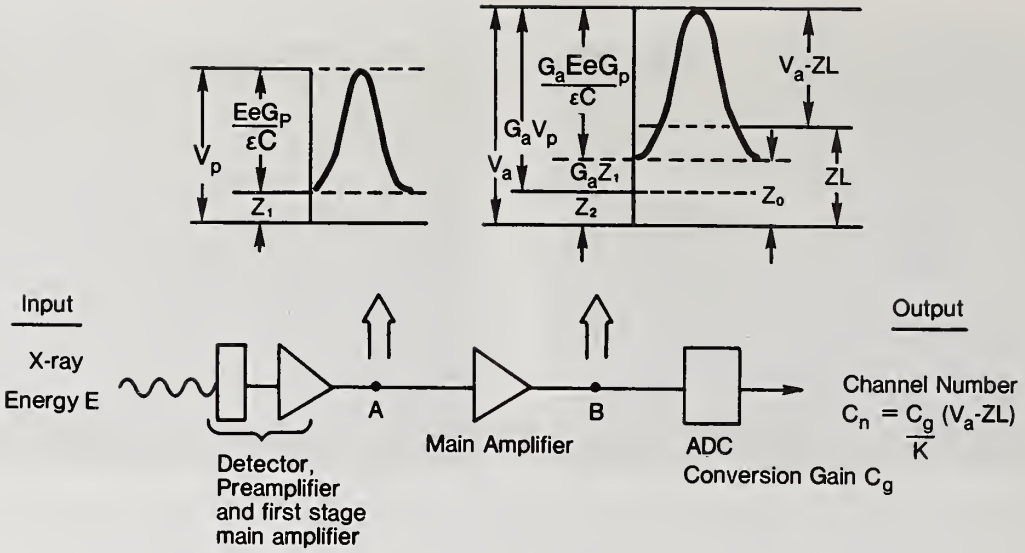

Figure 7. Schematic representation of factors determining the relationship between pulse energy and channel number.

It is this pulse which is seen by the ADC (waveform A in figure 3) which will be directed to channel C_n given by:

$$C_n = \frac{C_g}{k} (V_a - ZL) \tag{6}$$

where C_g is the conversion gain (number of channels used to span k volts (the maximum acceptable pulse size) and ZL and the user selected zero level setting (see figure 3 waveform B). In other words the conversion is done on a pulse whose effective height is V_a - ZL. Combining equations 3 and 6 gives the overall calibration equation:

$$C_n = \frac{C_g}{k}[(G_aG_p \frac{e}{\varepsilon C})E + G_aZ_1 + Z_2 - ZL] \tag{7}$$

for most calibration work ZL is adjusted such that:

$$ZL = Z_o = G_aZ_1 + Z_2 \tag{8}$$

and equation 7 transforms to:

$$E(\text{x-ray energy in eV}) = \frac{k\varepsilon C}{eC_gG_aG_p} (\text{eV per channel}) X\ C_n(\text{channel number}) \tag{9}$$

The actual calibration process by which equation 8 is satisfied and G_a chosen to give a valid preselected eV/channel cannot be accomplished by the use of a single peak. The reason is that any number of combinations of ZL and G_a can be used to put a known peak in a predetermined channel; however, such a calibration will generally not apply to any other peak since equation 8 may not be satisfied. Two peaks are therefore required with one usually selected at low energy and the other at high energy to cover a practical energy range. If the two peaks selected have energies E^1 and E^2 then the peak centroids channel numbers can be measured experimentally as C_n^1 and C_n^2. Rewriting equation 7 for each case gives

$$C_n^1 = \frac{C_g}{K} \left(G_a G_p \frac{e}{\varepsilon C}\right) E^1 + G_a Z_1 + Z_2 - ZL \qquad (10a)$$

$$C_n^2 = \frac{C_g}{k} \left(G_a G_p \frac{e}{\varepsilon C}\right) E^2 + G_a Z_1 + Z_2 - ZL \qquad (10b)$$

Subtracting equation 10a from 10b gives:

$$C_n^2 - C_n^1 = \frac{C_g}{k} \left(G_a G_p \frac{e}{\varepsilon C}\right)(E^2 - E^1) \qquad (11)$$

The significance of this equation (11) is that independently of Z_o and ZL the number of eV/channel corresponding to the difference between two peaks can be set by varying G_a to give the desired value (example: 10 eV/channel) even though the absolute placement of the spectrum with respect to zero may be wrong. The latter condition can be corrected by the ZL adjustment to satisfy equation (4). This procedure avoids the need for iteratively setting the controls to achieve calibration. As shown in figure 8 the process can be performed in a semiautomated mode in a computer based system which signals the operator how to make the needed adjustments. In those systems where the main amplifier gain and zero level are under computer control the process can be fully automated.

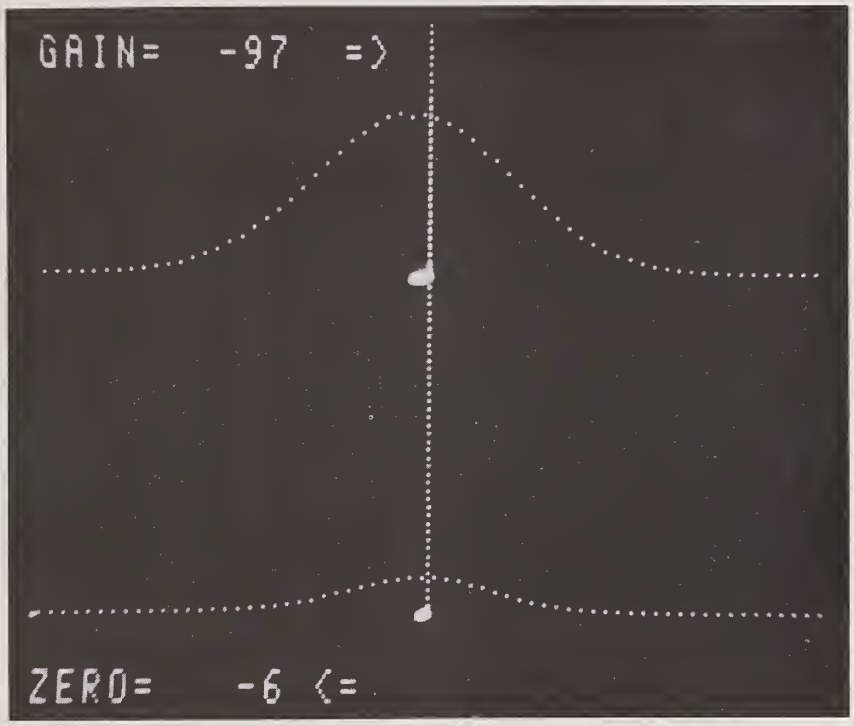

Figure 8. Visual output of automatic calibration program.

6. Multichannel Analyzer Evolution

The trend in advanced MCA development has been from completely hardwired to computer based units, with the latest systems containing the best features of both using a combination of minicomputers and microprocessors. In the earliest MCA's, the user literally had to count dots to determine channel numbers, which were then converted by hand to energy values. Elements were identified by comparing the calculated peak positions with tables of

known x-ray line energies. The next generation included a dial controllable feature known as a "bug" which made it possible to intensify the dot corresponding to the contents of any specific channel on the CRT. At the same time its position, in either channel number or energy, as well as the corresponding number of counts could be read directly from a numerical panel display. With the advent of low cost character generators, scale information and labels could also be displayed directly on the CRT. Later came a series of special features including regions of interest (ROI) displays, line markers, and access to a variety of auxiliary spectral storage and retrieval devices. The ROI approach allows the user, often with the help of the bug, to define a series of energy bands in which a running count of the integrated intensities are recorded. In this manner integrated peak intensities can be monitored either as a prerequisite for quantitative analysis, or pulses corresponding to specific elements can be coupled to SEM displays for line scans or area maps. Line markers are a series of vertical bars appearing at energies corresponding to the principal lines of any selected element. The line markers are introduced one element at a time and are manipulated by the bug control or keyboard. They can be superimposed over an unknown spectrum to facilitate rapid qualitative analysis. Figure 9 shows a composite of many of the types of information readily available to the user under keyboard control in addition to line markers. The area within the box shows the actual information that appears on the screen.

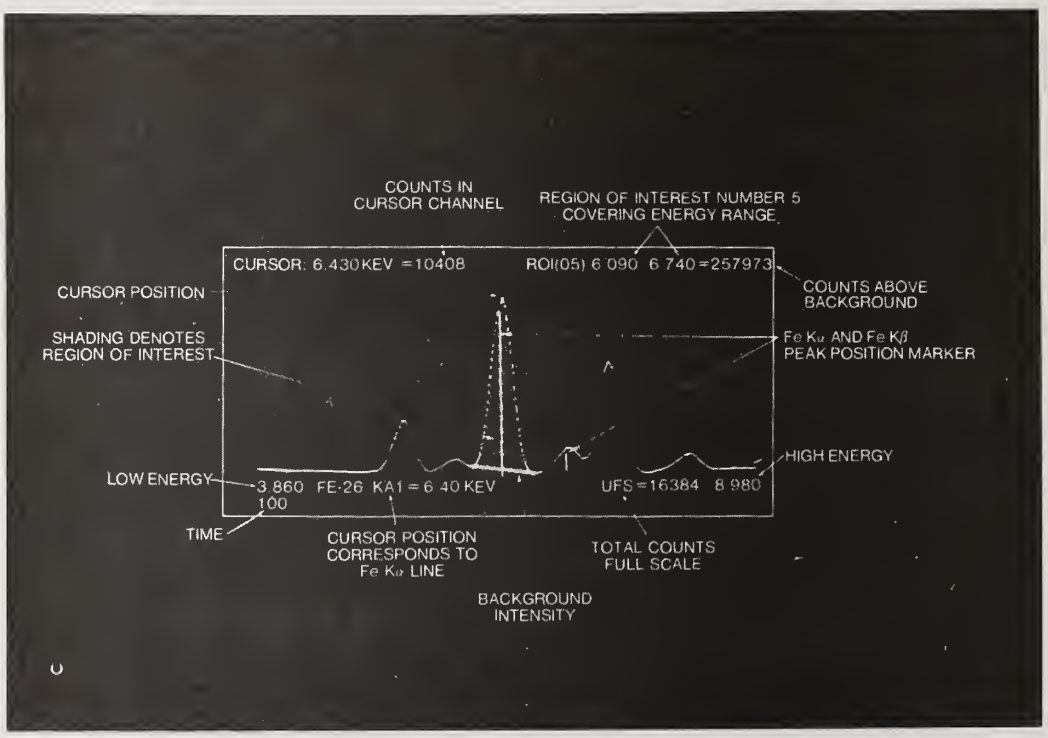

Figure 9. Composite illustration of CRT display aids.

Data readout with the earliest systems generally consisted of unlabeled x-y recordings, printed tables, or photographs of the CRT. Links to both large centralized computer systems and dedicated minicomputers were generally slow and awkward. Although there was some effort to interface the hardwired systems to auxiliary tape units for spectral storage and retrieval this approach also proved limited. In the exclusively computer based MCA, information from the ADC is transmitted directly to the central processor unit of a dedicated minicomputer which, through a combination of hardware and software, sees to it that pulse distribution information is directed to specified memory locations. The operator normally interacts with the system through an alphanumeric keyboard and/or various push button switches. Desired actions can then be initiated under computer control. These include data acquisition, spectral storage and retrieval on auxiliary devices and spectrum processing by

a variety of techniques. Central to this philosophy is the existence of an executive program with responds to specific mnemonic commands issued by the user. Unfortunately, unlike the more self-explanatory hardwired controls of early MCA's the software command structures of the computer based system tend to be more unique to each different manufacturer's product. The advantages are, however, much more flexibility and greater speed in data interpretation.

With the computer based MCA the operator normally has the option of changing parameters such as the memory group size, conversion gain, digital offset, the number of eV/channel and a number of CRT display features under program control. Furthermore, since the memory of the computer is used as the MCA memory, applications programs written in high level languages can readily access the stored data for quantitation. Typical programs presently available include ZAF, Bence-Albee, Cliff Lorimer and Rasberry-Heinrich calculations. The storage and retrieval of both spectral data and processing or control programs is also a relatively straightforward matter since devices like tape drives and floppy discs are easily interfaced to almost all minicomputers. The major shortcoming of such systems has been that simultaneous data collection and processing on an internal time shared mode tends to slow them down since pulse sorting and storage can be almost a full time job. The solution to this problem, as characterized by the latest generation of MCA's, has been to use a combination of minicomputers and microprocessors to handle specific tasks. For example, a dedicated microprocessor system with its own memory can be used for rapid pulse collection, sorting and storage, its memory can be coupled directly to a minicomputer which handles data processing. Other microprocessors can be used for controlling the CRT display or performing specific computational or control tasks. Looking ahead, the increased sophistication and reduced costs of semiconductor components will clearly lead to more integrated systems. Future microprobes, TEMs, SEMS, and x-ray fluorescence spectrometers will be digitally controlled. In this manner it will be possible for an instrument operator to supervise data collection, control, and processing through a single interface resulting in better reproducibility, speed, and hopefully accuracy.

Reference

[1] Williams, Garry, "Role of Multichannel Analyzer in Data Handling" Energy Dispersive X-ray Analysis: X-ray and Electron Probe Analysis, ASTM STP485, American Society for Testing and Materials, 1971, pp. 125-139.

National Bureau of Standards Special Publication 604. Proceedings of the Workshop on Energy Dispersive X-Ray Spectrometry held at NBS, Gaithersburg, Maryland, April 23-25, 1979. (Issued March 1981)

STATISTICAL CONSIDERATIONS OF DETECTABILITY LIMITS AND DECONVOLUTION IN ENERGY DISPERSIVE X-RAY SPECTROMETRY

P. L. Ryder

Department of Physics
University of Bremen
West Germany

Abstract

The first part of the paper considers theoretically the experimental errors due to counting statistics in the determination of line intensities by fitting Gaussian curves to the experimental values. The line positions and the background are assumed to be known, and the background level is taken to be constant over the relevant energy range. Expressions are derived for the standard deviations of the line intensities a) for a single line and b) for two overlapping lines. Numerical examples are given to illustrate the effect of line and background intensities on these errors. In the case of two overlapping lines, it is shown how the ultimate spectral resolution is limited by the statistical errors, which increase as the line separation decreases.

The second part of the paper is concerned with the effect of counting statistics on the deconvolution of unsmoothed ED spectra by Fourier methods, when no assumptions are made concerning the line positions or background spectrum. It is shown that a criterion for the resolution limit of two overlapping lines is provided by the requirement that the amplitude of the first maximum in Fourier spectrum of the line pair must be equal to or greater than the mean amplitude of the noise spectrum. In retransforming the Fourier spectrum the high-frequency noise must be eliminated by a suitable frequency filter. It is suggested that the filter shape should be that of the Fourier transform of the spectrometer function (in this case a Gauss curve). The consequences for computer evaluation of energy dispersion x-ray spectra are discussed.

1. Introduction

The accuracy with which the concentration C of a particular element may be determined by x-ray analysis techniques such as electron probe microanalysis, x-ray fluorescence, etc., is ultimately limited by the statistical error in the measured intensity. The detectability limit C_o is usually defined as the concentration at which the line intensity is equal to some arbitrarily chosen multiple (usually taken to be 3) of the standard deviation σ of the background intensity [1-8][1]. Assuming a linear relationship for small concentrations:

$$I = \gamma c \tag{1}$$

the detectability limit is given by

$$C_o = \frac{3\sigma}{\gamma} \tag{2}$$

[1]Figures in brackets indicate the literature references at the end of this paper.

In the case of energy dispersive x-ray spectrometry the situation is complicated by the fact that, due to the limited resolution of the solid state detection, overlapping lines are often encountered. The intensities of such lines must be determined by peak fitting, peak stripping or general deconvolution methods [9-13]. It is the purpose of the present paper to consider the effect of errors due to counting statistics in their processes, and to show how such errors limit the effective resolution attainable, i.e., the smallest line spacing for which the line intensities may be determined with a given required accuracy.

The problem is first discussed for the special cases of a single line and two overlapping lines on a constant background. Quantitative expressions are given for the relative errors as a function of the line counts, line separation and background level, and the results are illustrated by diagrams and numerical examples. The effect of statistical noise on the general Fourier deconvolution method is then considered.

2. Line Fitting Methods

2.1 Single Line on a Constant Background

We suppose that the intensity of a single line on a constant, known background is to be determined by fitting a curve of suitable shape to the experimental points. In energy dispersive x-ray analysis the line shape is described with sufficient accuracy by a Gaussian curve. The mean number of pulses collected in channel No. n is given by

$$P_n = B + If_{hn} \tag{3}$$

B is the number of background counts per channel (assumed to be constant), I is the total number of counts in the line (the parameter to be determined) and f_{hn} is given by

$$f_{hn} = \frac{1}{s\sqrt{2\pi}} \exp\left[\frac{-(h-n)^2}{2s^2}\right] \tag{4}$$

In this expression h denotes the position (channel No.) of the peak maximum and s is the line width parameter, related to the half-width by

$$w = 2.35\ s \tag{5}$$

We denote the actual number of counts collected in channel n by Q_n. The value of I is chosen so that the sum of the squares of the differences $(P_n - Q_n)$ is a minimum. The condition for this is

$$\frac{d}{dI} \sum_{n=1}^{N} \left\{B + If_{hn} - Q_n\right\}^2 = 0 \tag{6}$$

(N = total number of channels). The leads to the following expression for I:

$$I = (\Sigma_n Q_n f_{hn} - B\Sigma_n f_{hn})/\Sigma_n f_{hn}^2 \tag{7}$$

If we assume that the channel width is small compared with the line width (i.e., s>>1), which is indeed a condition for the validity of equation (3), then the sums Σf_{hn} and Σf_{hn}^2 in equation (7) may be replaced by integrals:

$$\sum_n f_{hn} \approx \frac{1}{s\sqrt{2\pi}} \int_{-\infty}^{\infty} \exp\,(-x^2/2s^2)\,dx = 1 \tag{8}$$

$$\sum_n f_{hn}^2 \approx \frac{1}{2\pi s^2} \int_{-\infty}^{\infty} \exp\,(-x^2/s^2)\,dx = 1/2s\sqrt{\pi} \tag{9}$$

Inserting these results in equation (7) we obtain

$$I = 2s\sqrt{\pi} \left\{ \sum_{n=1}^{N} Q_n f_{hn} - B \right\} \tag{10}$$

The standard deviation σ of the intensity I is given by

$$\sigma^2 = \sum_n \left(\frac{\partial I}{\partial Q_n}\right)^2 \sigma_n^2 \tag{11}$$

where σ_n is the standard deviation of the channel count Q_n. Assuming Poisson statistics and $Q_n \gg 1$, σ_n is equal to the square root of the mean value:

$$\sigma_n = \sqrt{P_n} \tag{12}$$

Substituting from (3), (10), and (12) in (11) gives

$$\sigma^2 = 4\pi s^2 \sum_n \left\{ B f_{hn}^2 + I f_{hn}^3 \right\} \tag{13}$$

Replacing the sums again by integrals, the following expression is finally obtained for the standard deviation of the line intensity as a function of the line and background intensities:

$$\sigma^2 = 2s\sqrt{\pi}\, B + 2I/\sqrt{3} \tag{14}$$

The product sB, which will be denoted by U, is the number of background counts in a range s of the spectrum and is therefore independent of the choice of the channel width of the multichannel analyzer. The relative standard deviation as a function of I and U is given by

$$\left(\frac{\sigma}{I}\right)^2 = \frac{2U\sqrt{\pi}}{I^2} + \frac{2}{I\sqrt{3}} \tag{15}$$

Figure 1 shows the relative standard deviation as a function of the line count for various values of the background parameter.

The horizontal dotted line at the value 0.33 indicates the level for which the 3σ-error becomes equal to 100 percent of the line intensity.

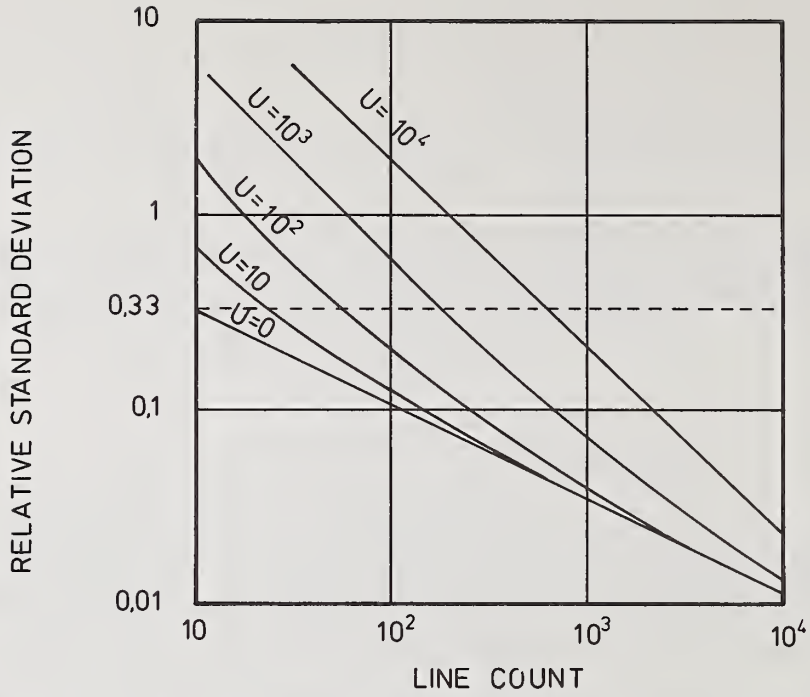

Figure 1. Relative standard deviation of the intensity of a single line as a function of the line count for various values of the background parameter U = sB.

2.2 Two Lines on a Constant Background

This problem has been treated extensively in an earlier paper [13]. The mean count in channel n is in this case

$$P_n = B + I_1 f_{1n} + I_2 f_{2n} \tag{16}$$

I_1 and I_2 ane the intensities of two lines centered on channel h_1 and h_2, respectively, and f_{1n} f_{2n} are abbreviations for $f_{h_1 n}$ and $f_{h_2 n}$. These parameters are chosen to give the best fit to the experimental points Q_n. The conditions for the minimum sum of the squares of the deviations are:

$$\frac{\partial}{\partial I_i} \sum_n \left\{ B + I_1 f_{1n} + I_2 f_{2n} - Q_n \right\}^2 = 0 \quad (i=1,2) \tag{17}$$

This given two simultaneous linear equations for I_1 and I_2. If we again replace the sums containing f_{1n}, f_{2n} and their products by integrals, we obtain the following solution:

$$I_1 = \frac{2s\sqrt{\pi}}{1-b^2} \left\{ S_1 - bS_2 - (1-b)\, B \right\}$$

$$I_2 = \frac{2s\sqrt{\pi}}{1-b^2} \left\{ S_2 - bS_1 - (1-b)\, B \right\} \tag{18}$$

with

$$S_i = \sum_n Q_n f_{in} \quad (i=1,2) \tag{19}$$

and

$$b = \exp\left\{-(h_1-h_2)^2/4s^2\right\}$$

The standard deviations of the intensities I_1 and I_2 are given by

$$\sigma_i^2 = \sum_n \left(\frac{\partial I_i}{\partial Q_n}\right)^2 \cdot P_n \quad (i=1,2) \tag{20}$$

From (18) and (20) we finally obtain

$$\sigma_1^2 = XU + YI_1 + ZI_2$$
$$\sigma_2^2 = XU + YI_2 + ZI_1 \tag{21}$$

with

$$X = \frac{2\sqrt{\pi}}{1-b^2}$$
$$Y = \frac{2(1-2b^{7/3} + b^{10/3})}{\sqrt{3}\ (1 - b^2)^2} \tag{22}$$
$$Z = \frac{2(b^{4/3}-2b^{7/3} + b^2)}{\sqrt{3}\ (1 - b^2)^2}$$

With the aid of equations (21) and (22) it is possible to calculate the errors as functions of the line intensities I_1 and I_2, the background count U (=Bs) and the line separation. The following figures show numerical examples for various values of these parameters. The line separation is denoted by the dimensionless quantity

$$\varepsilon = \frac{h_1-h_2}{s} \tag{23}$$

Figure 2 shows the relative error $\sigma_1/I_1 = \sigma_2/I_2$ as a function of the line count $I_1 = I_2$ for two lines of equal intensity with a separation $\varepsilon = 0.5$ (corresponding to about 1/5 half-width) and background counts of 0, 10, 10^2, 10^3, and 10^4 in the range s.

From such diagrams one may estimate how many counts are needed to obtain a given desired accuracy under specified experimental conditions.

Figure 3 is analogous to figure 2, the only difference being that the line separation ε was taken to be 2.5, corresponding approximately to the half-width. Comparison with figure 2 shows that the greater line separation leads, as one would expect, to lower experimental errors in the line intensities.

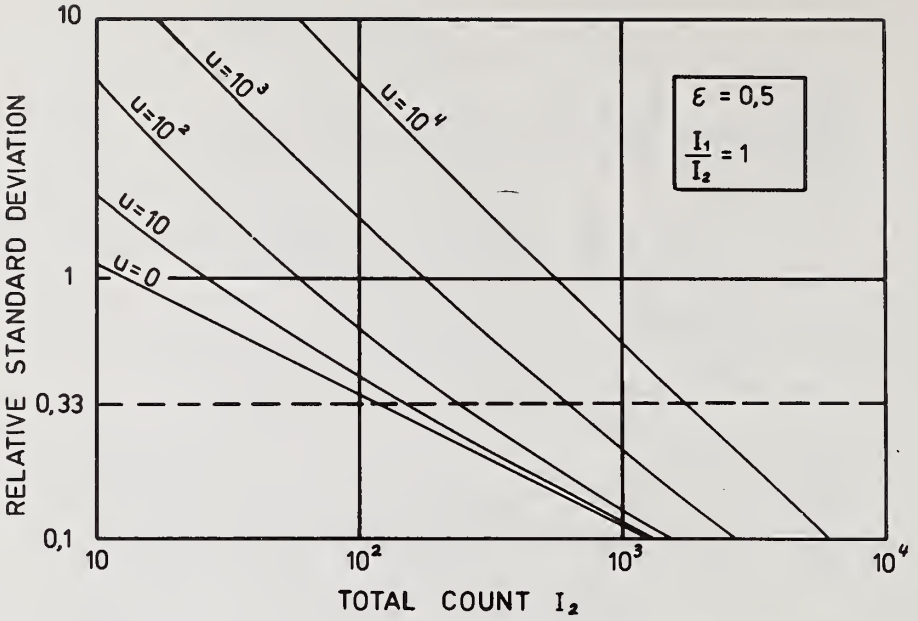

Figure 2. Relative standard deivation of the line intensities I_1 and I_2 as a function of I_2 calculated from equation (21) for $\varepsilon = 0.5$, $I_1 = I_2$ and $U = 0$, 10, 10^2, 10^3, and 10^4.

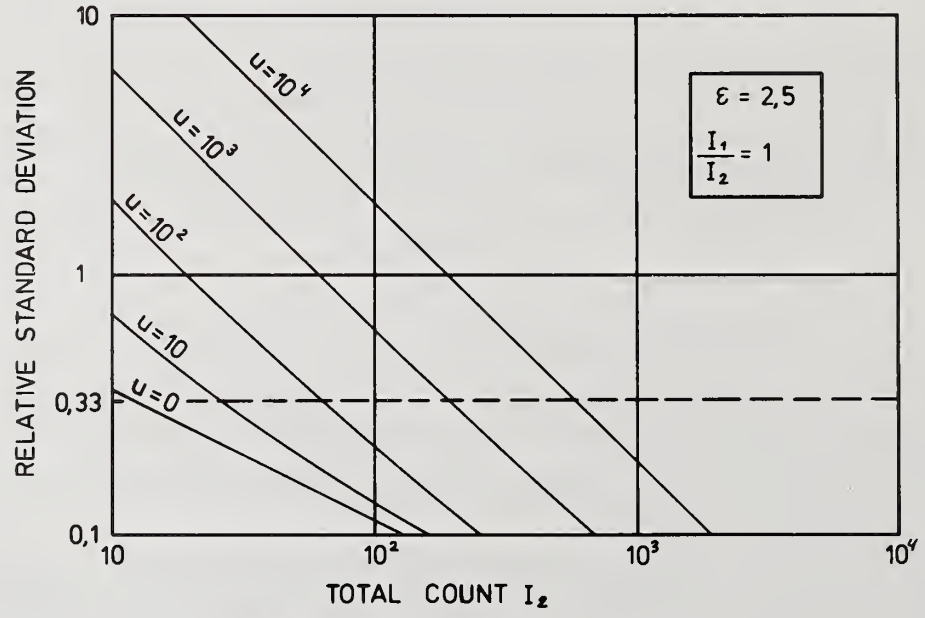

Figure 3. As for figure 2 with $\varepsilon = 2.5$.

Figures 4 and 5 are corresponding diagrams for two lines with an intensity ratio of 1:10. The relative standard deviation of the weaker line (continuous curves) and the stronger line (dashed curves) have been plotted against the total count of the stronger line (I_2) for the same background levels as in figures 2 and 3. The curves illustrate in particular the difficulty of detecting a weak line in the presence of a nearby strong line.

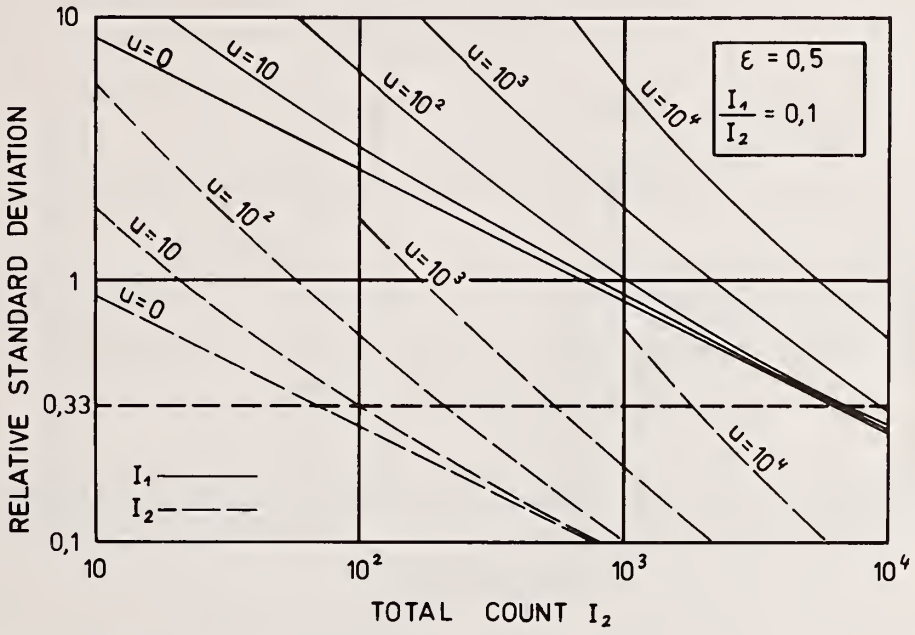

Figure 4. Relative standard deviation of the intensity I_1 (continuous curves) and I_2 (dashed curves) as a function of I_2 for $\varepsilon = 0.5$, $I_1 = 0.1\ I_2$ and U = 0, 10, 10^2, 10^3, and 10^4.

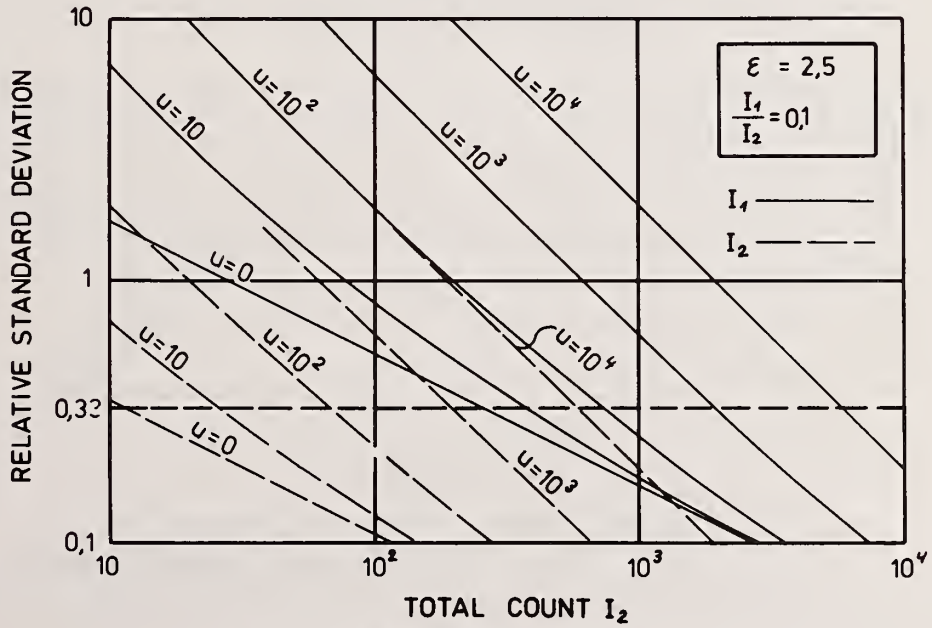

Figure 5. As for figure 4 with $\varepsilon = 2.5$.

The horizontal dashed line in figures 2 to 4 representa a 3σ limit of 100 percent. If the error is greater than this, the line may be regarded as "undetectable" under the given conditions. The points of intersection of curves with this horizontal line thus indicate the line counts for which the given line separation may be regarded as the "resolution limit", i.e., the smallest line separation for which the line concerned may still be detected under the given experimental conditions. Values of the resolution limit ε_0 obtained graphically from diagrams similar to figures 2 to 5 are shown in figures 6 and 7.

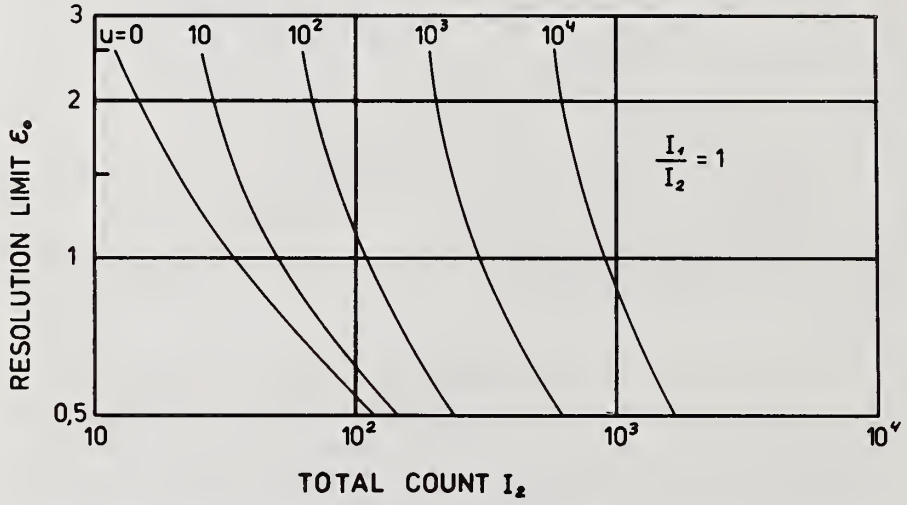

Figure 6. Resolution limit ε_0, determined graphically, as a function of I_2 for $I_1 = I_2$ and U = 0, 10, 10^2, 10^3, and 10^4.

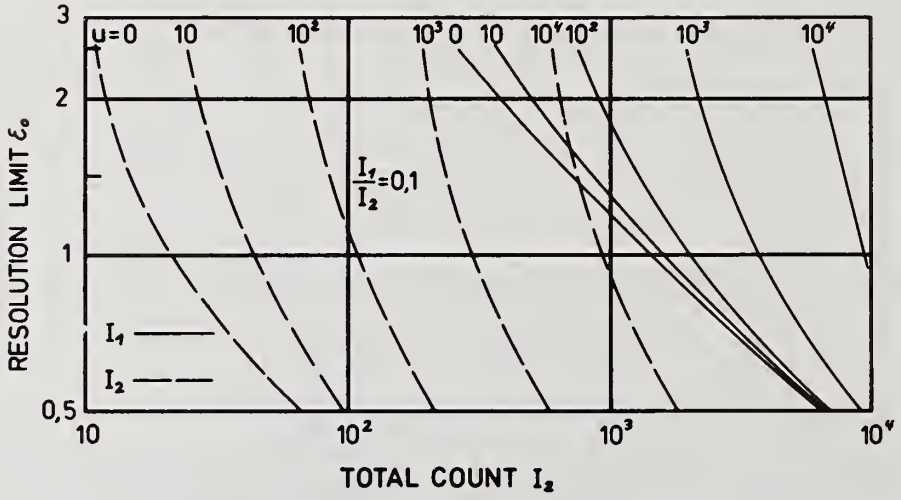

Figure 7. Resolution limit ε_0, determined graphically for the lines I_1 (continuous curves) and I_2 (dashed curves) with $I_1 = 0.1\ I_2$ and U = 0, 10, 10^2, 10^3 and 10^4.

Figure 6 shows, for example, that two lines with 100 counts each on a background of 100 counts may be detected separately in the sense defined above if their separation is greater than about 5. As may be seen from figure 7, in the case of two lines of unequal intensity, the value of the resolution limit depends upon whether one is trying to detect the weak line or the strong line. The values for the stronger line (dashed curves) are accordingly lower than those for the weaker line (continuous curves).

For small line separation ($\varepsilon \ll 1$) we may use the approximation

$$b^n \approx 1 - n\varepsilon^2/4 \tag{24}$$

which gives

$$\sigma_1 = \sigma_2 = \left\{4\sqrt{\pi}\ U + 8(I_1 + I_2)/3\sqrt{3}\right\}^{1/2}/\varepsilon \tag{25}$$

The resolution limit ε_o is defined as that value of ε for which $I_j = 3\sigma_j$ $(j = 1,2)$. This leads to the expression

$$\varepsilon_o = \frac{3}{I_j}\left\{4\sqrt{\pi}\ U + 8(I_1 + I_2)/3\sqrt{3}\right\}^{1/2} \tag{26}$$

with $j = 1$ for line 1 and 2 for line 2. For the special case $I_1 = I_2 = I$ and $U \ll I$ this equation takes on the simple form

$$\varepsilon_o = 3.72/\sqrt{I} \approx 4/\sqrt{I} \tag{27}$$

which may be used for estimating the ultimate resolution as a function of line intensity for small backgrounds.

3. General Fourier Deconvolution

3.1 Principle of the Method

We first review briefly the Fourier method of deconvolution, which makes use of the fact that the convolution of the spectrum is equivalent to multiplication of the Fourier coefficients, so that the deconvolution may be effected by division.

The original intensity distribution P(E) in the x-ray spectrum is modified by the spectrometer function G to give the measured spectrum P'(E)

$$P'(E) = \int_{-\infty}^{\infty} G(X)\ P(E - X)\ dX \tag{28}$$

with

$$G(X) = \frac{1}{\sqrt{2\pi}\ s}\ \exp\left(\frac{-x^2}{2s^2}\right) \tag{29}$$

This integral transformation is sometimes written in the abbreviated form

$$P' = G * P \tag{28a}$$

We assume that the spectrum is defined in the range $0 \leq E \leq E_o$ and expand all functions as Fourier series. With $\alpha = 2\pi/E_o$ we have

$$P(E) = \sum_{k=-\infty}^{\infty} p_k \exp(-ik\alpha E) \tag{30}$$

$$P'(E) = \sum_{k=-\infty}^{\infty} p'_k \exp(-ik\alpha E) \tag{31}$$

$$G(E) = \sum_{k=-\infty}^{\infty} g_k \exp(-ik\alpha E) \tag{32}$$

Replacing the functions in equation (28) by their Fourier series we obtain the following relationship between the Fourier coefficients:

$$p'_k = g_k p_k \tag{33}$$

The Fourier coefficients of the spectrometer function are given by

$$g_k = \frac{1}{E_o} \int_o^{E_o} \frac{1}{s\sqrt{2\pi}} \exp\left\{ik\alpha E - \frac{E^2}{2s^2}\right\} dE \tag{34}$$

For $s \ll E_o$ we may take the limits of integration to be $\pm\infty$ and obtain

$$g_k = \frac{1}{E_o} \exp\left(\frac{-\alpha^2 k^2 s^2}{2}\right) \tag{35}$$

The coefficients p'_k may be calculated from the measured spectrum and the coefficients p_k are then obtained by division

$$p_k = p'_k / g_k \tag{36}$$

The true spectrum is then reconstructed by Fourier synthesis from the coefficients p_k. Thus deconvolution is equivalent to division of the Fourier coefficients.

The limits to this process are set, as we will see, by the noise. To deal with this problem it is more convenient to handle a discrete spectrum. For a spectrum of N channels the Fourier series equivalent to equations (30 and 31) are

$$P_n = \sum_{k=-\infty}^{\infty} p_k \exp\left\{\frac{-2\pi ikn}{N}\right\} \tag{37}$$

$$P'_n = \sum_{k=-\infty}^{\infty} p'_k \exp\left\{\frac{-2\pi ikn}{N}\right\} \tag{38}$$

with

$$p'_k = p_k \exp\left\{\frac{-2\pi^2 k^2 s^2}{N^2}\right\} \tag{39}$$

3.2 Noise

Statistical noise may be represented by a random variable R_n added to the originally smooth spectrum. The Fourier coefficients of this contribution are

$$r_k = \frac{1}{N}\sum_{n=1}^{N} R_n \exp\left\{\frac{2\pi i k n}{N}\right\} \tag{40}$$

In general, it is not possible to determine the amplitude and phase of the Fourier coefficients r_k. One can, however, estimate the mean value of the amplitude $|\bar{r}_k|$. From (40) we have

$$|\bar{r}_k|^2 = \overline{r_k r_k}^* = \frac{1}{N^2}\sum_n \sum_m \overline{R_n R_m} \exp\left\{\frac{2\pi i k(n-m)}{N}\right\} \tag{41}$$

For $n \neq m$, the mean value of $R_n R_m$ is zero, since positive and negative values occur with equal probability. For Poisson statistics the mean value of R_n^2 is equal to P_n, the mean number of counts in the channel. Equation (41) therefore reduces to

$$|\bar{r}_k|^2 = \frac{1}{N^2}\Sigma P_n = \frac{M}{N^2} \tag{42}$$

where M denotes the total number of counts in the spectrum.

This calculation shows that the mean effect of the noise is a frequency-independent contribution to the Fourier spectrum.

3.3 Background

The background spectrum is – apart from steps due to absorption edges – a slowly varying function of the energy. As a simple extreme case we may take the number of background counts per channel (B_n) to be constant ($B_n = B$). The Fourier coefficients are

$$b_k = \frac{1}{N}\sum_{n=1}^{N} B_n \exp\left(\frac{2\pi i k n}{N}\right) = \begin{cases} 0 \text{ for } k \neq 0 \\ \\ B \text{ for } k = 0 \end{cases} \tag{43}$$

Thus the background gives rise to a peak at the low frequency end of the Fourier spectrum.

3.4 Signal

The Fourier transform of the signal is a general function, which is modulated by the transform of the spectrometer function according to equation (39). To illustrate the principle we will calculate the Fourier spectrum of a simple spectrum consisting of two lines of equal intensity separated by an energy interval a on a constant background.

The signal function is given in this case by

$$P_r = P_{r+a} = I$$
$$P_n = 0 \text{ for } n \neq r \text{ and } n \neq r+a \tag{44}$$

The Fourier coefficients are

$$p_k = \frac{I \exp\left(\frac{2\pi ikr}{N}\right)}{N} \left[1 + \exp \frac{2\pi ika}{N}\right] \tag{45}$$

The squares of the Fourier amplitudes are given by

$$\left|p_k\right|^2 = \frac{2I^2}{N^2} \left\{1 + \cos\left(\frac{2\pi ka}{N}\right)\right\} \tag{46}$$

and thus depend only on the separation of the two lines and not on their absolute position in the spectrum. In the measured spectrum the Fourier coefficients are modified by the spectrometer function:

$$\left|p'_k\right|^2 = \frac{2I^2}{N^2} \left\{1 + \cos\left(\frac{2\pi ka}{N}\right)\right\} \exp\left(\frac{-4\pi^2 k^2 s^2}{N^2}\right) \tag{47}$$

3.5 Deconvolution

Figure 8 is a schematic representation of the Fourier transform of the spectrum considered above. In this figure the square of the Fourier amplitude has been plotted against the frequency K. The background gives rise to the peak in the top left-hand corner of the figure. The signal gives an oscillating function which is modified by the spectrometer function, and the mean contribution of the noise to each Fourier amplitude is constant.

The effect of noise on the deconvolution process is illustrated in figure 9. The upper left-hand part of the figure shows the situation for an ideal spectrum without noise. The deconvolution is effected, as explained above, by dividing the Fourier coefficients of the measured spectrum by the Fourier coefficient of the spectrometer function. In the presence of noise, however, (see right-hand and lower part of figure 9) this leads to an exponential increase of the noise spectrum. This means that the deconvolution process magnifies the noise component. In the reverse Fourier transformation it is therefore necessary to use a frequency filter to cut off the high frequencies.

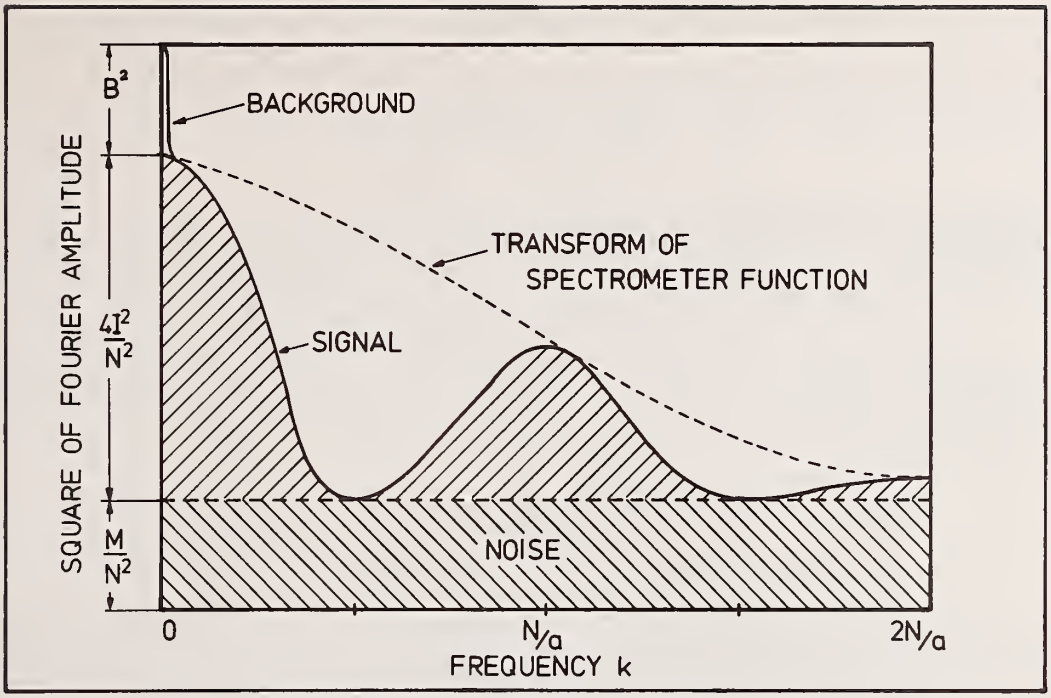

Figure 8. Schematic representation of the square of the Fourier amplitude as a function of the frequency for a spectrum consisting of two lines of intensity I and separation a on a constant background B. N is the total number of channels and M the total number of counts in the spectrum.

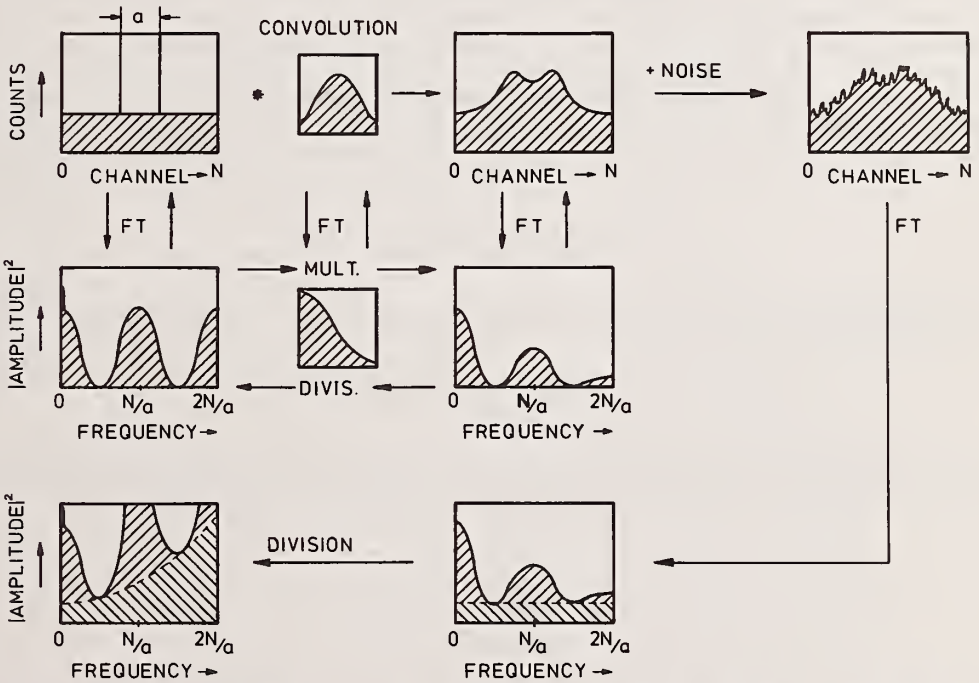

Figure 9. Schematic diagram showing the effect of noise on the Fourier deconvolution of a spectrum. The original spectrum is assumed to consist of two lines on a background (top left-hand figure). The next two figures to the right show the spectrometer function and the folded spectrum, with the Fourier transform (FT) below. The effect of Fourier deconvolution on a noisy spectrum (right) is shown in the lower part of the figure.

The limiting frequency and hence the resolution limit of the spectrum may be estimated from the criterion that the first maximum of the Fourier spectrum of the signal should be at least as great as the mean value of the noise level at the same frequency, i.e.,

$$\frac{4I^2}{N^2} \exp\left(\frac{-4\pi^2 s^2}{a^2}\right) \geq \frac{M}{N^2} \tag{48}$$

The corresponding line resolution limit is

$$\varepsilon_o = \frac{a}{s} = \frac{2\pi}{\sqrt{\ell n(4I^2/M)}} \tag{49}$$

For negligible background (M = 2I) this reduces to

$$\varepsilon_o = \frac{2\pi}{\sqrt{\ell n(2I)}} \tag{50}$$

This does not agree with equation (27). The reason is that, in deriving equation (27), it was assumed that the line positions and the background level were known, whereas the general Fourier deconvolution method assumes nothing except a knowledge of the spectrometer function.

3.6 Form of the Frequency Filter

It is well known that the shape of a frequency filter has a critical influence on the quality of the reconstructed spectrum. A sudden cut-off may lead to spurious oscillation which could be interpreted as lines. It is therefore suggested that the filter should have the same shape as the Fourier transform of the spectrometer function – see equation (35) – but with a different width. This may be regarded as a partial deconvolution, effectively reducing the line width of the spectrometer. Instead of multiplying by $\exp[2\pi^2k^2s^2/N^2]$, as required by equation (39), we multiply by $\exp[2\pi^2k^2(1-\beta^2)s^2/N^2]$ giving a

$$p''_k = p'_k \exp\left[2\pi^2k^2(1-\beta^2)s^2/N^2\right] \tag{51}$$

The relationship between p''_k and the Fourier coefficients p_k of the true spectrum is

$$p''_k = p_k \exp\left[-2\pi^2k^2(\beta s)^2/N^2\right] \tag{52}$$

Comparison with equation (39) shows that we have effectively reduced the spectrometer line by a factor β. The choice of β (<1) will depend upon the particular noise level.

4. Summary and Conclusions

The object of the present paper was to show how the resolution ultimately attainable by line fitting or Fourier transformation is affected by the counting statistics. The results may be used to estimate the theoretical resolution limit under various experimental conditions.

It was shown that, in the case of deconvolution by Fourier methods, a frequency filter must be used to eliminate the high-frequency contribution from the noise. It is suggested that the appropriate shape for the frequency filter is a Gauss curve corresponding to a reduced spectrometer line width. In a fast on-line deconvolution, the effective line width could be made variable and adjusted to the prevailing experimental conditions.

Independently of the method of deconvolution employed, all computer programmes used for evaluating energy-dispersive spectra should contain a test of the reliability of the results.

References

[1] Kaiser, H. and Specker, H., Anal. Chem., 149, 46-66 (1956).

[2] Kaiser, H., Anal. Chem., 209, 1-18 (1965).

[3] Kaiser, H., Anal. Chem., 216, 80-94 (1966).

[4] Ziebold, T. O., Anal. Chem., 39, 858-861 (1967).

[5] Svoboda, V. and Gerbatsch, R., 2. Anal. Chem., 242, 1-13 (1968).

[6] Hubeaux, A. and Vos, G., Anal. Chem., 42, 849-855 (1970).

[7] Kaiser, H., "Methodicum Chimicum", 1, Part 1, 1-20 (1973).

[8] Ryder, P. L., Scanning Electron Microscopy/1975 (Part 1), 111-117.

[9] Ergun, S., J. Appl. Cryst., 1, 19-23 (1968).

[10] Beevers, C. A., Acta Cryst., 5, 670 (1952).

[11] Stokes, A. R., Proc. Phys. Soc. (London), A61, 382-391 (1948).

[12] Cohen, J. B., "Diffraction Methods in Materials Science", 80-105, MacMillian, New York (1968).

[13] Ryder, P. L., Scanning Electron Microscopy/1977, Vol. 1, 273-280.

Table 1. List of symbols.

n	:	channel number
P_n	:	mean number of pulses in channel n
Q_n	:	actual number of pulses in channel n
B	:	background count per channel
I, I_1, I_2	:	total line counter
f_{hn}	:	Gauss function, see equation (4)
W	:	line half-width
s	:	2.35 W
N	:	total number of channels in spectrum
σ	:	standard deviation
U	:	background counts in range s ($U = sB$)
ε	:	line separation parameter $\varepsilon = (h_1-h_2)/s$
		(h_i = channel no. of maximum of line i)
K	:	Fourier frequency
$P(E)$	:	original energy spectrum
$P'(E)$	:	measured energy spectrum
$G(E)$	:	spectrometer function
k	:	Fourier frequency
p_k, p'_n, g_k	:	Fourier coefficients of P (or P_n), P' (or P'_n) and G, respectively
E_o	:	maximum energy of spectrum
α	:	$2\pi/E_o$
R_n	:	statistical deviation of channel n ("noise")
$\sqrt{k}$	:	Fourier coefficient of R_n
M	:	total number of counts in the spectrum

National Bureau of Standards Special Publication 604. Proceedings of the Workshop on Energy Dispersive X-Ray Spectrometry held at NBS, Gaithersburg, Maryland, April 23-25, 1979. (Issued March 1981)

CURVE FITTING TECHNIQUES AND THEIR APPLICATION TO THE ANALYSIS OF ENERGY DISPERSIVE SPECTRA

Frederick H. Schamber

Tracor Northern, Inc.
2551 W. Beltline Highway
Middleton, Wisconsin 53562

Abstract

Curve Fitting is a widely used procedure in many areas of analysis and has become one of the dominant methods employed in the analysis of energy dispersive spectra. Despite this popularity, curve fitting methods are not universally understood by x-ray analysts and there is thus the potential both for misapplication of the techniques and disagreement as to the interpretation of curve-fitted results.

Curve-fitting analysis can frequently produce spectacular results by extracting information which is not readily accessible by other techniques. Since the basic principles of the method are generally buried in the complexities of a computer program, the unfortunate impression is sometimes given that curve-fitting is a form of statistical alchemy which purports to extract unlimited information from minimal data. Enthusiasts have been known to make extravagant claims for the method, thereby confirming the worst fears of skeptics, who properly mistrust any technique which seems to offer "something for nothing."

The primary area of misunderstanding seems to be one which is addressed by the question: "What can curve fitting really do, and what can it not do?" It is the intent of this paper to deal with this primary question by discussing the basic theory and practice of curve fitting, at a common sense level and as it specifically applies to problems in extracting x-ray intensity information from energy dispersive spectra. In so doing, the following basic questions will be addressed:

(1) What actually is meant when we speak of "curve fitting?" What are the underlying principles?

(2) How does one actually implement a curve-fitting procedure? What are the basic algorithms and how do they differ? What are the practical considerations which determine which technique is most appropriate?

(3) What kind of information does one have to supply to the procedure and what kind of information can one obtain? What is the tradeoff between information supplied and information extracted?

(4) What are the practical problems encountered when one applies curve fitting methods to EDS spectra? How serious are these problems and how might one propose to deal with them?

(5) What kind of confidence can one have in curve-fitted results? How can one estimate statistical uncertainty and how reliable are such estimates? Does the technique have the ability to generate grossly erroneous results, and if so, what precautions must be exercised in interpreting fitted results?

It is clearly impossible to deal completely with each of these topics – indeed, unqualified answers cannot be given to many of these questions. It is instead the intent of this paper to clarify and briefly explore these issues as they specifically relate to the suitability of curve-fitting techniques for practical analysis of x-ray spectra.

1. Introduction

Curve fitting has become one of the major methods employed in the analysis of energy dispersive x-ray spectra. Despite this popularity, curve fitting methods are not universally understood by x-ray analysts and there exists the potential both for misapplication of the techniques and disagreement as to the interpretation of curve-fitted results.

It is the purpose of this paper to address two basic questions:

(1) What are the principles and practices of curve fitting?

(2) How reliable is curve fitting as an analysis technique?

2. Principles and Practices of Curve Fitting

This section of the paper will address itself to providing an overview of what curve fitting is and how it is performed. The primary intent will be to develop intuitive concepts and to provide a working vocabulary for the non-expert.

As the name implies, "curve fitting" is a procedure whose goal is to match a mathematical representation of a curve (i.e., a fitting function) to a collection of data points. Such procedures are applied to a wide variety of problems and for diverse reasons. For example, if you pick up a book written by a statistician or a theoretician, you will probably encounter curve-fitting used as a tool for functional analysis, that is, the practitioner is attempting to determine the "true" representation of an observed distribution of data by determining which function fits it best. (This is the kind of analysis which is concerned with significance tests.)

Another kind of curve fitting, commonly used in numerical analysis and engineering, is concerned with numerical approximation. Here one is interested only in obtaining a suitably simple approximation for a collection of data or a transcendental function. One does not worry about the "true" functional representation or about the "meaning" of the parameters. (This is the kind of application which makes frequent use of orthogonal polynomials and "spline fitting".)

In this paper we are concerned with a different type of curve-fitting application, which we will refer to as unfolding. This type of problem is fundamentally different from the first two types in that it is assumed that the functional representation of the curve (spectrum) being fitted is already known; the goal is to determine the values of specific parameters which are meaningful from an analytical viewpoint. Although the implementation of an unfolding problem often involves aspects of other types of application (e.g., determining the best function to represent peak shapes or approximating the background with a polynomial) these are only preparatory steps to the main analysis problem.

The analysis of an x-ray spectrum is a classic example of an unfolding problem. The spectrum consists of a "folding in" (summing) of a set of independent responses due to characteristic elemental emissions (peaks) and a relatively smooth underlying continuum (background), upon which is superimposed a "noise" component of random statistical variations. The spectrum is to be analyzed by "unfolding" it into its constituents so that the amplitudes of the relevant parameters (peak amplitudes) can be known. The "solution" to the problem is achieved when one determines the set of parameters which give the "best fit" to the unknown spectrum.

NOTE: This type of curve fitting problem has sometimes been referred to in the x-ray literature as "deconvolution" (a practice which this author has also been party to). Howeve, deconvolution is the accepted name for a specific process employed in Fourier Analysis (e.g., refer to the paper in this volume by P. L. Ryder). The use of this term to describe an entirely different type of analysis process should therefore be avoided.

We can describe the major considerations involved in implementing a curve fitting procedure as the following:

(1) Choosing the fitting function.

(2) Selecting a "best fit" criterion.

(3) Implementing an optimizing algorithm.

(4) Establishing the validity of the results.

These topics will now be discussed in some detail.

2.1 The Fitting Function

The first (and often the most difficult) step in implementing the analysis procedure is to choose a "fitting function" which provides an appropriate representation of the data to be fitted. We shall employ the following definitions:

$\bar{y}_j$ = the measured amplitude of the jth data value
(the "data points" to be fitted)

y_j = the functional approximation of the jth data value
(the "fitting function" being employed)

In general, a complete fitting function is made up of the sum of several component functions

$$y_j = (\text{function 1})_j + (\text{function 2})_j + \ldots + (\text{function n})_j$$

For example, a spectrum consisting of two peaks and a "background" function might be represented as:

$$y_j = (\text{peak 1})_j + (\text{peak 2})_j + (\text{background})_j$$

In turn, the peaks might be represented as Gaussian functions

$$(\text{peak i})_j = A_i e^{-\left[\frac{(C_i - x_j)^2}{2S_i^2}\right]} \qquad (1)$$

where A_i, C_i, and S_i are respectively the peak amplitude, centroid, and width parameters (S=FWHM/2.354; FWHM=Full Width of the peak at Half the Maximum amplitude).

A. Linear Functions

In many cases of practical interest, the fitting function can be expressed as a linear function of the parameters of interest. A fitting function is linear if it can be expressed in the form

$$y_j = A_1F_{1j}+A_2F_{2j}+\ldots+A_nF_{nj} \tag{2}$$

where the F_{ij} are predetermined functions of the j index and the A_i are the linear coefficients to be determined from the fit. For example, the background function might be chosen to be a quadratic function

$$(\text{background})_j = B_1+B_2x_j+B_3x_j^2 \tag{3}$$

where x_j is the energy-axis coordinate and the coefficients B_1,B_2,B_3 are the free parameters to be determined.

Similarly, if fitting with Gaussian peaks, one might be able to assume that the peak centroids (C_i) and widths (S_i) are known so that only the amplitude coefficients (A_i) need to be determined. The complete fitting function is then linear and can be written as

$$y_j = B_1+B_2x_j+B_3x_j^2+A_1g_{1j}+A_2g_{2j} \tag{4}$$

where g_{1j} and g_{2j} are Gaussian functions with fixed centroid and width parameters and B_1,B_2,B_3,A_1,A_2 are the free linear parameters to be determined.

Another example of a linear fitting function in x-ray analysis is the use of measured single-element spectra as the fitting functions (a subsequent paper in this volume by McCarthy and Schamber describes such a method).

B. Non-Linear Functions

Non-linear functions are those in which the parameters of interest appear in ways other than as simple multiplicative coefficients. Thus, the centroid C_1 and peak width S_i of the Gaussian function are non-linear parameters; if they are to be determined in the fit, then the fitting function is non-linear.

Non-linear fitting functions must be used in x-ray spectrum analysis when the centroid and/or width parameters are not predetermined. Such parameters would be variables if the x-ray detector's calibration and/or resolution are uncertain. (The SIMPLEX program described in a subsequent paper by Fiori, et al., employs non-linear Gaussian functions.)

In general, linear curve-fitting problems are much simpler to deal with than non-linear problems. It will become obvious in the following that nearly all of the complications in implementing a curve fitting program have to do with non-linear parameters.

2.2 The "Best Fit" Criterion

Another important consideration is to define what is meant by "best fit". For example, one might propose to seek the solution which minimizes the sum of the absolute errors, which is almost universally used in physical analysis problems is the "least-squares" criterion, which is the solution (set of parameter values) which minimizes the quantity

$$\sum_j (\bar{y}_j-y_j)^2w_j \tag{5}$$

where the w_j are suitably chosen "weights". The least-squares criterion is intuitively attractive since it tends to concentrate on eliminating large errors and is relatively insensitive to small errors.

If the weights w_j are all chosen to be one (or equivalently, all equal to the same value) then all errors will be given equal importance and minimizing this function will result in an unweighted fit. In practice, however, one knows that an error of 200 counts is more important when $\bar{y}_j$ is 10,000 than when it is 1,000,000 since the inherent statistical uncertainty (standard deviation) in the former is $\sigma \sim 100$ compared to $\sigma \sim 1000$ for the latter. Thus, the weights should account for the statistical precision of the data. It can be shown that when the weights are chosen such that

$$w_j = -\frac{1}{\sigma_j^2} \tag{6}$$

where σ_j^2 is the variance (standard deviation squared) of the jth data point, then the choice of parameters which minimizes

$$\chi^2 = \sum_j \frac{(\bar{y}_j - y_j)^2}{\sigma_j^2} \tag{7}$$

is the most probable solution [1][1]. This is intuitively reasonable since if σ_j is the uncertainty in the measured value $\bar{y}_j$ and if the fitted value y_j is the "true" value of this point (e.g., equal to the average $\bar{y}_j$ which would be obtained in an infinite number of trials) then it follows that

$$\frac{(\bar{y}_j - y_j)^2}{\sigma_j^2} \tag{8}$$

is the same (on the average) for all data points; thus all points receive "equal" weighting (in the sense of proportionality to statistical precision). It can be shown that if the measured points $\bar{y}_j$ are normally distributed about y_j with standard deviation σ then $\chi^2 \sim (N-n)$ where N is the number of data points fitted, and n is the number of free parameters.

It should be carefully noted that the quantity χ^2 has specific statistical properties and that strictly speaking, the quantity defined by Equation 7 is not χ^2 unless it possesses these properties [2]. In particular, Equation 7 is not the statistical χ^2 unless the y_j are the true solution points. On the other hand, the solutions obtained by minimizing Equation 1 are the most probable solutions only if this quantity is truly the χ^2 of statistical theory. Seldom (if ever) can we be certain of these facts. However, as long as we do not depart too far from these rigorous concepts, experience tells us that the set of parameter values which minimize an approximate expression for χ^2 will be reasonable approximations of the "true" solutions.

> A note on weighting seems appropriate at this point. It is often stated that (assuming Gaussian statistics) the standard deviation of a count is simply the square-root of the count. Therefore, it is common practice to use $\bar{y}_j$ as the weighting factor in Equation 1. This is not strictly accurate since it is the true count value (average of all possible meaments) whose square-root is equal to the standard deviation. This distinction can be safely ignored when the magnitude of $\bar{y}_j$ is large, but when it is small, the relative variation in $\bar{y}_j$ is substantial and the use

[1]Figures in brackets indicate the literature references at the end of this paper.

of $w_j = 1/\bar{y}_j$ is quite inaccurate; note particularly that when $\bar{y}_j$ deviates to a small value the point is weighted more strongly in the fit than when it deviates to a large value (e.g., for $\bar{y}_j = 100 \pm 10$, compare $w_j = 1/90$ versus $w_j = 1/110$. This means that the fit will be consistently biased towards low values. Fortunately, it is not hard to correct for this problem; one needs only to smooth the weights in some fashion to minimize their statistical fluctuations.

Although other "best fit" criteria are frequently used in some fields (such as numerical analysis) the "least-squares" criterion is so commonly used that is nearly synonymous with "curve fitting". Other designations which are also used to refer to the minimization of Equation 7 include "error-weighted least-squares" and "chi-squared minimization". In the remainder of this paper, it shall be assumed that the best-fit criterion to be employed is the error-weighted least-squares procedure defined by Equation 7; the term χ^2 will be used somewhat loosely, fully realizing that this may be only an approximation to the chi-squared function of statistics.

To reiterate, the "best" values for the parameters are assumed to be those which minimize χ^2; the problem is to obtain those parameter values. As an aid to understanding this problem it is useful to visualize the variation of χ^2 versus the parameters as describing a surface. Figure 1 illustrates such a "chi-squared surface" in two dimensions (parameters a and b). The least-squares solution is the point a_{min}, b_{min} which locates the lowest point on the surface. As a simple means of representing χ^2 surfaces, we often employ a "contour plot", as in figure 1 where the contours of constant χ^2 are projected onto the (a,b) plane. As additional parameters are introduced, the χ^2 surface must be represented as an n-dimensional surface. Obviously, such higher-dimensioned surfaces are difficult to visualize, but the concepts are the same as for the simple two-dimensional case.

2.3 Optimization Algorithms

Having defined the optimization criterion (minimum χ^2), it is now necessary to consider how this is to be accomplished. There are three main classes of methods which are commonly employed. These are:

(A) Pattern Search Methods

(B) Gradient Search Methods

(C) Analytic Solution Methods

A. Pattern Search Methods

Pattern-search methods are essentially "mechanical" methods of locating the minimum. They do not make explicit use of the mathematical properties of the χ^2 function.

Of the pattern search methods, the simplest conceptually is to divide the range of possible parameter values into a grid of appropriate "mesh" size and to compute the value of χ^2 for each point on the grid. One then determines by inspection which point on the grid has the smallest χ^2 and this is taken to be the best solution. For example, in figure 2, the value of χ^2 for a hypothetical problem is tabulated for each of 11 possible values of the parameters C_1 and C_2 respectively. The "best" solution is obtained in the vicinity of C_1=15, C_2=17 where χ^2=37. If we wish to locate the minimum with greater precision, we can create a new grid of smaller mesh in the vicinity of this solution and look for an even smaller value of χ^2.

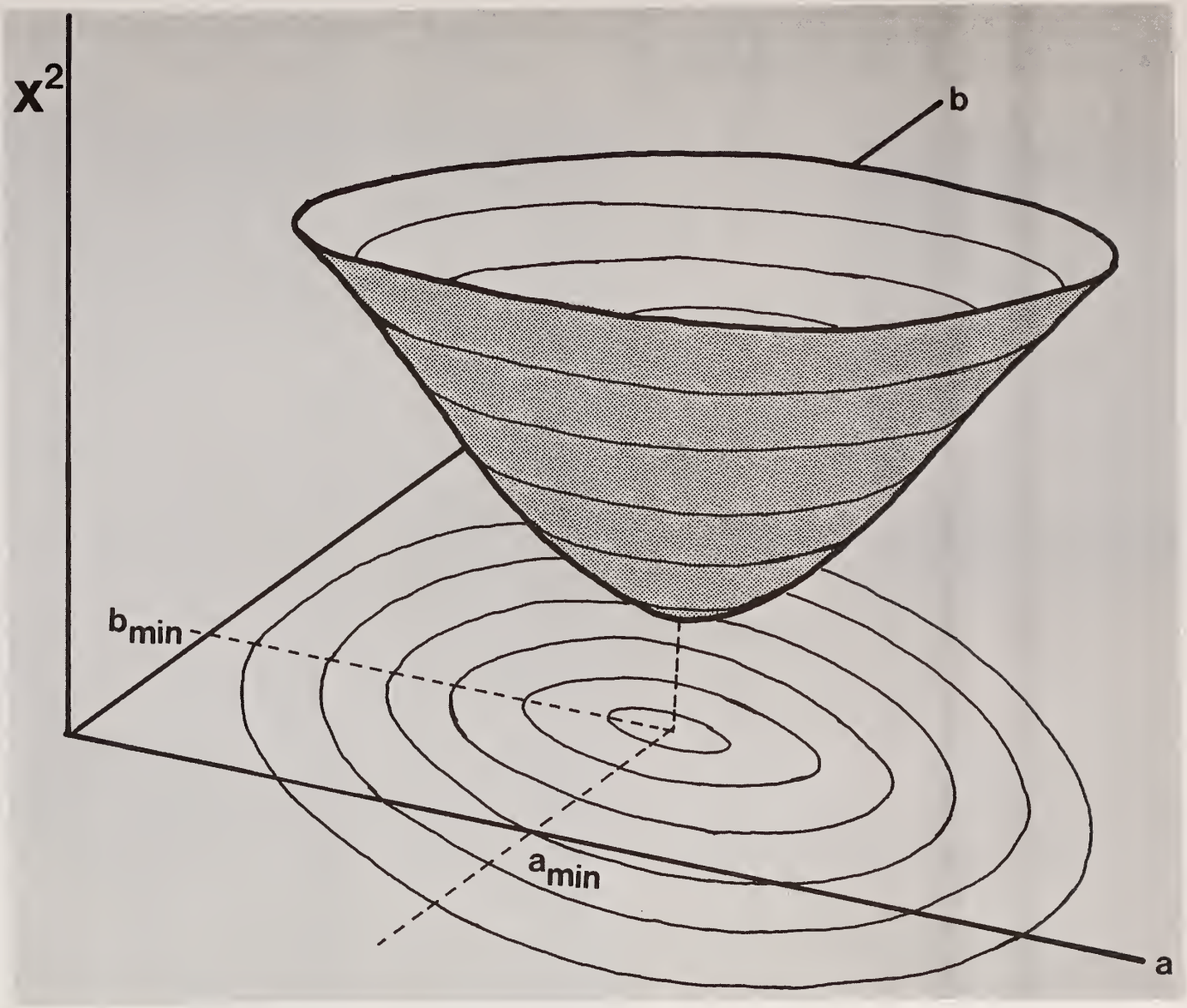

Figure 1. Representation of a two-dimensional χ^2 surface.

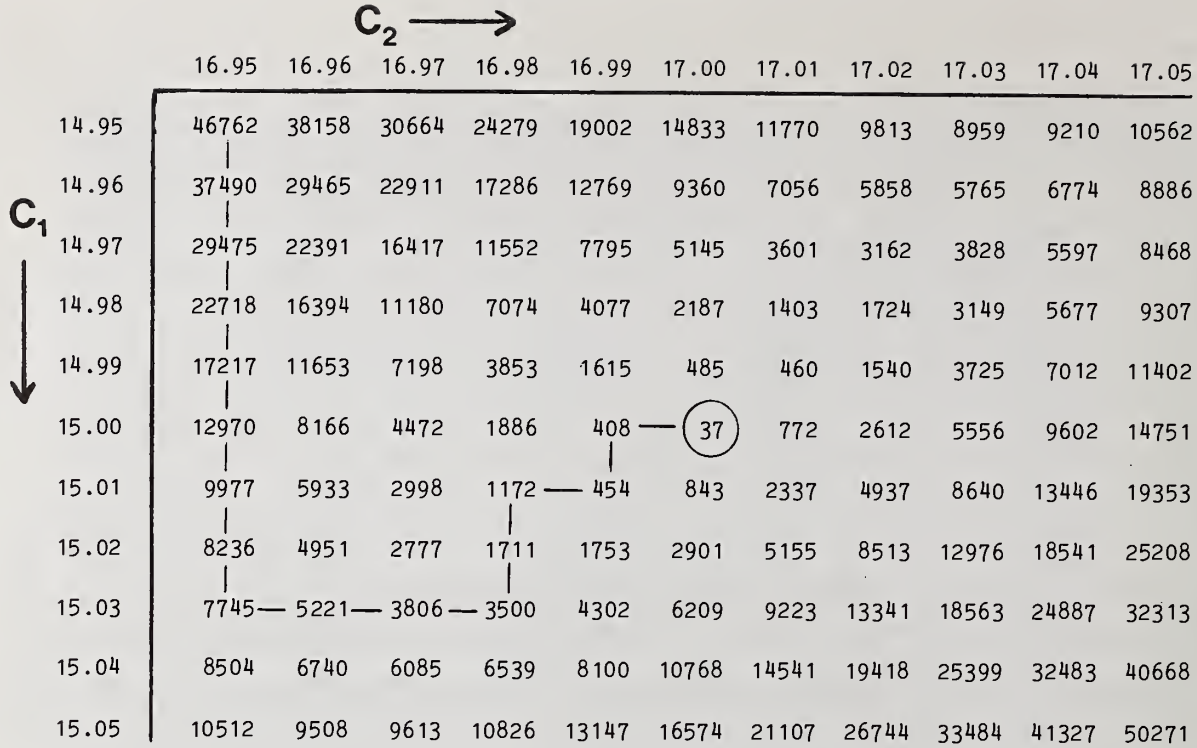

Figure 2. Grid of χ^2 values as a function of two parameters.

Such a "brute-force" procedure is infrequently used as a practical solution method simply because it is so inefficient. However, it is a valid optimization technique and illustrates how conceptually simple the problem really is. The more sophisticated methods described in the following are superior only in the speed with which they can locate the minimum.

Grid Search. An obvious improvement on the above crude method would be to inspect the grid only for those points which lie in the direction of decreasing χ^2 so as to eliminate a great deal of unproductive computation. One such simple method is a "grid search" which optimizes each of the parameters independently. This is illustrated in figure 2 for the same two-parameter example. Starting from the initial estimate C_1=14.95, C_2=16.95 one first optimizes C_1; the minimum in this column is found at C_1=15.03. Then C_2 is optimized while C_1 is held constant, and so forth along the path indicated in the figure. Again, when a grid minimum has been found, the mesh size can be decreased and the search repeated until the minimum has been located to the desired precision.

Grid Search Example. To illustrate the grid search procedure, a simple two-Gaussian test case was devised (figure 3). The "unknown" spectrum to be fitted (dotted spectrum in lower trace) consists of two Gaussians (top trace) of equal amplitudes (10,000) centered at channels 310 and 340 respectively, and of respective widths of 15 and 17 channels (FWHM). The fit was started with the initial "guesses" shown (bars) and all six of the peak parameters (two amplitudes, two centroids, two widths) were varied to obtain the best fit. (The actual fitting procedure is modelled after one described by Bevington [3], including the use of quadratic interpolation along an axis.) Figure 4 illustrates the six steps in the first iteration: proceeding left-to-right and top-to-bottom the fit is first optimized for the first peak amplitude (7277) and the second amplitude (12131), then for the first peak center (305.4) and the second (335.29), finally for the width of the first peak (14.70) and the second (19.73). In this first iteration, χ^2 decreased from its initial value of 6.8×10^8 to a value of 1.38×10^8, but the fit to the curve is still very poor.

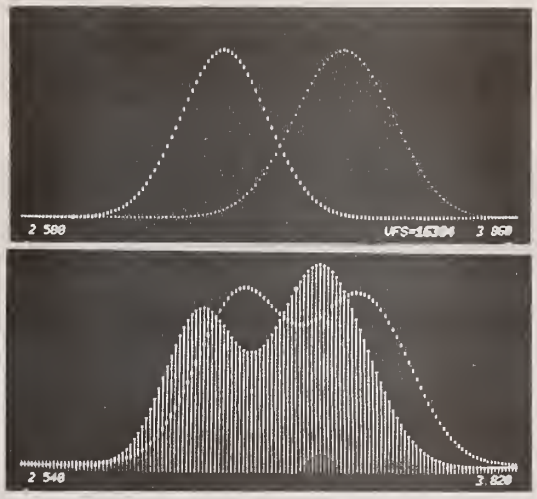

Figure 3. Two-Gaussian example problem: Upper — the individual "true" peaks. Lower — the composite "true" spectrum (dots) and the initial estimate (bars).

	TRUE PARAMETERS		INITIAL ESTIMATES	
	PEAK1	PEAK2	PEAK1	PEAK2
AMPLITUDE:	10000	10000	9000	12000
CENTER:	310	340	300	330
FWHM:	15	17	12	16

(FIT FROM CHANNEL 250 to 400)

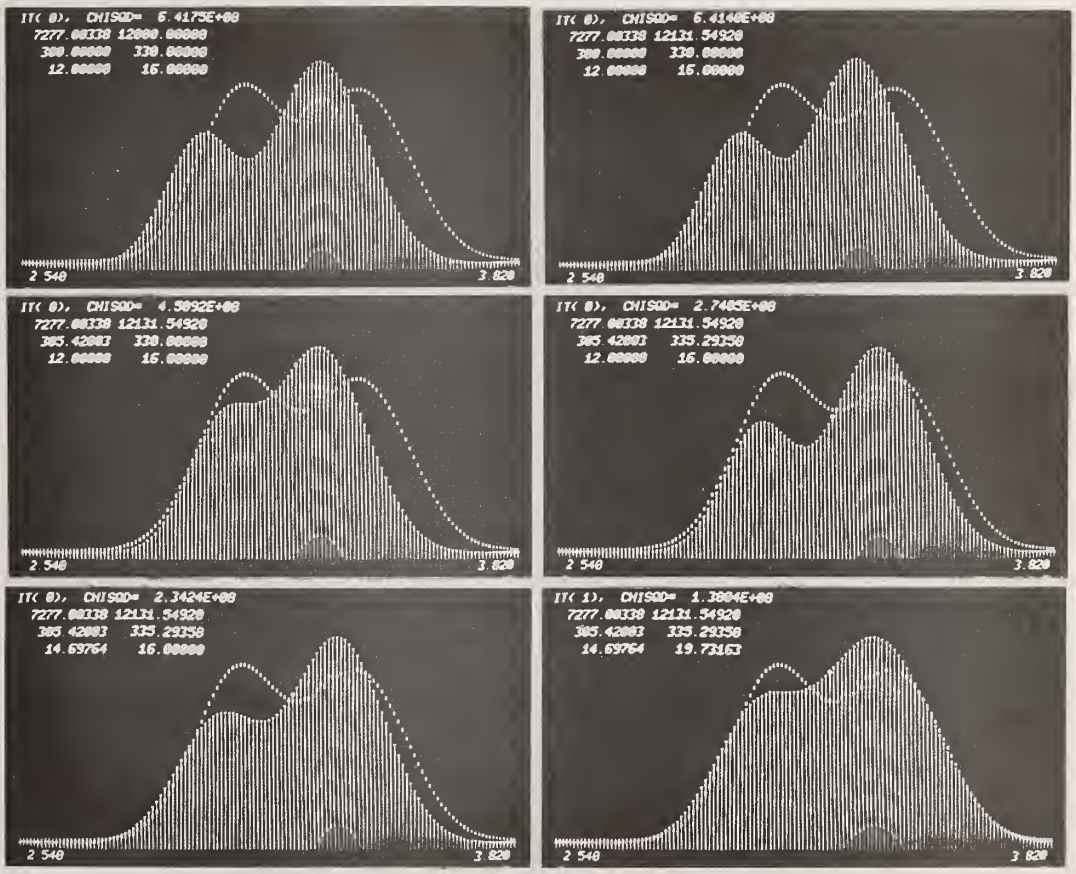

Figure 4. The six steps comprising the first iteration of a grid-search fit of the two-Gaussian problem.

Figure 5 illustrates the progress of the fit in subsequent iterations. By iteration 24 the fit is starting to look quite reasonable, but χ^2 is still 1.9×10^5. The fit will eventually converge to $\chi^2 = 6.2 \times 10^1$ on the 55th iteration. (This is a synthetic example with no statistical error so χ^2 is unrealistically small.)

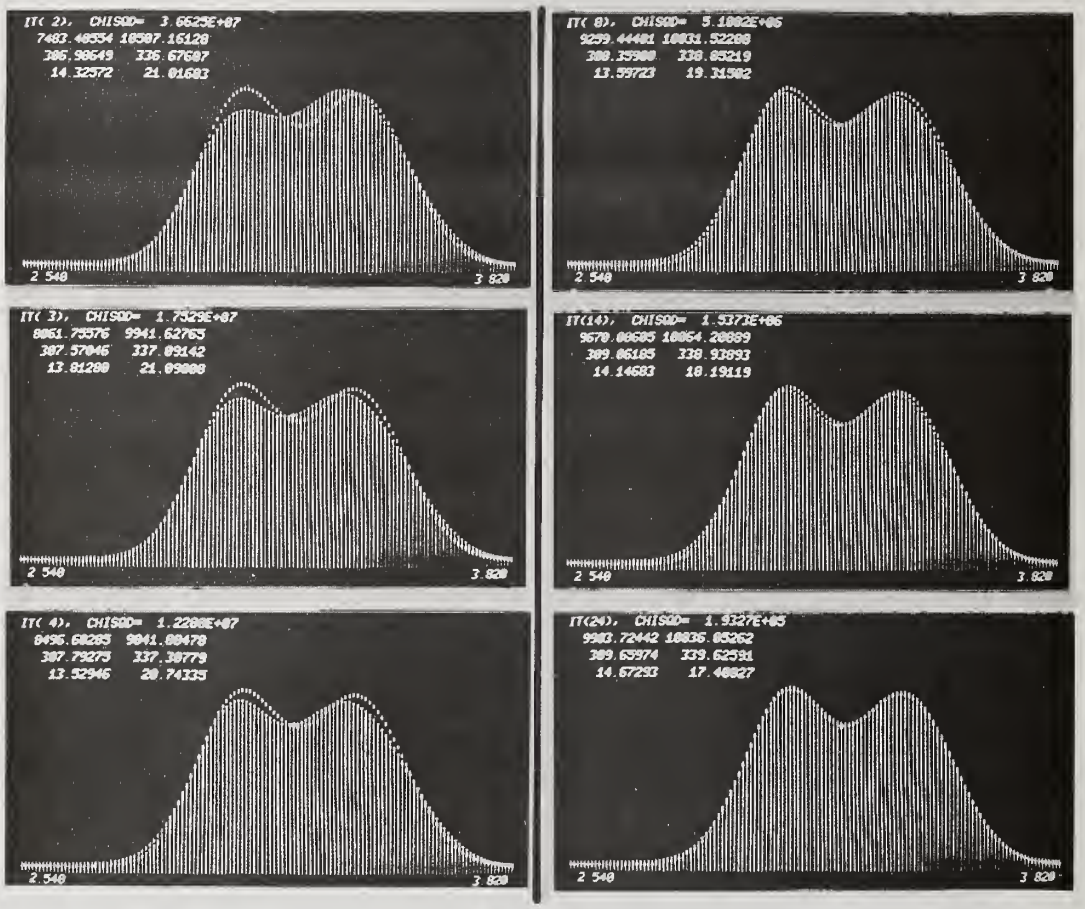

Figure 5. Grid-search solutions for the two-Gaussian problem at the end of 2, 3, 4 (left), 8, 14, and 24 (right).

This example illustrates how slowly the grid-search method may converge in a complex problem. Since each of the parameters is varied independently, the search for the χ^2 minimum describes a tortuous path of many small incremental variations rather than a smooth trajectory.

Simplex Method. The sequential simplex method is a particularly elegant pattern-search method. Like the grid-search, the simplex method is an intuitive geometric approach which involves only simple computations. But unlike the grid-search, the simplex method varies all parameters simultaneously. A simplex is defined as a geometrical figure of n+1 vertices, where n is the number of free parameters. For a single parameter the simplex is a straight line connecting two points, for a two parameter problem the simplex is a triangle, for three parameters a tetrahedron, etc. Figure 6 depicts the simplex for a two dimensional problem (triangle ABC). The optimization technique is to move the simplex across the parameter space in such a way that it always moves away from the least desirable vertex and thus (presumably) moves towards the optimum parameters. This procedure is governed by a set of simple rules (lucidly explained in reference 4) which will only be illustrated here. Referring to figure 6, assume that χ^2 is known for each of the three

points, A, B, C and that A has the largest value of χ^2. Since the response at A is less desirable than the response at either B or C a better response would presumably be found if one moves away from point A; point A is discarded and a new vertex is chosen as the reflection of point A across the line BC to obtain point D. The new simplex, BCD, is now evaluated, the least acceptable point is again reflected, and the process is repeated until the simplex arrives in the vicinity of the minimum.

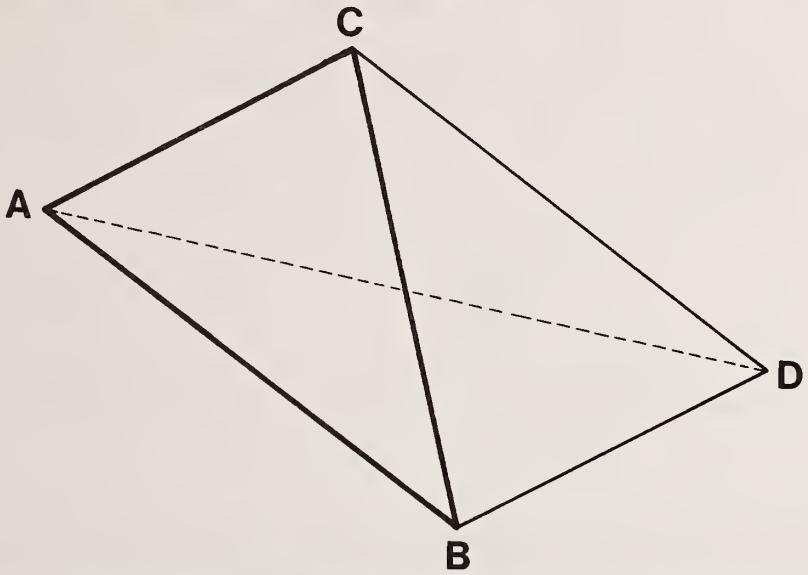

Figure 6. The basic two-dimensional simplex ABC, and its reflection to BCD.

An improved implementation of the basic simplex method employs "acceleration" which permits the dimensions of the simplex to be expanded or contracted along the direction of reflection. Figure 7 illustrates the moves in this modified simplex method (again a two-dimensional example). B. W, and N are respectively the Best, Worst, and Next-to-worst responses. The first step, as before, is to compute the response at point R, obtained by reflecting W across line BN. R is then compared with the other vertices according to precise rules [4] and expansion to point S, or contraction to points U or T can occur. Thus, the new simplex may be any of four possibilities: BNR – ordinary reflection, BNS – expanded reflection, BNU – contracted reflection, or BNT – contraction on the same side. These relatively simple modifications not only eliminate certain problems inherent in the basic method ("straddling" and "circling"), but they also enable the simplex to automatically adapt to the optimization surface; the simplex expands to move rapidly when distant and contracts as it nears the vicinity of the minimum.

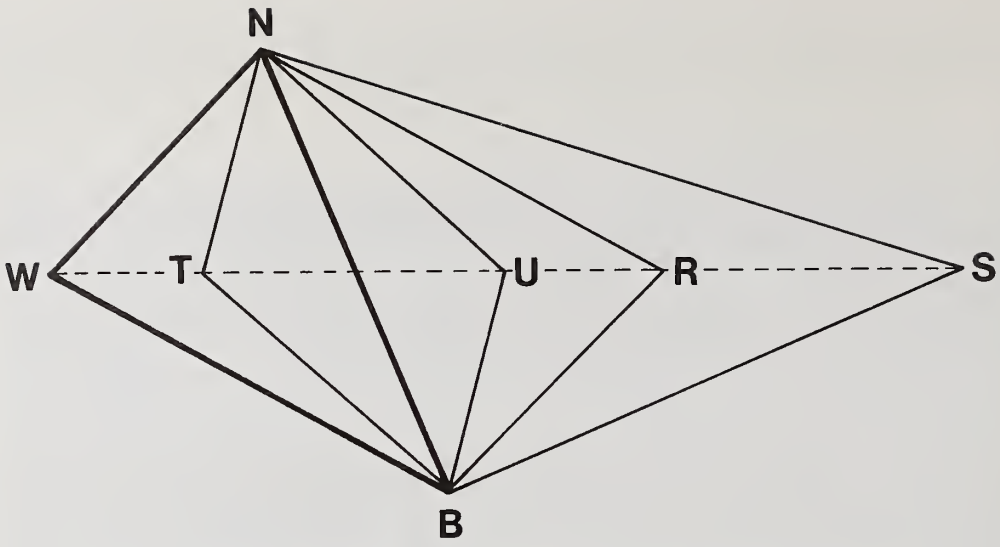

Figure 7. Possible moves of the accelerated simplex modification.

B. Gradient Search Methods

Gradient methods represent an increased level of sophistication over the pattern-search methods. Instead of relying upon "trial-and-error" to direct the search, the gradient methods attempt to predict the direction in which the minimum is to be found by making use of the gradient (slope) of the n-dimensional χ^2 surface. This is often referred to as the "method of steepest descent" since the idea is that for any given set of parameter estimates, the next set of estimates will be chosen along the direction of change which causes χ^2 to decrease most rapidly [3,5]. In two dimensions, this has a simple physical analog: referring to figure 1, think of releasing an object at any point on the χ^2 surface; the direction in which it would initially move under the influence of gravity is the direction of steepest descent (the negative of the gradient vector), and the path which it would follow to the bottom (disregarding inertia) is the ideal route of the minimizing procedure.

The mathematical basis of the method is illustrated in figure 8 for a two dimensional χ^2 surface. At an initial point, the negative components of the gradient are evaluated with respect to the parameters a and b:

$$D_a = -\frac{\partial \chi^2}{\partial a} \qquad D_b = -\frac{\partial \chi^2}{\partial b} \tag{9}$$

and the "steepest descent" vector D is the vector sum of D_a and D_b. (In practice, the gradient may either be obtained exactly by evaluating the partial derivatives of the χ^2 function, or approximated from the observed variation of χ^2 for small incremental changes in a and b.)

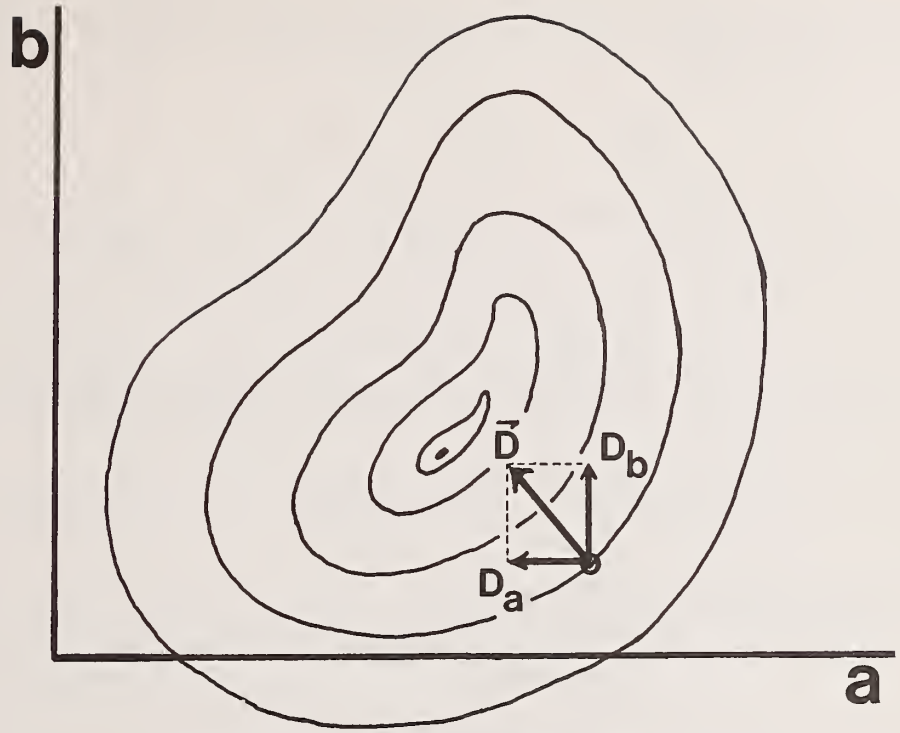

Figure 8. The steepest descent vector D.

The steepest-descent vector is always perpendicular to the local contour of constant chi-squared. For a "well-behaved" χ^2 surface with elliptically shaped contours (c.f., figure 22) the gradient vectors from all points on the surface will pass through the minimum. For an irregular surface (c.f., figure 19) the steepest descent vector at an arbitrary point may aim far from the true minimum and it will be necessary to recompute the gradient many times. In an "ideal" application of the method, the steepest descent trajectory would be composed of a continuous series of infinitesimal gradient vectors. In practice, one must use steps of finite size and therein lies a problem of the method; if one moves too far in the direction indicated by the steepest descent vector, one can overshoot the minimum, perhaps even to a point of higher χ^2. On the other hand, using very small increments and continuously recomputing the gradient is time-consuming. In short, although the steepest-descent method tells us what direction to move, it does not tell us how far to move in that direction. The usual procedure is to compute the steepest descent vector at an initial point and then move in this direction in small increments until χ^2 no longer decreases. It is then customary practice to use quadratic interpolation to estimate the minimum point along this vector and use this as the point from which to compute a new gradient vector.

Gradient methods would seem, in principle, to be very effective minimization procedures. This is not necessarily the case. First of all, gradient methods have difficulty with narrow curving valleys ("ravines"); such situations are quite common in peak fitting problems as will be seen in Part 2. Secondly, gradient methods converge slowly when the χ^2 surface is relatively flat, as tends to be the case in the vicinity of the minimum.

C. Analytic Solution Methods

The principle of the analytic method is to directly solve Equation 7 for the parameter values which will minimize χ^2. By definition, the gradient ("slope") of χ^2 with respect to each of the parameters must be zero at a minimum. To find the minimum, we solve for the set of parameters for which

$$\frac{\partial \chi^2}{\partial a_k} = 0 \qquad (k=1,n) \tag{10}$$

If y_j is a linear function of the parameters a_i

$$y_j = \sum_{i=1}^{n} a_i F_{ij} \tag{11}$$

then applying the condition of Equation 10 to Equation 7 results in the set of n coupled equations

$$\sum_j \frac{\bar{y}_j F_{kj}}{\sigma_j^2} = \sum_{i=1}^{n} a_i \sum_j \frac{F_{ij} F_{kj}}{\sigma_j^2} \tag{12}$$

which can be stated more compactly in the form

$$G_k = \sum_{i=1}^{n} a_i Z_{ik} \tag{13}$$

where the following definitions have been employed

$$G_i = \sum_j \frac{\bar{y}_j F_{ij}}{\sigma_j^2} \tag{14a}$$

$$Z_{ij} = \sum_j \frac{F_{ij} Z_{kj}}{\sigma_j^2} \tag{14b}$$

Z is an nxn matrix ("curvature matrix") and G is a column vector of n elements ("normal vector"). It should be noted that Equation 13 is nothing more than a set of n equations in n unknowns (often called the "normal equations").

For illustration, we will write the appropriate equations for the simple example of a quadratic fitting function.

$$y_j = a_1 + a_2 x_j + a_3 x_j^2 \qquad \text{(fitting function)} \tag{15}$$

$$\chi^2 = \sum_j \frac{(\bar{y}_j - a_1 - a_2 x_j - a_3 x_j^2)^2}{\sigma_j^2} \qquad \text{(object function)} \tag{16}$$

Using these definitions and approximating $\sigma_j^2 \cong \bar{y}_j$ we obtain for Equations 14a and 14b:

$$G_1 = \sum_j \frac{\bar{y}_j}{\bar{y}_j} \qquad G_2 = \sum_j \frac{\bar{y}_j x_j}{\bar{y}_j} \qquad G_3 = \sum_j \frac{\bar{y}_j x_j^2}{\bar{y}_j} \tag{17}$$

$$Z_{11} = \sum_j \frac{1}{\bar{y}_j} \qquad Z_{12} = \sum_j \frac{x_j}{\bar{y}_j} \qquad Z_{12} = \sum_j \frac{x_j^2}{\bar{y}_j}$$

$$Z_{21} = Z_{12} \qquad Z_{22} = \sum_j \frac{x_j x_j}{\bar{y}_j} \qquad Z_{23} = \sum_j \frac{x_j x_j^2}{\bar{y}_j}$$

$$Z_{31} = Z_{11} \qquad Z_{32} = Z_{23} \qquad Z_{33} = \sum_j \frac{x_j^2 x_j^2}{\bar{y}_j}$$

After computing the G and Z terms from these equations, one then obtains the optimum solutions for a_1, a_2, and a_3 by solving the normal equations:

$$\begin{aligned} G_1 &= a_1 Z_{11} + a_2 Z_{21} + a_3 Z_{31} \\ G_2 &= a_1 Z_{12} + a_2 Z_{22} + a_3 Z_{32} \\ G_3 &= a_1 Z_{13} + a_2 Z_{23} + a_3 Z_{33} \end{aligned} \tag{18}$$

Any reasonable method of solving the normal equations can be employed to obtain a solution. Most commonly, the solutions are obtained by first computing Z^{-1}, the matrix inverse of Z, and then solving for the a_i via

$$a_i = \sum_{i=1}^{n} G_i Z_{ij}^{-1} \tag{19}$$

(For this reason, the analytic method is sometimes referred to as "the matrix inversion method".)

One of the useful characteristics of this method is that it permits the uncertainty (standard deviation) in the fitted parameters a_i to be readily estimated from the relation

$$\sigma_{a_i}^2 \cong Z_{ii}^{-1} \tag{20}$$

Because of this property, Z^{-1} is often referred to as the "error matrix".

Unlike the preceding methods which proceed to the minimum by a stepwise iteration process, the analytic method obtains the optimum coefficients of a linear problem in a single computation. Not only is the analytic method invariably faster in such cases, but it has the additional advantage that it requires no initial guesses, step sizes, or other preparatory estimates. For this reason, linear least-squares problems are almost always solved by the analytic method, leading sometimes to an unfortunate tendency to use the

terms as synonyms (which can result in confusing statements such as "an advantage of the simplex method over the least-squares method is ...").

Analytic Solution of Non-linear Problems (Linearization). The above remarks are all relevant for the case of a linear fitting function. In the case of a non-linear function, application of Equation 10 to Equation 7 gives rise to a set of non-linear coupled equations which are generally non-analytic and cannot be solved directly.

In certain special cases, one can convert a non-linear function to a linear function by suitable manipulation of the problem. For example the case of fitting $\bar{y}_j$ with the function

$$y_j = Ae^{Bx_j} \tag{21}$$

can be transformed to a linear problem by fitting to $\ln(\bar{y}_j)$, in which case the fitting function is of the linear form $\ln(A)+Bx_j$ (note that the weighting function w_j also needs to be transformed appropriately). Such "tricks" are generally of quite limited utility and more general methods are needed for solution of routine problems.

The usual method used to solve non-linear problems by the analytic method is to "linearize" the problem by approximation in the vicinity of an estimate. The Taylor-series expansion for a function $f(x)$ about the point $x=x^o$ is given by:

$$f(x) = f(x^o)+(x-x^o)\left.\frac{\partial f}{\partial x}\right|_{x=x^o} + \frac{(x-x^o)^2}{2}\left.\frac{\partial^2 f}{\partial x^2}\right|_{x=x^o} + \ldots \tag{22}$$

As a first-order approximation we disregard high order terms and use only the linear expression (figure 9). For a function of n parameters

$$y(a)_j \cong y(a^o)_j + \sum_{i=1}^{n} \Delta a_i y'(a^o)_{ij} \tag{23}$$

where a represents the complete set of parameters $a_1,a_2,..,a_n$; where a^o represents the set of initial estimates $a_1^o,a_2^o,\ldots,a_n^o$ of these same parameters; where $y'(a^o)_{ij}$ is the first partial derivative of y_j with respect to a_i and evaluated at a^o; and where

$$\Delta a_i = a_i - a_i^o \tag{24}$$

is a "small" variation of the ith parameter relative to the estimated value a_i^o. Inserting this approximation into Equation 1, one than has an approximation for χ^2

$$\chi^2 \cong \sum_j \frac{\left(d_j - \sum_{i=1}^{n} \Delta a_i y'(a^o)_{ij}\right)^2}{\sigma_j^2} \tag{25}$$

where

$$d_j = \bar{y}_j - y(a^o)_j \tag{26}$$

is the residual error in the jth fitted point for the current estimates a^o. What we have accomplished is to approximate a non-linear function of the a_i parameters by a linear function of the new parameters Δa_i in the vicinity of the estimates a_i^o. One now proceeds

by treating the Δa_i as the fitting parameters. By requiring the first partial derivatives of χ^2 to be zero with respect to these new parameters, one again obtains a set of linear normal equations which can be solved for the increments Δa_i (simply replace $\overline{y}_j$ by d_j, F_{ij} by $y'(a^o)_{ij}$, and a_i by Δa_i in Equations 10 to 19). After solving for the Δa increments, one again computes new estimates a^o by adding the increments to the old a^o estimates. The process is then repeated until the fit converges (e.g., χ^2 is minimized when all Δa_i approach zero).

Linear approximation of the fitting function results in a parabolic approximation of χ^2 as shown in figure 10 for a one-dimensional case. The minimum of this approximation parabola is closer to the true minimum than is the original estimate. Generating a new approximation parabola at this improved estimation point results in a still closer approximation, etc. It is clear that such parabolic approximation is potentially quite poor when far from the minimum, but sufficiently close to the minimum any χ^2 surface is parabolic and the approximation is exact.

Equation 20 can still be employed for estimating the uncertainties in the computed parameters a_i (since a_i^o are treated as constants all of the uncertainty is in the Δa_i). However, the validity of this equation relies upon the premise that the "true" solution has been attained.

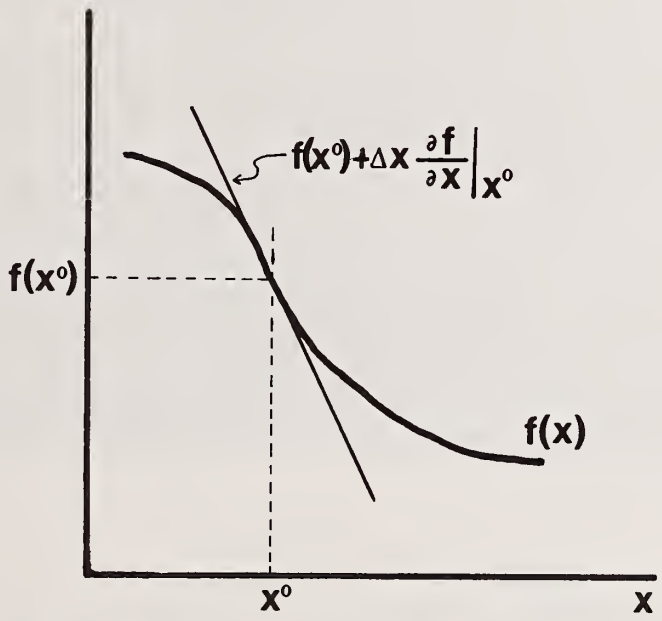

Figure 9. Linear approximation of an arbitrary function f(x) at the point x^o.

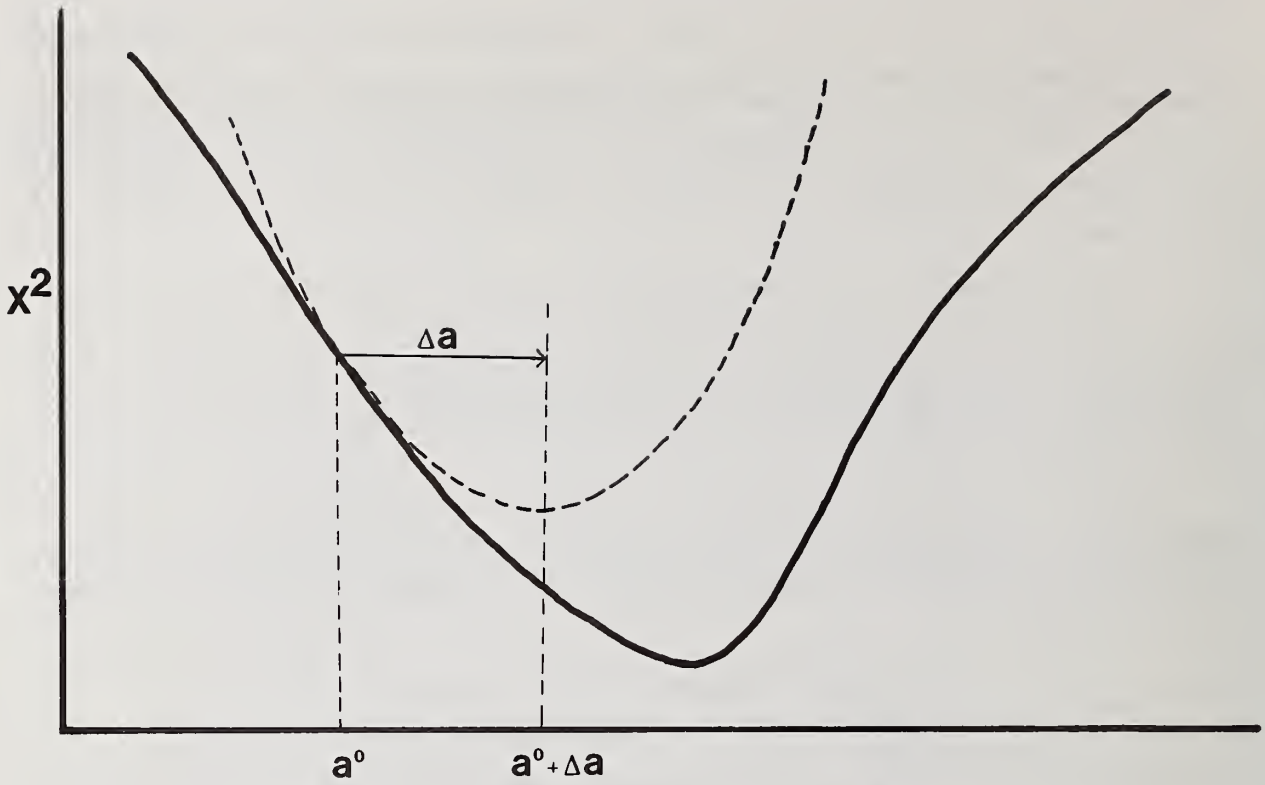

Figure 10. Parabolic approximation of the X^2 function at the point a^o.

Example of Linearized-Analytic Solution. To illustrate the application of the linear-expansion analytic solution method, we again consider the example of the two-Gaussian peak fit with six free parameters (the same problem as for the earlier grid-search example). For this problem, each Gaussian is linearized as follows:

$$\text{Gaussian}(A,C,S)_j \cong g_{0j} + \Delta A g_{1j} + \Delta C g_{2j} + \Delta S g_{3j} \tag{27}$$

where

$$g_{0j} = A^o \exp\left[\frac{-(C^o - x_j)^2}{2(S^o)^2}\right] \tag{28}$$

$$g_{1j} = \exp\left[\frac{-(C^o - x_j)^2}{2(S^o)^2}\right] \tag{29}$$

$$g_{2j} = -A^o \frac{(C^o - x_j)}{(S^o)^2} \exp\left[\frac{-(C^o - x_j)^2}{2(S^o)^2}\right] \tag{30}$$

$$g_{3j} = A^o \frac{(C^o - x_j)^2}{(S^o)^3} \exp\left[\frac{-(C^o - x_j)^2}{2(S^o)^2}\right] \tag{31}$$

The fitting was thus performed for the six linear parameters ΔA_1, ΔA_2, ΔC_1, ΔC_2, ΔS_1, ΔS_2 (alternate ways of dealing with the linear A parameters could also have been employed). Figure 11 illustrates the progress of the fit for the first five iterations: IT(0) (upper left frame) is the fit for the initial estimates (with the same starting parameters as for the grid-search fit); iterations 1 through 5 (IT(1) - IT(5)) then follow in a top-to-bottom sequence. The example converges to a final values of $\chi^2=1.8\times10^1$ on the 9th iteration.

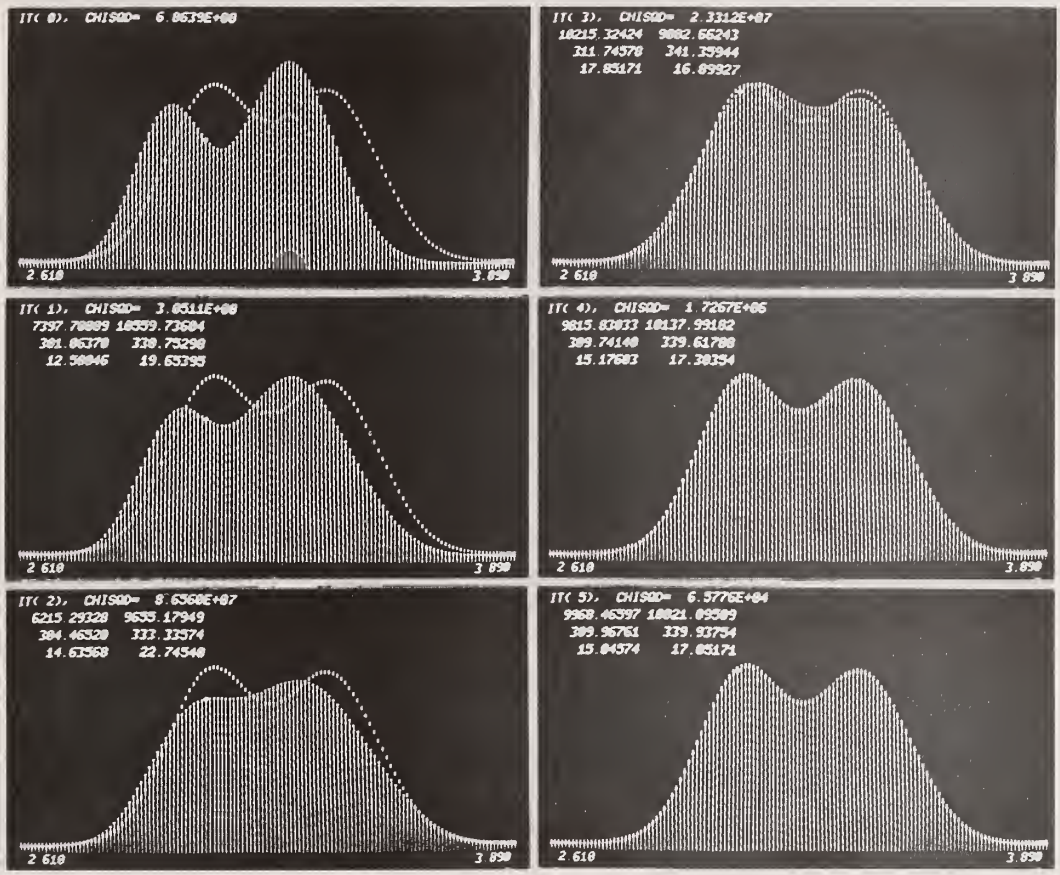

Figure 11. First six iterations of the linearized-analytic fit of the two-Gaussian example.

Failure of the Linearized-Analytic Solution Method (Damping). In view of the limited validity of the linear expansion used in this method, it is not surprising that the procedure encounters difficulty when the initial parameter estimates are far from the minimum. This is illustrated in figure 12 for a different example: the true solution in this case (dotted curve) is the same as for the earlier example (cf., figure 3) except the peak centers are now $C_1=310$, $C_2=315$; the starting estimates are as before (solid curve). Initially, $\chi^2=2.1\times10^9$ for the starting estimates, this decreases on the first iteration to 4.0×10^8 and then increases on the 3rd iteration to 5.6×10^8, to 9.7×10^8 on the 4th, and continues to increase on subsequent iterations! Instead of converging, the method has diverged. This behavior can be understood as a break-down of the linear approximation; the true χ^2 surface is so poorly approximated that the solution obtained from this approximation is farther from the true solution than was the original estimate. In short, the solution subsequent iteration (being even further from the minimum) overshoots by a greater amount.

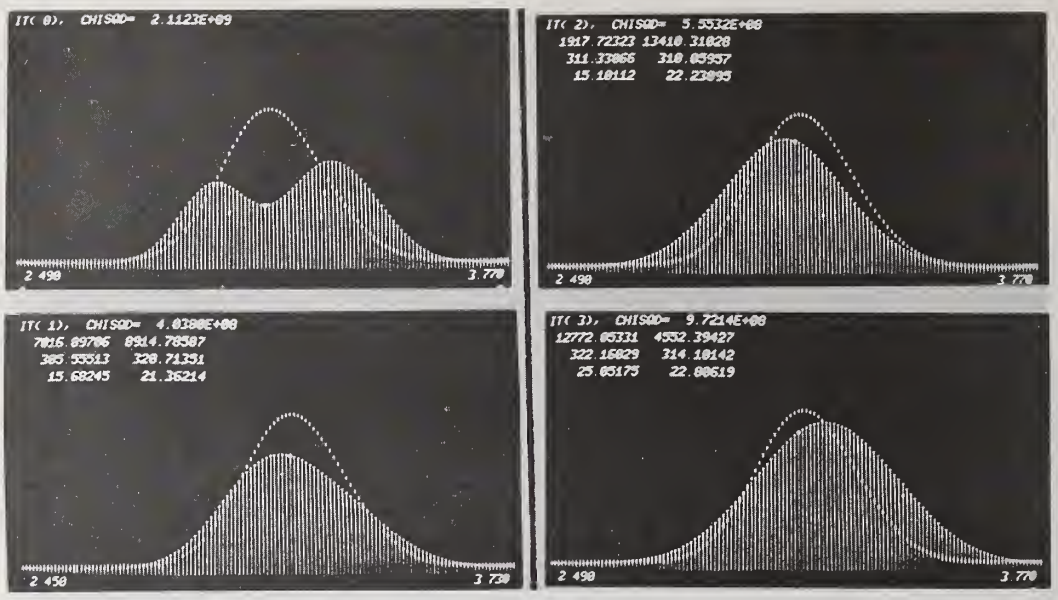

Figure 12. Example of divergent failure of the linearized-analytic method (no damping).

A simple way of dealing with this oscillatory behavior is to introduce "damping" into the procedure. The oscillations can be "damped" by changing the parameter estimates by a fraction Q (Q<1) of the computed Δa_i. Use of a Q factor of approximately 0.4 seems to be a safe choice for the majority of problems. To expedite the procedure, Q can be automatically increased by the program until Q~1 as convergence is approached. Figure 13 illustrates the solution of the above problem after damping has been incorporated in the program; the oscillations have been damped out and the fit will converge cleanly to the correct solution on the 10th iteration.

It should be clearly stated that the sort of divergence problems which can be encountered in the linearized-analytic method do not make the method unreliable in the sense of producing "wrong answers". When divergence is encountered, the problem is to obtain any solution at all since the program tends to either "wander" indefinitely or "blow-up" with attendant math overflow errors.

Comparison of the Algorithms. Four different solution method were programmed and applied to the solution of the six parameter two-Gaussian problem already discussed (see figure 3). The comparative performance data for these tests are summarized as follows:

Method	Rel. Time	Final χ^2	Iterations
Linearized Analytic	1	18	9
Accelerating Simplex	5	22	246
Grid-Search	10	62	55
Gradient-Search	10	365	67

The "Final χ^2" value refers to the value of χ^2 which was achieved when the program was stopped; these values depend on the precise formulation of the stopping criterion in each program and are thus somewhat arbitrary. The gradient-search method was stopped prematurely since it was minimizing χ^2 with excruciating slowness at this point; to obtain a χ^2 value as small as for the analytic method would surely have taken much longer than the factor of 10 indicated here!

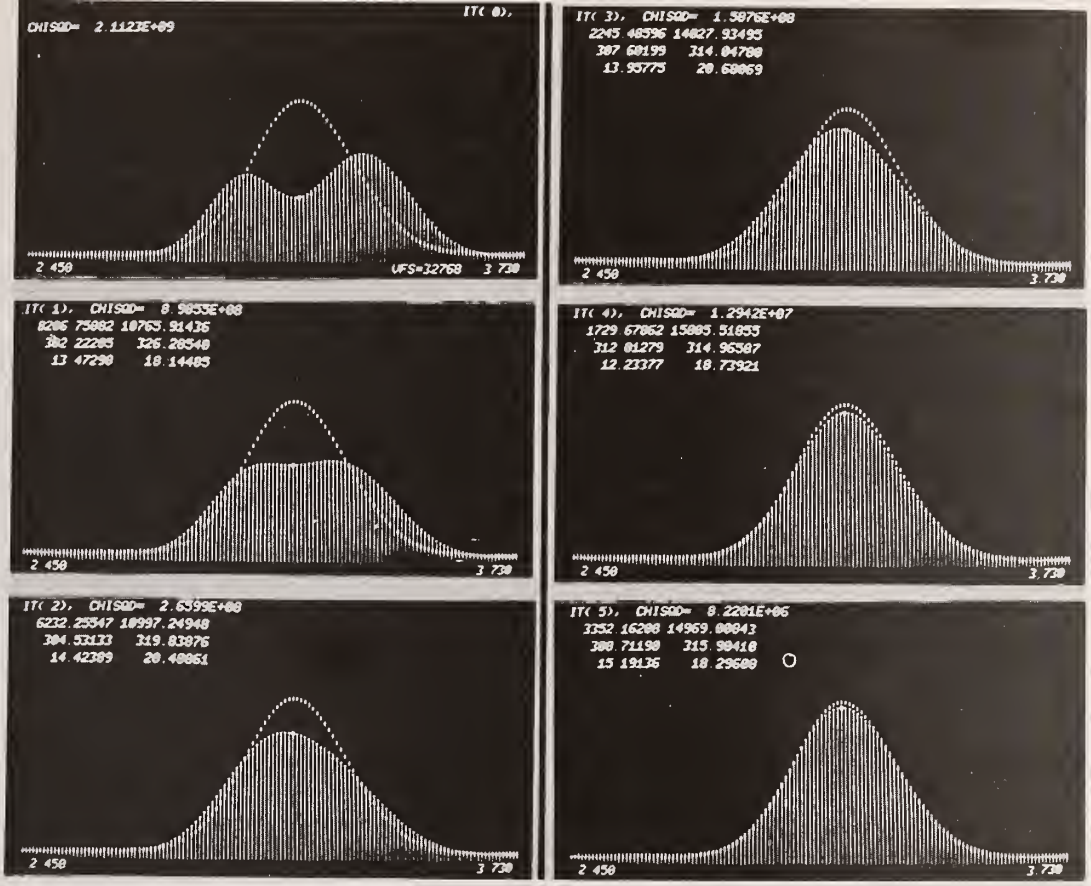

Figure 13. Successful solution of the prior example (c.f., figure 12) after the incorporation of damping.

"Relative Time" refers to the relative computation time for each program, arbitrarily normalized to the fastest method (linearized-analytic). All of the fitting programs were coded in the same higher-level language and run on the same computer. Actual computation times for a specific implementation will depend strongly on the programming language, the computation hardware used, and the details of program construction. The precise nature of the fitting problem, (number and type of parameters, quality of initial estimates, number of data points, stopping criterion, etc.) will influence both the absolute and relative speed of each method.

For most problems, the analytic solution method is the best choice in terms of performance. Not only does it converge faster, but it also provides estimation of the statistical uncertainties as a natural by-product of the computations.

A basic pattern-search procedure is probably the best choice for the user who is more interested in understanding curve-fitting technique than in absolute performance since the "moves" of such a method are more readily conceptualized. The grid-search procedure is varied. However, the simplex method is far more satisfactory in terms of performance.

Pattern-search methods are also a logical choice when optimizing is to be done via criteria other than minimization of χ^2 since these methods require only that some sort of "desirability" criteria be established.

The gradient-search method would seem to be a poor overall method. Not only is its convergence very sluggish in the region of the minimum, but its implementation is also fairly complex. One point in its favor is that it is quite good at approaching the minimum from afar (in the above comparison the initial rate of convergence of the gradient method was significantly faster than that of the simplex or the grid-search). For this reason a gradient method is sometimes employed for the first rough-approximation, followed by the linearized-analytic method for the final optimization.

2.4 Establishing the Validity of Fitted Results

It is an unfortunate fact that people tend to accept computed results uncritically ("If the number is printed to five decimal places, then the answer must be correct to five decimal places"). For this reason, the program designer should make every reasonable effort to provide the program user with relevant qualifying information.

It has already been noted the Equation 20 provides a useful estimate of statistical uncertainty when the solution is obtained via the analytic method. Obtaining uncertainties from the pattern and gradient-search methods is not so direct, but there do exist error estimation procedures for these methods also. Although statistical error estimates are just that, estimates which are not to be taken too literally, they do provide a useful indication of precision.

Another useful indicator which should be reported for any least-squares program is χ^2. For convenience, χ^2 is usually reported as "normalized chi-squared", that is divided by (N-n) where N is the number of data points fitted, and n is the number of free parameters. When normalized, $\chi^2 \sim 1$ indicates a "good" fit and $\chi^2 >> 1$ is indicative of a systematic error. χ^2 is not an ideal indicator since it is itself a statistical quantity which will vary from analysis to analysis. Moreover, a small χ^2 does not guarantee accurate results nor does a large χ^2 guarantee inaccurate results since the sensitivity of χ^2 to systematic error is directly related to the statistical precision of the data. This is because a systematic error of one percent in the measured content of a channel is not very significant when the statistical uncertainty is ±10 percent but is very signficant when the uncertainty is ±0.1 percent. As the statistics of a spectrum are improved (e.g., by longer counting times) small systematic errors in the data or inadequacies of the fitting function will be manifested in an increasing value of χ^2.

Of course, what a user would like is a fool-proof indicator of combined error (statistical and systematic), or at least a reliable way of knowing when the results are "bad". Unfortunately, there is no completely satisfactory way of doing this, and the program user must bear some of the burden for qualifying the results (see the concluding Summary).

3. Reliability of Non-Linear Least-Squares: An Investigation

The first section of this paper developed the concepts of curve-fitting and detailed specific methods of implementation. In this section, fundamental questions related to the reliability of the method are explored in the context of investigating a particular example.

Statement of the Problem

This investigation was motivated by a paper by Peter Statham in which he raised the question of whether non-linear peak-fitting programs can be trusted to give correct answers. As evidence, he cited a specific case in which non-linear fitting appears to fail spectacularly [6].

The illustration is as follows: A synthetic two-peak problem is constructed from Gaussian peaks of fixed widths (15 channels FWHM). The first peak has an amplitude of 5000 and is centered in channel 100, the second peak has an amplitude of 10000 and is centered in channel 104 (simulating EDS spectral peaks of 150 eV resolution, centered at 1.00 and 1.04 KeV for an assumed calibration of 10 eV/channel). Simulated counting statistics are applied and this synthetic "unknown" spectrum is then fitted with two Gaussian peaks of fixed width (150 eV) and unknown centers and amplitudes (4 free parameters).

Statham found that for one particular simulated spectrum the best fit was actually obtained for the (keV, amplitude) parameters: Peak 1, (1.012,9119); Peak 2, (1.050,5903) resulting in $\chi^2=0.925$. In comparison, the "true" solution parameters Peak 1, (1.000,5000); Peak 2, (1.040,10000) produce $\chi^2=1.173$. That is, a "false" solution is found for this case in which the amplitudes of Peak 1 and Peak 2 are almost exactly reversed!

It is well known that false minima can exist in non-linear least-squares fitting problems. Most commonly, however, false minima represent obviously absurd solutions, have larger χ^2 than the "true" minimum, and are encountered only when extremely poor starting estimates are employed (e.g., figure 14). This is clearly not the case here since the "false" solution is not only physically reasonable but has a lower χ^2 than the "true" solution. This is a most disturbing example since it raises the prospect of getting wildly wrong answers from a least-squares program and offers no apparent way to either prevent or sense such errors. The remainder of this paper describes an investigation of the important questions raised by this example.

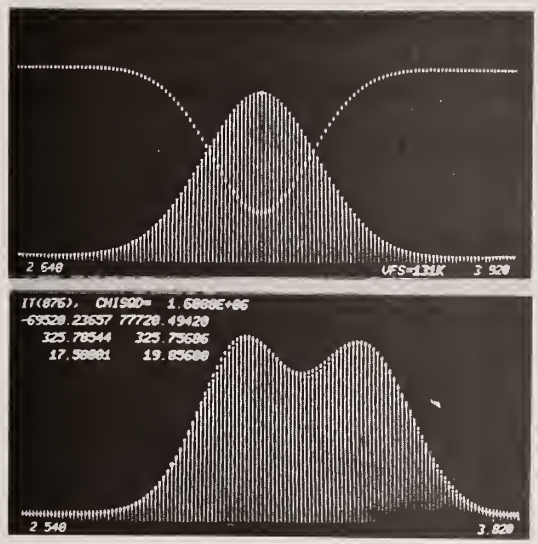

Figure 14. Illustration of an "abused" false solution of the two-Gaussian problem (c.f., figure 3) composed on one positive and one negative peak.

In figure 15, the upper left and upper right frames are the individual peaks for the "true" and "false" solutions respectively. Below, the composite solutions (dots) are overlayed on Statham's simulated spectrum data (bars). It is immediately clear that both the "true" and the "false" solutions are very good fits to the data. Although there are subtle differences in the shapes of the two solution curves, they are effectively obscured by statistical fluctuations in the data. There are several significant points to consider in this example:

1. The false solution has a smaller χ^2 in this instance simply because the statistical fluctuations in the data happen to favor this solution. This implies that the phenomenon is statistical in nature (rather than systematic) and should occur with a statistical probability distribution.

2. There is nothing particularly meaningful about the fact that the results are "reversed". If one peak amplitude is increased by 5000 then the other must naturally be decreased by 5000 to maintain the correct number of total counts in the spectrum. The important question is not why the amplitudes are reversed, but rather, whether such a large error is reasonable.

3. The choice of a relatively narrow fitting window (channels 90 through 116) may be a contributing factor since there is a substantial amount of information which is contained in the "skirts" of the Gaussians. Truncating the fitting region in this way reduces the amount of information available to the fitting routine. This reduces the precision of the analysis (i.e., increases σ for each of the computed parameters) and increases the probability of obtaining answers which deviate significantly from the "true" solution.

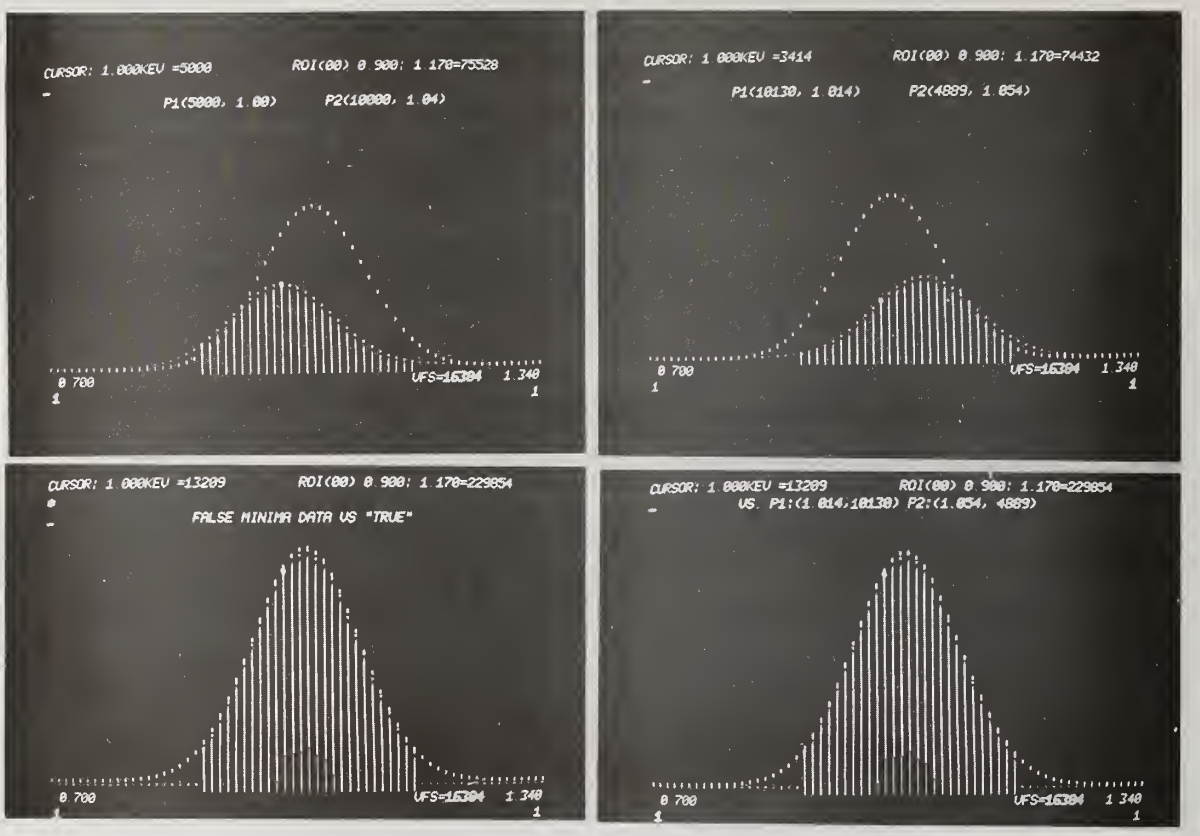

Figure 15. Illustration of the "true" and "reversed" solutions of Statham's example case (left and right): Upper — the individual solution peaks. Lower — comparison of the composite solutions (dots) with the simulated data (bars).

Taken together, these observations suggest that if the fitting problem were reformulated so as to include the skirts of the Gaussians, the precision of the determination would improve and the probability of obtaining the "false" solution would diminish (to "zero", one might hope). But there is a practical problem in broadening the fitting region; as one gets far enough out into the skirts, the Gaussian function approaches zero and the statistical distribution of the channel contents is governed by the Binomial distribution. Binomial statistics are not only difficult to simulate, they also create unique problems in weighting the least-squares fit properly. (It was for precisely this reason that Statham restricted the fitting region as he did.) The approach used to circumvent this difficulty was to change the definition of the problem somewhat and to superimpose the Gaussian peaks upon a constant "background" of 100 counts per channel. The fitting region was then extended to include channels 70 to 135 (roughly the portion of the spectrum depicted in figure 15).

Test 1

The test procedure was to generate a true spectrum using the following parameters:

Peak 1: amplitude = 5000, centroid = 1.00 keV, width = 150 eV

Peak 2: amplitude =10000, centroid = 1.04 keV, width = 150 eV

Background = 100 (each channel)

(calibration: 10 eV/channel)

(Note that the above amplitudes correspond to peak areas of approximately 80,000 and 160,000 counts respectively.)

This true spectrum was perturbed with random counting statistics (simulated via a commonly used computer algorithm) and the resulting "unknown" spectrum was then fitted using the linearized-analytic method with five free parameters (2 peak amplitudes, 2 peak centers, 1 background amplitude). In order to give the "reversed amplitude" solution plenty of opportunity to occur, the starting estimates for the peak parameters were deliberately chosen to be in the near vicinity of this false solution. This test was run repeatedly (with different statistics each time) to simulate a series of independent physical measurements. Figure 16 depicts the distribution of the Peak 1 amplitude for a series of 1604 such runs (the Peak 2 distribution is equivalent). The horizontal axis was divided into bins of 0.2 σ width and each "+" represents an event which was counted in that bin. The horizontal axis is labeled as follows: Bottom line – deviation from "true" in σ units; Center Line – number of results in each bin; Top Line – cumulative percentage of results which deviated to this point from "true". The solid bar below the plot indicates ±1σ. The open circles depict an ideal Gaussian distribution.

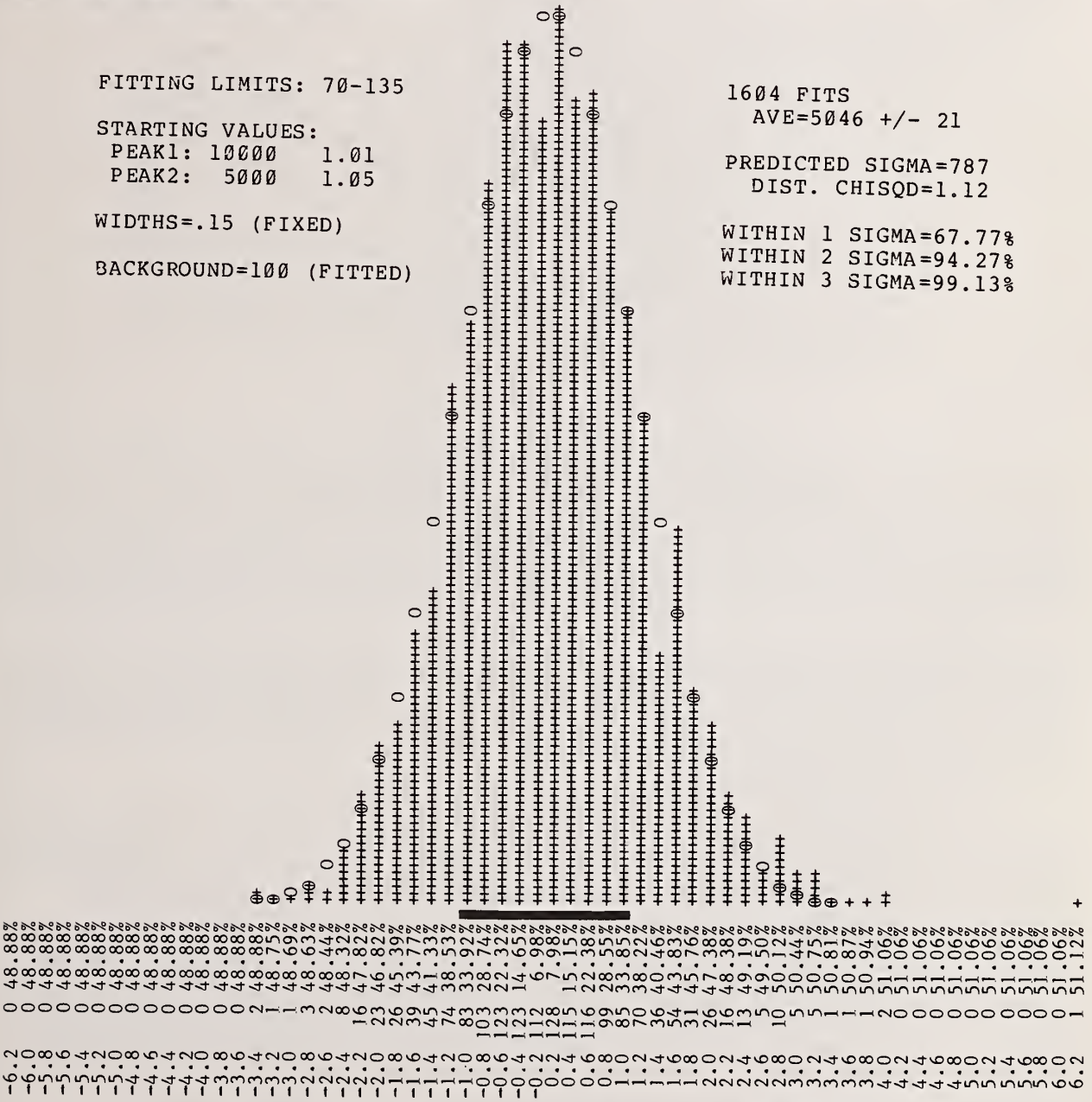

Figure 16. Distribution of 1604 solutions from Test 1.

"AVE=5046±21" is the observed average and observed standard deviation of the 1604 fitted values for the Peak 1 amplitude. "PREDICTED SIGMA=787" is the theoretical uncertainty (σ) in the Peak 1 amplitude obtained via Equation 20 by fitting the "true" spectrum (without simulated statistics) as if it were an unknown. "DIST. CHISQD" is a measure of how well the observed values of the fitted amplitudes correspond to the expected result of 5000±σ (σ=787).

$$\text{DIST. CHISQD} = \sum_{k=1}^{m} \frac{(A_k - 5000)^2}{(m-1)\sigma^2} \qquad (32)$$

where the $A_1, A_2, \ldots A_m$ are the 1604 independent measurements. Also tabulated on figure 16 are the percentage of results which fell within ±1, ±2, and ±3σ (ideally 68.2%, 95.4%, and 99.7%).

> (The reader may have noted that there is a single result which appears on the extreme right of the plot (+6.5σ). This point corresponds to a reversed-amplitude fit, nearly identical to the one reported by Statham. What is not apparent is the fact that this particular result occurred on the 26th trial! This incredible coincidence stimulated a great deal of effort in attempting to understand what was unique about <u>this</u> particular solution. It was only after hundreds of additional runs had been performed that it began to seem plausible that this false solution might only be a statistical anomaly. Eventually it was concluded that although the theoretical probability of a deviation of this magnitude is less than 2×10^{-7} and although the odds are strongly against encountering the error in <u>only</u> 1600 runs, it remains a valid statistical possibility. Furthermore, we are here working with only an approximation to ideal counting statistics.)

<u>Test 2</u>

Figure 17 is a plot of the distribution obtained using Statham's original fitting method; channels 90-116 for the fitting region, no background, and four free parameters (2 peak amplitudes, 2 peak centers). In this case, the ideal standard deviation of the Peak 1 amplitude is σ=1486 (nearly twice that of Test 1). A "reversed" solution (Peak 1 amplitude ~10000) corresponds to an error of approximately 3.4σ and we note that a number of fits did produce results in this vicinity. In this case, the plot contains 1198 results. Not included in the plot were four fits which were non-convergent (N.C.) and failed to produce any solution.

It seems clear that the main features of figures 16 and 17 are consistent with the predicted statistical distribution of errors. Although large deviations, such as the "reversed solution" case are improbable, they <u>can</u> occur and must be accepted as a normal hazard imposed by the random statistics of the physical process. However, a careful formulation will make maximum use of the available data and thereby minimize the probability of obtaining such large absolute errors.

One of the hazards of a detailed investigation is that it tends to create new questions. Specifically, one might ask, why do both figures 16 and 17 tend to show more large deviations on the positive than the negative side? Further, why is the average fitted result signficantly greater than 5000 in both cases (5046±21 and 5161±41 respectively)?

One explanation for this skewing is that the initial estimates used to start the fit were chosen on this side of the true result. We can visualize the progress of the iterations as moving along the floor of a valley which gently slopes to the minimum. If one introduces statistical perturbations in the data, the floor of this valley will be distorted and the gentle natural slope may be locally obscurred. If one adds to this picture the presence of tiny "ripples" in the computed χ^2 values due to computational round-off, etc. one can then imagine that the iteration procedure might well stumble into a local "pothole"

rather than proceeding to the "true" minimum. If this picture is correct, then the probability of getting a result which deviates to a particular side of the true solution is enhanced by starting the iteration from that side.

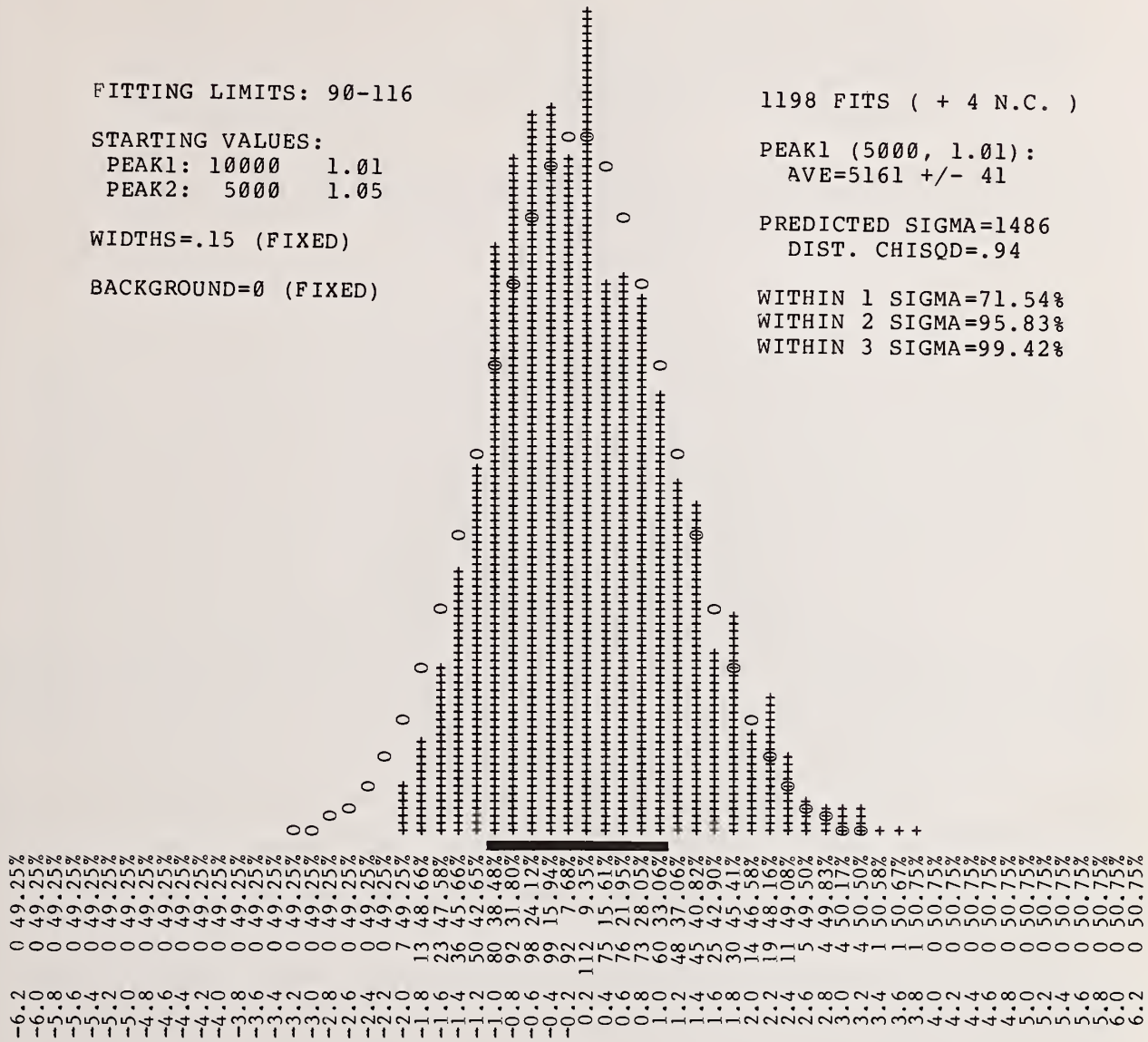

Figure 17. Distribution of 1198 solutions from Test 2.

Test 3

Test 3 was constructed in order to check this starting-point hypothesis. The procedure was identical to Test 1 except the starting estimates were chosen to be the "true" solution parameters. Figure 18 shows the resulting distribution for 711 trials. The computed average of the distribution (5032±29) is now within approximately one standard deviation of the true answer (compared to approximately two standard deviations for Test 1), tending to support the intuitive notion that the choice of starting estimates can be a factor in determining precisely where the solution converges.

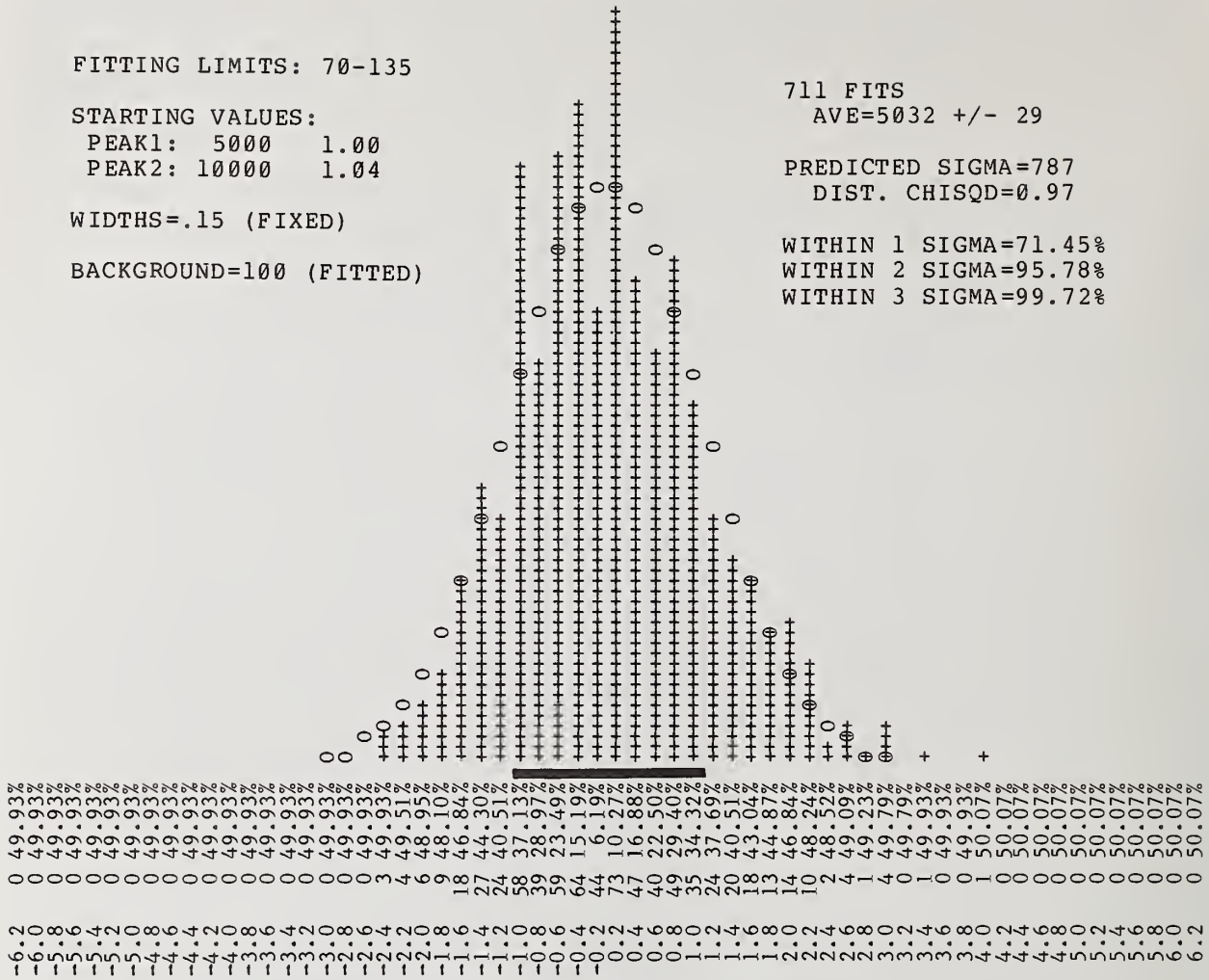

Figure 18. Distribution of 711 solutions from Test 3.

However, the distribution of figure 18 still seems somewhat skewed relative to a pure Gaussian distribution. Note in particular that there seems to be more points than expected above $+2\sigma$ and correspondingly less than expected below -2σ, and in turn, there seems to be more results within -1 than within $+1\sigma$ of the true. One explanation for this asymmetry is simply that the distribution is really Poisson, rather than Gaussian. (This seems to be borne out by figure 17 which has a decidedly Poisson-like distribution).

Interpretation of Uncertainty Estimates

In preparing distributions of fitted results such as figures 16, 17, and 18, one is confronted with a subtlety of interpretation which has to do with the actual meaning of the uncertainty estimates computed according to Equation 7. Consider, for example, the Peak 1 amplitude computed for the "anomalous" point in figure 16: 10135±445. A first inclination is to consider the deviation to be $(10135\pm5000)/445=11.5\sigma$! However, it so happens that large positive errors in Peak 1 area are always accompanied by smaller than normal uncertainty estimates and vice versa. This is consistent with the fact that all of the measurements are drawn from the same parent population and must all have the same uncertainty (since σ is a property of the distribution, not the individual measurement). From fundamental premises, the proper interpretation of a statement of the form "$X\pm\sigma_X$" is as follows: "Based upon available information, X is the best estimate of the "true" value. If X is the true value, then the distribution of possible results has standard deviation σ_X".

This conclusion is not confined to the interpretation of curve-fitted results; it applies in ordinary counting statistics as well. For example, assume that the "true" number of counts in a measurement is T, but that because of a statistical fluctuation, one obtains R=(T+ΔT) as a measured count. The true value of the standard deviation of the measurement is still given by σ^2=T, not σ^2=R as one would infer on the basis of one measurement. For a large relative value of ΔT this distinction is important.

This subtlety, though typically ignored, can potentially be important to the analyst. It is an additional reason to distrust a result based upon one measurement since, if that result should happen to be a statistical deviant, then its associated uncertainty estimate is also invalid.

Factors Affecting Precision

An interesting question to consider is precisely how the uncertainties of the fitted results are affected by specific conditions imposed upon the problem. Table 1 tabulates the computed uncertainty (σ) which would be obtained in fitting Peak 1, for various ways of parameterizing the problem, and for several separations of the peaks. The "unknown" spectrum was always generated with the first peak fixed at 1.00 keV with amplitude 5000, the second peak amplitude was always 10000, and both peaks had widths of 150 eV (calibration is again 10 eV/channel). A fixed background of 100 counts/channel was used, and no statistical perturbations were applied to the spectrum. This "unknown" spectrum was then fitted over a fixed broad range (channels 70 to 171) for 13 different positions of Peak 2 and nine different combinations of free parameters. The letters A, C, and S are used respectively to designate the amplitude, center, and width parameters for each peak. When circled, it means that this is a free parameter in the fit; when the parameters of both peaks are circled as one, it means that both were fitted jointly (as a single parameter). Uncircled parameters were held fixed at their "true" values. The "background" parameter was fitted in all cases.

Table 1. Uncertainty in Peak 1 area (5000) vs. fit method and Peak 2 position.

PEAK2 CENTER	(a) PEAK1: Ⓐ C S PEAK2: A C S	(b) PEAK1: (A) C S PEAK2: (A) C S	(c) PEAK1: Ⓐ C S PEAK2: Ⓐ C S	(d) PEAK1: Ⓐ (C) S PEAK2: Ⓐ (C) S	(e) PEAK1: Ⓐ C (S) PEAK2: Ⓐ C (S)	(f) PEAK1: ⒶⒸ S PEAK2: ⒶⒸ S	(g) PEAK1: Ⓐ (C (S) PEAK2: Ⓐ (C (S)	(h) PEAK1: ⒶⒸ (S) PEAK2: ⒶⒸ (S)	(i) PEAK1: ⒶⒸⓈ PEAK2: ⒶⒸⓈ
1.010	30.91	10.36	201.98	5884.94	202.49	47087.47	69957.66	*****.**	*****.**
1.020	30.47	10.36	101.97	1466.42	102.99	5996.48	8927.70	24243.80	*****.**
1.030	29.79	10.36	69.06	647.83	70.59	1812.37	2675.59	5085.41	*****.**
1.040	28.94	10.37	52.91	361.19	54.94	785.00	1147.28	1743.19	37149.46
1.050	28.00	10.37	43.45	228.49	45.98	414.77	599.64	785.22	12304.88
1.060	27.02	10.37	37.32	156.59	40.35	248.77	355.47	420.91	4994.08
1.080	25.16	10.39	30.01	85.84	33.96	114.00	158.63	167.75	1198.21
1.100	23.56	10.40	25.94	54.25	30.54	64.51	86.83	87.82	389.18
1.125	21.98	10.42	22.98	35.58	27.64	38.86	49.79	49.79	121.95
1.150	20.81	10.44	21.23	26.86	25.23	27.94	34.12	34.18	47.78
1.175	19.98	10.46	20.15	22.62	23.32	22.97	26.92	27.00	27.67
1.200	19.40	10.49	19.46	20.52	21.97	20.62	23.43	23.48	23.93
1.300	18.54	10.63	18.54	18.56	19.88	18.56	19.90	19.91	23.04

The meaning of "jointly fitted" parameters requires some elaboration:

(A) Jointly fitted amplitudes were constrained to maintain a constant proportionality (1:2 in this case). This can be a worthwhile strategy to use when fitting x-ray peak multiplets (e.g., K-alpha/beta pairs).

(C) When fitted jointly, the peak centers were constrained to vary with constant separation. This would be appropriate when peak separations were known accurately but there is uncertainty as to the "zero" of the energy scale.

(S) When fitted jointly, the widths were maintained at a constant ratio (1:1 in this case). This might be useful if the spectrometer resolution was uncertain.

One factor which is immediately obvious from this table is that the greater the number of free parameters the larger the uncertainty tends to be. This effect is especially pronounced for small separations and tends to become less important for larger peak separations.

As the peak separation increases, the uncertainty of Peak 1 area typically diminishes asymptotically (approaching the theoretical limit of $\sigma \sim 17.6$ in this case).

The special case (column b) where the amplitudes of the peaks are fitted jointly has its minimum uncertainty when the peaks are exactly overlapped and gets worse as the peaks are separated. This is logical because the two peaks are being treated as one structure; the best precision is achieved when the counts are localized in the fewest number of channels. The uncertainty of the joint-amplitude fit is always less than for any other case since the counts from both peaks contribute to its precision.

The ability to analyze a peak in the presence of another nearby peak will depend strongly upon how much prior knowledge can be brought to bear on the problem. For example, it is obvious that if every parameter except the unknown peak's amplitude is known (column a), precise analysis is possible for a separation of as little as 10 eV (1 channel). At the other extreme, if all six peak parameters are unknown (column i), one would need to have a separation of more than 150 eV to attain comparable precision. Precision is a measure of how well-defined the χ^2 minimum is. Large uncertainties therefore indicate shallow ill-defined minima and convergence problems can be expected.

Induced False-Minima

From Table 1 one notes that for Peak 2 located at 1.04 keV, fitting with constrained peak separation (column d) should result in a σ for Peak 1 of less than half that for the case where the peaks are fitted independently (column f). Assuming that the same factor-of-two relationship roughly holds for a narrower fitting region also (it does), then the magnitude of σ in Test 2 would be reduced by about half if the peak centers were constrained to a fixed separation in that fit. But Statham also reported observing a reversed-amplitude solution when fitting with constrained peak separations [6]. Statistically, this is quite improbable and it seems suprising that such a solution was observed.

However, if one repeats Test 2 for the case of constrained peak separation (3 free parameters) one finds that about half of the fits converge to the false "reversed" solution and about half converge to the "true"! (When Test 1 was repeated with the same constraint on peak separations, the "reversed" solution was not seen in a series of 130 trials and the observed distribution of fitted Peak 1 values was completely consistent with the σ predicted by Table 1.) Clearly, some systematic property of the truncated fitting region causes the constrained fit to consistently locate a false minimum.

In order to investigate this problem further, a simple computer program was constructed to plot contour maps of χ^2 surfaces for various conditions of interest. Figures 19 and 20 are such contour plots. They were obtained by fitting to the same statistics-less spectrum as was used as the basis of Tests 1, 2, and 3. In this case the Peak 1 and Peak 2 centers of the solution function were varied in fixed step sizes of 1 eV on a 31x31 grid; the Peak 1 and Peak 2 amplitudes were then optimized to give the best fit for each grid point, and the resulting value of χ^2 was tabulated. The program then interpolated between these

31x31 points to obtain contours of constant χ^2. The contour levels were selected on an arbitrary power-of-two scale so that each contour line represents a value of χ^2 which is two times larger/smaller than its neighbor. The minimum point is shown as a small circle. Innermost contour lines have been left out of the plot since they could not be resolved at this scale. (It must be noted that the "scalloped" appearance of the innermost contour lines is due to the crude linear interpolation technique used to generate these plots – the true χ^2 contours are assuredly not so jagged!)

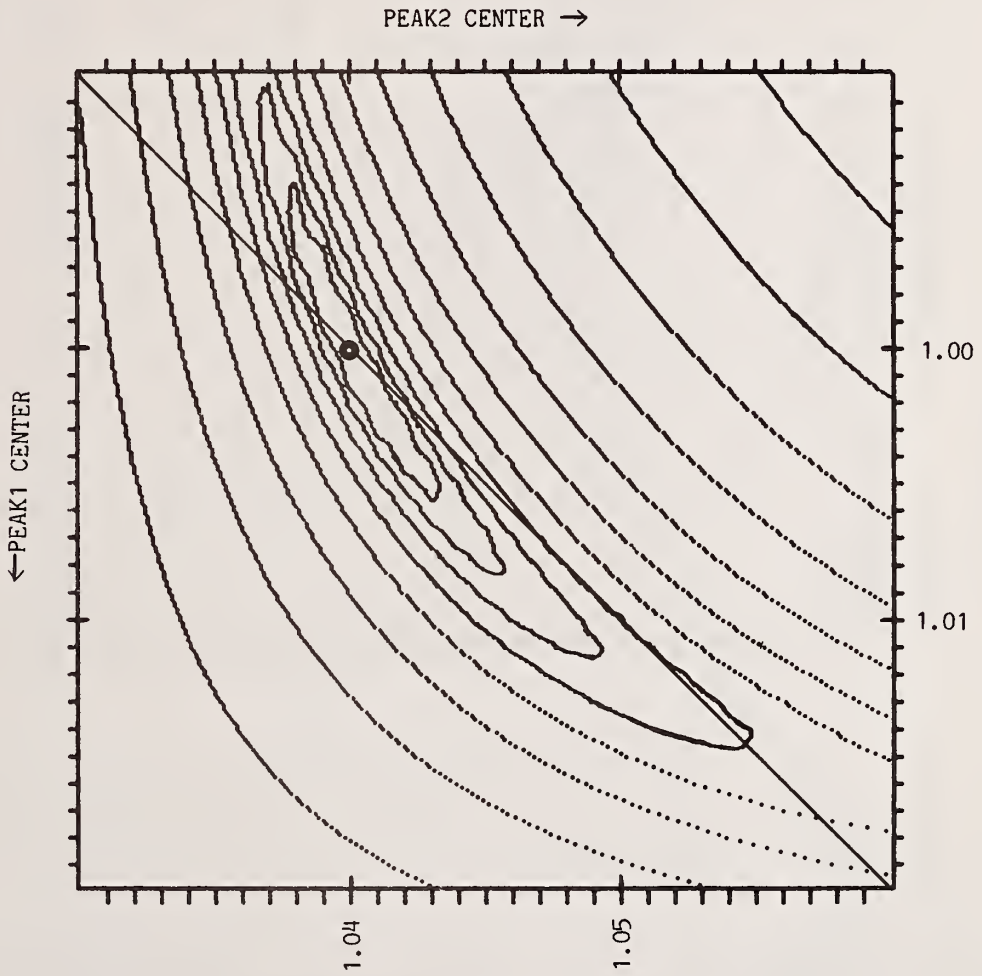

Figure 19. Contour plot of χ^2 surface obtained using a restricted fitting region.

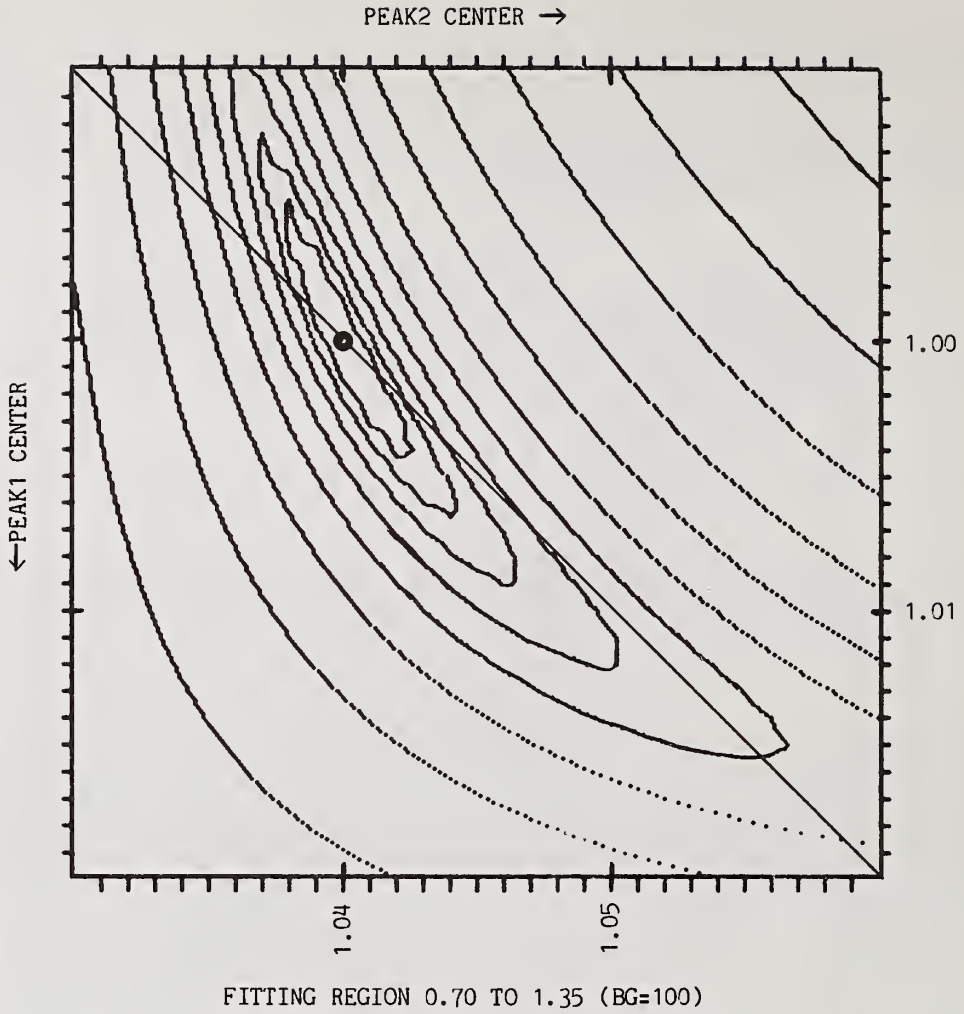

Figure 20. Contour plot of χ^2 surface obtained with an extended fitting region.

Figure 19 employs the truncated fitting region used in Test 2 and Figure 20 employs the broad fitting region used in Tests 1 and 3. If one visuallizes the solid surfaces with these contours one gets a picture of the minima located in the bottom of deep curving ravines. If one should initiate a least-squares fit with starting estimates of 1.02 and 1.06 respectively for the peak centers (lower-right-hand corner) one can imagine the solutions moving down these long curving valleys to the minimum at 1.00, 1.04. Now imagine the effect of constraining the peak separations to be fixed at 0.04 keV. The solution must now move along the diagonal line drawn from the lower-right to the upper-left corner of each plot. If one studies figure 19 carefully it is noted that this line intersects one of the contours more than once. This means that along this path χ^2 first decreases, then increases, and again decreases on its way to the true minimum. Careful inspection of figure 20 will show that the same diagonal path intersects each contour only <u>once</u> as it moves to the minimum.

The meaning of this difference is shown clearly in figure 21. Here the value of χ^2 is plotted as a function of the combined Peak 1/Peak 2 center position (equivalent to taking a vertical cross section of the χ^2 surface along the diagonal line of figures 19 and 20). One sees that for the truncated fitting region (solid line) the value of χ^2 shows a pronounced local minimum in the vicinity of 1.014/1.054. For the broader fitting region (dotted line) there is indication of an inflection in this region, but no minimum.

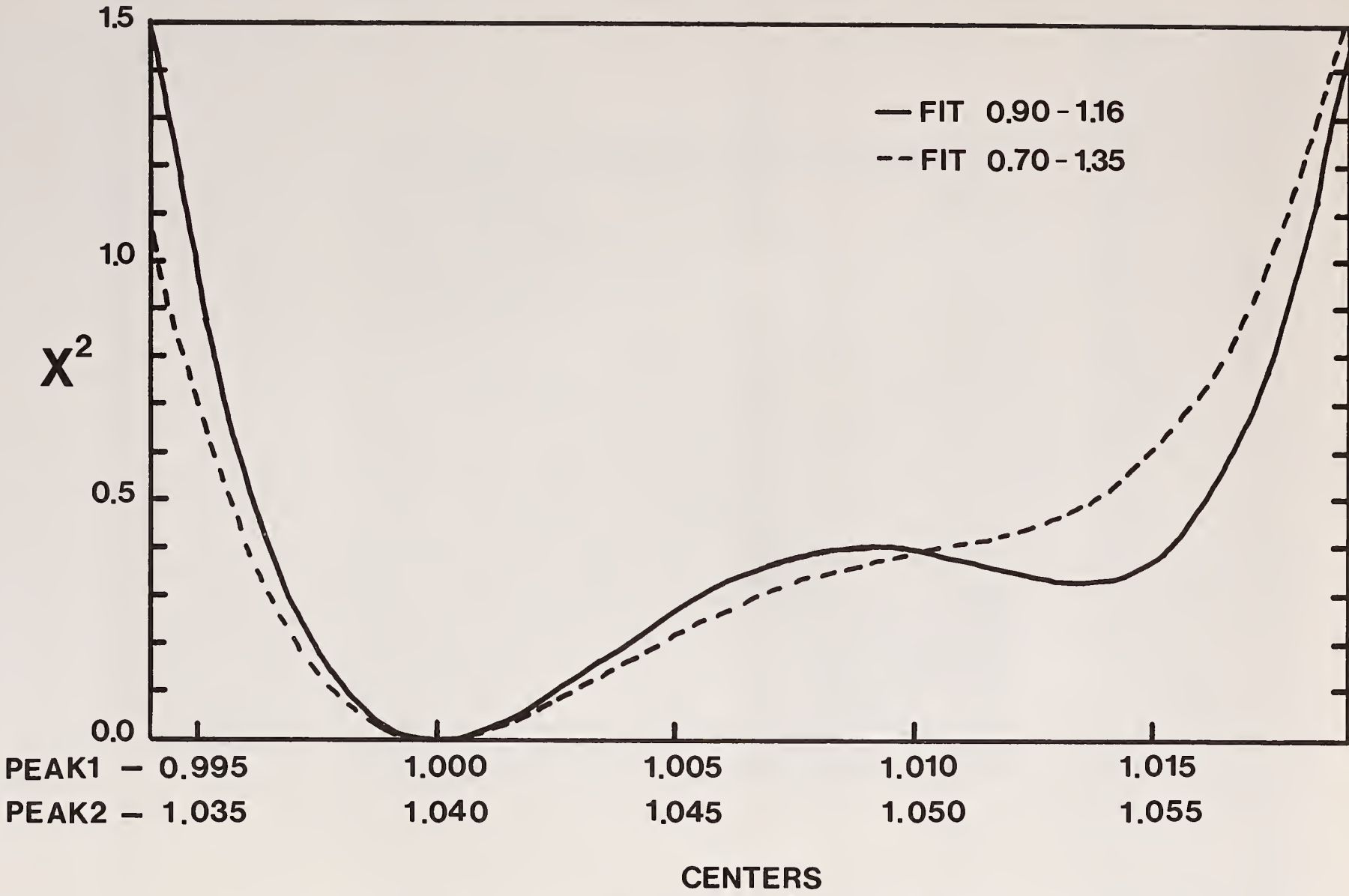

Figure 21. Plot of χ^2 along the line of fixed peak-separation constraint for two choices of fitting region.

These plots clearly indicate why a false solution is consistently obtained when attempting to fit Statham's test case with constrained peak separation. If the initial starting estimate for the joint peak position is too large, there is a very high probability of locating the "local" minimum in the vicinity of 1.014/1.054 rather than the "true" minimum at 1.000/1.040. The influence of statistics will be to further distort the χ^2 surface and it can even happen that χ^2 in the vicinity of 1.014/1.054 is smaller than in the vicinity of 1.000/1.040.

Figure 22 is a contour plot similar to figures 19 and 20. In this case the true peak centers are separated by 100 eV (10 channels) and the change in the shape of the contours is dramatic. The contours are now effectively elliptical. This is a classic example of a "well-behaved" χ^2 surface.

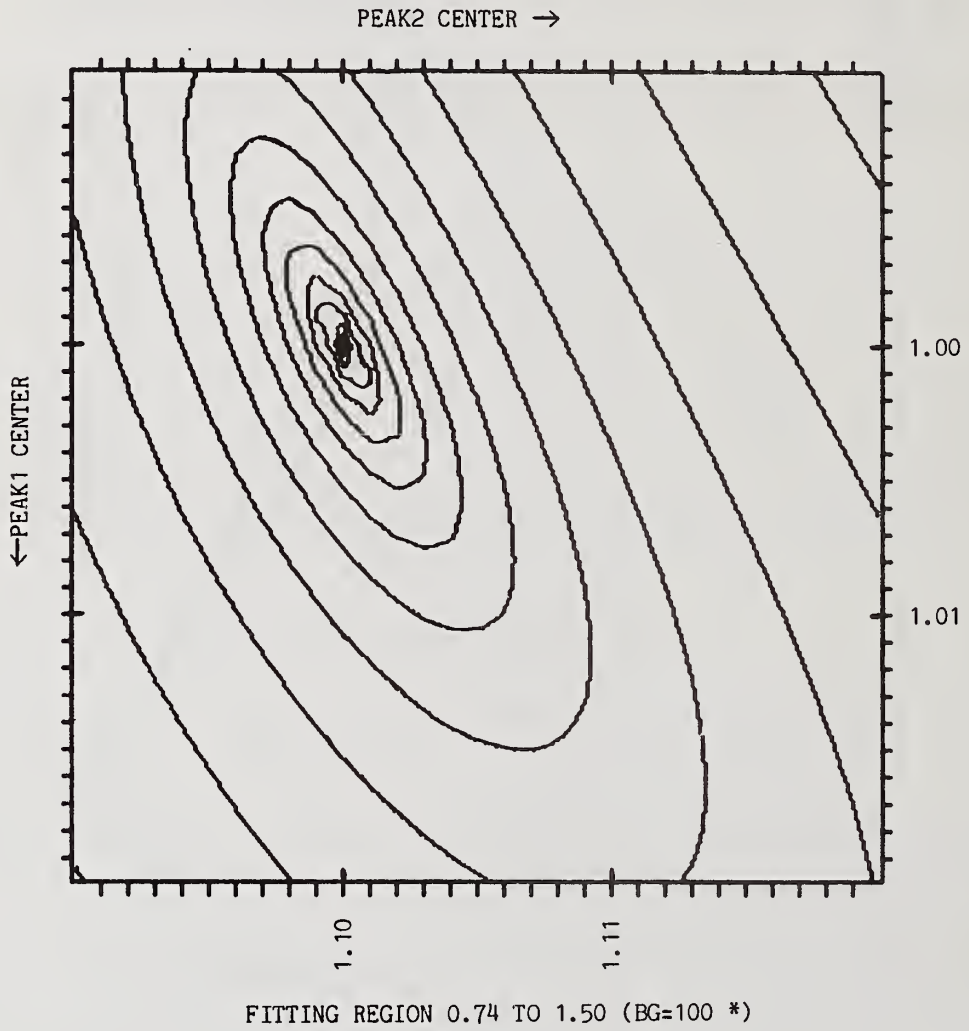

Figure 22. Contour plot of χ^2 surface obtained when peaks are separated by 100 eV.

Clearly, as one brings the peak centers closer together, the χ^2 surface gets increasingly "wild". Figures 23 and 24 illustrate part of the reason for this. These plots are merely larger views of the χ^2 surfaces depicted in figures 19 and 20 (the upper right hand corners of these plots correspond to the same portion of the surfaces depicted in 19 and 20). These plots clearly demonstrate that any two-peak problem has two valid minimum points since one can simply switch the roles of the two peaks to obtain an indentical fit. The broken diagonal line on these plots is a "singularity" line along which both peaks have identical centers; the roles of Peak 1 and Peak 2 reverse as one crosses this line. As the peak separations decrease, the minima must move closer to this line and the contours are increasingly distorted. When the fitting region is artificially restricted, this seems to exaggerate the contour distortions and increasingly warp the minima valleys.

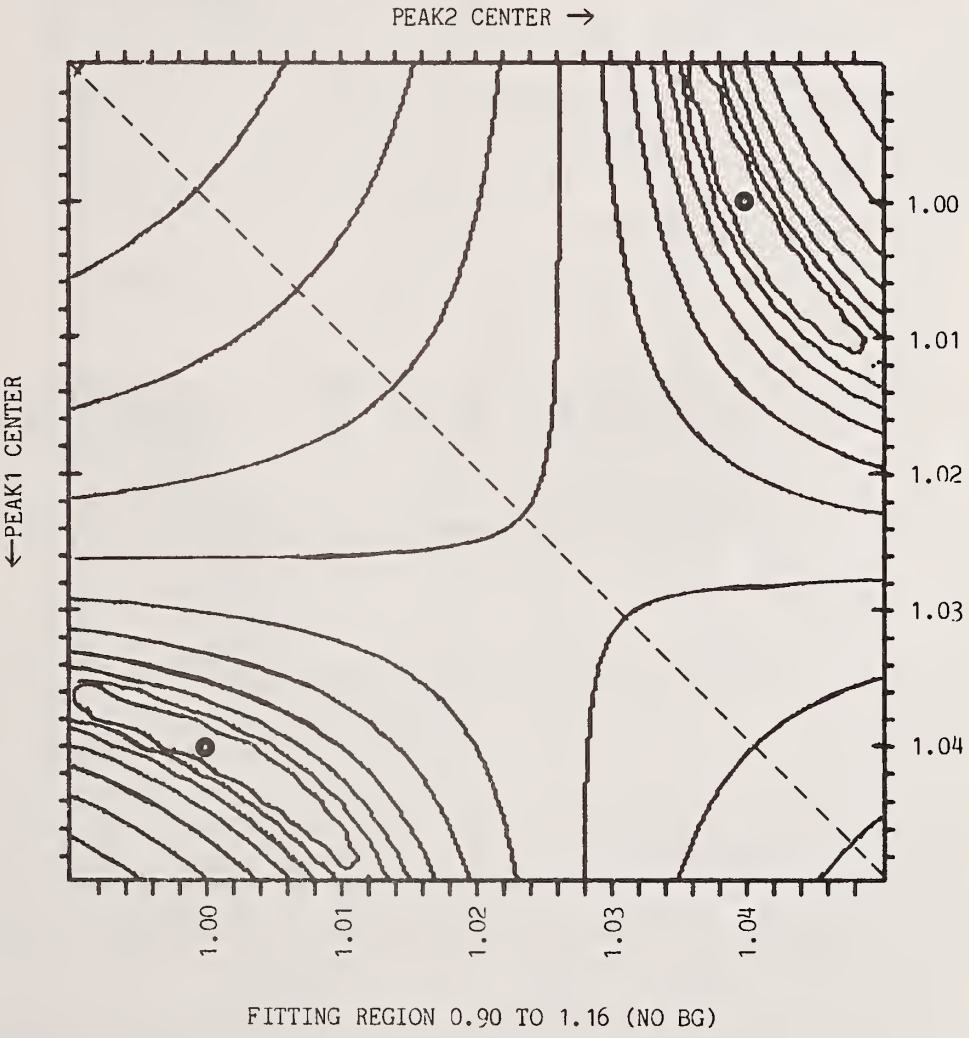

Figure 23. Expanded view of χ^2 surface for the narrow fitting region.

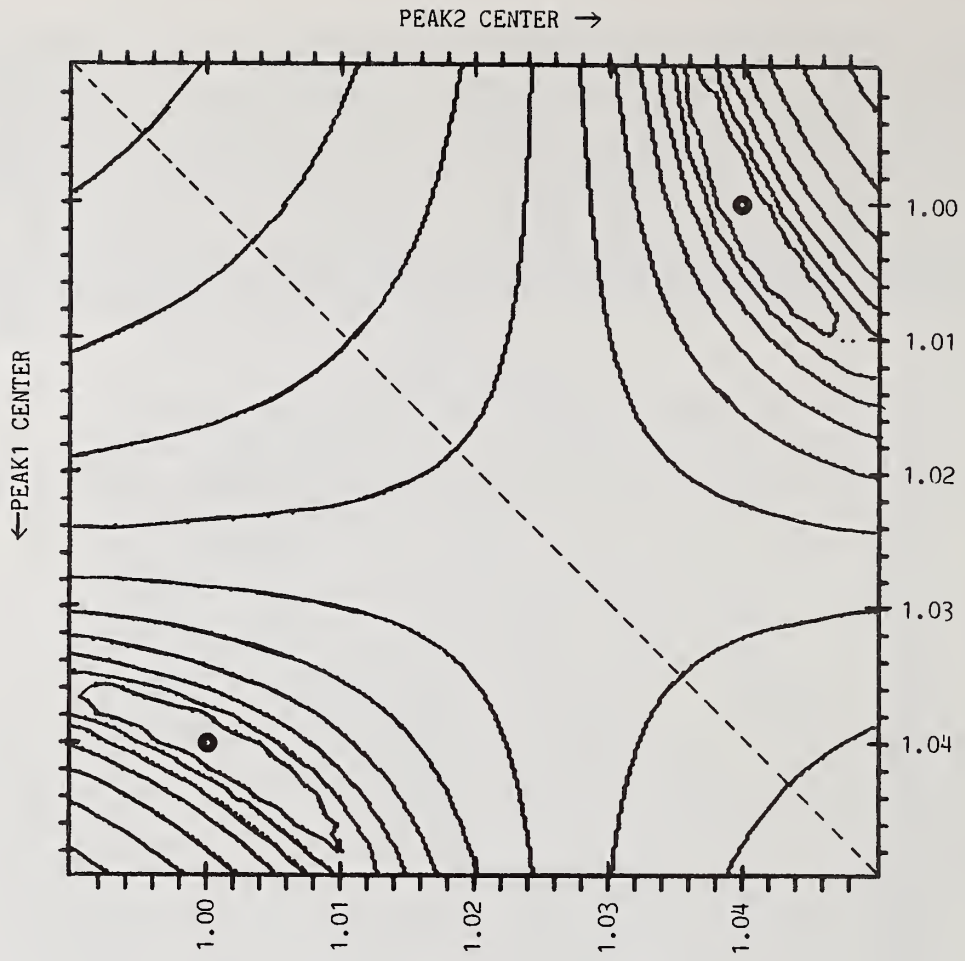

Figure 24. Expanded view of χ^2 surface for the extended fitting region.

Figure 25 compares the contour maps for four different choices of the fitting region. The top two plots of this figure are identical to figures 20 and 19. The lower plot is restricted strongly on the low-energy side of the peaks but generous on the high-energy side; the lower right plot is restricted strongly on both the low and high-energy sides of the fitting region. Again, it can be seen that the effect of truncating the fitting region is to stretch out and distort the valleys. As the valleys are elongated, the slope of the bottom towards the minimum is reduced, and as a consequence, the precision of the fitted parameters worsens and the probability of local statistical minima increases. This exaggerated curvature also creates false minima when the peak-separation constraint is imposed.

In summary then, one must recognize that there are a number of factors which are relevant to the successful solution of a least-squares problem. These include the uniqueness of potential solutions, the quantity and quality of available statistical information, the presence of constraints, the quality of initial estimates, etc. When the overall problem is basically well-determined (e.g., well separated peaks, good statistics, few free parameters, etc.) the solutions tend to be "robust" and it is possible to take liberties with some factors (e.g., poor starting estimates). However, when a problem is basically ill-defined, the solutions are quite sensitive to minor sources of bias and careful formulation is imperative.

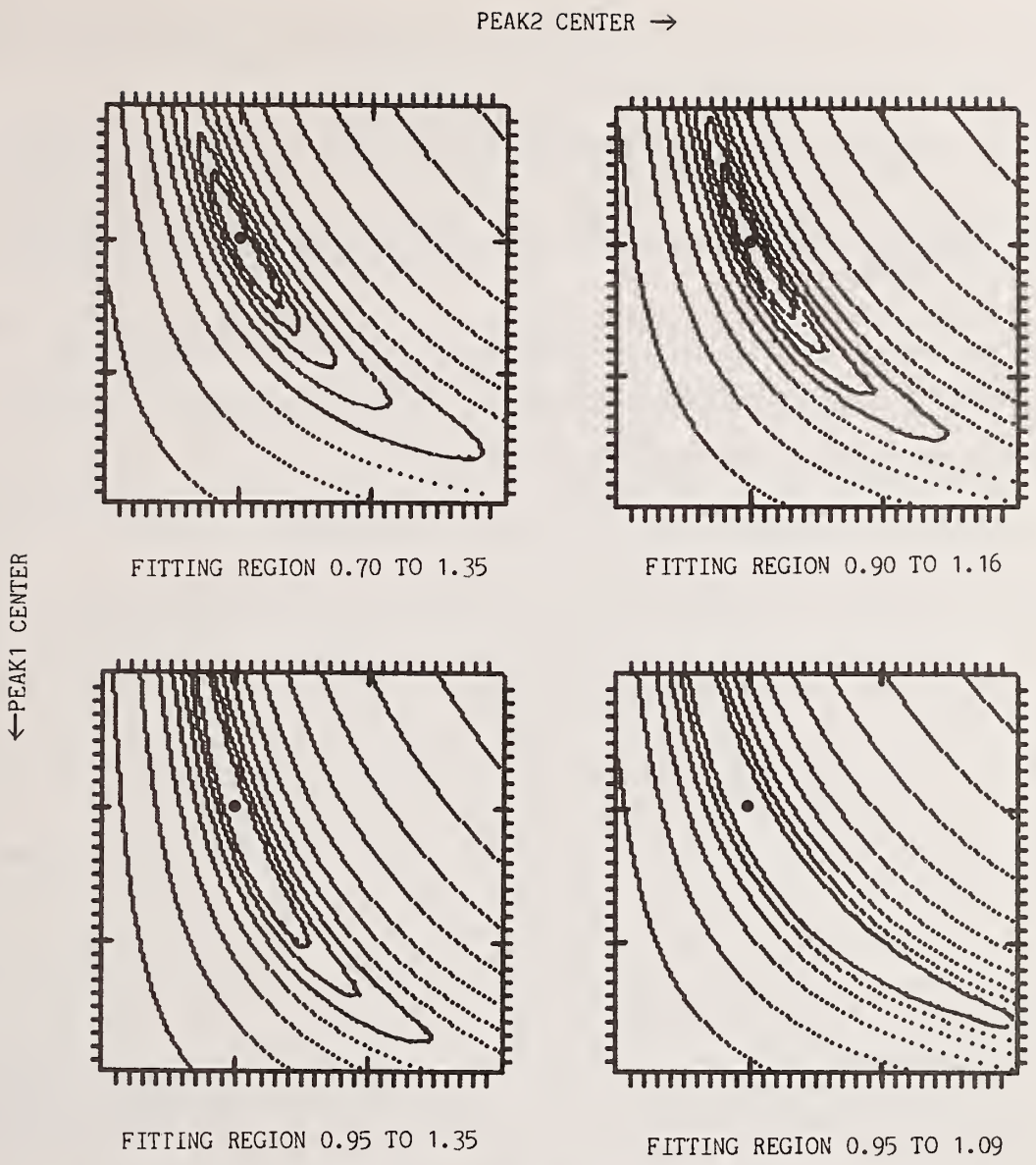

Figure 25. Comparison of χ^2 surface obtained with four choices of fitting region.

It is clearly possible to identify plausible circumstances under which non-linear least-squares methods will produce unacceptably inaccurate results, but this investigation has nonetheless given cause to feel reassured about the essential validity of the principles. Although there are certainly "pitfalls" which one can encounter in their application, these are not inexplicable hazards, but rather can be understood in terms of fundamental statistical limitations and/or systematic factors related to implementation.

Summary

Least-squares curve fitting is a powerful analytic tool for the analysis of complex spectra, yet inherently simple in concept. Linear fitting functions are particularly simple to work with and have unique solutions. Non-linear functions are more difficult to deal with and generally require an iterative optimization algorithm.

Assuming reasonable objectives and careful formulation, both linear and non-linear least-squares problems can be solved reliably. This is not to say that unacceptably large errors (from the viewpoint of the analyst) cannot occur. Rather, it must be recognized that the distribution of errors is governed by a statistical probability function and that any error is possible in principle, although deviations which exceed a few standard deviations are quite improbable.

The precision of the fitted results is ultimately limited by the statistical content of the data employed and the formulation of the problem. Precision is improved when:

(a) The statistics of the data are improved (more counts per channel).

(b) Redundant information is supplied (more channels).

(c) External information can be supplied to the procedure (e.g., use of "known" parameters and judicious constraints between parameters).

Systematic biases can be introduced into a least-squares fit by improper program design or careless formulation of the problem. Some factors which deserve consideration are:

(a) Care should be taken to ensure that the fitting region is sufficiently wide to include all of the information which is relevant to variations in the parameters.

(b) The choice of starting estimates in an iterative procedure can affect the distribution of results obtained.

(c) Imposing parameter constraints can, under certain conditions, create systematic false minima.

(d) Improper application of weighting can introduce biases into the solutions.

It is incumbent upon the user of any analysis program to exercise common sense and reasonable caution. Some basic guidelines are:

(a) Employ estimates of statistical uncertainty as a guide, but do not rely solely on them for crucial determinations. For maximum safety, perform several measurements and compute the average and standard deviation of these independent observations.

(b) Independently establish confidence in the performance of the analysis program by running a few "known" specimens under typical conditions. If you cannot consistently achieve good results for the "known" samples, you cannot expect to do any better with "unknowns" (regardless of what the program printout says).

(c) Use χ^2 as an "early warning" of systematic problems. If χ^2 begins to increase significantly, you should make an effort to understand why, and to what degree the accuracy of the results are being affected.

(d) Whenever possible, prevent systematic disturbances in the analysis rather than correct for them. For example, a stable spectrometer is always preferable to the introduction of non-linear parameters to accomodate calibration and/or resolution changes. Even if such parameters cannot be absolutely controlled and non-linear methods must be employed, the reliability of the correction is improved if such parameters do not deviate greatly from their expected values.

(e) Be critical. Always ask "Is this reasonable?" No device or procedure is ever completely without flaw.

References

[1] Orear, J., Notes on Statistics for Physicists, UCRL-8417, University of California Radiation Laboratory, Berkeley, Calif., (1958).

[2] Moore, R. H., "On the Meaning and Use of "Chi-Square" in Curve Fitting", in Applications of Computers to Nuclear and Radiochemistry, O'Kelley, G. D., Ed., NAS-NS 3107, Office of Technical Services, Department of Commerce, Washington, D. C., (1958), p. 305.

[3] Bevington, P. R., Data Reduction and Error Analysis for the Physical Sciences, mcGraw-Hill (1969), Chapters 6-12.

[4] Deming, S. N. and Morgan, S. L., "Simplex Optimization of Variables in Analytic Chemistry", Anal. Chem., 45, (3), 379A (1973).

[5] Hamming, R. W., Introduction to Applied Numerical Analysis, McGraw-Hill (1971), Chapters 9 and 10.

[6] Statham, P. J., "Pitfalls in Linear and Non-Linear Profile-Fitting Procedures, X-Ray Spectrom. 7, (3), 132 (1978).

National Bureau of Standards Special Publication 604. Proceedings of the Workshop on Energy Dispersive X-Ray Spectrometry held at NBS, Gaithersburg, Maryland, April 23-25, 1979. (Issued March 1981)

SEQUENTIAL SIMPLEX: A PROCEDURE FOR RESOLVING SPECTRAL INTERFERENCE IN ENERGY DISPERSIVE X-RAY SPECTROMETRY

C. E. Fiori, R. L. Myklebust* and K. Gorlen**

Division of Research Services
National Institutes of Health
Bethesda, MD 20205

*Center for Analytical Chemistry
National Bureau of Standards
Gaithersburg, MD 20234

**Division of Computer Research and Technology
National Institutes of Health
Bethesda, MD 20205

Abstract

A method is described for the fitting of Gaussian profiles to the pulse-height distributions of overlapping x-ray peaks measured with an energy-dispersive detector. The desired result is to know the areas under individual x-ray peaks in a spectrum in which the peaks are not resolved. A sequential simplex procedure for selection of the parameters in a mathematical expression that describes a spectral peak is used. Starting and stopping criteria and a method to reduce the number of independent variables for the procedure are discussed, and a computer program is included. Examples of the method applied to computer generated peaks and to peaks obtained from a lithium-drifted silicon Si(Li) detector are provided.

1. Introduction

The lithium-drifted silicon (Si(Li)) detector has become an established tool in x-ray spectro-chemical techniques such as x-ray fluorescence spectrometry and electron beam x-ray microanalysis. The popularity of the Si(Li) detector is due to a number of factors including high quantum efficiency and stability over the analytical energy range 1 - 20 keV, large collection solid angle (typically 0.05 - 0.3 steradian), operational simplicity, low cost and minimal maintenance.

The natural width of an x-ray line is in the order of several electron volts in the energy range of interest measured at half the maximum of the peak intensity (the measured quantity is designated "full width, half maximum" (FWHM)). However, the instrumental response function of the Si(Li) detector is closely approximated by a Gaussian distribution having a width (FWHM) of approximately 150 eV. Consequently, a natural peak of 1.5 eV width having 1000 counts amplitude would be degraded to a peak having a width of 150 eV and an amplitude of 10 counts. For some applications the available resolving power is sufficient. Often, however, peak overlap occurs in x-ray spectra observed using a Si(Li) detector. This paper will describe an application of an optimization procedure, the sequential simplex [1,2,3][1], which is used by us to resolve spectral overlaps in the x-ray energy range 1 - 20 keV.

[1]Figures in brackets indicate the literature references at the end of this paper.

A sequential simplex procedure is a technique which can be used for selection of the set of independent variables in a mathematical expression which cause the expression to be a "best" fit to a set of data points. In this procedure, each of the n independent variables in the function to be fitted is assigned an axis of an n-dimensional coordinate system. A simplex, in this coordinate system, is defined to be a geometric figure consisting of n + 1 vectors (in this discussion we will use the purely mathematical definition of a vector, i.e., an ordered n-tuple (X_1, X_2...Xn). In one dimension a simplex is a line segment; in two dimensions a triangle; and in three or more dimensions a polyhedron, the vertices of which are the above-mentioned n + 1 vectors. The simplex is moved toward the set of independent variables which optimize the fit according to a set of specific rules. The function used to determine the quality of the fit for any set of independent variables is called the "response function". The response function is a real valued function of n independent variables and is evaluated at the n + 1 vertices of a simplex. The value exhibiting the largest error (worst fit) is then replaced by another value, which is obtained by reflecting the discarded vertex across the hyperplane of the remaining vertices. The methods for expanding and contracting the simplex suggested by Nelder and Mead [2] have been adopted.

The procedure uses a minimum of information at each step, and no record is kept of past position of the simplex in the space being searched. Furthermore, only addition, subtraction, multiplication, and division are required in the simplex portion of the routine. Consequently the technique is well suited for use in a small computer.

We will use a simple example to demonstrate the essence of the method. Consider the problem of finding the "best" straight line through a set of data points. A straight line is defined by the two quantities m, the slope of the line and b, the y axis intercept of the line. The functional form is:

$$y = mx + b \tag{1}$$

The quantities we wish to optimize by a simplex search are m and b. We start the process by estimating, as best we can, three lines each defined by its own slope m_i and y-axis intercept b_i, figure 1. Each of these three lines can be characterized by a vector (m_i, b_i) on a m, b plane. The three vectors form a simplex – in this case a triangle – on the plane. If we now define a third orthogonal axis to represent the "response function" the simplex search can be visualized (figure 2). The search proceeds by calculating the response above each vertex of the simplex, discarding the vertex having the highest (worst) response, and reflecting this point across the line connecting the remaining two vertices. This defines a new simplex and the process repeats subject to the rules specified in the flow sheet (figure 3).

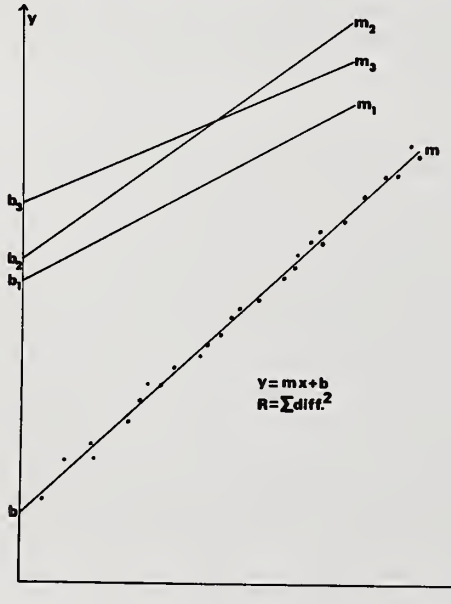

Figure 1. Linear data set with "best" fit line and 3 initial assumption lines.

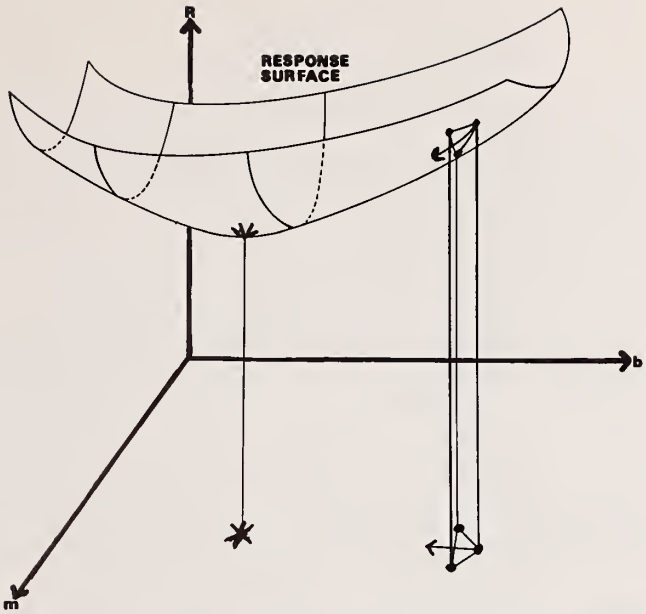

Figure 2. (m,b) plane and response surface showing a single, arbitrary, simplex.

The problem of fitting a straight line to a set of data points is a linear problem. However, the method of sequential simplex is an organized procedure to search for a minimum on a response surface and is usable whether the function describing the data set is linear in its coefficients or not. If the coefficients are linear, or can be made linear by a suitable transformation, the least squares determination can be accomplished analytically. In this case a search procedure would not be used and is done so here only for the purpose of explanation.

2. The Fitting Profile

The function we fit to a given set of N overlapping spectral peaks is the additive combination of N Gaussian profiles, i.e.,

$$y_j = \sum_{i=1}^{N} A_i \exp \left[-0.5 \left[\frac{E_j - E_i}{\sigma_i} \right]^2 \right] \qquad (2)$$

where y_j is the intensity at energy E_j, N is the number of x-ray peaks, A_i is the amplitude of each peak, E_i is the peak energy, and σ_i is the width (standard deviation) of each peak. The assumption of a Gaussian distribution is based on 1) the known distribution of noise in the preamplifier of the Si(Li) detector and 2) the discrete nature of the counting process of charge carriers created by capturing photons of a single energy in the active volume of the Si(Li) detector. A small error is introduced by virtue of the fact that each channel (data point) is in reality the integral of a Gaussian over a small energy range. This error is very small if less than 10 eV/channel is utilized.

The fitting procedure involves the calculation of the function which is then compared with the experimental data points. The purpose of the response function is to provide a measure of the goodness of fit y_j to the data points. The response function used is a normalized chi-squared function:

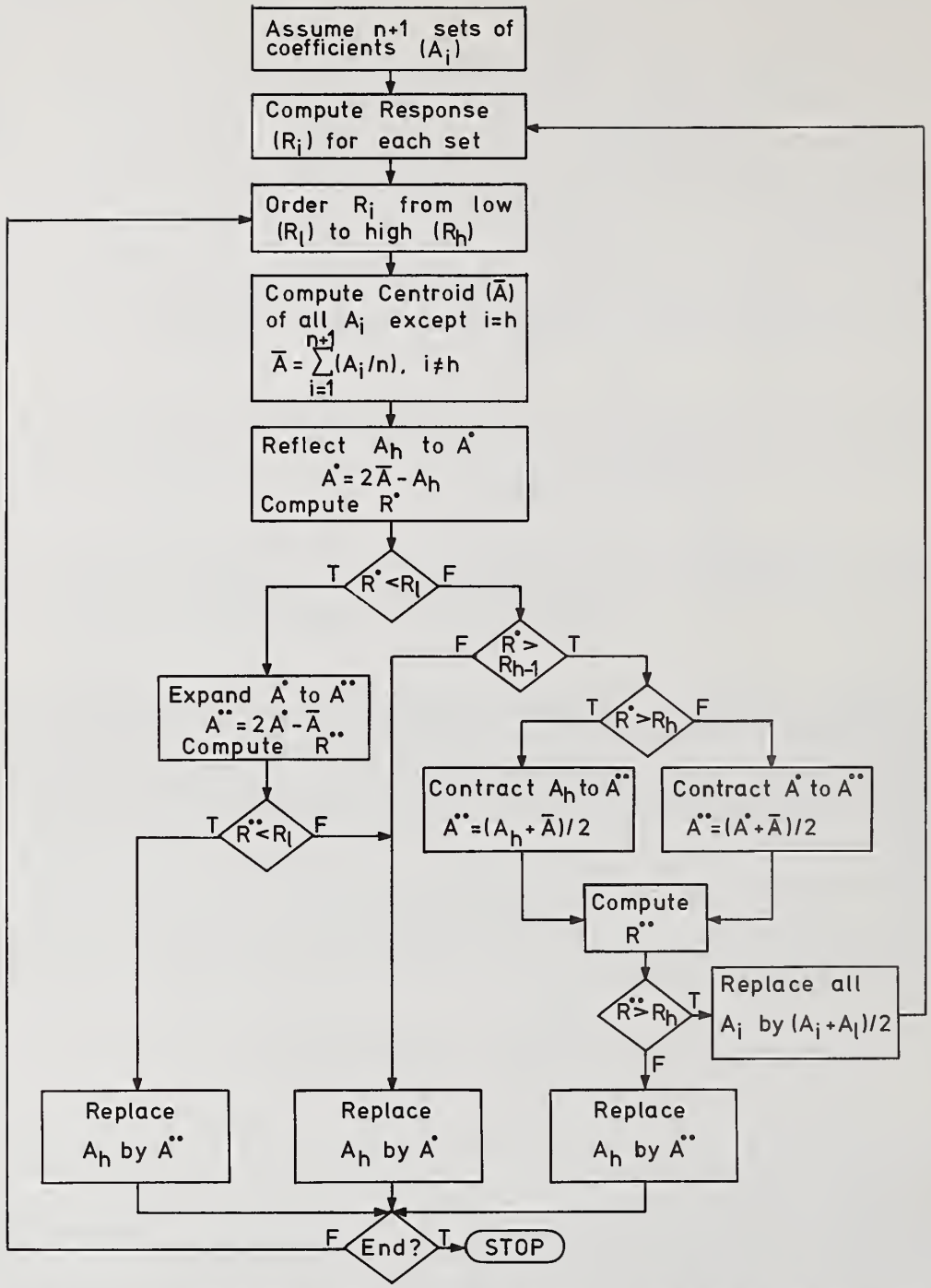

Figure 3. Flow diagram showing the logic necessary to minimize the response (R) by moving a simplex.

$$R = \sum_{j=1}^{M} \frac{1}{y} \frac{\left(z_j - y_j\right)^2}{M - f} \qquad (3)$$

where M is the number of data points, z_j is the number of counts at each data point and is consequently governed by Poisson counting statistics, y_j is defined by equation (2), and f is the number of fitted variables. The weighing factor, $1/y_j$, normalizes the effect of all data points used in the fit.

3. Reduction in the Number of Variables

From equation (2) we see that the independent variables (coefficients) A_i, E_i and σ_i must be determined for each peak; therefore, the total number of coefficients, n, is:

$$n = 3N \qquad (4)$$

here, values for n + 1 different sets of coefficients are chosen to create the initial simplex and the response, R, is determined for each set. The procedure outlined in figure 3 is then used to mimimize R to obtain the best set of coefficients.

We have introduced several simplifications which reduce the number of coefficients to be fitted. Since the energies of x-ray lines are well known, they are entered as known quantities and it is unnecessary to include all of the peak centroids (E_i) as coefficients. The energy of only the principal peak (E_p) is used as a coefficient to correct for small shifts in energy due to miscalibration of the electronics of the Si(Li) spectrometer. The energies of all other peaks are determined from the energy E_p, thereby reducing the number of coefficients required in the fit. The stability and linearity of present-day amplifiers permits this assumption. In addition, the width (σ_p) of only the principal peak must be included since the widths of the other peaks (σ_i) are related to σ_p (for a Si(Li) detector [3]) by:

$$\sigma_i = \left([2500(E_i - E_p) + (2355\ \sigma_p)^2] \right)^{1/2} \Big/ 2355 \qquad E(\text{keV}) \qquad (5)$$

The number of coefficients required is, therefore, reduced from 3N to N + 2. Consequently, only one more coefficient (amplitude) must be included for each additional peak used in a fit.

Since the energies and widths of small unresolved peaks are determined as functions of the principal peak, opportunities for obtaining false minima are considerably reduced. Significant savings in computation time are also realized.

4. Starting and Stopping Criteria

A difficulty common to all minimization methods is the possibility that a local minimum may be found before the global mimimum. As the number of peaks to be fitted increases so does the possibility of finding false minima. Consequently, the simplex must be started closer to the unique set of coefficients which determine the global minimum than to a set which determine a local (false) minimum.

The initial estimate of energy of a peak is considerably more important than estimates for amplitude or width. Figure 4 demonstrates the relative significance of estimates of these three parameters for a single Gaussian peak centered at 5 keV for three different widths. Twenty channels symmetrically placed across the peak, 10 eV per channel, are used for the fit. The amplitude is assumed to be 10,000 counts. Only one of the three parameters is varied for a given curve and the effect on the response function (equation 3) is shown on the vertical axis.

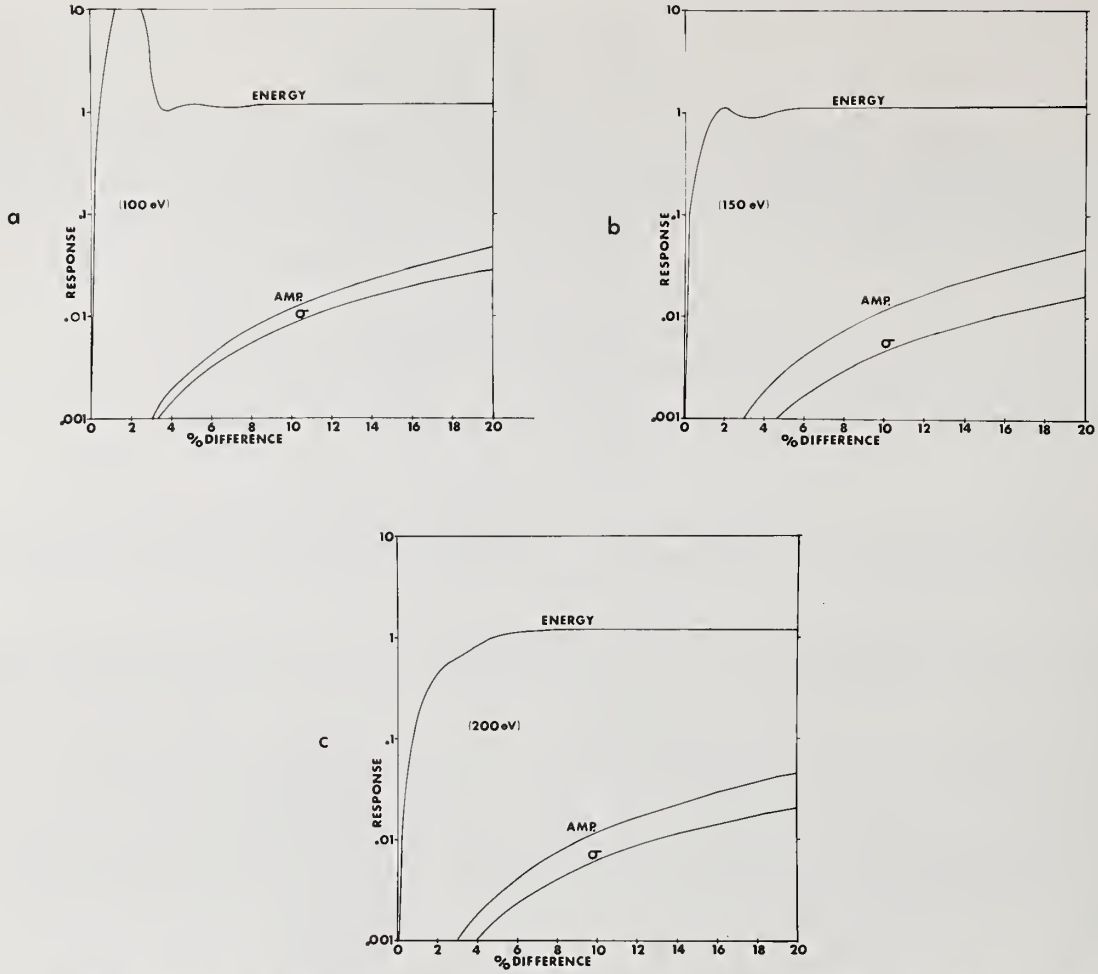

Figure 4. Relative change in response (R) for initial estimates of energy, amplitude, and standard deviation (σ) to three different peaks centered at 5 keV with amplitudes of 10,000 counts and widths (fwhm) of (a) 100 ev, (b) 150 eV, and (c) 200 eV, respectively. Twenty channels, 10 eV per channel, are used for the fit. The abscissa is the difference, in percent, between a given parameter of the theoretical Gaussian and the same parameter for the assumed Gaussian.

The results for the initial estimate of energy indicate that this parameter is at least four orders of magnitude stronger in influencing the response than either the amplitude estimate or width estimate. Fortunately, a good estimate of the energy of a peak is the most easily supplied of the three parameters.

The first estimate of each coefficient establishes one vertex of the initial simplex. The remaining n vertices are established by selectively perturbing several of the coefficients an appropriate distance. If the perturbations are too large the likelihood of obtaining false minima increases. On the other hand, if the perturbations are too small, computation time will be wasted as the simplex attempts to determine the direction in which it must move. This occurs when the size of the simplex is of the same magnitude as the statistical irregularity of the response surface. We have empirically determined that the true minimum on the response surface is most often found with a smaller number of moves of the simplex when the amplitude coefficients are initally perturbed by 10 percent; the width coefficient of the largest peak perturbed by 1.0 percent; and the energy of the largest peak perturbed by 0.1 percent.

A simplex search of a response surface can be terminated in at least two ways. A stopping criterion based on change of the response function for each new vertex of the simplex as it moves across the response surface is one method. Another method is to examine for changes in the coefficients as the simplex moves across the response surface. We use the second method. If all of the coefficients have changed by less than 10^{-6} in three moves of the simplex we assume convergence. This approach is less sensitive to changes in the number of channels used in a fit and the number of peaks being fit.

5. Presmoothing of the Data

The largest amount of computation time in our procedure is involved in the calculation of n Gaussian profiles at each data channel used in the fit. These calculations must be made each time the simplex requires a new vertex. We have found that a significant reduction in computation time (greater than 50 percent) can be realized by first presmoothing the data, we use an unweighted five point fit to a quadratic polynomial. The procedure then uses every other data channel until convergence is close (all coefficients changing less than 10^{-3} in three moves of the simplex). At this point the procedure switches and uses the original data from all channels until final convergence is reached.

6. Incomplete Charge Collection

The energy-dispersive x-ray peaks in our method are assumed to be Gaussian line profiles. This assumption ignores the distortion on the low energy side of the observed peak caused by incomplete charge collection in the detector [4,5,6]. The effect due to incomplete charge collection can be seen in figure 5 for chlorine Kα and potassium Kα peaks. The deviation from a Gaussian distribution (shown as a solid line) is a function of energy. For example, the magnitude of the effect is significantly different for chlorine and potassium, which are separated by only two atomic numbers. The distortion due to incomplete charge collection tends to diminish as the energy of the x-ray line increases. In general, incomplete charge collection is a second order effect and can be neglected. For those situations, however, in which it cannot (i.e., small peaks on the low energy side of large peaks), it is possible to determine an expression of the form

$$Y_j = aA_i\,(E_i - E_j)\,e^{-b(E_i - E_j)} \qquad E_j < E_i \tag{6}$$

for a particular detector in a given experimental situation [7]. This equation can be functionally added to the Gaussian profile used to fit each peak in a spectrum. The terms in equation 6 are as follows: E_i is the centroid of the particular Gaussian profile to be modified and A_i the amplitude, y_j is the contribution due to incomplete charge collection at energy E_j, and "a" and "b" are coefficients which will, in general, be different for peaks of different energy. The procedure to determine "a" and "b" for a given energy consists of the following. A series of Kα lines in the vicinity of the energy in question are each fitted with a Gaussian profile (K series lines are used because of their simplicity relative to other x-ray lines). Only data from half the peak maximum on the low energy side to the baseline on the high energy side are used for these fits. The fitted curve for a given peak is subtracted from the real data and equation 6 fitted to the residuals. An example of such residuals and fit for FeKα are shown in figure 6. The optimum "a" and "b" for any energy in the characterized range can be interpolated. As long as significant changes are not made in the experimental situation the values determined for "a" and "b" will remain valid.

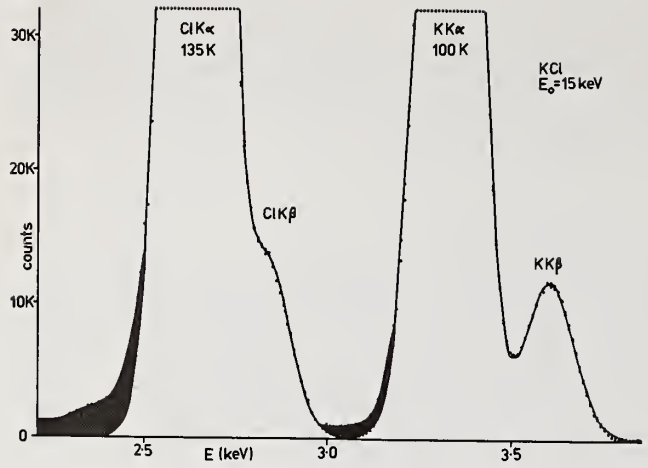

Figure 5. Energy-dispersive spectrum of KCl illustrating distortion caused by incomplete charge collection (shaded area). The solid line is a Gaussian fit to the data points.

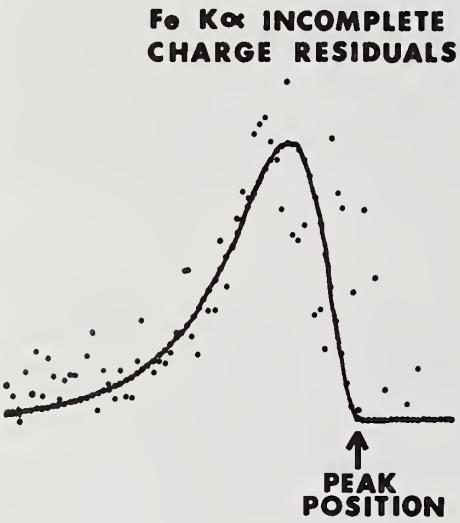

Figure 6. The iron Kα incomplete charge residuals remaining after subtracting a fitted Gaussian curve from a real peak. The smooth points are a fit to the residuals using equation 6.

An example of a complete fit including the correction for incomplete charge collection is shown in figure 7. The spectrum used in this figure is the same as used in figure 5.

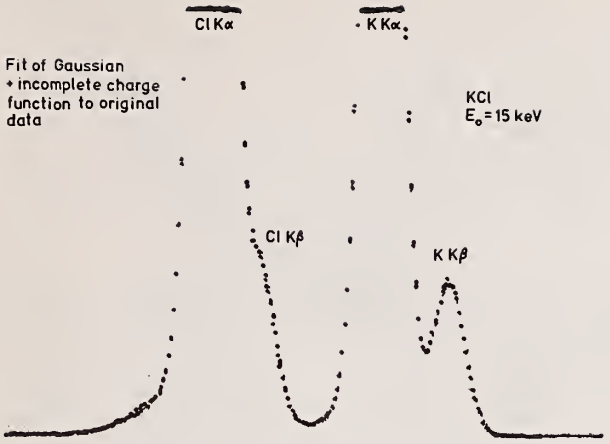

Figure 7. Example of a complete fit including the correction for incomplete charge collection.

7. Constraints

A constraint is defined to be a limit to the values which a given coefficient may assume as the simplex moves across the response surface. For example, it is known that peaks may not have negative amplitudes and it would seem reasonable to forbid any peak from assuming such a value. This can be accomplished by assigning a very high response to any vertex which contains a negative amplitude. Similarly, one may place constraints on the width and energy coefficients of the largest peak. The assumption made is that the simplex will reflect off the constraint and the search will be confined to a defined, physically meaningful, region. Constraints such as the above were suggested by Nelder and Mead [2] and give significant positive benefits.

Figure 8 is a computer generated spectrum of two Gaussian peaks of similar amplitude shown with their convolution. The peaks are separated by 50 eV and have the appropriate widths for peaks at 5.0 and 5.05 keV arising from a detector having a resolution (FWHM) of 150 eV at MnKα (5.895 keV). Equation 5 was used to determine the widths. No background has been superposed under the peaks nor have they been modulated by statistical uncertainty – other than that due to computer round off error. To assess the utility of placing constraints on amplitude, energy or width or a combination of all of these, the experiments shown in figures 9, and 12 through 14 were performed.

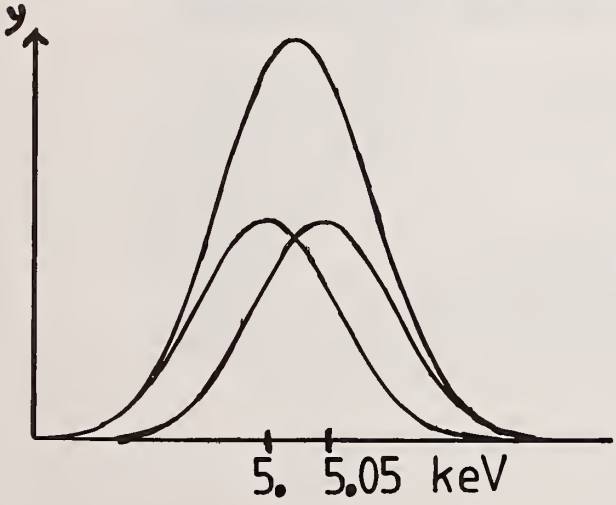

Figure 8. Computer generated spectrum of two Gaussian peaks of similar amplitude with their convolution. Peaks are separated by 50 eV and have energies of 5.0 and 5.05 keV arising from a detector saving a FWHM at MnKα of 150 eV.

In these experiments the convolution shown in figure 8 was subjected to a large number of simplex searchs with various constraints and without constraint. The initial estimates for width and energy were the correct values for the two peaks. Initial estimates for the two amplitudes, however, were allowed to vary from zero to nearly twice the known values (in increments of 10 counts) in both cases. The horizontal and vertical axis of the plots are respectively, the initial estimate for the amplitude of the low energy peak and the high energy peak. A successful search was arbitrarily defined as all variables being within one percent of the known values. A success is denoted, at each increment, by an asterisk and a failure by a solid circle. In cases where a vertical line of adjacent failure is encountered the solid circles are connected.

When the convergence test matrix for the no constraints situation is examined, as shown in figure 9, failures are found principally near the axis, where the initial estimate of at least one of the peaks differs greatly from the true value. Somewhat surprisingly, isolated failures are also observed in the region around the true value, with most of these failures corresponding to initial estimates above the true value. Determination of the exact origin of these failures will require additional work. It is felt that the extreme flatness of the response surface, when peaks are separated by less than about 50 eV, is the principal cause of the observed failures, figure 10.

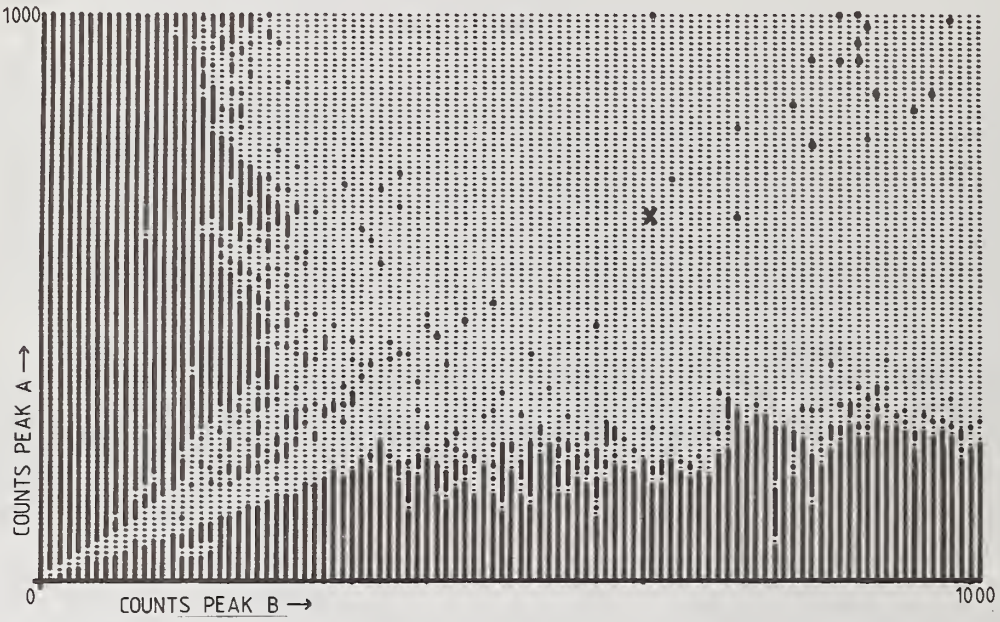

Figure 9. Convergence test matrix, no constraints.
X marks correct solution.

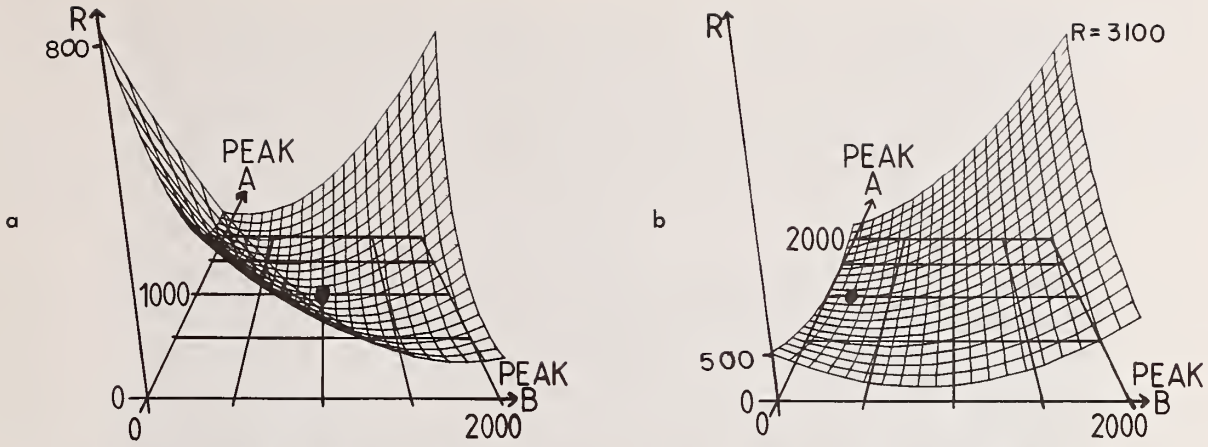

Figure 10. Three dimensional slice through a six dimensional volume. The response surface is shown above the two amplitude axes. The true peak amplitudes are denoted by the solid circle, (a) 1000 counts each peak; (b) 200 counts each peak. The response surface is essentially flat in the direction of opposite amplitude variation.

The convergence test matrix was then recalculated with various individual constraints placed upon the parameters. These constraints were (1) the peak energies were constrained to ± 20 eV, figure 11; (2) the width of the lower energy (largest amplitude) peak was constrained to ± 5 eV from the given by equation (5), figure 12; and (3) negative amplitudes were forbidden, figure 13.

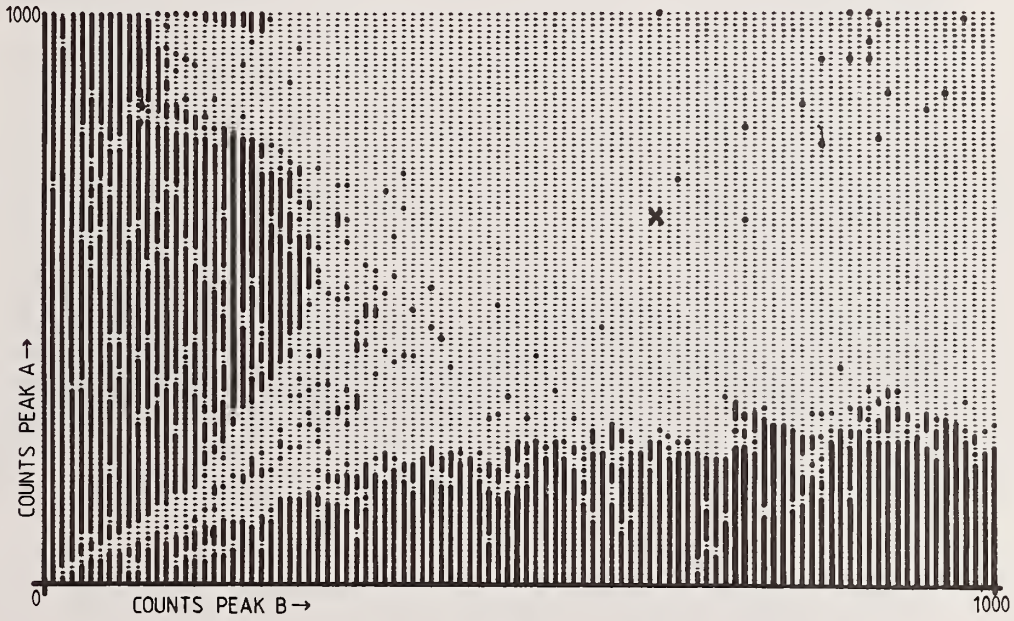

Figure 11. Convergence test matrix, energy constrained.

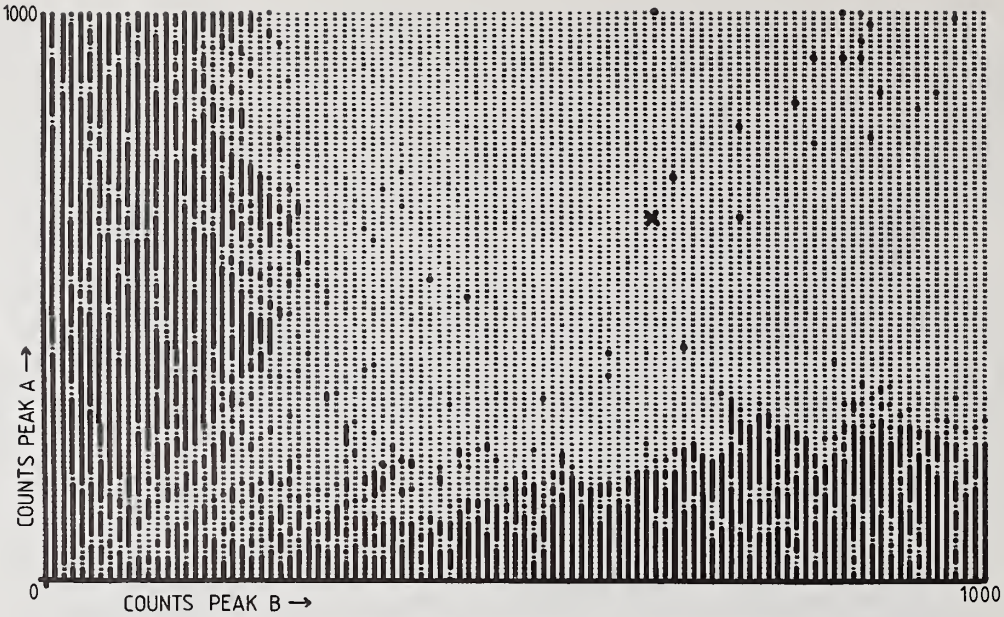

Figure 12. Convergence test matrix, width constrained.

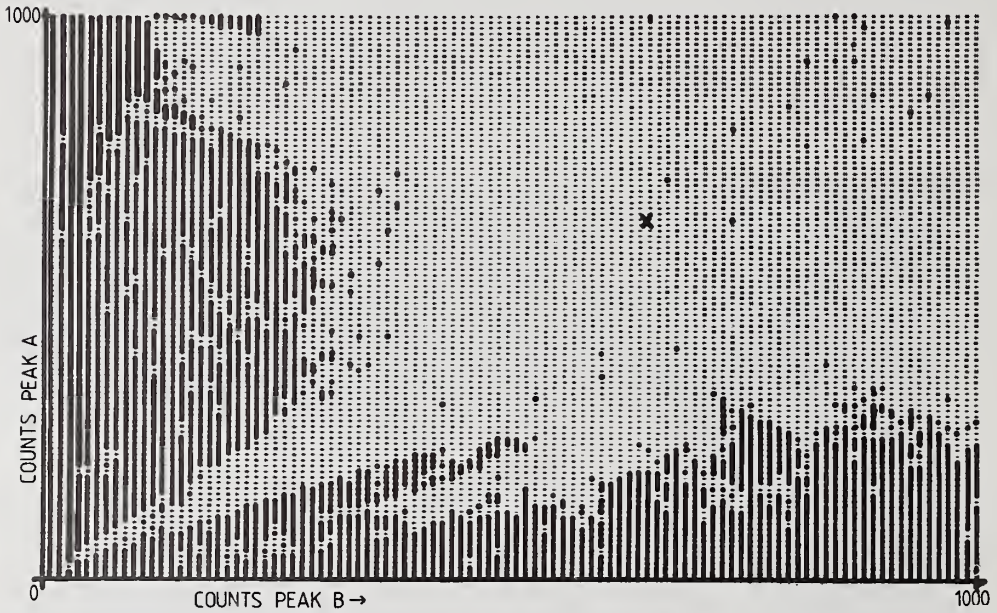

Figure 13. Convergence test matrix, positive amplitude constrained.

As can be seen from figures 11 - 13, the various individual constraints produce a marginal improvement when both starting estimates are well below the true amplitudes (denoted by a cross). For those failures where the starting estimates are both above the true amplitudes there is no improvement. A curious result occurs when all the constraints are included, figure 14. In this case there is a neglibibly small improvement over the case where no constraints are used at all. Clearly, more work needs to be done in this area as well. It must be noted, however, while only ten seconds is required for any one data point, that 15 days of central processor time were required (PDP 11-60 computer with high speed arithmetic capability) to produce the data used in figures 9 and 11 - 14.

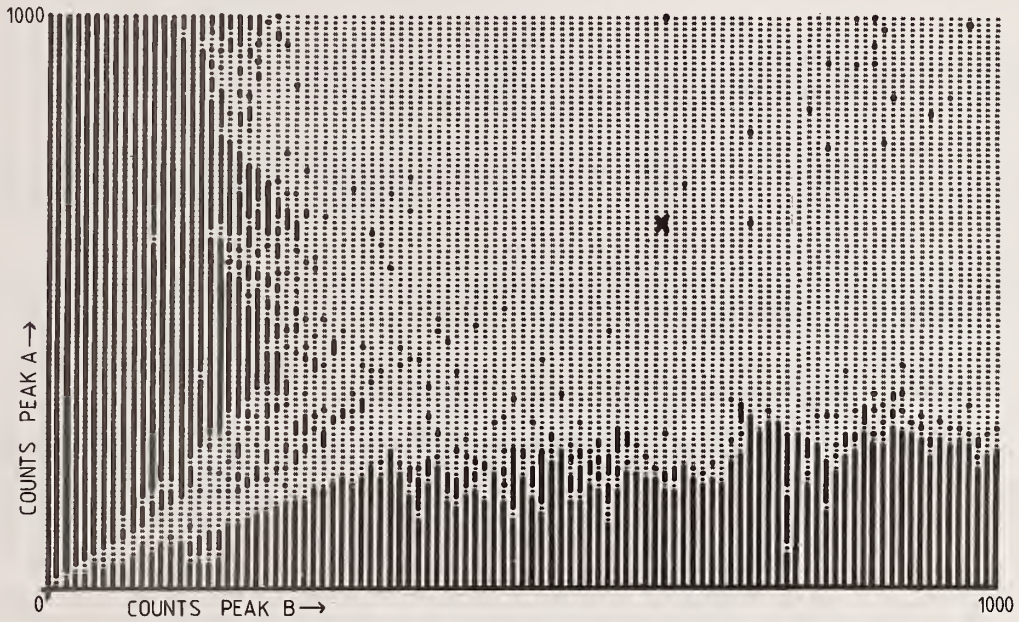

Figure 14. Convergence test matrix, all constraints included.

8. Fortran Program

A complete listing of our Simplex program is included in Appendix 1. This program is written in Digital Equipment Corporation Fortran IV plus. Very little of the program, however, is written in non-standard Fortran.

9. Conclusions

A sequential simplex procedure has been developed for the specific problem of unfolding peak overlaps encountered in energy dispersive x-ray spectrometry. This procedure has been tested to determine the importance of individual peak parameters, i.e., energy, width, and amplitude, on the simplex response. The initial estimate of energy was found to be at least four orders of magnitude more influential on the response than either the amplitude or width estimates.

An exhaustive study was conducted to determine the capability of the simplex procedure to find a correct solution for two computer generated overlapping Gaussian peaks separated by 50 eV. A convergence test matrix was developed to test the sensitivity to convergence on the initial amplitude estimates. Constraint of parameters, peak energy, peak width, and restriction to positive peak amplitude, caused an improvement in the convergence. Anomalous failures at individual points were observed in the region of the correct peak amplitudes. Due to the extreme flatness of the response surface when peaks are separated by less than about 50 eV it is recommended that great caution be exercised when attempting to resolve such a spectral interference in real data modulated by statistical uncertainty and the

effects of background. The authors would like to thank Daniel Ferner for doing the graphics utilized in figure 10.

References

[1] Spendley, W., Hext, G. R., and Himsworth, F. R., Sequential Application of Simplex Designs in Optimisation and Evolutionary Operation, Technometrics, 4, 441 (1962).

[2] Nelder, J. A. and Mead, R., A Simplex Method for Function Minimization, Comput. J., 7, 308 (1965).

[3] Fiori, C. E. and Myklebust, R. L., A Simplex Method for Fitting Gaussian Profiles, in Computers in Activation Analysis and Gamma-ray Spectroscopy, Technical Information Center/U. S. Dept. of Energy, 139-149 (1979).

[4] Fiori, C. E. and Newbury, D. E., Artifacts Observed in Energy Dispersive Spectrometry in the Scanning Electron Microscope, in Scanning Electron Microscopy/1978, Los Angeles, California, O. Johari, ed., Aug. 16-21, 1977, p. 401, S.E.M., Inc., O'Hare, Ill. (1978).

[5] Gedcke, D. A., The Si(Li) X-ray Energy Analysis System: Operating Principles and Performance, X-ray Spectrom., 1, 129 (1972).

[6] Elad, E., Inskeep, C. N., Sareen, R. A., and Nestor, P., Dead Layers in Charged Particle Detectors, IEEE Trans. Nucl. Sci., 20, 534 (1973).

[7] Myklebust, R. L., Fiori, C. E., and Heinrich, K. F. J., FRAME C: A Compact Procedure for Quantitative Energy-Dispersive Electron Probe X-ray Analysis, National Bureau of Standards Technical Note 1106, U. S. Government Printing Office, Washington, D.C. (1979), available from authors.

```
      C SIMPLX -- X-RAY SPECTRUM DE-CONVOLUTION VIA SIMPLEX METHOD
      C
      C
      C AUTHOR:
      C
      C       KEITH E. GORLEN
      C       DIVISION OF COMPUTER RESEARCH AND TECHNOLOGY
      C       NATIONAL INSTITUTES OF HEALTH
      C       BETHESDA, MD. 20205
      C       JUNE 11, 1979
      C
0001            INCLUDE 'SMAT.COM'
     *  C
     *  C       NAXES:  NUMBER OF AXES (= NPEAK+2)
     *  C       NVERT:  NUMBER OF VERTICES (= NPEAK+3)
     *  C       TOLER:  TOLERANCE FOR PARAMETER CONVERGENCE
     *  C       IL:     INDEX OF LOWEST RESPONSE VERTEX
     *  C       IH:     INDEX OF HIGHEST RESPONSE VERTEX
     *  C       A:      SIMPLEX MATRIX
     *  C               A(*,I) = ITH VERTEX OF THE SIMPLEX
     *  C               A(1,I) = SIGMA OF LARGEST PEAK (KEV)
     *  C               A(2,I) = ENERGY OF LARGEST PEAK (KEV)
     *  C               A(J,I), 3 >= J <= NPEAK+2 = AMPLITUDE OF JTH PEAK
     *  C       R:      R(I) IS THE RESPONSE OF THE ITH VERTEX
0002 *          COMMON /SMAT/ NAXES,NVERT,TOLER,IL,IH,A(16,17),R(17)
0003            INCLUDE 'SPECTB.COM'
     *  C
     *  C       NCHB:   TOTAL NUMBER OF DATA CHANNELS IN BUFFER
     *  C       ICHW:   INDEX OF FIRST CHANNEL IN ANALYSIS WINDOW
     *  C       NCHW:   NUMBER OF CHANNELS IN ANALYSIS WINDOW
     *  C       BKEVB:  ENERGY OF FIRST CHANNEL IN KEV (BUFFER)
     *  C       CHKEVB: ENERGY PER CHANNEL IN KEV (BUFFER)
     *  C       CHB:    ARRAY OF CHANNEL COUNTS (BUFFER)
0004 *          COMMON /SPECTB/ NCHB,ICHW,NCHW,BKEVB,CHKEVB,CHB(1028)
0005            LOGICAL INPAR
      C
      C       READ SPECTRUM
      C
0006  1000      CALL RDSPEC
      C
      C       READ PARAMETERS
      C
0007  1100      IF (.NOT. INPAR(0)) GO TO 1000
      C
      C       FIND PEAKS IN SPECTRUM
      C
0008            CALL FPEAKS(CHB(ICHW),NCHW,BKEVB,CHKEVB)
      C
      C       PERFORM SIMPLEX FIT
      C
0009            CALL SIMPLX(CHB(ICHW-2),NCHW+4,BKEVB,CHKEVB,ETIME)
      C
      C       REPORT RESULTS
      C
0010            CALL REPORT(A(1,IL),R(IL))
0011            WRITE (5,2000) ETIME
0012  2000      FORMAT (/' ELAPSED TIME= ',F7.1,' SECONDS'//)
      C
      C       DISPLAY RESULT OF FIT ON KEVEX 7000 SCREEN
      C
0013            CALL DSPFIT(A(1,IL))
0014            GO TO 1100
0015            END
```

```
0001              SUBROUTINE AUTOPK(LINLST)
                  C
                  C       ESTIMATE PEAK ENERGIES AND AMPLITUDE FROM ATOMIC NUMBERS
                  C
                  C ENTER:
                  C       LINLST = LIST OF LINE NUMBERS TO CONSIDER FOR FIT
                  C                LINLST(1): NUMBER OF LINES IN LIST
                  C                LINLST(2) - LINLST(LINLST(1)): LINE NUMBERS
                  C
                  C       NZ:      NUMBER OF ELEMENTS
                  C       IZ:      ARRAY OF ATOMIC NUMBERS
                  C       PE:      BEARDEN'S VALUES FOR PEAK ENERGIES OF AN ELEMENT
0002              DIMENSION IZ(10),PE(17),LINLST(18)
0003              INCLUDE 'PEAKS.COM'
                *   C
                *   C       NPEAK:  NUMBER OF PEAKS
                *   C       FWHMMN: FULL WIDTH AT HALF MAXIMUM FOR MANGANESE PEAK (EV)
                *   C       IBP:    INDEX OF BIGGEST PEAK
                *   C       PKA:    PKA(I) IS ESTIMATED AMPLITUDE OF ITH PEAK
                *   C       PKE:    PKE(I) IS ESTIMATED ENERGY (KEV) OF ITH PEAK
                *   C       PKS:    PKS(I) IS ESTIMATED SIGMA (KEV) OF ITH PEAK
                *   C       IZPK:   ATOMIC NUMBER OF ITH PEAK
                *   C       IDPK:   LINE CODE OF ITH PEAK
                *   C       IX:     ARRAY OF INDICES WHICH SORT PEAKS BY ENERGY
                *   C       DPKE:   DPKE(I) IS PKE(I) - PKE(IBP)
0004            *       COMMON /PEAKS/ NPEAK,FWHMMN,IBP,PKA(14),PKE(14),PKS(14),
                *      +  IZPK(14),IDPK(14),IX(14),DPKE(14)
0005              INCLUDE 'SPECT.COM'
                *   C
                *   C       NCH:    NUMBER OF DATA CHANNELS
                *   C       BKEV:   ENERGY OF FIRST CHANNEL IN KEV
                *   C       CHKEV:  ENERGY PER CHANNEL IN KEV
                *   C       CH:     ARRAY OF CHANNEL COUNTS
0006            *       COMMON /SPECT/ NCH,BKEV,CHKEV,CH(1024)
0007              DIMENSION T(14)
0008              EQUIVALENCE (T(1),PE(1))
0009          10  WRITE (5,20)
0010          20  FORMAT ('$ENTER NUMBER OF ELEMENTS (10 MAX): ')
0011              READ (5,30) NZ
0012          30  FORMAT (I4)
0013              WRITE (5,40)
0014          40  FORMAT ('$ENTER ATOMIC NUMBERS: ')
0015              READ (5,50) (IZ(I),I=1,NZ)
0016          50  FORMAT (10I5)
                  C
                  C       LOOK UP BEARDEN'S VALUES FOR PEAK ENERGIES
                  C
0017              NPEAK = 0
0018              DO 200 I=1,NZ
0019              IF (IZ(I) .LE. 0 .OR. IZ(I) .GT. 92) GO TO 900
0020              CALL BEARDN(IZ(I),PE)
0021              DO 100 K=1,LINLST(1)
0022              J=LINLST(K+1)
0023              IF (PE(J) .EQ. 0) GO TO 100
0024              IF (PE(J) .LT. BKEV .OR. PE(J) .GT. BKEV+CHKEV*NCH) GO TO 100
0025              NPEAK = NPEAK+1
0026              PKE(NPEAK) = PE(J)
0027              IZPK(NPEAK) = IZ(I)
0028              IDPK(NPEAK) = J
0029          100 CONTINUE
0030          200 CONTINUE
0031              IF (NPEAK .NE. 0) GO TO 400
0032              WRITE (5,300)
```

```
0033    300     FORMAT (' NO PEAKS FOUND')
0034            GO TO 10
        C
        C       COMPUTE AMPLITUDE ESTIMATES
        C
0035    400     CALL ESTAMP
        C
        C       COMPUTE PERMUTATION TO SORT PEAKS BY INCREASING ENERGY
        C
0036            CALL SORTPK(NPEAK,PKE,IX)
        C
        C       OUTPUT ESTIMATES TO BE USED IN SIMPLEX FIT
        C
0037            WRITE (5,600)
0038    600     FORMAT (/' PARAMETER ESTIMATES FOR SIMPLEX'/
             +  '  Z  LINE  AMPLITUDE  ENERGY  SIGMA')
0039            DO 800 I=1,NPEAK
0040            WRITE (5,700) IZPK(IX(I)),IDPK(IX(I)),PKA(IX(I)),
             +  PKE(IX(I)),PKS(IX(I))
0041    700     FORMAT (1X,I2,I5,F9.0,F9.3,F9.4)
0042    800     CONTINUE
0043            RETURN
        C
        C       ERROR PROCESSING
        C
0044    900     WRITE (5,910)
0045    910     FORMAT(' ATOMIC NUMBER OUT OF RANGE')
0046            GO TO 10
0047            END
0001            SUBROUTINE BEARDN(IZ,PE)
        C
        C BEARDN -- GET PEAK ENERGIES FROM BEARDEN TABLE
        C
        C ENTER:
        C       IZ = ATOMIC NUMBER
        C       PE = 17 ELEMENT ARRAY TO RECEIVE PEAK ENERGIES (KEV):
        C
        C               PE(1) = KA
        C               PE(2) = KB
        C               PE(3) = LA1
        C               PE(4) = LA2
        C               PE(5) = LB1
        C               PE(6) = LB2
        C               PE(7) = LB3
        C               PE(8) = LB4
        C               PE(9) = LG1
        C               PE(10) = LG3
        C               PE(11) = LN
        C               PE(12) = LL
        C               PE(13) = MA
        C               PE(14) = MB
        C               PE(15) = MG
        C               PE(16) = MZ
        C               PE(17) = M2N4
        C
0002            DIMENSION PE(17),E(890)
0003            REAL KALFA(48),KBETA(41),LALFA1(64),LALFA2(56),
             +  LBETA1(69),LBETA2(53),LBETA3(69),LBETA4(69),
             +  LGAMA1(53),LGAMA3(53),LETA(69),LLAMDA(69),
             +  MALFA(36),MBETA(36),MGAMA(52),MZETA(33),MIINIV(20)
0004            EQUIVALENCE
             +  (KALFA(1),E(1)),
             +  (KBETA(1),E(49)),
             +  (LALFA1(1),E(90)),
```

```
     +   (LALFA2(1),E(154)),
     +   (LBETA1(1),E(210)),
     +   (LBETA2(1),E(279)),
     +   (LBETA3(1),E(332)),
     +   (LBETA4(1),E(401)),
     +   (LGAMA1(1),E(470)),
     +   (LGAMA3(1),E(523)),
     +   (LETA(1),E(576)),
     +   (LLAMDA(1),E(645)),
     +   (MALFA(1),E(714)),
     +   (MBETA(1),E(750)),
     +   (MGAMA(1),E(786)),
     +   (MZETA(1),E(838)),
     +   (MIINIV(1),E(871))
0005       LOGICAL*1 IZL(17),IZU(17)
0006       DATA IZL/03,10,29,37,24,40,24,24,40,40,24,24,57,57,41,60,73/
0007       DATA IZU/50,50,92,92,92,92,92,92,92,92,92,92,92,92,92,92,92/
0008       DATA KALFA/.0543,.1085,.1833,.277,.3924,.5249,.6768,.8486,
     +  1.04098,1.25360,1.48656,1.73978,2.01341,2.30744,2.62185,
     +  2.95701,3.31290,3.69048,4.08910,4.50885,4.94968,5.41165,
     +  5.89505,6.3991,6.92531,7.47240,8.04112,8.63117,9.24277,
     +  9.87605,10.53181,11.20873,11.90867,12.632,13.37547,14.14263,
     +  14.93323,15.747,16.5837,17.4443,18.3283,19.2363,20.1686,
     +  21.1247,22.1054,23.1104,24.1405,25.1955/
0009       DATA KBETA/.8579,1.0711,1.30222,1.55745,1.83594,2.13908,
     +  2.46404,2.8156,3.1905,3.5896,4.0127,4.4605,4.93181,5.42729,
     +  5.94671,6.49045,7.05798,7.64943,8.26466,8.90529,9.5720,
     +  10.2642,10.9821,11.7262,12.4959,13.2914,14.112,14.9613,
     +  15.8357,16.7378,17.6678,18.6225,19.6083,20.619,21.6568,
     +  22.7236,23.8187,24.9424,26.0955,27.2759,28.486/
0010       DATA LALFA1/.9297,1.0117,1.09792,1.188,1.282,1.3791,1.48043,
     +  1.586,1.69413,1.80656,1.92256,2.04236,2.16589,2.29316,2.424,
     +  2.55855,2.69674,2.83861,2.98431,3.13373,3.28694,3.44398,
     +  3.60472,3.76933,3.93765,4.1099,4.2865,4.46626,4.65097,4.8402,
     +  5.0337,5.2304,5.4325,5.6361,5.8457,6.0572,6.2728,6.4952,
     +  6.7198,6.9487,7.1799,7.4156,7.6555,7.899,8.1461,8.3976,
     +  8.6525,8.9117,9.1751,9.4423,9.7133,9.9888,10.2685,10.5515,
     +  10.8388,11.1308,11.4268,11.727,12.0313,12.3397,12.652,
     +  12.9687,13.2907,13.6147/
0011       DATA LALFA2/1.69256,1.80474,1.92047,2.0399,2.163,2.28985,
     +  0.,2.55431,2.69205,2.83329,2.97821,3.12691,3.27929,3.43542,
     +  3.59532,3.7588,3.92604,0.,4.2722,4.45090,4.63423,4.823,
     +  5.0135,5.2077,5.4078,5.6090,5.8166,6.0250,6.2380,6.4577,
     +  6.6795,6.9050,7.1331,7.3673,7.6049,7.8446,8.0879,8.3352,
     +  8.5862,8.8410,9.0995,9.3618,9.6280,9.8976,10.1728,10.4495,
     +  10.73091,11.0158,11.3048,11.5979,11.895,12.1962,12.5008,
     +  12.8096,13.1222,13.4388/
0012       DATA LBETA1/.5828,.6488,.7185,.7914,.8688,.9498,1.0347,
     +  1.1248,1.2185,1.317,1.41923,1.5259,1.6366,1.75217,1.87172,
     +  1.99584,2.1244,2.2574,2.39481,2.5368,2.68323,2.83441,
     +  2.99022,3.15094,3.31657,3.48721,3.66280,3.84357,4.02958,
     +  4.22072,0.,4.6198,4.82753,5.0421,5.2622,5.4889,5.7216,5.961,
     +  6.2058,6.4564,6.7132,6.978,7.2477,7.5253,7.8109,8.101,
     +  8.4018,8.709,9.0227,9.3431,9.67235,10.0100,10.3553,10.7083,
     +  11.0707,11.4423,11.8226,12.2133,12.6137,13.0235,13.447,
     +  13.876,14.316,14.770,15.2358,15.713,16.2022,16.702,17.2200/
0013       DATA LBETA2/2.2194,2.3670,2.5183,0.,2.8360,3.0013,3.17179,
     +  3.34781,3.52812,3.71381,3.90486,4.10078,4.3017,4.5075,0.,
     +  4.9359,5.1565,5.3835,5.6134,5.850,6.0894,6.339,6.586,6.8432,
     +  7.1028,7.3667,7.6357,7.911,8.1890,8.468,8.7588,9.0489,9.3473,
     +  9.6518,9.9615,10.2752,10.5985,10.9203,11.2505,11.5847,11.9241,
     +  12.2715,12.6226,12.9799,13.3404,0.,0.,14.45,14.8414,0.,
     +  15.6237,16.024,16.4283/
```

```
0014            DATA LBETA3/0.638,0.705,0.790,0.869,0.942,1.0251,1.1077,
               +  1.196,1.2941,1.3884,1.490,1.569,1.707,1.82659,1.94719,2.0722,
               +  2.201,2.3348,2.473,0.,2.7634,2.9157,3.073,3.23446,3.40145,
               +  3.57311,3.75,3.9327,4.1204,4.3134,0.,4.7167,4.9269,5.1434,
               +  5.3651,5.5918,5.8294,6.071,6.318,6.5713,6.8311,7.0959,7.3702,
               +  7.6519,7.9392,8.231,8.5367,8.8469,9.1634,9.4875,9.8188,
               +  10.1598,10.5108,10.8674,11.2308,11.6103,11.9953,12.3904,
               +  12.7933,13.2098,13.638,14.067,14.512,14.976,15.4449,15.931,
               +  16.4258,16.930,17.4550/
0015            DATA LBETA4/0.638,0.705,0.790,0.869,0.942,1.0251,1.1077,
               +  1.196,1.2861,1.3884,1.490,1.596,1.697,1.81771,1.93643,2.06,
               +  2.1873,2.3194,2.4557,0.,2.7411,2.8908,3.0454,3.20346,3.36719,
               +  3.53528,3.7083,3.8864,4.0695,4.2575,0.,4.6494,4.8519,5.062,
               +  5.2765,5.4981,5.7216,0.,6.197,6.4389,6.6871,6.9403,7.2039,
               +  7.4708,7.7453,8.026,8.3132,8.6064,8.9054,9.2124,9.5252,
               +  9.8463,10.1754,10.5106,10.8543,11.2047,11.5630,11.9306,
               +  12.306,12.6912,13.086,0.,0.,0.,14.7472,0.,15.6429,16.104,
               +  16.5753/
0016            DATA LGAMA1/2.3027,2.4618,2.6235,0.,2.9645,3.1438,3.3287,
               +  3.51959,3.71686,3.92081,4.13112,4.34779,4.5709,4.8009,
               +  0.,5.2804,5.5311,5.7885,6.052,6.3221,6.6021,6.892,7.180,
               +  7.4803,7.7858,8.102,8.4188,8.747,9.089,9.426,9.7801,10.1434,
               +  10.5158,10.8952,11.2859,11.6854,12.0953,12.5126,12.9420,
               +  13.3817,13.8301,14.2915,14.7644,15.2477,15.744,16.251,
               +  16.770,17.303,17.849,18.488,18.9825,19.568,20.1671/
0017            DATA LGAMA3/2.5029,2.6638,2.8306,0.,3.1809,3.364,3.5533,
               +  3.7498,0.,4.1605,4.3768,4.5999,4.829,5.0657,0.,5.5527,
               +  5.8092,6.074,6.3409,6.616,6.902,0.,7.490,7.7961,8.105,8.423,
               +  8.7532,9.087,9.4309,9.779,10.1431,10.511,10.8907,11.2776,
               +  11.6743,12.0824,12.4998,12.9240,13.3613,13.8090,14.265,
               +  14.7368,15.218,15.7102,0.,0.,0.,0.,18.357,0.,
               +  19.507,20.098,20.7127/
0018            DATA LETA/.5102,0.5675,0.628,0.694,0.762,0.832,0.906,0.9842,
               +  1.068,1.155,1.2446,1.3396,0.,1.54177,1.64933,1.76095,
               +  1.87654,1.99620,2.1202,0.,2.38197,2.5191,2.6603,2.8061,
               +  2.95675,3.11254,3.27234,3.43661,3.60586,3.7801,0.,4.1421,
               +  4.3309,4.525,4.7315,4.935,5.1457,0.,5.587,5.8166,6.0495,
               +  6.2839,6.5342,6.7883,7.0579,7.3088,7.5802,7.8575,8.1393,
               +  8.428,8.7243,9.0272,9.3370,9.6522,9.975,10.3083,10.6512,
               +  10.9943,11.3493,11.7122,0.,0.,0.,0.,
               +  13.6630,0.,14.5099,14.946,15.3997/
0019            DATA LLAMDA/.5003,.5563,.6152,.6778,.7427,.8111,.884,.9572,
               +  1.0380,1.1198,1.2044,1.2935,0.,1.48238,1.58215,1.68536,
               +  1.79201,1.90225,2.01568,0.,2.2528,2.3765,2.5034,2.6337,
               +  2.76735,2.90440,3.04499,3.18860,3.33555,3.48502,0.,
               +  3.7950,3.9541,4.124,4.2875,4.4532,4.6330,0.,4.9945,
               +  5.1772,5.3621,5.5467,5.7431,5.9434,6.152,6.3419,6.5455,
               +  6.7528,6.9596,7.1731,7.3878,7.6036,7.8222,8.0458,8.268,
               +  8.4939,8.7210,8.9532,9.1845,9.4204,9.664,0.,0.,0.,
               +  10.6222,0.,11.1186,11.366,11.6183/
0020            DATA MALFA/.833,.883,.9292,.978,0.,1.081,1.131,1.185,
               +  1.24,1.293,1.348,1.406,1.462,1.5214,1.5813,1.6446,1.7096,
               +  1.7754,1.8425,1.9102,1.9799,2.0505,2.1229,2.1964,2.2706,
               +  2.3455,2.4226,0.,0.,0.,0.,0.,0.,2.9961,3.0823,3.1708/
0021            DATA MBETA/.854,0.902,0.95,0.977,0.,1.0998,1.1533,
               +  1.2091,1.2661,1.325,1.383,1.443,1.503,1.5675,1.6312,
               +  1.6976,1.7655,1.8349,1.9061,1.9783,2.0535,2.1273,2.2046,
               +  2.2827,2.3621,2.4427,2.5255,0.,0.,0.,0.,0.,0.,
               +  3.1458,3.2397,3.3367/
```

```
0022            DATA MGAMA/.356,0.,0.,.462,.496,.531,.568,.606,
               +  0.,.691,.733,.788,0.,0.,0.,.973,1.027,1.0749,
               +  1.1273,1.180,0.,1.291,1.346,1.402,1.461,1.522,
               +  1.576,1.643,0.,1.765,1.832,1.895,1.964,2.035,2.1067,
               +  2.182,2.254,2.331,2.410,2.490,2.571,2.6527,2.735,0.,0.,0.,
               +  0.,0.,0.,3.370,3.4657,3.563/
0023            DATA MZETA/.753,0.,.831,.872,.914,.955,.998,1.0450,
               +  1.0901,0.,1.183,0.,1.28,1.3303,1.3835,1.4368,1.4919,
               +  1.5458,1.6022,1.6605,0.,1.778,1.8395,1.901,
               +  0.,0.,0.,0.,0.,0.,2.364,2.435,2.507/
0024            DATA MIINIV/2.226,2.314,0.,2.502,2.594,2.695,2.797,
               +  0.,3.013,3.124,3.234,0.,0.,0.,0.,0.,0.,4.117,4.26,4.401/
0025            LBASE = 1
0026            DO 20 LN=1,17
0027            PE(LN) = 0.0
0028            IF ((IZ.LT.IZL(LN)) .OR. (IZ.GT.IZU(LN))) GO TO 10
0029            PE(LN) = E(LBASE+IZ-IZL(LN))
0030     10     LBASE = LBASE+(IZU(LN)-IZL(LN))+1
0031     20     CONTINUE
0032            RETURN
0033            END



0001            LOGICAL FUNCTION CONVRG(VERTEX)
       C
       C CONVRG -- TEST FOR CONVERGENCE
       C
       C ENTER:
       C       VERTEX = VERTEX WITH HIGHEST RESPONSE
       C
       C RETURNS:
       C       .TRUE. IF TERMINATION CRITERIA SATISFIED
       C       .FALSE. IF TERMINATION CRITERIA NOT SATISFIED
       C
0002            DIMENSION VERTEX(16),OLDV(16,3)
0003            INCLUDE 'SMAT.COM'
     *  C
     *  C       NAXES:  NUMBER OF AXES (= NPEAK+2)
     *  C       NVERT:  NUMBER OF VERTICES (= NPEAK+3)
     *  C       TOLER:  TOLERANCE FOR PARAMETER CONVERGENCE
     *  C       IL:     INDEX OF LOWEST RESPONSE VERTEX
     *  C       IH:     INDEX OF HIGHEST RESPONSE VERTEX
     *  C       A:      SIMPLEX MATRIX
     *  C               A(*,I) = ITH VERTEX OF THE SIMPLEX
     *  C               A(1,I) = SIGMA OF LARGEST PEAK (KEV)
     *  C               A(2,I) = ENERGY OF LARGEST PEAK (KEV)
     *  C               A(J,I), 3 >= J <= NPEAK+2 = AMPLITUDE OF JTH PEAK
     *  C       R:      R(I) IS THE RESPONSE OF THE ITH VERTEX
0004 *          COMMON /SMAT/ NAXES,NVERT,TOLER,IL,IH,A(16,17),R(17)
0005            INCLUDE 'COUNTS.COM'
     *  C
     *  C       ITER8:  ITERATION COUNTER (PER PASS)
     *  C       NRFLCT: REFLECTION COUNTER
     *  C       NXPAND: EXPANSION COUNTER
     *  C       NCONTR: CONTRACTION COUNTER
     *  C       NSHIFT: SHIFT COUNTER
     *  C       NTOTAL: TOTAL NUMBER OF ITERATIONS
0006 *          COMMON /COUNTS/ ITER8,NRFLCT,NXPAND,NCONTR,NSHIFT,NTOTAL
       C        EXIT IF MORE THAN 500 MOVES
0007            IF (ITER8 .GE. 500) GO TO 20
0008            CONVRG = .FALSE.
```

```
0009            I = 1+MOD(ITER8,3)
        C       REQUIRE THAT THE SIMPLEX MOVES AT LEAST THREE TIMES
0010            IF (ITER8 .LT. 3) GO TO 40
        C
        C       TEST FOR CONVERGENCE OF COEFFICIENTS
        C
0011            DO 10 J=1,NAXES
0012            D = OLDV(J,I)
0013            IF (D .EQ. 0) D = TOLER
        C       EXIT IF ALL THE COEFFICIENTS HAVE CHANGED BY LESS THAN
        C       TOLER IN THE LAST THREE MOVES.
0014            IF (ABS(VERTEX(J)-OLDV(J,I))/D .GE. TOLER) GO TO 40
0015    10      CONTINUE
0016    20      CONVRG = .TRUE.
0017    30      CONTINUE
0018            RETURN
        C
        C       SAVE CURRENT VERTEX
        C
0019    40      DO 50 J=1,NAXES
0020    50      OLDV(J,I) = VERTEX(J)
0021            RETURN
0022            END



0001            SUBROUTINE DSPFIT(VERTEX)
        C
        C DSPFIT -- DISPLAY SIMPLEX FIT ON KEVEX
        C
        C ENTER:
        C       VERTEX = VERTEX WITH LOWEST RESPONSE (I.E. A(I,IL))
        C
0002            DIMENSION VERTEX(16)
0003            INCLUDE 'PEAKS.COM'
     *  C
     *  C       NPEAK:  NUMBER OF PEAKS
     *  C       FWHMMN: FULL WIDTH AT HALF MAXIMUM FOR MANGANESE PEAK (EV)
     *  C       IBP:    INDEX OF BIGGEST PEAK
     *  C       PKA:    PKA(I) IS ESTIMATED AMPLITUDE OF ITH PEAK
     *  C       PKE:    PKE(I) IS ESTIMATED ENERGY (KEV) OF ITH PEAK
     *  C       PKS:    PKS(I) IS ESTIMATED SIGMA (KEV) OF ITH PEAK
     *  C       IZPK:   ATOMIC NUMBER OF ITH PEAK
     *  C       IDPK:   LINE CODE OF ITH PEAK
     *  C       IX:     ARRAY OF INDICES WHICH SORT PEAKS BY ENERGY
     *  C       DPKE:   DPKE(I) IS PKE(I) - PKE(IBP)
0004 *          COMMON /PEAKS/ NPEAK,FWHMMN,IBP,PKA(14),PKE(14),PKS(14),
     *       +  IZPK(14),IDPK(14),IX(14),DPKE(14)
0005            WRITE (5,10)
0006    10      FORMAT ('$QUADRANT NUMBER FOR SPECTRUM FIT DISPLAY:')
0007            READ (5,20) KQUAD
0008    20      FORMAT (I10)
0009            IF (KQUAD .LT. 1 .OR. KQUAD .GT. 4) RETURN
0010            KQUAD=(KQUAD-1)*1024
0011            DO 200 J=12,1023
0012            Y=0.
0013            E=J*.01
0014            DO 100 I=1,NPEAK
0015            Y=Y+VERTEX(I+2)*EXP(-0.5*((E-(DPKE(I)+VERTEX(2)))/
             +  PKSIG(VERTEX(1),DPKE(I)))**2)
0016    100     CONTINUE
0017            CALL KXWCH(J+KQUAD,Y)
```

```
0018    200     CONTINUE
0019            RETURN
0020            END



0001            SUBROUTINE ESTAMP
      C
      C ESTAMP -- COMPUTE AMPLITUDE ESTIMATES USING MULTIPLE LINEAR REGRESSION
      C
0002            DIMENSION A(14,14),B(14),C(14),T(14)
0003            EXTERNAL GAUSPK
0004            INCLUDE 'PEAKS.COM'
     *  C
     *  C       NPEAK:  NUMBER OF PEAKS
     *  C       FWHMMN: FULL WIDTH AT HALF MAXIMUM FOR MANGANESE PEAK (EV)
     *  C       IBP:    INDEX OF BIGGEST PEAK
     *  C       PKA:    PKA(I) IS ESTIMATED AMPLITUDE OF ITH PEAK
     *  C       PKE:    PKE(I) IS ESTIMATED ENERGY (KEV) OF ITH PEAK
     *  C       PKS:    PKS(I) IS ESTIMATED SIGMA (KEV) OF ITH PEAK
     *  C       IZPK:   ATOMIC NUMBER OF ITH PEAK
     *  C       IDPK:   LINE CODE OF ITH PEAK
     *  C       IX:     ARRAY OF INDICES WHICH SORT PEAKS BY ENERGY
     *  C       DPKE:   DPKE(I) IS PKE(I) - PKE(IBP)
0005 *          COMMON /PEAKS/ NPEAK,FWHMMN,IBP,PKA(14),PKE(14),PKS(14),
     *       +  IZPK(14),IDPK(14),IX(14),DPKE(14)
0006            INCLUDE 'SPECT.COM'
     *  C
     *  C       NCH:    NUMBER OF DATA CHANNELS
     *  C       BKEV:   ENERGY OF FIRST CHANNEL IN KEV
     *  C       CHKEV:  ENERGY PER CHANNEL IN KEV
     *  C       CH:     ARRAY OF CHANNEL COUNTS
0007 *          COMMON /SPECT/ NCH,BKEV,CHKEV,CH(1024)
      C
      C       COMPUTE PEAK SIGMAS
      C
0008            DO 10 J=1,NPEAK
0009            PKS(J) = PKSIG(FWHMMN*4.2466E-4,PKE(J)-5.895)
0010    10      CONTINUE
      C
      C       PERFORM MULTIPLE LINEAR REGRESSION
      C
0011            CALL REGRES(NCH,CH,NPEAK,GAUSPK,A,B,T,PKA)
0012            RETURN
0013            END



0001            SUBROUTINE FIT
      C
      C FIT -- PERFORM SIMPLEX FIT
      C
0002            DIMENSION ABAR(16),ASTAR(16),ASTAR2(16)
0003            LOGICAL CONVRG
0004            INCLUDE 'SMAT.COM'
     *  C
     *  C       NAXES:  NUMBER OF AXES (= NPEAK+2)
     *  C       NVERT:  NUMBER OF VERTICES (= NPEAK+3)
     *  C       TOLER:  TOLERANCE FOR PARAMETER CONVERGENCE
     *  C       IL:     INDEX OF LOWEST RESPONSE VERTEX
     *  C       IH:     INDEX OF HIGHEST RESPONSE VERTEX
```

```
      *  C        A:       SIMPLEX MATRIX
      *  C                 A(*,I) = ITH VERTEX OF THE SIMPLEX
      *  C                 A(1,I) = SIGMA OF LARGEST PEAK (KEV)
      *  C                 A(2,I) = ENERGY OF LARGEST PEAK (KEV)
      *  C                 A(J,I), 3 >= J <= NPEAK+2 = AMPLITUDE OF JTH PEAK
      *  C        R:       R(I) IS THE RESPONSE OF THE ITH VERTEX
0005  *           COMMON /SMAT/ NAXES,NVERT,TOLER,IL,IH,A(16,17),R(17)
0006              INCLUDE 'COUNTS.COM'
      *  C
      *  C        ITER8:  ITERATION COUNTER (PER PASS)
      *  C        NRFLCT: REFLECTION COUNTER
      *  C        NXPAND: EXPANSION COUNTER
      *  C        NCONTR: CONTRACTION COUNTER
      *  C        NSHIFT: SHIFT COUNTER
      *  C        NTOTAL: TOTAL NUMBER OF ITERATIONS
0007  *           COMMON /COUNTS/ ITER8,NRFLCT,NXPAND,NCONTR,NSHIFT,NTOTAL
         C
         C        ALPHA:  SIMPLEX REFLECTION COEFFICIENT
         C        BETA:   SIMPLEX CONTRACTION COEFFICIENT
         C        GAMMA:  SIMPLEX EXPANSION COEFFICIENT
0008             DATA ALPHA/1.0/,BETA/0.5/,GAMMA/2.0/
         C
         C        INITIALIZATION
         C
0009             ITER8 = 0
0010             IL = 1
0011             IH = 1
         C
         C        COMPUTE RESPONSES FOR ALL VERTICES
         C
0012     1000    DO 1100 I=1,NVERT
0013             R(I) = RESP(A(1,I))
0014     1100    CONTINUE
         C
         C        TEST FOR CONVERGENCE
         C
0015     1200    IF (CONVRG(A(1,IH))) RETURN
0016             ITER8 = ITER8+1
         C
         C        BEGIN NEXT ITERATION: FIND HIGHEST AND LOWEST RESPONSES
         C
0017             DO 1300 I=1,NVERT
0018             IF (R(I) .GT. R(IH)) IH=I
0019             IF (R(I) .LT. R(IL)) IL=I
0020     1300    CONTINUE
         C
         C        COMPUTE CENTROID (ABAR) OF ALL VERTICES EXCEPT A(,IH)
         C
0021             DO 1400 J=1,NAXES
0022     1400    ABAR(J) = 0
0023             DO 1600 I=1,NVERT
0024             IF (I .EQ. IH) GO TO 1600
0025             DO 1500 J=1,NAXES
0026     1500    ABAR(J) = ABAR(J)+A(J,I)
0027     1600    CONTINUE
0028             DO 1700 J=1,NAXES
0029     1700    ABAR(J)=ABAR(J)/(NVERT-1)
         C
         C        COMPUTE REFLECTION (ASTAR) OF ABAR
         C
0030             DO 1800 J=1,NAXES
0031     1800    ASTAR(J) = (1.+ALPHA)*ABAR(J)-ALPHA*A(J,IH)
```

```
0032              RSTAR = RESP(ASTAR)
          C
          C       TEST FOR EXPANSION
          C
0033              IF (RSTAR .LT. R(IL)) GO TO 2500
          C
          C       TEST FOR REFLECTION
          C
0034              DO 1900 I=1,NVERT
0035              IF (I .EQ. IH) GO TO 1900
0036              IF (RSTAR .LE. R(I)) GO TO 2700
0037      1900    CONTINUE
          C
          C       CONTRACT
          C
0038              IF (RSTAR .GT. R(IH)) GO TO 2100
0039              DO 2000 J=1,NAXES
0040      2000    A(J,IH) = ASTAR(J)
0041              R(IH) = RSTAR
          C
          C       COMPUTE CONTRACTION ASTAR2
          C
0042      2100    DO 2200 J=1,NAXES
0043      2200    ASTAR2(J) = BETA*A(J,IH)+(1.-BETA)*ABAR(J)
0044              RSTAR2 = RESP(ASTAR2)
          C
          C       TEST FOR CONTRACTION FAILURE
          C
0045              IF (RSTAR2 .LE. R(IH)) GO TO 2400
          C
          C       CONTRACTION FAILED, DO SHIFT
          C
0046              DO 2300 I=1,NVERT
0047              DO 2300 J=1,NAXES
0048              A(J,I) = (A(J,I)+A(J,IL))/2.
0049      2300    CONTINUE
0050              NSHIFT = NSHIFT+1
0051              GO TO 1000
          C
          C       CONTRACTION SUCCEEDED, REPLACE A(,IH) BY CONTRACTION (ASTAR2)
          C
0052      2400    NCONTR = NCONTR+1
0053              CALL REPLA(ASTAR2,RSTAR2)
0054              GO TO 1200
          C
          C       COMPUTE EXPANSION (ASTAR2) OF ASTAR
          C
0055      2500    DO 2600 J=1,NAXES
0056      2600    ASTAR2(J) = GAMMA*ASTAR(J)+(1-GAMMA)*ABAR(J)
0057              RSTAR2 = RESP(ASTAR2)
0058              IF (RSTAR2 .LT. R(IL)) GO TO 2800
          C
          C       REPLACE A(,IH) BY REFLECTION (ASTAR)
          C
0059      2700    NRFLCT = NRFLCT+1
0060              CALL REPLA(ASTAR,RSTAR)
0061              GO TO 1200
          C
          C       REPLACE A(,IH) BY EXPANSION (ASTAR2)
          C
0062      2800    NXPAND = NXPAND+1
0063              CALL REPLA(ASTAR2,RSTAR2)
0064              GO TO 1200
0065              END
```

```
0001              SUBROUTINE FPEAKS(CHB,NCHB,BKEVB,CHKEVB)
                  C
                  C FPEAK -- FIND PEAKS IN SPECTRUM
                  C
                  C ENTER:
                  C         CHB = DATA ARRAY TO BE FIT
                  C         NCHB = NUMBER OF CHANNELS TO BE FIT
                  C         BKEVB = ENERGY OF FIRST CHANNEL IN KEV
                  C         CHKEVB = ENERGY PER CHANNEL IN KEV
                  C
0002              INCLUDE 'SPECT.COM'
                *  C
                *  C         NCH:     NUMBER OF DATA CHANNELS
                *  C         BKEV:    ENERGY OF FIRST CHANNEL IN KEV
                *  C         CHKEV:   ENERGY PER CHANNEL IN KEV
                *  C         CH:      ARRAY OF CHANNEL COUNTS
0003            *         COMMON /SPECT/ NCH,BKEV,CHKEV,CH(1024)
0004              DIMENSION CHB(NCHB)
                  C         LINLST(,1): MAJOR PEAK ENERGIES, IE., KALPHA, KBETA, LALPHA1,
                  C         LBETA1, LGAMMA1, MALPHA, MBETA, MGAMMA.
0005              DIMENSION LINLST(18,2)
                  C         LINLST(,2) ALL PEAK ENERGIES.
0006              DATA LINLST/8,1,2,3,5,9,13,14,15,0,0,0,0,0,0,0,0,0,
                 +  17,1,2,3,4,5,6,7,8,9,10,11,12,13,14,15,16,17/
0007              WRITE (5,10)
0008    10        FORMAT ('$ENTER 1 FOR MANUAL MODE, 2 FOR AUTO MODE: ')
0009              READ (5,20) MODE
0010    20        FORMAT (I4)
0011              GO TO (100,200),MODE
                  C
                  C         MANUAL MODE
                  C
0012    100       CALL MANUPK
0013              RETURN
                  C
                  C         AUTO MODE
                  C
0014    200       NCH = NCHB
0015              BKEV = BKEVB
0016              CHKEV = CHKEVB
0017              DO 210 I=1,NCHB
0018              CH(I) = CHB(I)
0019    210       CONTINUE
0020              WRITE (5,220)
0021    220       FORMAT ('$ENTER 1 FOR MAJOR PEAKS, 2 FOR ALL PEAKS: ')
0022              READ (5,230) MODE
0023    230       FORMAT (I10)
0024              CALL AUTOPK(LINLST(1,MODE))
0025              RETURN
0026              END



0001              SUBROUTINE GAUSPK(M,T,I)
                  C
                  C GAUSPK -- GAUSSIAN PEAK FUNCTION
                  C
                  C ENTER:
                  C         M = NUMBER OF PEAKS
                  C         I = CHANNEL NUMBER
                  C
```

```
      C RETURNS:
      C       T = T(J) IS VALUE OF GAUSSIAN FOR PEAK J AT CHANNEL I
      C
0002          INCLUDE 'PEAKS.COM'
     *  C
     *  C       NPEAK:  NUMBER OF PEAKS
     *  C       FWHMMN: FULL WIDTH AT HALF MAXIMUM FOR MANGANESE PEAK (EV)
     *  C       IBP:    INDEX OF BIGGEST PEAK
     *  C       PKA:    PKA(I) IS ESTIMATED AMPLITUDE OF ITH PEAK
     *  C       PKE:    PKE(I) IS ESTIMATED ENERGY (KEV) OF ITH PEAK
     *  C       PKS:    PKS(I) IS ESTIMATED SIGMA (KEV) OF ITH PEAK
     *  C       IZPK:   ATOMIC NUMBER OF ITH PEAK
     *  C       IDPK:   LINE CODE OF ITH PEAK
     *  C       IX:     ARRAY OF INDICES WHICH SORT PEAKS BY ENERGY
     *  C       DPKE:   DPKE(I) IS PKE(I) - PKE(IBP)
0003 *          COMMON /PEAKS/ NPEAK,FWHMMN,IBP,PKA(14),PKE(14),PKS(14),
     *       +  IZPK(14),IDPK(14),IX(14),DPKE(14)
0004          INCLUDE 'SPECT.COM'
     *  C
     *  C       NCH:    NUMBER OF DATA CHANNELS
     *  C       BKEV:   ENERGY OF FIRST CHANNEL IN KEV
     *  C       CHKEV:  ENERGY PER CHANNEL IN KEV
     *  C       CH:     ARRAY OF CHANNEL COUNTS
0005 *          COMMON /SPECT/ NCH,BKEV,CHKEV,CH(1024)
0006          DIMENSION T(M)
0007          ENERGY = BKEV+(I-1)*CHKEV
0008          DO 10 J=1,M
0009          T(J) = EXP(-.5*((ENERGY-PKE(J))/PKS(J))**2)
0010     10   CONTINUE
0011          RETURN
0012          END



0001          LOGICAL FUNCTION INPAR
      C
      C INPAR -- INPUT PARAMETERS
      C
      C RETURNS:
      C       .TRUE. IF PARAMETERS RETURNED
      C       .FALSE. IF EOF ON INPUT REACHED
      C
0002          INCLUDE 'LIMITS.COM'
     *  C
     *  C       LIMSW:  1 = LIMITS ENABLED, 0 = LIMITS DISABLED
     *  C       SIGMAX: MAXIMUM SIGMA OF BIGGEST PEAK (EV)
     *  C       SIGMIN: MINIMUM SIGMA OF BIGGEST PEAK (EV)
     *  C       EMAX:   MAXIMUM ENERGY OF BIGGEST PEAK (KEV)
     *  C       EMIN:   MINIMUM ENERGY OF BIGGEST PEAK (KEV)
     *  C       AMAX:   MAXIMUM AMPLITUDE OF ANY PEAK
     *  C       LCODE:  LIMIT COUNTS
0003 *          COMMON /LIMITS/ LIMSW,SIGMAX,SIGMIN,EMAX,EMIN,AMAX,LCODE(16)
0004          INPAR = .FALSE.
0005          WRITE (5,10)
0006     10   FORMAT ('$ENABLE CONSTRAINTS? (1=YES, 0=NO): ')
0007          READ (5,20,END=99) LIMSW
0008     20   FORMAT (I1)
0009          INPAR = .TRUE.
0010     99   RETURN
0011          END
```

```
0001              SUBROUTINE INSIMP
                  C
                  C INSIMP -- INITIALIZE SIMPLEX MATRIX
                  C
0002              INCLUDE 'PEAKS.COM'
                  *  C
                  *  C       NPEAK:  NUMBER OF PEAKS
                  *  C       FWHMMN: FULL WIDTH AT HALF MAXIMUM FOR MANGANESE PEAK (EV)
                  *  C       IBP:    INDEX OF BIGGEST PEAK
                  *  C       PKA:    PKA(I) IS ESTIMATED AMPLITUDE OF ITH PEAK
                  *  C       PKE:    PKE(I) IS ESTIMATED ENERGY (KEV) OF ITH PEAK
                  *  C       PKS:    PKS(I) IS ESTIMATED SIGMA (KEV) OF ITH PEAK
                  *  C       IZPK:   ATOMIC NUMBER OF ITH PEAK
                  *  C       IDPK:   LINE CODE OF ITH PEAK
                  *  C       IX:     ARRAY OF INDICES WHICH SORT PEAKS BY ENERGY
                  *  C       DPKE:   DPKE(I) IS PKE(I) - PKE(IBP)
0003              *  COMMON /PEAKS/ NPEAK,FWHMMN,IBP,PKA(14),PKE(14),PKS(14),
                  *     +  IZPK(14),IDPK(14),IX(14),DPKE(14)
0004              INCLUDE 'SMAT.COM'
                  *  C
                  *  C       NAXES:  NUMBER OF AXES (= NPEAK+2)
                  *  C       NVERT:  NUMBER OF VERTICES (= NPEAK+3)
                  *  C       TOLER:  TOLERANCE FOR PARAMETER CONVERGENCE
                  *  C       IL:     INDEX OF LOWEST RESPONSE VERTEX
                  *  C       IH:     INDEX OF HIGHEST RESPONSE VERTEX
                  *  C       A:      SIMPLEX MATRIX
                  *  C               A(*,I) = ITH VERTEX OF THE SIMPLEX
                  *  C               A(1,I) = SIGMA OF LARGEST PEAK (KEV)
                  *  C               A(2,I) = ENERGY OF LARGEST PEAK (KEV)
                  *  C               A(J,I), 3 >= J <= NPEAK+2 = AMPLITUDE OF JTH PEAK
                  *  C       R:      R(I) IS THE RESPONSE OF THE ITH VERTEX
0005              *  COMMON /SMAT/ NAXES,NVERT,TOLER,IL,IH,A(16,17),R(17)
                  C
                  C       SET SIGMA OF BIGGEST PEAK ESTIMATE
                  C
0006              A(1,1) = PKSIG(FWHMMN*4.2466E-4,PKE(IBP)-5.895)
                  C
                  C       SET ENERGY OF BIGGEST PEAK ESTIMATE
                  C
0007              A(2,1) = PKE(IBP)
                  C
                  C       SET PEAK AMPLITUDE ESTIMATES
                  C
0008              DO 10 J=1,NPEAK
0009              A(J+2,1) = PKA(J)
0010     10       CONTINUE
                  C
                  C       COPY FIRST VERTEX TO ALL OTHERS
                  C
0011              DO 20 I=2,NVERT
0012              DO 20 J=1,NAXES
0013              A(J,I) = A(J,1)
0014     20       CONTINUE
                  C
                  C       PERTURB ONE PARAMETER ESTIMATE OF ALL BUT FIRST VERTEX TO
                  C       FORM INITIAL SIMPLEX.
                  C
                  C       PERTURB A SIGMA OF BIGGEST PEAK
                  C
0015              A(1,2) = A(1,2)*.99
                  C
                  C       PERTURB AN ENERGY OF BIGGEST PEAK
                  C
```

```
0016              A(2,3) = A(2,3)*.999
                  C
                  C       PERTURB PEAK AMPLITUDES
                  C
0017              DO 30 J=1,NPEAK
0018              A(J+2,J+3) = A(J+2,J+3)*.9
0019        30    CONTINUE
0020              RETURN
0021              END



0001              LOGICAL FUNCTION LIMIT(VERTEX)
                  C
                  C LIMIT -- TEST VERTEX AGAINST LIMITS
                  C
                  C ENTER:
                  C       VERTEX = VERTEX TO BE CHECKED
                  C
                  C RETURNS:
                  C       .TRUE. IF THE SPECIFIED VERTEX EXCEEDS A LIMIT
                  C       .FALSE. IF THE SPECIFIED VERTEX IS WITHIN LIMITS
                  C
0002              DIMENSION VERTEX(16)
0003              INCLUDE 'PEAKS.COM'
                  *   C
                  *   C       NPEAK:  NUMBER OF PEAKS
                  *   C       FWHMMN: FULL WIDTH AT HALF MAXIMUM FOR MANGANESE PEAK (EV)
                  *   C       IBP:    INDEX OF BIGGEST PEAK
                  *   C       PKA:    PKA(I) IS ESTIMATED AMPLITUDE OF ITH PEAK
                  *   C       PKE:    PKE(I) IS ESTIMATED ENERGY (KEV) OF ITH PEAK
                  *   C       PKS:    PKS(I) IS ESTIMATED SIGMA (KEV) OF ITH PEAK
                  *   C       IZPK:   ATOMIC NUMBER OF ITH PEAK
                  *   C       IDPK:   LINE CODE OF ITH PEAK
                  *   C       IX:     ARRAY OF INDICES WHICH SORT PEAKS BY ENERGY
                  *   C       DPKE:   DPKE(I) IS PKE(I) - PKE(IBP)
0004              *           COMMON /PEAKS/ NPEAK,FWHMMN,IBP,PKA(14),PKE(14),PKS(14),
                  *       +   IZPK(14),IDPK(14),IX(14),DPKE(14)
0005              INCLUDE 'SMAT.COM'
                  *   C
                  *   C       NAXES:  NUMBER OF AXES (= NPEAK+2)
                  *   C       NVERT:  NUMBER OF VERTICES (= NPEAK+3)
                  *   C       TOLER:  TOLERANCE FOR PARAMETER CONVERGENCE
                  *   C       IL:     INDEX OF LOWEST RESPONSE VERTEX
                  *   C       IH:     INDEX OF HIGHEST RESPONSE VERTEX
                  *   C       A:      SIMPLEX MATRIX
                  *   C               A(*,I) = ITH VERTEX OF THE SIMPLEX
                  *   C               A(1,I) = SIGMA OF LARGEST PEAK (KEV)
                  *   C               A(2,I) = ENERGY OF LARGEST PEAK (KEV)
                  *   C               A(J,I), 3 >= J <= NPEAK+2 = AMPLITUDE OF JTH PEAK
                  *   C       R:      R(I) IS THE RESPONSE OF THE ITH VERTEX
0006              *           COMMON /SMAT/ NAXES,NVERT,TOLER,IL,IH,A(16,17),R(17)
0007              INCLUDE 'LIMITS.COM'
                  *   C
                  *   C       LIMSW:  1 = LIMITS ENABLED, 0 = LIMITS DISABLED
                  *   C       SIGMAX: MAXIMUM SIGMA OF BIGGEST PEAK (EV)
                  *   C       SIGMIN: MINIMUM SIGMA OF BIGGEST PEAK (EV)
                  *   C       EMAX:   MAXIMUM ENERGY OF BIGGEST PEAK (KEV)
                  *   C       EMIN:   MINIMUM ENERGY OF BIGGEST PEAK (KEV)
                  *   C       AMAX:   MAXIMUM AMPLITUDE OF ANY PEAK
                  *   C       LCODE:  LIMIT COUNTS
0008              *           COMMON /LIMITS/ LIMSW,SIGMAX,SIGMIN,EMAX,EMIN,AMAX,LCODE(16)
```

```
0009              IF (LIMSW .EQ. 0) GO TO 100
        CD        L=1
0010              IF (VERTEX(1) .GT. SIGMAX) GO TO 200
        CD        L=2
0011              IF (VERTEX(1) .LT. SIGMIN) GO TO 200
        CD        L=3
0012              IF (VERTEX(2) .GT. EMAX) GO TO 200
        CD        L=4
0013              IF (VERTEX(2) .LT. EMIN) GO TO 200
        CD        L=5
        C         DO 10 I=1,NPEAK
        C         IF (VERTEX(I+2) .LT. 0) GO TO 200
        C         IF (VERTEX(I+2) .GT. AMAX) GO TO 200
0014    10        CONTINUE
        C
        C         ALL PARAMETERS ARE WITHIN LIMITS
        C
0015    100       LIMIT=.FALSE.
0016              RETURN
        C
        C         PARAMETER OUTSIDE LIMITS
        C
0017    200       CONTINUE
        CD        LCODE(L) = LCODE(L)+1
        CD        WRITE (5,*) L,(VERTEX(I),I=1,NAXES)
0018              LIMIT=.TRUE.
0019              RETURN
0020              END



0001              SUBROUTINE MANUPK
        C
        C MANUPK -- MANUAL ENTRY OF PEAK INFORMATION
        C
0002              INCLUDE 'PEAKS.COM'
     *  C
     *  C         NPEAK:  NUMBER OF PEAKS
     *  C         FWHMMN: FULL WIDTH AT HALF MAXIMUM FOR MANGANESE PEAK (EV)
     *  C         IBP:    INDEX OF BIGGEST PEAK
     *  C         PKA:    PKA(I) IS ESTIMATED AMPLITUDE OF ITH PEAK
     *  C         PKE:    PKE(I) IS ESTIMATED ENERGY (KEV) OF ITH PEAK
     *  C         PKS:    PKS(I) IS ESTIMATED SIGMA (KEV) OF ITH PEAK
     *  C         IZPK:   ATOMIC NUMBER OF ITH PEAK
     *  C         IDPK:   LINE CODE OF ITH PEAK
     *  C         IX:     ARRAY OF INDICES WHICH SORT PEAKS BY ENERGY
     *  C         DPKE:   DPKE(I) IS PKE(I) - PKE(IBP)
0003 *            COMMON /PEAKS/ NPEAK,FWHMMN,IBP,PKA(14),PKE(14),PKS(14),
     *       +    IZPK(14),IDPK(14),IX(14),DPKE(14)
0004    5         WRITE (5,10)
0005    10        FORMAT ('$ENTER NUMBER OF PEAKS (14 MAX): ')
0006              READ (5,20) NPEAK
0007    20        FORMAT (I2)
0008              IF (NPEAK .GT. 16-2) GO TO 5
0009              WRITE (5,30)
0010    30        FORMAT (' ENTER AMPLITUDE AND ENERGY (KEV) OF EACH PEAK: ')
0011              DO 50 I=1,NPEAK
0012              READ (5,40) PKA(I),PKE(I)
0013    40        FORMAT (2F15.0)
0014    50        CONTINUE
        C
        C         SORT PEAKS INTO ORDER OF INCREASING ENERGY
        C
```

```
0015              CALL SORTPK(NPEAK,PKE,IX)
0016              RETURN
0017              END



0001              FUNCTION PKSIG(SIGMAP,DELTAE)
                  C
                  C PKSIG -- COMPUTE SIGMA OF PEAK FROM SIGMA OF BIGGEST PEAK
                  C
                  C ENTER:
                  C       SIGMAP = SIGMA OF BIGGEST PEAK IN KEV
                  C       DELTAE = ENERGY DIFFERENCE FROM BIGGEST PEAK IN KEV
                  C
                  C RETURNS:
                  C       SIGMA OF THE PEAK IN KEV
                  C
0002              PKSIG=SQRT(2500*DELTAE+(2354.825*SIGMAP)**2)*4.2466E-4
0003              RETURN
0004              END



0001              SUBROUTINE RDSPEC
                  C
                  C RDSPEC -- READ SPECTRUM
                  C
                  C THIS ROUTINE READS THE SPECTRUM DATA TO BE FIT (IN THIS CASE FROM
                  C A KEVEX 7000 ANALYTICAL SPECTROMETER), DETERMINES THE ENERGY
                  C RANGE TO BE PROCESSED, PADS THE DATA AT BEGINNING AND END FOR
                  C POLYNOMIAL SMOOTHING, CHANGES ANY ZERO CHANNEL COUNTS TO ONE
                  C TO AVOID DIVIDE OVERFLOW, AND SETS FWHM(MN).
                  C
0002              INCLUDE 'PEAKS.COM'
                *  C
                *  C       NPEAK:  NUMBER OF PEAKS
                *  C       FWHMMN: FULL WIDTH AT HALF MAXIMUM FOR MANGANESE PEAK (EV)
                *  C       IBP:    INDEX OF BIGGEST PEAK
                *  C       PKA:    PKA(I) IS ESTIMATED AMPLITUDE OF ITH PEAK
                *  C       PKE:    PKE(I) IS ESTIMATED ENERGY (KEV) OF ITH PEAK
                *  C       PKS:    PKS(I) IS ESTIMATED SIGMA (KEV) OF ITH PEAK
                *  C       IZPK:   ATOMIC NUMBER OF ITH PEAK
                *  C       IDPK:   LINE CODE OF ITH PEAK
                *  C       IX:     ARRAY OF INDICES WHICH SORT PEAKS BY ENERGY
                *  C       DPKE:   DPKE(I) IS PKE(I) - PKE(IBP)
0003            *       COMMON /PEAKS/ NPEAK,FWHMMN,IBP,PKA(14),PKE(14),PKS(14),
                *      +  IZPK(14),IDPK(14),IX(14),DPKE(14)
0004              INCLUDE 'SPECTB.COM'
                *  C
                *  C       NCHB:   TOTAL NUMBER OF DATA CHANNELS IN BUFFER
                *  C       ICHW:   INDEX OF FIRST CHANNEL IN ANALYSIS WINDOW
                *  C       NCHW:   NUMBER OF CHANNELS IN ANALYSIS WINDOW
                *  C       BKEVB:  ENERGY OF FIRST CHANNEL IN KEV (BUFFER)
                *  C       CHKEVB: ENERGY PER CHANNEL IN KEV (BUFFER)
                *  C       CHB:    ARRAY OF CHANNEL COUNTS (BUFFER)
0005            *       COMMON /SPECTB/ NCHB,ICHW,NCHW,BKEVB,CHKEVB,CHB(1028)
                  C
                  C       INPUT QUADRANT NUMBER
                  C
0006              100     WRITE (5,110)
0007              110     FORMAT ('$ENTER QUADRANT NUMBER:')
```

```
0008              READ (5,120) KQUAD
0009     120      FORMAT (I10)
0010              IF (KQUAD .GE. 1 .AND. KQUAD .LE. 4) GO TO 140
0011              WRITE (5,130)
0012     130      FORMAT (' INVALID QUADRANT')
0013              GO TO 100
         C
         C        LOCATE "A" WINDOW
         C
0014     140      ICHNL=(KQUAD-1)*1024
0015              CALL KXWIN(ICHNL+12,ICHNL+1023,"001,ICHW,NCHW)
0016              IF (NCHW .GT. 0) GO TO 160
0017              WRITE (5,150)
0018     150      FORMAT (' NO WINDOW SPECIFIED')
0019              GO TO 100
         C
         C        READ CHANNEL DATA FROM KEVEX
         C
0020     160      CALL KXRCHS(ICHNL+12,1012,CHB(3))
         C
         C        SET PARAMETERS
         C
0021              CHKEVB=0.01
0022              BKEVB=ICHW*CHKEVB
0023              EKEVB=BKEVB+(NCHW-1)*CHKEVB
0024              ICHW=ICHW-12+3
0025              NCHB=ICHW-1+NCHW+2
         C
         C        ADD 2 ONES AT BEGINNING AND END FOR POLYNOMIAL SMOOTHING
         C
0026              CHB(1) = 1.
0027              CHB(2) = 1.
0028              CHB(2+1012+1) = 1.
0029              CHB(2+1012+2) = 1.
         C
         C        CHANGE ALL CHANNELS WITH 0 COUNTS TO HAVE 1 COUNT
         C
0030              DO 165 I=ICHW,ICHW+NCHW-1
0031              IF (CHB(I).EQ.0.) CHB(I)=1.
0032     165      CONTINUE
         C
         C        DISPLAY SPECTRUM INFORMATION
         C
0033              WRITE (5,170) NCHW,BKEVB,EKEVB
0034     170      FORMAT (1X,' PROCESSING',I4,' CHANNELS FROM',F7.3,
                +  ' TO',F7.3,' KEV')
         C
         C        GET FWHM(MN)
         C
0035              WRITE (5,180)
0036     180      FORMAT ('$ENTER FWHM(Mn) (EV): ')
0037              READ (5,190) FWHMMN
0038     190      FORMAT(F10.3)
0039              RETURN
         C
         C        ERROR PROCESSING
         C
0040     900      WRITE (5,910)
0041     910      FORMAT (' NO ANALYSIS WINDOW SPECIFIED')
0042              STOP
0043              END
```

```
0001            SUBROUTINE REGRES(N,Y,M,F,A,B,T,C)
                C
                C REGRES -- PERFORM MULTIPLE LINEAR REGRESSION
                C
                C ENTER:
                C       N = NUMBER OF DATA POINTS
                C       Y = Y(N) ARRAY CONTAINING DATA POINTS
                C       M = NUMBER OF PARAMETERS
                C       F = EXTERNAL SUBROUTINE F(M,T,I) TO RETURN THE M FUNCTION VALUES
                C               AT DATA POINT I IN ARRAY T
                C       A = A(M,M) SCRATCH MATRIX
                C       B = B(M) SCRATCH ARRAY
                C       T = T(M) SCRATCH ARRAY
                C
                C RETURNS:
                C       C = C(M) -- PARAMETER VALUES
                C
                C CALLS:
                C       MINV -- MATRIX INVERSION
                C       GMPRD -- GENERAL MATRIX PRODUCT
                C       (SEE THE SCIENTIFIC SUBROUTINES REFERENCE MANUAL,
                C       DIGITAL EQUIPMENT CORP. FOR DOCUMENTATION)
                C
0002            DIMENSION Y(N),A(M,M),B(M),T(M),C(M)
                C
                C       INITIALIZATION
                C
0003            DO 100 J=1,M
0004            B(J) = 0.0
0005            DO 100 K=1,M
0006            A(J,K) = 0.0
0007    100     CONTINUE
                C
                C       COMPUTE WEIGHTED SUMS OF CROSS PRODUCTS
                C
0008            DO 200 I=1,N
0009            CALL F(M,T,I)
0010            DO 200 J=1,M
0011            B(J) = B(J)+T(J)
0012            DO 200 K=1,M
0013            A(J,K) = A(J,K)+T(J)*T(K)/Y(I)
0014    200     CONTINUE
                C
                C       INVERT MATRIX A
                C
0015            CALL MINV(A,M,D,C,T)
                C
                C       COMPUTE PARAMETERS
                C
0016            CALL GMPRD(A,B,C,M,M,1)
0017            RETURN
0018            END



0001            SUBROUTINE REPLA(VERTEX,RESP)
                C
                C REPLA -- REPLACE A(,IH) BY SPECIFIED VERTEX
                C
                C ENTER:
                C       VERTEX = VERTEX TO REPLACE A(,IH)
                C       RESP = RESPONSE TO REPLACE R(IH)
                C
```

```
0002              DIMENSION VERTEX(16)
0003              INCLUDE 'SMAT.COM'
      *   C
      *   C       NAXES:  NUMBER OF AXES (= NPEAK+2)
      *   C       NVERT:  NUMBER OF VERTICES (= NPEAK+3)
      *   C       TOLER:  TOLERANCE FOR PARAMETER CONVERGENCE
      *   C       IL:     INDEX OF LOWEST RESPONSE VERTEX
      *   C       IH:     INDEX OF HIGHEST RESPONSE VERTEX
      *   C       A:      SIMPLEX MATRIX
      *   C               A(*,I) = ITH VERTEX OF THE SIMPLEX
      *   C               A(1,I) = SIGMA OF LARGEST PEAK (KEV)
      *   C               A(2,I) = ENERGY OF LARGEST PEAK (KEV)
      *   C               A(J,I), 3 >= J <= NPEAK+2 = AMPLITUDE OF JTH PEAK
      *   C       R:      R(I) IS THE RESPONSE OF THE ITH VERTEX
0004  *           COMMON /SMAT/ NAXES,NVERT,TOLER,IL,IH,A(16,17),R(17)
0005              DO 10 J=1,NAXES
0006      10      A(J,IH) = VERTEX(J)
0007              R(IH) = RESP
0008              RETURN
0009              END



0001              SUBROUTINE REPORT(VERTEX,RESP)
          C
          C REPORT -- REPORT RESULTS
          C
          C ENTER:
          C       VERTEX = VERTEX WITH LOWEST RESPONSE (I.E. A(1,IL))
          C       RESP = RESPONSE OF SPECIFIED VERTEX
          C
0002              DIMENSION VERTEX(16)
0003              INCLUDE 'PEAKS.COM'
      *   C
      *   C       NPEAK:  NUMBER OF PEAKS
      *   C       FWHMMN: FULL WIDTH AT HALF MAXIMUM FOR MANGANESE PEAK (EV)
      *   C       IBP:    INDEX OF BIGGEST PEAK
      *   C       PKA:    PKA(I) IS ESTIMATED AMPLITUDE OF ITH PEAK
      *   C       PKE:    PKE(I) IS ESTIMATED ENERGY (KEV) OF ITH PEAK
      *   C       PKS:    PKS(I) IS ESTIMATED SIGMA (KEV) OF ITH PEAK
      *   C       IZPK:   ATOMIC NUMBER OF ITH PEAK
      *   C       IDPK:   LINE CODE OF ITH PEAK
      *   C       IX:     ARRAY OF INDICES WHICH SORT PEAKS BY ENERGY
      *   C       DPKE:   DPKE(I) IS PKE(I) - PKE(IBP)
0004  *           COMMON /PEAKS/ NPEAK,FWHMMN,IBP,PKA(14),PKE(14),PKS(14),
      *         + IZPK(14),IDPK(14),IX(14),DPKE(14)
0005              INCLUDE 'SMAT.COM'
      *   C
      *   C       NAXES:  NUMBER OF AXES (= NPEAK+2)
      *   C       NVERT:  NUMBER OF VERTICES (= NPEAK+3)
      *   C       TOLER:  TOLERANCE FOR PARAMETER CONVERGENCE
      *   C       IL:     INDEX OF LOWEST RESPONSE VERTEX
      *   C       IH:     INDEX OF HIGHEST RESPONSE VERTEX
      *   C       A:      SIMPLEX MATRIX
      *   C               A(*,I) = ITH VERTEX OF THE SIMPLEX
      *   C               A(1,I) = SIGMA OF LARGEST PEAK (KEV)
      *   C               A(2,I) = ENERGY OF LARGEST PEAK (KEV)
      *   C               A(J,I), 3 >= J <= NPEAK+2 = AMPLITUDE OF JTH PEAK
      *   C       R:      R(I) IS THE RESPONSE OF THE ITH VERTEX
0006  *           COMMON /SMAT/ NAXES,NVERT,TOLER,IL,IH,A(16,17),R(17)
```

```
0007              INCLUDE 'COUNTS.COM'
     *  C
     *  C         ITER8:  ITERATION COUNTER (PER PASS)
     *  C         NRFLCT: REFLECTION COUNTER
     *  C         NXPAND: EXPANSION COUNTER
     *  C         NCONTR: CONTRACTION COUNTER
     *  C         NSHIFT: SHIFT COUNTER
     *  C         NTOTAL: TOTAL NUMBER OF ITERATIONS
0008 *            COMMON /COUNTS/ ITER8,NRFLCT,NXPAND,NCONTR,NSHIFT,NTOTAL
         C
         C        OUTPUT COUNTERS
         C
0009              WRITE (5,10) NTOTAL,NRFLCT,NXPAND,NCONTR,NSHIFT
0010     10       FORMAT (///1X,I5,' ITERATIONS',I5,' REFLECTIONS',I5,
               +  ' EXPANSIONS',I5,' CONTRACTIONS',I5,' SHIFTS')
         C
         C        OUTPUT FIT DATA FOR BIGGEST PEAK
         C
0011              FWHM = 2354.825*PKSIG(VERTEX(1),0)
0012              XFWHMM = 2354.825*PKSIG(VERTEX(1),5.895-VERTEX(2))
0013              WRITE (5,20) RESP,VERTEX(2),FWHM,XFWHMM
0014     20       FORMAT (1X,'RESPONSE=',G12.6,'  ENERGY=',F7.3,
               +  '  FWHM=',F7.2,'  FWHM(MN)=',F7.2)
         C
         C        OUTPUT FIT SUMMARY FOR ALL PEAKS
         C
0015              WRITE (5,30)
0016     30       FORMAT (/'  AMPLITUDE     ENERGY       SIGMA      A*SIGMA')
0017              DO 50 I=1,NPEAK
0018              ENERGY = DPKE(IX(I))+VERTEX(2)
0019              SIGMA = PKSIG(VERTEX(1),DPKE(IX(I)))
0020              ASIGMA = VERTEX(IX(I)+2)*SIGMA
0021              WRITE (5,40) VERTEX(IX(I)+2),ENERGY,SIGMA,ASIGMA
0022     40       FORMAT (1X,4G12.5)
0023     50       CONTINUE
0024              RETURN
0025              END



0001              FUNCTION RESP(VERTEX)
         C
         C RESP -- COMPUTE RESPONSE OF SPECIFIED VERTEX
         C
         C ENTER:
         C        VERTEX = VERTEX TO CALCULATE RESPONSE FUNCTION FOR
         C
         C RETURNS:
         C        RESPONSE OF THE SPECIFIED VERTEX
         C
0002              DIMENSION VERTEX(16)
0003              LOGICAL LIMIT
0004              INCLUDE 'PEAKS.COM'
     *  C
     *  C         NPEAK:  NUMBER OF PEAKS
     *  C         FWHMMN: FULL WIDTH AT HALF MAXIMUM FOR MANGANESE PEAK (EV)
     *  C         IBP:    INDEX OF BIGGEST PEAK
     *  C         PKA:    PKA(I) IS ESTIMATED AMPLITUDE OF ITH PEAK
     *  C         PKE:    PKE(I) IS ESTIMATED ENERGY (KEV) OF ITH PEAK
     *  C         PKS:    PKS(I) IS ESTIMATED SIGMA (KEV) OF ITH PEAK
     *  C         IZPK:   ATOMIC NUMBER OF ITH PEAK
```

```
     *  C        IDPK:    LINE CODE OF ITH PEAK
     *  C        IX:      ARRAY OF INDICES WHICH SORT PEAKS BY ENERGY
     *  C        DPKE:    DPKE(I) IS PKE(I) - PKE(IBP)
0005 *           COMMON /PEAKS/ NPEAK,FWHMMN,IBP,PKA(14),PKE(14),PKS(14),
     *         +  IZPK(14),IDPK(14),IX(14),DPKE(14)
0006             INCLUDE 'SMAT.COM'
     *  C
     *  C        NAXES:   NUMBER OF AXES (= NPEAK+2)
     *  C        NVERT:   NUMBER OF VERTICES (= NPEAK+3)
     *  C        TOLER:   TOLERANCE FOR PARAMETER CONVERGENCE
     *  C        IL:      INDEX OF LOWEST RESPONSE VERTEX
     *  C        IH:      INDEX OF HIGHEST RESPONSE VERTEX
     *  C        A:       SIMPLEX MATRIX
     *  C                 A(*,I) = ITH VERTEX OF THE SIMPLEX
     *  C                 A(1,I) = SIGMA OF LARGEST PEAK (KEV)
     *  C                 A(2,I) = ENERGY OF LARGEST PEAK (KEV)
     *  C                 A(J,I), 3 >= J <= NPEAK+2 = AMPLITUDE OF JTH PEAK
     *  C        R:       R(I) IS THE RESPONSE OF THE ITH VERTEX
0007 *           COMMON /SMAT/ NAXES,NVERT,TOLER,IL,IH,A(16,17),R(17)
0008             INCLUDE 'SPECT.COM'
     *  C
     *  C        NCH:     NUMBER OF DATA CHANNELS
     *  C        BKEV:    ENERGY OF FIRST CHANNEL IN KEV
     *  C        CHKEV:   ENERGY PER CHANNEL IN KEV
     *  C        CH:      ARRAY OF CHANNEL COUNTS
0009 *           COMMON /SPECT/ NCH,BKEV,CHKEV,CH(1024)
0010             IF (LIMIT(VERTEX)) GO TO 30
0011             RESP=0.
0012             DO 20 J=1,NCH
0013             Y=0.
0014             E=BKEV+CHKEV*(J-1)
0015             DO 10 I=1,NPEAK
0016             Y=Y+VERTEX(I+2)*EXP(-0.5*((E-(DPKE(I)+VERTEX(2)))/
               +  PKSIG(VERTEX(1),DPKE(I)))**2)
0017     10      CONTINUE
0018             RESP=RESP+(CH(J)-Y)**2/AMAX1(Y,1.0)
0019     20      CONTINUE
0020             RESP=RESP/(NCH-NAXES)
0021             RETURN
0022     30      RESP=1E19
0023             RETURN
0024             END



0001             SUBROUTINE SETLIM(CH,NCH)
                 C
                 C SETLIM -- SET PARAMETER LIMITS
                 C
                 C ENTER:
                 C        CH = ARRAY OF CHANNEL COUNTS
                 C        NCH = NUMBER OF DATA CHANNELS
                 C
0002             INCLUDE 'PEAKS.COM'
     *  C
     *  C        NPEAK:   NUMBER OF PEAKS
     *  C        FWHMMN:  FULL WIDTH AT HALF MAXIMUM FOR MANGANESE PEAK (EV)
     *  C        IBP:     INDEX OF BIGGEST PEAK
     *  C        PKA:     PKA(I) IS ESTIMATED AMPLITUDE OF ITH PEAK
     *  C        PKE:     PKE(I) IS ESTIMATED ENERGY (KEV) OF ITH PEAK
     *  C        PKS:     PKS(I) IS ESTIMATED SIGMA (KEV) OF ITH PEAK
     *  C        IZPK:    ATOMIC NUMBER OF ITH PEAK
     *  C        IDPK:    LINE CODE OF ITH PEAK
```

```
     *  C        IX:     ARRAY OF INDICES WHICH SORT PEAKS BY ENERGY
     *  C        DPKE:   DPKE(I) IS PKE(I) - PKE(IBP)
0003 *           COMMON /PEAKS/ NPEAK,FWHMMN,IBP,PKA(14),PKE(14),PKS(14),
     *        +  IZPK(14),IDPK(14),IX(14),DPKE(14)
0004             INCLUDE 'SPECTB.COM'
     *  C
     *  C        NCHB:   TOTAL NUMBER OF DATA CHANNELS IN BUFFER
     *  C        ICHW:   INDEX OF FIRST CHANNEL IN ANALYSIS WINDOW
     *  C        NCHW:   NUMBER OF CHANNELS IN ANALYSIS WINDOW
     *  C        BKEVB:  ENERGY OF FIRST CHANNEL IN KEV (BUFFER)
     *  C        CHKEVB: ENERGY PER CHANNEL IN KEV (BUFFER)
     *  C        CHB:    ARRAY OF CHANNEL COUNTS (BUFFER)
0005 *           COMMON /SPECTB/ NCHB,ICHW,NCHW,BKEVB,CHKEVB,CHB(1028)
0006             INCLUDE 'LIMITS.COM'
     *  C
     *  C        LIMSW:  1 = LIMITS ENABLED, 0 = LIMITS DISABLED
     *  C        SIGMAX: MAXIMUM SIGMA OF BIGGEST PEAK (EV)
     *  C        SIGMIN: MINIMUM SIGMA OF BIGGEST PEAK (EV)
     *  C        EMAX:   MAXIMUM ENERGY OF BIGGEST PEAK (KEV)
     *  C        EMIN:   MINIMUM ENERGY OF BIGGEST PEAK (KEV)
     *  C        AMAX:   MAXIMUM AMPLITUDE OF ANY PEAK
     *  C        LCODE:  LIMIT COUNTS
0007 *           COMMON /LIMITS/ LIMSW,SIGMAX,SIGMIN,EMAX,EMIN,AMAX,LCODE(16)
         C
         C       DFWHMM: FWHM(MN) UNCERTAINTY (EV)
         C       DEBPK:  ENERGY UNCERTAINTY OF BIGGEST PEAK (KEV)
0008             DATA DFWHMM/5./,DEBPK/.02/
         C
         C       SET MAXIMUM AND MINIMUM SIGMA OF BIGGEST PEAK
         C
0009             SIGMAX = PKSIG((FWHMMN+DFWHMM)*4.2466E-4,PKE(IBP)-5.895)
0010             SIGMIN = PKSIG((FWHMMN-DFWHMM)*4.2466E-4,PKE(IBP)-5.895)
         C
         C       SET MAXIMUM AND MINIMUM ENERGY OF BIGGEST PEAK
         C
0011             EMAX = PKE(IBP)+DEBPK
0012             EMIN = PKE(IBP)-DEBPK
         C
         C       FIND MAXIMUM AMPLITUDE
         C
0013             AMAX = -1.
0014             DO 10 I=3,NCHB-2
0015             IF (CHB(I) .GT. AMAX) AMAX = CHB(I)
0016     10      CONTINUE
         C
         C       SET AMPLITUDE LIMIT
         C
0017             AMAX = AMAX+3.2*SQRT(AMAX)
         C
         C       RESET LIMIT COUNTERS
         C
0018             DO 20 I=1,16
0019             LCODE(I)=0
0020     20      CONTINUE
0021             RETURN
0022             END
```

```
0001            SUBROUTINE SIMPLX(CHB,NCHB,BKEVB,CHKEVB,ETIME)
                C
                C SIMPLX -- SIMPLEX FIT CONTROL ROUTINE
                C
                C ENTER:
                C       CHB = DATA ARRAY TO BE FIT, INCLUDING 2 ADDITIONAL CHANNELS
                C             AT BEGINNING AND END
                C       NCHB = NUMBER OF CHANNELS TO BE FIT +4
                C       BKEVB = ENERGY OF FIRST CHANNEL (CHB(3)) IN KEV
                C       CHKEVB = ENERGY PER CHANNEL IN KEV
                C
                C       FOLLOWING COMMON VARIABLES MUST BE INITIALIZED:
                C
                C       NPEAK,FWHMMN,PKA,PKE
                C
                C RETURNS:
                C       ETIME = ELAPSED TIME TO PERFORM FIT IN SECONDS
                C
0002            DIMENSION CHB(NCHB)
0003            INCLUDE 'PEAKS.COM'
              * C
              * C       NPEAK:  NUMBER OF PEAKS
              * C       FWHMMN: FULL WIDTH AT HALF MAXIMUM FOR MANGANESE PEAK (EV)
              * C       IBP:    INDEX OF BIGGEST PEAK
              * C       PKA:    PKA(I) IS ESTIMATED AMPLITUDE OF ITH PEAK
              * C       PKE:    PKE(I) IS ESTIMATED ENERGY (KEV) OF ITH PEAK
              * C       PKS:    PKS(I) IS ESTIMATED SIGMA (KEV) OF ITH PEAK
              * C       IZPK:   ATOMIC NUMBER OF ITH PEAK
              * C       IDPK:   LINE CODE OF ITH PEAK
              * C       IX:     ARRAY OF INDICES WHICH SORT PEAKS BY ENERGY
              * C       DPKE:   DPKE(I) IS PKE(I) - PKE(IBP)
0004          *         COMMON /PEAKS/ NPEAK,FWHMMN,IBP,PKA(14),PKE(14),PKS(14),
              *       + IZPK(14),IDPK(14),IX(14),DPKE(14)
0005            INCLUDE 'SMAT.COM'
              * C
              * C       NAXES:  NUMBER OF AXES (= NPEAK+2)
              * C       NVERT:  NUMBER OF VERTICES (= NPEAK+3)
              * C       TOLER:  TOLERANCE FOR PARAMETER CONVERGENCE
              * C       IL:     INDEX OF LOWEST RESPONSE VERTEX
              * C       IH:     INDEX OF HIGHEST RESPONSE VERTEX
              * C       A:      SIMPLEX MATRIX
              * C               A(*,I) = ITH VERTEX OF THE SIMPLEX
              * C               A(1,I) = SIGMA OF LARGEST PEAK (KEV)
              * C               A(2,I) = ENERGY OF LARGEST PEAK (KEV)
              * C               A(J,I), 3 >= J <= NPEAK+2 = AMPLITUDE OF JTH PEAK
              * C       R:      R(I) IS THE RESPONSE OF THE ITH VERTEX
0006          *         COMMON /SMAT/ NAXES,NVERT,TOLER,IL,IH,A(16,17),R(17)
0007            INCLUDE 'SPECT.COM'
              * C
              * C       NCH:    NUMBER OF DATA CHANNELS
              * C       BKEV:   ENERGY OF FIRST CHANNEL IN KEV
              * C       CHKEV:  ENERGY PER CHANNEL IN KEV
              * C       CH:     ARRAY OF CHANNEL COUNTS
0008          *         COMMON /SPECT/ NCH,BKEV,CHKEV,CH(1024)
0009            INCLUDE 'COUNTS.COM'
              * C
              * C       ITER8:  ITERATION COUNTER (PER PASS)
              * C       NRFLCT: REFLECTION COUNTER
              * C       NXPAND: EXPANSION COUNTER
              * C       NCONTR: CONTRACTION COUNTER
              * C       NSHIFT: SHIFT COUNTER
              * C       NTOTAL: TOTAL NUMBER OF ITERATIONS
0010          *         COMMON /COUNTS/ ITER8,NRFLCT,NXPAND,NCONTR,NSHIFT,NTOTAL
                C
```

```
      C       INITIALIZATION
      C
0011          NAXES = NPEAK+2
0012          NVERT = NAXES+1
      C
      C       LOCATE BIGGEST PEAK
      C
0013          IBP = 1
0014          DO 100 I=2,NPEAK
0015          IF (PKA(I) .GT. PKA(IBP)) IBP=I
0016  100     CONTINUE
      C
      C       COMPUTE ENERGY DIFFERENCES FROM BIGGEST PEAK
      C
0017          DO 200 I=1,NPEAK
0018          DPKE(I) = PKE(I)-PKE(IBP)
0019  200     CONTINUE
      C
      C       SET SIMPLEX PARAMETER LIMITS
      C
0020          CALL SETLIM
      C
      C       SETUP INITIAL SIMPLEX MATRIX
      C
0021          ETIME = 0.
0022          TIME = SECNDS(0.)
0023          CALL INSIMP
      C
      C       APPLY POLYNOMIAL SMOOTHING TO INPUT SPECTRUM
      C
0024          NCH = 0
0025          DO 300 I=3,NCHB-2,2
0026          NCH = NCH+1
0027          CH(NCH) = (-3.0*CHB(I-2)+12.0*CHB(I-1)+17.0*CHB(I)
     +   +12.0*CHB(I+1)-3.0*CHB(I+2))/35.0
0028  300     CONTINUE
      C
      C       RESET COUNTERS
      C
0029          NREFLCT = 0
0030          NXPAND = 0
0031          NCONTR = 0
0032          NSHIFT = 0
      C
      C       FIT ALTERNATE POINTS OF SMOOTHED SPECTRUM
      C
0033          BKEV = BKEVB
0034          CHKEV = CHKEVB*2
0035          TOLER = 0.001
0036          CALL FIT
0037          NTOTAL = ITER8
0038          ETIME = ETIME+SECNDS(TIME)
      C
      C       OUTPUT RESULTS
      C
      C       CALL REPORT(A(1,IL),R(IL))
      C
      C       FIT RAW SPECTRUM
      C
```

```
0039            TIME = SECNDS(0.)
0040            DO 400 I=1,NCHB-4
0041            CH(I) = CHB(I+2)
0042    400     CONTINUE
0043            NCH = NCHB-4
0044            CHKEV = CHKEVB
0045            TOLER = 0.00001
0046            CALL FIT
0047            NTOTAL = NTOTAL+ITER8
0048            ETIME = ETIME+SECNDS(TIME)
        C
        C       OUTPUT RESULTS OF FINAL FIT
        C
        C       CALL REPORT(A(1,IL),R(IL))
0049            RETURN
0050            END



0001            SUBROUTINE SORTPK(N,AKEY,INDEX)
        C
        C SORTPK -- CALL SORTUP TO SORT SPECTRUM PEAKS
        C
        C ENTER:
        C       N = NUMBER OF KEYS TO SORT
        C       AKEY = KEY ARRAY TO COMPUTE PERMUTATION INDEX FOR
        C
        C RETURNS:
        C       INDEX = PERMUTATION WHICH SORTS KEY ARRAY INTO ASCENDING ORDER
        C
0002            DIMENSION AKEY(N),INDEX(N)
0003            DIMENSION TEMP(14)
0004            DO 10 I=1,N
0005            TEMP(I) = AKEY(I)
0006            INDEX(I) = I
0007    10      CONTINUE
0008            CALL SORTUP(N,TEMP,INDEX)
0009            RETURN
0010            END



0001            SUBROUTINE SORTUP(N,AKEY,IDATA)
        C
        C SORTUP -- SORT ARRAY INTO ASCENDING ORDER
        C
        C ENTER:
        C       N = NUMBER OF ITEMS IN ARRAY
        C       AKEY = ARRAY CONTAINING SORT KEY
        C       IDATA = AUXILIARY DATA ARRAY TO BE SORTED
        C
        C RETURNS:
        C       AKEY = INPUT ARRAY SORTED IN ASCENDING ORDER
        C       IDATA = INPUT ARRAY SORTED BY AKEY ARRAY
        C
```

```
0002            DIMENSION AKEY(N),IDATA(N)
0003            IF (N .LT. 2) RETURN
      C
      C         SELECTION SORT
      C
0004            L = N-1
0005            DO 20 I=1,L
0006            K = N
0007            DO 10 J=I,L
0008            IF (AKEY(J) .LT. AKEY(K)) K=J
0009    10      CONTINUE
0010            TEMP = AKEY(I)
0011            AKEY(I) = AKEY(K)
0012            AKEY(K) = TEMP
0013            TEMP = IDATA(I)
0014            IDATA(I) = IDATA(K)
0015            IDATA(K) = TEMP
0016    20      CONTINUE
0017            RETURN
0018            END
```

National Bureau of Standards Special Publication 604. Proceedings of the Workshop on Energy Dispersive X-Ray Spectrometry held at NBS, Gaithersburg, Maryland, April 23-25, 1979. (Issued March 1981)

LEAST-SQUARES FIT WITH DIGITAL FILTER: A STATUS REPORT

Jon J. McCarthy and Frederick H. Schamber

Tracor Northern, Inc.
2551 W. Beltline Highway
Middleton, WI 53562

Abstract

The technique of incorporating digital filtering within a linear least-squares fitting procedure was initially conceived and reported in 1973. At this time, it was one of the very few x-ray analysis procedures which attempted to perform quantitative analysis on spectra containing complex peak overlaps. Since then, the method has been used extensively in a number of applications and continues to be a powerful analysis technique.

The continued success of the filter-fit method is more than a little surprising in view of its essential simplicity of concept. Unlike continuum-modeling which achieves quantitative accuracy by careful attention to the details of the x-ray production and measurement process, the filter-fit method revolves about a single empirical fact: the continuum (background) components in a spectrum are relatively "smooth" structures compared to the characteristic x-ray peaks and thus can be selectively suppressed by application of an appropriate digital filter operator. In view of the considerable success which has been achieved with this very simple concept, it seems clearly worthwhile to analyze why the method works as well as it does.

It is the purpose of this paper to review the current state of knowledge of the technique, based upon the past five years of experience in its application. In addition to reviewing the basic concept of the technique and its application to spectral analysis, the presentation will focus attention on the inherent strengths and limitations of the technique and areas for future improvement.

1. Introduction

Quantitative analysis of the x-ray spectrum obtained with a solid-state silicon detector requires a procedure that can accurately unfold overlapped peaks in the presence of a relatively high background component. Linear least-squares fitting procedures may be applied to the problem of overlapped peaks provided that the continuum background can be eliminated by a suitable technique. A very simple, yet extremely powerful method for continuum suppression is embodied in the concept of digital filtering. A simple modification of the usual least-squares fitting procedure allows continuum suppression via an appropriate digital filter. The application of this technique to x-ray analysis was first described in 1973, and discussed in some detail in the following publications [1,2,3,4][1]. This method has been implemented for use in an on-line minicomputer-based x-ray analyzer. In this form, the technique has been applied with considerable success by a large number of users to problems in both electron and photon excited x-ray analysis [5,6,7,8].

[1]Figures in brackets indicate the literature references at the end of this paper.

This paper will review the basic concepts of the technique and discuss its application to analysis of x-ray spectra. Particular attention will be focused upon the effect of absorption edges in the continuum and sources of error in peak unfolding. In the following the technique will be referred to as the "filter-fit" method.

2. Basic Concept of the Filter-Fit Method

2.1 Linear least-squares fitting

The basic assumption of the linear least-squares method is that each channel of a measured spectrum can be represented by the sum of the corresponding channels of a set of reference spectra in correct proportions. We can express this basic assumption in the following manner:

$$\begin{aligned}\text{Measured Spectrum} = {} & A_1^* \text{ (Reference 1)} \\ & +A_2^* \text{ (Reference 2)} \\ & +A_3^* \text{ (Reference 3)} \\ & +\ldots \\ & +\text{statistical noise}\end{aligned}$$

Analysis of the measured spectrum requires a procedure that will determine the set of proportionality coefficients (A_1, A_2, A_3, ...) that provide the best fit to the measured spectrum. The reference spectra may be any set of curves that provide an accurate model of the shape and amplitude of the particular x-ray lines of interest. Normally such references are a set of measured pure element spectra.

If we denote channel j of the measured spectrum by $\bar{Y}_j$ and channel j of the i^{th} reference spectrum as R_{ij}, we may express the "word" equation given above in a conventional mathematical form:

$$\bar{Y}_j = \sum_{i=1}^{m} A_i R_{ij} + E_j \qquad (1)$$

where E_j is the statistical fluctuation in channel j.

Following the conventional least-squares procedure, we assume that the best set of values for the A_i coefficients are those that minimize the value of the quantity χ^2 (chi-squared), which is defined as follows:

$$\chi^2 = \sum_j E_j^2/\sigma_j^2$$

$$= \sum_j (\bar{Y}_j - \sum_{i=1}^{m} A_i R_{ij})^2/\sigma_j^2 \qquad (2)$$

σ_j is the standard deviation which represents the statistical uncertainty of $\bar{Y}_j$. When the measured values $\bar{Y}_j$ are normally distributed with variance σ_j^2, the set of A_i coefficients that minimize χ^2 are the "maximum-likelihood" solutions in a rigorous mathematical sense.

In the ideal case in which the reference spectra would provide a complete and exact description of the constituents of the unknown spectrum, the solution coefficients of Equation (2) would provide an accurate analysis of the unknown x-ray spectrum. Unfortunately, even when the reference spectra are obtained from pure elements and acquired under

identical conditions as the unknown spectrum, there is no assurance that the continuum in the references will sum to duplicate the continuum of the unknown spectrum. To obtain accurate results, any procedure which employs least-squares fitting must incorporate a treatment of these continuum differences.

Suppression of the Continuum

The filter-fit method approaches the problem of continuum removal by transforming the actual spectra in question into a set of related spectra to which least-squares fitting may be directly applied. This transformation is performed by the application of a digital filter to both the unknown and reference spectra prior to the least squares analysis. An obvious distinction between the continuum and the peaks of a spectrum is the slow variation of the former with energy compared with the much faster variation of the latter. A digital filter is a simple correlating function which can be applied to a spectrum to suppress particular "frequencies" in a digital data array in much the same way that electrical filter networks are used to suppress unwanted frequencies in an electrical signal. The effect of the filter operator used here is to suppress both low frequencies (primarily continuum) and higher frequencies (primarily statistical fluctuations) and pass the characteristic frequencies of the peak shapes. In this manner the continuum is effectively suppressed without the need for a detailed model of continuum shape. In addition, no errors due to subtraction of background are introduced into subsequent analysis procedures.

Digital Filtering

Mathematically, a digital filter is defined by a set of coefficients which are multiplied against corresponding channels of a spectrum. The sum of these products is the "filtered" value for one point in the spectrum and can be expressed as

$$\text{FILT}\,(\bar{Y}_j) = \sum_{s=-t}^{t} f_s \bar{Y}_{j+s}$$

where the f coefficients are the set of filter constants.

Figure 1 illustrates one of the most elementary such filters; the central lobe (upper width) consists of UW positive coefficients (f_s = C/UW); the outer (lower width) lobes contain LW negative coefficients (f_s = -C/2LW), where C is an arbitrary constant. With C = 1, such a filter is nothing more than the average of UW central channels minus the average of two regions of LW channels on either side. When this filter is applied to the spectrum in figure 1 (consisting of a Gaussian shaped peak superimposed on a straight line) it results in the filtered spectrum shown immediately below; there is a strong response to the peak and the straight line is suppressed entirely. It can be easily shown that all filters of this type (symmetric and zero-area) will filter linear components to exactly zero. Since a smooth curve can be approximated by a series of straight lines, and since the continuum is assumed to be a slowly varying smooth curve, it follows that the continuum component of a spectrum can be suppressed by the application of a filter of appropriate dimensions. This is illustrated in figure 2 and figure 3. Several complex spectra are shown before and after application of a digital filter of the type shown in figure 1. The spectrum of figure 2 was generated by electron excitation, while the spectrum of figure 3 was produced by photon excitation. In each case, despite the fact that the continuum shape is markedly different, the continuum has been effectively suppressed and only the peak structures remain.

Although digital filtering introduces obvious distortions to peak shapes, this distortion is predictable and consistent, and does not alter the primary information content of the peaks. Most importantly, digital filtering is a linear operation; a composite spectrum, after filtering, is still the linear sum of its individually filtered peak components. This is illustrated in figure 4. On the upper left of this figure is a composite spectrum which is a linear sum of the two Gaussian peaks and the smooth continuum traces shown below it. The right hand side of figure 4 shows the filtered composite

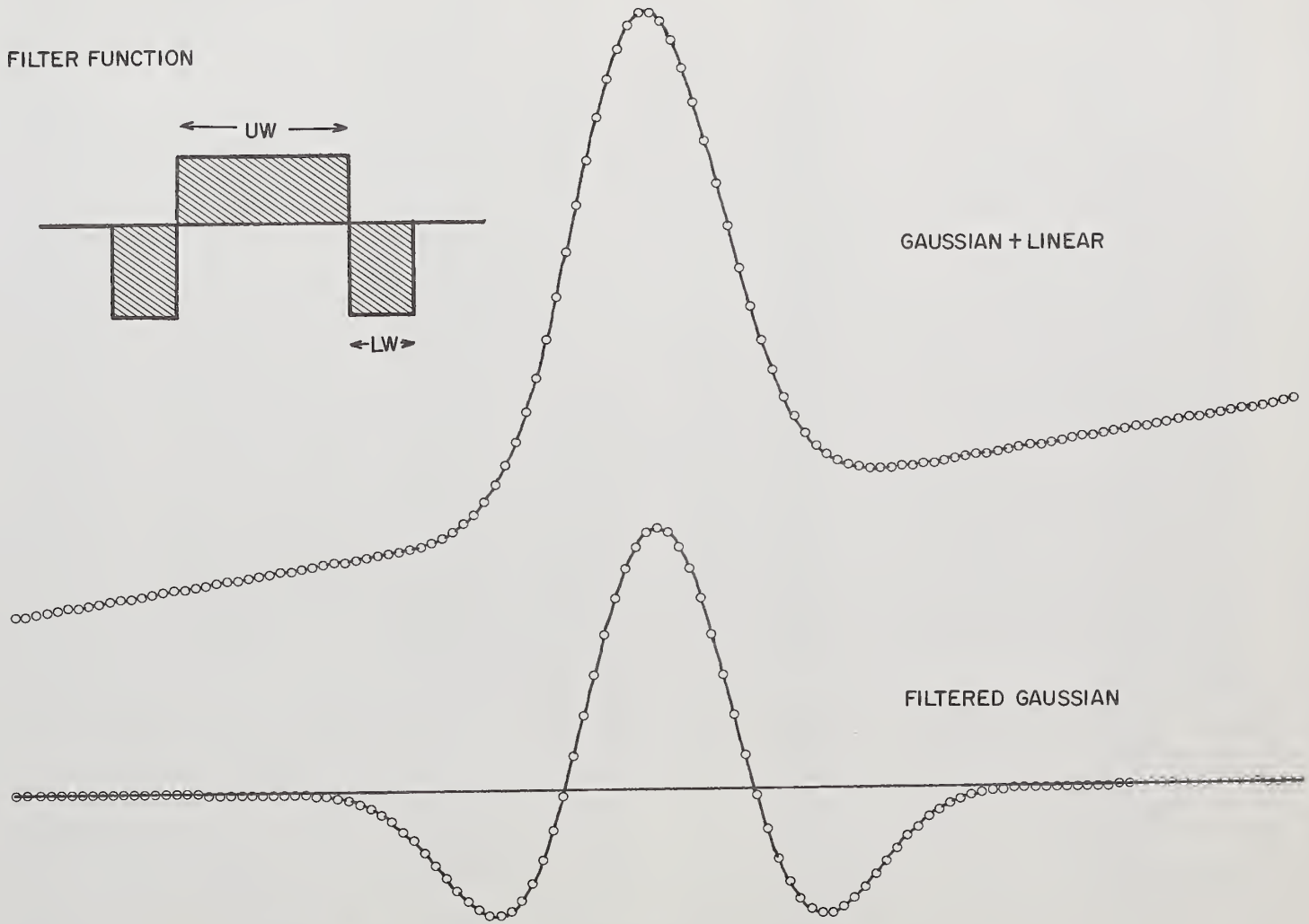

Figure 1. Gaussian peak with straight line background (above) and filtered result (below).

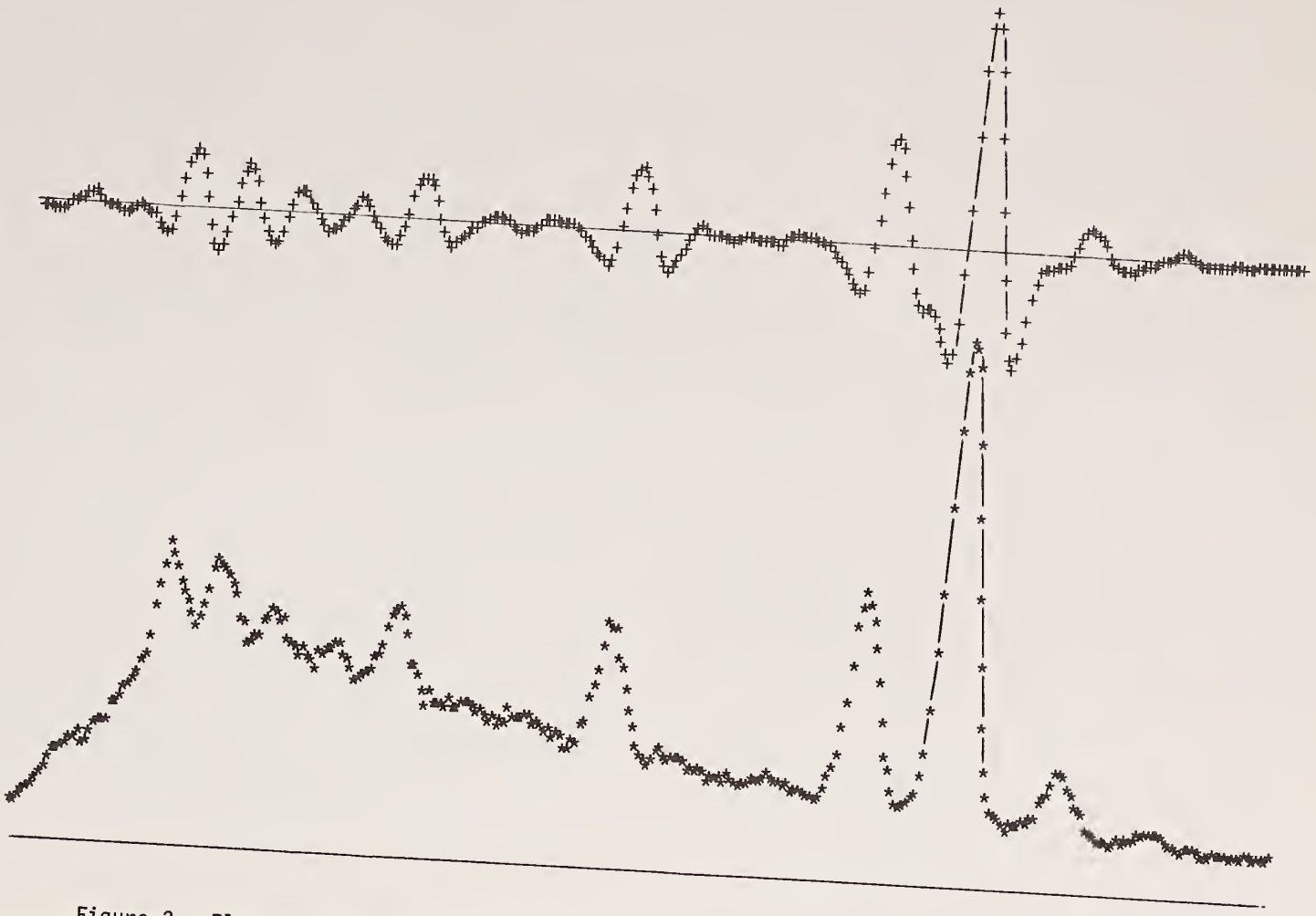

Figure 2. Electron excited spectrum before (below) and after (above) digital filtering.

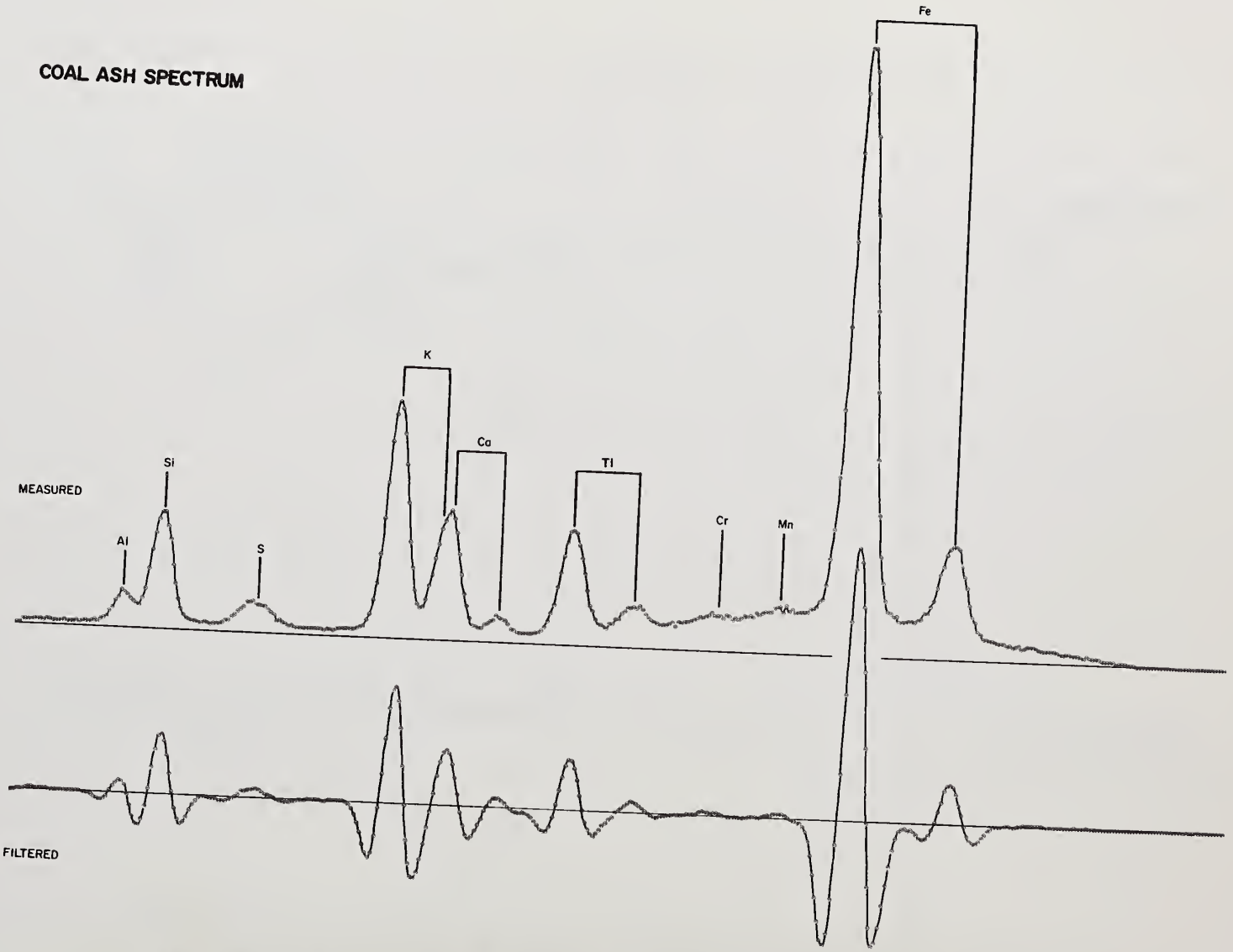

Figure 3. Photon excited spectrum before (below) and after (above) digital filtering.

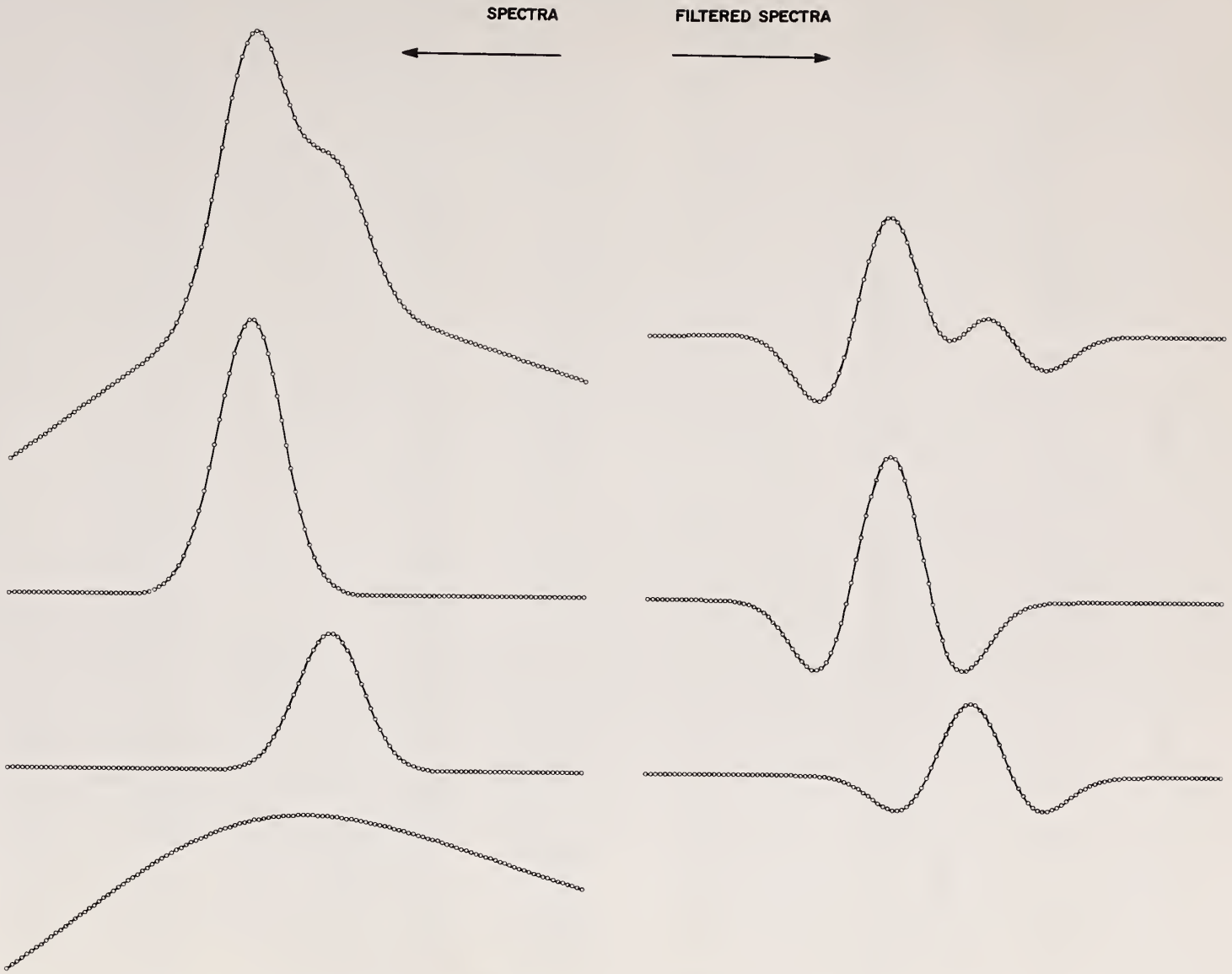

Figure 4. Illustration of the linear nature of digital filtering. The composite spectra (top trace).

spectrum, and the two filtered Gaussian peaks. The contribution of the filtered continuum is zero and can be ignored. To a very good approximation the filtered composite spectrum is the sum of the filtered peak spectra.

A detailed treatment of the effect of various filter dimensions in processing x-ray spectra has been discussed by Statham [4]. The optimum filter dimensions reported by Statham agree remarkably well with those first suggested by Schamber [2] from an empirical viewpoint. The filter dimensions used for the illustrations in this paper are those of Schamber.

The observations made in the preceding paragraphs form the basis for the filter-fit method of spectral processing. Since digital filtering is a linear operation that effectively suppresses background, the peak structure in a filtered measured spectrum can be represented by a linear sum of filtered reference spectra. If both the measured data and the reference peaks are digitally filtered a conventional least squares fitting procedure is justified to obtain the best fit of peak structure.

Filter-Fit Procedure

Consider the measured spectrum to be a linear sum of reference spectra, statistical noise, and a slowly-varying continuum component. We can then rewrite Equation 1 in the following manner:

$$\bar{Y}_j = \sum_{i=1}^{m} A_i R_{ij} + cont_j + E_j \qquad (3)$$

To suppress the continuum, we apply a digital filter to both sides of this equation, and obtain:

$$FILT\ (\bar{Y}_j) = \sum_{i=1}^{n} A_i[FILT(R_{ij})] + FILT(E_j) + FILT(cont_j)$$

Since the continuum is assumed to be a slowly-varying component,

$$FILT(cont_j) \cong 0$$

and then

$$FILT(\bar{Y}_j) = \sum_{i=1}^{n} A_i[FILT(R_{ij})] + FILT(E_j)$$

with the definitions

$$Y'_j = FILT(\bar{Y}_j)$$

$$R'_{ij} = FILT(R_{ij})$$

and

$(\sigma'_j)^2$, the variance of Y'_j

$$(\sigma'_j)^2 = \sum_m (\partial Y'_j/\partial Y_m)^2 \sigma_m^2$$

We can define a new chi-squared variable by

$$\chi^2 = \sum_j [Y'_j - \sum_{i=1}^{n} A_i R'_{ij}]^2/(\sigma'_j)^2$$

Assuming that observed errors are due to counting statistics of the unknown spectrum only, we have

$$(\sigma'_j)^2 \cong \sum_{s=-t}^{t} f_s^2 \bar{Y}_{j+s}$$

From this point, the mathematical development employs the well-known Chi-Squared minimization procedure, except that the filtered quantities Y'_j and R'_{ij} are substituted for the original channel variances σ_j^2.

In this format, the least squares method has been previously discussed in detail [2,4] and will not be treated further in this paper.

Estimate of Uncertainty

The results of any computerized data reduction procedure should not be accepted without an adequate estimate of the errors to be expected. It is therefore important that the procedure calculate and output the statistical uncertainty of the results. A virtue of the least-squares procedure is that it allows the uncertainties of the fitted coefficients to be estimated by use of a simple approximation [2].

Another useful indicator of error is the quantity Chi-Squared (χ^2). If χ^2 is normalized (by dividing by the number of fitted points minus degrees of freedom) it should have a value of about one (on the average) for an ideal fit. Values of χ^2 which are much greater than one are indicative of some systematic error in the fit. χ^2 can be quite useful in this regard as a figure of merit for the entire procedure. A more detailed discussion of the interpretation of Chi-Squared in the filter-fit procedure can be found in Reference 3.

3. Application to Spectral Analysis

The preceding development of the filter-fit method was based upon two key assumptions: 1) the continuum is adequately suppressed by a digital filter and 2) the measured reference spectra provide accurate peak models. In view of the simplicity of these assumptions, it is worthwhile to explore in some detail the performance of the method under various conditions.

In order to demonstrate the performance of the filter-fit method, a simulation was devised which requires that both continuum suppression and peak unfolding be carried out accurately. Six Gaussian peaks, each with a full width at half maximum (FWHM) of 150 eV, were constructed with their centroids separated by 150 eV. These Gaussians were summed into another spectrum which contained a broad continuum profile. Statistical noise was introduced into the resultant composite spectrum with a radioactive source. This composite spectrum is shown in figure 5. The final spectrum was then analyzed with the filter-fit method using the original Gaussian peaks as reference profiles. This entire process was repeated for a total of 54 trial cases. The results of the simulation are presented in Table 1. The high accuracy obtained illustrates the performance of the filter-fit procedure for peak unfolding and continuum suppression.

Additional simulations have been devised to explore in more detail the strengths and weaknesses of the filter-fit method. These simulations will be discussed briefly in the following. Particular emphasis will be placed on the relationship of each simulation to the key assumptions on which the filter-fit technique rests.

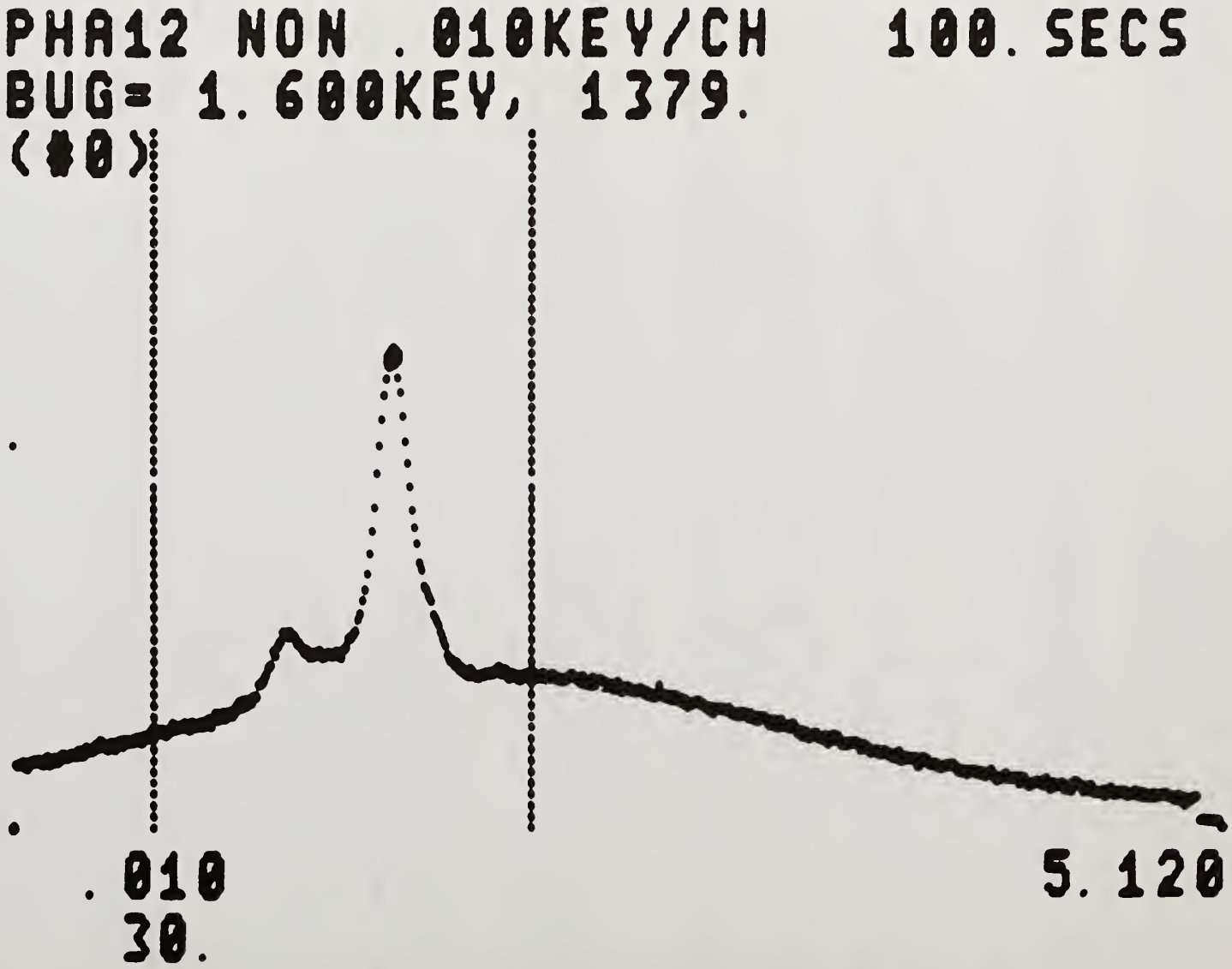

Figure 5. Deconvolution test case of six overlapped Gaussian peaks plus continuum and statistical noise.

Table 1. Six Overlapping Gaussian Test Case.

E_c (keV)	FWHM (eV)	True Ratio	Average ML Ratio[a]	Standard Deviation[a]
1.000	150	0.1	0.100 ± 0.004	0.033
1.150	150	1.0	1.002 ± 0.008	0.047
1.300	150	0.5	0.498 ± 0.005	0.042
1.450	150	0.6	0.599 ± 0.006	0.047
1.600	150	5.0	4.997 ± 0.005	0.038
1.750	150	1.0	1.000 ± 0.004	0.033

[a]Average of 54 independent noise-perturbed runs.

3.1 Discussion of continuum suppression

Two important considerations come to mind in respect to continuum suppression by digital filtering. The first is apparent in the low energy region of the spectrum where attenuation by the beryllium window of the detector causes an abrupt roll-off in the spectrum. This effect is most pronounced in electron-excited spectra due to the larger proportion of bremsstrahlung continuum at these energies. In order to perform well at these energies, the filter-fit must be insensitive to this continuum curvature. The second consideration is related to the appearance of steps in the continuum at the energies of the absorption edges of the various elements being excited. Despite the fact that these steps are smooth in appearance due to instrumental resolution, the abrupt appearance of an edge in the continuum represents a severe departure from linearity over a region of the spectrum.

Sensitivity to Continuum Curvature

Figure 6 is a plot comparing the filter-fit method with two other methods of removing continuum. To perform these comparisons, a Gaussian peak of fixed energy and width (REF) was superimposed upon a variable-width Gaussian peak (BGND) simulating a curving background. By varying the width of the BGND peak and plotting the error in measurement of the REF peak by each of the three methods, the inaccuracies of the three methods can be compared as a function of continuum curvature. The top trace was obtained by simple integration of the area above the straight line segment (A,B). This curve represents the error of a linear background interpolation and direct peak integration. The middle curve was obtained by performing an ordinary least-squares fit (without filtering) across the region (A,B), but introducing slope and intercept parameters into the fit to account for the background. This curve represents the error obtained using ordinary least-squares fitting with linear background. The bottom curve was obtained using the filter-fit method with the REF peak as the sole fitting reference (filter dimensions as shown in figure 1).

The vertical axis of the plot was normalized to 100 percent error for the case when the FWHM of the BGND curve was the same as the reference peak. As expected, the error of all three methods approaches zero as the FWHM of the BGND peak is increased. What is remarkable is the rapidity with which the error of the filter-fit method decreases with decreasing continuum curvature. Note that the filter-fit method is subject to an error of only ~1 percent when the BGND width is four times the peak width. When the BGND width is increased to eight times the REF peak width the analysis error has decreased to less than 0.05 percent. This demonstrates that digital filtering is highly effective in suppressing smooth continuum.

This plot illustrates why the filter-fit method has been successful in the analysis of low energy peaks which lie in the spectral region where detector window absorption causes a strong curvature in the observed bremsstrahlung spectrum. The plot also indicates that the filter-fit method is superior to linear-interpolation methods on the basis of continuum rejection alone, confirming the results reported by Beaman and Solosky [6].

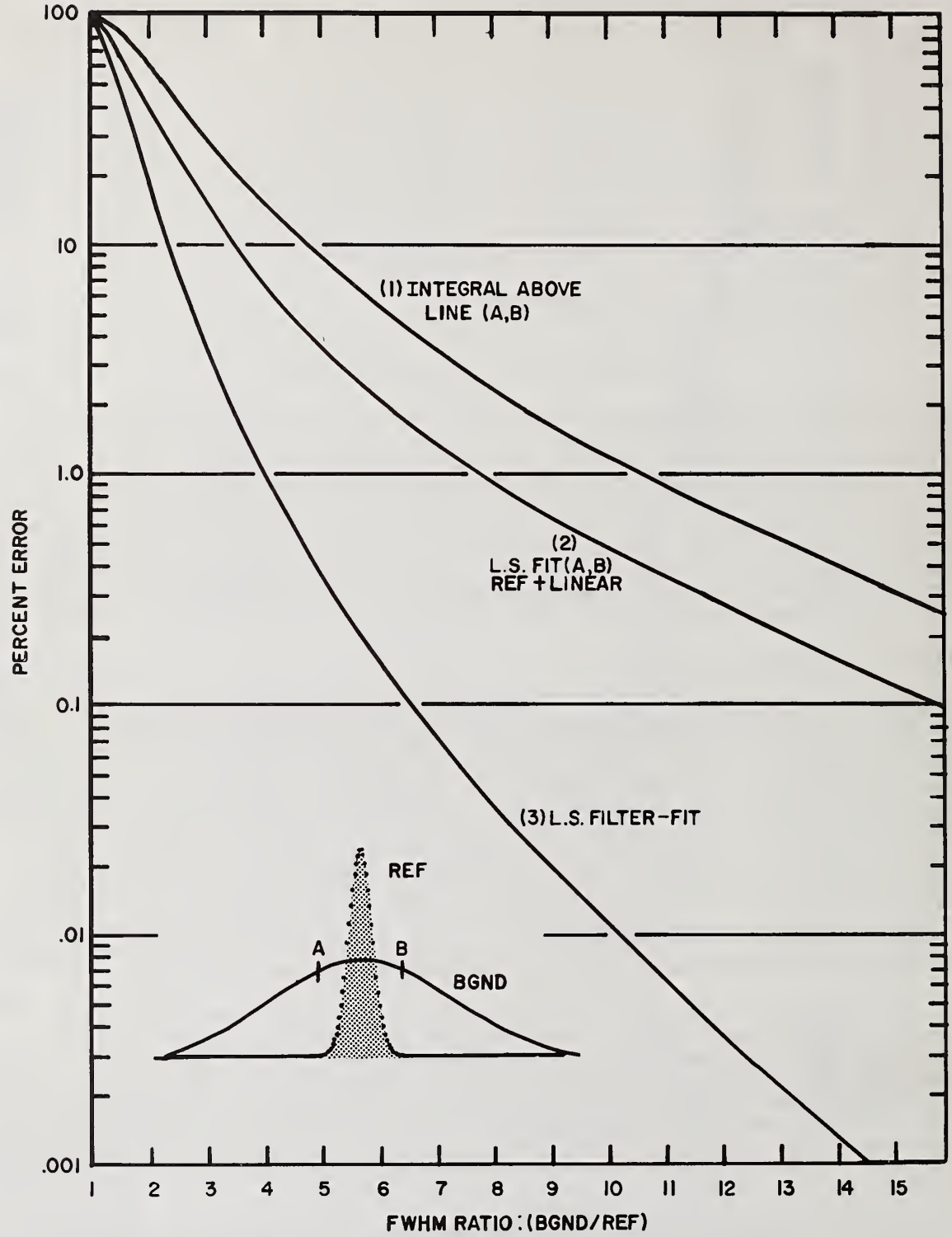

Figure 6. Comparison of continuum removal performance by three methods.

Sensitivity to Absorption Edge Steps in the Continuum

Matrix absorption introduces steps into the continuum due to elemental absorption edges. To first order, least-squares fitting with measured reference spectra compensates for these edges since the edges also appear in the references. However, the amplitude of an edge depends not only upon the concentration of the element, but also upon the amount of bremsstrahlung, and is therefore not strictly proportional to peak amplitude.

In order to estimate the maximum error expected due to absorption steps, several simulations were devised. In the first simulation, the continuum spectrum from a specimen of pure iron was constructed using the method suggested by Fiori et al., [9]. A portion of this spectrum which includes the step due to the iron K edge is shown in the lower trace of figure 7. The upper trace is the result of filtering this spectrum. This trace definitely shows a non-negative residual in the edge area after filtering. A single Gaussian peak was generated and used as a peak reference for filter-fitting to this continuum spectrum. The results of this study are shown in figure 8, where the area obtained by a filter-fit of the continuum step is plotted versus the center channel of the fitted peak. The maximum absolute value of the error yields a peak with area of about 45 counts, centered about 5 channels (approximately 1/2 of 0.5 FWHM) on either side of the edge. This represents an error of less than .01 percent of the Kα peak for pure iron. In a similar analysis [4], Statham concludes that the maximum error that can occur amounts to a peak height of less than 1/3 of the height of the step. It is well to remember at this point that these errors are the maximum expected because of the absence of an edge step in the reference spectrum. In normal work, the reference spectrum would include the edge step.

A second simulation was designed to explore the effects of edge steps in the region below 2 keV where the continuum is large and sloping due to detector absorption. The magnitude of this effect was investigated for mathematically synthesized aluminum-silicon spectra. This is a particularly interesting case since the absorption edges are large and the aluminum edge (1.56 keV) falls close to the silicon K-alpha peak (1.74 keV). Table 2 displays the k-ratios obtained using synthesized aluminum and silicon reference spectra to fit "unknown" spectra synthesized in 1:9, 5:5, and 9:1 proportions of aluminum to silicon. All spectra were generated using Gaussian peak shapes added to the bremsstrahlung continuum (including absorption edges) modeled by the method described by Fiori, et al., [9] (excitation voltage = 15 keV, take-off angle = 57.5 degrees). These results strongly suggest that absorption edge steps are not a significant source of error in the application of the filter-fit method.

Table 2. Effect of Continuum Absorption on Fitted K-Ratios of Al and Si for Concentration Ratios of 1:9, 5:5, and 9:1.

Reference	Expected	Fitted	Error
Al	0.10260	0.10269	-.09%
Si	0.82781	0.82882	-.12%
Al	0.49566	0.49588	-.04%
Si	0.34311	0.34353	-.12%
Al	0.89740	0.89747	-.01%
Si	0.05395	0.05397	-.04%

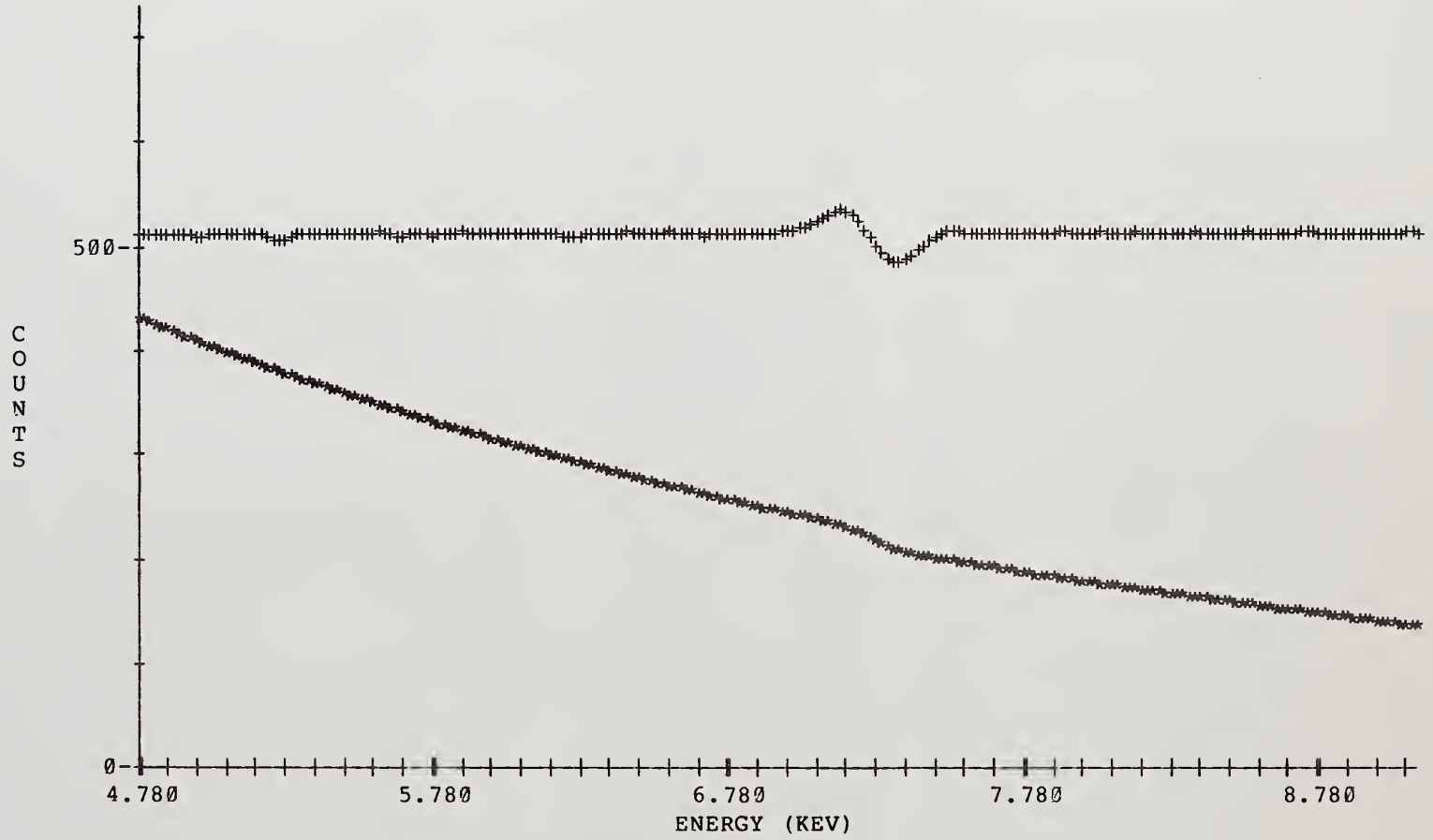

Figure 7. Portion of the continuum of pure iron including the step from the K edge. Upper trace is the result of filtering this continuum.

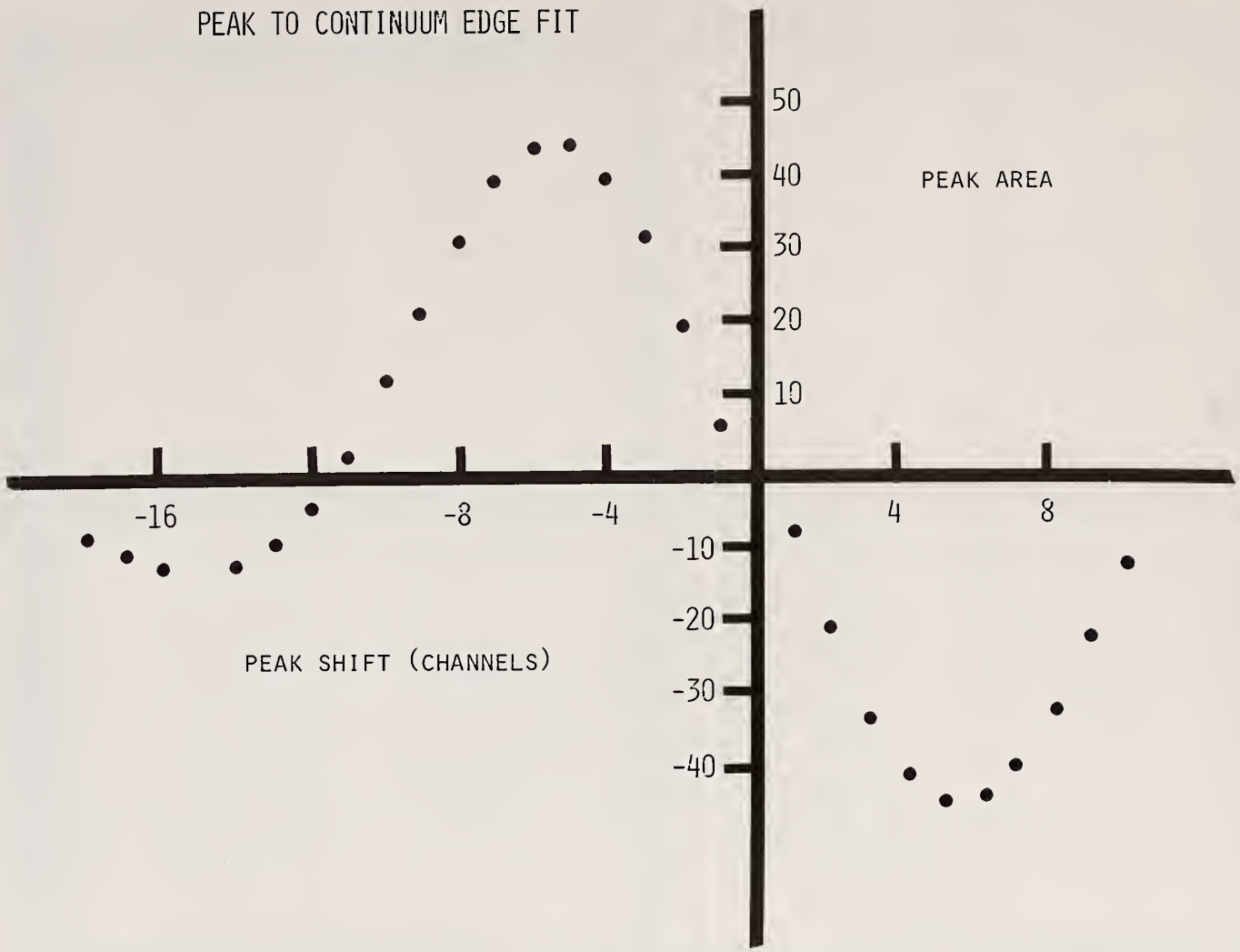

Figure 8. Area of a single peak fitted to the smoothed iron K edge step as a function of channel shift from the edge.

3.2 Discussion of peak shape models

The accuracy of a least-squares analysis is highly dependent upon how closely the peak models used as fitting references represent the actual peak profiles of the measured spectrum. Shifts in peak position due to electronic drift, slight changes in detector resolution, or inaccurate reference peak shapes will produce inaccurate results. Since a measured spectrum of good statistics provides the most accurate description of peak shapes and positions possible, the use of measured reference spectra as fitting functions results in an analysis method which is simple to implement and is nearly optimum in terms of accuracy and precision. Even certain spectral artifacts (such as escape peaks and peak tailing) are reproduced in measured reference spectra, and are thus compensated in the fit. For this reason, measured fitting references are normally employed in the filter-fit method. In cases where suitable pure-element standards are not available, appropriate compound standards or even synthesized pure-element spectra may be employed.

Despite the inherent advantages of using measured fitting references, various situations can arise which limit the accuracy obtained by any least-squares procedure, including the filter-fit method. Some examples of the effects of inaccurate peak models are discussed in the following.

Differential Absorption

Spectrum peaks due to emissions of different line series (K,L,M) do not normally appear in constant proportions in the spectra of different matrices due to the effect of matrix absorption. For example, since softer x-rays will be more strongly absorbed, it is wise to fit the K, L, and M lines of an element separately. Even if this precaution is observed, a question remains as to what degree lines within the same series can be affected by the appearance of an absorption edge between the lines. This problem will be most severe when a strong absorption edge lies between two characteristic peaks. Figure 9 depicts four such situations. Figure 9A illustrates the positions of the L-alpha and L-beta emissions of lead (top trace) and the L absorption edges of tungsten. The L1 and L2 edges of tungsten will absorb the lead L-beta line more strongly than the L-alpha, thereby altering the ratios of these lines. Similarly, figures 9B, C, and D illustrate differential absorption of the zinc K-beta line by the copper K edge, mercury L-beta by the tungsten L2 and L3 edges, and platinum L-beta by the zinc K-edge, respectively. Tests were conducted for these cases by synthesizing reference spectra with Gaussians. Unknown spectra were constructed for various concentrations of the absorbing and absorbed elements, with appropriate attenuation of the beta peaks. The relative errors in determination of the concentration as a function of absorbed element concentration are plotted in figure 10. As previously noted by Corlett and McDonald [5], differential absorption is more severe due to the rough parity in size of the L-alpha and L-beta lines. The most serious problem arises when a K absorption edge falls between the L-alpha and L-beta lines (case D).

It is clear from these results that differential absorption can be a significant source of error. A practical solution to this problem is to partition the fit when a strong absorption edge is known to be present. For example, if fitting low concentrations of platinum in the presence of large concentrations of zinc, it is advisable to prepare two reference spectra for platinum, one containing the L lines below, and the other containing the lines above the zinc K edge. This technique has been successfully employed in instances where such differential absorption was found to be a problem and is only a minor inconvenience.

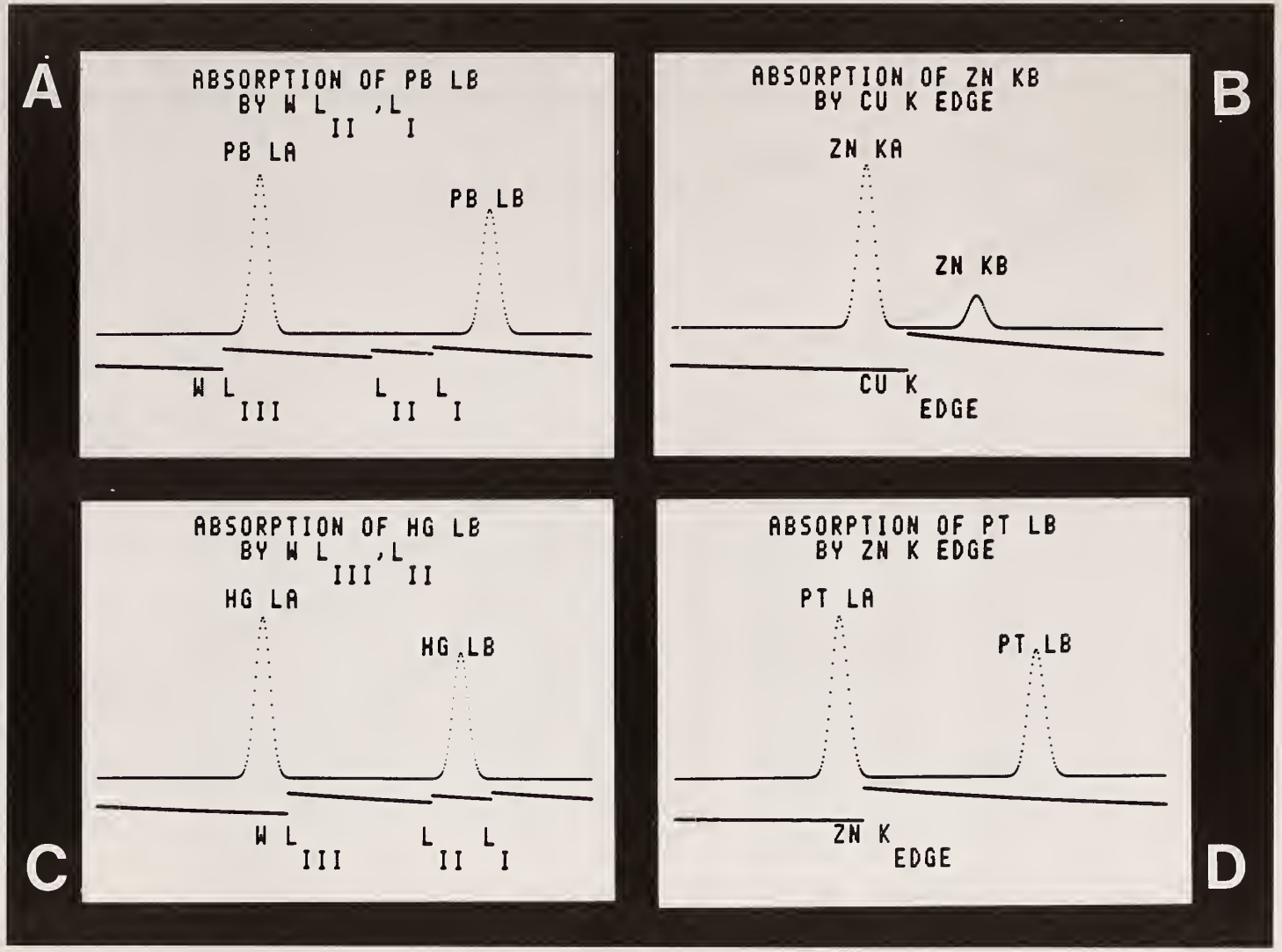

Figure 9. Four cases in which differential absorption strongly affects relative alpha/beta peak intensities.

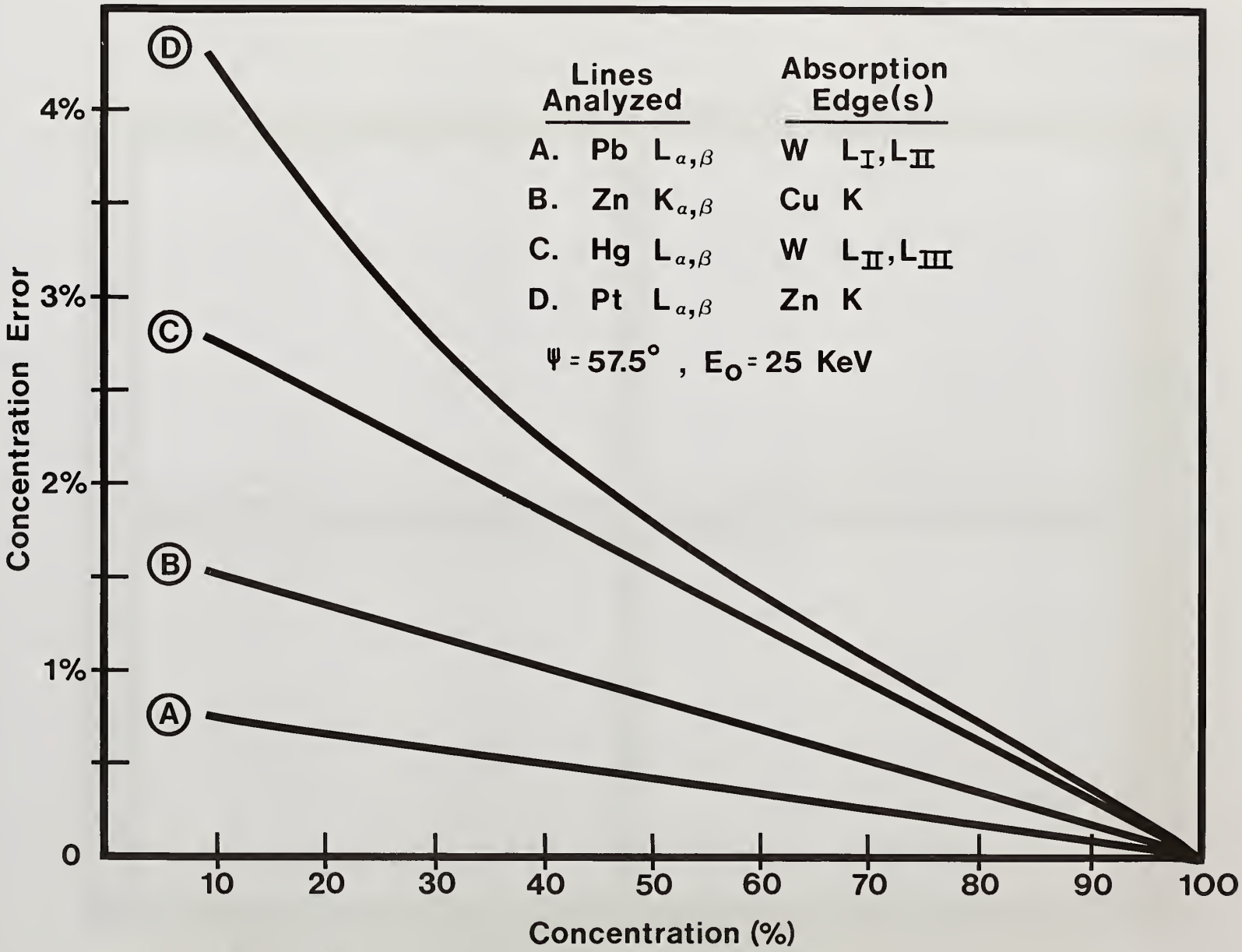

Figure 10. Relative concentration error from analysis of the four cases of figure 9.

Unreferenced Peaks

Figure 11 illustrates the response to an unexpected peak of three different peak-area measurement methods. This figure was constructed by determining the amplitude of a fixed peak (analyzed peak) at various separations from a movable "interference" peak of identical shape and size. The direct integration method simply used the area determined for a region, extending one FWHM on either side of the centroid of the analyzed peak. The (unfiltered) least-squares fit and the filter-fit curves were made with a single reference (for the analyzed peak). At zero separation, the analyzed and interference peaks overlap exactly and all three methods converge to 100 percent error. In the region of small peak separation (below about 1 FWHM) the filter-fit method has the least error of all methods tested. This is gratifying since it is here that a minor overlapped peak is likely to be overlooked and not referenced in the fitting procedure. At peak separations of 1 to 3 FWHM, the filter-fit performance is slightly worse than other methods, but the absolute errors are much smaller in this region. Beyond 3 FWHM all methods show little interference. The filter-fit method approaches the "no-interference" condition the most slowly since convolution with the filter function broadens the effective width of a peak shape. Because of this extended response, it is important that either: (1) all peaks present in the spectrum be fitted, or (2) the fitting region be carefully selected so that nonreferenced peaks are excluded. We conclude that for small peak separations the filter-fit method exhibits superior performance and is comparable to other methods at large peak separations.

An interesting characteristic of the filter-fit response is that it exhibits regions of both positive and negative correlation. Thus, the presence of an unreferenced peak might either increase or decrease the intensity determined for a nearby analyzed peak; there are even two nodes of orthogonality where an interfering peak does not affect the fitted amplitude of another peak at all. A large Chi-Squared value, of course will always be associated with the presence of such unreferenced peaks.

Spectral Energy Shift

Since the least-squares analysis method is predicated upon the assumption that the reference spectra provide an accurate peak-shape model, it is apparent that a difference in energy calibration between the analyzed and reference spectra will introduce fitting errors. Figure 12 illustrates the results of a study to determine the magnitude of this effect. A Gaussian line shape (FWHM $\sim$ 160 eV) was used as the unknown spectrum and a peak of identical width was used as the fitting reference. The position of the peak in the unknown spectrum was shifted by small increments and the resulting relative error and computed value of Chi-Squared were plotted.

A more realistic example of this type of error occurs in the case of analyzing a very small peak which is overlapped by a large one. An example of this type of difficult problem is the barium Lα and titanium Kα lines which are separated by only 44 eV. Spectra were obtained from barium and titanium under identical conditions (25 kV, 80° take-off angle, 10 eV/channel), and used as fitting references. Both references were used to analyze a spectrum of pure titanium using the filter-fit procedure. The analysis was repeated as the titanium spectrum was shifted in 10 eV steps with respect to the reference calibration. The purpose of the test was to determine how much false barium would be reported due to the energy shift. The results of these measurements are shown in figure 13. The value of the maximum barium concentration reported is about four percent and occurs when the titanium has been shifted approximately 0.5 FWHM.

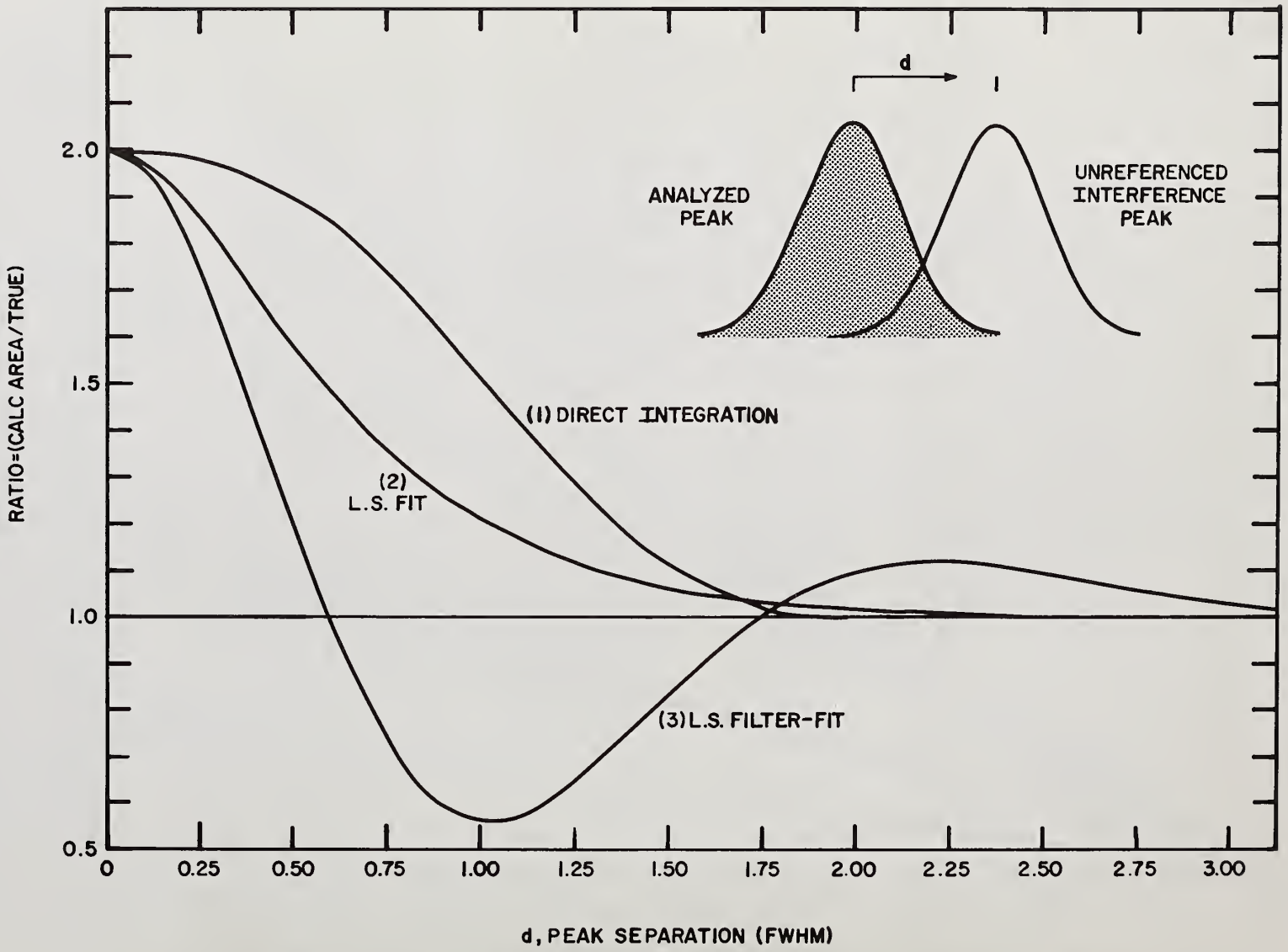

Figure 11. Response of three different peak area analysis methods to an unexpected peak.

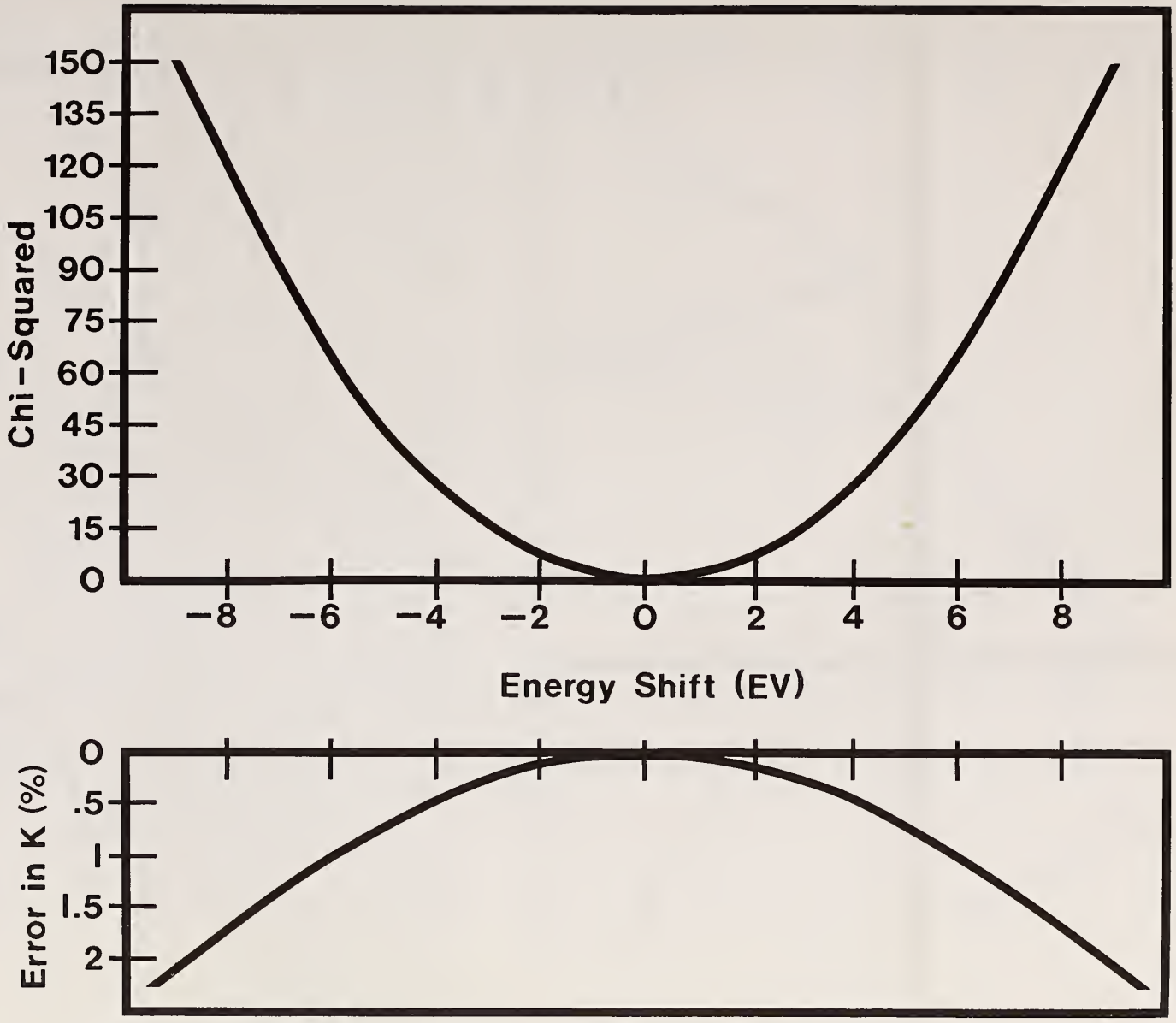

Figure 12. Relative error in measured K-ratio and value of Chi-Squared as a function of peak shift.

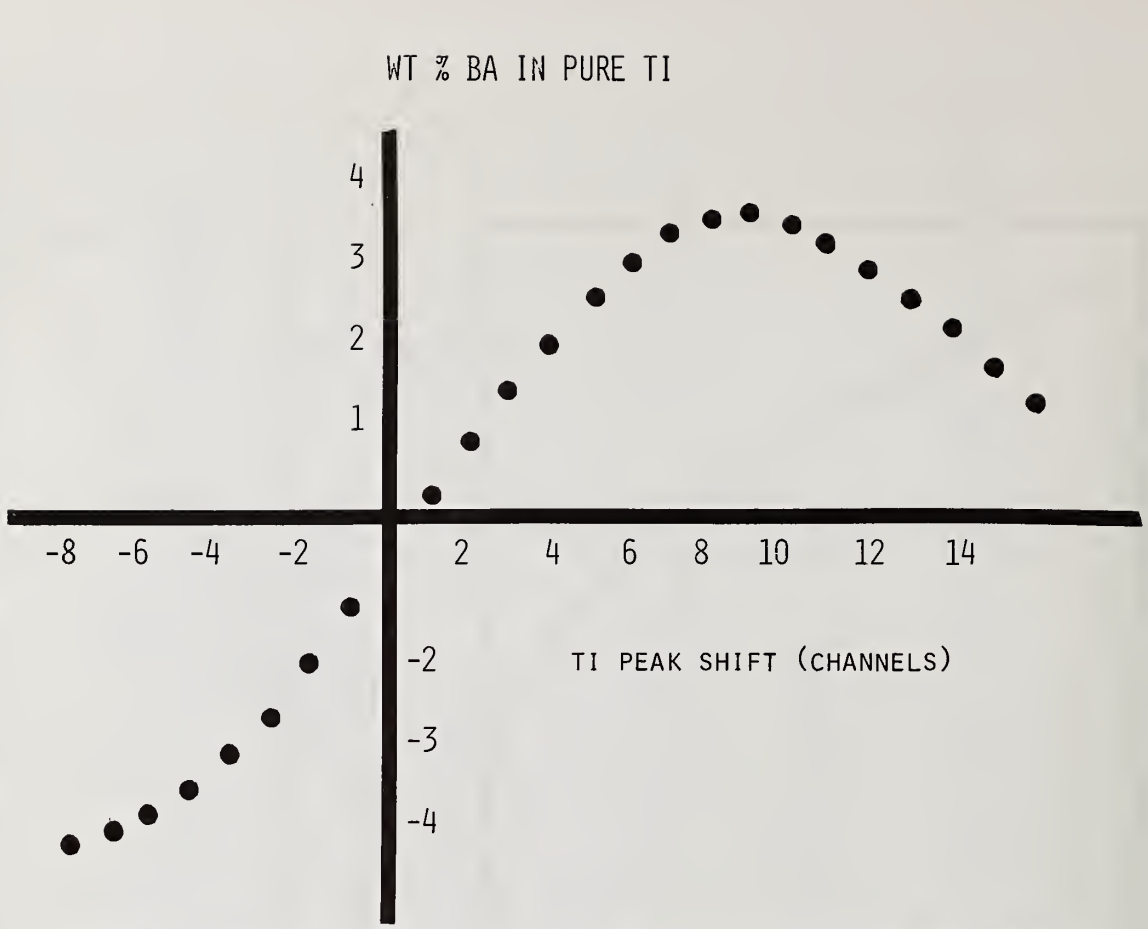

Figure 13. Measured concentration of barium in a pure titanium spectrum as a function of the energy shift of the titanium K alpha peak.

It is clear from the examples above that the filter-fit method is (like all least-squares techniques) quite sensitive to calibration shifts. Mathematical techniques for restoring the calibration of spectra have been developed and found to work quite well. Gain and zero-level shifts can be measured periodically by acquiring a calibration spectrum containing two known peaks. Using this information, subsequently acquired spectra can be restored to correct calibration by a quadratic interpolation procedure. A similar procedure may be employed to examine each spectrum after acquisition and restore it to true calibration automatically. An example of the result of such an automatic calibration is shown in figure 14. In this figure, the value of Chi-Squared obtained in an analysis of each of twelve data sets is plotted versus the data file index. The data were acquired on a spectrometer known to have substantial electronic drifts. The upper trace is the result of analysis without automatic calibration. The lower trace is the result of analysis with automatic calibration. The substantial reduction of Chi-Squared is an indication of the reduction of systematic error due to improper energy calibration.

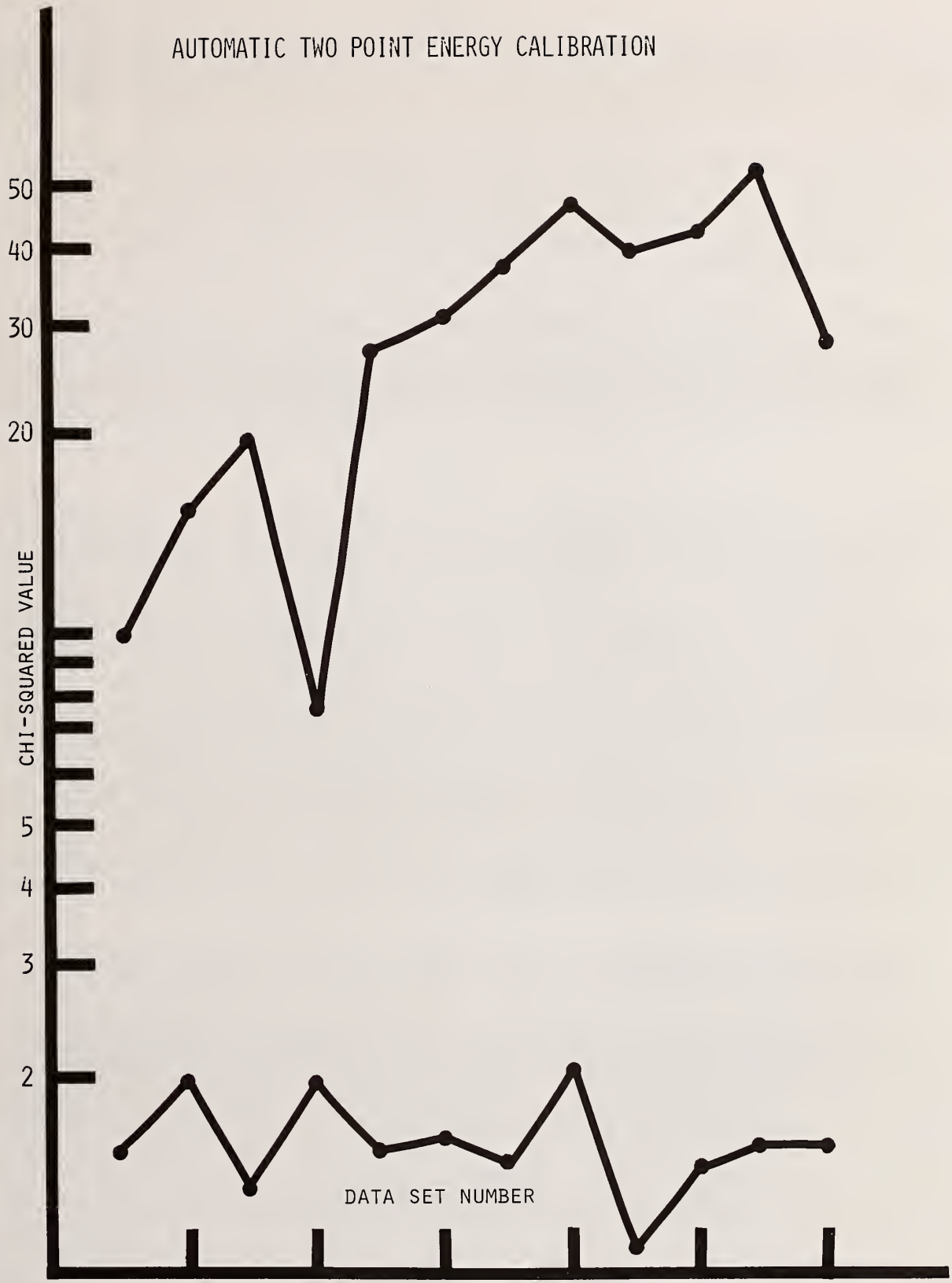

Figure 14. Illustration of the reduction of Chi-Squared by automatic two point energy calibration.

4. Summary

This paper has reviewed the development of the filter-fit method of spectral processing and its applications to the analysis of x-ray spectra obtained with the Si(Li) detector. The method has been used successfully for the last five years in a variety of applications.

The filter-fit method relies on the simple postulates that the spectrum continuum is essentially smooth and that measured reference spectra provide the best peak shape models. The consequence of these assumptions is that no explicit knowledge of the continuum shape or complex peak shape models are required for spectral analysis. The continued success of the filter-fit method can be attributed to the fact that most x-ray spectra do indeed satisfy these assumptions.

A number of practical concerns related to physical and instrumental effects has been considered and shown to produce systematic errors. When the errors are small, as are absorption edge effects, they can safely be ignored. More serious errors arise from incorrect energy calibration and differential absorption which require special procedures to reduce their size. Development efforts focused on eliminating these systematic errors offer the best direction for improvement of the filter-fit method.

References

[1] Schamber, F. H., "A New Technique for Deconvolution of Complex X-ray Energy Spectra," Proceedings of the Eighth National Conference on Electron Probe Analysis, New Orleans, Paper 85, 1973.

[2] Schamber, F. H., "A Modification of the Linear Least-Squares Fitting Method Which Provides Continuum Suppression," in X-ray Fluorescence Analysis of Environmental Samples, T. G. Dzubay, Ed., Ann Arbor Science Publishers, Inc., 1977, p. 241.

[3] Schamber, F. H., Wodke, N. F., and McCarthy, J. J., "Least-Squares Fit with Digital Filter: The Method and Its Application to EDS Spectra." Proceedings of the Twelfth Annual Conference of the Microbeam Analysis Society, Boston, Paper 98, 1977.

[4] Statham, P. J., "Deconvolution and Background Subtraction by Least-Squares Fitting with Prefiltering of Spectra," Anal. Chem., 49, No. 14, 2149-2154 (1977).

[5] Corlett, M. I., and McDonald, M., "Quantitative Analysis of Sulphides and Sulfosalts Using an Energy Dispersive Spectrometer," Proceedings of the Ninth Annual Conference of the Microbeam Analysis Society, Ottawa, Canada, Paper 23, 1974.

[6] Beaman, D. R., and Solosky, L. F., "Advances in Quantitative Energy Dispersive Spectrometry," Proceedings of the Ninth Annual Conference of the Microbeam Analysis Society, Ottawa, Canada, Paper 26, 1974.

[7] Servant, J. M., Meny, L., and Champigny, M., "Energy Dispersive Quantitative X-ray Microanalysis on a Scanning Electron Microscope," X-ray Spectrom., 4, 3, 99 (1975).

[8] Shuman, H., and Somlyo, A. P., "Quantitative Electron Probe Analysis of Ultra-Thin Biological Specimens," Proceedings of the Tenth Annual Conference of the Microbeam Analysis Society, Las Vegas, Paper 41, 1975.

[9] Fiori, C. E., Myklebust, R. L., Heinrich, K. F. J., and Yakowitz, M., "Prediction of Continuum Intensity in Energy-Dispersive X-ray Microanalysis, Anal. Chem., 48, 1, 172 (1976).

National Bureau of Standards Special Publication 604. Proceedings of the Workshop on Energy Dispersive X-Ray Spectrometry held at NBS, Gaithersburg, Maryland, April 23-25, 1979. (Issued March 1981)

MULTIPLE LEAST SQUARES FITTING FOR SPECTRUM DECONVOLUTION

John C. Russ

EDAX Laboratories
P.O. Box 135
Prairie View, IL 60069

The multiple least squares fitting approach to energy-dispersive x-ray spectrum deconvolution has been described by several authors [1-3][1] and is used in some commercial ED software [3]. It is also commonly used in nuclear spectroscopy [4]. The fundamental assumption in this method is that the measured spectrum is a summation of spectra measured on each of the pure element standards. For the peaks this is often a good first approximation as we shall see.

Since for x-ray spectra, and particularly for electron excited x-ray spectra, the background is quite significant and not a linear summation of the individual pure elements' spectral backgrounds, it is questionable whether the fitting should include the background. One approach [3] has been to fit not the measured spectrum, peaks and background, but a filtered spectrum. By passing a simple digital filter over the spectrum (similar to but much simpler than the background-removing frequency filter [5], used by EDAX), the spectrum is replaced by an approximation to its second derivative. This supresses the background which varies more slowly than the peaks. A typical filter is shown diagrammatically in figure 1. Each channel is replaced by the summation of itself and its neighbors multiplied by the function. Since all the coefficients are integers (in this example 1 or 2) the filtering procedure, if written in machine language using simple addition and subtraction, can be extremely rapid. Since the filtering process is linear, it seems that linear least squares fitting of the filtered library of spectra to the filtered unknown spectrum should also be possible, and this is done.

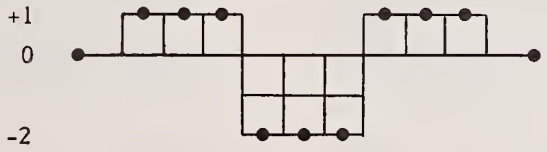

Figure 1. Typical "Digital Filter" used to weight channels to produce second derivative spectrum.

Another approach [6] has been to use weighted least squares fitting in which the individual data points in the measured spectrum and each library spectrum are weighted in importance according to their statistical precision. This is approximated as simply being the square root of the number of counts in that channel, so the peak areas are more strongly weighted than the background and major peaks more strongly than the minor ones. These methods discriminate against the background but do not remove it. They are therefore different from that used by the programs which calculate and/or fit background discretely [7] and we believe inferior both in their practical consequence and philosophic approach. Removal of the background by fitting or interpolating a line (straight or a simple function) can also be used on the measured spectrum and the library spectra before fitting, and gives good results.

[1]Figures in brackets indicate the literature references at the end of this paper.

It is the purpose of this article to illustrate the basic method and evaluate potential problem areas for it. Fitting of both generated and measured library spectra are considered. A series of applications are shown using spectra having different characteristics to test the performance of the various approaches. The particular features chosen are very severe overlaps of K and L lines where the peak separation is small, and families of lines are involved.

First let us consider a simple example showing the combination of pure copper and pure zinc spectra to match the spectrum measured on a copper zinc brass alloy. Figure 2 shows the measured spectra each analyzed for 40 seconds, at 25 kV with the specimen inclined at 20° with a 36° takeoff angle. Tables 1-3 show the results of the different fitting approaches with intensities and K ratios, that is, the ratios of the intensity of each element measured on the brass alloy divided by the intensity measured using the same methods on the pure element spectrum. Table 4 lists the resulting calculated concentrations. All of the fitting methods give reduced chi-squared values very close to 1.0 (between .9 and 1.6) indicating excellent fits. In this example all of the results are roughly similar and it is not obvious which method is to be preferred in general. Figure 3 shows typical fitting results.

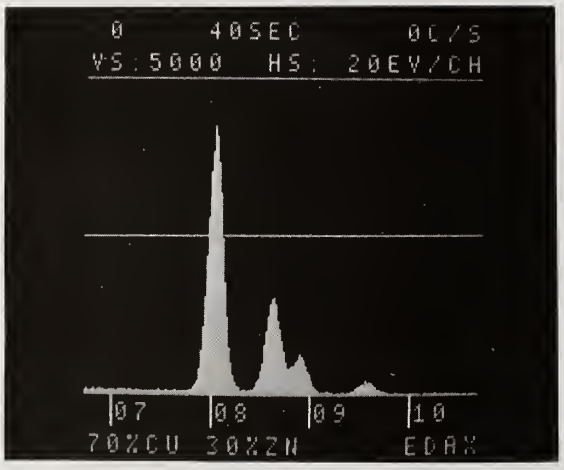

Figure 2a. Spectrum from 70 percent Cu – 30 percent Zn Brass.

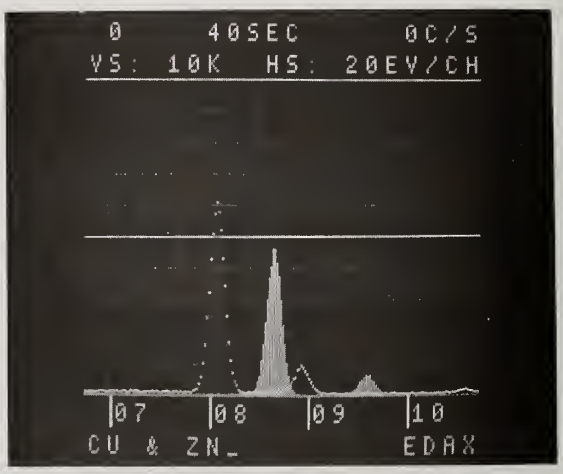

Figure 2b. Library spectra from pure Cu (dots) and Zn (bars).

Table 1. Intensities, ratios, and concentrations for 70 percent Cu – 30 percent Zn spectrum.

	Generated Peaks		Library Spectra		
	Linear	Weighted	Linear	Weighted	Digital Filter
Cu	37710	39503			
	5264	5750	0.67311	0.68978	0.68754
Zn	13719	14538			
	1658	1745	0.30432	0.32954	0.28563

Table 2. Intensities on pure Cu and Zn.

	Linear	Weighted
Cu	53706	53728
	7497	7537
Zn	42821	42783
	5886	5843

Table 3. K-ratios from intensities in Tables 1, 2.

	Linear	Weighted
Cu	0.7022	0.7390
Zn	0.3157	0.3349

Table 4. Normalized ZAF results from Tables 1, 3.

	Generated Peaks		Library Spectra		
	Linear	Weighted	Linear	Weighted	Digital Filter
%Cu	69.12	68.92	69.03	67.81	70.80
%Zn	30.88	31.08	30.97	32.19	29.20

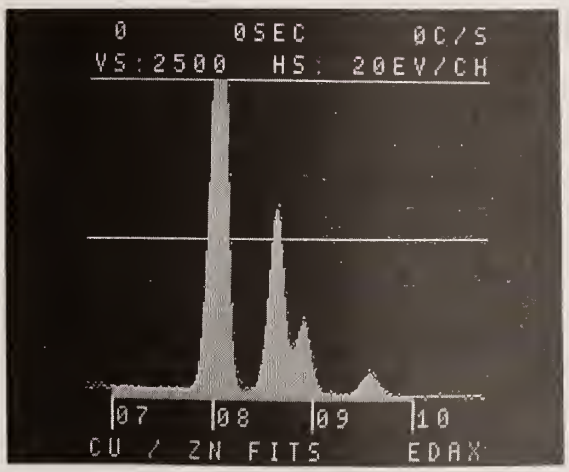

Figure 3a. Fit of individually generated peaks (bars) to Brass spectrum (dots).

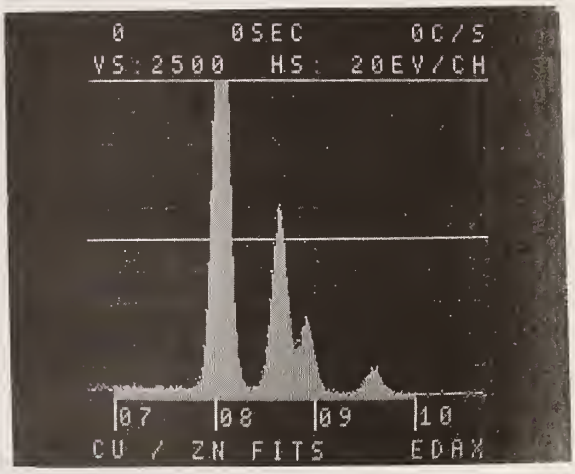

Figure 3b. Fit of summation of library Cu and Zn spectra (bars) to measured Brass spectrum (dots).

Applying the same method to nominal 90 percent Cu – 10 percent Zn and 95 percent Cu – 5 percent Zn alloys (figure 4) produces the results summarized in Table 5. As there was some indication above that the weighting method introduces bias when mixtures of very large and small peaks are present (this will become more apparent in a subsequent example), it was not used for these calculations.

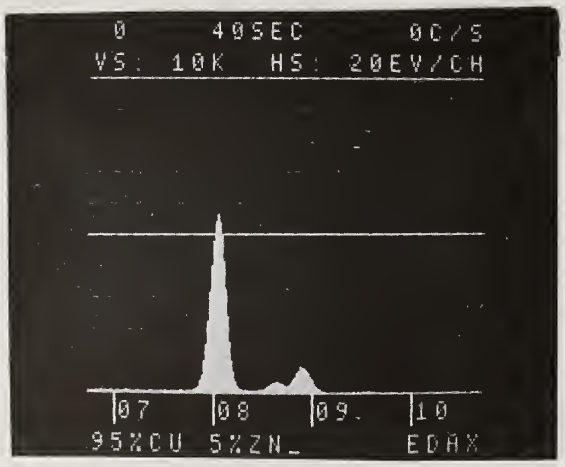

Figure 4a. Spectrum from 95% Cu – 5% Zn Brass.

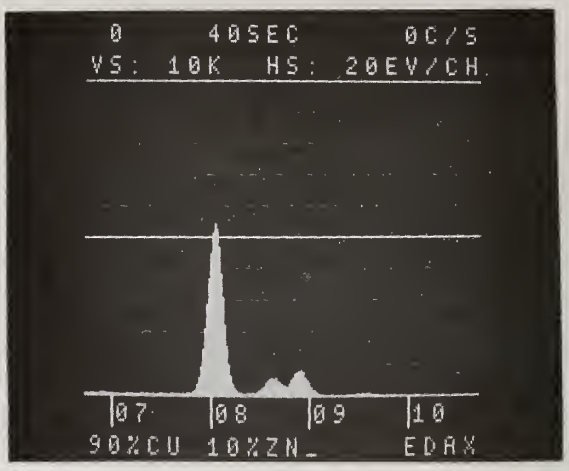

Figure 4b. Spectrum from 90% Cu – 10% Zn Brass.

Table 5. Fitting results on 90-10 and 95-5 Brass alloys.

			Generated Peaks	Library Spectra	
				Linear	Digital Filter
90-10		Cu	0.90874	0.86402	0.87298
	K ratio	Zn	.11086	.10054	.08893
		Cu	89.19	89.65	90.82
	%	Zn	10.81	10.35	9.18
95-5		Cu	.96969	.91481	.91744
	K ratio	Zn	.05942	.05112	.04772
		Cu	94.26	94.10	95.09
	%	Zn	5.74	5.90	4.91

The next example is a sample containing lead and arsenic, as a mixture of arsenic trioxide and lead acetate (figure 5). This presents a major problem in the interference of the AsKα and PbLα. Fitting of generated peaks was tried using one Kα and one Lα peak, at 10.53 and 10.55 keV respectively and also using separate $K\alpha_1$, $K\alpha_2$, $L\alpha_1$, and $L\alpha_2$ peaks at 10.541, 10.505, 10.551, and 10.448 keV. The results listed in Table 6 are accompanied by chi-squared values of 1.036 and 1.004 for the two fits, and excellent appearance of the fitted result (figure 6). However, they are clearly wrong. In the one case the ratios of $K\alpha_1$ to $K\alpha_2$ and $L\alpha_1$ to $L\alpha_2$ are wrong, and in the other, the ratio of As to Pb is about 3.5 while from all of the other peak ratios (and results of library fits to be shown below) the ratio should be about 2.60. Furthermore, the values are extremely sensitive to changes in peak position of as little as one eV, and even careful calibration cannot guarantee adequate reliability.

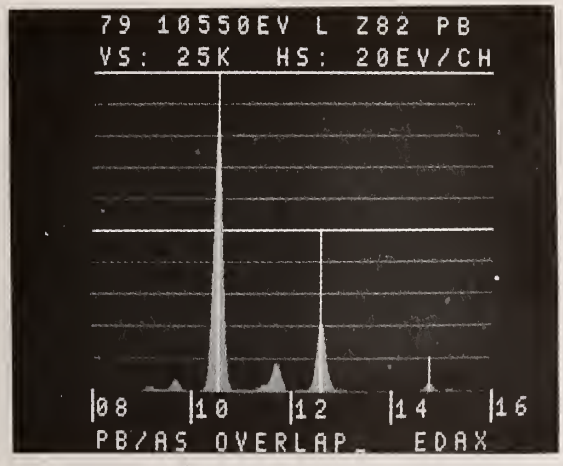

Figure 5a. Spectrum measured on lead-arsenic mixture, showing major Pb peaks.

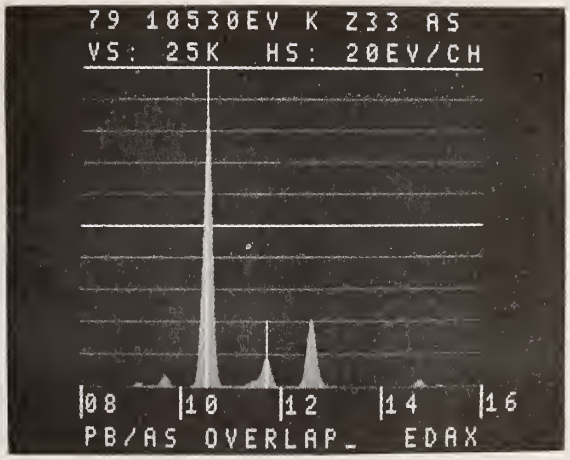

Figure 5b. Spectrum measured on lead-arsenic mixture, showing major As peaks.

Table 6. Intensities from generated peak fits to Pb-As overlap.

	Peak	keV	Total Counts
Case 1	AsKα	10.53	179720
	PbLα	10.55	52418
Case 2	$AsK\alpha_1$	10.541	24567
	$AsK\alpha_2$	10.505	77377
	$PbL\alpha_1$	10.551	128945
	$PbL\alpha_2$	10.448	1234

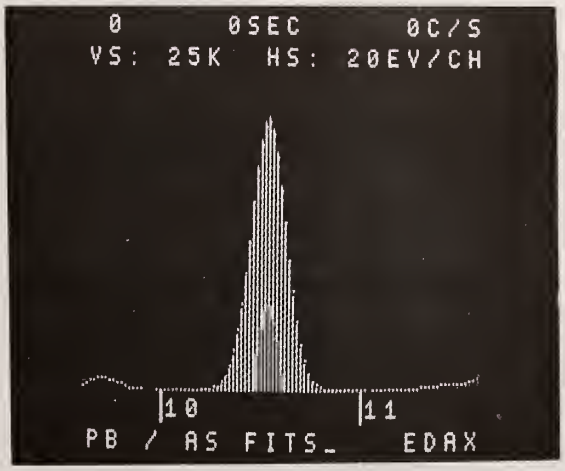

Figure 6a. Fit of two generated peaks (bars) to AsKα – PbLα overlap (dots).

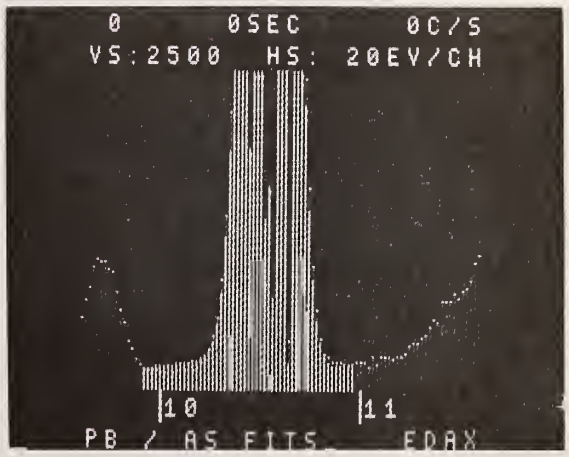

Figure 6b. Detail near baseline of figure 6a.

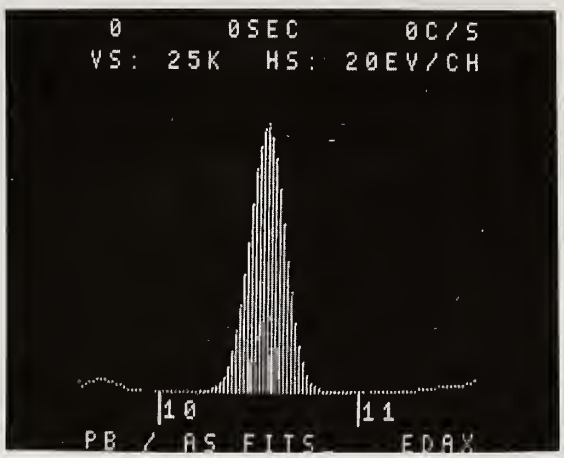

Figure 6c. Fit of four generated peaks (bars) to AsKα – PbLα overlap (dots).

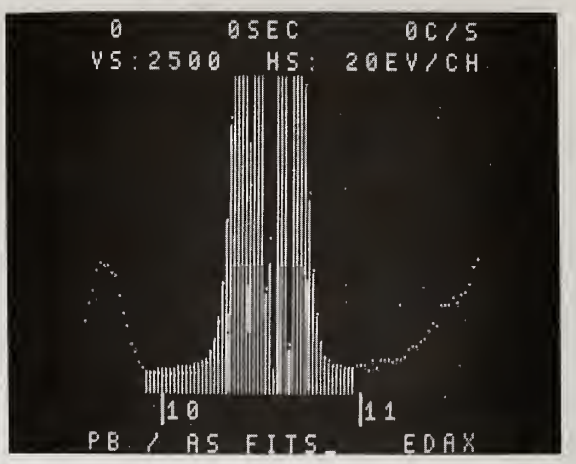

Figure 6d. Detail near baseline of figure 6c.

To judge the effect of miscalibration, the As Kα and Pb Lα peaks were fit at energies varying over a narrow range, in one eV steps, keeping the separation of the peaks and their widths constant. The results (Table 7, figure 7) shows huge variations in intensities, with only slight variations in the reduced chi-squared value. Note that the minimum chi-squared value occurs for nearly equal size As and Pb peaks, which again does not agree with the more probable ratio of about 2.6. Statham has shown another example of minimum chi-squared occuring at the "wrong" answer [8].

Table 7. Variation of Pb Lα/As Kα with position.

(Energy in eV)	As-Pb Mixture		
	Chi-squared	I_{As}	I_{Pb}
-10	1.0167	-11317	242794
9	1.0159	-115	231590
8	1.0153	11081	220394
7	1.0147	22297	209177
6	1.0142	33492	197981
5	1.0137	44700	186772
4	1.0133	55906	175565
3	1.0130	67124	164345
2	1.0127	78341	153128
- 1	1.0125	89546	141922
0	1.0124	100761	130705
+ 1	1.0123	111979	119487
2	1.0123	123198	108266
3	1.0124	134415	97048
4	1.0125	145636	85827
5	1.0127	156853	74608
6	1.0130	168077	63383
7	1.0134	179297	52163
8	1.0138	190525	40934
9	1.0142	201745	29713
10	1.0148	212975	18482
11	1.0154	224206	7249
12	1.0160	235423	-3969
13	1.0168	246660	-15206
+14	1.0176	257878	-26425

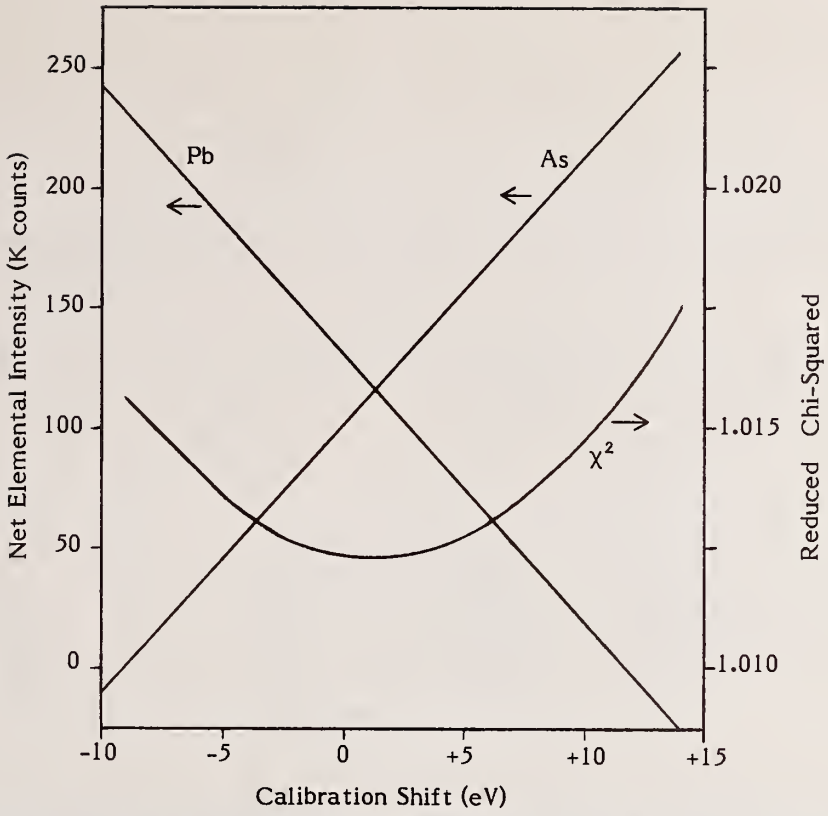

Figure 7. Effect of calibration shift on chi-squared and intensity values for overlapped peak.

If we use the same series of energies for generated peaks of both elements to fit the pure element spectra measured on a pressed pellet of arsenic trioxide and a metallic lead disc, respectively, we find results as shown in Table 8 and figure 8. Again note that the absent element can have either positive or negative values, and that the reduced chi-squared value varies only slightly, and is not at its minimum when the absent elements's intensity passes through zero.

Table 8. Variation in intensities measured on pure elements.

Energy in eV	Pb			As		
	Chi-squared	Pb int.	"As Int."	Chi-squared	As int.	"Pb Int."
-5	1.0337	136516	-10052	1.0011	425197	202411
-4	1.0329	130549	-4086	1.0013	456201	171388
-3	1.0322	124566	1897	1.0017	487244	140359
-2	1.0315	118588	7874	1.0020	518196	109393
-1	1.0309	112611	13851	1.0025	549272	78324
0	1.0304	106633	19829	1.0031	580292	47302
+1	1.0299	100647	25805	1.0037	611359	16232
+2	1.0295	94655	31797	1.0044	642340	-14752
+3	1.0292	88669	37783	1.0051	673368	-45779
+4	1.0289	82679	423772	1.0059	704438	-76849
+5	1.0288	76683	49769	1.0068	735405	-107816

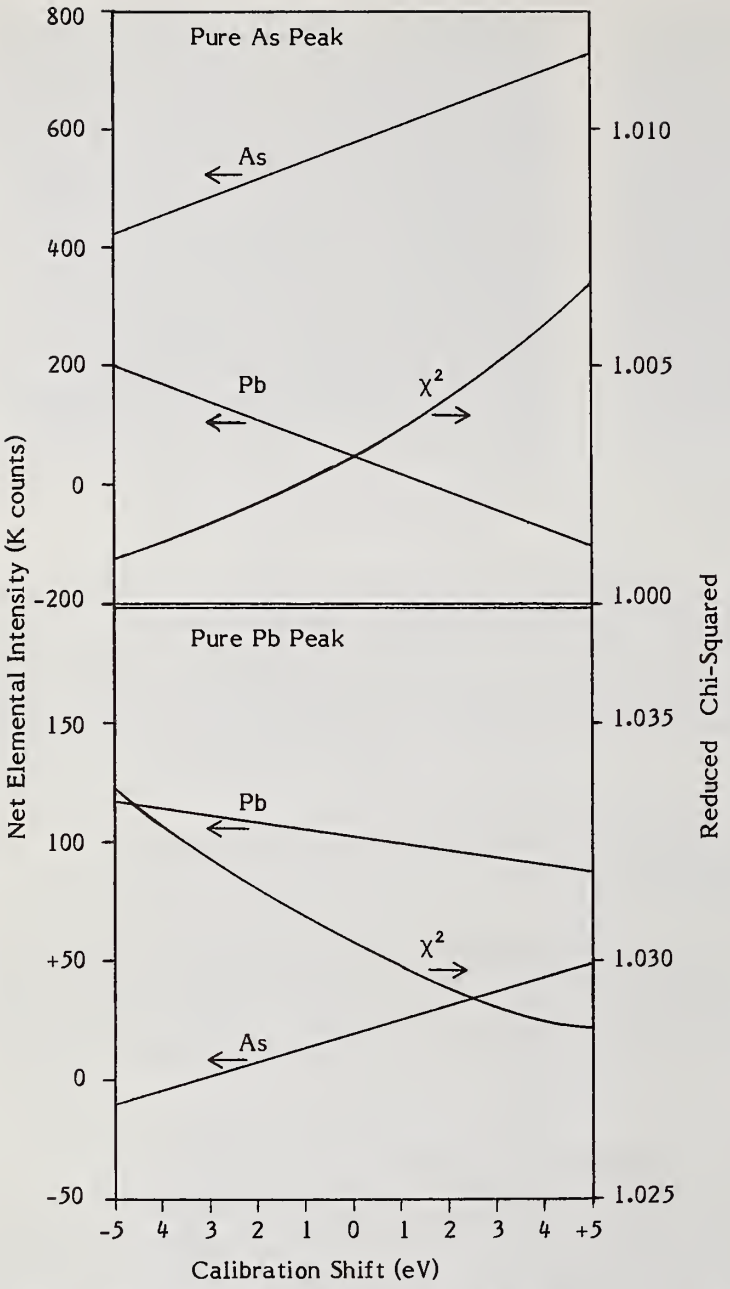

Figure 8. Effect of calibration shift on chi-squared and intensity values for individual element peaks.

If we choose the value of the pure intensities at the energy position where the absent element's peak is zero, then we obtain ratios of intensities on the mixture (determined at minimum chi-squared) to pure intensities equal to 0.1874 for As and 0.8609 for Pb. These are very different from the more likely values determined, for example, from a consideration of the arsenic Kβ and lead Lβ lines (values typically about .25 for As and .65 for Pb). The mixture of lead acetate and As_2O_3 contained by weight 76.44 percent lead acetate and 23.56 percent As_2O_3, from which we might expect ratios of 0.236 for the arsenic spectrum and about 0.55 for the lead spectrum (taking into account the fraction of lead in lead acetate).

We would have to conclude from this that generated peaks cannot separate this overlap by themselves, and either knowledge of peak ratios to the other α and β peaks, or the use of those other peaks by themselves, would be required.

Using library spectra measured on the pure arsenic and lead compounds gives generally more reliable results, but still with some variations. Since they were measured immediately before and after the mixture, the calibration of peak positions has not changed, (although it may be 1 or 2 eV off, even with careful adjustment used in this example). A major variable left to the user's discretion is still the energy range to be used for making the fit. Table 9 shows the change in results using linear fitting as the range is increased from the major KαLα peak to the entire family of lines. Note that the As:Pb ratio increases as more and more Pb lines are included in the fit. Figure 9 shows the library spectra. These data indicate the ability of fitting of library spectra to give fairly consistent and useful results if all of the available lines are used, but in this case equally useful and less potentially questionable values could be obtained using only the As Kβ and Pb Lβ lines, which are not overlapped.

Table 9. Variation of Pb-As fitting factors with energy range.

Limits (keV)		As	Pb
Low	High		
10	11	0.2889	0.4238
10	12	.2535	.6011
10	13.5	.2432	.6533
11	13.5	.2395	.6673
8.1	14.0	.2444	.6584
8.1	15.9	.2451	.6623

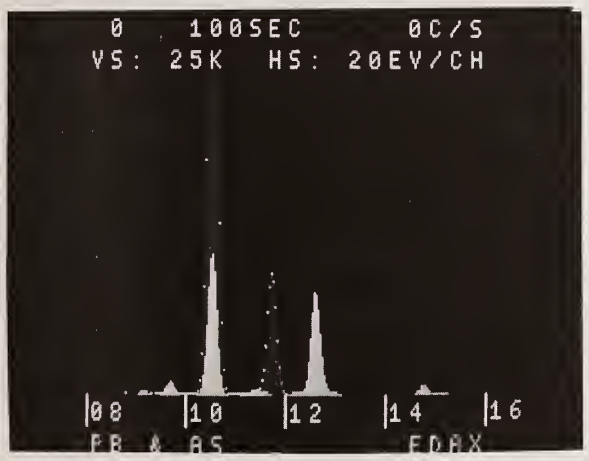

Figure 9a. Library spectra measured for lead (bars) and arsenic (dots).

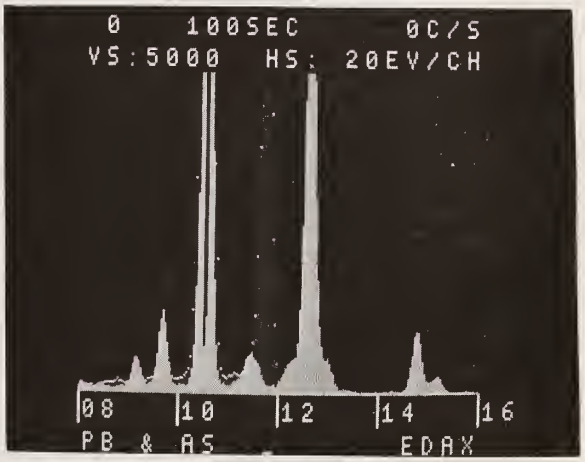

Figure 9b. Detail of figure 9a showing background and minor peaks.

Using the weighting method over the full 8.1-15.9 keV range, introduces a significant error because of the assemblage of very large and small peaks. Table 10 shows the results, and figure 10 illustrates the problem; the fit is strongly influenced by the larger α peaks which have the major error because of the close overlap. This results in a too large As Kβ and too small Pb Lβ. The chi-squared results for the weighted fit are correspondingly poor, while for the linear and filtered fits, the values are 1.09 and 1.63 respectively. Figure 11 shows the filter fit results; note that the background is not well fit, while the major peak areas are quite close, showing the general discrimination against the background regions. The opportunity for biased results from the weighted fits argue against that method, and in fact it has been dropped from subsequent examples.

Table 10. Variation of Pb - As fitting factors with method.

	Linear	Weighted	Filter
As	0.2451	0.2746	0.2369
Pb	.6623	.6791	.6683

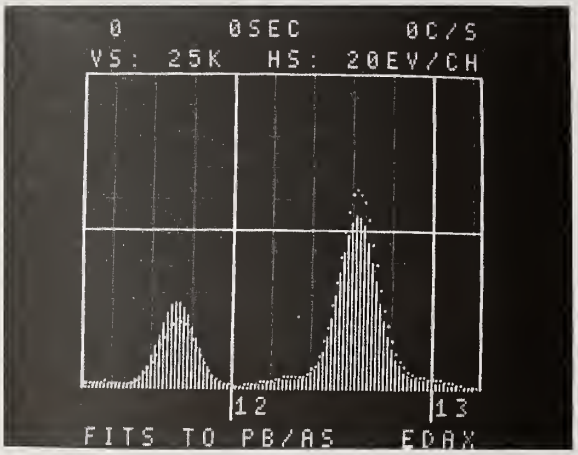

Figure 10. Comparison of composite spectra (bars) obtained by weighted fit. AsKβ (11.7 keV) is larger and PbLα (12.6 keV) smaller than measured spectrum (dots).

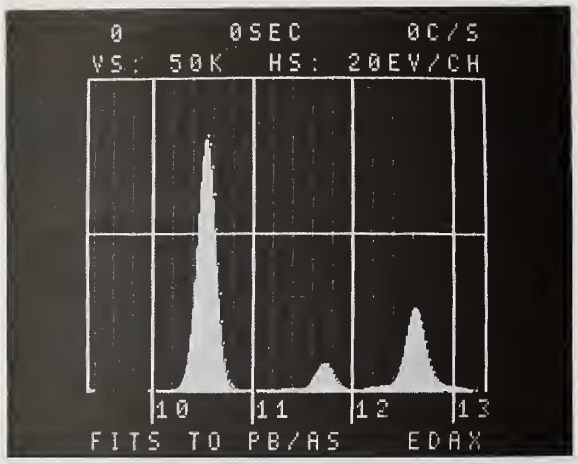

Figure 11a. Comparison of composite from filtered fit (bars) with measured spectrum (dots) showing agreement on major peaks but not background and minor.

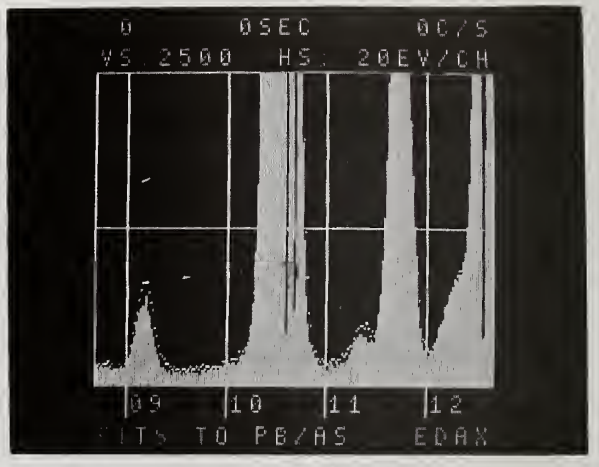

Figure 11b. Detail of figure 11a, showing background and minor peaks.

A further useful test is to evaluate the purely statistical effects of fitting, figure 12. For the Pb-As mixture, and for each of the pure samples, duplicate spectra were recorded. Each had a total of at least one-half million counts in the 8.2-15.6 keV fitting region. Using all possible combinations of spectra gave the results shown in Table 11. The variance is approximately one percent, while from a simple consideration of the number of counts we would expect about half that value. Note also that there is a consistent difference between the linear and digital filter results.

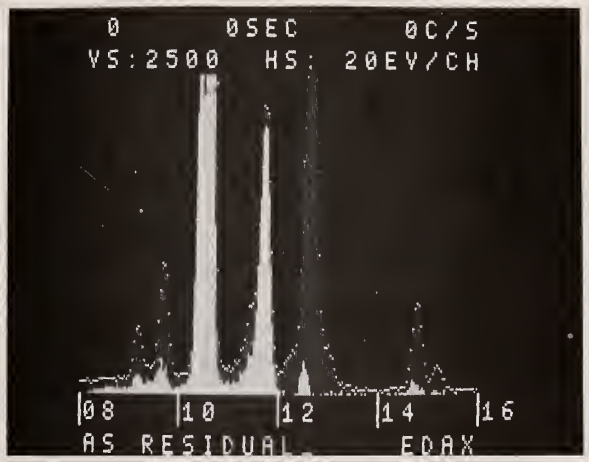

Figure 12a. Residual spectrum (bars) for As left after subtracting fitted library standard for Pb, showing effect of changed peak ratios.

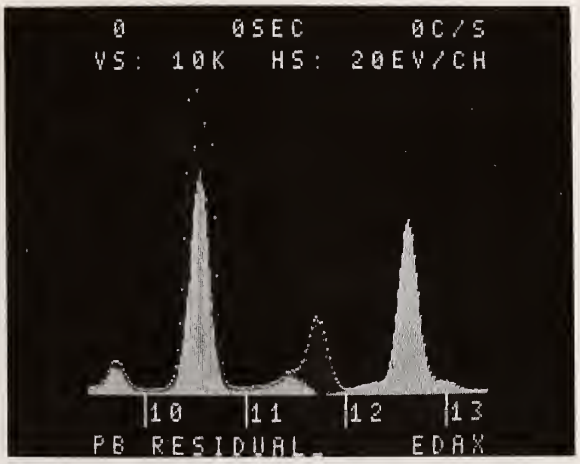

Figure 12b. Residual spectrum (bars) for Pb left after subtracting fitted library standard for As, showing effect of changed peak ratios.

Table 11. Results of fitting of duplicate spectra.

Spectrum No.			Fitting Factors			
			Linear		Filter	
As	Pb	As-Pb	As	Pb	As	Pb
1	1	1	0.2451	0.6623	0.2396	0.6758
1	1	2	.2470	.6622	.2423	.6733
1	2	1	.2454	.6669	.2389	.6830
1	2	2	.2473	.6668	.2416	.6807
2	1	1	.2422	.6513	.2380	.6616
2	1	2	.2440	.6512	.2401	.6607
2	2	1	.2424	.6559	.2373	.6686
2	2	2	.2443	.6558	.2394	.6677
		Mean	.2447	.6591	.2396	.6714
		var.	.0019	.0064	.0017	.0082
			(0.8%)	(1.0%)	(0.7%)	(1.2%)

As a third example, figure 13 shows library spectra of Ca K and Sn L peaks. The main overlap here is between the Ca Kα and Sn $L\beta_1$ measured on a sample composed of $CaCO_3$ and SnO_2 in H_3BO_3. Since the Sn Lα, is relatively free from interference, we may expect it to determine the Sn contribution fairly well, but the Ca intensity will depend strongly on the ratio of the Sn Lβ, to Lα peak heights. Table 12 shows the fitting ratios for varying ranges, illustrated in figure 14; these are a) the Sn Lα, b) the Sn Lβ – Ca Kα, c) the Ca Kα and Kβ with Sn Lβ lines, d) the entire range. All of the fits give reduced chi-squared values between .97 and 1.03, indicating excellent fits.

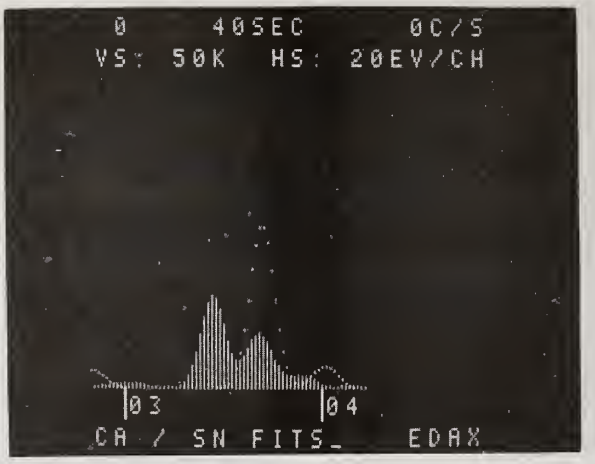

Figure 13. Library spectra for Ca (dots) and Sn (bars).

Table 12. Ca-Sn fits to overlapped spectrum.

	Range (keV)		Linear		Filtered	
	From	To	Ca	Sn	Ca	Sn
a)	3.2	3.56	0.15827	0.60213	0.15853	0.60158
b)	3.56	3.86	.16831	.57355	.16247	.60073
c)	3.56	4.28	.16276	.61625	.15607	.61721
d)	3.2	4.28	.16265	.56756	.15558	.59801

Figure 14a. Fit from 3.2 to 3.56.

Figure 14b. Fit from 3.56 to 3.86.

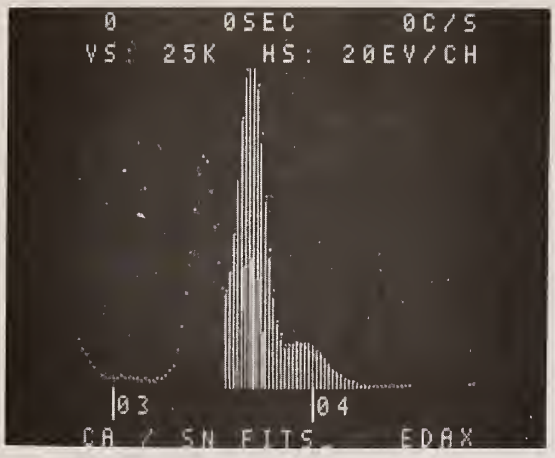

Figure 14c. Fit from 3.56 to 4.28.

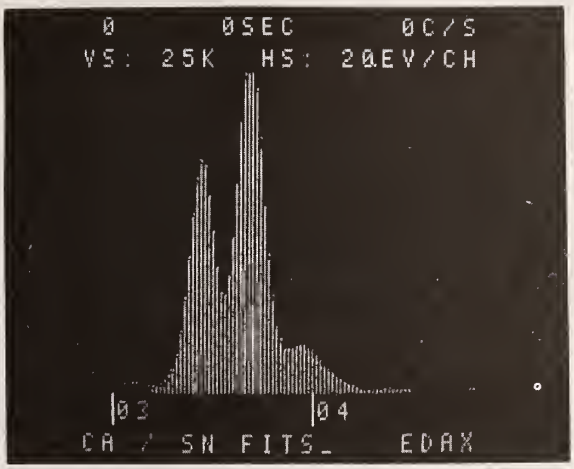

Figure 14d. Fit from 3.2 to 4.28.

Figure 14. Ca:Sn library fits (bars) compared to measured spectrum (dots) over different energy ranges. Note variation of ratios of minor peaks.

Note however, that the factors obtained vary substantially. Figure 13 illustrates the fits, and shows the reason for the variation. The composite fitted spectrum does not match the peak ratios of the measured one (note for instance the lower Sn Lα and higher Ca Kβ – Sn $L\beta_2$ at 4 keV); this is due to changes in the peak ratios of these elements in the mixture, as compared to the pure elements. The same problem was also evident in the As-Pb overlaps, since the As K absorption edge lies between the Pb Lα and Lβ, and reduces the Lβ in the composite.

This problem is increased if the excitation conditions are not the same for the mixture and the pure library spectra. We analyzed the Ca-Sn mixture again using monoenergetic nickel Kα excitation. The fitting coefficients (Table 13) show a different ratio of Ca to Sn for fits performed over the entire overlap range 3.2-4.6 keV. Figure 15 shows that the generated composite has greater discrepancies with the measured spectrum, because the different L edges of Sn are differently excited in this case.

Table 13. Ca-Sn fits to monoenergetically excited spectrum.

	Linear	Filtered
Ca	0.17416	0.17512
Sn	.57871	.58742

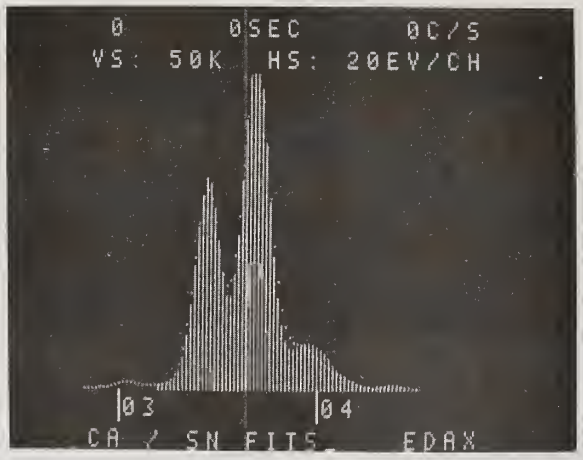

Figure 15. Fit of library spectra (bars) to spectrum measured on Ca:Sn mixture (dots) using quasi-monoenergetic excitation which changes peak ratios.

The examples shown so far have all had quite large peaks and low backgrounds. The fourth example concerns the overlap of Cr Kβ – Mn Kα, complicated by low concentrations of both unknowns and standards. This gives small peaks, and the samples have organic matrices which scatter significant amounts of background. Figure 16 shows the standard spectra, each measured for 400 seconds with quasi-monoenergetic excitation obtained by placing a gold filter in front of a gold-target x-ray tube operated at 25 kV, 500 μA. The Mn standard contains 100 μg Mn in a 2 gram sample, or 50 ppm by weight. The Cr standard contains 20 μg Cr, or 10 ppm, with a significant Fe contaminant peak.

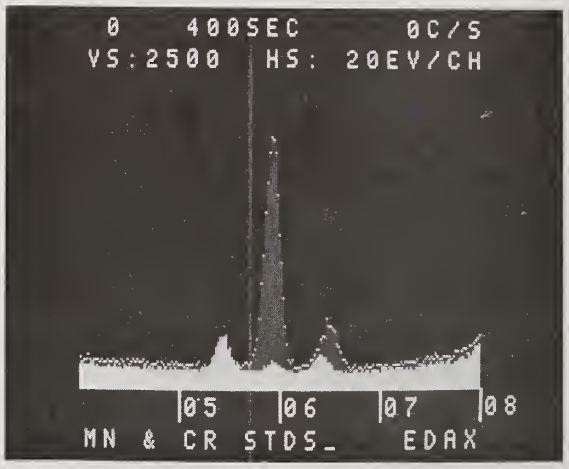

Figure 16. Standard (library) spectra for trace Mn (dots) and Cr (bars).

The unknown spectrum (figure 17) was obtained from a sample containing 20 μg Mn, 100 μg, Cr. This spectrum is clearly not a simple linear sum of the two standards; figure 18 shows the results of fitting from 5 to 6.2 keV, using the standard spectra. The coefficients are 2.1066 and 0.0466 for Cr and Mn respectively (the ratios of concentrations are 5.0 and 0.2, respectively). Figure 19 shows the fit obtained using the digitally filtered spectra; the coefficients are 0.9416 and 0.0909, for Cr and Mn. The filtering out of the background changes the ratios of Cr to Mn dramatically, but the values are not "better". It also changes the reduced chi-squared from 0.88 to 0.47. (The low number of counts in these spectra make the chi-squared values appear better than for spectra with

higher intensities.) However, it is obvious that the result does not match the measured spectrum. It appears from these results that background suppression using filtering is only useful when the background is in fact small relative to the peaks to begin with.

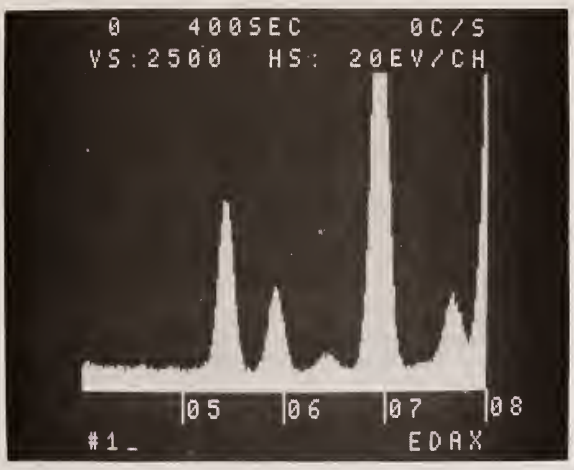

Figure 17. Spectrum measured on sample containing Mn and Cr.

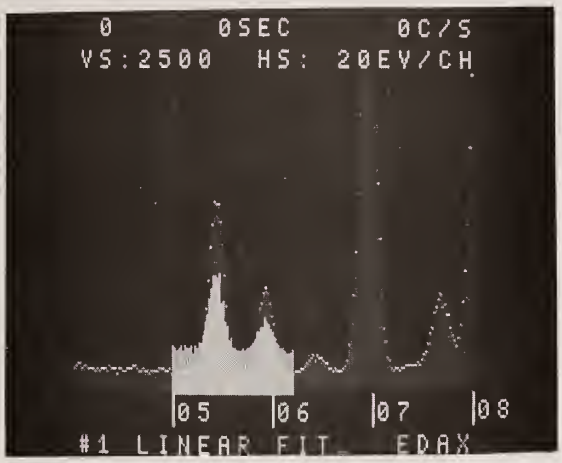

Figure 18. Linear fit (bars) of library Cr and Mn spectra to unknown composite (dots).

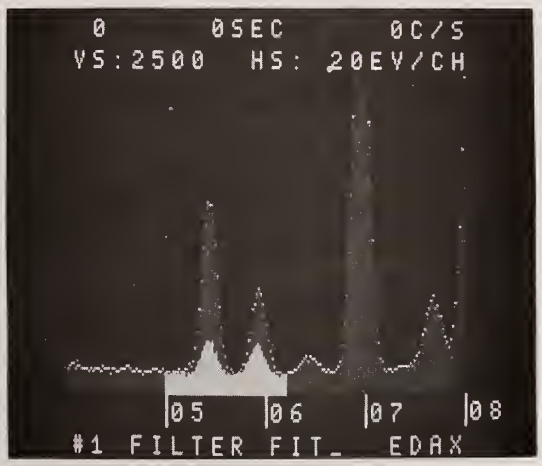

Figure 19. Fit of library spectra (bars) to composite (dots), using digital filter.

In cases like this, the use of generated modified-Gaussian peaks with a separate removal of background gives substantial improvement. Generating five peaks (Cr Kα and Kβ, Mn Kα and Kβ, and Fe Kα) above a linear background interpolated from 4.9 to 6.66 keV, returned intensities as listed below and gave a reduced chi-squared of 0.98 (Table 14). Figure 20 shows the overall fit, and the lines for each element singly.

Table 14. Intensities of simultaneously fit generated peaks.

Element/Line	Intensity (Counts per 400 seconds)		
	Unknown	Cr std.	Mn std.
Cr Kα	11421	2311	-4
Cr Kβ	1782	349	63
Mn Kα	3715	202	15148
Mn Kβ	312	62	2221
Fe Kα	791	1018	665

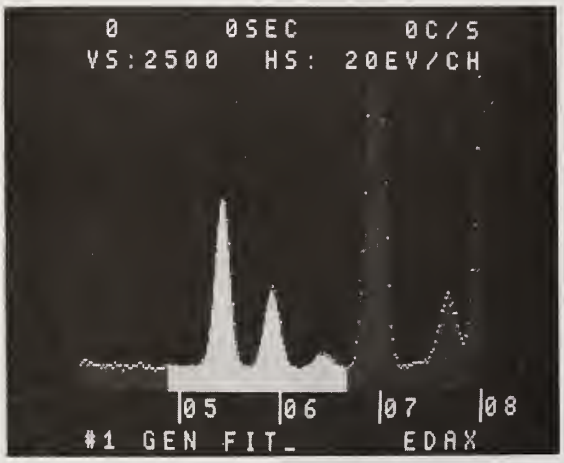

Figure 20a. Agreement of individually generated Cr, Mn, and Fe peaks to measured composite spectrum.

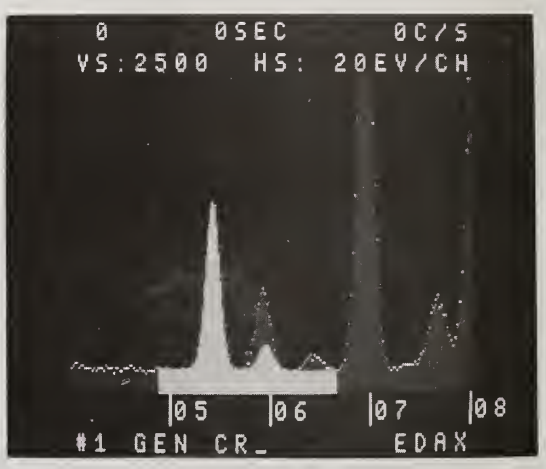

Figure 20b. Detail of figure 20a showing only generated Cr peak.

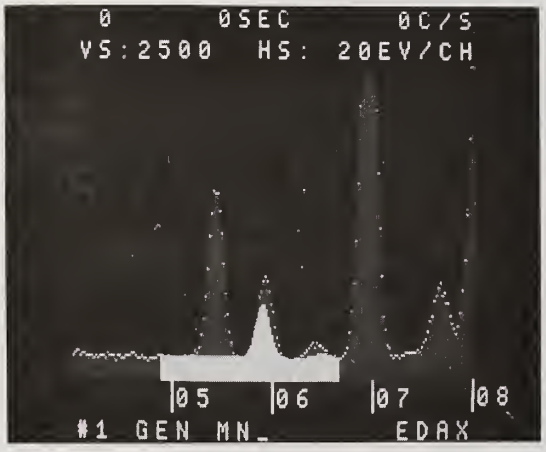

Figure 20c. Detail of figure 20a showing only generated Mn peak.

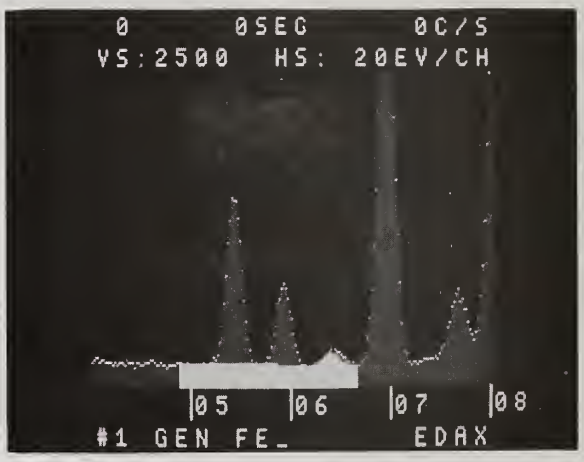

Figure 20d. Detail of figure 20a showing only generated Fe peak.

The β/α ratios are reasonable, confirming the general success of the fit; the low value obtained for the absent element in each standard is a measure of the error of fitting. The ratios of intensities in unknown to standard are within the error expected from statistics and the chemical preparation procedure. For such low concentration specimens, the intensity ratio (using the sum of Kα and Kβ) should be close to the concentration ratio so we predict 97.5 µg of Cr and 23.1 µg of Mn (the amounts expected from preparation are 1-- and 20 µg, or 50 and 10 ppm, respectively).

Similar computation on a total of sixteen "unknown" samples confirmed the applicability of fitting individual peaks with a separate background removal [9]. The same conclusion would be expected for much larger concentrations of elements excited by an electron beam, since the background is larger; this is particularly true at low energies (1-3 keV) where the background shape is strongly influenced by concentration.

In summary, these examples show that multiple least squares fitting of library spectra can be useful in cases where overlaps are too complete, or involve too many lines, for practical peak generation. However, calibration is absolutely critical, as errors of even 1 or 2 eV can cause large changes in results. Fitting over all the lines involved is perhaps the most consistent and defensible method, but introduces errors if peak ratios change. This will happen even if the identical excitation conditions are used, and changes in excitation conditions exacerbate the errors. Fitting of generated peaks would be equivalent if all the major and minor peaks were used and their ratios known. If the overlap involves only a few lines and others are available without overlaps, it may be preferable to ignore the overlapped region altogether. The digital filtering of the spectrum changes the fitting ratios slightly, but does not appear to significantly increase the overall error. It may improve results somewhat in cases of varying and/or large backgrounds. Although the filter and fit method may be used for this type of deconvolution, in most cases of practical analysis methods involving peak generation after discrete background removal are preferred because of their greater versatility and lesser dependence on availability of appropriate library spectra with identical peak positions and ratios.

References

[1] Applications of Computers to Nuclear and Radiochemistry, NAS-NS 3107 (U.S. Dept. Commerce, Office of Technological Services, 1962).

[2] Gehrke, R. J. and Davies, R. C., Anal. Chem., 47, 1537-1541 (1975).

[3] Schamber, F. H., in "X-Ray Fluorescence Analysis of Environmental Samples", T. Dzubay (ed.) Ann Arbor Press, 1977, p. 241-257.

[4] Gunnink, R. and Niday, J. B., Computerized Quantitative Analysis by Gamma-Ray Spectrometry. Volume 1, Lawrence Livermore Laboratory, March 1, 1972.

[5] Russ, J. C., "Processing of X-Ray Spectra", EDAX EDIT or Volume 6, Number 3, page 4-39.

[6] Arinc, F., Gardner, R. P., Wielopolsi, L., and Stiles, A. R., Advances in X-Ray Analysis, 19, 367 (1976).

[7] Russ, J. C., A Fast Self-Contained No-Standards Quantitative Program for EDS, Proc. 9th Annual MAS Meeting, 1978, p. 46.

[8] Statham, P. J., X-Ray Spectrometry, 7, 132-137 (1978).

[9] Specimens courtesy of Dr. W. Wegscheider, U. Graz, Austria.

National Bureau of Standards Special Publication 604. Proceedings of the Workshop on Energy Dispersive X-Ray Spectrometry held at NBS, Gaithersburg, Maryland, April 23-25, 1979. (Issued March 1981)

ARTIFACTS OBSERVED IN ENERGY DISPERSIVE X-RAY SPECTROMETRY IN ELECTRON BEAM INSTRUMENTS – A CAUTIONARY GUIDE

C. E. Fiori*, D. E. Newbury, and R. L. Myklebust

*Division of Research Services
National Institutes of Health
Bethesda, Maryland 20205

Center for Analytical Chemistry
National Bureau of Standards
Gaithersburg, Maryland 20234

Abstract

Microanalysis with the energy dispersive x-ray spectrometer on electron beam instruments is complicated by the existence of spectral artifacts which are introduced during the x-ray detection, amplification and display processes. The artifacts of the x-ray detection mechanism include absorption in the window and silicon dead layer, peak broadening, formation of parasitic peaks by escape of silicon x-rays, sum peaks due to pulse coincidence, and effects due to system deadtime. Pulse coincidence effects are exacerbated when high energy (> 30 keV) x-rays strike the detector. In the transmission electron microscope high energy x-rays cause pulse saturation to occur. Artifacts arising from interactions of the spectrometer with its environment include microphonics, electromagnetic interference, ground loops, and stray radiation in the sample chamber. Spectral artifacts influence the strategy for qualitative analysis since artifact peaks may be misassigned to a chemical element not actually present in the specimen.

Key Words: Energy dispersive x-ray spectrometry, microanalysis, electron probe microanalysis, qualitative analysis, quantitative analysis, scanning electron microscopy, spectral artifacts, transmission electron microscopy.

1. Introduction

1.1 The x-ray spectrum

In carrying out microanalysis with the energy dispersive x-ray spectrometer attached to the scanning electron microscope, electron probe microanalyzer, or transmission electron microscope, the analyst is frequently confronted with artifacts introduced into the spectrum by the measurement process [1][1]. These artifacts can adversely affect both qualitative analysis, leading, for example, to misidentification of peaks, and quantitative analysis, causing improper measurement of x-ray intensities. To aid the analyst both in recognizing these artifacts in spectra and properly accounting for them, we shall provide a catalogue of typical artifacts, listing their characteristics and providing examples of them in real spectra. It is beyond the scope of this paper to give details of the physical origin of these artifacts; references to more complete descriptions of each artifact will be provided. Following the catalogue of artifacts, a systematic approach to qualitative analysis will be described, with attention given to the recognition of artifacts. The treatment of artifacts in measuring x-ray intensities for quantitative analysis will be considered.

[1]Figures in brackets indicate the literature references at the end of this paper.

As a starting point, it is useful to consider the nature of the x-ray spectrum generated in the sample by the incident beam. For a target such as copper bombarded with electrons at an energy of 20 keV, the form of the x-ray spectrum generated in the specimen is illustrated in figure 1. The spectrum consists of two constituents: (1) characteristic peaks which result from electron transitions following ionization of an inner shell of an atom by a beam electron; (2) Bremsstrahlung ("braking radiation") or continuous x-radiation which is formed when a beam electron undergoes deceleration in the coulombic field of an atom [2]. The continuous x-radiation forms a background extending from zero energy up to the energy of the incident beam. In the context of this paper, it must be pointed out that the x-ray continuum is not an artifact since it is a product of the beam interaction with the solid, and that it carries information about the average atomic number of the sample. Artifacts are the deviations from the natural spectrum introduced into the observed spectrum by the measurement process. The generated continuum of energy E can be reasonably well described by the equation of Kramers [3]:

$$I \propto \bar{Z}(E_o - E)/E \qquad (1)$$

where I is the continuum intensity in an energy interval ΔE, $\bar{Z}$ is the average atomic number of the target, E_o is the incident beam energy, and E is any energy less than E_o. At very low energies, the continuum intensity predicted by equation (1) increases toward infinity.

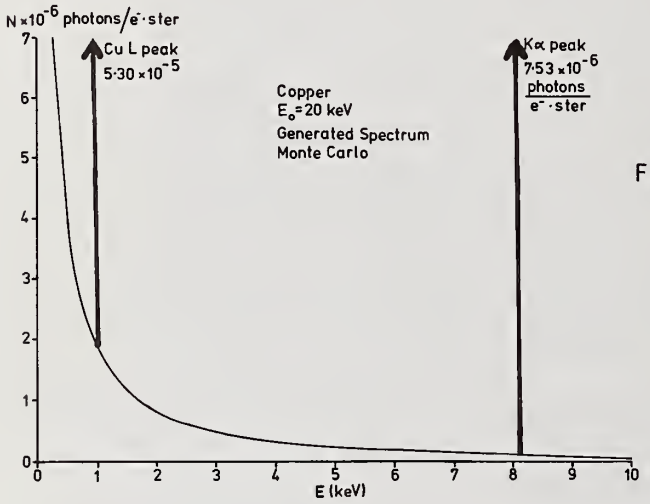

Figure 1. Characteristic and continuum x-ray spectrum generated in a bulk copper target by a 20 keV electron beam as calculated by Monte Carlo electron trajectory simulation. Note that only the alpha member of the characteristic x-ray family is plotted.

The x-rays are generated over a range of depth in the sample, and during propagation out of the sample, absorption occurs. Absorption significantly alters the shape of the emitted spectrum, which is shown in figure 2(a), as calculated by a Monte Carlo electron trajectory simulation [4]. Low energy x-rays (<300 eV) are very strongly absorbed, and only those low energy x-rays generated near the surface escape. High energy x-rays are less likely to be absorbed. The mass absorption coefficient for x-rays decreases with increasing x-ray energy, except near the energy of an absorption edge. An absorption edge corresponds to the ionization energy of an inner shell; x-rays at an energy just above the absorption energy are very strongly absorbed relative to energies just below the edge.

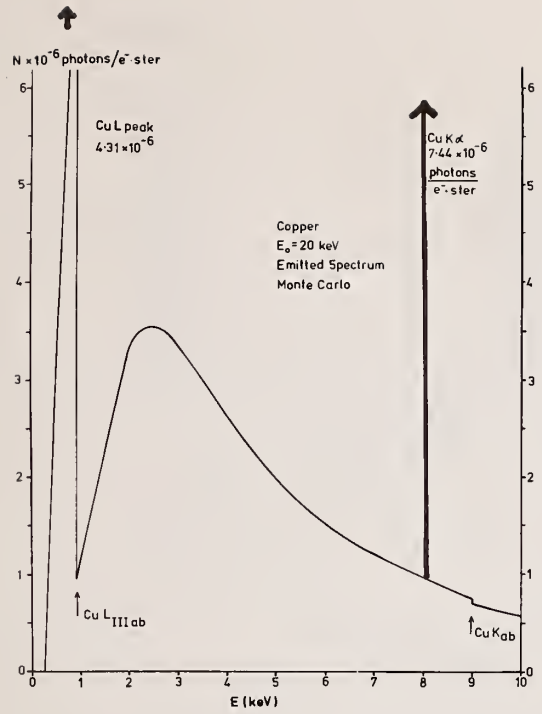

Figure 2(a). Characteristic and continuum x-ray spectrum emitted from a bulk copper target excited with a 20 keV electron beam as calculated by a Monte Carlo electron trajectory simulation.

The x-ray spectrum which is finally observed with the energy dispersive x-ray spectrometer is further modified by the measurement process. The artifacts introduced by the measurement process can be broadly classified into two main categories: (1) those which arise during the detection process and (2) those associated with the signal manipulation following the detector. In addition, artifacts may arise because of certain unfortunate interactions between the energy dispersive x-ray spectrometer and the instrument environment in which it operates.

2. Artifacts of the Detection Process

2.1 Absorption effects

The structure of a typical energy dispersive x-ray spectrometer containing a lithium-drifted silicon detector is illustrated in figure 3. In order to enter the active portion of the detector, x-rays must pass through a beryllium window with a nominal thickness of 7.6 μm (0.3 mil), which maintains the vacuum integrity of the spectrometer, a gold surface electrode about 20 nm thick, and an inactive or dead layer of silicon, 20 - 200 nm thick. The absorption which occurs during passage through those layers eliminates virtually all x-rays with an energy below 500 eV. Above an energy of about 2 keV the absorption becomes relatively insignificant so that nearly all x-rays pass into the active detector region. For intermediate energies the transmission is about 45 percent at 1 keV and 70 percent at 1.5 keV. The modifications to the spectrum which result from absorption in the detector components can be seen in figure 2(b) for the calculated copper spectrum and in an experimentally measured spectrum, figure 2(c). These effects are further illustrated in the experimentally measured spectrum from high purity carbon, figure 4. The decrease in the measured continuum below 1 keV is evident, and discontinuities are observed in the continuum at the absorption edges of silicon and gold, where the abrupt change in mass absorption coefficient is observed as a discontinuity in the continuum. In the windowless variety of the energy dispersive x-ray spectrometer, the measurable x-ray range extends as low as carbon Kα (0.282 keV), although absorption still occurs in the silicon dead layer and gold electrode [6].

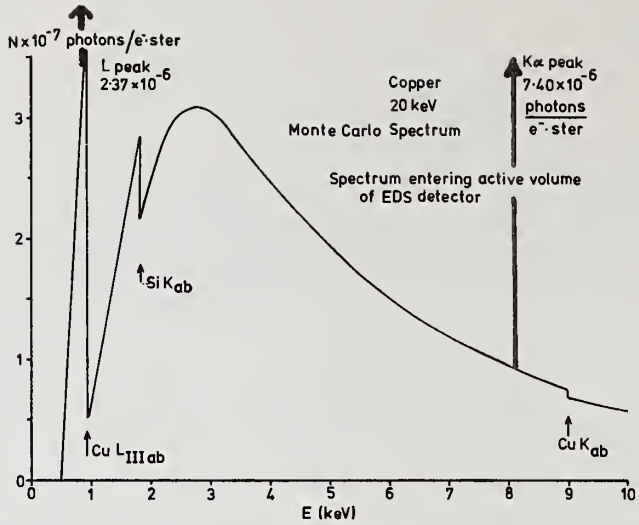

Figure 2b. Spectrum of 2a corrected for absorption in the beryllium window and silicon dead layer.

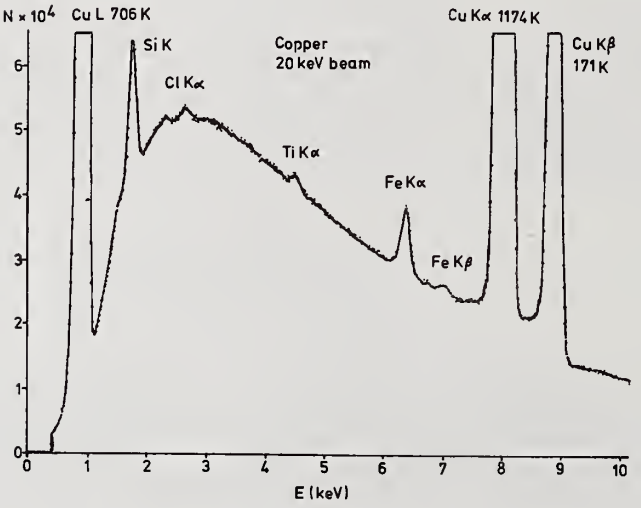

Figure 2c. Experimental spectrum of copper; 20 keV beam. Chlorine, titanium, and iron are trace contaminants in the specimen or mounting medium. Note that the CuKα escape peak at 6.30 keV is obscured by the FeKα peak at 6.40 keV. In the peak intensities "K" equals 1000.

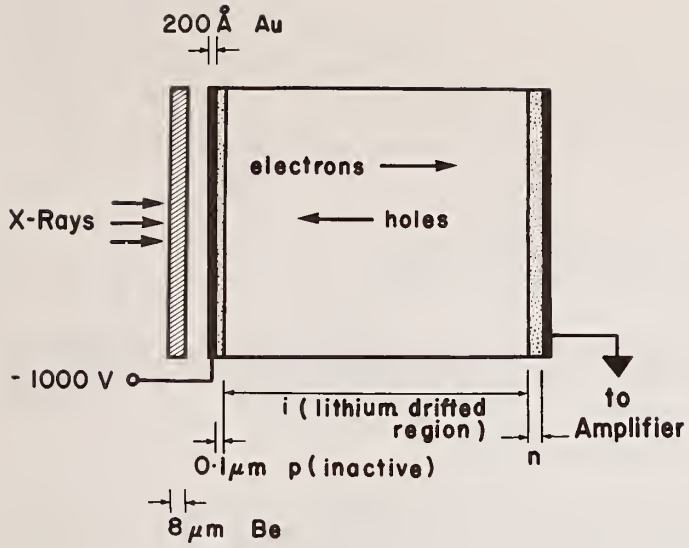

Figure 3. Schematic diagram of a typical lithium-drifted detector of an energy dispersive x-ray spectrometer.

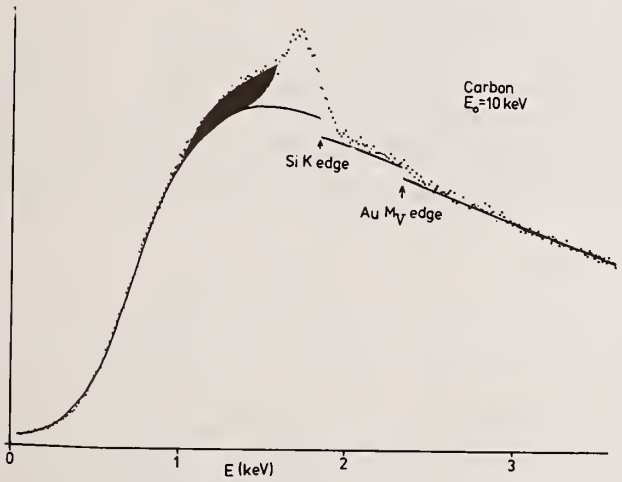

Figure 4. EDS spectrum from carbon excited by a 10 keV electron beam. The silicon and gold absorption edges can be observed as well as a silicon peak resulting from internal fluorescence of the silicon dead layer. The solid line is a theoretical fit to the continuum; the shaded region is the distortion caused by incomplete charge collection of the silicon internal fluorescence peak.

The absorption of x-rays in the inactive silicon layer leads to fluorescent emission of silicon K x-rays which are detected in the active region of the spectrometer. This causes the production of a small artifact silicon peak in the spectrum which is not representative of a silicon constituent in the specimen. In the analysis of a bulk specimen, this artifact silicon peak is typically equivalent to an apparent concentration of about 0.2 percent or less by weight of silicon in the sample.

2.2 Peak broadening

In the Si(Li) detector the process of detection consists of converting the energy of the incident photon into charge carriers (electron-hole pairs), proportional in number to the photon energy, within the detector material [7]. The charge carriers are collected by applying a suitable bias to the faces of the detector. All subsequent operations involve the measurement of this charge.

The natural width of an x-ray peak is in the order of 1 eV in the energy range of interest, measured at half the maximum peak intensity (the measurement is designated full width, half maximum, "FWHM"). The detection process in the energy dispersive x-ray detector results in statistical uncertainty being introduced which distributes the x-ray information over a range of energies such that the measured peak has a FWHM about two orders of

magnitude greater than the natural width [8]. For example, a typical detector will produce a peak for manganese Kα with a FWHM of 150 eV. The natural width of Mn Kα is 2.3 eV. Consequently, a natural peak of 2.3 eV width having an amplitude of 1000 counts will be degraded to a peak of 150 eV width having 15 counts in the peak channel (assumed to be 10 eV in width). The natural x-ray line would be totally contained in one, or at most two, such channels. The peak width varies as a function of peak energy, and a convenient measure of the FWHM for any peak is given by [1]:

$$FWHM_1 = \sqrt{2.5(E_1 - E_2) + FWHM_2^2} \qquad (2)$$

where $FWHM_1$ and E_1 are the peak width and energy (eV) of the peak of interest, and $FWHM_2$ and E_2 are the known values for a reference peak, usually manganese Kα, recorded with the same detector under similar conditions.

2.3 Peak distortions

The peak produced by the detector is reasonably well described by a Gaussian function, figure 5. Deviations from the ideal Gaussian shape occur on the low energy side of the peak due to the phenomenon of incomplete charge collection [9,10]. Incomplete charge collection produces a noticeable shoulder on the low energy side of the peak, figure 6. The relative magnitude of this shoulder is dependent on the energy of the peak. A second consequence of the incomplete charge collection phenomenon is the formation of a "background shelf" of counts lost from the peak extending from the peak energy down to zero energy. The background shelf is normally obscured by the continuous x-ray background present in electron-excited spectra. The effect is illustrated in the spectrum of figure 7, where the manganese radiation is obtained with virtually no x-ray continuum from a radioactive ^{55}Fe source. The background shelf at half the peak energy has an intensity of about 0.1 percent of the peak intensity. The total intensity distributed in the background shelf is about 1 percent of the integrated peak intensity.

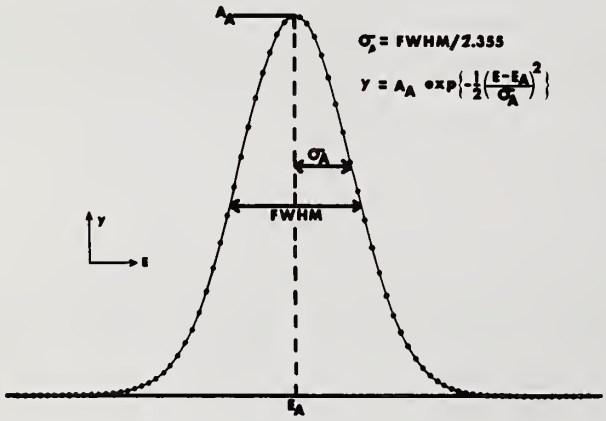

Figure 5. Theoretical Gaussian distribution which describes an EDS peak. σ is the standard deviation of the distribution, A_A is the peak amplitude, and y is the amplitude at any energy, E.

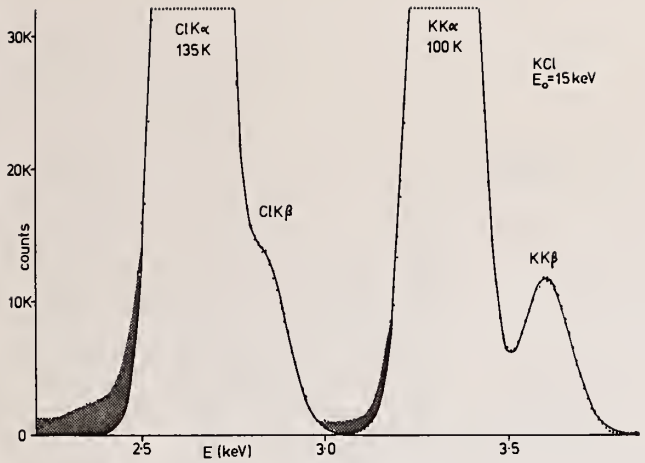

Figure 6. EDS spectrum of KCl illustrating (1) peak overlap and (2) the incomplete charge collection distortion. The Cl Kα and Kβ peaks are not resolved while the K Kα and Kβ are nearly resolved. The solid line is a Gaussian fit to the data points. The shaded areas are the distortions introduced by incomplete charge collection.

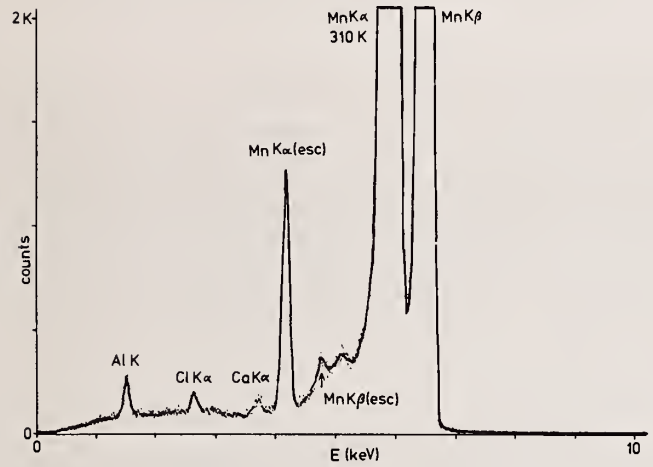

Figure 7. EDS spectrum derived from ^{55}Fe radioactive source. The background shelf is easily observed at energies below Mn Kα to the threshold energy, 300 eV. The silicon escape peaks from the Mn Kα and Kβ are noted. Extraneous characteristic peaks from the source holder are observed (aluminum, chlorine, and calcium signals).

2.4 Silicon escape peaks

The process of capturing an x-ray in the detector involves the ionization of a silicon atom. De-excitation of the ionized atom involves the emission of a silicon K x-ray in about 4 percent of the ionizations. Because an element has a relatively low absorption for its own characteristic x-rays, these silicon x-rays have a significant probability of escaping the active detector area, robbing the x-ray pulse being measured by an amount corresponding to the silicon K energy, 1.74 keV for Si Kα and 1.83 keV for Si Kβ. An artifact peak is formed, the so-called silicon escape peak, at an energy of E_1 - 1.74 keV, where E_1 is the energy of the parent peak. Due to the low detector resolution and the low probability for silicon Kβ formation, only one escape peak per parent is observed. The escape peaks for manganese Kα and Kβ radiation can be seen in the radioactive source spectrum in figure 7 and the electron-excited spectrum of manganese in figure 8. The relative magnitude of the silicon-escape peak varies with the energy of the parent peak, ranging from about 1 percent of the integrated parent peak intensity for phosphorus Kα to 0.01 percent for zinc Kα x-rays. Below the excitation energy for silicon, 1.840 keV, the silicon K escape peak cannot be generated.

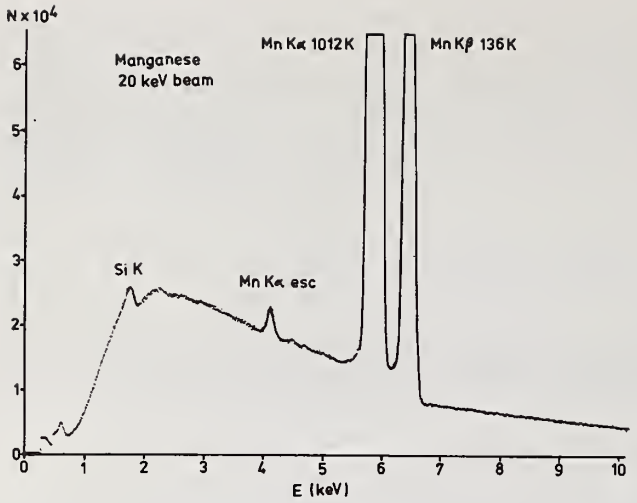

Figure 8. EDS spectrum of manganese excited by a 20 keV electron beam. As compared to figure 7, the continuum spectrum makes the observation of the distortion due to incomplete charge collection difficult except near the peak. The background shelf is obscured in this spectrum but it is still present.

3. Artifacts Introduced During Signal Processing

The task of amplifying the small charge collected during the capture of a photon by the detector to yield a signal which is useful for classification by a multichannel analyzer (MCA) requires extensive signal processing [11]. Moreover, in order to minimize the effects of noise to produce an amplified signal capable of yielding a high resolution spectrum, long pulse widths must be employed, in the range 10 - 100 μs. Since the amplification circuits are occupied for such a relatively long time with the pulse developed from a single photon, there is a high probability that a second photon may enter the detector during this occupied period (or deadtime) and lead to a distorted signal. Artifacts of the signal processing chain arise principally from pulse coincidence effects.

3.1 Pulse pileup

If x-rays of a peak energy E_1 are being measured, pulse coincidence can lead to a continuous band of overlapping pulses in the range E_1 to $2E_1$, the so-called pulse pileup continuum, figure 9 [12]. A modern system contains an efficient pulse pileup rejector which functions to eliminate overlapping pulses. However, there is a limitation in the capability of the rejector to separate two pulses closely spaced in time. Therefore, even an optimally adjusted rejector will allow a pile-up sum peak, which is composed of pulses in nearly exact coincidence, to appear in the spectrum, figure 10. Moreover, for low energy pulses, the pileup rejector may fail. For example, a properly adjusted pileup rejector may function adequately for silicon, figure 10, and fail badly for magnesium, figure 9, due to the differences in the energies of the pulses. If a spectrum contains major peaks of energy E_1, E_2, and E_3, sum peaks may be found at $2E_1$, $2E_2$, $2E_3$, $(E_1 + E_2)$, $(E_2 + E_3)$, and $(E_1 + E_3)$.

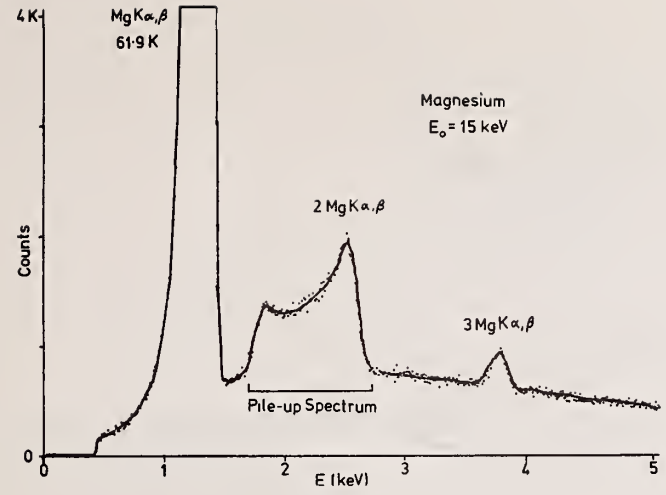

Figure 9. EDS spectrum of magnesium excited by a 15 keV electron beam. Pile-up peaks and pile-up continuum can be observed.

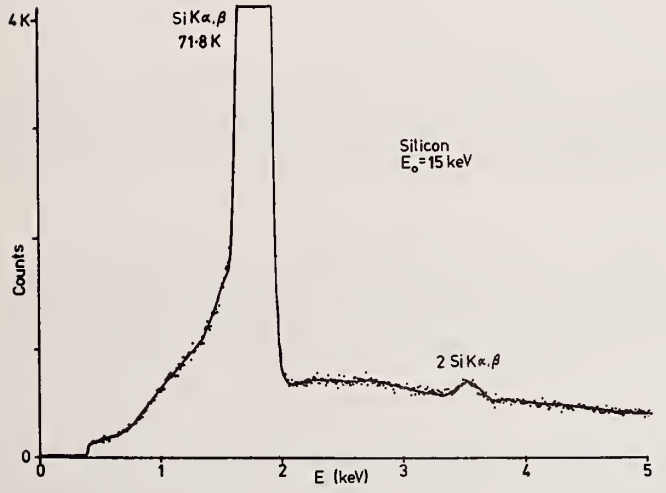

Figure 10. EDS spectrum of silicon excited by a 15 keV electron beam. Only a small sum peak can be observed, and the pile-up continuum is not significant.

3.2 Deadtime Correction

The system deadtime which results from the long pulse widths is normally compensated automatically by the signal processing system through the function known as "live time correction". If the desired live time is T seconds, the clock time is allowed to run to $T + \sum_i n_i \tau_i$, where τ_i is the pulse width appropriate to each different energy pulse E_i and n_i is the number of each type of pulse. The circuitry of the deadtime correction section of a signal processing system is capable of making a sufficiently accurate correction to satisfy most practical analysis situations. The analyst must not, however, presume that he can use an arbitrarily high count rate with the assumption that the deadtime correction will automatically accommodate that rate. Indeed, at high count rates, sum peak loss becomes significant. Every pulse in a double energy peak represents the loss of two pulses from the parent peak. In general, pulses lost from a peak due to pile-up are not correctly accounted by the deadtime circuit. However by using a count rate where the sum peaks are not in evidence in the spectrum, this effect is reduced to an acceptable level.

For those applications where the output pulses of the amplifier are used directly, such as intensity modulation of a cathode ray tube for x-ray area mapping and x-ray line profiling, which are applications where a high count rate is especially useful, the analyst

should be aware of the following insidious artifact. In figure 11, the output count rate from a processing system is plotted versus input count rate for several different pulse widths. For the longest pulse widths (which would yield the highest spectral resolution), the output count rate actually begins to decrease above an input count rate of about 10,000 cps. Such a system should not be operated above a count rate of about 15,000 cps. Above the maximum in response, a situation could be encountered where two widely differing input count rates, which could correspond, for example, to the signals obtained for an element from regions of radially different composition, yield the same output count rate, and hence, the same apparent composition in an area or line scan.

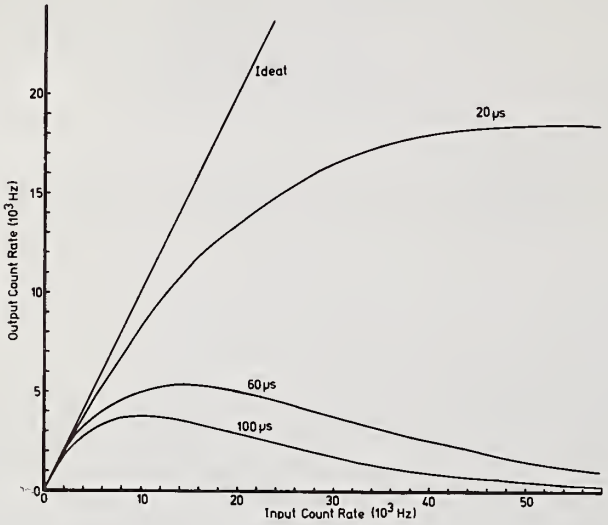

Figure 11. Relationship of output and input count rates for a generalized EDS system for three different values of pulse width.

A second important point about figure 11 is the fact that the input count rate considered is the total spectrum count rate, from the minimum cutoff energy of the discriminator, about 500 eV, to the incident beam energy. All x-rays entering the detector, characteristic as well as continuum x-rays, contribute to the limitation on input signal rate.

3.3 High energy x-ray effects

The extension of energy dispersive x-ray spectrometry to the transmission electron microscope operating at 100 keV or more raises the problem of processing pulses derived from the capture of x-rays of very high energy, as well as x-rays in the practical analytical range of 1 - 20 keV. Under normal operation, the main amplifier is adjusted so that the useful x-ray energy range (1 - 20 keV) spans a specified group of channels (typically quarter, half or full memory) in the multichannel analyzer. Under bombardment with high energy electrons, the specimen will emit a continuum spectrum with x-ray energies up to the beam energy, and possibly high energy characteristic x-rays as well (Kα - Kβ). Significant numbers of high energy x-rays will strike the detector which will produce voltage pulses outside the allowed range as specified above. These high energy pulses will produce electronic saturation, figure 12, and can lead to two undesirable effects, (1) loss of resolution and (2) incorrect operation of the deadtime circuit. The loss of resolution, which results from electronic artifacts caused by the sharp transitions associated with pulse cut-off, can be of the order of 5 eV at MnKα. The high energy pulses are proportionally wider than the low energy pulses of interest. For an acceptable deadtime, the amplifier will spend a significant amount of its time processing the wide high energy pulses leaving less time for the low energy pulses of interest.

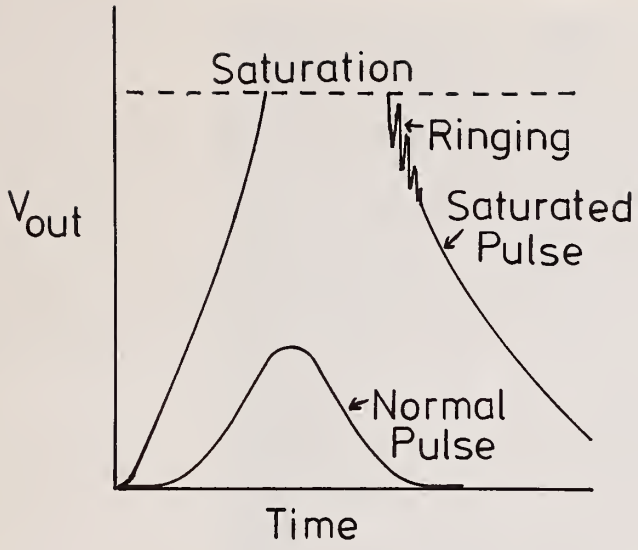

Figure 12. Schematic illustration of signal saturation showing a normal pulse and a saturated pulse. Note transient "ringing" of signal decaying from saturated condition.

4. Artifacts of the Detector-Microscope System

Several artifacts may be observed in spectra which result from certain interactions of the EDS detector and/or amplifier with the microscope environment. These artifacts can, in principle, be removed by employing suitable precautions. In order to aid the analyst in recognizing these artifacts, examples will be given.

4.1 Microphonics

The extraordinary sensitivity of the detector and amplifier of the EDS system produces a marked susceptibility to interference from mechanical and acoustic vibration and stray electromagnetic radiation. One form of artifact introduced into the spectrum from these sources is shown in figure 13. Figure 13a is the spectrum of a chromium-iron alloy obtained in the absence of interference. In figure 13b, the same spectrum recorded with an acoustic noise source (a telephone) operating contains an enormous noise background extending from zero energy up to about 2 keV, which eliminates all useful spectral information in this region. Further, the peaks in the high energy region of the spectrum of figure 13b are broadened, i.e., the resolution has degraded in the presence of the acoustic noise source, and consequently the peak amplitudes have been diminished.

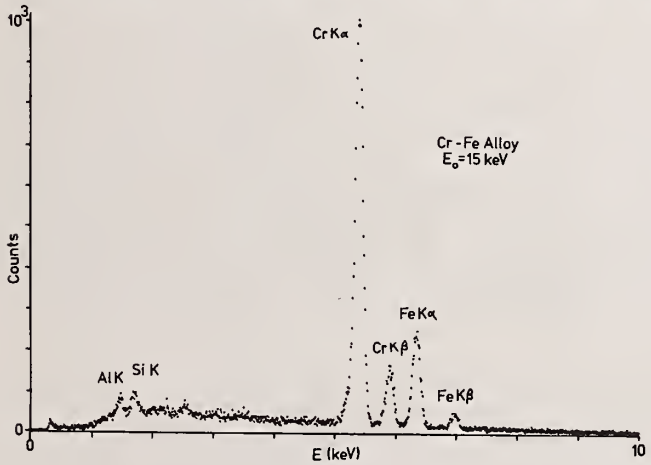

Figure 13(a). EDS spectrum of a chromium-iron alloy excited by a 15 keV electron beam. For Al and Si, the Kα - Kβ pair is unresolved.

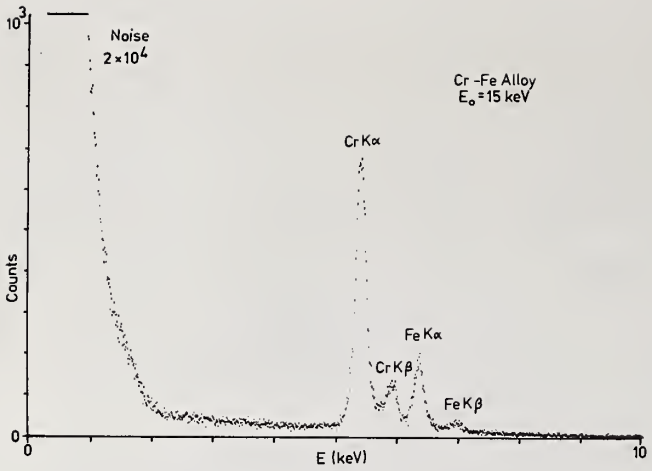

Figure 13(b). EDS spectrum obtained under identical conditions to 13a, except with a source of acoustic interference operating (nearby telephone). Note the noise spectrum exciting to about 2 keV and the degradation in resolution as compared to 13a.

4.2 Electromagnetic interference

One does not normally think of the electron beam instrument as a source of electromagnetic interference. However, several intrinsic components of electron beam systems can be sources of electromagnetic radiation which can couple with the silicon detector system and introduce artifacts. If the silicon detector-cryostat assembly, main amplifier, or interconnecting cable between these components is placed in proximity to a source of electromagnetic radiation, difficulties can arise. Typical instrumental sources for this radiation include power supply transformers, scan generators, scan coils, computers and logic circuits, and motors. For example, a poor location for the main amplifier of the EDS system would be in the same electronic bin as the SEM scan generator or placed near a computer. An example of a particularly difficult electromagnetic interference problem is that arising from interaction of the beam scan coils with the silicon detector. While the problem is not usually manifest in low beam energy SEM's the problem can be observed on high energy (200 keV) STEM-TEM instruments where the scan coil excitation is necessarily much higher and where the instrument configuration places the silicon detector adjacent to the scan coils, figure 14. The electromagnetic interference can introduce a spurious peak, figure 15, whose apparent energy is a function of the STEM magnification, since the scan coil excitation varies with magnification. Reversal of the flow of current in the scan coils would eliminate the obvious manifestation of the artifact, namely the spurious peak, but close examination of the spectrum would reveal the resolution still degraded and the deadtime correction adversely affected.

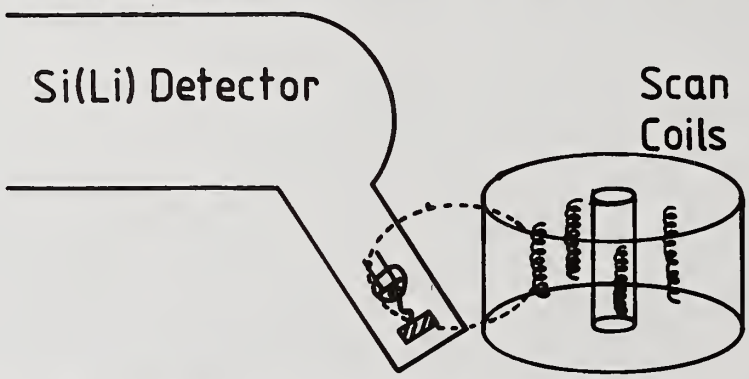

Figure 14. Schematic explanation of anomalous peak in figure 15 arising from electromagnetic coupling of scan coils.

Figure 15. Anomalous peak observed in 0 - 2 keV region in an analytical electron microscope; the peak position varied with the magnification setting (magnification 9500X, 7200X, and 5000X, left to right peaks, frame time 1/s).

This type of artifact is a member of a class of problems which result from the marriage of two independently designed systems, the x-ray spectrometer and the electron microscope. Generally, the user must be prepared to recognize and correct such problems, since it is unlikely that the manufacturers of the individual systems have had the opportunity to test the composite instrument.

4.3 Ground loops

We might normally assume that the metal components of the spectrometer/microscope system are all at ground potential with no current flowing between them. In fact, small differences in potential of the order of millivolts to volts, can exist between the components. The potential differences cause currents to flow, ranging from microamperes of dc current to many amperes of high frequency ac current. These extraneous currents are commonly referred to as "ground currents" or "ground loops" since they are flowing in components of the system which are supposedly at ground potential, such as the chassis or outer shields of co-axial cable. Since high frequency ground currents have associated electromagnetic radiation, such currents flowing in co-axial cable shielding can modulate low level signals passing through the center conductor. In EDS systems, the signals being processed are at extremely low levels, hence ground loops must be carefully avoided. The interference from a ground loop can manifest itself as degraded spectrometer resolution, peak shape distortion, background shape distortion, and/or deadtime correction malfunction. An example of peak shape distortion is shown in figure 16, where a normal MnKα - Kβ pair appears to be split into subsidiary peaks in the presence of a ground loop.

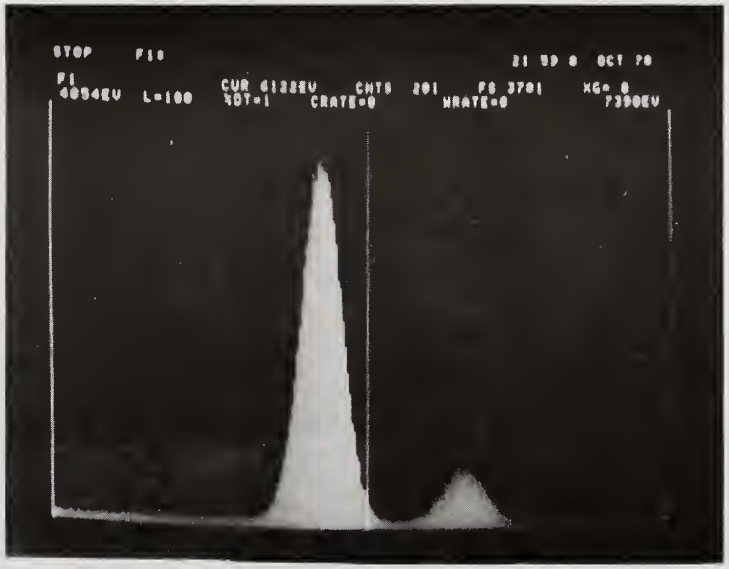

a

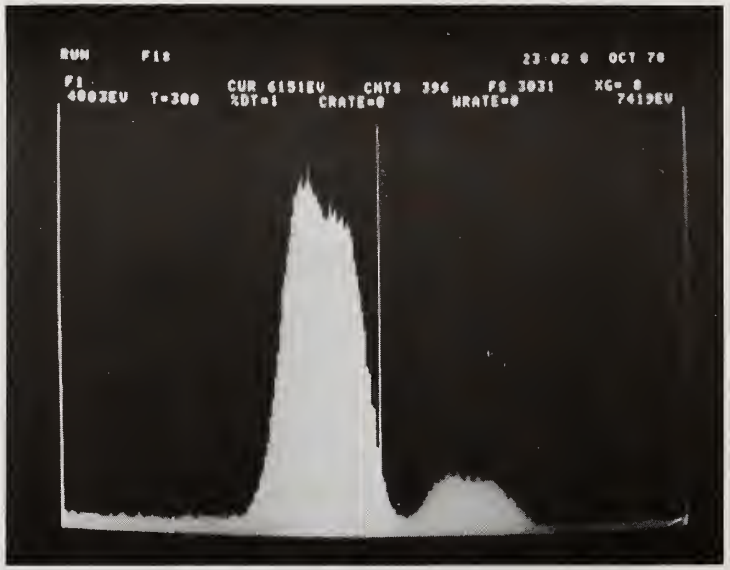

b

c

Figure 16. Electron-excited spectra of manganese showing Mn Kα - Kβ peaks. 16a. Normal spectrum. 16b. Distorted with peaks introduced by severe ground loop. 16c. As 16b, but an intermediate case.

Ground loop artifacts are best dealt with by prevention rather than cure. At the time of installation of the detector, care should be taken to insure that ground loops are not inadvertently introduced. For example, as shown in figure 17, the grounding path should be created in a logical fashion avoiding cross-connections between microscope components and spectrometer components. An important ground loop path to avoid is that between the cryostat housing (preamp) and the microscope. The resistance between the cryostat assembly (disconnected from its cabling) and the microscope column should typically exceed 5 x $10^6\Omega$. Cross connections can be inadvertently introduced when the EDS amplifier and/or multichannel analyzer units share common racks with microscope components such as scan generators, video amplifiers, power supplies, etc. Ideally, it is best to keep the two systems electrically isolated through the use of separate racks. A logical ground path should be established in the sub-systems to a high quality ground. Note that a high quality ground is not typically available at the wall power plug. A high quality ground might consist of a 1 cm diameter, or greater, copper wire leading through the shortest distance possible to an external assembly consisting of three separate 5 m or longer copper rods driven vertically into the ground and reaching into the water table. The EDS user should note that modifications to establish a high quality ground necessarily involve altering the electrical distribution network of the microscope/EDS system, and as a result, such modifications must be carried out under supervision of a qualified electrician.

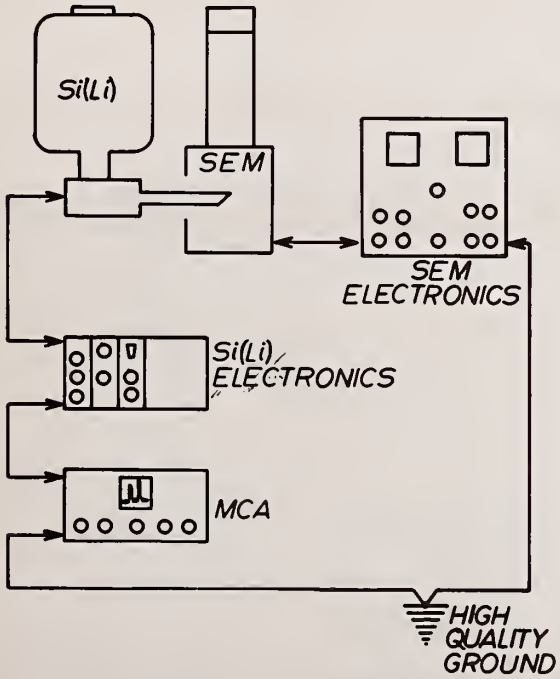

Figure 17. Schematic illustration of ideal ground paths in a SEM instrument equipped with an x-ray detector.

4.4 Stray radiation

The EDS detector accepts any x-rays emitted in a large solid angle, illustrated schematically in figure 18. This fact makes the spectrometer sensitive to stray x-rays generated over a wide portion of the sample as well as parts of the specimen stage and sample chamber [13,1]. Several potential sources of stray radiation which can excite areas remote from the beam impact point are shown in figure 19. Electrons may scatter out of the beam after interacting with the final aperture. Backscattered electrons can strike the chamber walls or stage, and upon scattering a second time, they can excite the specimen at large distances from the focused beam. Characteristic and continuous x-rays generated in the aperture can cause x-ray fluorescence effects over the entire sample. Collimation of the detector can serve to minimize these effects, but the analyst should be aware that even a well collimated detector may have an effective acceptance area several millimeters in diameter at the position of the sample. The key to avoiding difficulties with artifacts introduced into the spectrum by stray radiation is recognition of the problem. Two specimens serve as suitable tests for stray radiation: (1) It is useful to obtain the spectrum

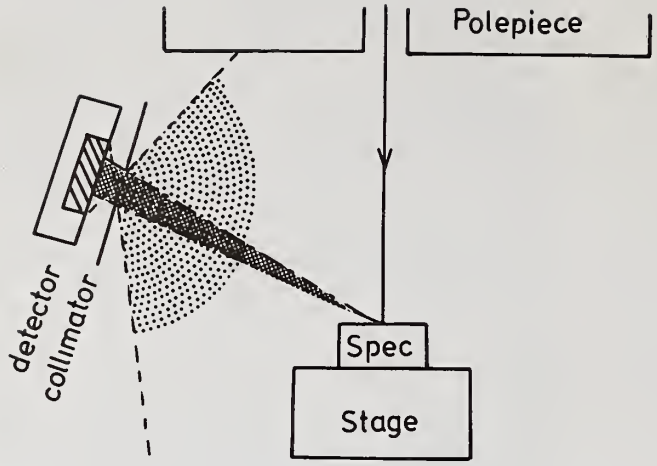

Figure 18. Solid angle of x-ray collection from the point of view of the specimen (dark shading) and the detector (light shading).

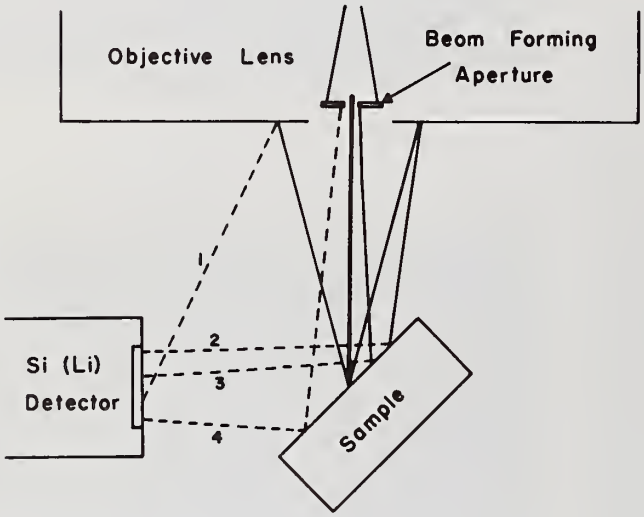

Figure 19. Possible sources of remote x-ray excitation in an electron beam/EDS system. Solid lines – electron paths; dashed lines – x-ray paths.

of spectrographically pure carbon. The appearance of characteristic x-ray peaks in the carbon spectrum is an indication of stray radiation striking the surroundings of the specimen. (2) For assessing the magnitude of stray radiation near the beam, a special Faraday specimen cup is useful, figure 20. The Faraday cup consists of a small aperture (10 - 100 μm diameter) pressed into a blind hole drilled in a block of material dissimilar to that of the aperture. Spectra are recorded for a fixed live time with the beam striking on the block, figure 21(a), on the aperture material, figure 21(b), and in the hole, figure 21(c). If the "in-hole" spectrum contains characteristic x-rays for the block and/or aperture materials, a stray radiation problem exists. In the example of figure 21, the stray radiation represents about 0.6 percent of the production of the direct beam. Elimination of such problems is entirely dependent on the nature of the individual instrument.

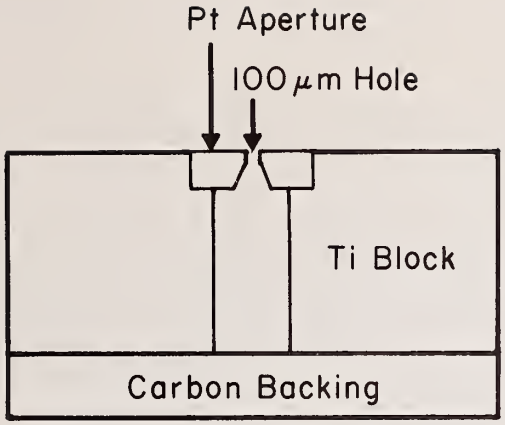

Figure 20. Schematic illustration of a cross-section through a Faraday cup suitable for detecting remote sources of x-ray excitation in an electron beam instrument.

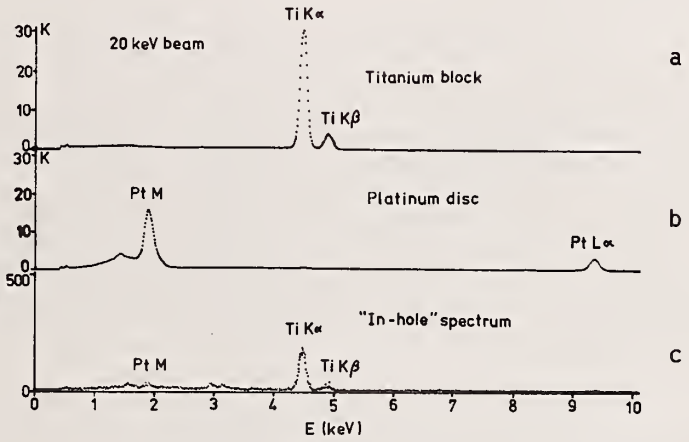

Figure 21. Spectra obtained in an electron probe microanalyzer from the components of a Faraday cup: (a) titanium block, directly excited; (b) platinum aperture (c) "In-hole" spectrum. The spectra indicate a source of stray radiation at a long range from the incident beam since only titanium x-rays are observed in the "in-hole" spectrum. The stray radiation represents about 0.6 percent of that excited by the direct beam.

Electrons backscattered from the specimen may penetrate the beryllium window of the energy dispersive spectrometer and be measured by the detector. Just as in the case of an x-ray, the detector will produce a signal pulse proportional to the energy of the electron and add this to the x-ray spectrum being measured. Because electrons are scattered from a specimen with a continuum of energies, measurement of stray electrons from the specimen has the effect of increasing the background above that expected from the normal x-ray continuum. A spectrum containing a significant electron contribution is shown in figure 22. The background under the peaks of interest is mainly due to the electron contribution. The predicted x-ray continuum, extrapolated by the method of Fiori et al., [14] from the high energy region above 25 keV, which is unaffected by the electrons, is shown for comparison. The scattered electron problem is most significant for high atomic number specimens. For such targets, a larger fraction of the incident electrons are backscattered and these electrons retain a significant portion of their incident energy. The problem of direct electron entry into the detector becomes insignificant for beam energies less than about 25 keV, since the beryllium window on the detector is effective at stopping electrons up to this energy. For windowless detectors, a magnet is used to deflect the electrons away from the detector.

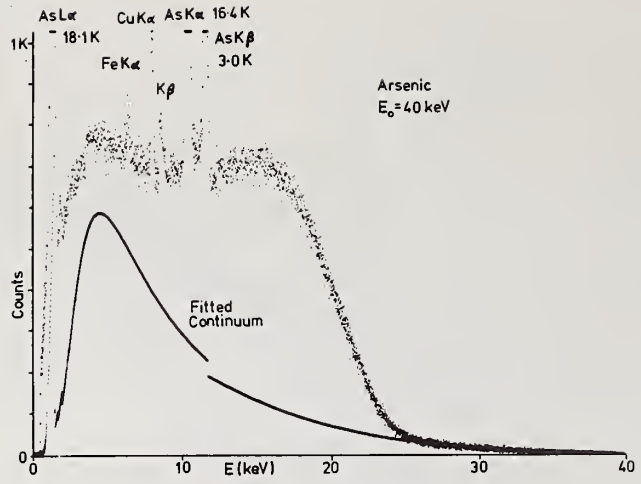

Figure 22. EDS spectrum of arsenic excited by a 40 keV electron beam showing an anomalous background below 25 keV due to direct entry of electrons scattered from the specimen into the detector. The x-ray continuum was fitted from the high energy end of the spectrum.

5. Artifacts in Qualitative Analysis

A correct qualitative analysis forms the basis for an accurate quantitative analysis. Artifacts principally influence qualitative analysis through misidentification of peaks which may be taken to represent elements not actually present in the specimen. With the important exception of artifact peaks generated by stray electrons which excite remote portions of the sample and/or surroundings and which may produce major peaks in the spectrum, all of the artifacts described in previous sections will be present at a level of the order of one percent or less of the parent peak. Thus, artifact peaks primarily cause difficulty in the identification of low intensity peaks which usually represent minor constituents of a sample. In order to properly account for artifact peaks, the following general scheme for qualitative analysis is useful [1].

5.1 General guidelines for qualitative analysis

(1) An adequate spectrum must be accumulated in order to give statistically valid peaks. This condition is especially important for the low intensity peaks which are close to the background intensity. If it is difficult to determine whether a peak exists above the statistical fluctuations, the analyst should either ignore it or else accumulate more counts in the spectrum to "develop" the peak against the background.

(2) In order to comply with condition (1), the tendency of the analyst is to operate the system at a high count rate. However, the energy dispersive spectrometer becomes increasingly prone to pulse coincidence-related artifacts as the input count rate increases. For a typical system, the input count rate should be kept below 5,000 cps for the full spectrum. Further, it must be noted that the "full" spectrum includes all x-rays up to the incident beam energy. Thus, if a 100 keV beam is employed but the analyst monitors only the region 0 - 10 keV in the multichannel analyzer, x-rays in the range 10 - 100 keV still contribute to system deadtime.

(3) The most important principle of qualitative analysis with EDS is to identify the family of lines produced by an element. With the exception of light elements with atomic numbers less than 16 (sulfur), each element produces at least two x-ray lines which are sufficiently separated in energy to be resolved with an ordinary EDS system (150 eV FWHM at manganese Kα). When the principal lines of an element are noted, all minor lines of the family, which can be quite extensive for a heavy element, should also be marked. This makes the task of identifying the low intensity peaks belonging to minor elements easier and reduces the chance of misidentifying a low intensity peak. The degree of confidence which can be placed in assigning an element as present in a specimen goes up rapidly as the number of lines identified increases. In the following specific guidelines, families of x-ray lines which can be observed under practical analysis conditions (high quality spectra with 5×10^6 counts in the full spectrum) are noted along with the approximate weights (relative transition probabilities) of the lines. These weights are only approximate, since they vary

with the atomic number of the element. When the weights observed in an analysis differ radically from these values, an interference or misidentification should be suspected.

(4) The energies of x-ray lines for qualitative analysis are usually obtained from charts, "slide rules", tables, or "KLM" markers available on some multichannel analyzers. Generally, all of these sources have deficiencies, either in terms of incomplete data or lack of simultaneous display. The analyst generally must use several sources of information. The ultimate reference is a definitive compilation of x-ray energies, such as Bearden's table [15], but the detail in such a table is too great for quick reference; for example, twenty-five L series lines are listed for heavy elements whereas at most nine are observed in practical analysis. To augment the existing sources, we present a plot of x-ray line energies for all lines observed in spectra obtained under practical conditions, including the silicon x-ray escape peak energy of the principal line for each series, figure 23. The utility of this plot is that the analyst can look at a particular energy and note all possible peaks which can occur. The FWHM produced by a 155 eV (Mn Kα) detector is shown as a bar for each keV segment at the top of the plot. It should be noted, however, that for a heavy atomic number specimen, such as uranium, and sufficient counts in the full spectrum (5.10^6 counts) a quite complex spectrum results, shown in figure 24, which requires the use of a table such as that of Bearden [15].

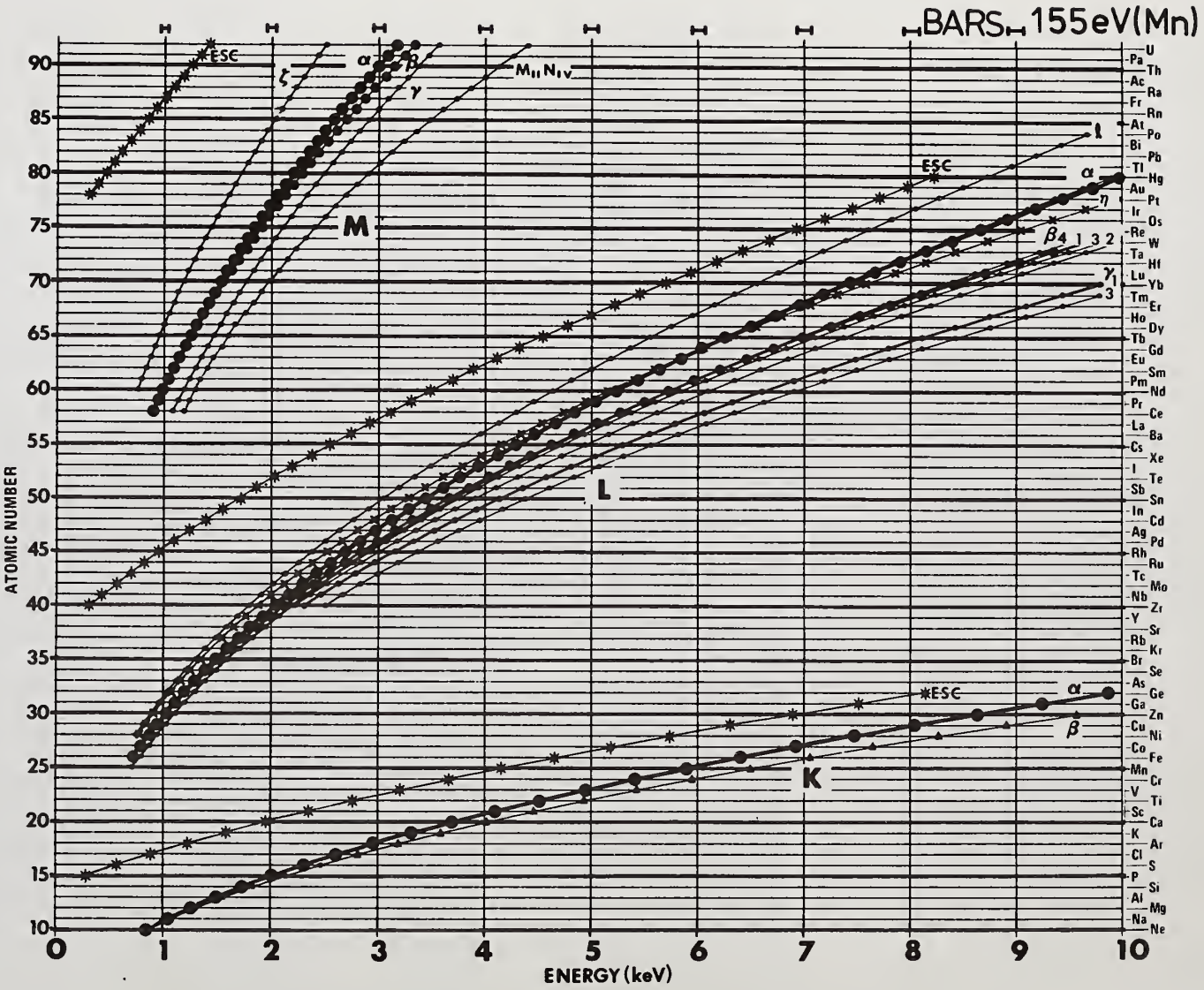

Figure 23. Plot of the x-ray lines likely to be observed in EDS spectra containing about 5,000,000 counts in the full spectrum. The silicon escape peak energies for the major line in each family, K, L, or M are indicated. The solid bars at the top are the FWHM of a 155 eV (MnKα) detector.

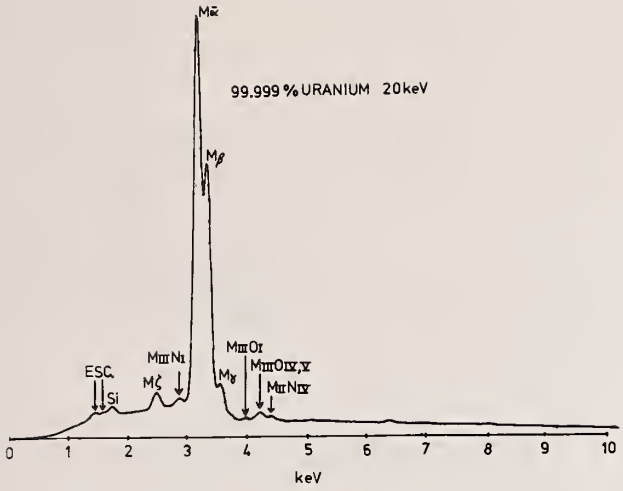

Figure 24. Spectrum of high purity uranium containing 5×10^6 counts in full spectrum.

5.2 Specific guidelines – major peaks

(1) The analyst should begin with the peaks of high intensity, working from the high energy end of the spectrum toward the low energy end. The reason for this approach is that the members of a family of lines are separated by the largest differences in energy at high energy and are likely to be resolved by the energy dispersive spectrometer.

(2) The energy at which a large amplitude peak occurs should be determined. If it is suspected to be a Kα peak, look immediately for a Kβ peak at the proper energy and at approximately 10 percent of the Kα peak height. For K lines of elements with atomic number 16 (sulfur) and above, the Kα - Kβ peaks will be resolved with an ordinary 150 eV detector. If a peak is identified as a K peak of an element, try to find the L series of lines for this element; L lines become visible for atomic number 26 (iron). Always locate the complete family of lines for each element.

(3) If a Kα - Kβ pair doesn't fit, L lines should be examined. If an Lα peak is suspected, look for the series $L\alpha_{1,2}$ (1), $L\beta_1$ (0.7), $L\beta_2$ (0.2), $L\gamma_1$ (0.08), $L\gamma_3$ (0.03), Lℓ (0.04), and Lη (0.01). If a high energy L family is located, look for M series lines which may occur. M series lines become visible for atomic number 58 (cerium).

(4) If neither K series or L series lines fit the observed lines, M series lines should be examined. The observed lines are Mα (1), Mβ (0.6), Mζ (0.06), Mγ (0.05), and the line obtained from the transition $M_{II}N_{IV}$ (0.01).

(5) At energies below 3 keV, the L and M series lines are not well resolved by an EDS detector. Because several of the peaks of the family have similar weights $L\alpha_{1,2}$ (1), $L\beta_1$ (0.7); Mα (1), Mβ (0.6)) the resulting composite L or M peaks are frequently assymmetrical. This asymmetry aids in distinguishing L or M peaks from K peaks, figure 25 (a), (b), (c). At low energies, the Kβ weight decreases toward one percent of the Kα intensity and the energy separation becomes less, so that the low energy composite Kα - Kβ peak is nearly symmetrical, figure 25(a). Near 1 keV, nearly all K, L, and M peaks appear symmetrical and distinguishing the different types becomes difficult.

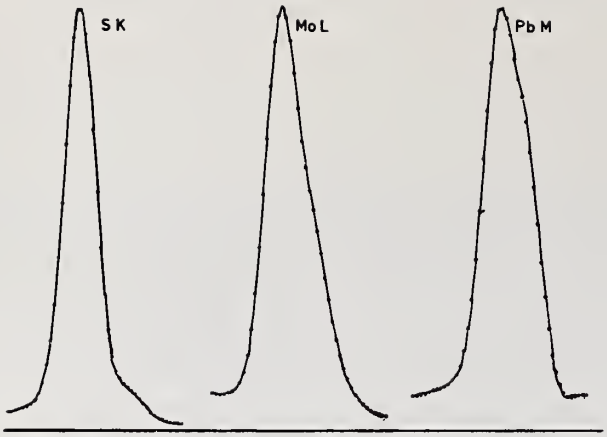

Figure 25. Low energy x-ray peaks in the region of 2.3 keV. The K family in this region appears as a single, nearly symmetric peak, while the L and M families appear distinctly asymmetric.

5.3 Specific guidelines – minor peaks

Only after all of the high intensity peaks have been satisfactorily identified, and the complete family of lines for each element so identified has been noted, is the analyst ready to proceed with the remaining low intensity peaks.

(1) Spectral artifacts associated primarily with high intensity peaks should be systematically identified. Each peak with an energy above the silicon K-absorption energy (1.84 keV) has an associated silicon escape peak at 0.1 - 1 percent of the main peak intensity. The silicon escape peak is likely to be seen only for high intensity peaks. The energies of silicon escape peaks associated with principal lines are plotted in figure 23.

(2) If the spectrum was obtained at a high counting rate, pulse coincidence effects will lead to the formation of sum peaks. Only high intensity peaks will have a sufficient count rate to give significant pulse coincidence. If major peaks exist at energies E_A, E_B, and E_C, low level coincidence peaks can be expected at $2E_A$, $2E_B$, $2E_C$, $(E_A + E_B)$, $(E_B + E_C)$, and $(E_A + E_C)$.

(3) A low level silicon peak will be found as an inevitable result of the fluorescence of the silicon dead layer following absorption of x-rays. This silicon signal represents an apparent silicon constituent in a bulk sample at a level of 0.2 weight percent or less, in a good detector.

(4) Artifact peaks due to stray radiation, previously determined on known samples, should be noted as extraneous to the sample being investigated.

(5) Any low intensity peaks remaining after the above procedures have been carried out have a reasonable chance of arising from an elemental constituent of the sample. The same procedures are repeated to identify these peaks as described above for major elements. However, the level of confidence with which the identification of a minor element can be made is generally poorer than for major elements, since the peak intensities are usually so low that only the main peak of a family is visible.

5.4 Example

As an example of the application of the above guidelines to the qualitative analysis of a complicated spectrum, we shall analyze the spectrum of NBS glass K-252 [16].

The spectrum is shown in figure 26.

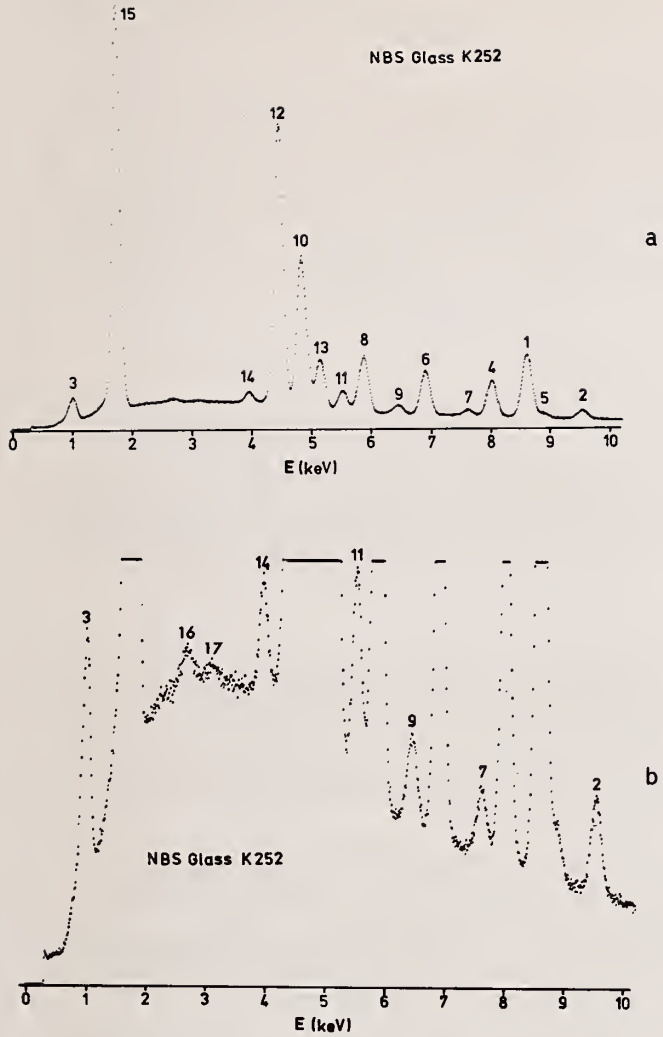

Figure 26(a,b). Spectrum of NBS glass K-252 at two different scale expansions. The qualitative analysis identifying the numbered peaks is described in the text.

(1) Starting at the high energy end of the spectrum, figure 26(a), peak (1) has an energy which corresponds to zinc Kα (8.64 keV) and the appearance of peak (2) at the proper energy for zinc Kβ (9.57 keV) and at about 10 percent of the intensity of peak (1) confirms the assignment. Next we look for a zinc L line, and find peak (3) at the energy for zinc Lα (1.01 keV).

(2) Peak (4) is found to correspond to copper Kα (8.04 keV); the corresponding Kβ peak at 8.91 keV, peak (5), appears unresolved from the zinc Kα peak and is only seen as a distortion on the high energy side of that peak. Copper Lα (0.93 keV) is not resolved from zinc Lα (1.01 keV).

(3) Peak (6) is found to be cobalt Kα (6.93 keV) with peak (7) as cobalt Kβ (7.65 keV). The peaks are found to be in the correct ratio which confirms the assignment. Similarly, peaks (8) and (9) are found to correspond to manganese Kα (5.89 keV) and Kβ (6.49 keV).

(4) At first appearance, we seem to have two additional Kα - Kβ pairs, peaks (10) - (11) and (12) - (13), since the peak ratios are approximately correct. However, the energies of the nearest candidate elements, vanadium and titanium, are sufficiently different from the measured energies to throw out these assignments. When L energies are examined, we find that barium Lα (4.47 keV) fits peak (12), $L\beta_1$ (4.83 keV): peak (10); $L\beta_2$ (5.15 keV): peak (13); and $L\gamma_1$ (5.53 keV): peak (11). To complete the barium L series, we locate barium Ll (3.95 keV) at peak (14). Barium Lη is unresolved.

(5) The last major peak, (15), is identified as silicon Kα (1.74 keV); the detector will not resolve silicon Kβ (1.83 keV) and so only one peak is available for identification. Peak (15) might be confused with tantalum M, except for the difference in energy (1.71 keV compared to 1.74 keV), the symmetry of the observed peak, which implies a K peak, and the absence of a tantalum L series at 8.15 keV.

(6) Expansion of the vertical scale, figure 26(b), reveals only two additional peaks, (16) and (17). Searching first for artifacts of the major peaks, we identify peak (16) as the silicon escape peak of barium Lα and peak (17) as the escape peak of barium $L\beta_1$. No other peaks remain unidentified, so the qualitative analysis is complete. Due to the large number of major elements in the specimen, the available regions of the spectrum where minor elements might be observed are very limited. This example points out that a consequence of the poor resolution of the detector is the difficulty in recognizing minor elements in complicated spectra.

6. Conclusions

Successful x-ray microanalysis with the energy dispersive x-ray spectrometer requires knowledge of the types of artifacts which can occur. Artifacts which originate in the physical process of x-ray detection cannot be eliminated from the spectrum. Artifacts arising from the specimen environment can frequently be reduced to an insignificant level. Accurate analysis can be carried out with a logical method for proper peak assignments and artifact recognition.

References

[1] Fiori, C. E. and Newbury, D. E., "Artifacts Observed in Energy-Dispersive Spectrometry in the Scanning Electron Microscope", SEM/78, Om Johari, ed., 1978, pp. 401-422.

[2] Reed, S. J. B., Electron Microprobe Analysis, Cambridge University Press, Cambridge, England, 1975.

[3] Kramers, H. A., "On the Theory of X-ray Absorption and of the Continuous X-ray Spectrum", Philosophical Magazine, 46, 1923, p. 836.

[4] Heinrich, K. F. J., Newbury, D. E., and Yakowitz, H., Use of Monte Carlo Calculations in Electron Probe Microanalysis and Scanning Electron Microscopy, NBS Special Publication 460, U.S. Government Printing Office, Washington, D.C. 20402, 1975.

[5] Woldseth, R., X-ray Energy Spectrometry, Kevex Corporation, 1101 Chess Dr., Foster City, California 94494, 1973.

[6] Freund, H. U., Hansen, J. S., Karttunen, E., and Fink, R. W., "Photon Spectrometry in the Low Energy Region of 500 eV to 100 keV", Proceedings Inter. Conference on Radioactivity and Nucl. Spect., 1969, p. 623.

[7] Gedke, D., "The Si(Li) X-ray Energy Analysis System: Operating Principles and Performance", X-ray Spect., 1(4), 129 (1972).

[8] Heath, R. L., "The Applications of High-Resolution Solid State Detectors to X-ray Spectrometry – A Review", Advan. X-ray Anal., 15(1), 1 (1972).

[9] Elad, E., Inskeep, C. N., Sareen, R. A., and Nestor, P., "Dead Layers in Charged Particle Detectors", IEEE Trans. on Nucl. Sci., 20(1), 534 (1973).

[10] Jaklevic, J. M and Goulding, F. S., "Detection of Low Energy X-rays with Si(Li) Detectors", IEEE Trans. on Nucl. Sci., NS-18(1), 187 (1971).

[11] Fitzgerald, R. and Gantzel, P., "X-ray Energy Spectrometry in the .1 to .10 A Range", Energy Dispersion X-ray Analysis: X-ray and Electron Probe Analysis, ASTM-STP-485, American Society for Testing and Materials, 1971, p. 3.

[12] Statham, P. J., "Pile-up Rejection: Limitations and Corrections for Residual Errors in Energy-Dispersive Spectrometers", X-ray Spect., 6(2), 94 (1977).

[13] Bolon, R. B. and McConnell, M. D., "Evaluation of Electron Beam Tails and X-ray Special Resolution in the SEM" in Scanning Electron Microscopy, 1, O. Johari, ed., 163 (1976).

[14] Fiori, C. E., Myklebust, R. L., Heinrich, K. F. J., and Yakowitz, H., "Prediction of Continuum Intensity in X-ray Dispersive Microanalysis", Anal. Chem., 48(1) (1976).

[15] Bearden, J. A., "X-ray Wavelengths and X-ray Atomic Energy Levels", Rev. Mod. Phys., 31(1) (1967).

[16] Fiori, C. E., Heinrich, K. F. J., Marinenko, R. B., Darr, M. M., Blackburn, D. H., Newbury, D. E., and Small, J. A., "An Overview of the Glass Standards Program for Microanalysis at the National Bureau of Standards", Proc. 11th Annual Conference of MAS, Miami Beach, Florida, 1976.

[17] Henoc, J., Heinrich, K. F. J., Myklebust, R. L., "A Rigorous Correction Procedure for Quantitative Electron Probe Microanalysis (COR 2)", NBS Technical Note 769, U.S. Government Printing Office, Washington, D.C., 1973.

[18] Yakowitz, H., Myklebust, R. L., and Heinrich, K. F. J., "FRAME: An On-Line Correction Procedure for Quantitative Electron Probe Microanalysis", NBS Technical Note 796, U.S. Government Printing Office, Washington, D.C., 1973.

[19] Schamber, F. H., "A Modification of the Linear Least-Squares Fitting Method which Provides Continuum Suppression" in X-ray Fluor. Analysis of Environmental Samples, T. G. Dzubay, ed., Ann Arbor Science Pub., Ann Arbor, Mich., 1977, p. 241.

[20] Smith, D. G. W., Gold, C. M., and Tomlinson, D. A., "The Atomic Number Dependence of the X-ray Continuum Intensity and the Practical Calculation of Background in Energy Dispersive Electron Microprobe Analysis", X-ray Spect., 4, 149 (1975).

[21] Fiori, C. E., Myklebust, R. L, and Heinrich, K. F. J., "A Method for Resolving Overlapping Energy-Dispersive Peaks of an X-ray Spectrum; Application to the Correction Procedure FRAME B", Proc. 11th Annual Conf. MAS, Miami Beach, Florida, 1976, paper 12.

[22] Heinrich, K. F. J. and Yakowitz, H., "Absorption of Primary X-rays in Electron Probe Microanalysis", Analyt. Chem., 47(14), 2408 (Dec. 1975).

[23] Reed, S. J. B. and Ware, N. G., "Escape Peaks and Internal Fluorescence in X-ray Spectra Recorded with Lithium Drifted Silicon Detectors", J. Phys. E: Sci. Instru., 5, 582 (1972).

[24] Myklebust, R. L., Fiori, C. E., and Heinrich, K. F. J., "FRAME C: A Compact Procedure for Quantitative Energy-Dispersive Electron Probe X-ray Analysis", Proc. 12th Annual Conf. MAS, Boston, Mass., 1977, p. 96A.

National Bureau of Standards Special Publication 604. Proceedings of the Workshop on Energy Dispersive X-Ray Spectrometry held at NBS, Gaithersburg, Maryland, April 23-25, 1979. (Issued March 1981)

ARTIFACTS ENCOUNTERED IN ENERGY DISPERSIVE X-RAY SPECTROMETRY IN THE ANALYTICAL ELECTRON MICROSCOPE

D. B. Williams and J. I. Goldstein

Metallurgy and Materials Engineering Department
Lehigh University,
Bethlehem, PA 18015

Abstract

The analytical electron microscope (AEM), consisting of an energy dispersive spectrometer interfaced to a scanning transmission electron microscope, produces its own particular spectral artifacts. These artifacts are due specifically to the use of high kV electrons and thin foil specimens. The detection of these artifacts, the identification of their source, and the minimization of their effects are discussed. It is concluded that an ideal microanalytical configuration for an AEM exists and that now it is possible to reduce the effect of spectral artifacts to the level where they do not limit quantitation of the x-ray data.

1. Introduction

The interfacing of an energy dispersive x-ray spectrometer (EDS) to a scanning transmission electron microscope (STEM) is one of the principal configurations for analytical electron microscopy (AEM). Ideally in the AEM the measured characteristic x-ray intensity above background is related to the specimen composition directly through a known constant of proportionality. For this to occur the source of x-rays measured by the EDS must be the region of the specimen interacting with the primary electron beam. This is not routinely the case in AEM where x-rays generated from other sources are often detected. This undesired signal is the major artifact in the EDS and is sometimes called the spurious x-ray signal. Spurious x-rays are insidious because they often seem to be part of the desired spectral information and are thus not immediately obvious. Unless very specific precautions are taken, AEM x-ray microanalysis is <u>not</u> quantitative under these conditions and therefore the applications of AEM are limited.

The problem of spurious x-rays has received much attention recently [1,2][1]. It appears that the spurious x-ray signal is caused by two major effects, 1) stray radiation in the AEM illumination system, and 2) specimen interaction with the primary electron beam. The resultant spectral artifacts are specific to AEM because the system uses high kV electrons and the specimen is transparent to the high kV beam. These points contrast with other instruments (e.g., scanning electron microscope and electron microprobe) in which EDS is used, where bulk specimens are typically irradiated by electrons with energy $\leq$ 30 keV.

This paper summarizes the present state of knowledge and describes how the instrument-specific sources can be identified and eliminated or minimized. In the ideal configuration that is described in the conclusion of the paper, it is considered that AEM x-ray microanalysis using EDS can be free of quantitation-limiting spectral artifacts and that quantitation is then a straightforward process.

---

[1]Figures in brackets indicate the literature references at the end of this paper.

2. Sources of Spurious X-rays

2.1 Artifacts due to stray radiation in the AEM illumination system

The existence of this type of spurious x-rays is easy to determine. Figure 1a shows a typical EDS spectrum obtained in ~60 seconds from a thin Ag disc specimen in a Phillips 300 TEM-STEM operated at 100 kV. Figure 1b shows a similar spectrum obtained when the primary beam was placed down a hole in the foil. Since it can be assumed that the primary beam continued uninterrupted down the microscope, it is clear that something other than the primary beam is exciting specimen-characteristic x-rays. This and similar phenomena have been reported by many investigators and the effect has been ascribed to both uncollimated electrons [3-5] and stray x-rays [6-8]. However it is possible to distinguish between the two sources because the Ag spectrum contains high and low energy x-ray lines (Kα at 22.2 keV and Lα at 3.0 keV) and the relative height of the lines is a useful indicator of the source of the spurious x-rays [2]. By performing this type of experiment and observing the 'hole-count' spectral artifact, it is possible to identify unambiguously the sources of the spurious x-rays from the illumination system as described below.

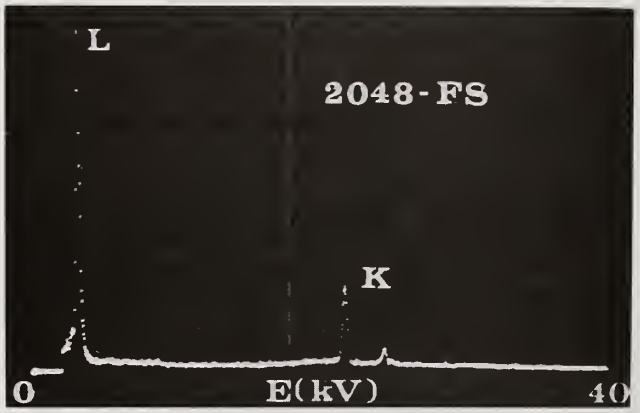

Figure 1a. Typical spectrum from the thin region of a Ag disc (FS = full scale).

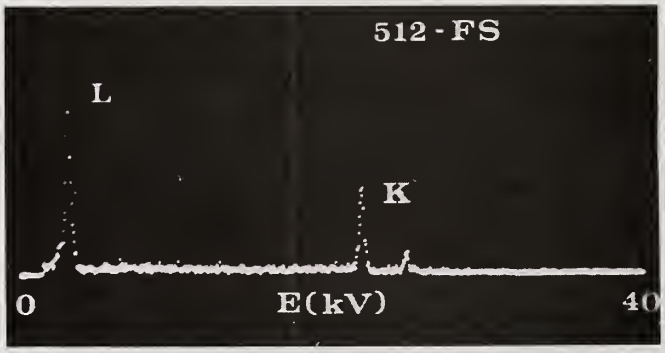

Figure 1b. Spectrum obtained when the primary beam is placed down a hole in the same Ag specimen as figure 1a.

The use of 100 kV electrons in STEM gives rise to x-rays detected from areas other than the point of interest on the specimen, primcipally in the following two ways shown schematically in figure 2:

1. The STEM electron optical system is not always designed to collimate the electron beam completely. In normal TEM and STEM imaging and diffraction operation, it is of little consequency if stray electrons hit the specimen and holder at distances well away from the point of interest. However this is clearly undesirable in an AEM when the EDS can detect x-rays from a wide area of the specimen chamber.

2. 100 kV electrons generate continuum (bremsstrahlung) and characteristic x-rays from various apertures as they are collimated by the illumination system. If these x-rays reach the specimen chamber, they can act as efficient sources of fluorescent x-rays from large areas of the specimen and its surroundings.

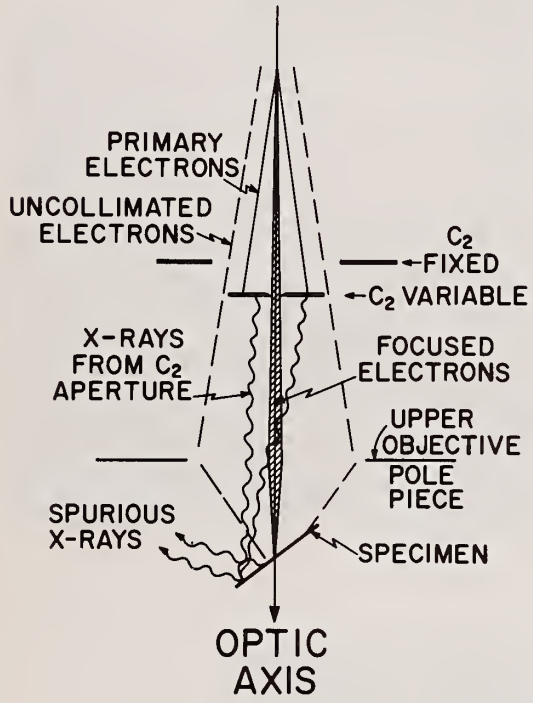

Figure 2. Principal sources of spurious x-rays in the illumination system of an AEM.

The two problems outlined above are instrument dependent, since illumination systems differ. Therefore solutions to eliminate 'hole count' spectra are instrument dependent. The first problem is to determine the existence of the spurious x-rays and identify their source(s). After that one can attempt to minimize the effect.

In the silver spectrum (figure 1a) obtained with the primary beam incident on a thin region of the disc, it is assumed that the Lα to Kα peak height ratio is primarily characteristic of an electron-induced spectrum. Observing the hole spectrum (figure 1b), a similar conclusion might be drawn. Thus in this instrument (a Phillips EM 300) some of the uncollimated electrons are not stopped by the C_2 aperture and are focussed onto the specimen. This effect is particularly acute in that series of Phillips instruments and was first determined in 1976 [4]. A simple solution to stop uncollimated electrons (which are in fact scattered around the beam-defining apertures) is the insertion of a spray aperture or plug beneath the variable C_2 aperture. If this is done, the hole count spectrum is as shown in figure 3. The reduction in scale (x4) compared with figure 1b indicates that a substantial proportion of the spurious contribution to the specimen spectrum has been eliminated.

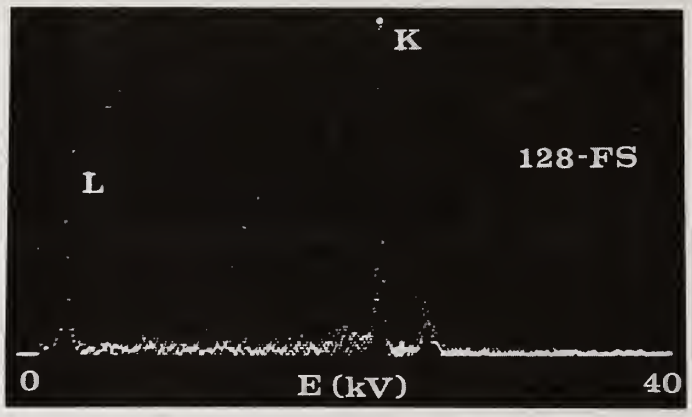

Figure 3. The hole-count spectrum obtained after the contribution of uncollimated electrons has been removed by a spray aperture. Compare the F.S. with figure 1b.

There is still a detectable hole count but, as shown in figure 3, the Kα peak is now substantially higher then the Lα (compare with figures 1a and 1b). The remaining source of stray radiation is the hard x-radiation generated in the illumination system. A simple calculation [1] shows that even conventionally thick platinum apertures (∿25 μm in the vicinity of the hole) transmit substantial fractions of the continuum x-rays generated. Figure 4 shows the calculated spectrum of continuum x-rays which would travel down the column through increasing thicknessess of a platinum aperture. Since the efficiency of x-ray fluorescence depends on the energy of the exciting x-rays, it is clear that the continuum x-ray intensity from the aperture will excite the high energy Ag Kα line more efficiently than the low energy Ag Lα line. This explains the hole spectrum shown in figure 3.

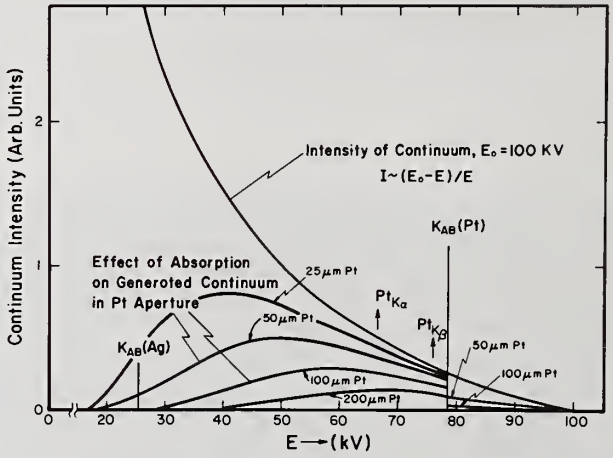

Figure 4. Calculated spectrum of bremsstrahlung x-rays generated by 100 kV electrons at the final beam-defining C_2 aperture. The reduction in intensity due to absorption by increasing thickness of Pt is shown as well as the relative position of the AgKα and Lα x-ray lines.

This problem of fluorescence due to continuum x-rays is inherent in all AEMs, but will be reduced if thin film specimens are used, since x-ray absorption is minimized. However, in metallurgical and ceramic specimens, which are usually thick discs with a central electron transparent zone, the fluorescence problem will always be significant.

Two ways to combat the fluorescence problem have been proposed. First the source may be removed by using extra thick [9] or cylindrical (no taper) [10] apertures. Figure 5 shows an SEM image of a 200 μm thick, 20 μm wide aperture designed for this application and produced by Microengineering[2]. In this case the hole count is further reduced using both a spray aperture and an extra thick C_2 aperture by a factor of four as shown in figure 6 (compare scale with figure 4). Extra thick apertures are now available for Phillips EM 300 and 400 series AEMs. The second approach to the hard x-ray problem is to insert non beam-defining apertures further down the column [7]. This has the effect of cutting down substantially on the area fluoresced. This solution is incorporated into all JEOL 100CX and 200CX 'hard x-ray kits'.

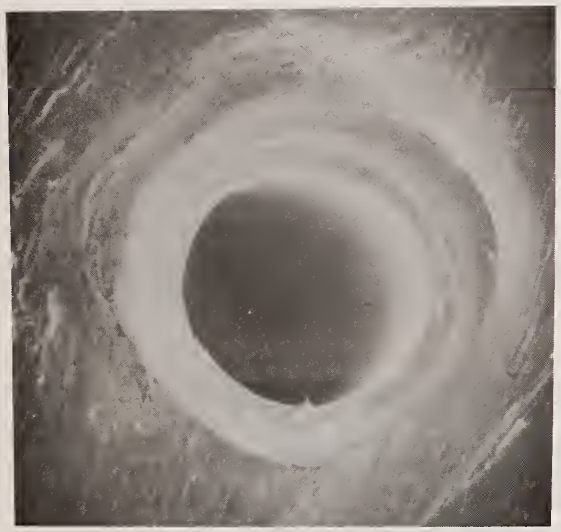

Figure 5. SEM image of extra-thick Pt C_2 variable aperture. The aperture is cylindrical, no regions being <200 μm thick.

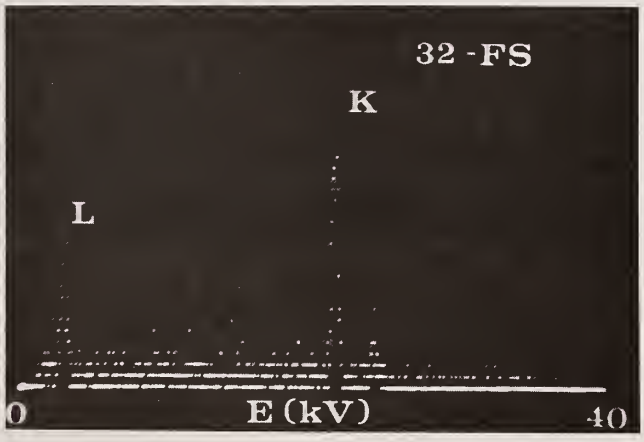

Figure 6. The hole-count spectrum obtained with both a spray aperture and extra thick C_2 aperture. There is still a small amount of AgKα and Lα due to residual stray radiation.

[2]Microengineering, Inc., R.D. #3, Box 501, Williston, VT 05495.

With all the modifications to the illumination system discussed above, the problems of spurious x-rays from electron and x-ray sources can be reduced to acceptable levels. Two criteria of acceptability have been defined [2,11] but they have the same aim – i.e., to ensure that these spurious x-rays are not the limiting factor in the accuracy of x-ray quantitation. Given a reasonable microanalysis situation, if the spurious hole count for a given element is less than the continuum background generated when the beam is on the specimen, then at least the spurious contribution to the spectrum is of the order of the detection limit of the characteristic line of interest. For example, selecting a thin region of a specimen such that 10,000 counts (statistically significant) can be accumulated in ~60 seconds (reasonable time) with a typical probe size (70 - 100 Å) used for microanalysis, then the characteristic x-ray hole count, using the same probe for the same time, should be less than the background for all peaks of interest in the specimen spectrum.

The modifications described above are currently being incorporated in the latest AEM instruments. However, all earlier first generation AEMs suffered from the problem of spurious x-rays induced by stray radiation and the individual user should check his instrument in the way outlined above and correct the problem accordingly.

2.2 Artifacts due to beam interaction with the specimen

Assuming that the illumination system problems are removed, it is still not certain that all the detected characteristic x-rays are generated solely from the point of interest. The primary reason for this is that the thin specimens allow transmission of high kV electrons, and also scatter electrons in both the forward and backward directions.

The sources of x-rays that can reach the EDS due to this effect are summarized in figures 7a and 7b. These problems can be identified as follows.

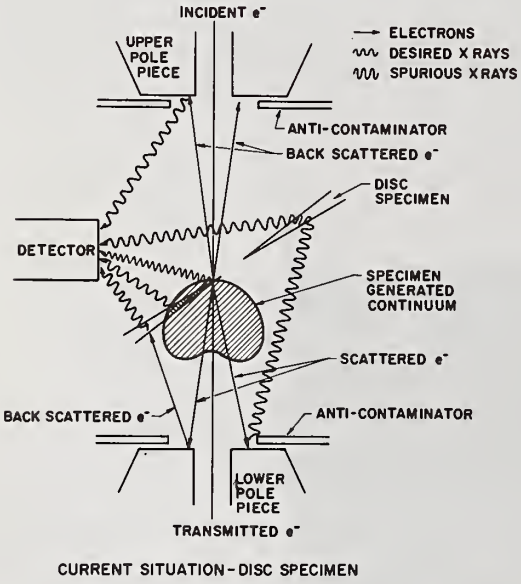

Figure 7a. Sources of spectral artifacts due to electron beam-thin disc specimen interaction in an AEM.

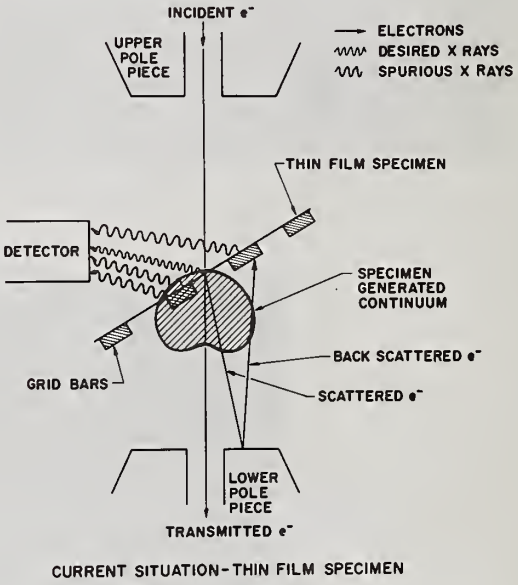

Figure 7b. Sources of spectral artifacts due to electron beam interaction with a thin foil specimen mounted on a support grid.

1. Incident high energy electrons are backscattered into the microscope specimen chamber and generate x-rays from this region (e.g., cold trap, upper pole piece, EDS collimator). The possibility of direct backscatter into the EDS itself also cannot be discounted, although the strong prefield of upper objective polepiece should prevent this.

2. Incident high energy electrons are transmitted, scattered or diffracted into the specimen chamber (or specimen support grid if it is very close to the region of interest), and generate a) characteristic and continuum x-rays, b) backscattered electrons from, e.g. lower objective polepiece, objective aperture drive.

3. Characteristic and high energy bremsstrahlung from the point of interest on the specimen fluoresce the specimen environment. This is probably the most important problem. If the specimen is a disc and is tilted to some non-horizontal orientation to permit detection of the characteristic x-rays, then the possibility of self-fluorescence (i.e., fluorescence induced by the continuum radiation generated in the sample) exists (figure 7a). This of course depends on the specimen shape, thickness, and microstructure, and the actual energy and intensity distribution of the bremsstrahlung x-rays. If a specimen support grid is used (figure 7b), then this radiation will fluoresce the grid. This probably accounts for the observation of copper peaks in otherwise 'clean' STEM systems, when a copper support grid is used. Figure 8 which is a spectrum from a 200 nm particle of Fe-Ni sulphide in a silicate matrix illustrates this problem. A Cu Kα peak is still clearly visible although the primary beam is confined totally within the particle and the grid bar is $\geq$ 200 μm away from the focussed beam. The use of beryllium support grids will remove the Cu Kα peak in the spectrum since a) there will not be efficient fluorescence of beryllium, and b) beryllium characteristic x-rays cannot be detected by EDS. However, even using beryllium support grids, there is still a danger of backscatter of scattered (diffracted) 100 kV electrons from this grid into the bulk of the specimen, if the grid is very close to the region of interest.

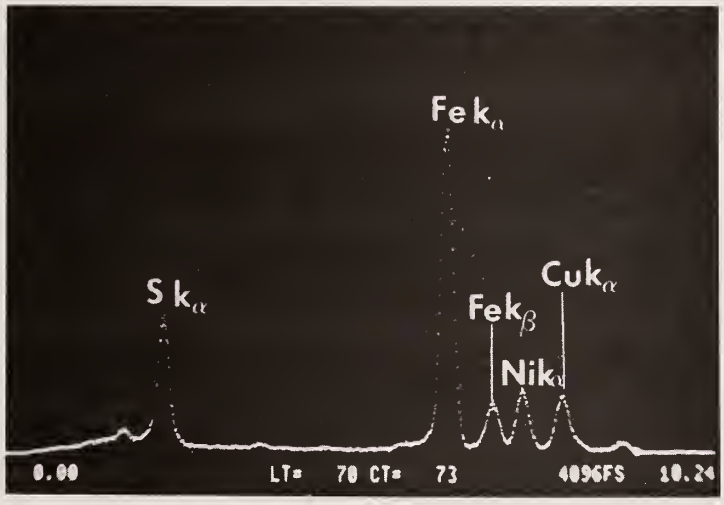

Figure 8. Spectrum from an analysis situation as in figure 7b. The Cu peak due to the Cu grid bars is clealy bisible.

The minimization of problems 1 and 2 above, will again be somewhat instrument dependent. For example, the JEOL 100C produced system counts from pole pieces, anticontaminator and the guard tube in the stigmator coils [12]. All of these contributions to the spectrum may be minimized by suitable light element inserts which either reduce the backscatter, or produce x-rays which are not detectable. Conversely, in some instruments, no such systems peaks have been detected.

The use of thin foil specimens rather than discs may cut down the possibility of specimen self-fluorescence. Furthermore, the development of high take-off angle detectors (standard on some STEM/AEMs and being developed on others) is an essential step. Specimen interaction with its own bremsstrahlung is thus minimized. There is, however, the possibility of increased backscatter directly into the detector in this configuration, but to-date, no conclusive evidence exists for this effect. The use of beryllium grids, when grids are necessary, is of paramount importance, but even in this case, microanalysis should be performed at least 0.1 mm away from any grid bars to minimize any backscatter of diffracted or scattered electrons. Electron backscatter and x-ray production from the lower objective polepiece can be minimized by covering it with an element of low atomic number such as carbon, boron, or beryllium. The same could be done to minimize x-ray production from the upper objective polepiece and/or anticontaminator. Taking all these points into account, an ideal microanalysis situation from the specimen chamber point of view is shown in figure 9.

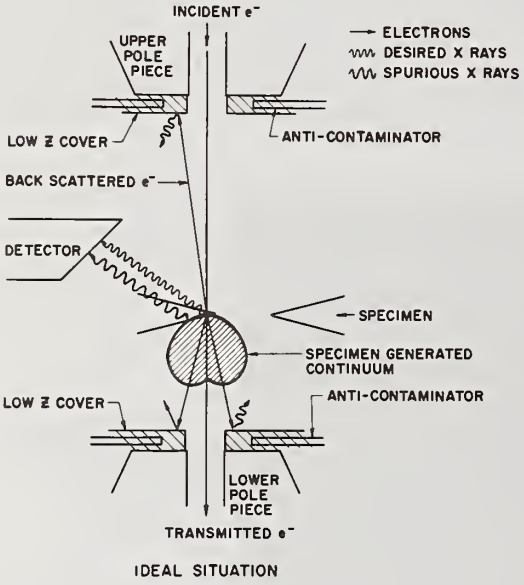

Figure 9. Ideal microanalytical configuration which minimizes spectral artifacts in an AEM. The configuration shown is attainable in current AEMs, and assumes that any stray radiation from the illumination system has been effectively suppressed.

3. Summary

To the unwary operator, spectral artifacts due to spurious x-rays in EDS in the AEM can contribute significantly to errors in quantitation. The spurious x-rays unique to AEM are insidious in their effect because more often than not, the signals they generate are similar to that expected from the point of interest, although often originating from far away on the specimen. Careful operation and ideal microanalytical configurations have now been identified and it is possible to reduce spurious contributions to the specimen to levels at which they do not limit the accuracy of quantitation. It is considered that at this stage of development EDS in the AEM is fully quantitative and may be confidently applied to a whole range of materials problems awaiting the advent of the superior spatial resolution of this technique.

This work was supported by NASA Grant NGR 39-007-043.

References

[1] Goldstein, J. I. and Williams, D. B., SEM (IITRI), 1, 651 (1977).

[2] Bentley, J., Kenik, E. A., Zaluzec, N. J., and Carpenter, R., SEM, 1 (1979).

[3] Geiss, R. H. and Huang, T. C., X-ray Spectrometry, 4, 196 (1975).

[4] Shuman, H., Somlyo, A. V., and Somlyo, A. P., Ultramicroscopy, 1, 317 (1976).

[5] Russ, J. C., SEM (IITRI), 1, 335 (1977).

[6] Hren, J. J., Ong, P. S., Johnson, P. F., and Jenkins, E. J., Proc. 34th EMSA Meeting, Claitor's Publishing Division, 418 (1976).

[7] Zaluzec, N. J. and Fraser, H. L., Proc. 34th EMSA Meeting, Claitor's Publishing Division, 420 (1976).

[8] Kenik, E. A. and Bentley, J., Proc. 8th ICXOM/12th Annual MAS Conference, Boston, 114A (1977).

[9] Joy, D. C. and Maher, D. M., Proc. Specialist Workshop on AEM, Cornell University, 111 (1976).

[10] Williams, D. B. and Goldstein, J. I., Proc. Specialist Workshop on AEM, Cornell University, 174 (1978).

[11] Williams, D. B., Goldstein, J. I., Proc. 8th ICXOM/12th Annual MAS Conference, Boston, 113A (1977).

[12] Nicholson, W. A. P., Robertson, B. W., and Chapman, J. N., Developments in Electron Microscopy and Analysis, The Institute of Physics, Bristol and London, 373 (1977).

National Bureau of Standards Special Publication 604. Proceedings of the Workshop on Energy Dispersive X-Ray Spectrometry held at NBS, Gaithersburg, Maryland, April 23-25, 1979. (Issued March 1981)

UNCOLLIMATED FLUORESCING RADIATION IN AN ANALYTICAL ELECTRON MICROSCOPE (100-1000 KEV): SOURCES AND SOLUTIONS[1]

Nestor J. Zaluzec

Oak Ridge National Laboratory
Metals and Ceramics Division
Radiation Effects and Microstructural Analysis Group
Oak Ridge, Tennessee 37830

Abstract

The interfacing of a solid state energy dispersive spectrometer (EDS) to the column of a modern transmission or scanning transmission electron microscope (TEM/STEM) can potentially provide an extremely powerful analytical tool for the microcharacterization of materials. Unfortunately, there are sometimes serious instrumental limitations involved in this seemingly straightforward modification of a TEM/STEM instrument into an analytical electron microscope (AEM) of the simplest kind. The limitations arise due to the presence of uncollimated radiation, consisting of both hard x-rays and electron tails, which is generated within the probe forming system of the microscope. In an unmodified instrument this radiation can reach the specimen area and thus produce characteristic x-ray emission by fluorescence of the specimen and its environment. Clearly, in any quantitative analysis scheme such an effect is undesirable. Fortunately, these complications can be minimized by judicious modification to the electron-optical column of the AEM system. The correction procedures employed in instruments with incident electron beam energies from 100 to 1000 keV will be outlined and their effects on quantitative analysis discussed.

1. Introduction

The interfacing of a solid-state energy-dispersive x-ray spectrometer (EDS) to the column of a modern transmission or scanning transmission electron microscope (TEM/STEM) can potentially provide an extremely powerful analytical tool for the microcharacterization of materials. Such an instrument is complementary to a conventional electron microprobe in that it can provide high spatial resolution ($\lesssim$100 nm) x-ray analysis of microvolumes of material. This increased spatial resolution is derived from the use of minute electron probes (<20 nm), high incident beam energies (100-1000 keV), and thin electron transparent specimens (<200 nm). Furthermore, the quantitative interpretation of data produced under these conditions is fundamentally simpler than bulk analysis since the specimen thicknesses employed are such that absorption and fluorescence corrections are usually negligible. Unfortunately, there are sometimes serious instrumental limitations involved in this seemingly straightforward modification of a TEM/STEM instrument into an analytical electron microscope (AEM) of the simplest kind. The limitations arise due to the presence of uncollimated radiation, consisting of both hard x-rays and electrons, which is generated within the probe-forming system of the microscope. In an unmodified instrument this radiation can reach the specimen area and produce characteristic x-ray emission by fluorescence of the specimen and its environment. In any quantitative analysis scheme such an effect is undesirable. Fortunately, these complications can be minimized by judicious modifications to the electron-optical column of the AEM system. The correction procedures employed in

[1]Research sponsored by the Division of Materials Sciences, U. S. Department of Energy, under contract No. W-7405-eng-26 with the Union Carbide Corporation and the E. P. Wigner Fellowship at ORNL.

2. Uncollimated Fluorescing Radiation: Sources

In an ideal AEM all of the information recorded by the x-ray detector system is produced solely by the interaction of the incident electron probe and the region of interest of the specimen. However, the current generation of AEMs have evolved from the addition of analytical attachments to TEM/STEM instruments, and as such are not necessarily optimized for x-ray work. The most detrimental aspect of this is the nonlocalized fluorescence of the specimen and its immediate surroundings by uncollimated radiation (i.e., electrons and/or x-rays not confined to the immediate diameter of the incident probe). The presence of this radiation is most easily detected by allowing the incident electron probe to pass through a hole in an appropriate test specimen. In this situation one would expect all x-ray emission from the specimen to cease. This, unfortunately, is usually not observed. The x-ray emission detected during such an "in-hole" experiment is produced by fluorescence of the specimen by remotely produced radiation. The source, amount, and nature (i.e., electrons versus x-rays) of this radiation vary from instrument to instrument. Nevertheless, the net result is the same – a degradation of the high spatial resolution and accuracy of the quantitative analysis ultimately obtainable in the AEM.

In order to produce the minute electron probes used in an AEM, it is necessary to intercept a relatively large electron flux by a series of beam-defining apertures. If the geometry and/or operating conditions of the microscope are appropriate, these apertures act as the principal sources of uncollimated radiation. Two types of radiation have been identified as originating from this source: electrons (not confined to the focused incident probe) and x-rays (both characteristic and continuum).

Depending on the specific design of the condenser aperture system of the prospective AEM, it may be possible for electrons (at a significant fraction of the incident beam energy) to scatter around the periphery of the fixed and variable aperture support mechanisms. These electrons together with any that are scattered from the bore of contaminated or thick apertures can result in the formation of significant electron tails and can become an important factor in the production of characteristic x-ray emission from regions of the specimen other than that defined by the electron probe. These beam-defining apertures can also act as a source of a second type of fluorescing radiation. In this case, one can consider the apertures not as electron collimators but rather as a source of hard x-ray (both characteristic and bremsstrahlung) emission. Typical condenser apertures in modern microscopes are relatively thin, high-atomic-number materials of sufficient mass thickness to completely stop the incident electron probe. Conditions such as this are nearly perfect for these apertures to act as thin target x-ray sources. The situation is further complicated by the fact that the emission of bremsstrahlung (continuum) radiation is highly anisotropic and at the electron energies typical of AEM investigations ($\gtrsim$100 keV) this emission is peaked in the forward scattering direction. Thus, in an AEM one can find the conditions and geometry nearly ideal for x-ray fluorescence of the specimen and its environment. Figure 1(a) schematically illustrates these sources of uncollimated radiation.

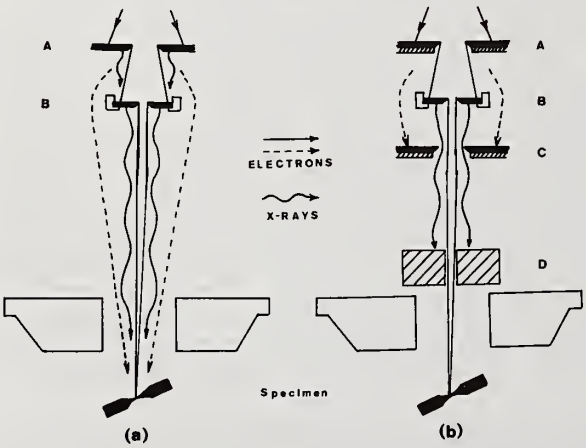

Figure 1. (a) Schematic illustration of remote sources of uncollimated fluorescing radiation from Fixed (A) and Variable (B) beam-defining apertures.

(b) Modifications to reduce the intensity of uncollimated fluorescing radiation using: Thick Fixed apertures (A) above the Variable beam-defining aperture (B) and Thick Spray apertures (C) below, as well as non-beam defining apertures (D) just above the Objective Lens Pole Piece.

3. Uncollimated Fluorescing Radiation: Solutions

In order to assess the amount, nature, and detrimental effects of uncollimated radiation on quantitative analysis, the choice of test specimen used to observe the phenomenon is an important consideration. Regardless of the nature of the radiation, the type of specimen which most dramatically illustrates these effects if of the self-supporting thinned disc variety. In this case, the periphery of the specimen is essentially a thick (~0.1 mm) rim of material representing a bulk sample. The thin electron transparent region of these specimens is confined to the edge of a small hole near the central area of the disc and is usually produced by preferentially electrochemically thinning using a fine jet of electrolyte [1][2]. An additional factor influencing the magnitude of fluorescence effect is the specimen composition. The most pronounced effects are observed in specimens composed of medium-to-high atomic number elements (or suitably homogeneous alloys) having both a low-energy ($\leq$3 keV) as well as a medium-energy ($\gtrsim$7 keV) characteristic x-ray emission line. In selecting a suitable specimen, it is advantageous to choose a material which has characteristic x-ray lines in the 0 - 18 keV range (above ~20 keV, the transmission of high-energy x-rays by the solid state detector becomes significant and thus their efficiency of detection decreases). Some suggested systems are molybdenum and its alloys (MoKα ~17.4 keV, MoLα ~2.3 keV), or some of the homogeneous aluminum nickel alloys such as βNiAl (NiKα ~7.5 keV, AlKα ~1.5 keV).

There are four steps in the elimination of remotely produced uncollimated radiation. They are: (1) identification of the fluorescing species; (2) consultation with the instrument manufacturer as to their solutions to the problem; (3) modifications to the electron optical column; and (4) corrections to measured spectra for quantitative analysis. It is beyond the scope of this review to discuss at length the details of such modifications, and the prospective investigator is referred to the recent tutorial specifically devoted to that subject; however, the most important points are discussed below [2].

The identification of the fluorescing species is probably the most difficult task of the four steps outlined above, because the procedures are more qualitative than quantitative in their interpretation. One first examines the design of the probe-forming system of the microscope to ascertain if it is physically possible for electrons to reach the specimen by scattering around the periphery of the various aperture mechanisms. Next, with the variable second condenser (C_2) aperture in its normal position and using a thick solid disc in place of the normal aperture, one should attempt to detect electron scattering around the aperture supports using a suitable Faraday cup and sensitive electrometer (the currents involved may be less than 10^{-13} A). Third, using a suitable test specimen as previously described, acquire a representative in-hole spectrum and carefully note its characteristics. If x-rays are the principal fluorescing species, then one would expect the intensity of the low energy characteristic line to be extremely small relative to the higher energy line. This result is to be expected because the x-ray production cross sections for fluorescence by x-ray photons favors excitation of the higher energy lines, while electrons favor the lower energy lines. This can be seen by reference to Tables 1 and 2 which document the relative cross-section ratio of a high to low energy x-ray lines for the elements molybdenum and nickel due to excitation by x-ray photons and electrons, respectively. In addition, the relatively weak interaction of x-rays with solids (relative to electrons) results in the majority of characteristic x-ray production of x-ray fluorescence occurring deep within the sample. Thus, the lower energy lines will suffer significant absorption effects (relative to the higher energy line), making their detection more difficult. In comparison, the cross sections for electron excitation favor the lower energy lines and, although absorption effects will reduce their intensity, they will also be of greater relative intensity since generation will occur nearer the sample surface. The final test in the qualitative evaluation is to irradiate the bulk regions of the test specimen with the incident beam and record an x-ray spectrum resulting from electron excitation of this area. The overall characteristics of this (bulk specimen) electron-excited spectrum can then be compared qualitatively with the "in-hole" spectrum. The combination of the results of all these tests is usually sufficient to identify the dominant source.

---

[2]Figures in brackets indicate literature references at the end of this paper.

Table 1. Cross section ratios $\sigma_{K\alpha}/\sigma_{L\alpha}$ for molybdenum and nickel.

Characteristic x-rays by x-ray excitation

X-ray Photon Energy (keV)	Mo $\left(\frac{\text{x-ray } \sigma_{K\alpha}}{\text{x-ray } \sigma_{L\alpha}}\right)$	Ni $\left(\frac{\text{x-ray } \sigma_{L\alpha}}{\text{x-ray } \sigma_{L\alpha}}\right)$
25	205	625
50	230	610
75	235	590

Table 2. Cross Section Ratios $\sigma_{K\alpha}/\sigma_{L\alpha}$ for molybdenum and nickel.

Characteristic x-rays by electron excitation

Incident Electron Energy (keV)	Mo $\left(\frac{\text{electron } \sigma_{K\alpha}}{\text{electron } \sigma_{L\alpha}}\right)$	Ni $\left(\frac{\text{electron } \sigma_{K\alpha}}{\text{electron } \sigma_{L\alpha}}\right)$
25	0.002	0.010
50	0.011	0.012
75	0.014	0.013
100	0.016	0.015

The various AEM manufacturers have begun to offer modifications or accessory attachments to their respective AEM instruments in order to reduce the magnitude of uncollimated radiation. These modifications are based on the various solutions proposed in the literature to reduce this problem; these modifications include: the insertion of spray apertures above and below the variable (C_2) drive assembly to reduce electron tails [3], the use of thick apertures in the probe-forming system to reduce the emitted hard x-ray flux [4] and finally the addition of non-beam defining apertures between the condenser aperture system and the top of the objective lens pole piece [5]. Figure 1(b) illustrates the use of these solutions to reduce the intensity of the uncollimated radiation. The details of these modifications can be found in the paper by Bentley et al., (1979) [2].

It is pertinent to note the fluorescence effects by uncollimated radiation have been reported in every transmission or scanning transmission electron microscope in which the interfacing of an EDS system for quantitative analysis has been reported. The experimental evidence includes the following instruments:

- Philips EM-400 FEG (Carpenter and Bentley, 1979) [6]
- Philips EM-400 (Clarke, 1978) [7]
- Philips EM-301 (Geiss and Huang, 1975) [8]
- Philips EM-300 (Shuman et al., 1976) [3]
- JEOL 100-B (Joy and Maher, 1976) [4]
- JEOL 100-C (Kenik and Bentley, 1977) [9]
- JEOL 100-CX (Headley and Hren, 1978) [10]

- JEOL JSEM-200 (Zaluzec and Fraser, 1976) [11]
- VG HB-5 (Fraser, 1979) [12]
- Siemens ST-100F (Oppolzer and Knauer, 1979) [13]
- Hitachi H-700 (Fiori and Joy, 1979) [14]
- Hitachi HU-1000 (Zaluzec et al., 1978) [15]

Although this discussion may be taken as discouraging for x-ray microanalysis in an AEM, it is important to point out that the situation is correctable. In the worst case reported for a TEM/STEM instrument it was possible to reduce the "in-hole" spectrum to $\lesssim 2$ percent of the measured spectrum from a 100 nm thick region of an appropriate test specimen [16]. Initial studies on an HVEM indicate that the situation in this case is also correctable [15].

Figures 2 and 3 show an example of the reduction of the in-hole spectrum to an acceptable level (the term "acceptable level" will be defined shortly) in a modified AEM. The data presented to illustrate this effect and its solution was chosen from an extreme case. It should not be taken as representative of all microscopes or even for newer versions of the instrument used herein. The results presented here were obtained from a JEOL JSEM 200 TEM/STEM instrument (circa 1973) capable of operating up to incident beam energies of 200 keV. The test specimen used was a 3 mm diameter single crystal of β-NiAl (50/50 at. %) of the self-supporting disc variety and was mounted in a modified stage designed for x-ray analysis [11]. All measurements were performed in the STEM mode at 200 keV with a probe diameter of ∿10 nm, and exciting an area of approximately 100 nm thick. The spectra shown in figure 2 were obtained from the instrument in its "as-received" condition. Spectrum 2(a) was measured with the electron probe positioned on a 100 nm thick region of the specimen, while 2(b) is the corresponding in-hole signal (both spectra were acquired for a detector live time of 200 s). The fluorescing species in this instrument was identified as hard x-rays and reduction of the uncollimated radiation was accomplished using a non-beam defining aperture (0.5 mm in diameter, 2 cm long) positioned just above the upper objective lens pole piece (see figure 1(b)) [11]. Figure 3 shows the resulting changes in the measured specimen (3(a)) spectra after this modification. By comparing these data with figure 2 one can see that the in-hole signal was reduced by nearly two orders of magnitude. For example, in figure 2(b) the NiKα in-hole intensity makes up over 95 percent of that signal measured when the probe is interacting with the specimen, while in figure 3(b) the in-hole NiKα intensity is ∿3 percent. Furthermore, a substantial change in the relative NiKα/AlKα intensity ratio for the two cases is also apparent, indicating that in the initial experimental conditions quantitative analysis were seriously compromised.

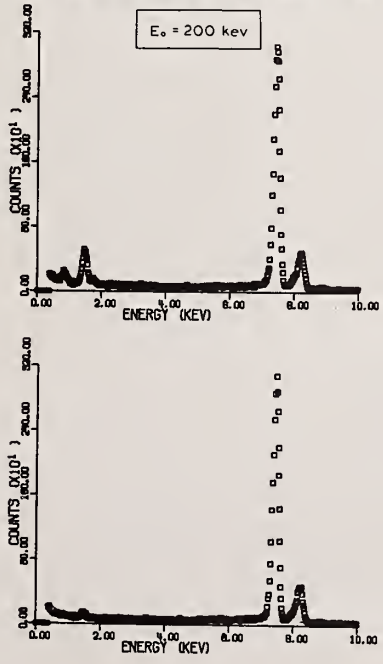

Figure 2. Specimen (a) and in-hole (b) spectra obtained in an "as-received" AEM (see text for details).

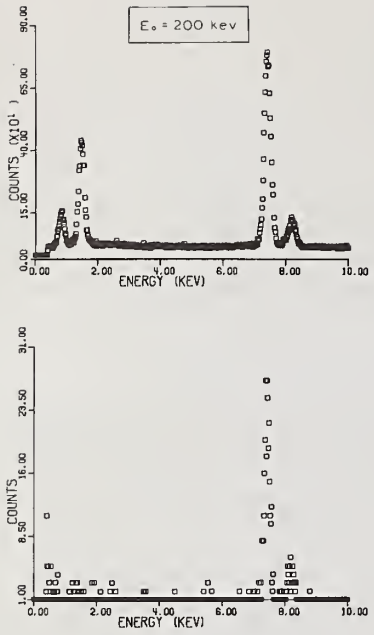

Figure 3. Specimen (a) and in-hole (b) spectra obtained in an AEM modified to reduce uncollimated fluorescing radiation. Note the changes relative to figure 2.

The effect of this large in-hole spectrum on quantitative analysis is shown in greater detail in figure 4. The measured intensity ratio of th NiKα/AlKα lines is shown as a function of specimen thickness for the unmodified instrument (curve A). Also plotted on this figure is a theoretically calculated variation of the NiKα/AlKα intensity ratio (curve C). These calculations were based purely on electron excitation of the sample and, as one would expect, initially begins with the ratio being nearly constant and then slowly increasing as absorption effects become important [17]. In the as-received state of the microscope, quantitative analysis using the thin-film electron excitation model is invalid. The initial decrease of the Ni/Al ratio in curve A results from the increasing contribution of the electron probe excited signal with specimen thickness relative to the nearly constant in-hole signal. As this signal begins to dominate and finally exceed that produced by the uncollimated radiation, the measured ratio will approach but not necessarily reach that corresponding to electron excitation. The amount of the discrepancy will depend on the magnitude of the "in-hole" signal and, as seen in this case, may be in error by a substantial amount. The ratio eventually goes through a relative minimum and then begins to increase as absorption effects become important. Although this particular example was a result of x-ray fluorescence, identical trends will be observed if electron tails are the problem. The results of the reduction of the uncollimated radiation on quantitative analysis are also shown in figure 4 (curve B) and one can see that the agreement is now reasonable. The discrepancy in the thinner regions of the foil is related to the detrimental aspects of contamination [18]. The deviations at the last few points investigated can be attributed to errors in the thickness measurement as well as a neglect of beam broadening effects in the calculations.

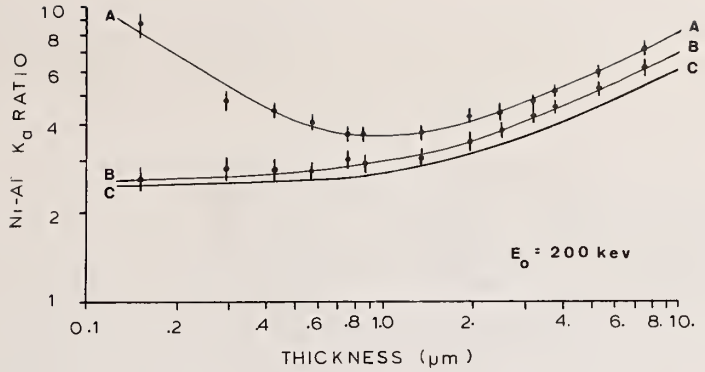

Figure 4. The effects of an in-hole signal on the measured intensity ratio in a NiAl alloy as a function of specimen thickness. A – as-received instrument; B – modified instrument; C – calculated variation based on electron excitation model.

Ideally, one would like to completely eliminate the in-hole signal in order to perform quantitative analysis. Realistically, this may be extremely difficult. The pertinent question to then ask is: At what level does one reach an acceptable in-hole signal for which the errors in quantitative analysis will be small and hence correctable or negligible? There is obviously no general answer to this question, principally due to the wide range of materials as well as AEM instruments used in the scientific community. The following general criteria is a reasonable definition of "acceptable" in-hole signal; however individual investigators may wish to propose more stringent requirements. When the integrated intensity (above background) of each characteristic x-ray line recorded during an "in-hole" measurement is less than ∿2 percent of the intensity of its corresponding line with the incident electron probe positioned on the thinnest area of the specimen to be studied, then the in-hole signal is acceptable. It is assumed that both spectra are measured under identical operating conditions which include: constant geometry, incident beam energy, emission current, and detector "live time". For example, typical metallurgical specimens usually involve the analysis of regions 100 - 500 nm thick; thus, if the in-hole signal is $\lesssim$2 percent of the signal measured from the specimen where the probe is exciting a region $<\sim$100 nm thick, then one can consider this as an acceptable "in-hole" spectrum for all measurements when the specimen thickness is $\gtrsim$100 nm.

An alternative definition of an acceptable in-hole signal has also been suggested [19]. In this definition, when the peak intensity of each characteristic x-ray line in the in-hole spectrum is less than the average continuum intensity generated by the incident probe exciting the region of interest of the specimen, then the in-hole signal is deemed neglibible. Under an ideal set of experimental conditions, this average specimen bremsstrahlung criterion and the previous definition based on a fraction of the integrated peak intensity are in fact related. This is due to the fundamental relationship between the generation of characteristic and continuum x-rays in a thin specimen by electron excitation [17]. The definition of acceptability based on integrated peak intensities in this author's opinion is a more suitable choice for several reasons. First, by using the integrated peak intensity criterion one is comparing the in-hole signal to the actual quantity of interest for analysis rather than an indirect measure using the continuum. Furthermore, the specific experimental conditions used – namely, incident beam energy and detector-specimen geometry – have more pronounced effects on the measured continuum intensity [17] than on characteristic x-ray emission. Finally, the detected continuum intensity is extremely sensitive to specimen contamination effects [18,3]. It was shown that the accumulation of foreign material on the specimen surface results in a net increase in the generated continuum intensity with neglibible effects to characteristic emission. Based on these considerations, these two criteria can easily yield different results. For example, consider the spectra shown in figure 3. The net peak intensity of the in-hole signal for the NiKα line (∿7.5 keV) in figure 3(b) is 28 counts, while the corresponding average specimen bremsstrahlung under this peak (figure 3(a)) is 35 counts. This result implies (using the average bremsstrahlung criterion) that the in-hole signal has reached an acceptable level and can be

neglected. On the other hand, the ratio of the integrated peak intensities of NiKα for the in-hole/specimen spectra yields a value of 0.035, thus exceeding the integrated peak intensity criterion. The errors involved are not extremely large; however, it is ultimately up to the investigator to propagate the errors through the quantitative analysis schemes and clearly the lower the in-hole signal the better.

It should also be re-emphasized that the thinner the region of interest the more pronounced is the detrimental effect of the in-hole signal. This can be simply understood by recalling that the in-hole signal is, to a first approximation, independent of the position of the incident electron probe. The specimen-related signal is, on the other hand, directly related to specimen thickness. Thus, an in-hole signal which may be unacceptably high for a region of the specimen ∿50 nm thick may be acceptable at a thickness of ∿100 nm. There are, however, compromises in analyzing thicker regions of a specimen since bream-broadening effects will ultimately decrease the attainable spatial resolution, as well as the need to include absorption effects in quantitative analysis schemes [20].

Even though we have defined an acceptable in-hole signal it is still important to correct all subsequent specimen measurements for the small but still detectable in-hole spectrum. This is particularly relevant during analysis of heterogeneous specimens since any residual in-hole peaks (which reflect the average specimen composition) may be erroneously interpreted as trace elements in the inhomogeneous specimen being studied. To a good approximation the specimen measurement may be corrected by the simple subtraction of the reduced in-hole spectrum for each successive specimen measurement [18]. An important assumption in this case is that the in-hole signal essentially remains constant over the same period of machine time as the sample measurement. Furthermore, it is tacitly assumed that the locally produced uncollimated radiation resulting from the interaction of the electron probe with the sample itself (i.e., secondary and backscattered electrons, specimen generated characteristic and continuum x-rays, etc.) are important only to second order. The first of these assumptions is usually the most important, and it is assumed that the remotely produced uncollimated radiation is directly related to the emission/probe current which is taken to be constant during both sample and in-hole measurements. This is a good approximation for stable thermionic guns; however, for AEM instruments using field emission sources, particularly cold field emission, this may be quite inaccurate. In such instruments, the emission current can vary substantially and the data acquistion time should be controlled by a measurement of the integrated electron dose rather than using the conventional live-time corrections [12].

Four points are important to remember when applying this subtraction correction for quantitative analysis. First, the in-hole spectra will change from one specimen to another; thus, it must be monitored for each sample. Second, for each specimen measurement, one should acquire a corresponding in-hole spectrum to ensure that long-term changes in the emission/probe current do not invalidate the subtraction assumptions. Third, for the case of trace element analysis, extreme care must be taken to ensure the statistical validity of minor peaks which may be detected both in specimen and in-hole data. Fourth, it is essential to stress that the in-hole signal must be first reduced before subtraction; otherwise, additional errors may be introduced into the data.

Figure 5 is an example of the improper subtraction of the in-hole signal to correct for uncollimated fluorescence effects. The curve labeled (A) in this figure is a measurement of the NiKα/AlKα intensity ratio as a function of specimen thickness in the unmodified instrument described previously. Curve (C) is the result of a simple subtraction of the in-hole data from the data of curve (A) without first reducing the in-hole intensity. The middle curve (B) is the result of first reducing the in-hole signal to an acceptable level and then subtracting it from each successive sample measurement. The error bars indicated on each curve were taken from the specimen data after subtraction of the in-hole signal.

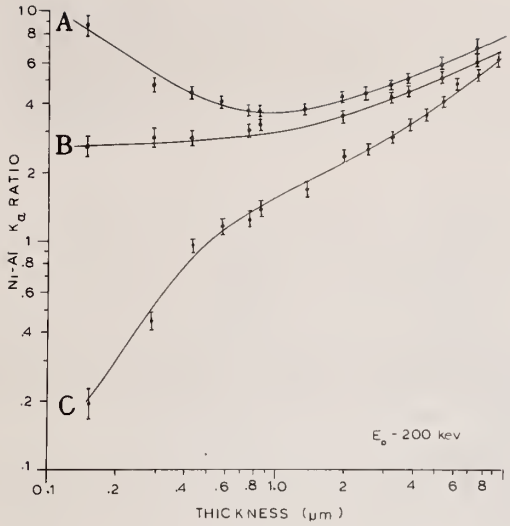

Figure 5. Subtraction of the in-hole signal to correct for uncollimated fluorescence. A – as-received instrument; B – modified instrument with reduced in-hole signal subtracted; C – erroneous subtraction of in-hole signal without reduction of in-hole signal.

Up to this point we have considered the problem of uncollimated fluorescing radiation in commercially available AEMs with incident beam energies ≤200 keV. There is considerable interest in employing High Voltage Transmission Electron Microscopes (HVEMs) for x-ray microanalysis where the incident beam energies are ≥1000 keV. This interest stems from the potential advantages in thin-film x-ray analysis using the highest energy electron probes available. One of these advantages is the decrease in the detrimental beam broadening effects with increasing electron energies [26,22], which serves as the ultimate limit to the spatial resolution of thin-film analysis. Secondly, theoretical calculations [17,23] as well as experimental measurements [15,25] have shown that the characteristic peak-to-background (P/B) ratio in thin specimens increases with incident beam energy. This result becomes important when considering the mass sensitivity of x-ray analysis which is directly related to the measured P/B ratio. Figure 6 illustrates the variation in the calculated P/B ratio for Kα x-rays from thin specimens of nickel, calcium, and aluminum as a function of the overvoltage (U_0) for the geometry found in most AEMs (i.e., the detector axis perpendicular to the electron-optical axis). Here, the overvoltage has its conventional definition, $U_0 = E_0/E_c$, that is, the ratio of the incident probe energy (E_0) to the critical excitation energy (E_c) of the x-ray line in question. From this figure one can see that the calculated P/B ratio for nickel at 1000 keV is ~2.5 times the value at 100 keV. Combining these factors with the relatively large pole piece gaps and the availability of a wide variety of in situ experimental stages (heating, cooling, straining, etc.) makes an HVEM a potential candidate for real-time microanalytical measurements during controlled phase transformation studies.

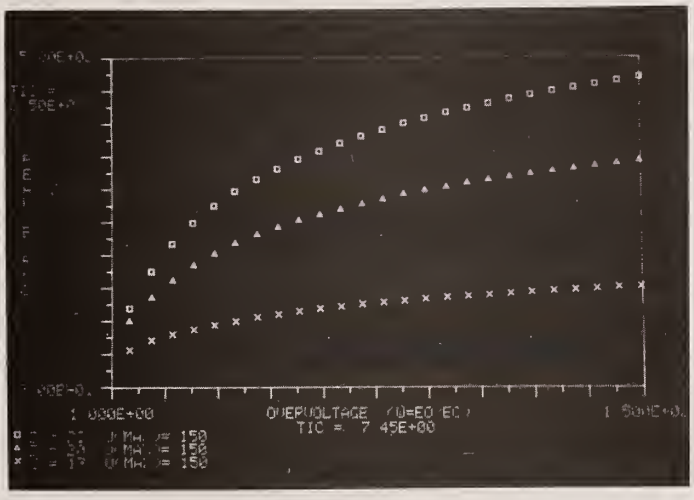

Figure 6. Calculated Kα peak-to-background for thin specimens of nickel, calcium, and aluminum as a function of overvoltage of incident electron beam energy.

As in the case of conventional AEMs the specific details of the probe-forming lens system of the HVEM will have a great influence on the magnitude of any uncollimated radiation present in the instrument. Unfortunately, there have been very few systematic studies made on the optimization of an HVEM for x-ray analysis [15,24]. As such at the present time it is difficult to generalize this discussion to cover all HVEMs; therefore, the remainder of this text will concentrate on the author's own experience with a Hitachi HU-1000 HVEM at ORNL.

The source of uncollimated radiation in this instrument is fundamentally the same as in the lower voltage AEMs; however, the problems it produces are different. In addition to fluorescing the specimen and producing characteristic x-ray emission, there is also a more serious problem in an HVEM based system - namely, the detection of an anomalously high continuum intensity in all measured spectra. This continuum is most likely a result of a large high energy x-ray flux produced by the interaction of the 1000 keV electron beam and the various beam defining apertures in the probe-forming lens system of the microscope. This hypothesis is substantiated by the detection of the continuum x-ray spectrum shown in figure 7 which was obtained by operating the instrument in the TEM mode using a probe diameter of 0.75 μm and a probe current of 2.5×10^{-9} A, and positioning the x-ray detector physically outside of the microscope at the nominal height of its insertion. These results demonstrate quite clearly that there is a substantial x-ray flux at this level, which undoubtedly is greater inside the electron-optical column. Figure 8(a) is a typical x-ray spectrum from a self-supporting TEM disc specimen of β-NiAl acquired after the detector has been appropriately interfaced to the microscope while figure 8(b) is the corresponding in-hole spectrum. These and all subsequent spectra were acquired at an incident electron energy of 1000 keV, a probe current of 2.5×10^{-9} A, a probe diameter of ∿0.75 μm, and a detector live-time of 400 s. One can see that the continuum distribution obtained during the excitation of the β-NiAl test specimen (8(a)) is essentially identical to that obtained during the in-hole measurement. Furthermore, characteristic fluorescence of the specimen by the uncollimated radiation is low (≤10% for the NiKα line) and exhibits preferential excitation for higher energy x-rays indicating the presence of a hard x-ray flux rather than electron tails.

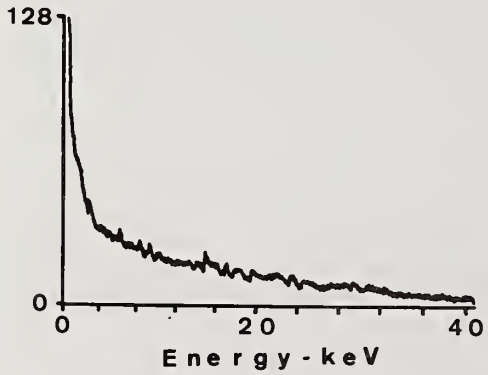

Figure 7. Measured continuum intensity external to microscope column for a Hitachi HU-1000 HVEM instrument operating at 1000 keV (see text for details).

Since most Si(Li) detectors are enclosed in relatively thin stainless steel casings, the first step toward reducing the magnitude of the detected bremsstrahlung flux consists of increasing the shielding around the detector. This can be accomplished, for example, by wrapping thin lead sheets around the detector head. Figures 8(c) and (d) show the resulting changes in the specimen and in-hole spectra obtained by the addition of 3 mm lead to this part of the detector. The overall continuum intensity drops by nearly a factor of two relative to figures 8(a) and (b). After this modification, it was no longer possible to increase shielding at this position and therefore a remote non-beam-defining collimator was added between the condenser and objective lenses. Modifications to the beam-defining aperture at this time were not considered feasible due to their inaccessibility. The last set of spectra (8(e) and (f)) were obtained after the insertion of lead non-beam-defining collimators (1/2 mm bore diameter, 2 cm long) above the upper objective pole piece and the addition of 2 cm of lead sheet over the remaining cross section; furthermore, the detector collimator thickness was also increased to 1.5 cm from the 0.4 cm previously used. These modifications, which are shown schematically in figure 9, successfully reduced the original in-hole signal by ∿90 percent; however, the continuum distribution between the specimen

and in-hole signal is still essentially indistinguishable, indicating that additional shielding is still required. As well as reducing the anomalous continuum intensity, one can also observe in spectra 8(a), (b) and (c) an apparent improvement in the energy resolution of the system as each modification was implemented. This is also consistent with a large high energy x-ray flux degrading the detector system performance.

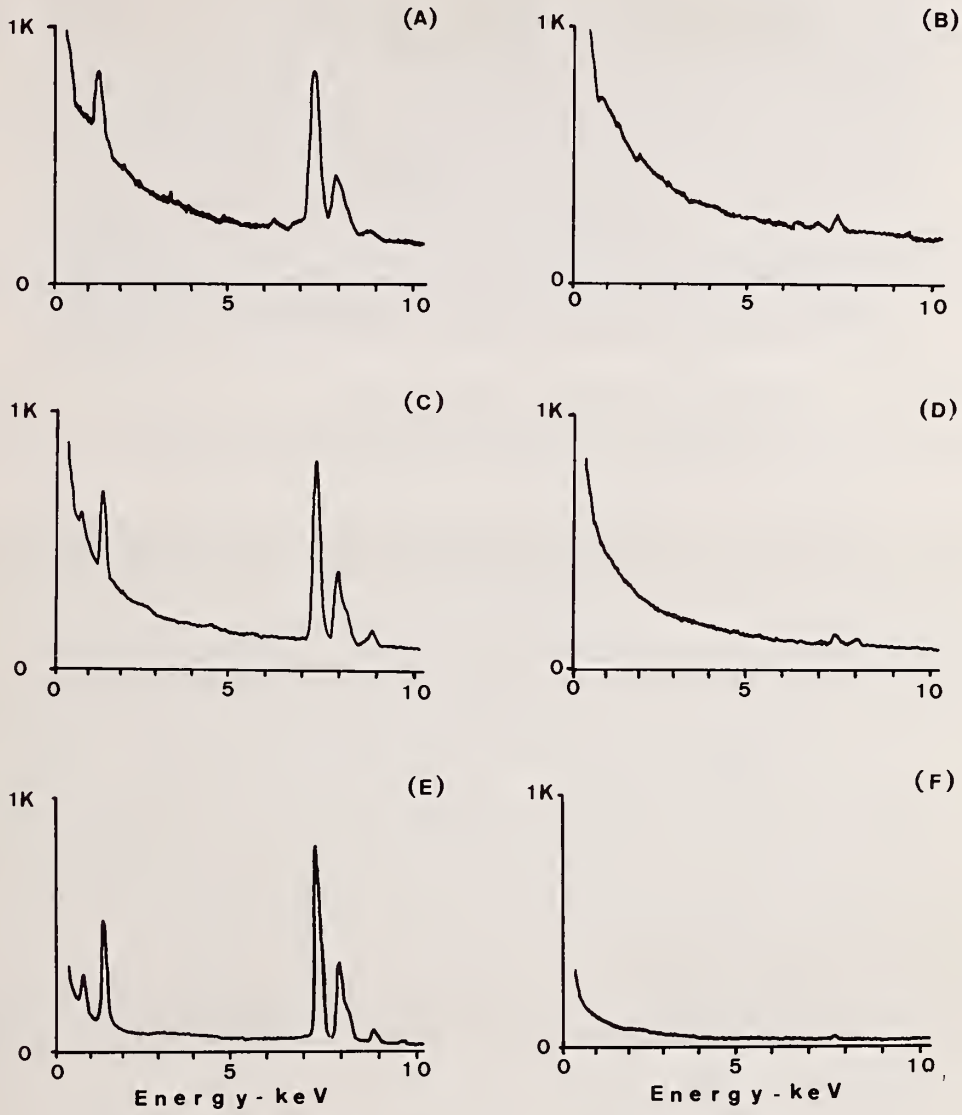

Figure 8. Variation in specimen and in-hole spectra recorded in an HVEM as a function of modifications to the electron-optical column to reduce uncollimated radiation. (a), (b) unmodified instrument, (c), (d) after installation of shielding around detector head, (e), (f) after installation of non-beam-defining collimator and additional shielding between the condenser and objective lens (see text for details).

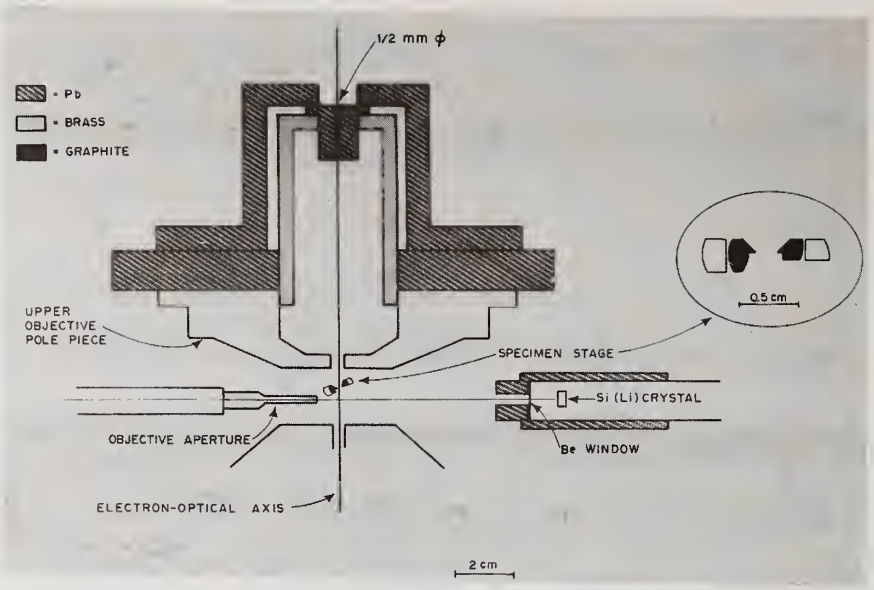

Figure 9. Schematic diagram of modifications to electron-optical column of an HVEM to reduce the intensity of uncollimated radiation reaching the specimen area (see text for details).

In order to continue it becomes necessary to decrease the incident probe current from 2.5×10^{-9} A to 2.5×10^{-11} A which reduces the magnitude of the uncollimated radiation to nearly manageable levels as shown in figure 10. Here in in-hole continuum signal (figure 10(b)) is $\lesssim$25 percent of the corresponding specimen continuum (figure 10(a)) and it was possible to qualitatively assess the proposed advantages of HVEM-based analysis on the P/B ratio. By subtracting this reduced in-hole signal from the corresponding specimen measurement, an increase relative to 100 keV measurements of 2.4 and 1.6 times was experimentally measured for the NiKα and AlKα lines, confirming qualitatively the expected increase. The 100 keV data used for comparison was obtained from the same specimen in a JEOL JSEM 100 C TEM/STEM instrument operating at nearly the same geometry. The characteristic fluorescence problem in the HVEM is also reduced after these modifications as the in-hole signal for the NiKα line is now ~5 percent and is essentially zero for the AlKα line relative to the specimen measurement. The feasibility of replacing the remote lead shielding by appropriately machined depleted uranium is being investigated as well as possible modifications to the condenser aperture assembly to further reduce the magnitude of the hard x-ray flux closer to its most probable source.

ORNL-DWG 79-11916

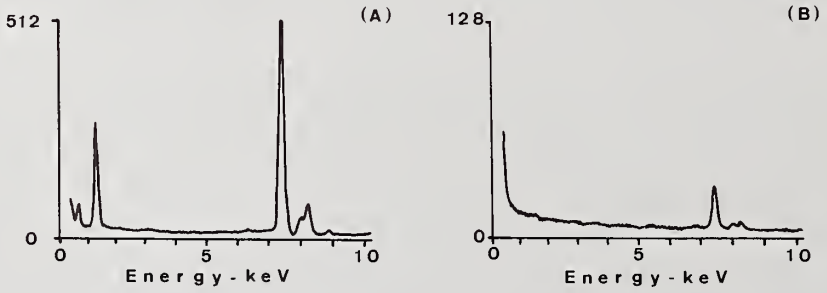

Figure 10. Specimen (a) and in-hole spectra (b) measured after reduction of bremsstrahlung production by decreasing incident probe current and addition of non-beam-defining collimators (note scale changes between the two spectra).

4. Summary

The presence of uncollimated fluorescing radiation in an Analytical Electron Microscope is the most serious problem in the application of x-ray microanalysis to thin electron transparent specimens. The magnitude of this radiation varies from one instrument to another, and its detrimental effects to a particular analysis can be judged easily by performing an "in-hole" experiment on the specimen under investigation. Should the intensity of any characteristic x-ray peak in this in-hole spectrum be greater than 2 percent of the intensity of the same line when performing a specimen measurement, then steps should be taken to reduce the magnitude of the uncollimated radiation by modifications to the electron-optical column. Once the uncollimated radiation is reduced to an "acceptable level", each subsequent specimen measurement can be corrected to a good first approximation for any residual, yet still detectable, in-hole signal by the simple subtraction of the two spectra.

The author would like to acknowledge the invaluable assistance and discussions with Drs. E. A. Kenik, J. Bentley, and R. W. Carpenter, as well as the support of the E. P. Wigner Fellowship at ORNL under contract no. W-7405-eng-26, U. S. Department of Energy, with the Union Carbide Corporation.

References

[1] Hirsch, P., Howie, A., Nicholson, R., Pashley, D., Whelan, M., Electron Microscopy of Thin Crystals, Krieger Pub. Co., New York (1979).

[2] Bentley, J., Zaluzec, N. J., Kenik, E. A., Carpenter, R. W., SEM/1979/II, Washington, D.C., O. Johari, ed., Chicago Press (1979), p. 581.

[3] Shuman, H., Somlyo, A. V., Somlyo, A. P., Ultramicroscopy, 1, 317-339 (1976).

[4] Joy, D. C., Maher, D. M., Analytical Electron Microscopy: Report of a Specialist Workshop, Cornell University (August 1976), Materials Science Center, Clark Hall, Cornell University, Ithaca, New York 14850.

[5] Zaluzec, N. J. and Fraser, H. L., Phys. E., 9, 1051-1052 (1976).

[6] Carpenter, R. W. and Bentley, J., SEM/1979/I, Washington, D.C., O. Johari, ed., Chicago Press (1979), p. 153.

[7] Clarke, D. R., SEM/1972/I, O. Johari, ed., Los Angeles, Chicago Press (1978).

[8] Geiss, R. H. and Huang, T. C., X-ray Spectr., 4, 196-201 (1975).

[9] Kenik, E. A. and Bentley, J., 35th Annual Proceedings of EMSA, G. W. Bailey, ed., Claitor's Publishing Company, Baton Rouge (1977), p. 328-329.

[10] Headley, T. J. and Hren, J. J., Ninth Inter. Conf. on Electron Microscopy, J. M. Sturgess, ed., Microscopical Society of Canada, Toronto (1978), Vol. 1, pp. 504-505.

[11] Zaluzec, N. J. and Fraser, H. L., Analytical Electron Microscopy: Report of a Specialist Workshop, Cornell University (August 1976), pp. 118-120, Materials Science Center, Clark Hall, Cornell University, Ithaca, New York 14850.

[12] Fraser, H. L. and Woodhouse, J. B., Electron Microscopy: Proc. of 2nd Workshop, Cornell University, Ithaca, New York (1978), p. 191.

[13] Oppolzer, H. and Knauer, U., SEM/1979/I, Washington, D.C., O. Johari, ed., Chicago Press (1979), p. 111.

[14] Fiori, C. and Joy, D. C., National Institute of Health, Bethesda, Maryland, private communication (1979).

[15] Zaluzec, N. J., Kenik, E. A., Bentley, J., Analytical Electron Microscopy: Proc. of 2nd Workshop, Cornell University (July 1978), p. 179.

[16] Zaluzec, N. J., Ninth Inter. Conf. on Electron Microscopy, J. M. Sturgess, ed., Microscopical Society of Canada, Toronto (1978), Vol. 1, p. 548-549.

[17] Zaluzec, N. J., An Analytical Electron Microscopy Study of the Omega Phase Transformation in a Zirconium-Niobium Alloy, PhD Thesis, University of Illinois, 1978; also published as Oak Ridge National Laboratory Report ORNL/TM-6705. Copies available from NTIS, U. S. Department of Commerce, Springfield, Virginia 22161.

[18] Zaluzec, N. J. and Fraser, H. L., 8th Inter. Conf. on X-ray Optics and Microanalysis, Boston (1977), Beaman, Ogilivie, Wittry, eds., Science Press, Princeton, New York (in press).

[19] Goldstein, J. E. and Williams, D. B., SEM/1978/I, O. Johari, ed., SEM, Inc., AMF O'Hare, Illinois (1978), pp. 427-434.

[20] Zaluzec, N. J., Introduction to Analytical Electron Microscopy, Hren, Joy and Goldstein, eds., Plenum Press, New York (1979), chapter 4.

[21] Goldstein, J. I., Costley, J. L., Lorimer, G. W., Reed, S. J. B., SEM 1 (1977), 315.

[22] Hutchings, R., Loretto, M. J., Jones, L. P., Smallman, R. E., Analytical Electron Microscopy, Proc. of 2nd Workshop, Cornell University, Ithaca, New York (1978), p. 166.

[23] Joy, D. C., Maher, D. M., SEM/1977, O. Johari, ed., IITRI, Chicago, Illinois (1977), p. 325.

[24] Cliff, G., Nasir, M. J., Lorimer, G. W., Ridley, N., 9th Inter. Conf. on Electron Microscopy, J. M. Sturgess, ed., Microscopical Society of Canada, Toronto (1978), pp. 540-541.

[25] Zaluzec, N. J. and Fraser, H. L., Analytical Electron Microscopy: Proc. of the 2nd Workshop, Cornell University, Ithaca, New York (July 1978), p. 122.

[26] Goldstein, J. I. and Williams, D. B., SEM/1977/I, O. Johari, ed., Chicago Press, IIT Research Institute, Chicago, Illinois (1977), pp. 651-662.

National Bureau of Standards Special Publication 604. Proceedings of the Workshop on Energy Dispersive X-Ray Spectrometry held at NBS, Gaithersburg, Maryland, April 23-25, 1979. (Issued March 1981)

SPECTRAL PROCESSING TECHNIQUES IN A QUANTITATIVE ENERGY DISPERSIVE X-RAY MICROANALYSIS PROCEDURE (FRAME C)

R. L. Myklebust, C. E. Fiori* and K. F. J. Heinrich

National Measurement Laboratory
National Bureau of Standards
Gaithersburg, MD 20234

*Division of Research Services
National Institutes of Health
Bethesda, MD 20205

Abstract

The correction procedure FRAME C was developed for quantitative electron probe microanalysis with an energy dispersive detector. Algorithms incorporated to compute the background due to the x-ray continuum and to correct for overlaps due to x-ray peaks will be described in detail. The method employed to determine the detector efficiency for the x-ray continuum calculation will be discussed as well as the computation of the continuum.

1. Introduction

The application of quantitative analysis procedures to x-ray data obtained with an energy-dispersive x-ray spectrometer (EDS) requires two computations not normally needed for wavelength-dispersive spectrometer (WDS) data. First, since the peak-to-background ratio in EDS is approximately an order of magnitude less than the peak-to-background ratio in WDS, the background subtraction in EDS is of much greater importance than in WDS [1][1]. Second, there must be a method of resolving overlapping peaks in the EDS since the resolution of the EDS system is much poorer than in a WDS system and thus, peak overlaps frequently occur in practical analytical situations [2].

We will describe the methods used in the NBS theoretical matrix correction procedure, FRAME C, for handling these two problems [2].

1.1 Background prediction

The problems associated with calculation of the background in the EDS spectrum can be divided into three parts: (1) the continuum x-rays generated within the specimen, (2) the absorption of the continuum x-rays by the sample, and (3) the losses of x-rays within the Si(Li) detector (detector efficiency).

1.2 Generation of continuous radiation

Kramers proposed a relation describing the intensity distribution of the continuum which, as a function of the energy of the emitting photons, is

$$I_E \Delta E = k_E \bar{Z} (E_o - E) \Delta E \qquad (1)$$

[1]Figures in brackets indicate the literature references at the end of this paper.

In this equation, $I_E \Delta E$ is the average energy of the continuous radiation, produced by one electron, in the energy range from E to E + ΔE. The constant k_E is Kramers' constant [3] transformed for the energy scale, $\bar{Z}$ is the average atomic number of the target, and E_o is incident electron energy in keV. As shown by Green [4], k_E varies moderately with $\bar{Z}$, but this effect is not germane to the present communication. The value of the photon energy, E (keV), ranges from zero to E_o. Kulenkampff [5] obtained measurements which, except for a small term involving $\bar{Z}^2$, agreed with equation 1. The probability, IΔE, that one electron will produce one photon of energy between E and E + ΔE is equal to

$$I\Delta E = k_E \bar{Z} \frac{E_o - E}{E} \Delta E \tag{2}$$

The number of photons, N(E), within the energy range E to E + ΔE, produced in time t with a beam current i (electrons per second) and observed by a detector of efficiency P_E, subtending a solid angle L, is equal to

$$N(E) = \frac{\Omega}{4\pi} itf_E P_E I\Delta E$$

$$= \frac{\Omega}{4\pi} itf_E P_E k_E \bar{Z} \frac{E_o - E}{E} \Delta E \tag{3}$$

Here, the term f_E (absorption factor) denotes the probability of absorption of a photon of energy E within the target. In equation 3, the term $\Omega/4\pi$ is equal to the fraction of photons emitted towards the detector only if the generation of the continuum is isotropic in thick targets. This assumption is a reasonable approximation, although some degree of anisotropy does exist [5-7]. If we define $a \equiv (\Omega/4\pi) itk_E \Delta E$, then we obtain

$$N(E) = af_E P_E \bar{Z} \frac{E_o - E}{E} \tag{4}$$

Lifshin, Rao-Sahib and Wittry, and Hehenkamp and Böcker [7-10] have shown that the energy dependence of N(E), expressed by equation 4, is only approximate. For a detailed discussion of the subject, the reader is referred to reference [11] by Rao-Sahib and Wittry who also show that the atomic-number dependence of N(E) is more complex than indicated by Equation 4.

The residual correction has been carried out in at least two ways: (1) Applying more refined theoretical calculations [11], and modifying the exponents, from unity, on the energy term and atomic number $\bar{Z}$ in Kramers' equation (7,8); or (2) Using an additive energy-dependent correction term in equation 4 as proposed by Ware and Reed [12] as follows:

$$N(E) = a\left[f_E P_E \bar{Z} \frac{E_o - E}{E} + F(E)\right] \tag{5}$$

where F(E) is taken from an empirically determined table. The authors indicated that for continuum photon energies above 3 keV, the additive energy term was unnecessary. Lifshin [10] empirically developed and tested a more general relation for N(E):

$$N(E) = f_E P_E \bar{Z} \left[a \frac{E_o - E}{E} + b \frac{(E_o - E)^2}{E}\right] \tag{6}$$

in which b is a fitting factor, and the remaining terms are as defined for equation 4.

We have found that it is possible to determine a and b for any target by measuring N(E) at two separate photon energies, and solving the resulting two equations in two unknowns. This procedure presumes that both f_E and P_E in equation 6 are known. Since the determination of N(E) is made from measurements on the target of interest only, the inaccuracies of Kramers' equation with respect to atomic number do not affect the proposed method.

The points chosen for measurement of N(E) must be free of peak interference and detector artifacts (incomplete charge collection, pulse pile-up, double-energy peaks, and escape peaks) and they should be the same for standard and specimen. With moderate count rates and reasonable counting statistics, these limitations are not very restrictive.

1.3 The absorption factor, f_E

For characteristic primary x-ray photons, the absorption within the target is taken into account by a factor called f_p or f(x). This factor has been expressed by [13] as

$$1/f_p = (1 + a\gamma x)^2 \tag{7}$$

where γ is $E_o^{1.65} - E_q^{1.65}$, E_q is the excitation potential in keV for the shell of interest, and $x = \mu \cdot \csc \psi$ (μ is the mass attenuation coefficient of the target for the line of interest, and ψ is the x-ray emergence angle with respect to the specimen surface). The presently used value for the coefficient a is:

$$a = 1.2 \times 10^{-6} \ (g/cm^2)/kV^{1.65} \tag{8}$$

If it is assumed that the generation of the continuum has the same depth distribution as that of characteristic radiation, which Monte Carlo calculation suggests is a reasonable assumption [14] and if $E \cong E_q$, then equation 7 can be modified to

$$1/f_E = (1 + a(E_o^{1.65} - E^{1.65})x_C)^2 \tag{9}$$

where $x_C = \mu_E \csc \psi$, μ_E is the mass attenuation coefficient of the target for continuum photons of energy E and f_E is the absorption factor for these photons. Similar assumptions and expressions have been used by other authors [8,10,12].

The criterion for assessing the usefulness of equation 9 is that it should remove the effects of all absorption edges over the energy range of interest.

As pointed out by Ware and Reed [12], the absorption term f_E is dependent upon the composition of the target. Consequently, when the composition of the target is unknown, it is necessary to include equation 6 in an iteration loop, as shown in figure 1.

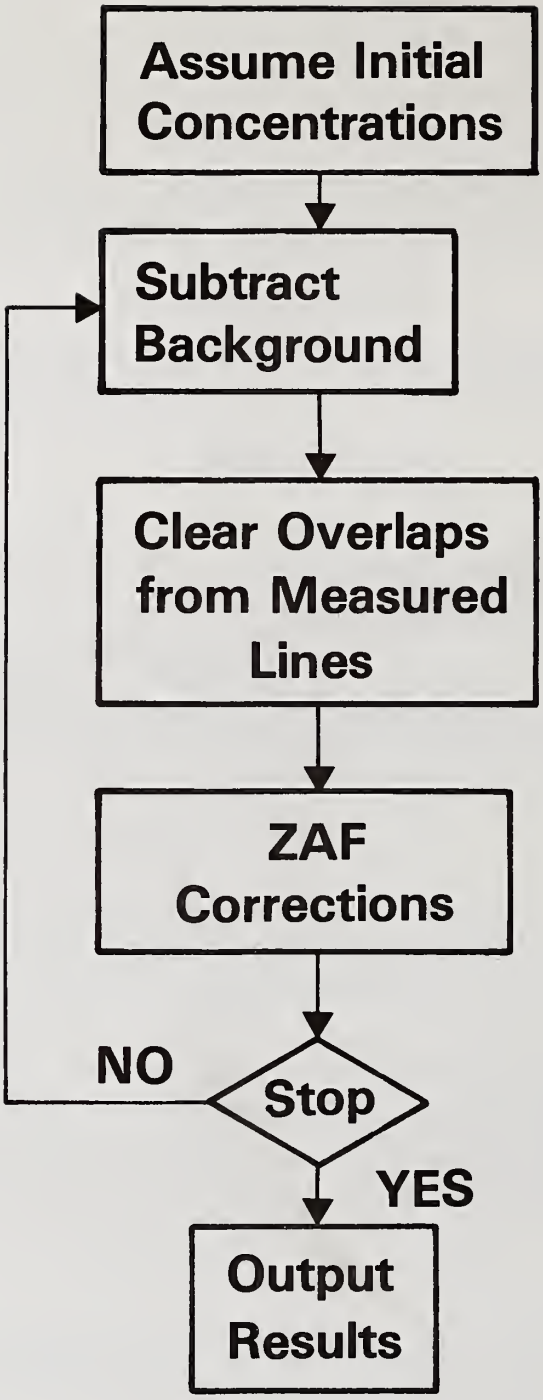

Figure 1. Short block diagram showing the principal operations within the FRAME C iteration loop.

1.4 The detector efficiency, P_E

The continuous radiation emitted from the target towards the detector traverses a beryllium window, typically on the order of 8 μm thick, a surface-barrier contact (< 20 nm of Au), and an inactive layer of silicon extending 200 nm or less into the detector. Then, the radiation enters the active (intrinsic) region of the detector which has a thickness typically between 2 and 5 mm. The absorption losses in the beryllium window, the gold, the silicon dead layer, and the transmission through the active silicon zone can therefore be calculated as follows:

$$P_E = \exp - [\mu(Be,E)t_{Be} + \mu(Si,E)t^D_{Si} + \mu(Au,E)t_{Au}][1 - \exp - (\mu Si,E)t_{Si})] \qquad (10)$$

In this equation, t^D_{Si}, t_{Si} are the thicknesses (g/cm^2) of the silicon dead layer, and of the active detector region, respectively. t_{Be} and t_{Au} are the thicknesses (g/cm^2) of the beryllium window and the gold contact layer. The mass attenuation coefficients of beryllium, silicon and gold at the energy E, μ(Be,E), μ(Si,E) and μ(Au,E) are calculated as described in reference 15.

Since sufficiently accurate values were not available from the manufacturer, estimates of the thicknesses of the beryllium window and the dead layer of the detector were adjusted to optimize the fit between the calculated and the experimental spectra at energies below 2 keV.

The detection efficiency and, hence, the shape of the recorded background are also affected by incomplete or slow charge collection, by Compton scattering and by the escape mechanism for SiK photons [16]. However, for radiation below 25 keV, the Compton effect is negligible. Incomplete charge collection can produce minor increases in the background at energies less than major peaks and, thus, affect the accuracy of trace analysis. The effects of the escape mechanism are negligible for our purposes. All of these effects should be considered, however, where the detector efficiency must be determined for absolute measurements. It should also be noted that the theoretical curves shown in figures 2 and 3 do not take into account the effects of limited detector resolution.

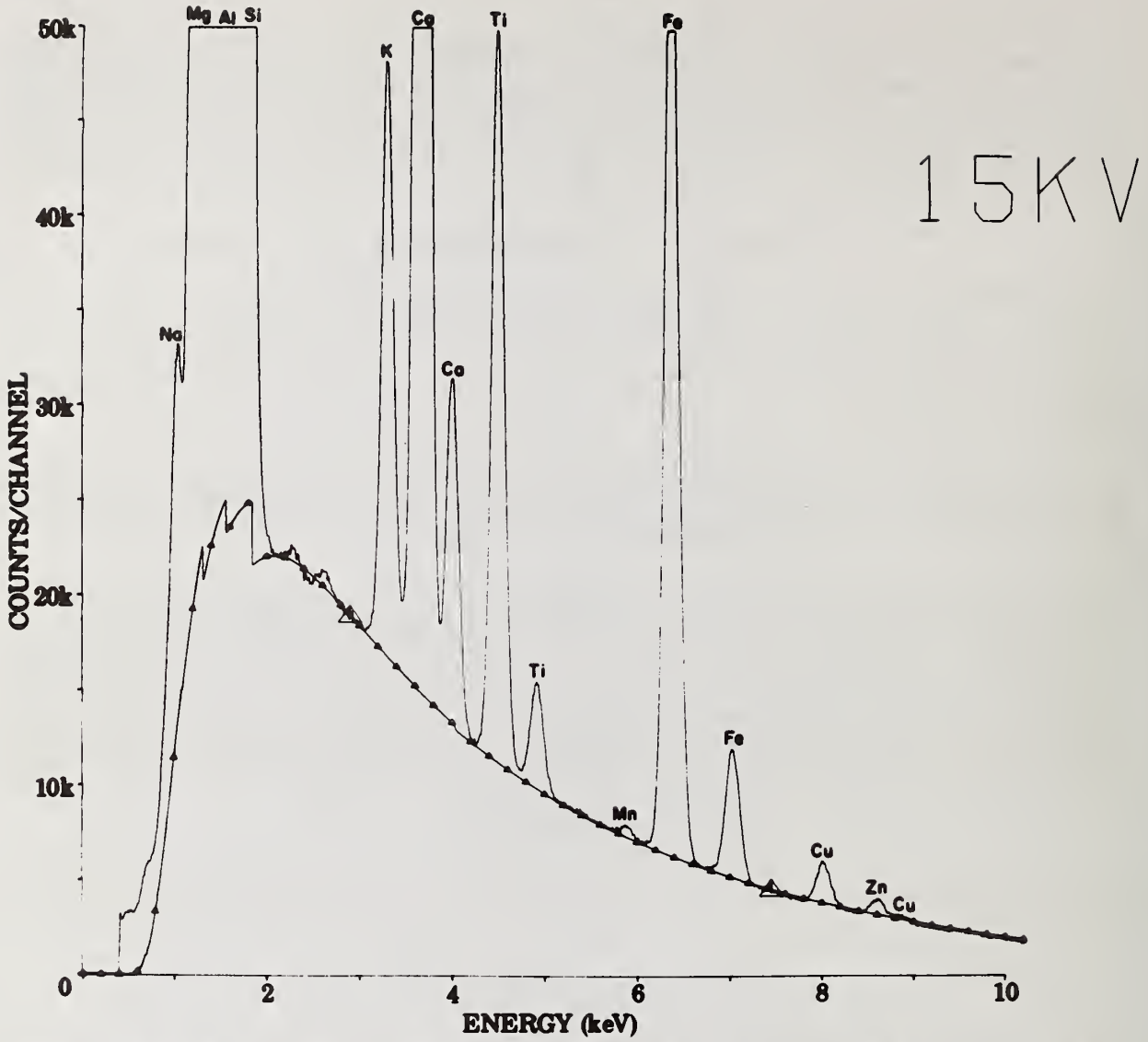

Figure 2. Spectrum of Kakanui hornblende with the fitted x-ray continuum background. The large open triangles are the fit points.

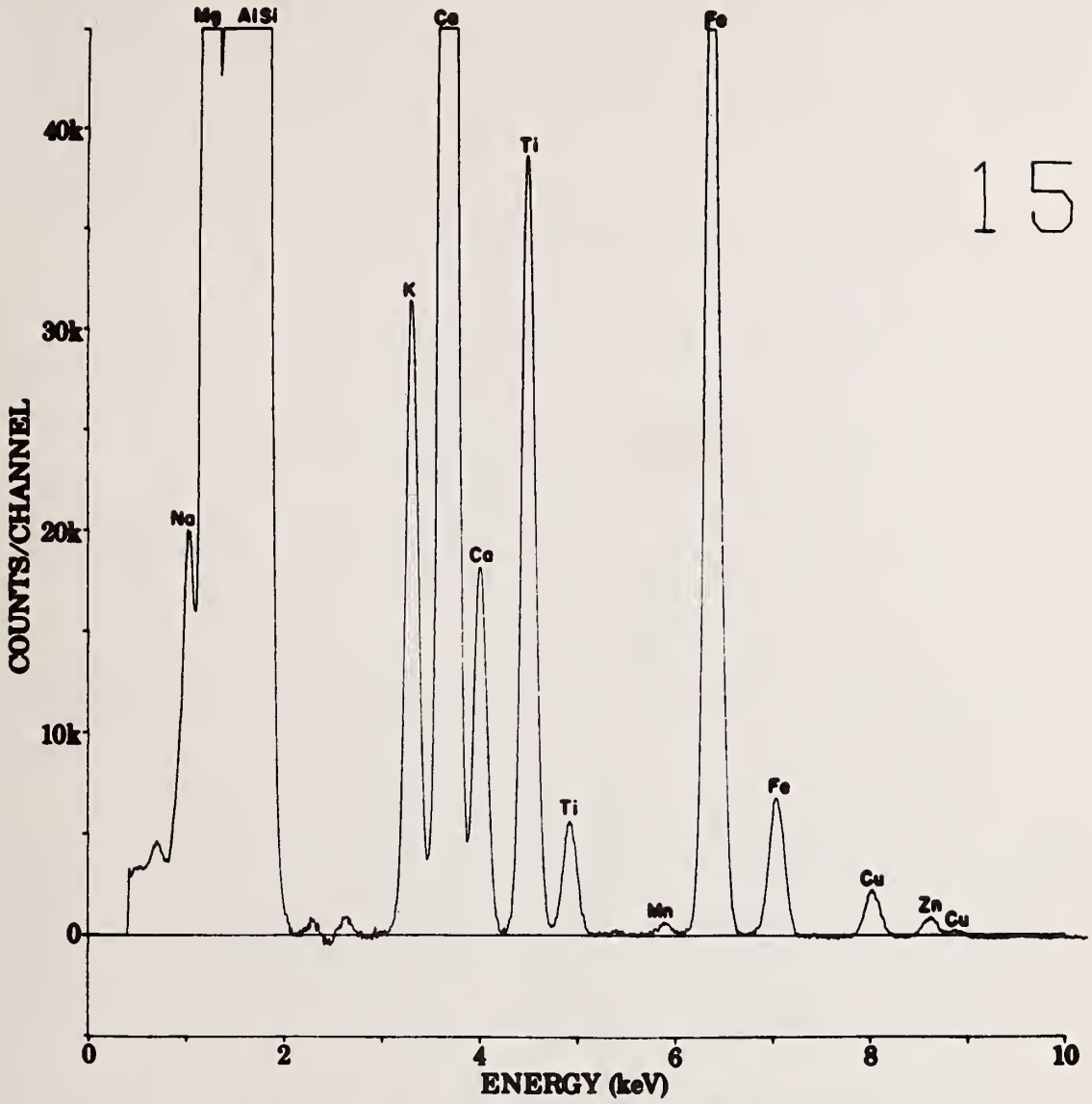

Figure 3. Spectrum of Kakanui hornblende shown in figure 2 but with continuum removed.

1.5 Line interferences

The original EDS version of the FRAME program, FRAME B, [17] required that all analytical x-ray peaks be clearly resolved from other x-ray peaks in the spectrum. This condition often cannot be met in energy-dispersive spectra. We have developed a simple method [18] to overcome this limitation which involves integrating peaks between the energy limits of the regions of interest for each analytical x-ray line. One x-ray line from each element is used for the analytical procedure; however, all lines are potential interferences which must be accounted for if they fall within the region of interest of an analytical line, i.e., one that has been assigned a region of interest.

Given an x-ray peak near a region of interest, the fraction of this peak which falls within the region depends only on the relative positions of peak and region of interest, and the width resolution (σ) of the Gaussian peak but not on the composition of the specimen. Therefore, this factor can be computed once early in the procedure and stored for all subsequent measurements. For simplicity we will develop the argument for two unresolved peaks, A and B (see figure 4). E_A is the center of peak A and E_B is the center of peak B.

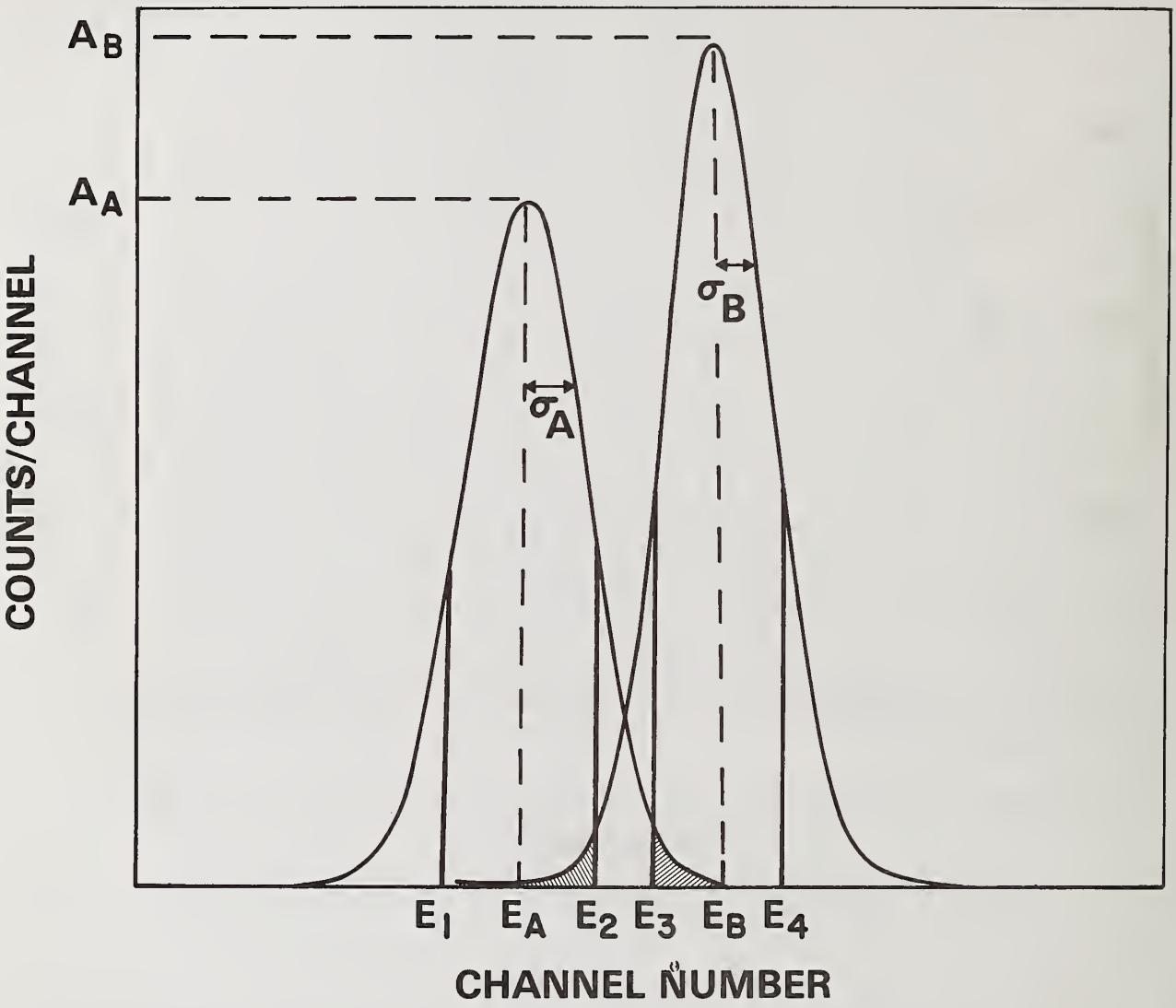

Figure 4. Schematic representation of two overlapping Gaussian shaped peaks. Shaded areas are the overlaps of each peak into the region of interest of the other peak.

We can calculate the width resolutions σ_A and σ_B as a function of E_A and E_B [18] if the detector resolution has been measured for a peak at any energy (e.g., Mn Kα). Since peak B contributes counts to the region of interest for peak A and vice versa, the correction procedure must be iterative.

The number of counts due to peak A at any channel whose energy is E_i is:

$$N_i = A_A \exp\left[-1/2\left(\frac{E_A - E_i}{\sigma_A}\right)^2\right] \tag{11}$$

Consequently, the integrated counts N_A between the limits E_1 and E_2 which define the region of interest of element A, are:

$$N_A = A_A \int_{E_1}^{E_2} \exp\left[-1/2\left(\frac{E_A - E_i}{\sigma_A}\right)^2\right] dE_i \tag{12}$$

and the integrated counts between the limits E_3 and E_4 of the region of interest of element B are:

$$N_{AB} = A_A \int_{E_3}^{E_4} \exp\left[-1/2\left(\frac{E_A - E_i}{\sigma_A}\right)^2\right] dE_i \tag{13}$$

The interference factor is defined as:

$$H_{AB} = \frac{N_{AB}}{N_A} \tag{14}$$

This factor is multiplied by the number of counts measured in peak A between the limits E_1 and E_2 to obtain the number of counts contributed to the region of interest of peak B by peak A.

A different type of interference occurs when a peak from element A which is not used for data reduction falls within the region of interest selected for element B (figure 5). In this case, the intensity of the interfering peak from element A must be obtained from the count rate within the region of interest of the analytical peak for element A. If the analytical line and the interfering line are both generated from ionization of the same subshell, their generated intensities are related by their respective relative transition probabilities. A transition probability is the intensity of the line of interest divided by the sum of the intensities of all other lines arising from the ionization of the same subshell,

$$\Phi_{AK\beta} = I_{AK\beta} / \left(I_{AK\beta} + I_{AK\alpha}\right). \tag{15}$$

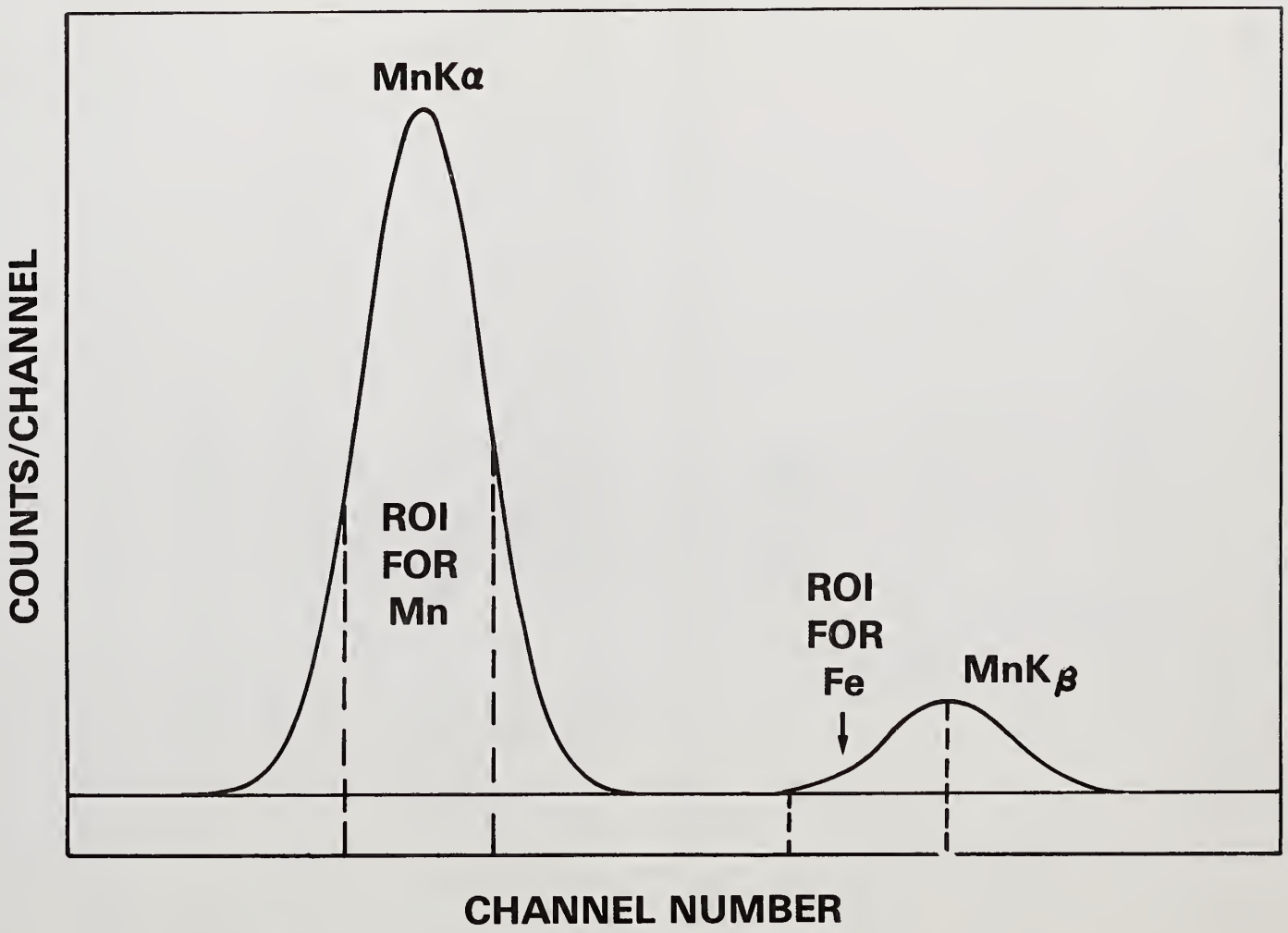

Figure 5. Spectrum of manganese showing the region of interest (ROI) for FeKα overlapped by MnKβ.

The measured intensities are also affected by the absorption of the x-rays within the specimen and the efficiency of the detector. For example, if the interfering line is a Kβ peak of element A, then to relate the interference of AKβ upon another peak BKα to the measured intensity of AKα, the overlap factor of AKβ into the region of interest of BKα is obtained by:

$$H_{AB} = \frac{I_{AK\beta}}{I_{AK\alpha}} \cdot \frac{f_{P(AK\alpha)}\ P_{E(AK\alpha)}}{f_{P(AK\beta)}\ P_{E(AK\beta)}} \cdot \frac{N_{AB}}{N_A} \qquad (16)$$

where $I_{AK\beta}/I_{AK\alpha}$ is derived from the transition probabilities, f_p is the absorption within the specimen for each line energy, and P_E is the detector efficiency at each energy. The transition probabilities for the Kβ and Kα x-ray lines of elements of atomic number 15 through 30 have been determined by us (see Table 1) as well as by others [19,20] and are better known than those of the L or M x-ray lines.

Table 1. Relative transition probabilities for Kβ x-ray lines [19].

Atomic Number	Kβ/(Kα + Kβ)
15	.050
16	.063
17	.085[a]
18	.097[a]
19	.104
20	.113[a]
21	.114[a]
22	.114
23	.116
24	.116
25	.119
26	.119
27	.120
28	.121
29	.123
30	.128

[a]Interpolated value.

We have estimated the transition probabilities for the L and M series of x-ray lines up to 10 keV. These estimates were made on five pure elements measured at three different beam voltages. Since the L-lines (and the M-lines) were all related to the $L\alpha_1$ line (or the Mα line), these are not the true transition probabilities. However, the transition probability is incorporated within this factor.

To compute overlap factors for all the L x-ray lines, we relate the intensity of each L line to the $L\alpha_1$ line (the measured line). We must, however, take into account that the ratios of line intensities of the L spectra vary with excitation potential. This is due to the fact that these lines arise from three subshells each of which has a different critical excitation potential. To relate the intensity of any line to the measured $L\alpha_1$ line, we compute an intensity factor which is the intensity of the line "i" divided by the intensity of the $L\alpha_1$ line ($I_{L_i}/I_{L\alpha_1}$). To introduce an energy-dependent term into this factor, we have integrated the expression:

$$Y_{nl} = \frac{N}{A} \int_{E_o}^{E_c} \frac{Q(E)}{[dE/ds]}\, dE \qquad (17)$$

where s is the mass thickness along the electron path (g/cm^2), in the same manner as Philibert and Tixier [21] to obtain the number of ionizations, Y_{nl}, in the level nl.

$$Y_{nl} = \frac{N}{A} \frac{Z_{nl}}{M} \left\{ U_o - 1 - \frac{1}{W} \ln W[li(U_o W) - li(W)] \right\} \tag{18}$$

M and N/A are constant and can be eliminated since we are calculating the ratios of the x-ray lines for the same element. U_o is the overvoltage E_o/E_{nl} where E_{nl} is the ionization energy of the edge nl, W is 1166 E_{nl}/J where J is the mean ionization potential, $U_o W$ is 1166 E_o/J and li is the logarithmic integral. We have fitted an expression which approximates the logarithmic integral ($li(x) \simeq 2.905 \sqrt{x - 3.063}$) over the range of interest. The number of electrons in each subshell, Z_{nl}, is determined from basic quantum theory, and the pertinent values for the subshells of interest are as follows:

Subshell	Number of Electrons
K	2
L_1	2
L_2	2
L_3	4
M_1	2
M_2	2
M_3	4
M_4	4
M_5	6

The ratios of lines arising from different absorption edges are then corrected for differences in overvoltage by multiplying each line by Y_{nl} (Equation 18). The total L line intensity factor, for any L line, thus becomes:

$$S_L = \frac{I_L \, Y_L}{I_{L\alpha_1} \, Y_{L\alpha_1}} \tag{19}$$

The first step in computing the L overlaps is to determine the area of the $L\alpha_1$ line within its region of interest by subtracting the areas of all other L lines of the same element from the region of interest. This is done by calculating all the overlap factors for these lines and stripping them out in the same manner as is used for overlaps from other elements. Since the computed overlap factor for each L line is relative to the $L\alpha_1$ line alone, this step is necessary. Overlap factors for the measured lines of other elements are then computed in the same manner as for K lines except that the overlapping area of an interfering peak is multiplied by that peak's intensity factor, S_L. In the case of the ratio $L\alpha_1/K\alpha$, the ratio must be multiplied by the ratio of fluorescence yields, ω_L/ω_K, and an atomic number dependent factor which is at least partly due to the Coster-Kronig transitions.

$$y_L = 0.095Z - 1.69 \tag{20}$$

M lines are treated in a similar manner. There are also provisions for determining the intensity of an M line from an L line or vice versa. Since we were unable to find an appropriate cross section for the M-series of x-ray lines, we fitted an empirical expression to the generated $M\alpha/L\alpha_1$ ratio for three elements at five different operating voltages.

$$Y_{nl}y_M = \exp\left[\frac{34.17}{\ln(U_p)} - \frac{30.03}{\sqrt{\ln(U_p)}} + 8.527\right] \tag{21}$$

U_p is the product of the L overvoltage, E_o/E_{L_3}, and the M overvoltage, E_o/E_{M_5}. Approximate results can be obtained by this technique; however, the factors used are not well known at this time.

In the previous discussion, we have assumed that the peaks have simple Gaussian shapes. In reality, however, the peaks are distorted on the low-energy side by the effect of incomplete charge collection. Consequently, the x-ray peaks observed by a Si(Li) detector are the convolutions of several contributions. Some peaks consist of several x-ray lines of the same series (such as $K\alpha_1$ and $K\alpha_2$). In most cases of multiple peaks (except $K\alpha_{1,2}$ and $K\beta_{1,3,5}$), we compute the peaks separately for each x-ray line in the same manner as the overlapping peaks from other elements. For the incomplete charge collection at the low-energy shoulder of each peak, we have developed an empirical expression:

$$I_{c_i} = A_A a(E_A - E_i) \exp[-b(E_A - E_i)] \tag{22}$$

in which a and b are energy-dependent coefficients fitted for a particular detector and the other terms are as previously defined. A_A was previously obtained as a measure of line intensity from Equation 13.

The remaining case of overlap that is computed is the interference of the escape peak of a characteristic x-ray line with an analytical line. The expression used to predict the number of counts in an escape peak based on the number of counts in the parent peak is that due to Reed and Ware [22]:

$$k_{esc} = 0.038\varepsilon/(1 - 0.038\varepsilon) \tag{23}$$

where k_{esc} is the integrated intensity ratio of the escape peak to the parent peak and

$$\varepsilon = 1/2 \left\{1 - \frac{\mu(Si,Si)}{\mu(Si,E_A)} \ln \left[1 + \frac{\mu(Si,E_A)}{\mu(Si,Si)}\right]\right\} \tag{24}$$

$\mu(Si,Si)$ is the mass absorption coefficient for SiKα in silicon and $\mu(Si,E_A)$ is the mass absorption coefficient for the parent peak in silicon. An overlap coefficient is then computed in the same manner as previously described for a peak that has no region of interest. The standard deviation of the escape peak is that corresponding to its energy rather than of the parent energy; k_{esc} is the intensity ratio of escape peak to parent peak.

2. Conclusions

The effectiveness of the corrections is shown in Table 2 where several pure materials have been analyzed for elements that are not present in the material. The last two columns are the amounts of the absent element found with and without the overlap correction. The results are satisfactory except when two measured peaks overlap almost completely (e.g., Ta + Cu in Table 2).

Table 2. Overlap corrections.

Specimen	E_o in keV	Analyzed for	Overlap with	Mass fraction found before correction	Mass fraction found after correction
MgO	15	Al	MgKβ	.0026	.0016
Al_2O_3	15	Mg	AlKα	.0132	.0058
SiO_2	15	Al	SiKα	.0072	-.0010
Cr	15	Mn	CrKβ	.1311	-.0024
Mn	15	Fe	MnKβ	.1045	.0019
Fe	15	Co	FeKβ	.0653	.0062
Cu	20	Zn	CuKβ	.0206	.0039
Zr	15	Bi	$ZrL\beta_2$, $L\gamma_1$,$L\gamma_3$	.0214	-.0113
Bi	15	Zr	BiMα,Mβ, Mζ	.0213	-.0009
Zn	20	W	ZnKα	.1329	.0010
Ta	20	Cu	$TaL\alpha_1$ [a]	.1968	.0700

[a] The regions of interest for Cu Kα and Ta Lα overlap. These lines are too close to be separated well by this method.

The electron beam incidence angle is 90° and the x-ray emergence angle is 52.5°.

References

[1] Fiori, C. E., Myklebust, R. L., and Heinrich, K. F. J., Analytical Chemistry, 48 (1), 172-176 (Jan. 1976).

[2] Myklebust, R. L., Fiori, C. E., and Heinrich, K. F. J., FRAME C: A Compact Procedure for Quantitative Energy-Dispersive Electron Probe X-ray Analysis, NBS Tech. Note 1106, Sept. 1979.

[3] Kramers, H. A., Phil. Mag., 46, 6th series (July-Dec. 1923).

[4] Green, M., PhD Thesis, University of Cambridge (1962).

[5] Kuhlenkampff, H., Ann Phys., 69, 548 (1922).

[6] Dyson, N. A., Proc. Phys. Soc., 73, 924 (1959).

[7] Rao-Sahib, T. S. and Wittry, D. B., Proc. 6th Int. Conf. on X-ray Optics and Microanalysis, Tokyo, 1972.

[8] Rao-Sahib, T. S. and Wittry, D. B., J. Appl. Phys., 45, 5060, 5068 (1975).

[9] Hehenkamp, Th. and Bocker, J., Mikrochim Acta Suppl., 5, 29 (1974).

[10] Lifshin, E., Proc. Ninth Annual Conference of Microbeam Analysis Society, Ottawa, Canada, paper 53 (1974).

[11] Duncumb, P. and Reed, S. J. B., Quantitative Electron Probe Microanalysis, K. F. J. Heinrich, ed., U. S. National Bureau of Standards Special Publication 298, U. S. Government Printing Office, Washington, D.C. 20402, 1967, p. 133.

[12] Ware, H. G. and Reed, J. B., J. Phys. E., 6, 286-288 (1973).

[13] Heinrich, K. F. J. and Yakowitz, H., Analytical Chemistry, 47 (14), 2408-2411 (1975).

[14] Reed, S. J. B., X-ray Spectrometry, 4, 14 (1975).

[15] Yakowitz, H., Myklebust, R. L., and Heinrich, K. F. J., U. S. National Bureau of Standards Technical Note 796, U. S. Government Printing Office, Washington, D.C. 20402 (1973).

[16] Freund, H. U., Hansen, J. S., Karttunen, E., and Fink, R. W., Proc. Int. Conf. on Radioactivity and Nuclear Spectroscopy (1969).

[17] Fiori, C. E., Myklebust, R. L., and Heinrich, K. F. J., Proc. 11th Annual Conf. of Microbeam Analysis Society, Miami Beach, Florida (August 9-13, 1976) paper 12.

[18] Fiori, C. E., Myklebust, R. L., and Heinrich, K. F. J., Proc. 10th Annual Conf. of Microbeam Analysis Society, Las Vegas, Nevada (August 11-15, 1975), paper 20.

[19] Heinrich, K. F. J., Fiori, C. E., and Myklebust, R. L., J. Appl. Phys., 50 (9), 5589-5591 (Sept. 1979).

[20] Smith, D. G. W., Reed. S. J. B., and Ware, N. G., X-ray Spectrometry, 3, 149 (1974).

[21] Philibert, J. and Tixier, R., in Quantitative Electron Probe Microanalysis, NBS Special Publication 298, K. F. J. Heinrich, ed., 13-33 (1968).

[22] Reed, S. J. B. and Ware, N. G., J. Phys. E: Sci. Inst., 5, 582-584 (1972).

National Bureau of Standards Special Publication 604. Proceedings of the Workshop on Energy Dispersive X-Ray Spectrometry held at NBS, Gaithersburg, Maryland, April 23-25, 1979. (Issued March 1981)

THE EFFECT OF ELECTRON INCIDENCE ANGLE ON QUANTITATIVE ELECTRON PROBE MICROANALYSIS

J. D. Brown

Faculty of Engineering Science and
The Centre for Interdisplinary Studies in Chemical Physics
The University of Western Ontario
London, Canada

Abstract

ϕ (ρz) curves have been measured at 25 and 30 keV electron energies and electron incidence angles from 60 to 90°. These data can be used to establish the effect of changing incidence angle on quantitative correction procedures and will be invaluable for comparison with Monte Carlo predictions. None of the factors currently used to correct for inclined electron incidence adequately compensates for this effect.

1. Introduction

The usual ZAF procedure for converting x-ray intensities to composition involves separate correction for differences between unknown and standard in average atomic number, in x-ray absorption and in fluorescence due to absorption of characteristic or continuum x-rays. When measurements are made with non-normal electron incidence, electron backscattering and diffusion are modified. This results in a decrease in depth and a change in shape and magnitude in the production of x-rays as a function of depth. To account for these changes, several geometric factors have been proposed to modify the absorption parameter χ in the absorption correction [1-3][1] and the backscatter factor R in the atomic number correction [4,5]. Several authors [6,7] have commented on the inaccuracy of these factors. Originally Castaing [8] proposed that quantitative analysis could be based on knowledge of the production of x-rays as a function of depth in the specimen. To measure x-ray production, Castaing and Descamps [9] proposed a sandwich sample technique. Characteristic x-rays generated by electrons in a thin tracer layer of one element buried at different depths in a second (matrix) element were measured at a fixed take-off angle ψ outside the specimen. From this angle, the overlayer thickness, and the mass absorption coefficient, the measured intensity could be corrected for absorption to yield the x-ray intensity generated in the thin layer. For normalization, the intensity from the identical thickness of tracer layer isolated in space was measured. The ratio of intensity in the thin layer in the specimen relative to the isolated layer plotted as a function of depth in the specimen was defined as the ϕ (ρz) curve. If the ϕ (ρz) curves are known for both the unknown and pure element standard, then the measured relative x-ray intensity K_A can be calculated from the equation:

$$K_A = W_A \frac{\int_0^\infty \phi_S(\rho z) \exp(-\mu_S \rho z \operatorname{cosec} \psi)\, d\rho z}{\int_0^\infty \phi_A(\rho z) \exp(-\mu_A \rho z \operatorname{cosec} \psi)\, d\rho z} \qquad (1)$$

where subscript S refers to the unknown specimen and subscript A refers to the pure element A.

[1]Figures in brackets indicate the literature references at the end of this paper.

W_A is the weight fraction of A in the unknown and μ is the mass absorption coefficient for the characteristic x-ray line of element a used in the analysis.

In the absence of fluorescence effects, equation (1) is exact and includes both the atomic number and absorption corrections. Fluorescence due to characteristic lines can be simply calculated if the $\phi(\rho z)$ curves are known [6].

If the $\phi(\rho z)$ curves are measured with an instrument in which the electron beam is inclined with respect to the normal to the specimen surface, then the effects on the absorption and atomic number corrections can be evaluated. This paper will discuss measurements of $\phi(\rho z)$ curves for both normal and inclined electron incidence angle and the effects of changing electron incidence angle on the absorption and atomic number corrections.

2. The Measurement of $\phi(\rho z)$ Curves

Several sets of sandwich samples have been prepared for the measurement of $\phi(\rho z)$ curves in different electron energy ranges. The tracer layer must be thick enough for sufficient x-ray intensity but thin enough that the resolution in the depth distribution is not degraded at the lowest electron energy.

The specimens were prepared by polishing carefully to a final stage of 0.25 μm diamond paste sets of 2 cm diameter pieces of pure matrix elements. The tracer layer was evaporated simultanously on all matrix elements from a thermal source in a vacuum apparatus in which the polished matrix pieces rotated during the evaporation about their own axis and about an axis through the evaporation source. The distance from source to specimen was great enough that the expected variation in tracer layer thickness over the specimen surface and from specimen to specimen due to the geometry of the evaporation apparatus was less than two percent in the absence of specimen rotation. The rotation during evaporation should have ensured better uniformity. Tracer layer uniformity was maintained for the measurement of $\phi(\rho z)$ curves for the same tracer layer in different matrices. A tracer layer thickness of 10-15 $\mu g/cm^2$ was used for the measurements at electron energies from 6-15 keV while a thickness of 30-40 $\mu g/cm^2$ was used from 15-30 keV.

The matrix overlayers were similarly evaporated. The specimens were appropriately masked and the thickness of each successive evaporation doubled so the 2^n different overlayer thicknesses were obtained. The thickness was measured from duplicate glass slides masked to a standard area and exposed to the evaporation source at the same distance as the sandwich specimens during the overlayer evaporation. The mass per unit area evaporated onto the glass slides was determined by weighing on a microbalance, by x-ray fluorescence analysis using an appropriate characteristic x-ray line of the matrix element and by atomic absorption using the proper hollow cathode lamp and spectral line. The three methods of measurement agreed to about two percent of the mass thickness. Table 1 lists the specimens prepared for the measurement of $\phi(\rho z)$ curves.

Table 1. Sandwich samples used in $\phi(\rho z)$ measurements.

Tracer	Line	Tracer Thickness ($\mu g/cm^2$)	Matrices	Electron Energies KeV
Zn	Kα	∿ 40	Al,Cu,Ag,Au	15-30
Si	Kα	∿ 40	Al,Cu,Ag,Au	15-30
Cd	Lα	∿ 40	Al,Cu,Ag,Au	15-30
Bi	$L\alpha_1, M\alpha_1$	∿ 40	Al,Cu,Ag,Au	15-30
Si	Kα	∿ 15	Al,Ni,Ag,Au	6-15
Cu	Kα	∿ 15	Al,Ni,Ag	12-15
Cd	Lα	∿ 15	Al,Ni,Ag,Au	6-15
Bi	$L\alpha_1, M\alpha_1$	∿ 15	Al,Ni,Ag,Au	6-15

The x-ray intensity from the tracer layer for each overlayer was measured. The pure tracer element was used as standard which was measured frequently to serve as a correction for any beam current changes. The background was measured at the peak position of the characteristic line for the tracer element on the pure matrix element. The data were corrected for dead time, background, drift and absorption in the overlaying matrix layers to obtain the x-ray generation curves.

Four different electron microprobes were used in measuring the ϕ (ρz) curves. In two of the instruments, an Applied Research Laboratories electron microprobe and a Cambridge Microscan-5, the electron beam is incident normal to the specimen surface while in the other two, an Associated Electrical Industries SEM2A and a Materials Analysis Company electron microprobe, the sample is inclined to the electron beam. The geometry of the four instruments is shown in figure 1. In addition a special specimen holder was constructed for the AEI SEM2A so that the electron incidence angle could be accurately changed in the range from about 50° to 80°. Table 1 indicates the energy ranges for which ϕ (ρz) curves have been measured during the past few years. Some of these have been published in the literature [10-13].

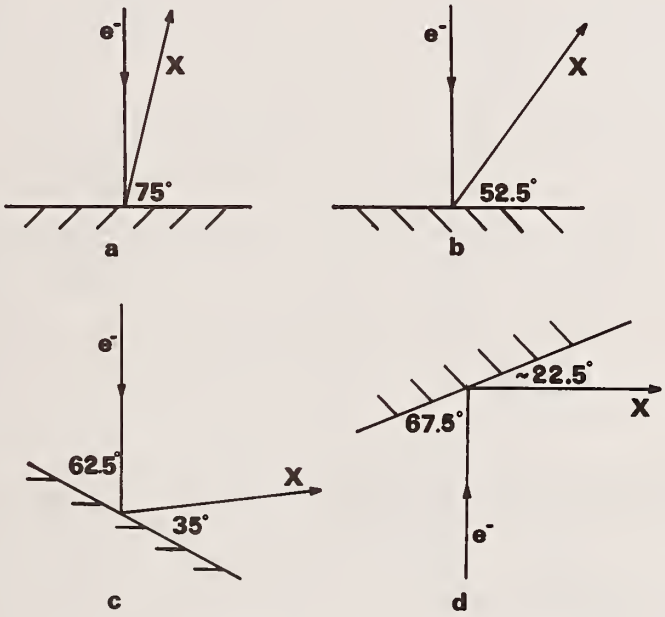

Figure 1. Geometry of ϕ (ρz) measurements.

(a) Applied Research Laboratories

(b) Cambridge Microscan- 5

(c) Materials Analysis Co.

(d) Associated Electrical Industries SEM-2A

The curves of the ratio of intensity from the thin tracer layer to the intensity of the pure element are correct on a relative scale when compared from matrix to matrix. They contain all the information about the atomic number and absorption corrections. However, to put them on the same basis as the ϕ (ρz) curves as defined by Castaing, it is necessary to normalize to the proper ϕ (0) value, i.e., relative to a thin isolated layer. The ϕ (0) values chosen for normalization are those of Hutchins [14] and Reuter [15] – at least in the case for normal incidence. For non-normal electron incidence the situation is not as satisfactory. The ϕ (0) value will be affected by changes in backscattering as electron incidence angle changes but it is not clear exactly how the ϕ (0) value will be affected. Love et al. [2] have suggested an equation for calculating ϕ (0) as a function of incidence angle and their equation has been used for normalization. A careful study of the resultant ϕ (ρz) curves would suggest that a better function for ϕ (0) needs to be found.

3. Experimental Results

Figure 2 is a plot of the ϕ (ρz) curve for the ZnKα line from a zinc tracer in a silver matrix measured in the two instruments with normal electron incidence. The agreement of the measured curves is indeed striking. The agreement proves that the tracer and matrix layer thicknesses are accurately known since many of the points on the curve are the sum of several individual layer thicknesses and that the electron energies were the same for both instruments. The agreement in the tail of the curve would suggest that the background is being measured correctly and that the absorption correction applied is also accurate.

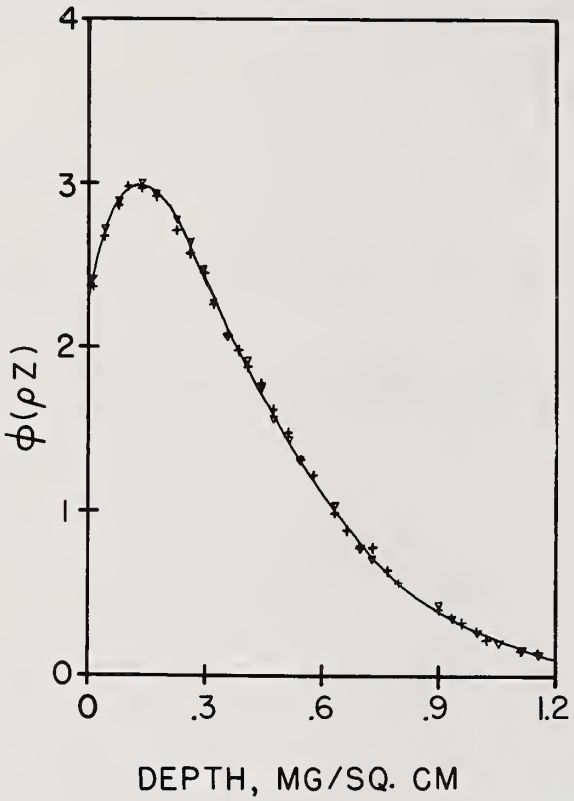

Figure 2. Comparison of measured ϕ (ρz) in ARL and Cambridge Microprobes. ZnKα from a zinc tracer in silver at 25 KeV electron energy. + Cambridge, Δ ARL.

Figure 3 shows the effect of the matrix element on the ϕ (ρz) curve, in this case for the $CdL\alpha_1$ line from a cadmium tracer in the four matrix elements whose atomic number varies from 13 to 79, measured in the Cambridge Microscan 5. These curves show clearly the effect of atomic number on the ϕ (ρz) curves: a shift to greater depths of the maximum of the curve and a broadening of the distribution as matrix atomic number decreases. An integration of the area under the curves gives the atomic number effect since the differences in these ϕ (ρz) curves result from differences in electron backscattering and stopping power as a function of atomic number.

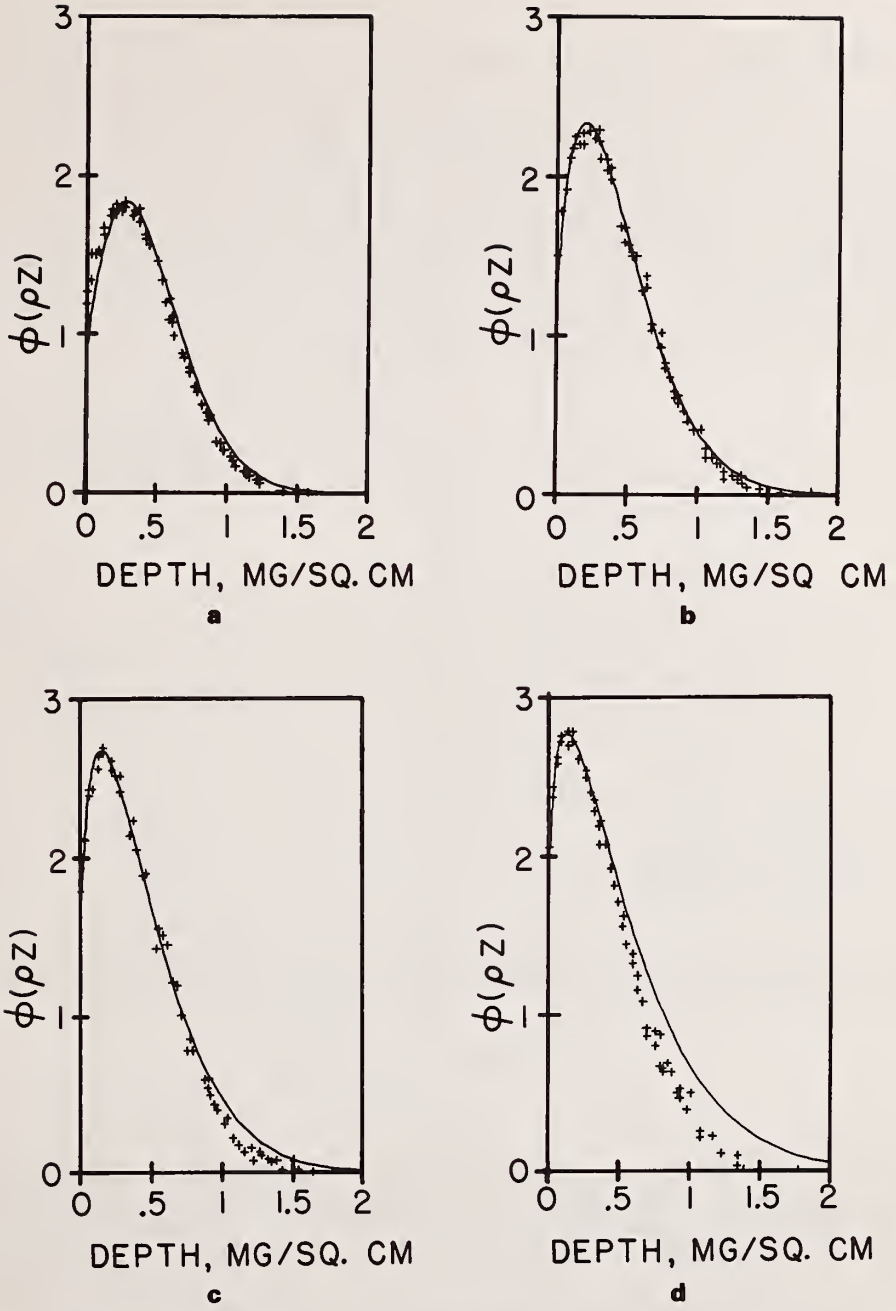

Figure 3. Effects of matrix atomic number on ϕ (ρz) curves.
CdLα from cadmium tracer in
(a) aluminum (b) copper (c) silver (d) gold.

Figure 4 illustrates the effect of electron energies on the ϕ (ρz) curves, in this case at much lower electron energies. These curves were measured using the specimens with thin tracer and overlayer thicknesses in the Cambridge Microscan 5. They show clearly, even down to 6 keV for the SiKα line, the characteristic shape of an increase in ϕ (ρz) from the surface value, through a maximum, then a decay to zero intensity. The same shape is apparent for the CuKα line at 12 keV even though the overvoltage ratio is less than 1.5.

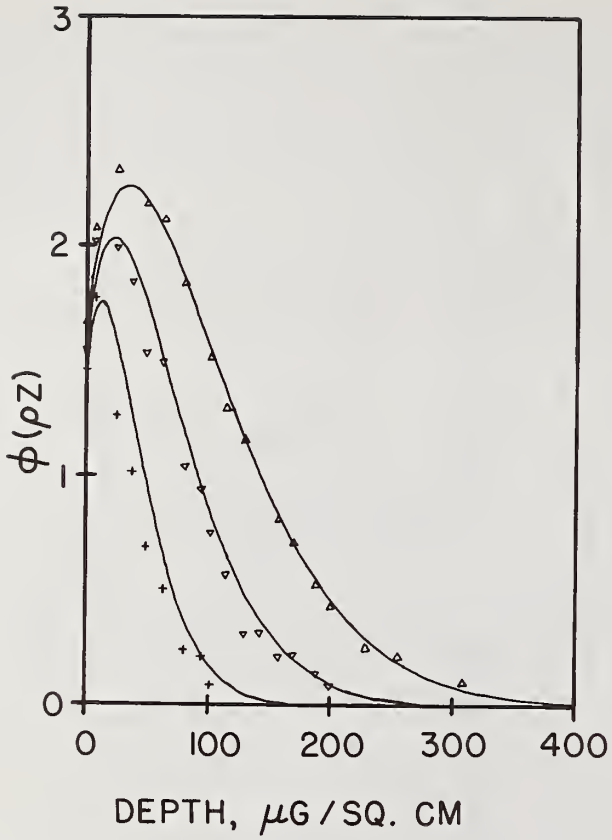

Figure 4. Effect of electron energy on ϕ (ρz) curves. SiKα from a silicon tracer in nickel at 6, 8, and 10 KeV electron energy.

The data for the many ϕ (ρz) curves measured at normal electron incidence as a function of electron energy, exitation potential and matrix atomic number, have been fitted to the empirical equation

$$\phi (R) = D \cdot k \cdot n \, (kR)^{n-1} \exp (-(kR)^n)$$

where $R = \rho z + \rho z_o$.

The parameters ρz, D, k, and n were obtained for each ϕ (ρz) curve by computer optimization of the parameters. The dependence of these parameters on Eo, Ec, Z, and A was established by appropriate plots and the constants for the dependence established by least squares linear regression [16]. One set of constants is required for low electron energies (below 15 keV) and a slightly different set for the higher electron energies [17]. The curves plotted in figures 2-4 are those for the ϕ (R) equation. Quantitative analysis using this equation yields excellent results when compared with the more conventional ZAF method with a significant improvement at low electron energies [16].

4. The Effect of Electron Incidence Angle

When the electron beam is inclined relative to the normal to the specimen surface, the ϕ (ρz) curve changes and x-rays are produced somewhat closer to the specimen surface. This can be seen in figure 5 where the electron incidence angle has changed by 27.5° for the two curves. Note that no simple geometric factor can reconcile the differences in the curves. The ϕ (ρz) curves can be converted to absorption correction curves by calculating the fraction of x-rays which will escape from the specimen as a function of the absorption parameter χ. An example of the dependence of $f(\chi)$ on electron incidence angle Φ is shown in figure 6. Geometric factors such as $1 + 1/2 \cos^2\Phi$ or $\sin\Phi$ have been suggested to change the χ scale to convert the $f(\chi')$ curves for non-normal incidence. Although these factors may be satisfactory for specific cases, in general they cannot be expected to compensate for the changes in shape of the ϕ (ρz) curves, with electron incidence angle which are different for different matrix atomic number, electron energy and excitation potential.

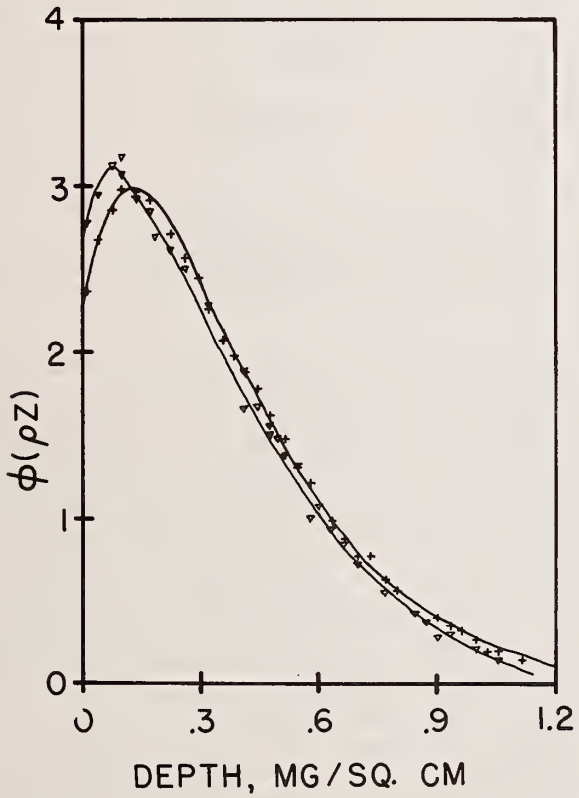

Figure 5. Effect of electron incidence on ϕ (ρz) curves. ZnKα from a zinc tracer in silver at 25 KeV electron energy + Cambridge $\Phi = 90°$, Δ MAC. $\Phi = 62.5°$.

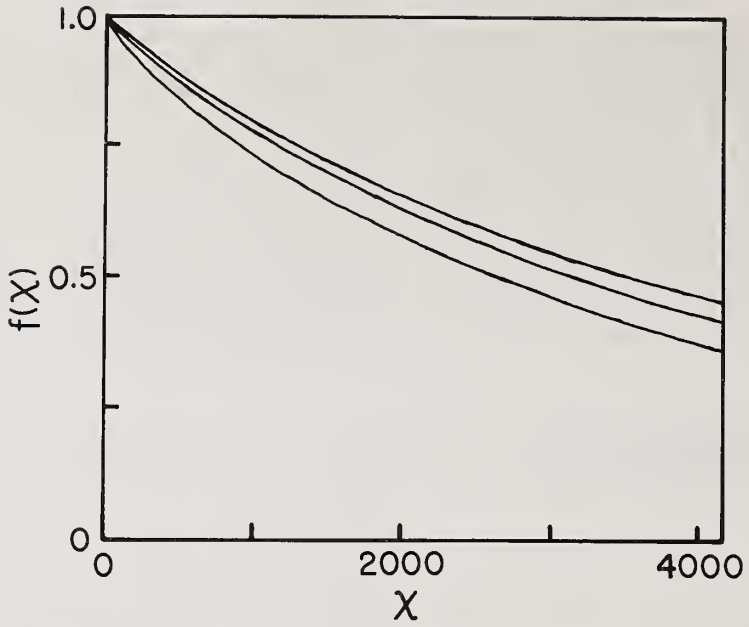

Figure 6. f(χ) curves from φ (ρz) curves. Effect of electron incidence angle. ZnKα in silver at 25 KeV electron energy. (a) Φ = 90° (b) Φ = 67.5°.

The situation for the atomic number effect is even less satisfactory. The φ (ρz) curves can be measured for different matrix elements with the same thin tracer layer to establish the magnitude of the atomic number effect at a specific Φ. To place the φ (ρz) curves on the basis of Castaing's definition relative to the thin isolated layer, the φ (0) value must be known for the tracer layer in the same matrix element. φ (0) as a function of electron incidence angle is not well known. Love et al. [4] have proposed a formula for φ (0) which takes into account changes in backscattering and up to this time, we have used φ (0) values predicted by this equation. The shape of the curves and in particular the crossing of the tails of the curves as incidence angle increases suggests that the φ (0) values are not accurate. More work needs to be done either experimentally or perhaps by Monte Carlo calculations to better establish the dependence of φ (0) on electron incidence angle. In practical analysis, errors fortunately tend to compensate provided all measurements are made at the same electron incidence angle as is normally the case in an electron microprobe. In scanning electron microscopes fitted with energy dispersive x-ray detectors, there is real danger since analyses are frequently performed on fracture surfaces. Even though there are methods to determine electron incidence and x-ray take-off angles from stereo measurements, calculation of quantitative analysis will give less accurate results when the unknown and standard are measured at different electron incidence angles since the compensation of errors will not occur.

5. Conclusions

Changing the electron incidence angle affects the shape and magnitude of x-ray generation as a function of depth. These changes differ for different electron energies, average atomic number matrices and x-ray energies. Simple geometric factors cannot be expected to exactly compensate for non-normal incidence. Fortunately for the usual analysis conditions in an electron microprobe where both the unknown and standard are measured in the same geometry, errors in the correction equations tend to cancel. In the SEM with energy dispersive analysis where this is frequently not the case, accuracy can be expected to suffer. Additional work needs to be done to establish more accurately the effect of electron incidence angle on x-ray generation and on φ (0). This work should lead to more reliable analysis in the variable geometries used in scanning electron microscopes.

References

[1] Bishop, H. E., Proc. Phys. Soc. (London) 85, 855 (1965).

[2] Moll, S. H., Baumgarton, N., Donnelly, W., Proc. 8th Int. Conf. X-Ray Optics and Microanalysis, Boston, Paper 33 (1977).

[3] Colby, J. W., Proc. 6th Nat. Conf. on Electron Probe Microanalysis, Paper 17 (1971).

[4] Love, G., Cox, M. G. C. and Scott, V. D., J. Phys. D 11, 7 (1978).

[5] Russ, J. C., in Scanning Electron Microscopy, IITRI, Chicago, 1973, p. 114.

[6] Brown, J. D., in Electron Probe Microanalysis, (Tousimis, A. J. and Marton, L. L., eds.) Academic Press, N. Y., 1969, p. 73.

[7] Bishop, H. E., J. Phys. D. 1, 673 (1968).

[8] Castaing, R., in Advances in Electronics and Electron Phys., (Marton, L. L. and Marton, C., eds.) Academic Press, N. Y., 13, 317 (1960).

[9] Castaing, R. and Descamps, J., J. Phys. Radium, 16, 304 (1955).

[10] Brown, J. D. and Parobek, L., in Proc. 6th Int Conf X-Ray Optics and Microanalysis, (Shinoda, G., Kohra, K., and Ichinokawa, T., eds.) U. of Tokyo Press, 1972, p. 163.

[11] Brown, J. D. and Parobek, L., Adv. X-Ray Anal., 16, 198 (1973).

[12] Parobek, L. and Brown, J. D., Adv. X-Ray Anal., 17, 479 (1974).

[13] Brown, J. D. and Parobek, L., X-Ray Spect., 5, 36 (1976).

[14] Hutchin, G. A., 2nd Nat. Conf on Electron Probe Microanalysis, Boston, Mass. (1967).

[15] Reuter, W., in Proc. 6th Int. Conf. X-Ray Optics and Microanalysis, (Shinoda, G., Kohra, K., and Ichinokawa, T., eds.) U. of Tokyo Press, 1972, p. 121.

[16] Parobek, L. and Brown, J. D., X-Ray Spect., 7, 26 (1978) errata 8 V (1979).

[17] Brown, J. D. and Robinson, W. H., Proc. 14th Nat. Conf. Microbeam Anal. Soc., San Francisco Press (1979).

National Bureau of Standards Special Publication 604. Proceedings of the Workshop on Energy Dispersive X-Ray Spectrometry held at NBS, Gaithersburg, Maryland, April 23-25, 1979. (Issued March 1981)

ENERGY AND WAVELENGTH DISPERSIVE X-RAY FLUORESCENCE ANALYSIS OF HEAVY ELEMENTS USING RADIOACTIVE, SECONDARY FLUORESCENCE AND X-RAY TUBE SOURCES, AND WITH GERMANIUM, SILICON, AND SCINTILLATION DETECTORS

M. A. Short and S. Bonfiglio

Engineering and Research Staff
Ford Motor Company
Dearborn, Michigan 48121

Abstract

Comparative analytical results are presented for the analysis of barium/lanthanum/cerium and osmium/iridium/platinum using both K and L series characteristic lines for four different excitation/detection systems. These systems include a radioactive source with an intrinsic germanium detector, a radioactive source fluorescing a secondary target with an intrinsic germanium detector, an x-ray tube fluorescing a secondary target with a lithium drifted silicon detector, and an x-ray tube used in a conventional wavelength dispersive spectrometer. The two principal advantages of K lines of heavy elements are discussed: the relative simplicity of the K spectra and the relatively great penetrating power of high energy K radiation. It is concluded that better resolution is obtained for L series lines using wavelength dispersive spectrometry. An example of the high penetrating power is shown in the in-laboratory analysis for platinum and lead on an automobile catalyst contained within a stainless steel can.

Key Words: Catalysts automotive; energy dispersive analysis; heavy element fluorescence analysis; intrinsic germanium detectors; secondary target fluorescence analysis; source excited fluorescence analysis; x-ray fluorescence analysis.

1. Introduction

In the automobile industry, a considerable effort has been invested in recent years in the elemental analysis of automotive catalytic converters. Artz [1][1] has discussed the quantitative determination of 17 elements ranging from phosphorus to lead in such catalysts using a wavelength dispersive x-ray fluorescence technique. His method, which may be described as "semi-destructive", that is the catalyst was pulverized but the powder itself was not consumed in the analysis, utilized the L series characteristic lines for the heavier elements ranging from barium to lead. Artz used these L lines because his x-ray tube and generator, like those in the majority of wavelength dispersive x-ray fluorescence analysis systems, had an upper limit of 60 kV (although systems are available going up to 80 kV and 100 kV). A tube voltage of 60 kV corresponds to a bremsstrahlung maximum intensity in the region of 40 kV. Consequently, not only will the characteristic K lines of elements such as barium, lanthanum, and cerium be inefficiently excited, the K lines of elements such as iridium, platinum and lead will not be excited at all. In addition, the angular dispersion of available analyzing crystals for the K lines of barium to lead is poor.

Recently, we have been investigating the development of alternative x-ray fluorescence techniques which would excite, detect, and measure the intensities of heavy element K lines and examining the advantages which would result from the use of such lines. The techniques

[1]The number in brackets refers to the literature reference at the end of this paper.

include the use of radioactive and secondary fluorescence sources and the use of lithium drifted silicon and intrinsic germanium detectors. There are two clear advantages. First, the K spectra of these heavy elements are relatively simple and free from interference with L series lines, whereas the heavy element L lines are complex, overlap with other L lines and overlap with the K lines of elements scandium (Z=21) through selenium (Z=34). Second, the higher penetrating power of the K lines, and in particular of platinum (E∿67 keV) and lead (E∿74 keV) is so great that, by suitably collimating the excitation and fluorescence x-rays, the platinum and lead contents of geometrically isolated volumes within a solid material, particularly where the material is of a low average atomic number and/or density such as is the case for a ceramic based monolithic catalyst, can be examined.

Additionally, because the absorption of platinum and lead K x-rays in steel is relatively low, the platinum and lead contents of automotive converters could perhaps be examined in the laboratory, non-destructively, while the catalyst itself is encased within the steel container which holds it in the automobile exhaust system. Such an analysis might be useful in both catalyst development and testing. The ability to undertake this analysis non-destructively means that the same catalyst could be examined before and after use, thus obviating any possible variations in precious metal content from one catalyst to another.

2. Experimental

Four different experimental techniques have been investigated:

(1) A cobalt-57 radioactive source emitting 122 keV gamma rays in conjunction with an intrinsic germanium detector of nominal resolution 189 eV (at 5.9 keV) used in an energy dispersive mode. Tin or uranium apertures were utilized to limit the count rate and to reduce the dead time of the system to 60 percent to 70 percent. Tungsten or tungsten-monel (monel is a nickel-copper alloy) shielding was employed to screen the detector from the source.

(2) A cobalt-57 source fluorescing a uranium secondary target and an americium-241 source fluorescing a dysprosium secondary target, both used with an intrinsic germanium detector (189 ev) in the energy dispersive mode. Tin or uranium apertures were again utilized to limit the count rate; tungsten was employed to screen the detector from the source.

(3) X-ray tubes fluorescing secondary targets, specifically tungsten fluorescing gadolinium, tungsten fluorescing nickel, and silver fluorescing zirconium, were used in conjunction with a lithium drifted silicon detector of nominal resolution 175 eV (at 5.9 keV), in the energy dispersive mode.

And for comparative purposes:

(4) A chromium or molybdenum x-ray tube used in a conventional wavelength dispersive spectrometer. For the longer wavelengths a PET crystal/flow detector combination was utilized and for the shorter wavelengths a LIF (220) crystal/scintillation detector combination was used. A fine collimator was moved into the primary fluorescence beam.

Synthetic samples were prepared specifically to demonstrate differences in wavelength/energy resolution shown by the four techniques described above and to show the effect of a light element matrix. Two sets of samples were prepared: one related to a comparison of K and L spectra for elements in the region barium/lanthanum/cerium, and another for elements in the region of osmium/iridium/platinum. The samples were not "infinitely thick" with respect to the K series x-rays.

Not all combinations of techniques, samples, and x-ray lines were examined. Table 1 shows those combinations that were examined. The combinations not examined were those that either preliminary experiments or intuition predicted to be of lesser interest. Peak and background measurements to determine the optimum technique for any particular analysis were not made.

Table 1. Experimental configurations used for the analysis of barium/lanthanum/cerium and osmium/iridium/platinum.

	Barium/Lanthanum/Cerium		Osmium/Iridium/Platinum	
	K Series	L Series	K Series	L Series
Wavelength Dispersive Spectrometry:	—	Mo tube, 50 kV, PET crystal fine collimator	Cr tube, 95 kV, LiF (220) crystal fine collimator	Mo tube, 50 kV, LiF (220) crystal fine collimator
Energy Dispersive Spectrometry:				
Lithium drifted silicon detector X-ray tube and secondary target	W tube, 60 kV Gd secondary	W tube, 50 kV, Ni secondary	—	Ag tube, 50 kV, Zr secondary
Intrinsic germanium detector, Radioactive source	—	—	Co-57 source (122 keV gammas)	—
Intrinsic germanium detector, Radioactive source Secondary target	Am-241 source (60 keV gammas) Dy secondary	—	Co-57 source (122 keV gammas) U secondary	—

3. Results – Energy Resolution

The relative simplicity of heavy element K series lines as compared with L series lines is illustrated in figures 1 and 2. Figure 1 shows an energy dispersive (ED) platinum K spectrum, figure 2 shows a wavelength dispersive (WD) platinum L spectrum. Note that the spectra contain 4 and 13 resolved peaks respectively. Note also the evident loss in resolution shown by WD platinum K series and ED platinum L series spectra shown in figures 3 (right) and 4 respectively as compared with figures 1 and 2. Figures 1 and 3 (right) illustrate graphically the superior resolution of energy dispersive spectroscopy over wavelength dispersive spectroscopy for short wavelength/high energy characteristic lines. The WD spectrum of platinum in a light element matrix (lithium tetraborate), as shown in figure 3 (left), shows the high background introduced by the bremsstrahlung from the x-ray tube, a discouragement for good quantitative analysis.

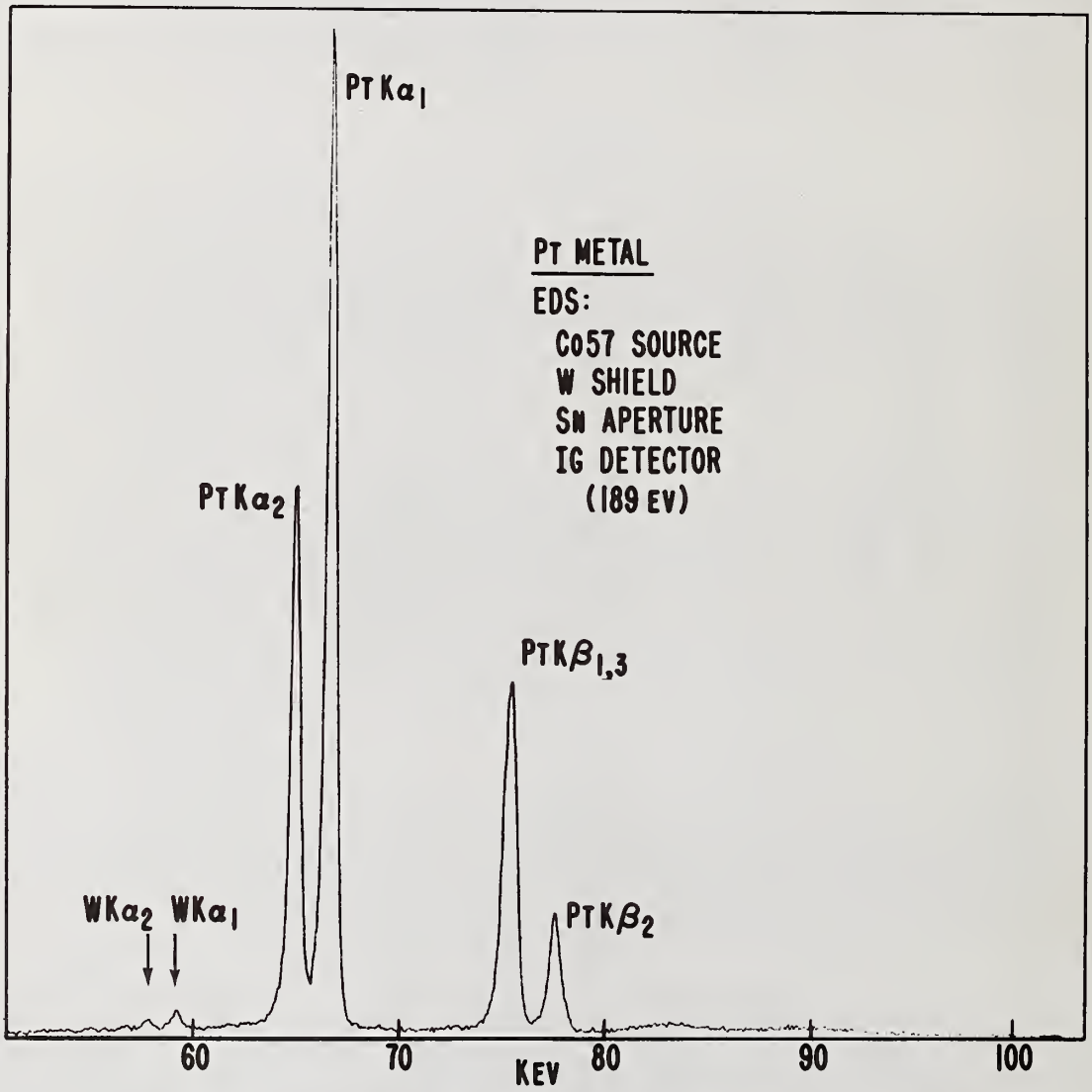

Figure 1. ED spectrum of Pt K lines: Co-57 source, intrinsic Ge detector.

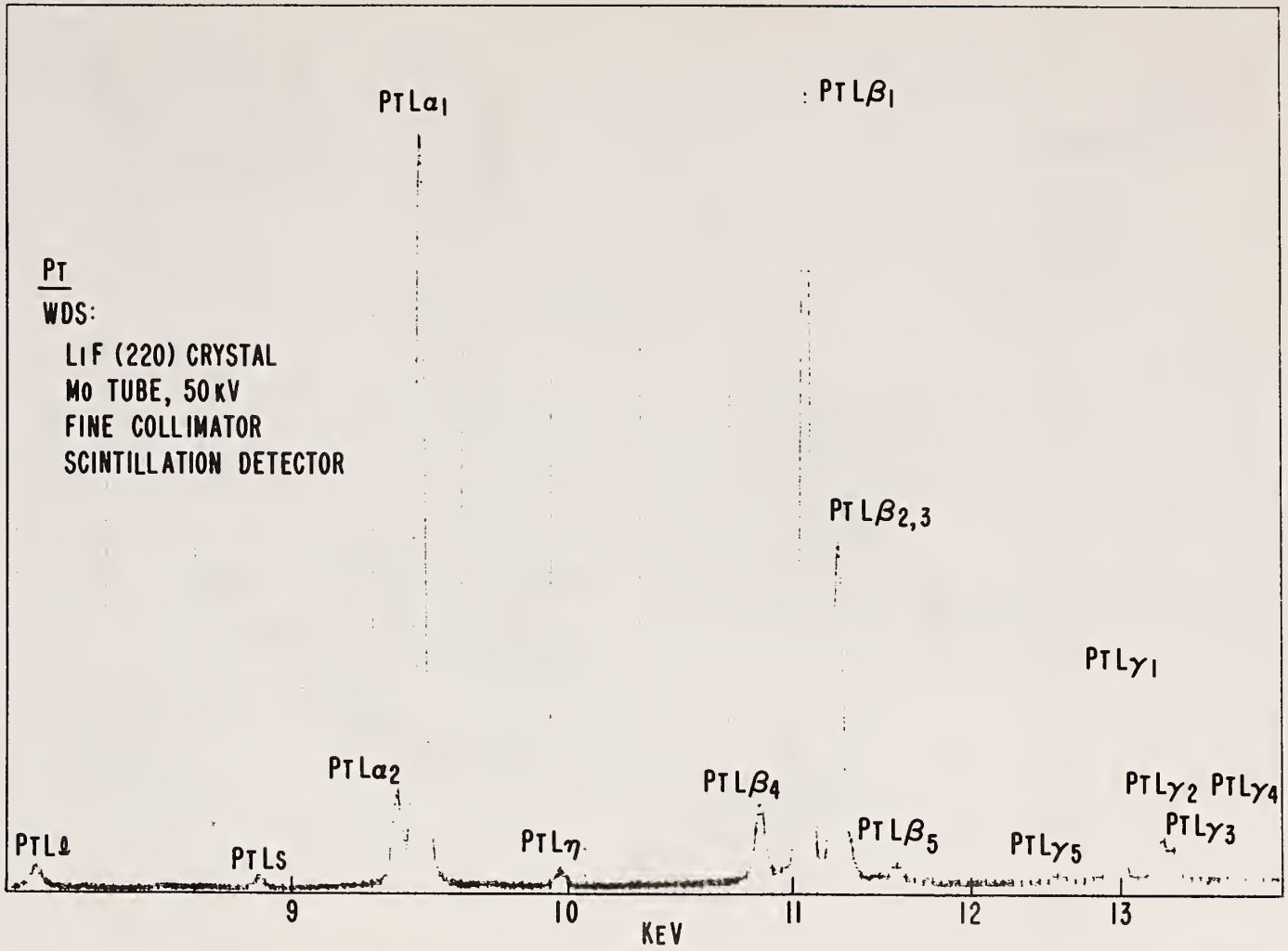

Figure 2. WD spectrum of Pt L lines: Mo tube at 50 kV, LiF(220) crystal.

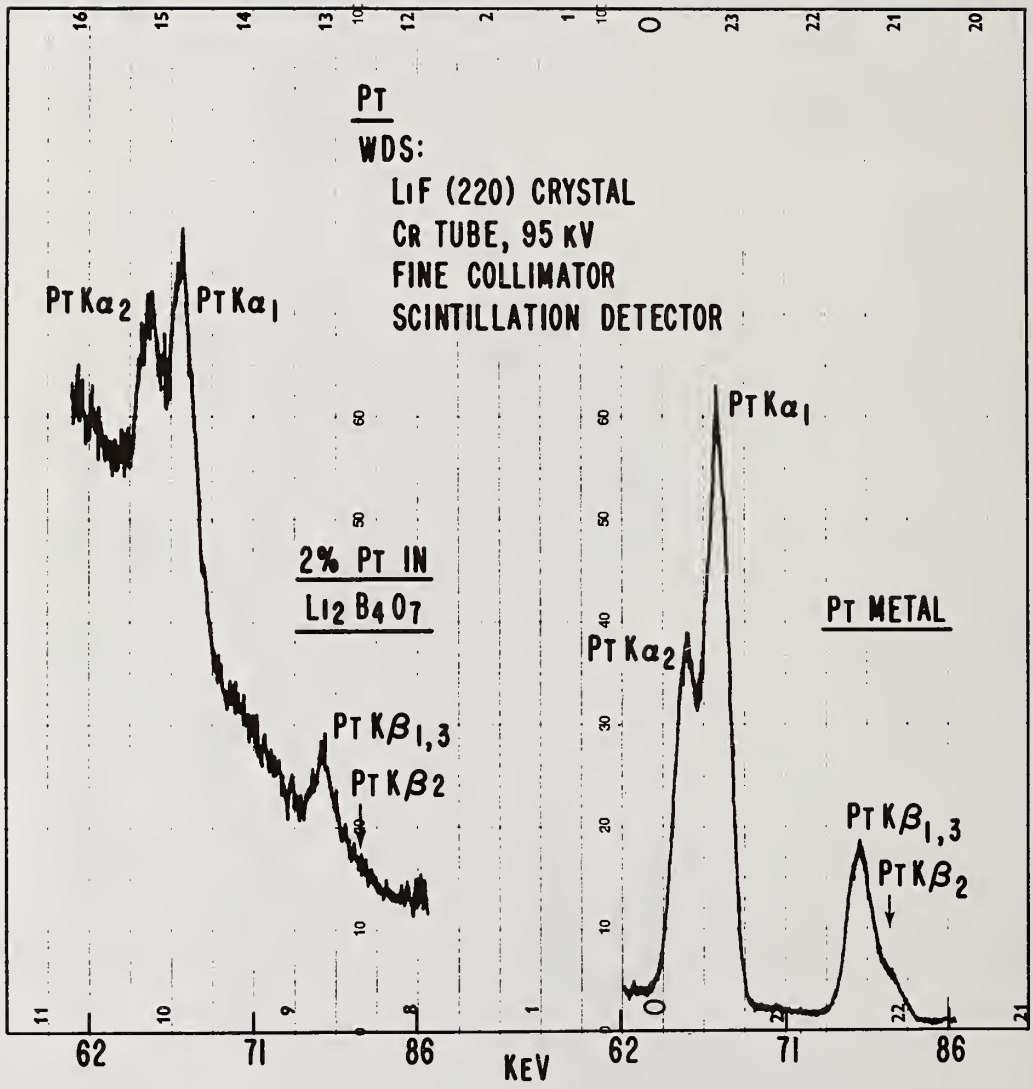

Figure 3. WD spectra of Pt K lines: Cr tube at 95 kV, LiF(220) crystal.

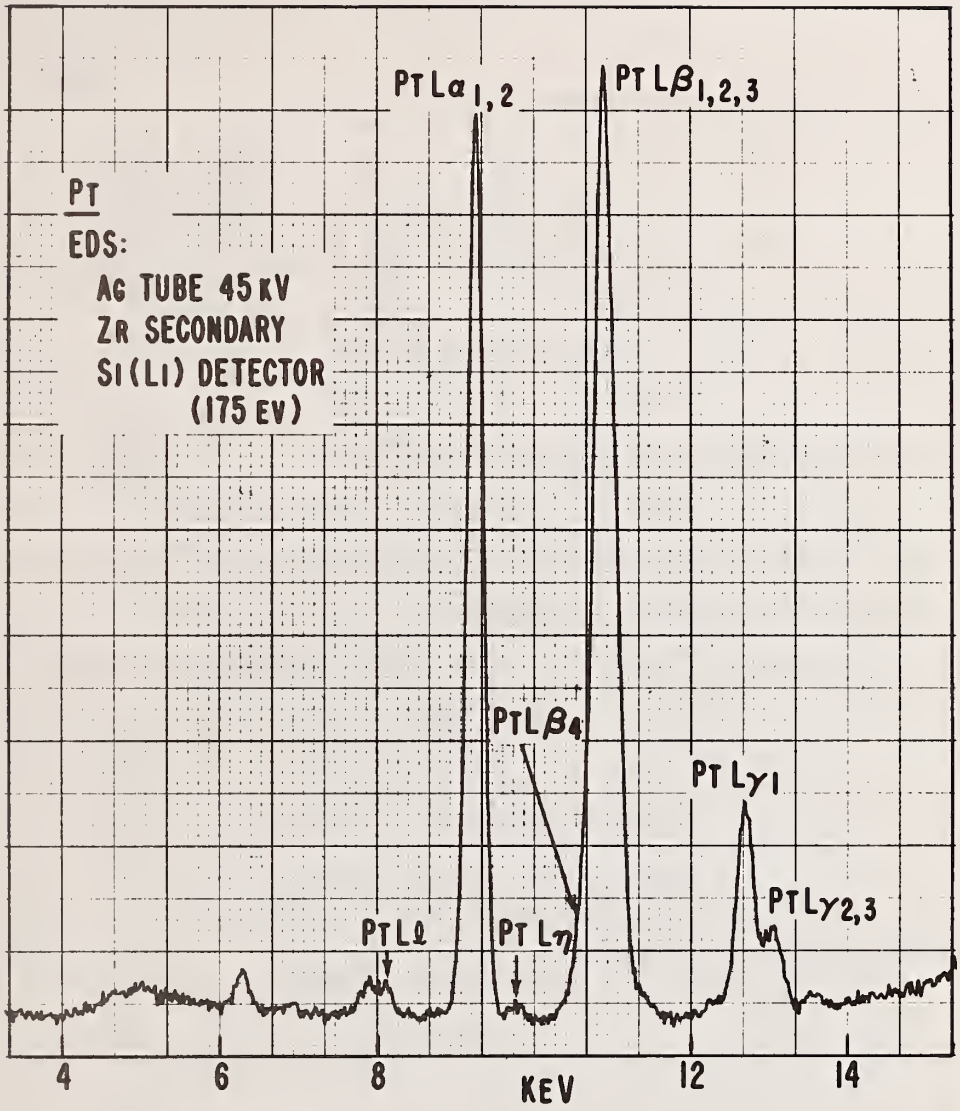

Figure 4. ED spectrum of Pt L lines: Ag tube, Zr secondary, Si(Li) detector.

Resolution becomes important in the analysis of elements with close or overlapping characteristic lines such as might be exhibited by elements adjacent in the periodic table. Osmium, iridium, and platinum, for example, in admixture, give a complex wavelength dispersive L spectrum (figure 5). Nevertheless, as may be seen there is sufficient resolution between the three $L\alpha_1$ lines of these elements that a good quantitative analysis could be made. The positions of the osmium, iridium, and platinum L_I, L_{II}, and L_{III} absorption edges are also indicated on this figure. Figure 5 may be contrasted with an energy dispersive L series spectrum of the same admixture, shown in figure 6, where there is little resolution between the same lines. No quantitative analysis of osmium/iridium/platinum could be made using energy dispersive analysis of the L series lines without utilizing a least squares or stripping technique.

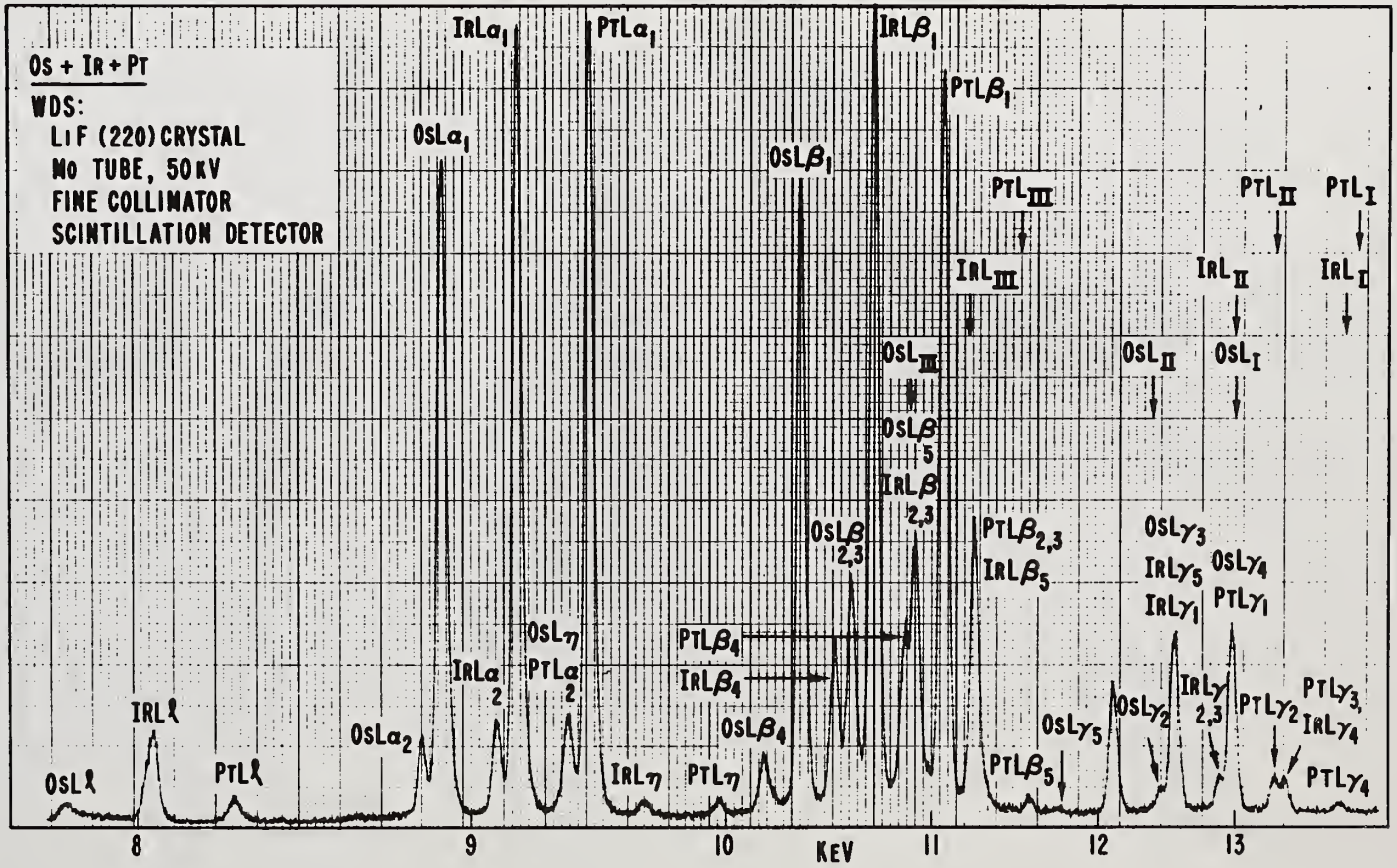

Figure 5. WD spectrum of Os/Ir/Pt L lines: Mo tube at 50 kV, LiF(220) crystal.

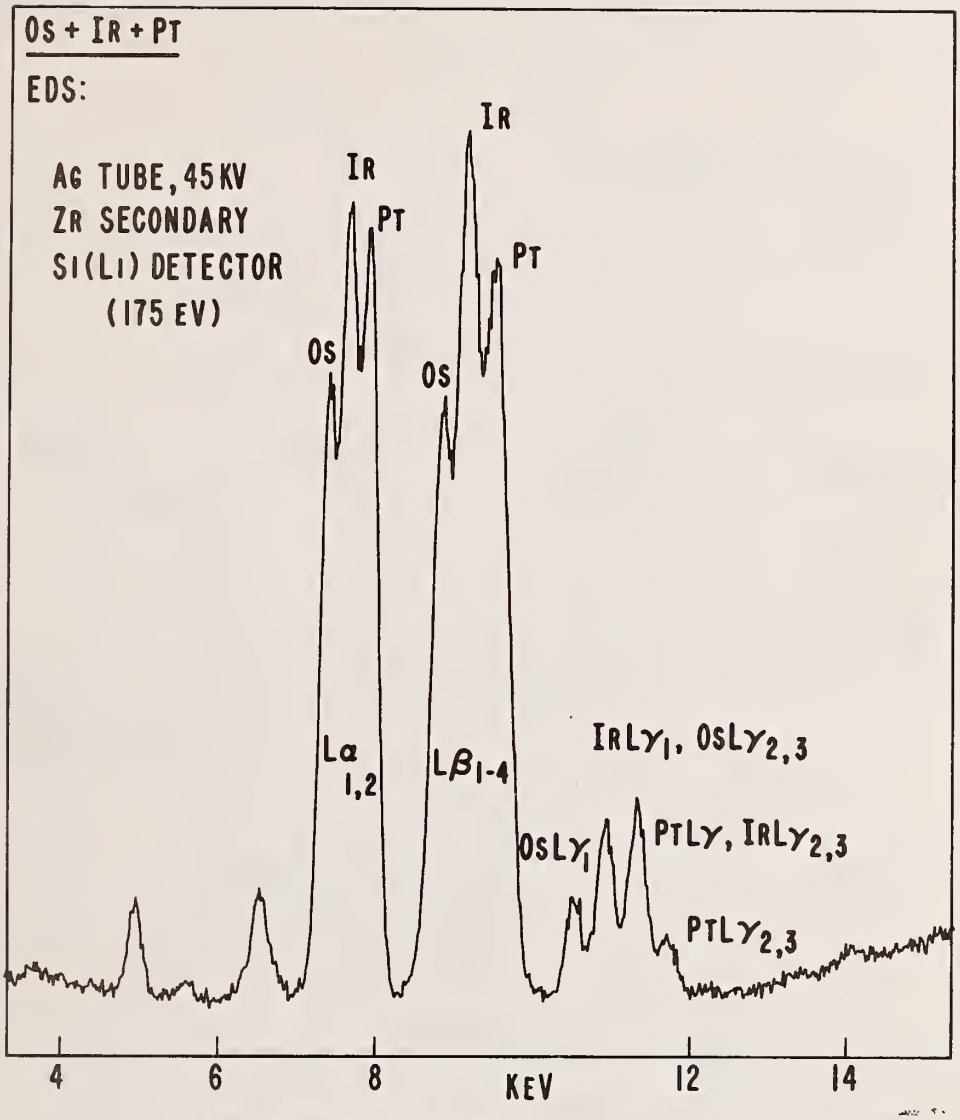

Figure 6. ED spectrum of Os/Ir/Pt L lines: Ag tube, Zr secondary, Si(Li) detector.

In the analysis of platinum on catalytic converters, we are concerned with small amounts of platinum (of the order of 0.2%) on light element ceramic substrates. Figure 7 shows a much higher concentration of platinum (2%) in a light element matrix (lithium tetraborate). This is an ED spectrum obtained using a cobalt-57 source and an intrinsic germanium detector. The superiority of this ED spectrum over the WD spectrum of the same sample shown in figure 3 (left) with regard to both resolution and peak-to-background is readily apparent. It can be seen, however, that there is a substantial tungsten peak arising from the tungsten shield and also a small amount of lead from the general shielding. A pellet containing a mixture of tungsten, platinum, and lead was made up to show the interference between these elements in ED spectroscopy. The spectrum obtained is shown in figure 8. The principal interferences are between tungsten $K\beta_{1\ 3}$ and Platinum $K\alpha_1$, and between platinum $K\beta_{1\ 3}$ and lead $K\alpha_1$. If these interferences cannot be removed a good quantitative analysis can still be made for both platinum and lead using the $K\alpha_2$ lines. It was found that if the tungsten shield surrounding the cobalt-57 source when used in the primary excitation mode was replaced with the tungsten-monel shield, then the tungsten

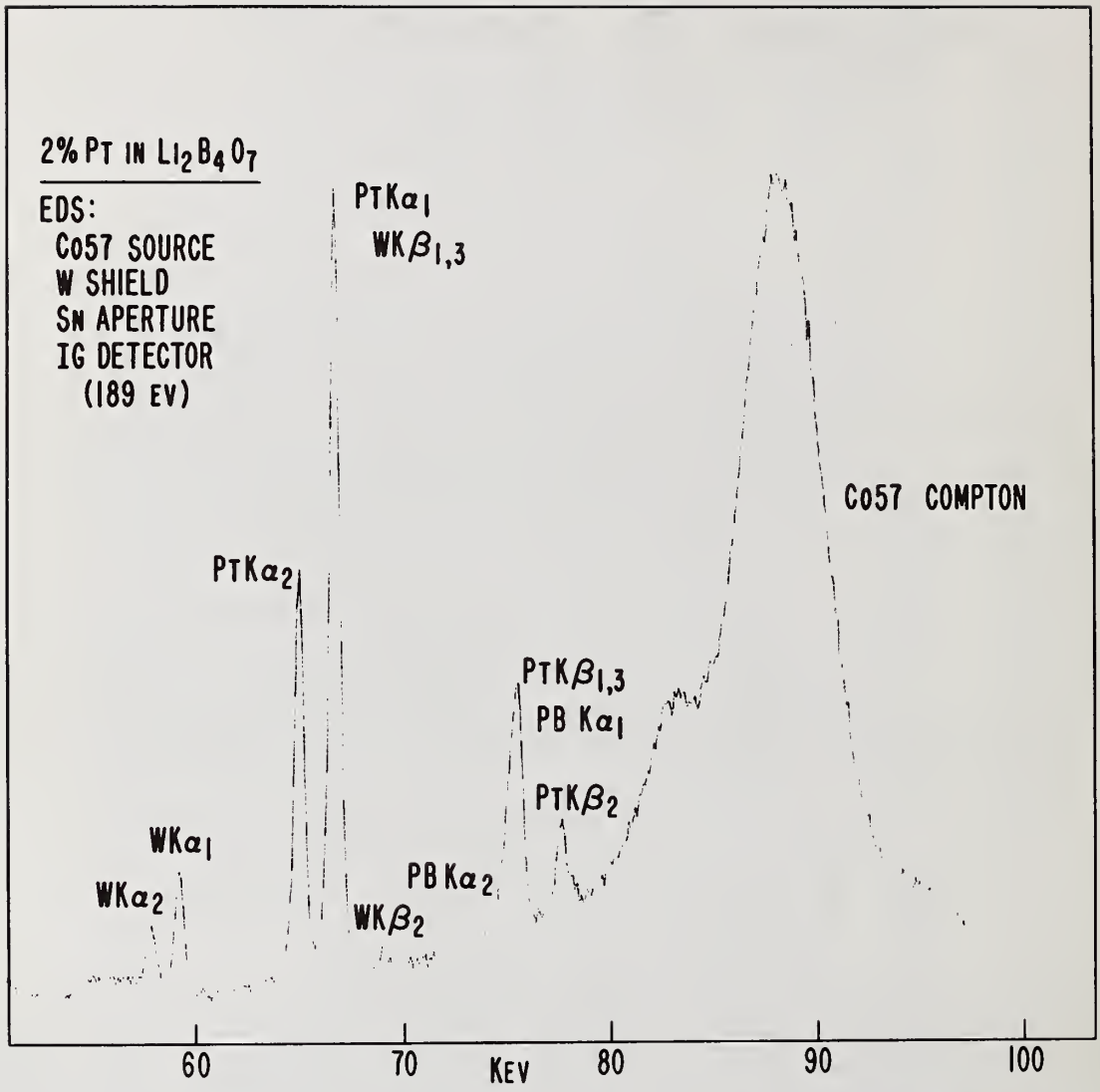

Figure 7. ED spectrum of Pt K lines: Co-57 source, intrinsic Ge detector.

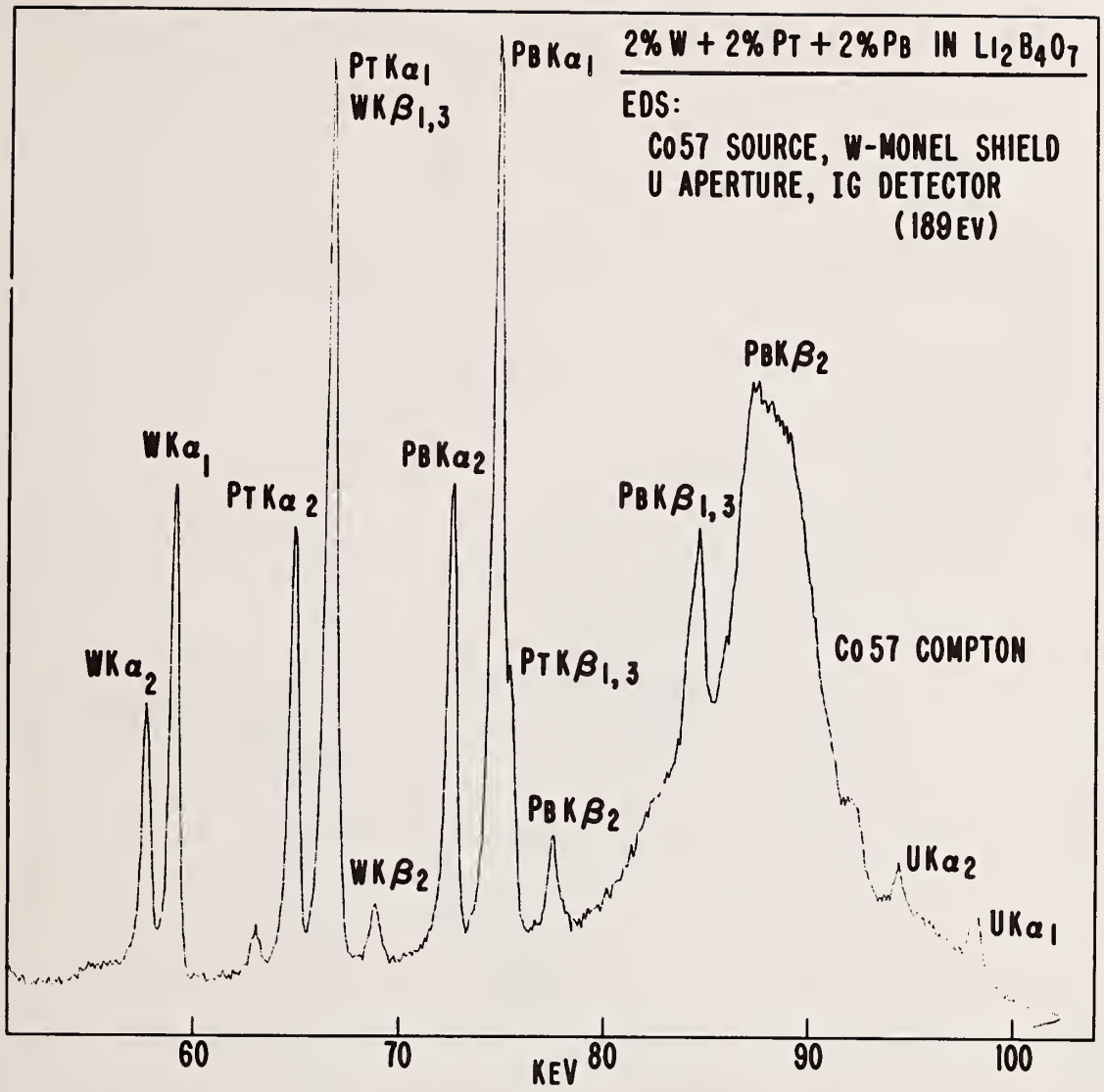

Figure 8. ED spectrum of W/Pt/Pb lines: Co-57 source, intrinsic Ge detector.

lines were reduced to a very low intensity, as can be seen in figure 9. Recently, a better alternative has been found – to construct a shield of depleted uranium; no tungsten peaks were observed and the uranium K and L series lines at 94/115 keV and 13/18 keV respectively do not interfere with most heavy element spectra. Unfortunately, neither the tungsten-monel nor the uranium shields would fit in the radioactive source holder in the secondary excitation configuration, and even with a sample of pure platinum the tungsten shield gave a substantial tungsten peak (figure 10). A simple subtraction procedure was therefore employed to remove the tungsten lines from the spectrum. The success of this procedure can be seen in figure 11.

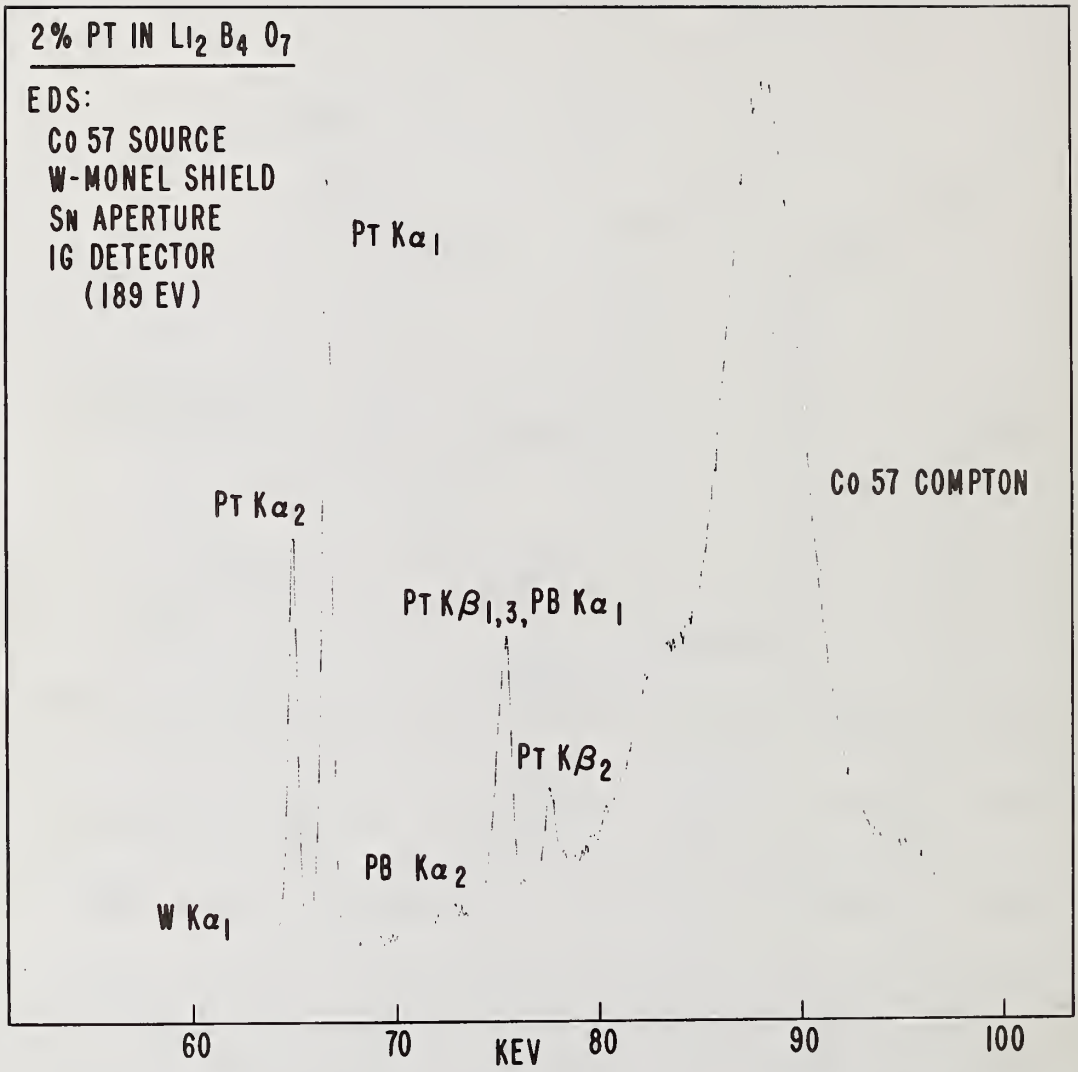

Figure 9. ED spectrum of Pt K lines: Co-57 source, intrinsic Ge detector.

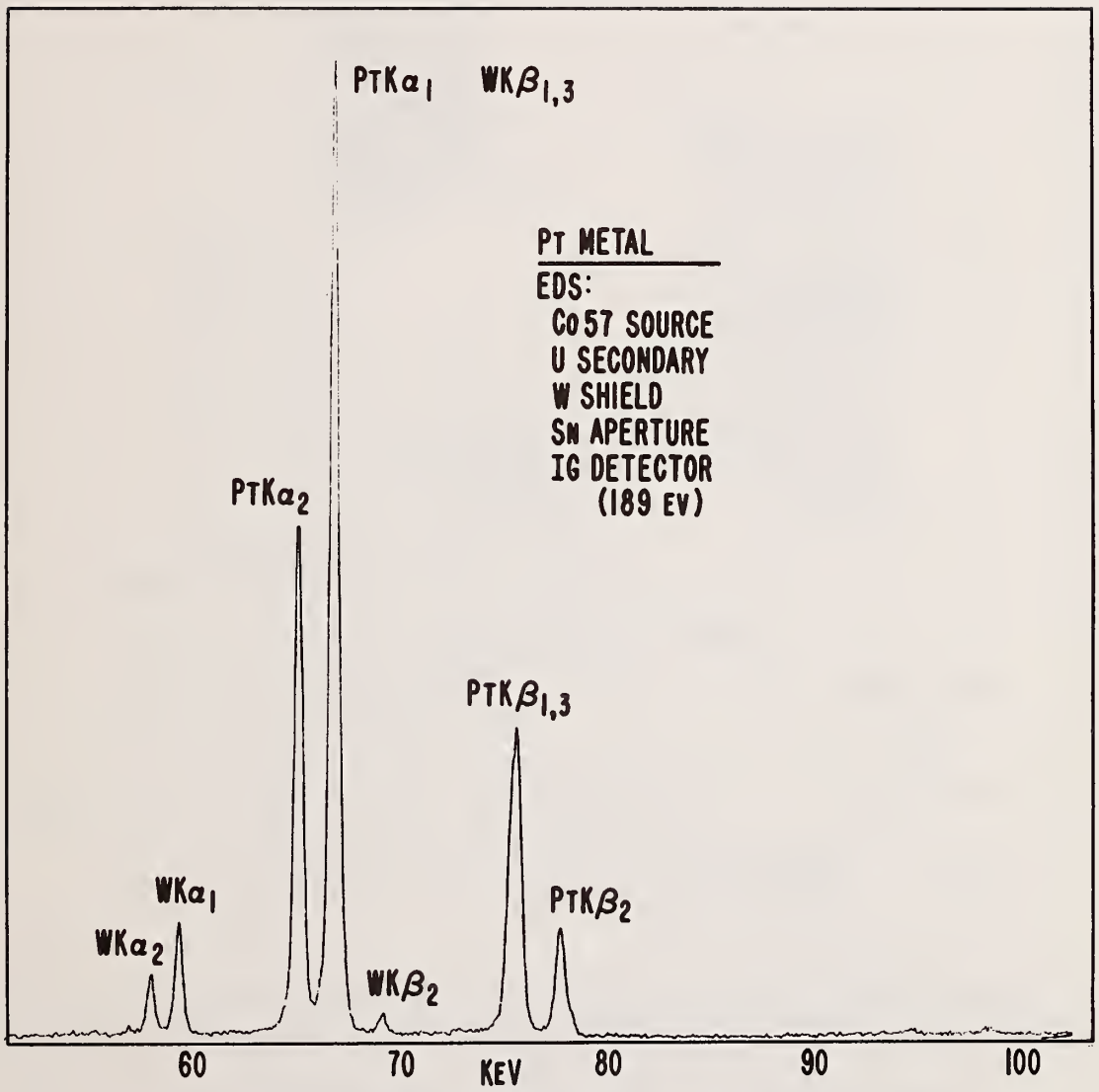

Figure 10. ED spectrum of Pt K lines: Co-57 source, U secondary, intrinsic GE detector.

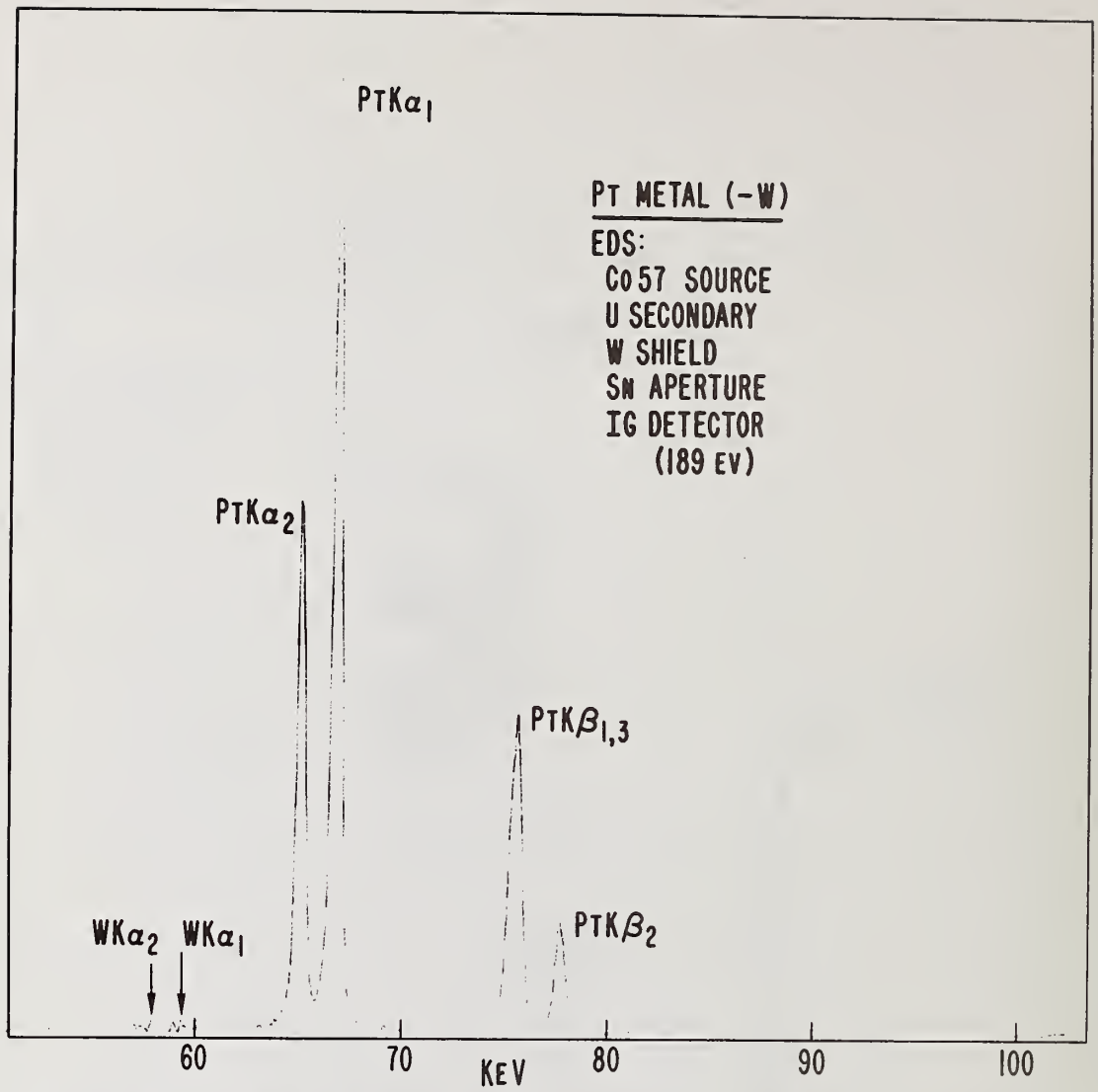

Figure 11. ED spectrum of Pt less W K lines: Co-57 source, U secondary, intrinsic Ge detector.

Very large tungsten Kα peaks were obtained for a mixture of two percent platinum and two percent iridium in a lithium tetraborate matrix, see figure 12. The tungsten peaks were again substantially removed by subtraction, as is shown in figure 13. The diminution in height of the platinum $K\alpha_1$ peak resulting from this subtraction may be noted. Figure 14 shows a three element mixture of osmium, iridium, and platinum using the alternative approach of a primary cobalt-57 source and the tungsten-model shield. It may be deduced that energy dispersive analysis using K lines would only permit analysis of the end-members osmium (using Os $K\alpha_2$) and platinum (using Pt $K\alpha_1$) unless a least squares or stripping procedure is used.

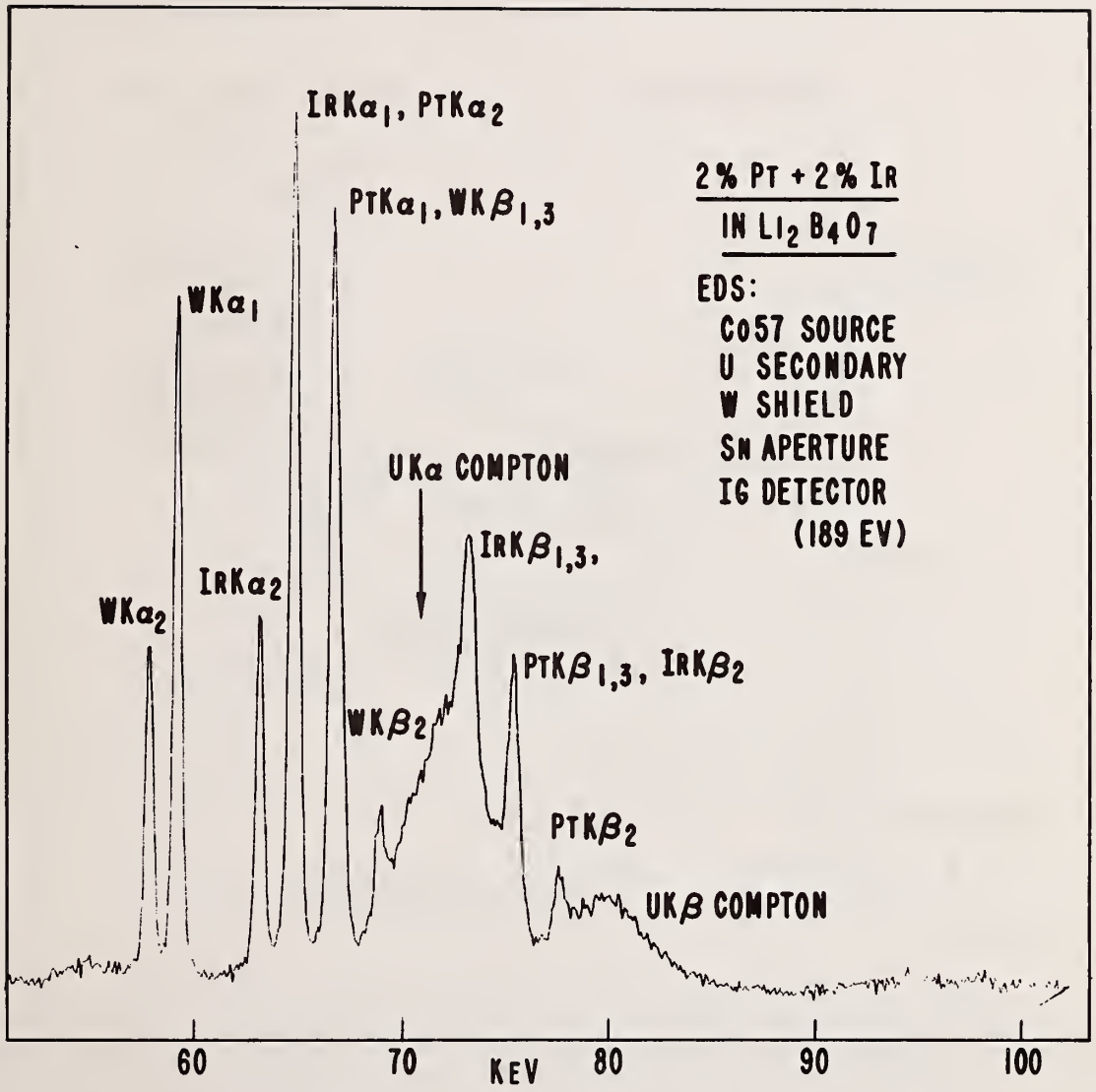

Figure 12. ED spectrum of Pt/Ir K lines: Co-57 source, U secondary, intrinsic Ge detector.

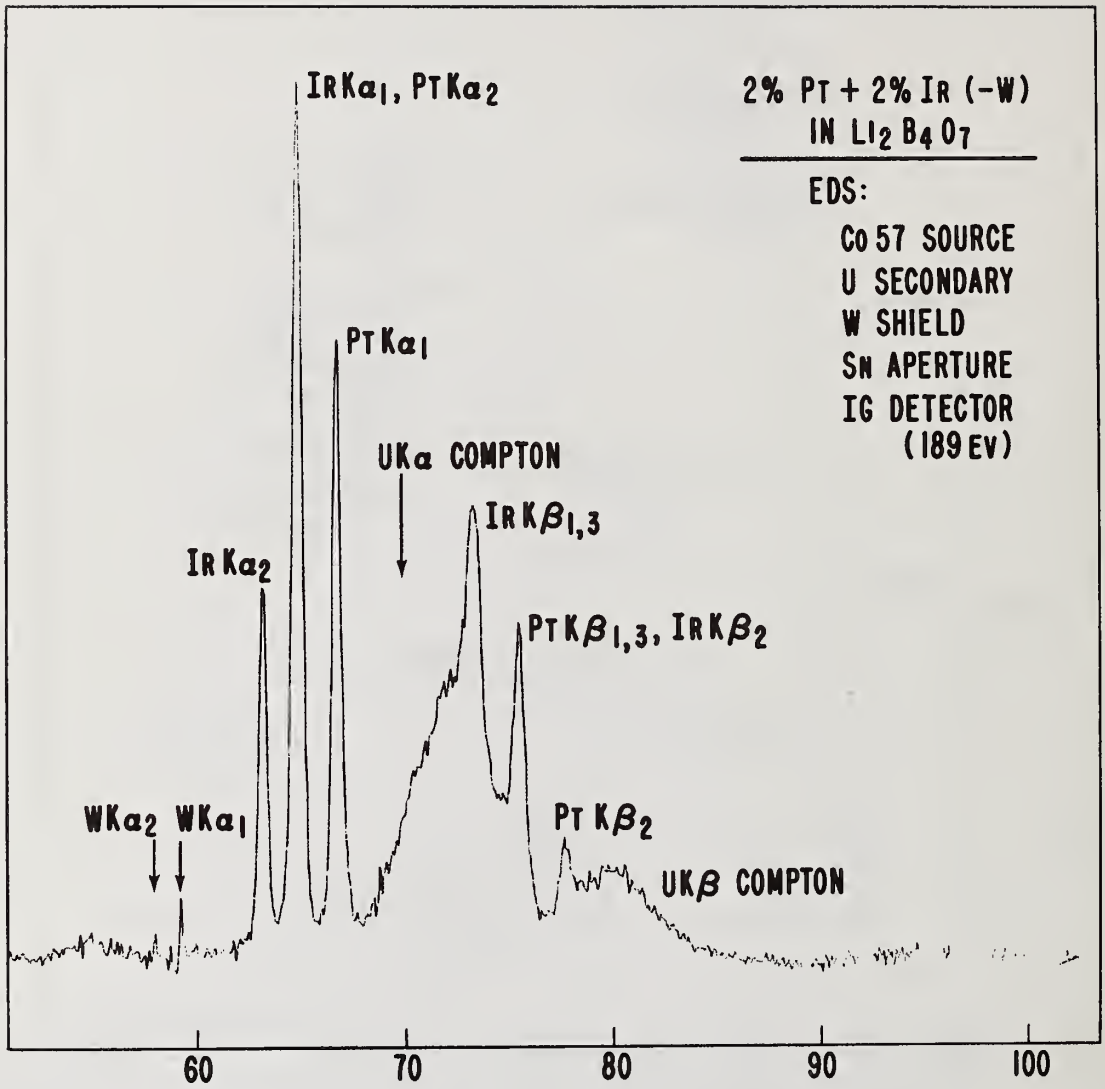

Figure 13. ED spectrum of Pt/Ir less W K lines: Co-57 source, U secondary, intrinsic GE detector.

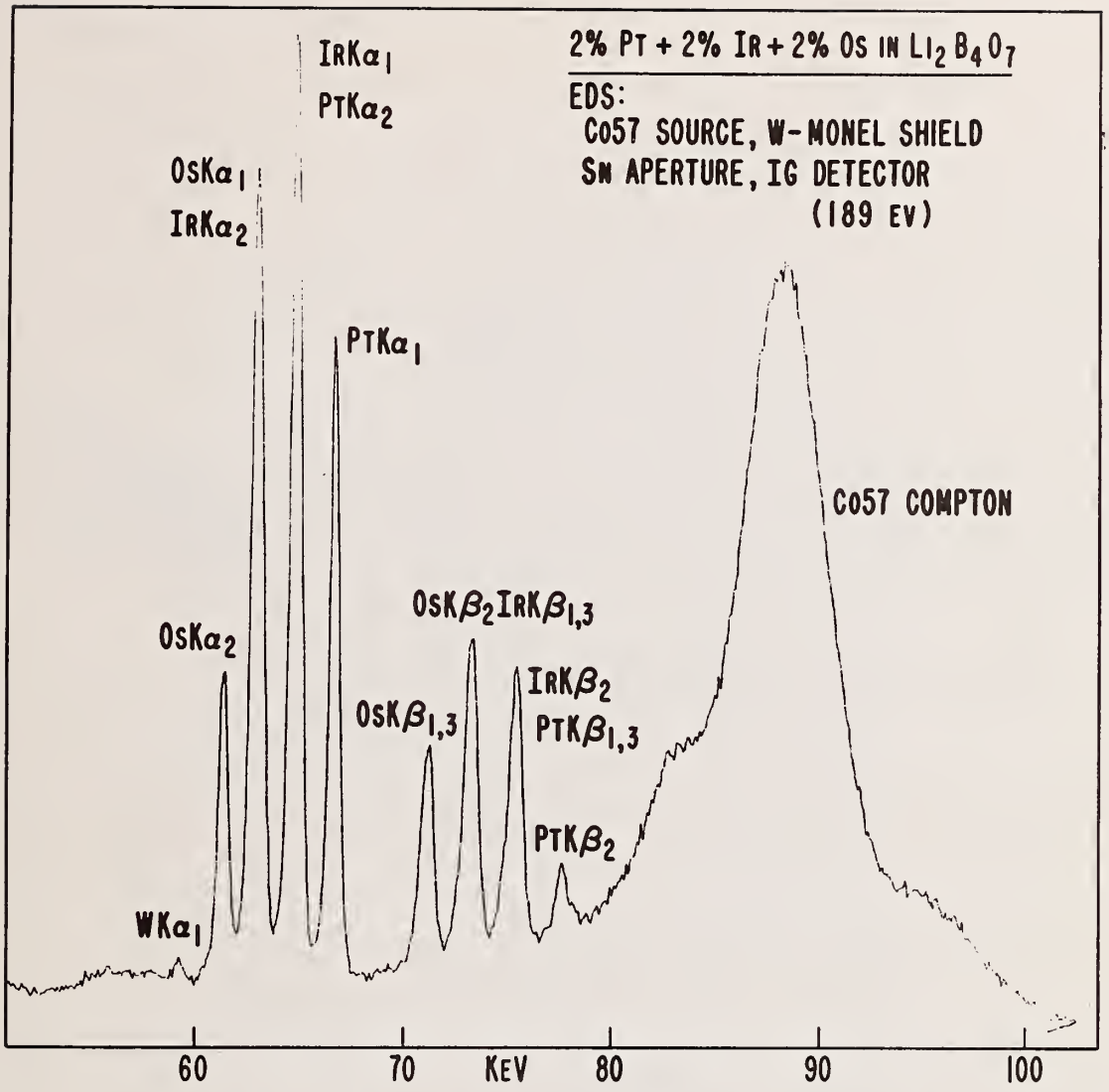

Figure 14. ED spectrum of Pt/Ir/Os K lines: Co-57 source, intrinsic Ge detector.

WDS is superior with respect to resolution for L series lines in the region of barium/lanthanum/cerium. Figures 15 and 16 show WD and Ed spectra, respectively, for cerium. The superiority of WDS is especially marked for a mixture of barium, cerium, and lanthanum. Figure 17 shows a WD spectrum, figure 18 shows an ED spectrum. It can be readily seen that a quantitative analysis for these three elements could be made by WDS using a Ba $L\alpha_{1\ 2}$, La $L\alpha_{1\ 2}$, and Ce $L\beta_{1\ 4}$. Also indicated in figure 17 are the positions of the barium, lanthanum, and cerium L_I, L_{II}, and L_{III} absorption edges. The ED spectrum would require a very sophisticated least squares stripping program to obtain quantitative information. Excellent resolution of the K series lines of barium, lanthanum, and cerum can be achieved with EDS. Figures 19 and 20 show spectra obtained with a tungsten tube, a gadolinium secondary target, and a lithium drifted silicon detector, and with an americium-241 source, a dysprosium secondary target, and an intrinsic germanium detector, respectively. The resolution given by the two systems is very similar.

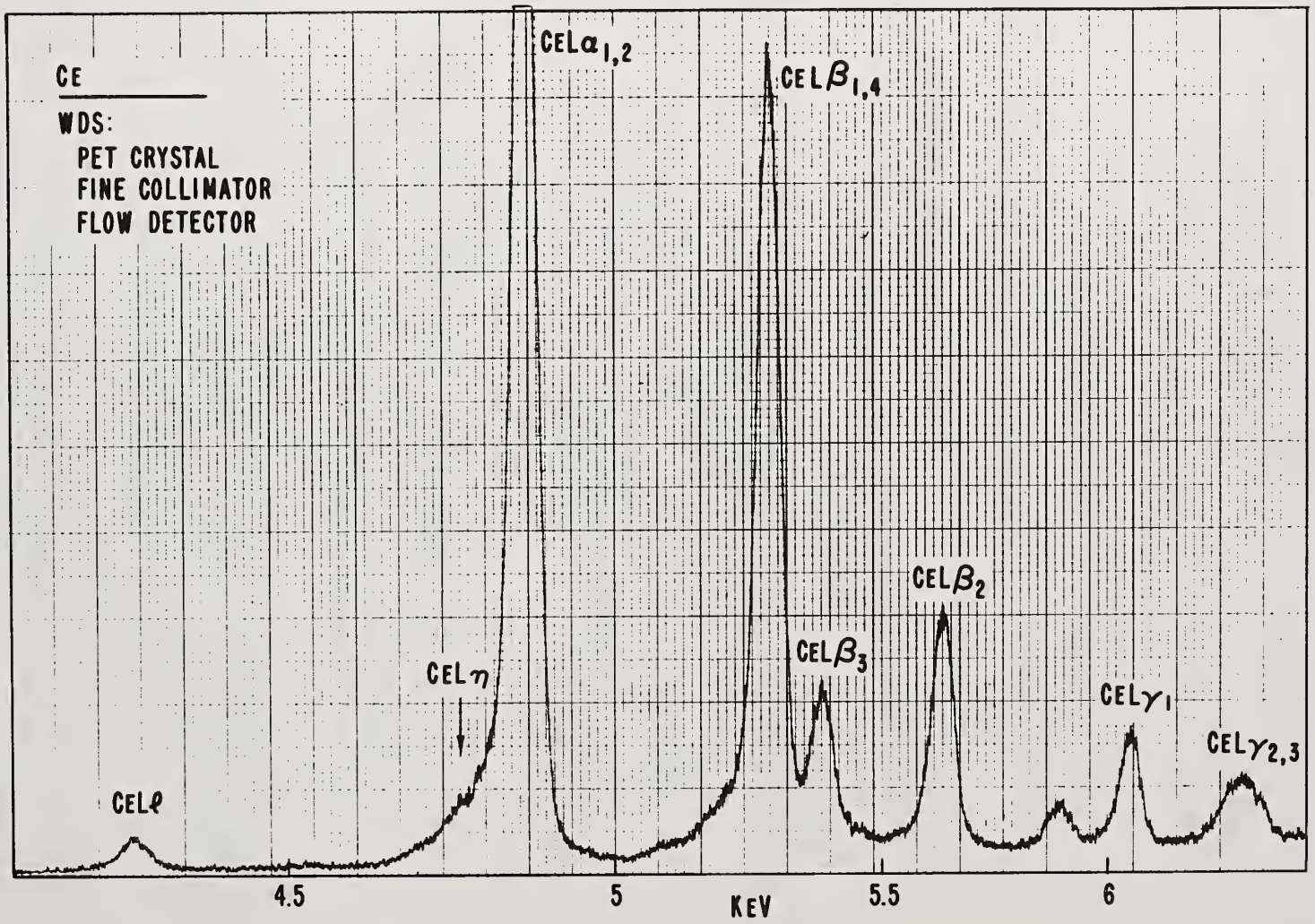

Figure 15. WD spectrum of Ce L lines: Cr tube, PET crystal.

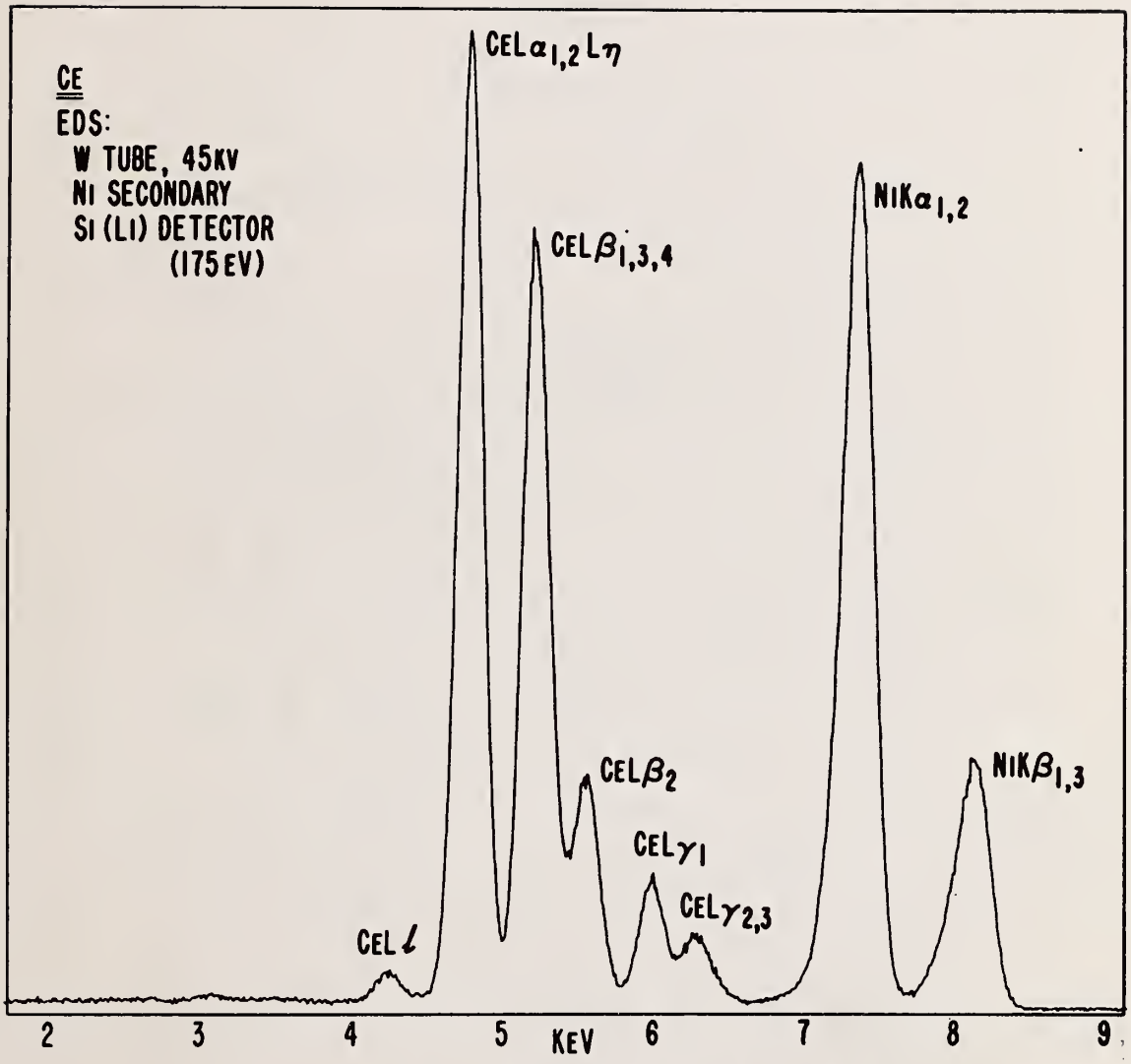

Figure 16. ED spectrum of Ce L lines: W tube at 45 kV, Ni secondary Si(Li) detector.

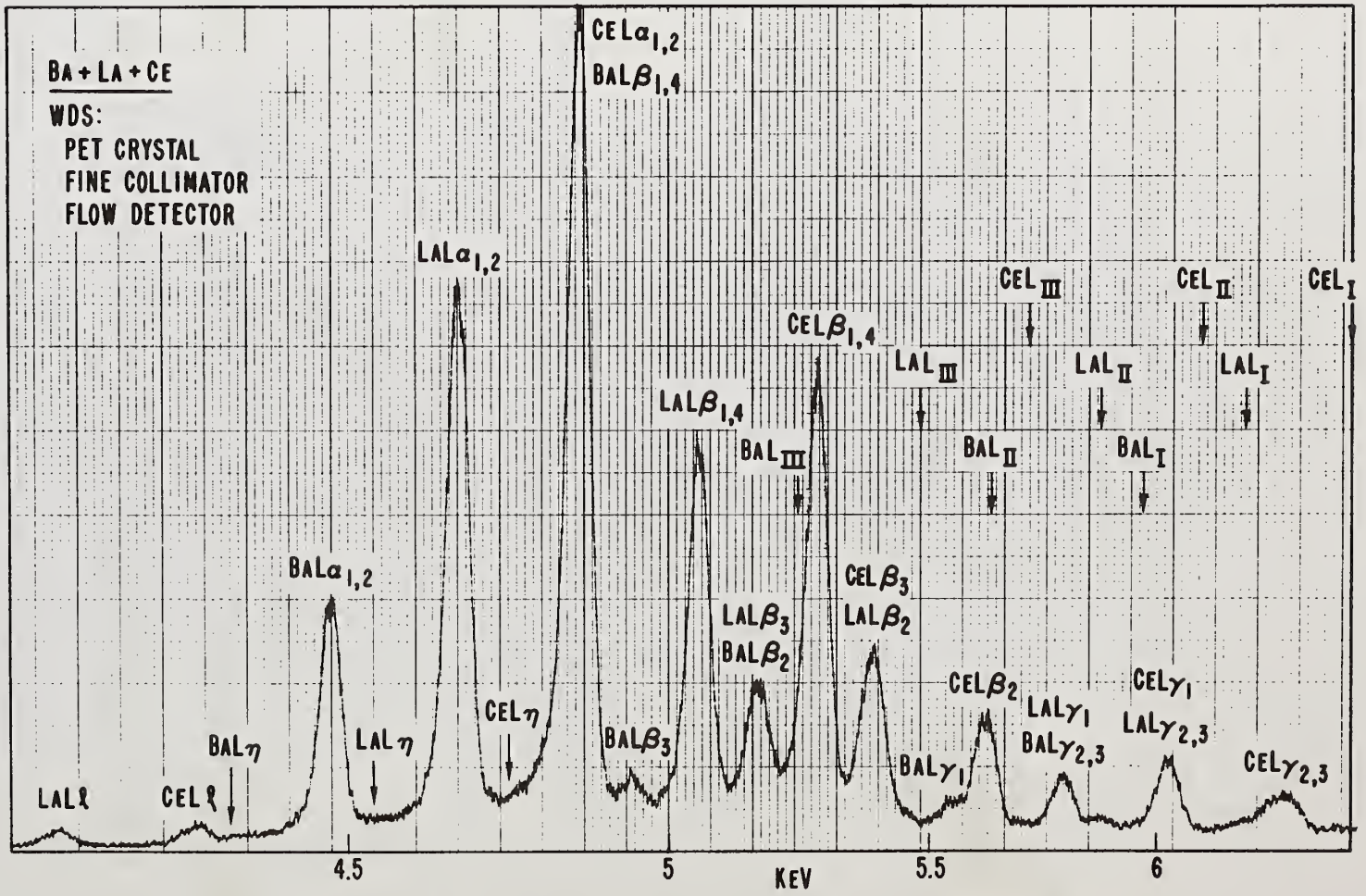

Figure 17. WD spectrum of Ba/La/Ce L lines: Cr tube, PET crystal.

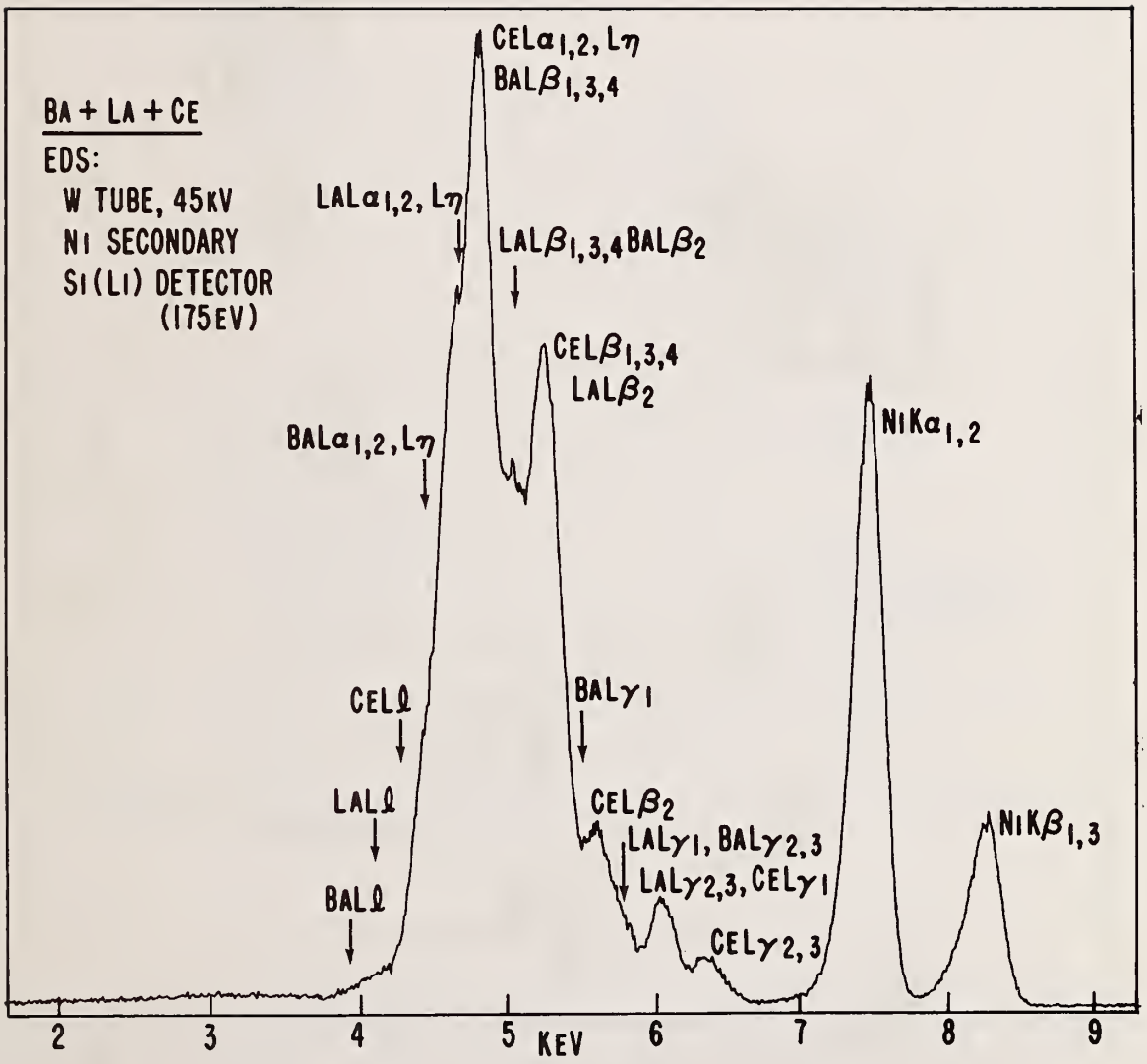

Figure 18. ED spectrum of Ba/La/Ce L lines: W tube at 45 kV, Ni secondary Si(Li) detector.

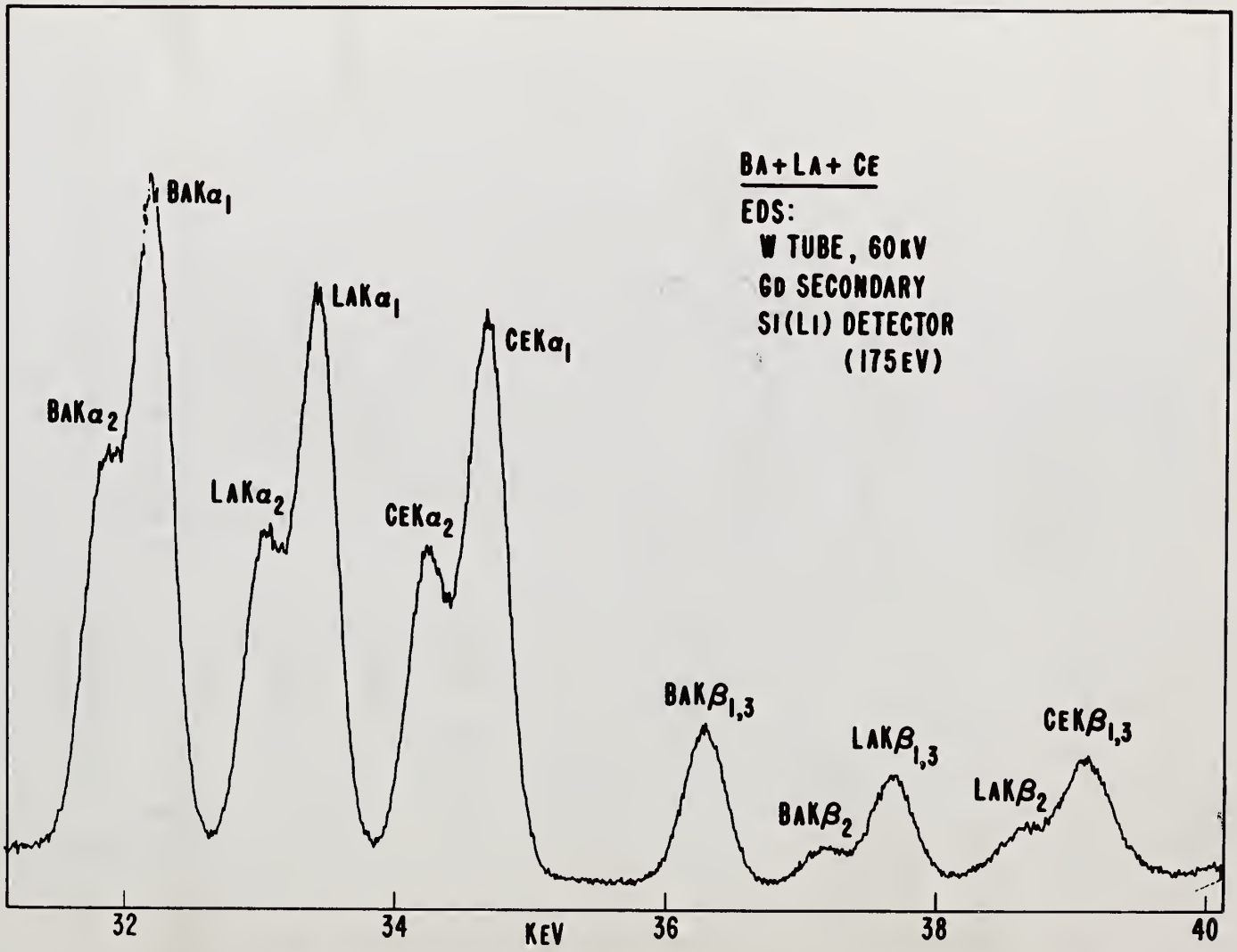

Figure 19. ED spectrum of Ba/La/Ce K lines: W tube at 60 kV, Gd secondary, Si(Li) detector.

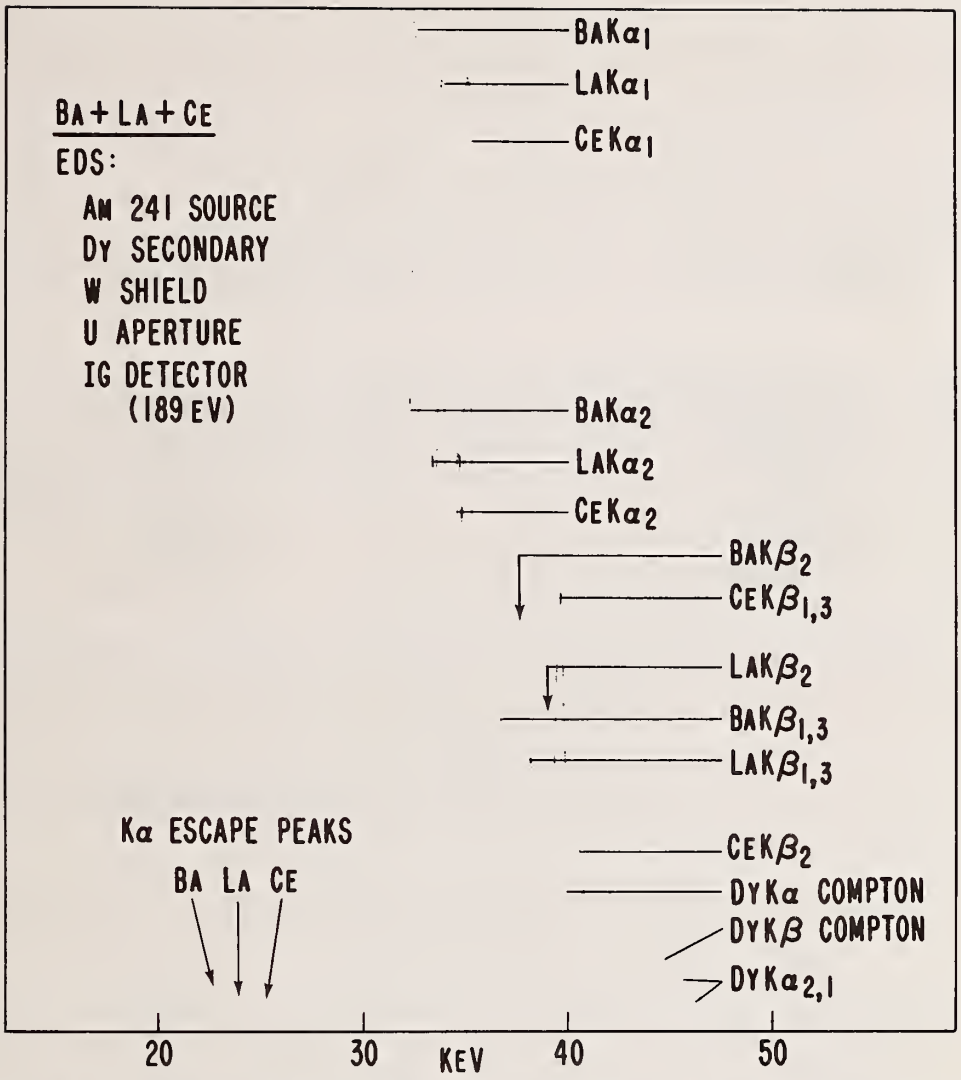

Figure 20. ED spectrum of Ba/La/Ce K lines: Am-241 source, Dy secondary, intrinsic Ge detector.

4. Results – High Energy Penetration

To demonstrate the high penetration power of platinum and lead K series x-rays and to illustrate the possible usefulness of the technique, two automobile converters were examined under laboratory conditions using the cobalt-57 source (122 keV gamma rays) to excite the platinum and lead, and the intrinsic germanium detector to detect the platinum and lead fluorescence K radiation. One catalyst was fresh and unused, the second had, for test purposes, been run in a car on leaded gasoline. Both contained in the region of 0.2 percent by weight of platinum and both were contained within a standard stainless steel can in which they are normally connected to the engine exhaust. The x-ray examinations were made through the can. The resulting spectra, shown in figure 21, each took approximately 50 minutes to collect (1000 seconds "live time" at a 60% to 70% "dead time"). The experimental conditions were not optimized to reduce the counting time to a minimum. It can be seen that platinum is readily detected at this low level (note the change in full scale for the lead containing catalyst) and that there is a substantial amount of lead present. No attempts have been made to analyze converters in situ. Possible complications of in situ analysis include:

the additional attenuation of the x-rays by the converter heat shield, radiant heat damage to the detector, and unacceptably long analysis times. Even a successful in situ analysis for lead would provide no immediate information as to the timing or quantity of leaded gasoline which had been consumed by the engine.

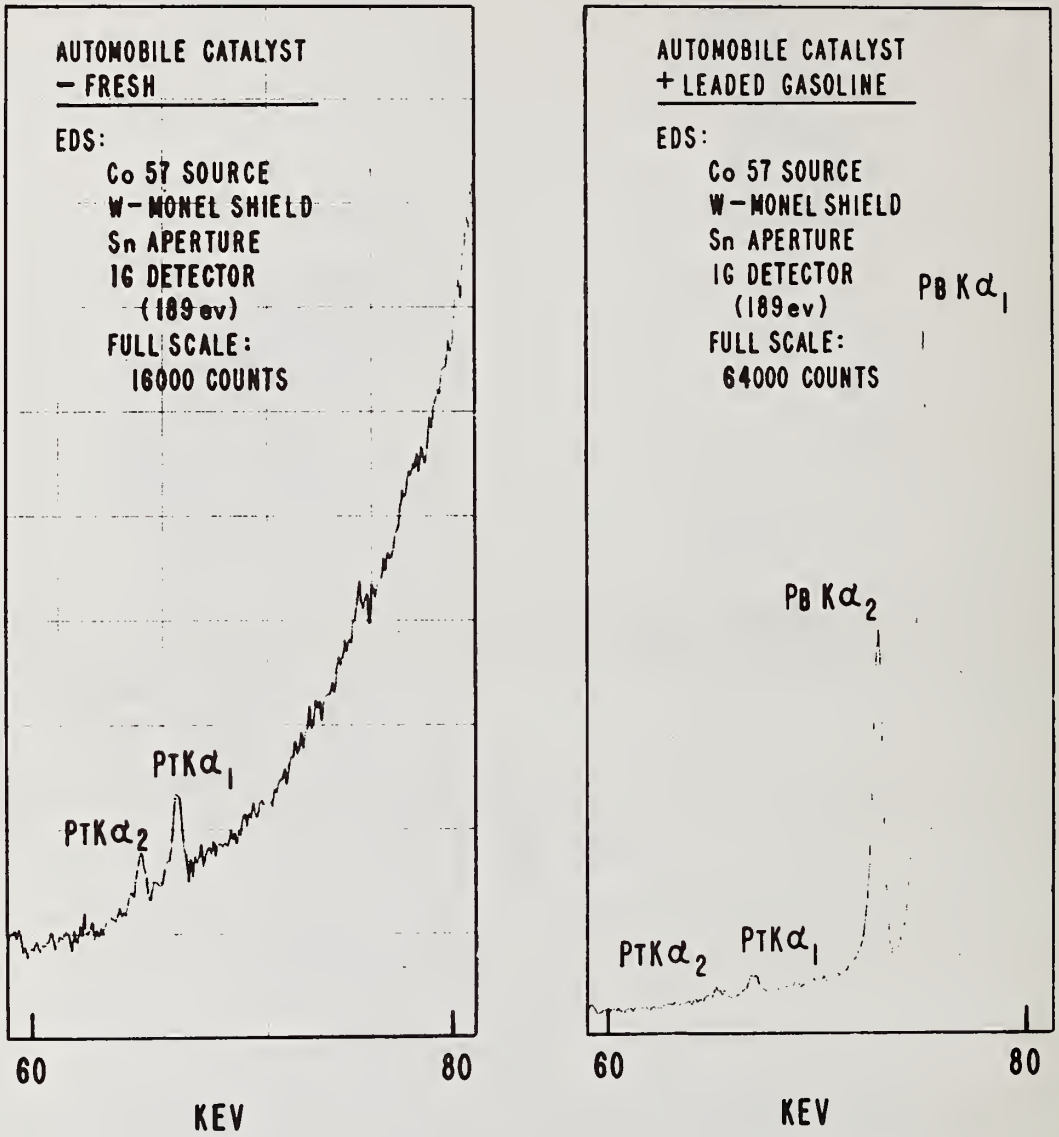

Figure 21. ED spectra of Automobile Catalysts: Co-57 source, intrinsic Ge detector.

5. Discussion

Wavelength dispersive and energy dispersive spectra have shown that better resolution for barium/lanthanum/cerium and osmium/iridium/platinum L series lines is provided by wavelength dispersive spectroscopy, while better resolution for the K series lines is given by energy dispersive spectroscopy. For barium/lanthanum/cerium K lines, there is little to choose between the W tube/Gd secondary/Si(Li) detector system and the Am-241/Dy secondary/intrinisic germanium detector system; they both give good resolution. For osmium/iridium/platinum, both cobalt-57 used as a primary source and cobalt-57 used with uranium as a secondary target give good resolution for the K lines; in the case of the light element matrix, the Co-57/U secondary combination suffers from a worse peak/background ratio and from the proximity of the uranium K Compton scattering when compared with Co-57 used as a primary source.

With cobalt-57 as a primary source and an intrinsic germanium detector, lead/platinum ratios have been measured in the laboratory, through the can, on a test converter after removal from a car run on leaded fuel. Useful semi-quantitative results for lead are currently being obtained under laboratory conditions using a computer-based multichannel analyzer program which integrates peak heights and subtracts backgrounds based on an assumed platinum content.

We would like to thank Drs. M. F. Elgart and R. G. Hurley for a number of useful discussions and Drs. B. E. Artz and J. L. Bomback for commenting on the manuscript.

Reference

[1] Artz, B. E., X-ray Spectrometry, 6, 165 (1977).

National Bureau of Standards Special Publication 604. Proceedings of the Workshop on Energy Dispersive X-Ray Spectrometry held at NBS, Gaithersburg, Maryland, April 23-25, 1979. (Issued March 1981)

ENERGY DISPERSIVE DETECTORS – A BIBLIOGRAPHY (1981)

C. E. Fiori and C. R. Swyt

Biomedical Engineering and Instrumentation Branch
Division of Research Services
National Institutes of Health
Bethesda, Maryland 20205

This paper is an expanded and updated bibliography of references relating to energy dispersive detectors for electron column instruments with more complete cross-referencing by subject than the previous bibliography by the first author[1]. The bibliography is not all-inclusive and is meant only to give the reader a starting point from which to become familiar with the large body of literature which exists on the topic of energy dispersive detectors. Papers from the more relevant journals, e.g., X-Ray Spectrometry, Review of Scientific Instruments, Scanning Electron Microscopy, etc., have been cited most heavily but a number of historical papers of general interest from many sources are also included. Both new citations and references from the previous bibliography are listed because of the nature of the workshop resulting in this volume.

Among the types of detectors covered are Si, Ge, Cd Te, Hg I_2, windowless Si(Li) and gas proportional. References treating the physics of Si(Li) detectors and their application to the electron microprobe and scanning and transmission microscopes are extensively included. Papers treating their applications, such as x-ray fluorescence and proton induced x-ray fluorescence, are less comprehensively referenced.

Broad areas covered in the cited literature are the physics of energy dispersive detectors, quantitative applications, characterization and calibration, and applications in fundamental physical measurement.

REFERENCES

Physics of Detectors, Si: 3, 4, 32, 40, 70, 87, 88, 99, 127, 150, 154, 163, 164, 172, 174, 177, 185, 202, 223, 224, 241, 243, 248, 252, 256, 258, 261, 279, 285, 296, 387, 423, 425, 429, 430, 434, 435, 436, 467, 468, 469, 470.

Physics of Detectors, Ge: 43, 64, 67, 81, 87, 88, 144, 166, 167, 169, 170, 171, 172, 173, 174, 175, 178, 179, 180, 181, 182, 195, 196, 197, 198, 244, 247, 256, 258, 261, 279, 292, 293, 294, 295, 301, 321, 366, 381, 382, 422, 423, 425, 430, 449.

Windowless Si(Li) Detectors: 12, 15, 273, 274, 340, 346, 347, 361.

Cd Te: 76, 123, 124, 201, 261, 373, 426.

Hg I_2, Hg O_2, Pb I_2: 75, 77, 137, 201, 254, 255, 299, 311, 373, 374, 388, 426, 427, 448.

Gas Proportional, Ionization, Scintillation Detectors: 7, 34, 38, 39, 45, 48, 63, 73, 87, 111, 113, 183, 209, 216, 246, 251, 260, 267, 268, 269, 270, 321, 323, 326, 386, 388, 391, 402, 424, 439, 450.

Fano Factor, Ionization Energy: 94, 112, 290, 291, 382, 436, 441, 464.

Calibration and Characterization: 49, 50, 51, 52, 56, 57, 58, 59, 70, 71, 114, 176, 217, 246, 256, 263, 272, 277, 324, 325, 365, 399, 419, 422, 440, 445.

[1]Fiori, C. E., "Energy-Dispersive Detectors: A Bibliography" in Microbeam Analysis–1979, ed. D. E. Newbury (San Francisco Press, 1979) p. 361.

BIBLIOGRAPHY

1. Admon, U., "Specimen Stage for Energy-dispersive Analysis for the S-600 Scanning Electron Microscope," J. of Phys. E 12: 749-751, 1979.

2. Aitken, D.W., "Recent Advances in X-ray Detection Technology," IEEE Trans. Nucl. Sci., NS-15(3): 10-46, 1968.

3. Aitken, D., Emerson, D. and Zulliger, H.R., "Response of the Lithium-Drifted Silicon Radiation Detector to High Energy Charged Particles," IEEE Trans. Nucl. Sci. NS-15(1): 456, 1968.

4. Aitken, D., Lakin, W., and Zulliger, H.R., "Energy Loss and Straggling in Silicon by High Energy Electrons, Positive Pions and Protons," Phys. Rev. 179: 393, 1969.

5. Aitken, D.W. and Woo, E., "The Future of Silicon X-Ray Detectors," STP 485, American Society for Testing and Materials, 36-56, 1971.

6. Albee, A.L. et al., "Quantitative Analysis of Petrographic Properties and of Mineral Compositions with a Computer-Controlled Energy-Dispersive System," Proc. 8th Intern. Conf. X-Ray Optics and Microanalysis; Proc. 12th MAS Conf., 1977, 181.

7. Aldargazelli, S.S., Ariyaratne, T.R., Breave, J.M., and Nandi, B.C., "A Study of Gas Scintillation Multiwire Proportional Counter," J. Phys. D 11(13): 1773-1780, 1978.

8. Armantrout, G.A., Swierkowski, S.P., Sheroman, J.W., and Yee, J.H., "What Can be Expected from High-Z Semiconductor Detectors?," IEEE Trans. Nucl. Sci. NS-24(1), 121-125, 1977.

9. Armantrout, G.A. and Thompson, H.W., "Spectrum Degradation Effects in Ge(Li) Detectors," IEEE Trans. Nucl Sci. NS-17(3): 165-175, 1970.

10. Awasthi, S.K., Chada, A., and Chackraburtty, S.M., "Energy-dispersive XRF Analysis of Rare Earths Using K X-Rays," Bhabha Atomic Res. Cntr. Report I.415., 11, 1976.

11. Balland, J.C. et al, "Problems Related to Charge Collection Variations in GE(Li) Detectors with Special Reference to Timing," IEEE Trans. Nucl. Sci. NS-17(3): 405-424, 1970.

12. Barbi, N.C. and Russ, J.C., "Analysis of Oxygen on an SEM Using a Windowless Energy Dispersive X-Ray Spectrometer," SEM/75 (Part I), Om Johari, Ed., (IITRI) Chicago, IL, 85-91, 1975.

13. Barbi, N.C. and Russ, J.C., "Applications of Energy Dispersive Analysis on the Transmission Electron Microscope in Pathology and Pollution Studies," Proc. of the Electron Microscopy Society of America, 32nd Annual Meeting, 110, 1974.

14. Barbi, N.C. and Skinner, D.P., "Techniques for Electron Microscopic Identification of Small Particles," SEM/76 (Part III), Om Johari, Ed., (IITRI) Chicago, IL, 393-400, 1976.

15. Barbi, N.C. et al., "Light Element Analysis on the Scanning Electron Microscope Using a Windowless Energy Dispersive X-Ray Spectrometer," SEM/74 (Part I), Om Johari, Ed., (IITRI), Chicago, IL, 151-158, 1974.

16. Barbi, N.C., and Goldman, L., "Contributions to the Spectral Background in Energy Dispersive X-Ray Microanalysis at Higher Accelerating Voltages," Proc. of a Specialist Workshop in Analytical Electron Microscopy, Cornell University, Ithaca, NY, 121, 1976.

17. Barbi, N.C., Foster, M. and Goldman, L., "Semiquantitative Energy Dispersive Analysis in STEM Using Generated Reference Spectra and Empirical Scale Factors," SEM/78 (Part I), Om Johari, Ed., (SEM Inc., A.M.F. O'Hare, IL), 307-314, 1977.

18. Barbi, N.C., Foster, M., Skinner, D.P., "A Technique for Rapid Semiquantitative Energy Dispersive Microanalysis," Proc. 8th Intern. Conf. X-Ray Optics and Microanalysis; 12th MAS Conf., 1977, 100.

19. Barbi, N.C., Giles, M.A., and Skinner, D.P., "Estimating Elemental Concentration in Small Particles Using X-Ray Analysis in the Electron Microscope," SEM/78 (Part I), Om Johari, Ed., (SEM Inc., A.M.F. O'Hare, IL), 193-200, 1978.

20. Barbi, N.C., Skinner, D.P. and Blinder, S., "The Calculation of Pure Element X-Ray Intensities from Empirically Derived Expressions and its Application to Quantitative SEM/EDS Analysis," Proc. 11th MAS Conf., 1976, 8.

21. Beaman, D.R. and File, D.M., "Quantitative Determination of Asbestos Fiber Concentrations," Anal. Chem. 48(1): 110, 1976.

22. Beaman, D.R. and Isasi, J.A., "Electron Beam Microanalysis," STP 506, Amer. Soc. for Testing and Materials, 1972.

23. Beaman, D.R. and Nagatani, T., "Developments in Instrumentation," in The Electron Microanalyzer and its Applications, proc. of a meeting sponsored by the National Science Foundation and the Japan Soc. for Promotion of Science, Honolulu, Hawaii, Sept. 1973, p. 5-20.

24. Beaman, D.R. and Solosky, L.F., "Accuracy of Quantitative Electron Probe Microanalysis with Energy Dispersive Spectrometers," Anal. Chem. 44(9): 1598-1610, August, 1972.

25. Beaman, D.R. and Solosky, L.F., "Advances in Quantitative Energy Dispersive Spectrometry," in Proc. 9th MAS Conf., 1974, p. 26.

26. Beaman, D.R., "Analytical Transmission Electron Microscopy and its Application in Environmental Science," in Environmental Pollutants, Y. Taft et al, Eds., 255-295, Plenum, 1978.

27. Beaman, D.R., Solosky, L.F., and Settlemeyer, L.A., "X-Ray Analysis with Energy Dispersive Spectrometers," in Tutorial Proc. 8th National Conf. on Electron Microprobe Analysis, New Orleans, Aug., 1973, 73-85.

28. Berdikov, V.V., Grigor'ev, O.I., and Iohin, B.S., "Energy-dispersive XRF Analysis of Highly Radioactive Samples with Small Tubes and Pyrographite Crystals," Nucl. Instrum. Meth. 155:, 313-315, 1978.

29. Bender, S.L. and Duff, R.H., "Energy Dispersion X-Ray Analysis with the Transmission Electron Microscope," STP 485, American Society for Testing and Materials, 180-196, 1971.

30. Bertolini, G. and Coche, A., Semiconductor Detectors, Netherlands, Wiley 1968.

31. Bertolini, G. et al., "Lithium Drifted Semiconductor Detectors in Nuclear Spectroscopy," EUR 2580-e, 1965.

32. Bertolini, G. Cappelani, F., and Restelli, G., "Construction and Performances of Silicon Lithium Drifted Detectors," Nucl. Instrum. Meth. 32: 86-92, 1965.

33. Birks, L.S. and Gilfrich, J.V., "Evolution of Commercial Energy-dispersive X-Ray Analysers for Water Polution," Appl. Spectrom. 32(2): 204-208, 1978.

34. Bisi, A., Zappa, L., "Statistical Spread in Pulse Size of the Proportional Counter Spectrometer," Nuovo Cimento 10: 988-94, Italy, 1955.

35. Black, W.W., "A Precision, Computer-Controlled Pulse Generator and its Application," Nucl. Instrum. Meth. 53: 249-256, 1967.

36. Blum, F. and Brandt, M.P., "The Evaluation of the Use of a Scanning Electron Microscope Combined with an Energy Dispersive X-Ray Analyzer for Quantitative Analysis," X-Ray Spectrom. 2: 121-124, 1973.

37. Borders, R.A. et al, "High Speed Pulse Amplifier/Discriminator and Counter for Photon Counting," Anal. Chem. 52(8): 1273-1278, 1980.

38. Borkowski, C.J. and Kopp, M.K., "Electronic Discrimination of the Effective Thickness of Proportional Counters," IEEE Trans. Nucl. Sci. NS-24(1): 287-292, 1977.

39. Borley, G.D., Bullen, G., and O'Hara, K., "A Method of Producing Mounted Thin Windows for X-Ray Spectrometer Flow Counters," X-Ray Spectrom. 5(4): 13-15, 1976.

40. Brombach, J.D., "Appearance of the Gold iv,v Absorption Edges in the Back-Ground of Energy-dispersive X-Ray Spectra," X-Ray Spectrom. 7(2): 81-85, 1978.

41. Bowman, H.R. et al, "Application of High-Resolution Semiconductor Detectors in X-Ray Emission Spectrography," Science 151: 562-568, 1966.

42. Bromba, M.U.A. and Ziegler, H., "Efficient Computation of Polynomial Smoothing Digital Filters," Anal. Chem. 51(11): 1760-1761, 1979.

43. Bruening, N., Fretwurst, E., and Lindstrom, N., "Detailed Investigations on Abnormal Pulse Shapes in Ge(Li)-Detectors," IEEE Trans. Nucl. Sci. NS-22(1): 173-176, 1975.

44. Brummer, O., "Mikroanalyse mit Elektronen-und Ionensonden," VEB Deutcher Verlag fur Grundstoffindustrie, Leipzig, 73-88, 1978.

45. Campbell, A.J., "Proportional Counter Resolution," Norelco Reporter 14, 103-106, 1967.

46. Campbell, J.L. and Crosse, L.A., "Non-Destructive Analysis of Lead on Apartment Walls," Can. J. Public Health 67: 506-510, 1976.

47. Campbell, J.L. and Crosse, L.A., "Portable Instrumentation for the Determination of Lead in Painted Surfaces," Bull. Env. Sci. Toxicology 16: 469-473, 1976.

48. Campbell, J.L. and Ledingham, K.W.D., "Pulse Height Distributions from Proportional Counters," Brit. J. Appl. Phys. 17: 769-774, 1966.

49. Campbell, J.L. and McNelles, L.A., "Americium-241 as a Low-Energy Photon Intensity Standard," Nucl. Instrum. Meth. 117: 519-532, 1974.

50. Campbell, J.L. and McNelles, L.A., "An Inter-Comparison of Efficiency Calibration Techniques for Semiconductor X-Ray Detection," Nucl. Instrum. Meth. 125: 205-233, 1974.

51. Campbell, J.L. and McNelles, L.A., "Construction of Efficiency Curves for Semiconductor X-Ray Detectors," Nucl. Instrum. Meth. 98: 433-444, 1972.

52. Campbell, J.L. et al, "Fabrication of Thin Radioactive Sources Using Biological Staining Techniques," Nucl. Instrum. Meth. 93: 173-174, 1971.

53. Campbell, J.L. et al, "Some Biomedical Applications of Proton-Induced X-Ray Fluorescence Analysis," Adv. X-Ray Anal. 17: 457-466, 1976.

54. Campbell, J.L. et al, "Trace Element Analysis of Fluids by Proton-Induced X-Ray Spectrometry," Anal. Chem. 47: 1542, 1975.

55. Campbell, J.L., "Pulse Rise Time Discrimination in X-Ray Proportional Counters," Nucl. Instrum. Meth. 65: 333-337, 1968.

56. Campbell, J.L., Goble, R.J., and Smith, H.J., "Efficiency of Planar Ge(Li) Detectors at Very Low Energy," Nucl. Instrum. Meth. 82: 183-186, 1970.

57. Campbell, J.L., Jorch, H.H., and Thompson, J.A., "Parametric Representation of X-Ray Detector-Efficiency Curves," Nucl. Instrum. Meth. 140: 167-173, 1977.

58. Campbell, J.L., O'Brien, P., and McNelles, L.A., "On the Efficiency Calibration of Semiconductor X-Ray Detectors," Nucl. Instrum. Meth. 92: 269-275, 1971.

59. Campbell, J.L., Smith, H.J., and MacKenzie, I.K., "A Coincidence Technique for Study of Ge(Li) Detector Profiles," Nucl. Instrum. Meth. 92: 237-245, 1971.

60. Carlton, D.T. and Russ, J.C., "Trace Level Water Analysis by Energy Dispersive X-Ray Fluorescence," X-Ray Spectrom. 5(3): 194-174, 1976.

61. Carr-Brion, K.G., "On-stream Energy Dispersion X-Ray Analysis," X-Ray Spectrom. 2(2): 63-68, 1973.

62. Catura, R.C. and Smithson, R.C., "Single Photon X-Ray Detection with a CCD Image Sensor," Rev. Sci. Instr. 50(2): 219-220, 1979.

63. Chew, W.M., McGeorge, J.C., and Fink, R.W., "A Multiwire Proportional Counter Technique for Standardization of Low-Energy Photon Sources," Nucl. Instrum. Meth. 106: 499-501, 1973.

64. Christensen L. H., "Comparison Between Experimental and Calculated Relative Escape Peak Intensities for an Intrinsic Ge Detector in the Energy Region 11-25 keV," X-Ray Spectrom. 8(4): 146-148, 1979.

65. Ciccarelli, M.F., Bolon, R.B., and Lifshin, E., "Quantitative Analysis with an Energy Dispersive Detector," Proc. 10th MAS Conf., 1975, 23.

66. Ciccarelli, M.R. and Goehner, R.P, "A Diffractometer Based Energy Dispersive Elemental Analyzer," Adv. X-Ray Anal. 21, 1978.

67. Cline, J.E., "Studies of Detection Efficiencies and Operating Characteristics of Ge(Li) Detectors," IEEE Trans. Nucl. Sci. 15(3):198-213, 1968.

68. Cohen, E.J., "Live Time and Pile-Up Correction for Multichannel Analyzer Spectra," Nucl. Instrum. Meth. 121: 25-32, 1974.

69. Comins, N.R. and Thirlwall, J.T., "A Critical Investigation of Energy-dispersive Microprobe Analysis of Steels Using the Reed/Fiori Method of Background Calculation," X-Ray Spectrom. 7(2), 92-96, 1978.

70. Corallo, D.M., Creek, D.M., and Murray, G.M., "The X-Ray Calibration of Silicon p-i-n Diodes Between 1.5 and 17.4 keV," J. of Phys. E 13: 623-626, 1980.

71. Cotherm, C.R., Manuel, H.L., and Millette, J. R., "Determination of Overall System Efficiency of an Energy-dispersive X-Ray Fluorescence Spectrometer Using a Bremsstrahlung Exciting Source," X-Ray Spectrom. 3(2): 53-58, 1974.

72. Covell, D.F., "Determination of Gamma-Ray Abundance Directly from the Total Absorption Peak," Anal. Chem. 31: 1785-1790, 1959.

73. Culhane, J.L. et al, "Advances in the Design and Performance of X-Ray Proportional Counters," J. Sci. Inst. 43: 908-912, 1966.

74. Currie, L.A., "Detection and Quantitation in X-Ray Fluorescence Spectroscopy," in X-Ray Fluorescence Analysis of Environmental Samples, T.G. Dzubay, Ed., Ann Arbor Sci., 289-307, 1977.

75. Dabrowski, A.J. and Huth, G., "Toward the Energy Resolution Limit of Mercuric Iodide in Room Temperature Low Energy X-Ray Spectrometry," IEEE Trans. Nucl. Sci. NS-25(1): 205-211, 1978.

76. Dabrowski, A.J. et al, "n-Type Cadmium Telluride Surface Barrier Nuclear Detectors," Revue de Physique Appliquee 12: 297-302, 1977.

77. Dabrowski, A.J. et al, "Characteristic X-Ray Spectra of Sodium and Magnesium Measured at Room Temperature Using Mercuric Iodide Detectors," Appl. Phys. Lett. 33(2): 211-213, 15 July 1978.

78. Damljanovic, D., "New System for the Reduction of Dead Time Losses," J. of Phys. E 13: 291-293, 1980.

79. Day, R.B., Dearnley, G. and Palms, J.M., "Noise, Trapping and Energy Resolution in Semiconductor Gamma-Ray Spectrometers," IEEE Trans. Nucl. Sci. NS-14(1): 487-491, 1967.

80. Dearnaley G. and Northrop, D.C., "Semiconductor Counters for Nuclear Radiation," E. and F.N. Son. Ltd., London, 1966.

81. Dearnaley, G., Gibbons, P.E. and Ellis, R., "Large Diameter Germanium Crystals for Gamma-Ray Spectroscopy," IEEE Trans. Nucl. Sci. NS-17(3): 282-286, 1970.

82. Deighton, M.O., "Statistical Errors Arising from Use of a Gated Pulse Train for Total Live Time Measurement During Pulse Amplitude Analysis," Nucl. Instrum. Meth. 14: 48-52, 1961.

83. Deighton, M.O., "A Time-Domain Method for Calculating Noise of Active Integrator Used in Pulse Amplitude Spectrometry," Nucl. Instrum. Meth. 58: 201-212, 1968.

84. de Jesus, A.S.M., "A Correction for Interelemental Background Contributions in Energy-dispersive X-Ray(EDX) Spectroscopy," X-Ray Spectrom. 2(4), 173-178, 1973.

85. Desborough, G.A. and Heidel, R.H., "Characteristics, Performance, and Quantitative Analytical Capability of an Energy-Dispersive Spectrometer on an Electron Microprobe Using Low Operating Voltages," Appl. Spectrosc. 27: 456-463, 1973.

86. Desborough, G.A. and Heidel, R.H., "Energy Dispersive Spectrometry for Quantitative Mineralogical Analyses - An Ancillary System on an Electron Microprobe," J. Rsch. U.S. Geol. Sur. 2(4): 441-446, 1974.

87. Deslattes, R., Simson, B., LaVilla, R., "Gas Density Stabilizer for Proportional Counters," Rev. Sci. Int. 37(5): 596-599, 1966.

88. Drummond, W.E. and Moll, J.L., "Hot Carriers in Si and Ge Radiation Detectors," J. Appl. Phys. 42(13): 5556-5562, 1971.

89. Dunham, A.C. and Wilkinson, F.C.F., "Accuracy, Precision and Detection Limits of Energy-dispersive Electron-microprobe Analysis of Silicates," X-Ray Spectrom. 7(2): 50-56, 1978.

90. Dunham, A. and Wilkinson, F., "The Suitability of Energy-dispersive Electron- microprobe Analysis for the Investigation of Stainless Steels," X-Ray Spectrom. 9(1): 8-12, 1980.

91. Dyer, G.R., Gedcke, D.A., and Harris, T.R., "Fluorescence Analysis Using a Si(Li) X-Ray Energy Analysis System with Low-Power X-Ray Tubes and Radioisotopes," Adv. X-Ray Anal. 15: 228, 1972.

92. Dzubay, T.G., Jarrett, B.V., and Jaklevic, J.M., "Background Reduction in X-Ray Fluorescence Spectra Using Polarization," Nucl. Instrum. Meth. 115: 297-299, 1974.

93. Ebel, H. and Drabseh, S., "Application of the Method of Variable Take-off Angle to Rapid Quantitative XRFA with Energy Dispersive Systems," X-Ray Spectrom. 4(2): 62-64, 1975.

94. Eberhardt, J.E., "Fano Factor in Silicon at 90K," Nucl. Instrum. Meth. 80(2): 291-292, 1970.

95. Ekelund, S., Thuren, A., and Werlefors, T., "A Fast and Simple Procedure for the Evlauation of Net Intensities from Energy-dispersive X-Ray Spectra," X-Ray Spectrom. 8(1): 1-8, 1979.

96. Elad, E. and Gedcke, D.A., "Light Element Analysis with Si(Li) X-Ray Energy Analyzers," Proc. of the Sixth International Conference on X-Ray Optics and Microanalysis, Osaka, Japan, September 5-10, 1971. University of Tokyo Press, 263, 1972.

97. Elad, E. and Nakamura, M., "Germanium FET-A Novel Element for Low Noise Preamplifiers," Nucl. Instrum. Meth. 54(2): 308, 1967.

98. Elad, E. and Nakamura, M., "Germanium FET-A Novel Low Noise Active Device," IEEE Trans. Nucl. Sci. NS-15 (1): 283, 1968.

99. Elad, E. and Nakamura, M., "High Resolution X-Ray and Electron Spectrometer," Nucl. Instrum. Meth. 41: 161, 1966.

100. Elad, E. and Nakamura, M., "Hypercryogenic Detector-FET Unit--Core of High Resolution Spectrometer," IEEE Trans. Nucl. Sci. NS-15(3): 488, 1968.

101. Elad, E. and Nakamura, M., "Low Energy Spectra Measured with 0.7 keV Resolution," Nucl. Instrum. Meth. 42: 315, 1966.

102. Elad, E. et al., "The Use of a Non-Dispersive X-Ray Spectrometer in Scanning Electron Microscopy," IEEE Trans. Nucl. Sci. NS-17(1): 354, 1969.

103. Elad, E. et al, "Dead Layers in Charged-Particle Detectors," IEEE Trans. Nucl. Sci. NS-20(1): 535-544, 1973.

104. Elad, E., "A Preamplifier with 0.7 keV Resolution for Semiconductor Radiation Detectors," Nucl. Instrum. Meth. 37: 327, 1965.

105. Elad, E., "Drain Feedback - A Novel Feedback Technique for Low-Noise Cryogenic Preamplifiers," IEEE Trans. Nucl. Sci. NS-19(1): 403-411, 1972.

106. Elad, E., "FET Preamplifiers for Semiconductor Radiation Detectors," Proc. ISPRA Nuclear Electronics Symposium, Ispra Italy, p. 21, 6-9 May, 1969.

107. Elad, E., "Low-Noise Cryogenic Preamplifiers," STP 485, American Society for Testing and Materials, 57-81, 1971.

108. Elad, E., "Recent Developments in Low Noise Preamplifiers," Proc. of International Symposium on Nuclear Electronicis and Radioprotection, Toulouse, Vol. 1, p. 13, (UCLRL Report 18005), 1978.

109. Elette, V. et al, "Energy Dispersion X-Ray Analysis Using a Scanning Electron Microscope," Metallography 5: 557-561, 1972.

110. El-Wahab, M.A. and Sakka, M., "Time Resolution in Semiconductor Detectors," IEEE Trans. Nucl. Sci. 24(1): 117-120, 1977.

111. Fabricant, D.G., Goddard, R.E., Harnden, Jr., F.R., and Gorenstein, P., "Lexan Coating to Eliminate the UV Sensitivity of Soft X-Ray Proportional Counters with a Polypropylene Window," Rev. Sci. Instrum. 50(6): 727-729, 1979.

112. Fano, U., "Ionization Yield of Radiations II. The Fluctuations of the Number of Ions," Phys. Rev. Vol. 72(1): 26-29, 1947.

113. Fink, R.W., "Proportional-Counter Spectrometer," in Atomic Inner-Shell Processes II, Experimental Approaches and Applications, 169-186, Academic Press, 1975.

114. Fink, R.W., "Radioactive X-Ray Standards," Nucl. Instrum. Meth. 112: 243, 1973.

115. Fiori, C.E. et al, "Observations on the Quantitative Electron Probe Microanalysis of Particles," Proc. of the 7th Materials Research Symp., Gaithersburg, MD, Oct. 7-11, 1974, NBS Spec. Publ. 422, 1975.

116. Fiori, C.E., and Newbury, D.E., "Artifacts Observed in Energy-Dispersive X-Ray Microanalysis with the Lithium-Drifted Silicon Detector," SEM/78 (Part I), Om Johari, Ed., (SEM, Inc., A.M.F. O'Hare, IL), 401-422, 1978.

117. Fiori, C.E. and Newbury, D.E., "Artifacts in Energy-dispersive X-Ray Spectrometry in the Scanning Electron Microscope(II)," SEM/80 (Part II), Om Johari, Ed., (SEM, Inc., A.M.F. O'Hare, IL), 251-250, 1980.

118. Fiori, C.E., Myklebust, R.L., and Heinrich, K.F.J., "A Method for Resolving Overlapping Energy-Dispersive Peaks of an X-Ray Spectrum; Application to the Correction Procedure FRAME B," Proc. 11th MAS Conf., 1976, 12.

119. Fiori, C.E., Myklebust, R.L., and Heinrich, K.F.J., "Prediction of Continuum Intensity in Energy-Dispersive X-ray Microanalysis," Anal. Chem. 48(1): 172-176, 1976.

120. Fiori, C.E., Myklebust, R.L., and Newbury, D.E., "A Catalog of Artifacts Observed in Energy Dispersive X-Ray Spectrometry and their Influence on Analysis," in Microbeam Analysis in Biology, C. Lechene and R. Warner, Eds., Academic Press, Inc., 1979, 225-263.

121. Fitzgerald, R. and Gantzel, P., "X-ray Energy Spectrometry in the 0.1 to 10A Range," STP 485, American Society for Testing and Materials, 3-35, 1971.

122. Fitzgerald, R., Keil, K., Heinrich, K.F.J., "Solid-State Energy-Dispersion Spectrometer for Electron-Microprobe X-Ray Analysis," Science 159(3814): 528-530, 1968.

123. Folkman, F., "Analytical Use of Ion-induced x Rays," J. of Phys. E 8: 429-444, 1975.

124. For a general review of CdTe detectors see: Proc. 2nd Intern. Symp. on CdTe, Rev. Appliquee 12(2): 1977.

125. Frankel, R.S., "Detection of Art Forgeries by X-Ray-Fluorescence Spectroscopy," Isotopes and Radiation Resch. 8(1): 1970.

126. Frankel, R.S., and Aitken, D.W., "Energy-Dispersive X-Ray Emission Spectroscopy," Appl. Spectrosc. 24(6): 557-566, 1970.

127. Freund, H.U. et al, "Photon Spectrometry in the Low Energy Region 500 eV to 100 keV," in Radioactivity in Nuclear Spectroscopy 2: 623-649, Hamilton, J.H. and Manthuruthil, J.C. (Eds.), Gordon and Breach Sci. Publ., New York, 1972.

128. Friel, J.J., Goldstein, J.I. and McCarthy, J.J., "Combined EDX and WDX Analysis with an Automated Microprobe," 8th Int. Conf. X-Ray Optics and Microanalysis; 12th MAS Conf., 1977, 50.

129. Gardner, R.P., Wielopolski, L., and Verghese, K., "Mathematical Techniques for Quantitative Elemental Analysis by Energy-dispersive XRF," J. Radioanal. Chem. 43(2): 611-643, 1978.

130. Gedcke, D.A., "The Si(Li) X-Ray Energy Analysis System: Operating Principles and Performance," X-Ray Spectrom. 1(4): 129-141, 1972.

131. Gedcke, D. and Elad, E., "An Intercomparison of Trace Element Excitation Methods for Energy Dispersive Fluorescence Analyzers," X-Ray Spectrom. 6(1): 21, 1977.

132. Gedcke, D.A. and Elad, E., "The Si(Li) X-Ray Energy Analysis Technique: Principles and Applications," Proc. of the Sixth International Conference on X-Ray Optics and Microanalysis, Osaka, Japan, Sept. 5-10, 1971. University of Tokyo Press, 253, 1972.

133. Gedcke, D.A., "The High Counting Rate Limits on Analytical Precision Due to Deadtime Losses," Proc. 10th MAS Conf., 1975, 25.

134. Gedcke, D.A., "The Si(Li) X-Ray Energy Spectrometer for X-Ray Microanalysis," in Quantitative Scanning Electron Microscopy, D. Holt, M. Muir, P. Grant, Eds., Academic Press, London, 1974.

135. Gedcke, D.A., Elad, E., and Dyer, G.R., "Limitations on the Si(Li) X-Ray Energy Analysis Systems at High Counting Rates," Proc. 6th National Conference on Electron Probe Analysis, 1971, 5.

136. Geiss, R.H. and Huang, T.C., "Quantitative X-Ray Energy Dispersive Analysis with the Transmission Electron Microscope," X-Ray Spectrom. 4: 196, 1975.

137. Gelbart, U., Yacoby, Y., Beinglass, I., and Holzer, A., "Study of Imperfections in Mercury Iodide by the Thermally Stimulated Currents Method," IEEE Trans. Nucl. Sci. NS-24(1): 135-141, 1977.

138. Geller, J.D., "A Comparison of MDL Limits Using Energy and Wavelength Dispersive Detectors," SEM/77 (Part I), Om Johari, Ed., (SEM Inc., A.M.F. O'Hare, Il.) 281-287, 1977.

139. Geller, J.D., "Energy Dispersive Filteration for Simultaneous Energy and Wavelength Dispersive Analysis," SEM/78 (Part I), Om Johari, Ed., (SEM Inc., A.M.F. O'Hare, Il.), 201-206, 1978.

140. Geller, J.D., "Minimum Detection Limits in an Automated Microprobe," Proc. 11th MAS Conf., 1976, 73.

141. Giaque, R.D., Garret, R.B., and Goda, L.Y., "Calibration of Energy-Dispersive X-Ray Spectrometers for Analysis of Thin Environmental Samples," in X-Ray Fluorescence Analysis of Environmental Samples, T.G. Dzubay, Ed., Ann Arbor Sci. 153-164.

142. Giaque, R.D., Goulding, F.S., Jaklevic, J.M. and Pehl, R.H., "Trace Element Analysis with Semiconductor Detector X-Ray Spectrometers," Anal. Chem. 45(4): 671-681, 1973.

143. Giles, M.A. and Barbi, N.C., "Estimating Mass Thickness in Semi-Thin Sections," Proc. 13th MAS Conf. 1978, 57.

144. Glasow, P.A. and Haller, E.E., "The Effect of Dislocation on the Energy Resolution of High-Purity Germanium Detectors," IEEE Trans. Nucl. Sci. NS-23(1): 92-96, 1976.

145. Goldstein, J.I. and Williams, D.B., "Spurious X-Rays Produced in the Scanning Transmission Electron Microscope," SEM/77 (Part I), Om Johari, Ed., (SEM, Inc., A.M.F. O'Hare, IL), 427-482, 1978.

146. Goldstein, J.I. and Williams, D.B., "X-Ray Analysis in the TEM/STEM," SEM/77 (Part I), Om Johari, Ed., (SEM, Inc., A.M.F. O'Hare, IL), 561- 662, 1977.

147. Goldstein, J.I. and Yakowitz, H., Practical Scanning Electron Microscopy, New York: Plenum Press, 1975.

148. Goldstein, J.I. et al, "Quantitative X-Ray Analysis in the Electron Microscope," SEM/77 (Part I), Om Johari, Ed., (SEM, Inc., A.M.F. O'Hare, IL), 315- 324, 1977.

149. Goldstein, J.I., Lorimer, G.W., and Cliff, G., "Quantitative Analysis of Thin Foils--Calibration Standards and Application to Iron Meteorites," Sixth European Congress on Electron Microscopy Proceedings 1: 56-58, 1976.

150. Goulding, F.S. and Hansen, W.L., "Leakage Current in Semiconductor Junction Radiation Detectors and its Influence on Energy-Resolution Characteristics," Nucl. Instrum. Meth. 12: 249-262, 1961.

151. Goulding, F.S. and Jaklevik, J.M., "XRF Analysis - Some Sensitivity Comparisons Between Charged-Particle and Photon Excitation," Nucl. Instrum. Meth. 142: 323-332, 1977.

152. Goulding, F.S. and Landis, D., "Nuclear Spectroscopy and Reactions," Part A, Chap III, in Semiconductor Spectrometer Electronics, J. Cerny, Ed., Academic Press, Inc., New York, 1974.

153. Goulding, F.S. and Landis, D.A., "Some Electronic Aspects of Energy Measurements with Solid-State Detectors," IEEE Trans. Nucl. Sci. NS-25(2): 896-901, 1978.

154. Goulding, F.S. and Lothrup, R.P., "Some Observations of Radiation Damage in Lithium-Drifted Silicon Detectors," Semiconductor Nuclear- Particle Detectors and Circuits, p. 337, National Academy of Sciences Pub. No. 1593, 1969.

155. Goulding, F.S. and Pehl, R.H., "A Survey of Radiation Damage in Semiconductor Detectors," IEEE Trans. Nucl. Sci. NS-19(1): 91-99, 1972.

156. Goulding, F.S. and Stone, Y., "Semiconductor Radiation Detectors," Science 170: 280-289, 1970.

157. Goulding, F.S. et al, "Detector Background and Sensitivity of X-Ray Fluorescence Spectrometers," Proc. 20th Ann. Denver X-Ray Conf, Aug 11-13, 1971.

158. Goulding, F.S., "Pulse-Shaping in Low-Noise Nuclear Amplifiers: A Physical Approach to Noise Analysis," Nucl. Instrum. Meth. 100: 493-536, 1972.

159. Goulding, F.S., "Semiconductor Detectors - An Introduction," IEEE Trans. Nucl. Sci. NS-25(2): 916-920, 1978.

160. Goulding, F.S., Jaklevic, J.M. and Loo, B.W., "Development of Air Particulate Monitoring Systems," UCID-8090 Preprint, EPA Report IAG-D6-0377, Jan. 1978.

161. Goulding, F.S., Jaklevic, J.M., and Thompson, A.C., "Semiconductor Detectors for Fluorescent EXAFS," presented at the Workshop on X-Ray Instrumentation for Synchrotron Radiation Research, SLAC, Stanford, CA, April 3, 1978 (LBL-7542 Preprint).

162. Goulding, F.S., Walton, J. and Malone, D., "An Opto-Electronic Feedback Preamplifier for High-Resolution Nuclear Spectroscopy," Nucl. Instrum. Meth. 71: 273-279, 1969.

163. Gruhn, C.R., "Epitaxial Silicon Semiconductor Detectors Past Developments, Future Prospects," IEEE Trans.Nucl. Sci. NS-24(1): 93-103, 1977.

164. Guislan, H.J. and De Laet, L.H., "Lithium Driftability and Precipitation in Silicon," IEEE Trans. Nucl. Sci. 19(1): 323-328, 1971.

165. Hall, R.N., "Electron-Hole Recombination," General Electric Research Laboratory, Report 55-RL-1316, Publ. Research Information Services Section, The Knolls, Schenectady, NY, 1955.

166. Hall, R.N., "Characterization of Pure Germanium for Detector Fabrication," IEEE Trans. Nucl. Sci. NS-19(3): 266-270, 1972.

167. Haller, E.E., Hansen, W.L., and Goulding, F.S., "Evaluation of High-purity Germanium by Pulse Measurements on Detectors," IEEE Trans. Nucl. Sci. 19(3): 271-274, 1972.

168. Haller, E.E. and Goulding, F.S., "Nuclear Radiation Detectors," in Handbook on Semi-conductors, E.E. Haller and F.S. Goulding, Eds., N. Holland Publishing Co., 1978, (LBL-7521 Preprint March 1978).

169. Haller, E.E. and Hansen, W.L., "High Resolution Fourier Transform Spectroscopy of Shallow Acceptors in Ultra-Pure Germanium," Solid State Communications 15: 687-692, 1974.

170. Haller, E.E. et al, "Divacancy-Hydrogen Complexes in Dislocation-Free High Purity Germanium," in Radiation Effects in Semiconductors 1976, N.B. Urli and J.W. Corbett, Eds., 309-318, Inst. of Physics, Bristol and London, 1977.

171. Haller, E.E. et al, "Origin and Control of the Dominant Impurities in High- Purity Germanium," IEEE Trans. Nucl. Sci. NS-23(1): 81-87, 1976.

172. Haller, E.E., "Recent Advances in Common Semiconductor Materials," IEEE Trans. Nucl. Sci. NS-25(2): 921-926, 1978.

173. Haller, E.E., Hansen, W.L., and Goulding F.S., "Distribution of Donors and Acceptors in High-Purity Germanium Crystals," IEEE Trans. Nucl. Sci. NS-20(1): 481-487, 1973.

174. Haller, E.E., Hansen, W.L., and Goulding, F.S., "Photothermal Ionization Spectroscopy," IEEE Trans. Nucl. Sci. NS-22(1): 127, 1975.

175. Haller, E.E., Hubbard, G.S. and Hansen, W.L., "Hydrogen-Multivalent Acceptor Complexes in High Purity Germanium," IEEE Trans. Nucl. Sci. NS-24(1): 48-52, 1977.

176. Hansen, J.S. et al, "Accurate Efficiency Calibration and Properties of Semiconductor Detectors for Low-Energy Protons," Nucl. Instrum. Meth. 106: 365-379, 1973.

177. Hansen, W. and Goulding, F.S., "Leakage, Noise, Guard Rings and Resolution in Detectors," Proc. Asheville Conf. NAS-NRC Report No. 32, p. 202, 1961.

178. Hansen, W.L. and Haller, E.E., "Amorphous Germanium as an Electron or Hole Blocking Contact High-Purity Germanium Detectors," IEEE Trans. Nucl. Sci. NS-24(1): 61-63, 1977.

179. Hansen, W.L. and Haller, W.L., "High-Purity Germanium-Observations on the Nature of Acceptors," IEEE Trans. Nucl. Sci. NS-19(1): 260-269, 1972.

180. Hansen, W.L., "High-Purity Germanium Crystal Growing," Nucl. Instrum. Meth. 94: 377-380, 1971.

181. Hansen, W.L., "Selection of Germanium for Lithium-Drifted Radiation Detectors by Observation of Etch-Pit Distributions," Nucl. Instrum. Meth. 80(2): 181-186, 1970.

182. Hansen, W.L., Haller, E.E., "A View of the Present Status and Future Prospects of High Purity Germanium," IEEE Trans. Nucl. Sci. NS-21(1): 279, 1974.

183. Hanson, J.A. and Kopp, M.K., "Design and Properties of a Multianode, Cylindrical Proportional Counter for Position Sensing at High Count Rates," Rev. Sci. Intrum. 50(10): 1318-1319, 1979.

184. Harms, J., "Automatic Dead-time Correction for Multichannel Pulse-Height Analyzers at Variable Counting Rates," Nucl. Instrum. Meth. 53: 192-196, 1967.

185. Harvey, N.P. and Pernou, J.P., "The Traverse-Field Silicon Detector," IEEE Trans. Nucl. Sci. NS-17(3): 306-309, 1970.

186. Hayashi, S.R. and Bolon, R.B., "Backscatter Electron Detectors on Energy-dispersive X-Ray Spectrometers," 310, Microbeam Analysis - 1979, D.E. Newbury, Ed., San Francisco Press, 1979.

187. Headley, T.J. and Hren, J.J., "Sources of Background X-Radiation in Analytical Electron Microscopy," 9th Intn. Cong. on Electron Microscopy 1: 504-505, 1978.

188. Heath, R.L., "The Application of High-Resolution Solid State Detectors to X-Ray Spectrometry - A Review," Adv. X-Ray Anal. 15(1): 1-35, 1972.

189. Heinrich, K.F.J., Fiori, C.E., and Myklebust, R.L., "Progress in the Measurement of Relative X-ray Line Intensities," Proc. 11th MAS Conf. 1976, 29.

190. Heinrich, K.F., Fiori, C.E., and Myklebust, R.L., "Relative Transition Probabilities for the x-ray Lines from the K Level," J. Appl. Phys. 50(9): 5589-5591, 1979.

191. Henck, R. et al, "Trapping Effects in Ge(Li) Detectors and Search for a Correlation with Characteristics Measured on the P-Type Crystals," IEEE Trans. Nucl. Sci NS-17(3): 149-159, 1970.

192. Herman, A.W., McNelles, L.A., and Campbell, J.L., "Choice of Physical Parameters in Charged Particle Induced X-Ray Fluorescence Analysis," Int. J. App. Rad. Iso. 24: 677-688, 1973.

193. Herman, A.W., McNelles, L.A., and Campbell, J.L., "Target Backings for Charged Particle Induced X-Ray Fluorescence Analysis," Nucl. Instrum. Meth. 109: 429-437, 1973.

194. Hewka, P.V., Huth, G.C., and Swinth, K.L., "Biomedical Applications of Avalanche Semiconductor Radiation Detectors," IEEE Trans. Nucl. Sci. NS-17(3): 265-275, 1970.

195. Hubbard, G.S., Haller, E.E., and Hansen, W.L., "Characterization of Poly-crystalline Zone-Refined Ingots of High-Purity Germanium," Nucl. Instrum. Meth. 130: 481-485, 1975.

196. Hubbard, G.S., Haller, E.E., and Hansen, W.L., "The Effect of Crystal Growth Direction on the Energy Resolution of High-Purity Germanium Detectors," IEEE Trans. Nucl. Sci. NS-26(1): 303-307, 1979.

197. Hubbard, G.S., Haller, E.E. and Hansen, W.L., "Ion Implanted N-Type Contact for High-Purity Germanium Detectors," IEEE Trans. Nucl. Sci. NS-24(1): 161-164, 1977.

198. Hubbard, G.S., Haller, E.E., and Hansen, W.L., "Zone Refining High-Purity Germanium," IEEE Trans. Nucl. Sci. 24: 161-164, 1977.

199. Hurley, R.G. and Goss, R.L., "Quantitative Energy-Dispersive Analysis Using Relative k-Ratios," X-Ray Spectrom. 7: 70-72, 1978.

200. Ingamells, C.O. and Fox, J.J., "Deconvolution of Energy-Dispersive X-Ray Peaks Using the Poisson Probability Function," X-Ray Spectrom. 8(2): 79-84, 1979.

201. Iwanczyk, J., and Dabrowski, A.J., "The Effect of Charge Trapping on the Spectrometric Performance of n-Type CdTe Surface-Barrier Detectors," Nucl. Instrum. Meth. 134: 505-512, 1976.

202. Jaklevic, J.M. and Goulding, F.S., "Detection of Low Energy X-Rays with Si(Li) Detectors," IEEE Trans. Nucl. Sci. NS-18(1): 187-191, 1971.

203. Jaklevic, J.M. and Goulding, F.S., "Semiconductor Detector X-Ray Fluorescence Spectrometry Applied to Environmental and Biological Analysis," IEEE Trans. Nucl. Sci. NS 19(3): 384-391, 1972.

204. Jakelovic, J.M., Goulding, F.S., and Landis, D.A., "High Rate X-Ray Fluorescence Analysis by Pulsed Excitation," IEEE Trans. Nucl. Sci. NS-19(3), 392-395, 1972.

205. Jaklevic, J.M. et al, "Application of X-Ray Fluorescence Techniques to Measure Elemental Composition of Particles in the Atmosphere," 165th Am. Soc. Meeting on Anal. Methods Applied to Air Pollution Measurements, Dallas, April 8-13, 1973.

206. Jaklevic, J.M. et al, "Small X-Ray Tubes for Energy Dispersive Analysis Using Semiconductor Spectrometers," Adv. X-Ray Anal. 15: 266- 275, K.F.J. Heinrich et al, Eds., New York: Plenum Press.

207. Jaklevic, J.M. et al, "X-Ray Fluorescence Analysis Applied to Small Samples," Adv. X-Ray Anal. 21: 171-185, C.S. Barrett et al, Eds., Plenum Press, 1978.

208. Jaklevic, J.M., Loo, B.W., and Goulding, F.S., "Photon-Induced X-Ray Fluorescence Using Energy-Dispersive Detector and Dichotomous Sampler," in X-Ray Fluorescence Analysis of Environmental Samples, T.G. Dzubay, Ed., Ann Arbor Science Publ., Ann Arbor, Michigan, 3-17, 1977.

209. Johnson, H. and Deslattes, R., "Production of Alumina Windows," Rev. Sci. Inst. 36: 1381-82, 1965.

210. Jorch, H.H. and Campbell, J.L., "Analytic Fitting of Full Energy Peaks from Ge(Li) and Si(Li) Photon Spectrometers," Nucl. Instr. Meth. 143: 551-559, 1977.

211. Kandiah, K., "Some Limitations of Energy Dispersive X-Ray Spectrometers," Proc. 8th Nat. Conf. on Electron Probe Analysis, New Orleans, 12, 1963.

212. Kandiah, K., Smith, A. J., and White, G., "A Pulse Processor for X-Ray Spectrometry with Si(Li) Detectors," Proc. 2nd ISPRA Nucl. Electronics Symposium, Stresa, Italy, 1975, and IEEE Trans. Nucl. Sci. NS-22 (Oct.), 1975.

213. Karlovac, N. and Gedcke, D.A., "Improvements in High Counting Rate Performance of Si(Li) Energy spectrometers with a Novel Baseline Restoration Technique," Proc. 8th Conf. on Electron Probe Analysis, 1973, 17.

214. Katsanos, A. et al, "An External Beam Technique for Proton-Induced X-Ray Emission Analysis," Nucl. Instrum. Meth. 137: 119-124, 1976.

215. Kaufmann, L., Price, D.C., Holliday, M.A., Payne, B., Camp, D.C., Nelson, J.A., and Deconninck, F., "Fluorescence Excitation Analysis in Medicine," J. Radional. Chem. 43(2): 321-46, 1978.

216. Kellogg, E., Henry, P., Murray, S., and Van Speybroeck, L., "High Resolution Imaging X-Ray Detector," Rev. Sci. Instrum. 47(3): 282-290, 1976.

217. Keith, H.D. and Loomis, T.C., "Calibration and Use of a Lithium-Drifted Silicon Detector for Accurate Analysis of X-Ray Spectra," X-Ray Spectrom. 5: 93-103, 1976.

218. Kern, H.E. and McKenzie, J.M., "Methods of Reducing Noise of Junction Field Effect Transistor (JFET) Amplifiers," IEEE Trans. Nucl. Sci. NS-17(1): 260-268, 1970.

219. Kern, H.E. and McKenzie, J.M., "Noise Studies of Ceramic Encapsulated Junction Field Effect Transistors (JFETs)," IEEE Trans. Nucl. Sci. NS-17(3): 425-432, 1970.

220. Keyser, R.M., Bartell, D.M. and Moneymaker, R.S., "A Computer Program for Spectrum Analysis," Proc. 10th MAS Conf., 1975, 22.

221. Khan, MD. R. and Karimi, M., "K beta/K alpha Ratios in Energy-dispersive Emission Analysis," X-Ray Spectrom. 9(1): 32-35, 1980.

222. Kirkendall, T.D., "Comprehensive Qualitative and Quantitative Analysis of Energy Dispersive X-Ray Spectra," Proc. 9th MAS Conf., 1974, 24.

223. Kraner, H.W., "Si(Li) Coaxial Detectors," IEEE Trans. Nucl. Sci. NS-17(3): 215-220, 1970.

224. Kramer, B.R. and Hubbard, E.L., "The Effects of Long Term Storage on Lithium Drifted Silicon Detectors," IEEE Trans. Nucl. Sci. NS-16(4): 16-19, 1969.

225. Kubo, H., Bernthal, R., and Wildeman, T.R., "Energy-dispersive XRF Spectro- metric Determination of Trace Elements in Oil Samples," Anal. Chem. 50(7): 899-903, 1978.

226. Kurz, R., "Low Noise Preamplifier for High Count Rates," IEEE Trans. Nucl. Sci. NS-19(3), 418-422, 1972.

227. Landis, D.A. et al, "Pulsed Feedback Techniques for Semiconductor Detector Radiation Spectrometers," IEEE Trans. Nucl. Sci. NS-18(1): 115-124, 1971.

228. Langhernrich, A.P., Forster, J.W., and Linn Jr., T.A., "Energy Dispersion X-Ray (EDX) Analysis in the Non-Ferrous Mining Industry Analysis Instrumentation," Proc. of the 17th Annual ISA Analysis Inst. Symposium Vol. 9, Houston, Texas, April 19-21, 1971.

229. Leyden, D.E. and Lennox, J.C. Jr., "Data Acquisition and Control of Wavelength and Energy Dispersive X-Ray Spectrometers Using a Single Minicomputer," X-Ray Spectrom. 5: 137-141, 1976.

230. Lifshin, E., "The Generation and Detection of X-Rays in the Electron Microprobe and Scanning Electron Microscope," Proceedings of the Tutorial Session 7th Conf. on Electron Probe Analysis, 1969, 51.

231. Lifshin, E. and Ciccarelli, M.F., "Present Trends in X-Ray Analysis with the SEM," SEM/1973 (Part I), Om Johari, Ed., (IITRI), Chicago, IL, 89- 96, 1973.

232. Lifshin, E., "An Evaluation of a Solid-State X-Ray Detection System for Microprobe Analysis," Proc. 4th Conf. on Electron Microprobe Analysis, 51, 1969.

233. Lifshin, E., "Computer Processing of Solid-State X-Ray Detector Data," Proc. 8th Conf. on Electron Probe Analysis, 1970, 8.

234. Lifshin, E., "Factors Affecting Sensitivity of X-Ray Analysis with Electron Microbeam Instrumentation," in Microbeam Analysis in Biology, C. Lechene and R. Warner, Eds., Academic Press, Inc., 1979, 225-263.

235. Lifshin, E., "Quantitative Microprobe Analysis with Energy Dispersive Detectors - A Status Report," Proc. Denver X-Ray Conf., 1975.

236. Lifshin, E., "X-Ray Generation and Detection in the SEM," Scanning Electron Microscopy, O.C. Wells, Ed., New York, McGraw Hill, Ch. 10, 1974.

237. Lifshin, E., Ciccarelli, M.F. and Bolon, R.B., "New Measurements of the Voltage Dependence of Absolute X-Ray Yields," Proc. 12th MAS Conf., 1977, 104.

238. Lifshin, E., Ciccarelli, M.F. and Bolon, R.P., "Determinations of the Energy Distribution of the Continuum and the Ratio of Indirect to Direct X-ray Fluorescence," Proc. 8th Nat. Conf. on Electron Probe Analysis, 29, 1973.

239. Lifshin, E., Ciccarelli, M.F., and Bolon, R.B., "Measurement of Characteristic and Continuum X-Ray Production Efficiences," 7th Int. Conf. on X-Ray Optics and Microanalysis in Moscow-Kiev, July 9-16, 1974.

240. Lifshin, E., Ciccarelli, M.F., and Bolon, R.B., "X-ray Spectral Measurement and Interpretation," in Practical Scanning Electron Microscopy, Goldstein, J., Ed., New York: Plenum, 1975.

241. Liu, Y.M. and Coleman, J.A., "Electron Radiation Damage Effects in Silicon Surface-barrier Detectors," IEEE Trans. Nucl. Sci. NS-18(1), 192-199, 1971.

242. Llacer, J., "Accurate Measurement of Noise Parameters in Ultra-Low Noise Opto-Feedback Spectrometer Systems," IEEE Trans. Nucl. Sci. NS-22(5): 2033, 1975.

243. Llacer, J., "Geometric Control of Surface Leakage Current and Noise in Lithium Drifted Silicon Radiation Detectors," IEEE Trans. Nucl. Sci. NS-13(1): 103, 1966.

244. Llacer, J., Haller, E.E. and Cordi, R.C., "Entrance Windows in Germanium Low- Energy X-Ray Detectors," IEEE Trans. Nucl. Sci. NS-24(1): 53-60, 1977.

245. Llacer, J., "Optimum Filtering in the Presence of Dominant 1/f Noise," Nucl. Instrum. Meth. 130, 565-570, 1975

246. Loomis, T.C. and Keith, H.D., "Accurate Calibration of Efficiencies of X-Ray Detectors: Flow Proportional and Scintillation Counters," Appl. Spectrosc. 29(4): 316-322, 1975.

247. Lopes da Silva, G. et al, "Lithium Driftability in Germanium," IEEE Trans. Nucl. Sci. NS-15(1), 448-455, 1968.

248. Lothrop, R.P., "The Effects and Control of Surface States During Lithium Ion Drift in Silicon," UCRL Report No. 19413, 1969.

249. Lucas, C.H., "A Stable ADC for Use with Ge(li) Detectors," IEEE Trans. Nucl. Sci. NS-21(1): 798-804, 1974.

250. Lucke, R.L., "Counting Statistics for Nonnegligible Dead Time Corrections," Rev. Sci. Instrum. 47(6): 1976.

251. Lukirskii, A.P., Ershov, O.A., and Brytov, I.A., "Operation of Proportional Counters in the Ultra-soft X-Ray Region," Izv. Akad. Naur, SSSR, Ser. Fiz 27: 798-807, 1963.

252. Madden, N.W. et al, "A High-Resolution Si(Li) Spectrometer with Thermoelectric Cooling," submitted to Nucl. Instrum. Meth. (LRL- 7550 Preprint), July 1978.

253. Malm, S., "A Systematic Error in Energy-dispersive Microprobe Analysis of Ni in Steel Due to the Method of Background Subtraction," X-Ray Spectrom. 5(3): 118-122, 1976.

254. Manfredotti, C., Murri, R., Quirini, A., and Vasanelli, L., "PbI2 as Nuclear Particle Detectors," IEEE Trans. Nucl. Sci. NS-24(1): 126-129, 1977.

255. Manfredotti, C., Murri, R., Quirini, A., and Vasanelli, L., "The Photo-magnetoelectric Effect in Mercuric Iodide," IEEE Trans. Nucl. Sci. NS-24 (1): 158-160, 1977.

256. Maor, D. and Rosner, B., "Efficiency of Ge and Si(Li) Detectors at Very Low Energies by an X-Ray Doublet Method," J. Phys. E 11: 1141-1144, 1978.

257. Marshall, A.T. and Forrest, Q.G., "X-Ray Microanalysis in the Transmission Electron Microscope at High Accelerating Voltages," Micron. 8(3): 135-138, 1977.

258. Martini, M., McMath, T.A. and Fowler, I.L., "The Effects of Operating Temperature on the Behavior of Semiconductor Detectors," IEEE Trans. Nucl. Sci. NS-17(3): 139-148, 1970.

259. Masters, C.F. and East, L.V., "An Investigation Into the Harms Dead Time Correction Procedure for Pulse Height Analyzers Using Monte-Carlo Modeling Techniques," IEEE Trans. Nucl. Sci. 17: 383-389, 1970.

260. Mathieson, E. and Sanford, P.W., "Point Anode Proportional Counters," J. Sci. Inst. 40: 446-449, 1963.

261. Mayer, J.W. et al, "Influence of Trapping and Detrapping Effects in Si(Li), Ge(Li) and CdTe Detectors," IEEE Trans. Nucl. Sci. NS-17(3): 221-234, 1970.

262. McMath, T.A. and Martini, M., "The Effect of Charge Trapping on the Spectrometer Performance of p-i-n Semiconductor Detectors," Nucl. Instrum. Meth. 86(2): 245-252, 1970.

263. McNelles, L.A. and Campbell, J.L., "Absolute Efficiency Calibration of Coaxial Ge(Li) Detectors," Nucl. Instrum. Meth. 109: 241-251, 1973.

264. McNelles, L.A. and Campbell, J.L., "Analytic Approximations to Peak Shapes Produced by Ge(Li) and Si(Li) Spectrometers," Nucl. Instrum. Meth. 127: 73-81, 1975.

265. Middleman, L.M. and Geller, J.D., "Trace Element Analysis Using X-Ray Excitation with an Energy Dispersive Spectrometer on a Scanning Electron Microscope," SEM/76 (Part I), Om Johari, Ed., (IITRI), Chicago, IL: 171-178, 1976.

266. Miehe, J.A. and Siffert, P., "Timing Performance of Ge(Li) Detectors," IEEE Trans. Nucl. Sci. NS-17(5): 8-17, 1970.

267. Mitra, S., Sinha, A.K., and Roy, S.C., "Proportional Response Photon Counter," Rev. Sci. Instrum. 51(6): 821-823, 1980.

268. Moll, S.H., Baumgarten, N., and Donnelly, W., "Geometrical Considerations for ZAF Corrections in the SEM," Proc. of 85h International Conf. on X-Ray Optics and Microanalysis and 12th Annual MAS Conf., Boston, Mass., 1977.

269. Morgenstern, P., "Proportional Scintillation Detector for Spectrometry of Ultra Weak X-Rays," Isotopenpraxis 17(5): 159-160, 1978.

270. Mulvey, T. and Campbell, A.J., "Proportional Counters in X-Ray Spectro-Chemical Analysis," B. J. of Appl. Phys. 9: 406-410, 1958.

271. Murray, R.T., "A Filter to Remove Backscattered Electrons for Energy-dispersive Analysis in a Scanning Microscope," J. of Phys. E 12: 1141, 1979.

272. Musket, R.G. and Bauer, W., "Determination of Gold-Layer and Dead-Layer Thicknesses for a Si(Li) Detector," Nucl. Instrum. Meth. 109: 593-595, 1973.

273. Musket, R.G. and Bauer, W., "Determinations of Oxide Thickness on Tritiaded Erbium Films Using Beta-Induced X-Ray Fluorescence," J. of Appl. Phys. 47(1): 353-356, 1976.

274. Musket, R.G., "Detection of Proton-Induced Boron X-Rays with a Si(Li) Detector," Nucl. Instrum. Meth. 117: 385-389, 1974.

275. Myklebust, R.L. and Heinrich, K.F.J., "Rapid Quantitative Electron Probe Microanalysis with a Nondiffractive Detector System," STP 485, American Society for Testing and Materials, 232-242, 1971.

276. Myklebust, R.L. et al, "Data Reduction Procedure for Monochromatic X-Ray Fluorescence Analysis with a Si(Li) Detector," Proc. 3rd Ann. Conf., Federation of Analytical Chemistry and Spectroscopy Societies, paper 241, 1976.

277. Myklebust, R.L., Fiori, C.E., and Heinrich, K.F.J., "FRAME C: A Compact Procedure for Quantitative Energy-Dispersive Electron Probe X-ray Analysis," Proc. of the 8th Intern. Conf. on X-ray Optics and Microanalysis and the 12th MAS Conf., 1977, 18.

278. Myklebust, R.L. and Newbury, D.E., "The Use and Abuse of a Quantitative Analysis Procedure for Energy-dispersive X-Ray Miroanalysis," Microbeam Analysis-1979, 231-237, D.E. Newbury, Ed., San Francisco Press, 1979.

279. Namenson, A.I., "Statistical Treatment of Damage Factors for Semiconductor Devices," IEEE Trans. Nucl. Sci. NS-26(5): 4691-4694, 1979.

280. Nass, M.J., Lurio, A., and Ziegler, J.F., "Computer Analysis of X-Ray Spectra," Nucl. Instrum. Meths. 154: 567-571, 1978.

281. Neumann, B., Reimer, L., and Wellmans, B., "A Permanent Magnet System for Electron Deflection in Front of an Energy Dispersive X-Ray Spectrometer," Scanning 1(2): 130, 1978.

282. Nielson, K.K., "Applications of Direct Peak Analysis to Energy-dispersive X-Ray Fluorescence Spectra," X-Ray Spectrom. 7(1): 15-22, 1978.

283. Noble, A.C. et al, "Trace Element Analysis of Wine by Proton-Induced X-Ray Fluorescence Spectrometry," J. Agric. Food Chem. 24: 532-535, 1976.

284. Nowlin, C.H. and Blankenship, J.L., "Elimination of Undesirable Undershoot in the Operation and Testing of Nuclear Pulse Amplifiers," Rev. Sci. Inst. 36(12): 1830-1839, 1965.

285. Nowotny, R. and Reiter, W.L., "A Comparison of Commercial PIN-Photodiodes for X-Ray Spectrometry," Nucl. Instrum. Meths. 153(E): 597-598, 1978.

286. Nullens, H., Van Espen, P. and F. Adams, "Linear and Non-linear Peak Fitting in Energy Dispersive X-Ray Fluorescence," X-Ray Spectrom. 8(3): 104-109, 1979.

287. Parker, M.A. and Warke, W.R., "Determination of the Effective Take-off Angle on Scanning Electron Microscope Energy-dispersive X-Ray Analysis Systems," Microbeam Analysis-1980, 65-67, D.B. Wittry, Ed., San Francisco Press, 1980.

288. Parus, J.L., Raynski, W., Zoltowski, T., Tys, J., Kierzek, J., Ceslak, E.K., and Kownacki, J., "Data Evaluation in Non-dispersive XRF Analysis of Copper Ore Processing Materials," J. Radioanal. Chem. 44(1): 1978.

289. Pawley, J., Statham, P.J., and Menzel, T., "Use of Beam Blanking and Digital Scan-Stop to Speed the Microanalysis of Particles," SEM/77 (Part I), Om Johari, Ed., (IITRI), Chicago, IL., 297-306, 1977.

290. Pehl, R.H. and Goulding, F.S., "Recent Observations on the Fano Factor in Germanium," Nucl. Instrum. Meth. 81(2): 329, 1970.

291. Pehl, R.H. et al, "Accurate Determination of the Ionization Energy in Semiconductor Detectors," Nucl. Instr. Meth. 59: 45-55, 1968.

292. Pehl, R.H., "Radiation Damage of Germanium Detectors," Proc. of Gamma Ray Spectroscopy in Astrophysics Symposium, Goddard Space Flight Center, Greenbelt, MD, April 28-29, 1978.

293. Pehl, R.H., Cordi, R.C. and Goulding, F.S., "High-Purity Germanium: Detector Fabrication and Performance," IEEE Trans. Nucl. Sci. NS-19(1): 265-269, 1972.

294. Pehl, R.H., Haller, E.E. and Cordi, R.C., "Operational Characteristics of Germanium Detectors at Higher Temperatures," IEEE Trans. Nucl. Sci. NS-20(1): 494-499, 1973.

295. Pehl, R.H., Varnell, L.S. and Metzger, A.E., "High-Energy Proton Radiation Damage of High-Purity Germanium Detectors," IEEE Trans. Nucl. Sci. NS-25(1): 409-417, 1978.

296. Pell, E.M., "Ion Drift in an n-p Junction," J. of Appl. Phys. 31(2): 291-302, 1960.

297. Phillips, G.W. and Marlow, K.W., "Peak Search and Analysis of Gamma-Ray Spectra with Very Low Statistics," IEEE Trans. Nucl Sci. NS-24(1): 154-157, 1977.

298. Picot, A., "Some Remarks on the Determination of Dead Time by the Two Sources Method," Rev. Sci. Instrum. 47(3): 385-386, 1976.

299. Pinsky, E., Halpern, A., Beinglass, I., and Schieber, M., "X-Ray Luminescence of Mercuric Iodide Nuclear Detectors," IEEE Trans. Nucl. Sci. NS-24 (1): 260-263, 1977.

300. Plant, A.G. and Lachance, G.R., "Quantitative Electron Microprobe Analysis Using an Energy Dispersive Spectrometer," Proc. 8th Nat. Conf. Electron Probe Analysis, 1972, 13.

301. Poenaru, D.N., Stuck, R. and Siffert, P., "Collection Efficiency and Charge Carrier Losses in Coaxial and Planer Ge(Li) Detectors: Influence on the Time Resolution," IEEE Trans. Nucl. Sci. NS-17(3): 176-186, 1970.

302. Porter, D.E. and Woldseth, R., "X-Ray Energy Spectrometry," Anal. Chem. 45(7): 604a-614a, June 1973.

303. Quinton, P.M., "EDS X-ray Analysis of Liquid Microdroplets," Microbeam Analysis-1980, D.B.Wittry, Ed., San Francisco Press, 115-119, 1980.

304. Quinton, P.M., "Ultramicroanalysis of Biological Fluids with Energy-dispersive X-Ray Spectrometry," Micron. 9(2): 57-69, 1978.

305. Radeka, V. and Karlovac, N., "Time-Varient Filters," in Semiconductor Radiation Detectors and Circuits, National Academy of Sciences Pub. No. 1593, p. 553, 1969.

306. Radeka, V., "Charge Amplification Without Charge Leak Resistor," IEEE Trans. Nucl. Sci. NS-17(3): 433-439, 1970.

307. Radeka, V., "Field Effect Transistor Noise as a Function of Temperature and Frequency," Semiconductor Nuclear Particle Detectors and Circuits, N.A.S. Publ. 1593, Washington, D.C., p. 393, 1969.

308. Radeka, V., "Overload Recovery Circuit for Charge Amplifiers," IEEE Trans. Nucl. Sci. NS-17(1): 269-275, 1970.

309. Radeka, V., "Trapezoidal Filtering of Signals from Large Germanium Detectors at High Rates," IEEE Trans. Nucl. Sci. NS-19(1), 412-428, 1972.

310. Radeka, V., "High Resolution Liquid Argon Total-absorption Detectors: Electronic Noise and Electrode Configuration," IEEE Trans. Nucl. Sci. NS-24(1): 293-298, 1977.

311. Randtke, P.T. and Ortale, C., "The Effects of Dislocations and Crystal Detectors on the Energy Resolution and Response Uniformity of Mercuric Iodide Detectors," IEEE Trans. Nucl. Sci. NS-24(1): 129-134, 1977.

312. Reed, S.J.B., "The Shape of the Continuous X-Ray Spectrum and Background Corrections for Energy Dispersive Electron Microprobe Analysis," X-Ray Spectrom. 4(1): 14-17, 1975.

313. Reed, S.J.B. and Ware, N.G., "Escape Peaks and Internal Fluorescence in X-Ray Spectra Recorded with Lithium Drifted Silicon Detectors," J. Phys. E 5: 582-584, 1972.

314. Reed, S.J.B. and Ware, N.G., "Quantitative Electron Microprobe Analysis of Silicates Using Energy-Dispersive X-Ray Spectrometry," J. Petrol. 16: 499-519, 1975.

315. Reed, S.J.B. and Ware, N.G., "Quantitative Electron Microprobe Analysis Using a Lithium Drifted Silicon Detector," X-Ray Spectrom. 2: 69-74, 1973.

316. Reed, S.J.B. and Ware, N.G., "The Measurement of X-ray Peak Intensities with a Lithium Drifted Silicon Detector by Integration Over a Fixed Energy Range," J. Phys. E 5: 1112-1114, 1972.

317. Reed, S.J.B., "Dead Time Corrections for X-Ray Intensity Measurements with a Si(Li) Detector," J. Phys. E 5: 994-996, 1972.

318. Reed, S.J.B., "Electron Microprobe Analysis," Cambridge University Press, Chapters 9, 10 and 17, 1975.

319. Reed, S.J.B., "Pulse Pile-Up Rejection in Si(Li) X-Ray Detection Systems," J. Phys. E 5: 997-999, 1972.

320. Renan, M.J., "Optimization of Trace Analysis by PIXE: Angular Dependence of the Background Continuum," X-Ray Spectrom. 9(2): 90-94, 1980.

321. Rhodes, J.R., "Design and Application of X-ray Emission Analyzers Using Radioisotope X-ray or Gamma Ray Sources," STP 485, American Society for Testing and Materials, 243-285, 1971.

322. Rhodes. J.R., "Energy-dispersive X-Ray Spectrometry for Multielement Pollution Analysis," IEEE Trans. Nucl. Sci. NS-21(1): 608-617, 1974.

323. Rose, M.E. and Korff, S.A., "An Investigation of the Properties of Proportional Counters I," Phys. Rev. 59: 850-859, 1941.

324. Rosner, B., and Gur, D., "Determination of the Efficiency Curve of a Ge(Li) Detector Near the Germanium K-edge (E=11.04 keV)," Nucl. Instrum. Meth. 111: 577-580, 1973.

325. Rosner, B.,Gur, D. and Shabason, L., "Efficiency of Ge(Li) and Si(Li) Planer Detectors in the 2-5 keV Energy Range," Nucl. Instrum. Meth. 131: 81-85, 1975.

326. Rossi, B.B. and Staub, H.H., Ionization Chambers and Counters, McGraw Hill, New York, 1949.

327. Russ, J.C., Ed., Energy Dispersion X-ray Analysis: X-ray and Electron Probe Analysis, STP 485, American Society for Testing and Materials, Philadelphia, 1970.

328. Russ, J.C. and Barbi, N.C., "Removing Substrate Background in TEM Micro-analysis," Proc. of the Electron Microscope Society of America, 32nd Annual Meeting, 568-579, 1974.

329. Russ, J.C. and Barnhart, M.W., "The EDIT System for Computer Reduction of Energy-Dispersive X-Ray Data," 6th International Conf. on X-Ray Optics and Microanalysis, Osaka, Sept., 271-278, 1971.

330. Russ, J.C. and Kabaya, A., "Use of a Non-Dispersive X-ray Spectrometer on the Scanning Electron Microscope," SEM/1969, Om Johari, Ed., (IITRI), Chicago, IL, 1969, 57-64.

331. Russ, J.C. et al., "An Integrated System for Elemental X-Ray Analysis of Materials," Advances in X-Ray Analysis 16: 1973.

332. Russ, J.C., "A Fast Self-Contained No-Standards Quantitative Program for EDS," Proc 12th MAS Conf. 1978, 46.

333. Russ, J.C., "A Simple Correction for Backscattering from Inclined Samples," Proc. 10th MAS Conf. 1975, 7.

334. Russ, J.C., "Background Subtraction for Energy-Dispersive X-Ray Spectra," Proc. 7th National Conference on Electron Probe Analysis, 1972, 76.

335. Russ, J.C., "Energy-Dispersion X-ray Analysis on the Scanning Electron Microscope," STP 485, American Society for Testing and Materials, Philadelphia, 154-179, 1970.

336. Russ, J.C., "Energy-Dispersion X-Ray Detection in the Scanning Electron Micro- scope," 7th International Congress on Electron Microscopy, Grenoble, 1970, 231-232.

337. Russ, J.C., "Erroneous Si Peaks in Energy Dispersive Spectra," Proc. 24th Annual Denver X-Ray Conference,Denver, Colorado, August 1975, 161-165.

338. Russ, J.C., "Evaluation of the Direct Element Ratio Calculation Method," Jour. De Microscopie 22(2-3): 283-286, 1973.

339. Russ, J.C., "Interactive Displays and Simple Algorithms as an Aid to Qualitative Analysis of Energy Dispersive Spectra," Proc. 13th MAS Conf. 1978, 54.

340. Russ, J.C., "Light Element Analysis Using the Semiconductor X-Ray Energy Spectrometer with Electron Excitation," STP 485, American Society for Testing and Materials, 217-231, June 1970.

341. Russ, J.C., "Microanalysis of Thin Sections in the TEM and STEM Using Energy-Dispersive X-Ray Analysis," Electron Microscopy and Cytochemistry, Proc. 2nd International Symposium, Drienerio, 1973, E.Wisse, W. Th. Daems, I. Molennar, P. van Duijn, Eds., 1974, 223-228.

342. Russ, J.C., "Microanalysis of Thin Sections, Coatings and Rough Surfaces," SEM/1973, Om Johari, Ed., (IITRI) Chicago, IL, 1973.

343. Russ, J.C., "Obtaining Quantitative Information from an SEM Equipped with an Energy-Dispersive X-Ray Analyzer," Proc. SEM 1973, Conference Series No. 18, Institute of Physics, London and Bristol, 238-241, 1973.

344. Russ, J.C., "Performance Characteristics of the Non-Dispersive X-ray Spectrometer," Proc. 27th Annual Meeting, EMSA, 1969, 92-93.

345. Russ, J.C., "Problems in Using Fixed Energy Windows to Get Intensity Values from Energy Dispersive X-Ray Spectra," Proc. Annual Denver X-Ray Conference, p. 96, 1977.

346. Russ, J.C., "Procedures for Quantitative Ultralight Element Energy Dispersive X-Ray Analysis," SEM/77 (Part I), Om Johari, Ed., (A.M.F. O'Hare, IL), 289, 1977.

347. Russ, J.C., "Procedures for Quantitative Ultralight Element Energy Dispersive X-Ray Spectra Using Fixed Energy Windows," Proc. 12th MAS Conf., 1977, 97.

348. Russ, J.C., "Processing of Energy Dispersive X-Ray Spectra," Proc. Annual Denver X-Ray Conference, p. 81, 1976.

349. Russ, J.C., "Processing of Energy Dispersive X-Ray Spectra," X-Ray Spectrom. 6(1): 37-55, 1977.

350. Russ, J.C., "Progress in the Design and Application of Energy-Dispersion X-Ray Analyzers for the Scanning Electron Microscope," SEM/1971, Om Johari, Ed., (IITRI) Chicago, IL, 65-72, 1971.

351. Russ, J.C., "Quantitative Results with X-Ray Fluorescence Spectrometry Using Energy-Dispersive Analysis of X-Rays," X-Ray Spectrom. 1(3): 119, 1971.

352. Russ, J.C., "Resolving Spectrum Interferences Using Non-Gaussian Peaks," Canadian Spectroscopy, February 1976.

353. Russ, J.C., "TEM and STEM Microanalysis," Proc. 34th Annual EMSA Meeting, p. 562, 1976.

354. Russ, J.C., "Use of Energy-Dispersion X-Ray Analysis on the Electron Micro- probe," 6th International Symposium on Microtechniques, Graz, September, 1970, 221-225.

355. Russ, J.C., "X-Ray Methods in the Scanning Electron Microscope," Scanning Electron Microscopy/Methods and Phenomena, W.R. Bottoms, Ed., 1974.

356. Russ, J.C., "X-Ray Microanalysis at High Beam Voltages," SEM/76 (Part I), Om Johari, Ed., (IITRI), Chicago, 1976, 143-150.

357. Russ, J.C., "X-Ray Microanalysis in the Biological Sciences," J. of Submicroscopic Cytology 6(1): A. Bairati, B. Baccetti, and R. Laschi, Eds., April, 1974.

358. Russ, J.C., "X-Ray Spectroscopy on the Electron Microscope," X-Ray Spectrom. 2(1): 1973.

359. Russ, J.C., and Sandborg, A.O., "Evaluation of Pulse Pileup Rejection," Proc. Annual Denver X-Ray Conference, p. 93, 1977.

360. Russ, J.C., and Shen, R.B., "An Efficient Combined ED/WD X-ray Analysis System," Proc.13th MAS Conf., 1978, 86.

361. Russ, J.C., Baerwaldt, G.C., and McMillan, W.R., "Routine Use of a Second Generation Windowless Detector for Energy Dispersive Ultra- Light Element X-Ray Analysis," X-Ray Spectrom. 5(3): 212-222, 1976.

362. Russ, J.C., Sandborg, A.O., and Barnhart, M.W., "Energy-Dispersive X-Ray Fluorescence Analysis: Use of Multi-Element Detection for Rapid On-Line Classification and Sorting," XVII Colloquium Spectroscopicum International 1973, Florence, September, 1973.

363. Russ, J.C., Shen, R.B. and Jenkins, R., "EXAM: Principles & Experiments," published by EDAX International, Inc., 1977.

364. Russ, J.C, "Automatic Fitting of Calculated Backgrounds in Energy Dispersive X-Ray Spectra," Proc. 8th MAS Conf. 1977, 102.

365. Russ, J.C, "Measuring Detector Entrance Windows," Proc. 8th MAS Conf. 1977, 105.

366. Sakai, E., "Slow Pulses from Germanium Detectors," IEEE Trans. Nucl. Sci. NS-18(1): 208-218, 1971.

367. Sandborg, A.O. and Lichtinger, R.W., "An Energy Dispersive Spectrometer for Elements from 6 to 92," Proc. 8th MAS Conf. 1977, 107.

368. Sandborg, A.O. and Russ, J.C., "Counting Rate Performance of Pulsed- Tube Systems," Proc. Annual Denver X-Ray Conference, p. 65, 1976.

369. Sandborg, A.O., "Energy Dispersion X-ray Analysis with Electron and Isotope Excitation," STP 485, American Society for Testing and Materials, 113-124, 1971.

370. Savitzky, A. and Golay, M.J.E., "Smoothing and Differentiation of Data by Simplified Least Squares Procedures," Anal. Chem. 36: 1627-1639, 1964.

371. Schamber, F.H., "A New Technique for Deconvolution of Complex X-Ray Energy Spectra," Proc. 8th Nat. Conf. on Electron Probe Analysis, 1973, 85.

372. Schamber, F.H., "A Modification of the Linear Least-Squares Fitting Method Which Provides Continuum Suppression," in X-Ray Fluorescence Analysis of Environmental Samples, T.G. Dzubay, Ed., Ann Arbor Sci., 241-257.

373. Schieber, M., Ed., "Proc. Intern. Workshop on HgI2 and CdTe Nuclear Detectors," Jerusalem, June 6-8, 1977.

374. Schieber, M., Beinglass, I., Holzer, A., and Dishon, G., "The Behavior of HgI2 Nuclear Detectors Irradiated with High X-Ray Fluences," IEEE Trans. Nucl. Sci. NS-24(1): 148-153, 1977.

375. Schwartz, L.M., "Calibration Curves with Nonuniform Variance," Anal. Chem., 51(6): 691-694, 1979.

376. Schwartz, L.M., "On Round-Off Error," Anal. Chem. 52(7): 1141-1151, 1980.

377. Semiconductor Nuclear Particle Detectors and Circuits, National Academy of Sciences Publication number 1593, Washington, DC 1969.

378. Servant, J.M., Meny, L., and Champigny, M., "Energy Dispersion Quantitative X-Ray Microanalysis on a Scanning Electron Microscope," X-Ray Spectrom. 4: 99-100, 1975.

379. Shen, R.B., "A Simplified Fundamental Parameters Method for Quantitative Energy Dispersive X-Ray Fluorescence Analysis," X-Ray Spectrom. 6(1): 56, 1977.

380. Shen, R.B., Russ, J.C., and Stroeve, A.W., "Modelling Intensity and Concentration in Energy Dispersive X-Ray Fluorescence," Proc. Annual Denver X-Ray Conference, p. 129, 1978.

381. Sher, A.H. and Coleman, J.A., "Lithium Driftability in Detector-grade Germanium," IEEE Trans. Nucl. Sci. NS-17(3): 125-129, 1970.

382. Sher, A.H. and Keery, W.J., "Variation of the Effective Fano Factor in a Ge(Li) Detector," IEEE Trans. Nucl. Sci. NS-17(1): 39-40, 1970.

383. Sherry, W.M. and Vandersande, J.B., "A Background Correction for Energy-dispersive X-Ray Analysis of Thin Sections," X-Ray Spectrom. 6(3): 154-160, 1977.

384. Short, J.M., "Time-Shared Computer Treatment of Energy Dispersive X-Ray Data," SEM/1973, Om Johari, Ed., (IITRI), Chicago, IL, 1973, 95-112.

385. Short, M.A., "Optimum 'Windows' in Quantitative Energy Dispersive Analysis," X-Ray Spectrom. 5: 169-171, 1976.

386. Sikkema, C.P., "Elimination of End Effects in Proportional Counters," Nucl. Inst. 1: 148-151, North Holland Pub. Co., 1957.

387. Sioshansi, P. and Lodhi, A.S., "Escape Peak Losses in Si(Li) Detectors," X-Ray Spectrom. 8(2): 65-67, 1979.

388. Sipla, H., "The Statistics of Gas Gain in Penning Mixtures," IEEE Trans. Nucl. Sci. NS-26(1): 181-185, 1979.

389. Slapa, M., Huth, G.C., Seibt, W., Schieber, M.M., and Randtke, P.T., "Capabilities of Mercuric Oxide as a Room Temperature X-Ray Detector," IEEE Trans. Nucl. Sci. NS-23(1): 102-111, 1976.

390. Small, J.A. et al, "The Production and Characterization of Glass Fibers and Spheres for Microanalysis," SEM/78 (Part I), Om Johari, Ed., (SEM Inc., A.M.F. O'Hare, IL), 445-454, 1978.

391. Smith, C.F. and Conway, D.C., "Distortion of Proportional Counter Spectra by Counter Poisons," Rev. Sci. Inst. 33(7) 726-729, July 1962.

392. Smith, D.G.W., "An Approach to Fully Quantitative Energy Dispersive Electron Microprobe Analysis," Proc. 10th MAS Conf., 1975, 21.

393. Smith, D.G.W., "Applications of Quantitative Energy Dispersive Electron Microprobe Analysis in the Study of Mineral Chemistry," Proc. 11th Mtg. Internat. Mineral. Assoc., Novosibirsk, USSR (in press), 1978.

394. Smith, D.G.W., "Quantitative Energy Dispersive Microanalysis," Short Course Handbook, Vol. 1: Microbeam Techniques, D.G.W. Smith, Ed., 63- 106, Mineralogical Association of Canada, 1976.

395. Smith, D.G.W., and Cavell, P.A., "An Energy Dispersive Technique for the Quantatitive Analysis of Clay Minerals by the Electron Microprobe," Proc. 13th MAS Conf., 1978, 45.

396. Smith, D.G.W., and Gold, C.M., "A Scheme for Fully Quantitative Energy Dispersive Microprobe Analysis," Adv. in X-ray Anal. 19: 191-201, 1976.

397. Smith, D.G.W., Gold, C.M., and Tomlinson, D.A., "The Atomic Number Dependance of the X-ray Continuum Intensity and the Practical Calculation of Back- ground in Energy Dispersive Electron Microprobe Analysis," X-Ray Spectrom. 4: 149-156, 1975.

398. Smith, D.G.W., Reed, S.J.B., and Ware, N.G., "KB/KA Intensity Ratios for Elements of Atomic Number 20 to 30," X-Ray Spectrom. 3: 149-150, 1974.

399. Solosky, L.F. and Beaman, D.R., "A Simple Method for Determining the Acceleration Potential in Electron Probes and Scanning Electron Microscopes," Rev. of Sci. Inst. 43(8): 1100-1102, Aug. 1972.

400. Spatz, R. and Lieser, K.H., "Matrix Correction of Siliceous Samples by Means of the Compton-scattering Peaks for Energy-dispersive XRFA," Fresenius Z. Anal. Chem., (293) 25-29, 1978.

401. Spatz, R. and Lieser, K.H., "Optimization of a Spectrometer for Energy-dispersive X-Ray Fluorescence Analysis by X-Ray Tubes in Combination with Secondary Targets for Multielement Determination," X-Ray Spectrom. 8(3): 104-109, 1979.

402. Spielberg, N., "Effect of Anode Material on Intensity Dependent Shifts in Proportional Counter Pulse Height Distributions," Rev. Sci. Instr. 38(2): 291, Feb. 1967.

403. Sprys, J.W., "Specimen Holder for Energy Dispersive X-Ray Analysis in the Transmission Electron Microscope," Rev. Sci. Instr. 46(6): 773, 1975.

404. Statham, P.J. et al, "Quantitative Analysis with an Energy Dispersive Detector Using a Pulsed Electron Probe and Active Signal Filtering," X-Ray Spectrom. 3: 153-158, 1974.

405. Statham, P.J., "A Comparative Study of Techniques for Quantitative Analysis of the X-Ray Spectra Obtained with a Si(Li) Detector," X-Ray Spectrom. 5: 16-28, 1976.

406. Statham, P.J., "A Comparison of Some Quantitative Techniques for Treating Energy Dispersive X-Ray Spectra," Proc. 9th MAS Conf., 1974, 21.

407. Statham, P.J., "Beam Switching: A Technique to Improve the Performance of Pulse Processing Electronics for EDS," Proc. 11th MAS Conf., 1976, 11.

408. Statham, P.J., "Corrections for the Bremsstrahlung Background in EDS Microprobe Analysis of Thick Specimens," Proc. 11th MAS Conf., 1976, 10.

409. Statham, P.J., "Deconvolution and Background Subtraction by Least Squares Fitting with Prefiltering of Spectra," Anal. Chem. 49: 2149, 1977.

410. Statham, P.J., "Escape Peaks and Internal Fluorescence for a Si(Li) Detector and General Geometry," J. Phys. E. 9: 1023, 1976.

411. Statham, P.J., "Measurement and Use of Peak-to-Background Ratios in X-Ray Analysis," Proc. "Neuntes Kolloquim Uber Metallkundliche Analyse," Vienna, Austria, Oct. 1978.

412. Statham, P.J., "Pile-up Rejection: Limitations and Corrections for Residual Errors in Energy Dispersive Spectrometers," X-Ray Spectrom. 6: 94-103, 1977.

413. Statham, P.J., "Pitfalls in Linear and Non-Linear Profile-Fitting Procedures for Resolving Severely Overlapped Peaks," X-Ray Spectrom. 7: 132-137, 1978.

414. Statham, P.J., "Reliability in Data-Analysis Procedures for X-Ray Spectra," Proc. 8th Intn. Conf. on X-ray Optics and Microanalysis; 12th MAS Conf., 1977, 95.

415. Statham, P.J., "Resolution Enhancement of X-Ray Spectra," Proc. 8th Intn. Conf. on X-Ray Optics and Microanalysis; 12th MAS Conf., 1977, 103.

416. Statham, P.J., "The Application of the Harwell Active Pulse Processor to Energy Dispersive X-Ray Analysis in the Electron Microprobe," Proc. 9th MAS Conf., 1974, 55.

417. Statham, P.J., "The Generation, Absorption and Anisotropy of Thick-Target Bremsstrahlung and Implications for Quantitative Energy Dispersive Analysis," X-Ray Spectrom. 5: 154-168, 1976.

418. Statham, P. J. and Pawley J. B., "A New Method of Particle X-Ray Micro-Analysis Based on Peak to Background Measurements," SEM/78 (Part I), Om Johari, Ed., (SEM Inc., A.M.F. O'Hare, IL), 469-478, 1978.

419. Stein, J.D. and White, F.A., "Window Thickness Measurement of Surface Barrier Detectors," IEEE Trans. Nucl. Sci. NS-17(7): 37-39, 1970.

420. Stewart, J.E., "Resolution Enhancement of X-Ray Fluorescent Spectra with a Computerized Multichannel Analyzer," Appl. Spectrosc. 29(2): 171-174, 1975.

421. Stewart, J.E., Zulliger, H.R., and Drummond, W.E., "Energy Dispersive X-Ray Fluorescence Spectrometry at High Count Rates with Recovery of Resolution by Computer Processing," Proc. of the 24th Ann. Conf. on Applications of X-Ray Analysis, Denver, Aug. 6-8, 1975.

422. Strauss, M.G., Sherman, I.S., Cattelino, M.J., Brenner, R., and Pehl, R.H., "Intrinsic Efficiency of Germanium - A Basis for Calculating Expected Detector Efficiency," IEEE Trans. Nucl. Sci. NS-24(1): 89-92, 1977.

423. Strokhan, N.B., Yeryomin, V.K., Lomashevich, S.A., and Tisnek, N.I., "Final Results on the Nature of the Pulse-height Spectrum from Semiconductor Detectors," IEEE Trans. Nucl. Sci. NS-19(3): 365-379, 1972.

424. Sutfin, L.V. and Ogalvie, R.E., "Role of the Gas Flow Proportional Counter in Energy Dispersive Analysis," STP 485, American Society for Testing and Materials, 197-216, 1971.

425. Swierkowski, S.P., "A Comprehensive Model For Predicting Semiconductor Detector Performance," IEEE Trans. Nucl. Sci. NS-23(1): 11-137, 1976.

426. Swierkowski, S.P. and Armantrout, G.A., "Prognosis for High-Z Semiconductor Detectors," IEEE Trans. Nucl. Sci. NS-22(1): 205-210, 1975.

427. Swierkowski, S.P., et al, "Recent Advances with HgI2 X-Ray Detectors," IEEE Trans. Nucl. Sci. NS-21(1): 302, 1974.

428. Tenny, H., "Rapid Analysis of Particles Using a Non-Dispersive X-Ray Analyzer," Metallography 1: 221-225, 1968.

429. Tove, P.A., Cho, Z.H. and Huth, G.C., "The Importance of the Time Scale in Radiation Detection Exemplified by Comparing Conventional and Avalanche Semiconductor Detectors," Physica Scripta 13: 83-92, 1976.

430. Trammel, R.C., "Semiconductor Detector Fabrication Techniques," IEE Trans. Nucl. Sci. NS-25(2): 910-915, 1978.

431. Trammel, R. and Walter, F.J., "The Effects of Carrier Trapping in Semiconductor Gamma-Ray Spectrometers," Nucl. Instrum. Meth. 76: 317-321, 1969.

432. Van der Heide, J.A., Kivits, H.P.M., and Beuzekom, D.C., "The PIXE Facility at Eindhoven University of Technology" X-Ray Spectrom. 8, No. 2, 63-64, 1979.

433. Van Espen, P. and Adams, F., "Evaluation of a Practical Background Calculation Method in X-Ray Energy Analysis," X-Ray Spectrom. 5(3): 123-128, 1976.

434. Van Espen, P., Nullens, H. and Adams, F., "Radiative Auger Effect in X-Ray Fluorescence Analysis," Anal. Chem. 51(8): 1325-1328, 1979.

435. Van Espen, P., Nullens, H. A. and Adams, F. C., "Possible Errors in Energy-dispersive X-Ray Spectrometry Due to Raman Scattering," Anal. Chem. 51(9): 1580-1583, 1979

436. Van Espen, P., Nullens, H., and Adams, F., "An In-depth Study of Energy-dispersive X-Ray Spectra" X-Ray Spectrom. 9(3): 126-133, 1980.

437. Van Espen, P., Van't Dack, L., Adams, F. and Van Grieken, R., "Effective Sample Weight from Scatter Peaks in Energy-dispersive X-Ray Fluorescence," Anal. Chem. 51(7): 961-966, 1979.

438. Verbeke, P., Nullens, H., and Adams, F., "Energy-dispersive XRF of Metals - a Simple Fundamental Parameters Approach," Anal. Chim. Acta. 97: 283-294, 1978.

439. Vogel, R. and Fergason, L., "Gas Flow Proportional Counter for Electron Probe Light Element Analysis," Rev. Sci. Inst.: 934-938, July 1966.

440. Walter, F.J., "Characterization of Semiconductor X-ray Energy Spectrometers," STP 485, American Society for Testing and Materials, 82-112, 1971.

441. Walter, F.J., "Comments on Measurements of Epsilon and the Fano Factor," in Semiconductor Nuclear-Particle Detectors and Circuits, National Academy of Sciences, Pub. No. 1593, p. 63, 1969.

442. Walter, F.J., "The Impact of Semiconductor Detectors on X-Ray Spectroscopy," IEEE Trans. Nucl. Sci. NS-17(3): 196-214, 1970.

443. Ware, N.G. and Reed, S.J.B., "Background Corrections for Quantitative Electron Microprobe Analysis Using a Lithium Drifted Silicon Detector," J. Phys. E. 6: 286-288, 1973.

444. Ware, N.G., "Annotated Computer Programs for Electron Probe Microanalysis Using a Lithium Drifted Silicon Detector," Special Report, Research School of Earth Sciences, Australian National University, 1973.

445. Webb, P.P. et al, "Use of Collimated Gamma-Ray Beams in the Study of Ge(Li) Detectors," Nucl. Instr. Meth. 63: 125-135, 1968.

446. Wendt, M., "Advances in Energy Dispersive X-Ray Microanalysis," Kristall und Technik 13(11): 1259-1275, 1978.

447. White, G., "An Autoranging Digital Ratemeter," Nucl. Instr. Meth. 125, 313-317, 1975.

448. Whited, R.C. and van den Berg, L., "Native Defect Compensation in HgI2 Crystals," IEEE Trans. Nucl. Sci. NS-24(1): 165-167, 1977.

449. Wichner, R., Armantrout, G.A. and Brown, T.G., "Ge Crystal Growth and Evaluation as Ge(Li) Detector Material," IEEE Trans. Nucl. Sci. NS-17(3): 160-164, 1970.

450. Williams, A. and Sara, R.I., "Parameters Affecting the Resolution of a Proportional Counter," Int. J. of Ap. Rad. & Isotopes 13: 229-38, 1962.

451. Williams, C.W., "Reducing Pulse-Height Spectral Distortion by Means of DC Restoration and Pile-Up Rejection," IEEE Trans. Nucl. Sci. NS-15(1): 297-302, 1968.

452. Williams, G., "Role of Multichannel Analyzer in Data Handling," STP 485, American Society for Testing and Materials, 125-139, 1971.

453. Woldseth, R. and Meyer, G.W., "Multi-Element Quality Control," Industrial R/D, June 1978.

454. Woldseth, R., "X-Ray Energy Spectrometry: New Applications in Industry and Medicine," American Laboratory 11: 1975.

455. Woldseth, R., Everything You Always Wanted to Know About XES, Foster City, California, Kevex Corp., 1973.

456. Woldseth, R., Porter, D.E., and Frankel, R.S., "The Analytical X-Ray," Industrial Research, Feb. 1971.

457. Woodhouse, J.B., "Escape Peaks in Si(Li) Detectors," Proc. 7th Nat. Conf. on Electron Probe Analysis, 79, 1972.

458. Yakowitz, H., "Energy-Dispersive X-Ray Spectrometry," J. de Microscopie et de Biologies Cellulaire 22: 1975.

459. Yakowitz, H., "X-Ray Microanalysis in Scanning Electron Microscopy," SEM/1974, Om Johari, Ed., (IITRI), Chicago, Ill, 1029-1042, 1974.

460. Yin, L.I., Trombka, J.I., and Seltzer, S.M., "New Position Sensitive Hard X-Ray Detector," Rev. Sci. Instrum. 51(6): 844-845, 1980.

461. Zaluzec, N.J. and Fraser, H.L., "A Modified Specimen Stage for X-Ray Analysis in a TEM," J. of Phys. E 9: 1051-1052, 1976.

462. Zaluzec, N.J. and Fraser, H.L., "Microchemical Analysis of Thin Metal Foils," 34th Ann. Proc. Electron Microscopy Soc. Amer., Miama Beach, Florida, G.W. Bailey, Ed., 1976.

463. Zulliger , H.R. and Aitken, D.W., "Charge Collection Efficiencies for Lithium- Drifted Silicon and Germanium Detectors in the X-Ray Energy Region," IEEE Trans. Nucl. Sci. NS-15(1): 466, 1968.

464. Zulliger, H.R. and Aitken, D., "Fano Factor, Fact and Fallacy," IEEE Trans. Nucl. Sci. NS-17(3): 187, 1970.

465. Zulliger, H.R. and Aitken, D., "The Linearity of the Charge Conversion Function for Cooled Lithium-Drifted Silicon Detectors in Response to X-Ray and Low Energy Gamma Ray Excitation," IEEE Trans. Nucl. Sci. NS-14(1): 563, 1967.

466. Zulliger, H.R. and Stewart, J.E., "X-Ray Fluorescence Analysis with Transmission Target Tubes," Adv. in X-Ray Anal. 18: 278, 1975.

467. Zulliger, H.R. et al, "Electric Field Profile and Electron Drift Velocities in Lithium Drifted Silicon," Nucl. Instrum. Meth. 70(2): 125-133, 1969.

468. Zulliger, H.R., "Hole-Electron Production in Semiconductors," J. of Appl. Phys. 42(13): 5570, Dec. 1971.

469. Zulliger, H.R., et al, "Electric Field Profile and Electron Drift Velocities in Lithium-Drifted Silicon," Nucl. Instrum. Meth. 70(2): 125, 1969.

470. Zulliger, H.R., Drummond, W.E., and Middleman, L.M., "Properties of Ion-Implanted Silicon Detectors," IEEE Trans. Nucl. Sci. NS-19(3), 1972.

471. Zulliger, H.R., Middleman, L., and Aitken, D., "Linearity and Resolution of Semiconductor Radiation Detectors," IEEE Trans. Nucl. Sci. NS-16(1): 47, 1969.

William G. Banfield
National Cancer Institute
9000 Rockville Pike
Bldg. 10, Rm 8B19
Bethesda, MD 20014

Nicholas C. Barbi
Princeton Gamma Tech, Inc.
P. O. Box 641
Princeton, NJ 08540

Irene K. Berezesky
University of Maryland
31 S. Greene St.
Baltimore, MD 21201

Roger B. Bolon
General Electric CRD
Bldg. K1, Rm 2C20
Schenectady, NY 12345

James D. Brown
Univ. Western Ontario
London, Ontario
Canada N6A5B9

B. Stephen Carpenter
National Bureau of Standards
B-118 Reactor Bldg.
Washington, DC 20234

William F. Chambers
Sandia Laboratories, Org. 5822
P. O. Box 5800
Albuquerque, NM 87185

Arthur A. Chodos
California Institute of Technology
Caltech 170-25
Pasadena, CA 91125

J. W. Colby
Kevex Corp.
1101 Chess Drive
Foster City, CA 94404

Lawrence P. Cook
National Bureau of Standards
Room B214/223
Washington, DC 20234

Louis Costrell
National Bureau of Standards
Washington, DC 20234

Andrzej J. Dabrowski
University of Southern California
4676 Admiralty Way, Suite 932
Marina Del Rey, CA 90291

William E. Drummond
United Scientific Corp.
1400 D Stierlin Road
Mountain View, CA 94043

Richard W. Fink
School of Chemistry
Georgia Institute of Technology
Atlanta, GA 30332

Ronald F. Fleming
National Bureau of Standards
B108, Bldg. 235
Washington, DC 20234

Chuck Fiori
National Institutes of Health
Bethesda, MD 20014

Robin P. Gardner
North Carolina State University
Nuclear Engineering Department
Raleigh, NC 27650

Dale Gedcke
EG&G Ortec
100 Midland Road
Oak Ridge, TN 37830

Joseph D. Geller
JEOL, Inc.
477 Riverside Avenue
Medford, MA 02155

David George
Geophysical Laboratory
2801 Upton St., NW
Washington, DC 20008

J. I. Goldstein
Metallurgy Dept.
Lehigh University
Bethlehem, PA 18015

Robert R. Greenberg
National Bureau of Standards
Bldg. 235, Rm B108
Washington, DC 20234

Sally Harrison
National Bureau of Standards
B108 Reactor
Washington, DC 20234

Kurt Heinrich
National Bureau of Standards
Gas and Particle Science Division
Washington, DC 20234

Edwin C. Kuehner
National Bureau of Standards
Washington, DC 20234

Eric Lifshin
General Electric Corporation
Research & Development
Rm 2A18 K-1
Schenectady, NY 12301

Daniel Lister
PGT, Inc.
Box 641
Princeton, NJ 08540

B. G. Lowe
Link Systems Ltd.
Halifax Road, Cressex Industrial Estate
High Wycombe, Bucks,
England

Jon McCarthy
Tracor Northern, Inc.
2551 W. Beltline Hwy.
Middleton, WI 53562

R. Marinenko
National Bureau of Standards
Washington, DC 20234

Harold Marr
Princeton Gamma-Tech
Princeton, NJ 08540

R. A. Miller
Princeton Gamma-Tech
Washington St.
Rocky Hill, NJ 08553

Tom Moore
Dept. of Materials Science
University of Virginia
Thornton Hall
Charlottesville, VA 22901

Ronald G. Musket
Kevex Corp.
1101 Chess Drive
Foster City, CA 94404

Robert Myklebust
National Bureau of Standards
Gas and Particle Science Division
Washington, DC 20234

Dale Newbury
National Bureau of Standards
Gas and Particle Science Div.
Washington, DC 20234

David L. Neylan
U.S. Bureau of Mines
4900 Lasalle Rd.
Avondale, MD 29782

Timonthy Padfield
Conservation Analytical Lab
Smithsonian Institution
Washington, DC 20560

P. Pella
National Bureau of Standards
Washington, DC 20234

Ivor L. Preiss
RPI - Dept. of Chemistry
Troy, NY 12181

Jacqueline M. Rams
EG&G Ortec
6406 Elray Drive
Baltimore, MD 21209

Carl Robbins
National Bureau of Standards
Washington, DC 20234

John C. Russ
EDAX Labs
P. O. Box 135
Prairie View, IL 60069

Peter L. Ryder
University of Bremen
Bremen, W. Germany

R. A. Sareen
Link Systems Ltd.
Halifax Road, Cressex Industrial Estate
High Wycombe, Bucks
England

Fred Schamber
Tracor Northern
2551 W. Beltline Hwy.
Middleton, WI 53562

Michael A. Short
Ford Motor Company
Engineering & Research Staff
P. O. Box 2053
Dearborn, MI 48121

Manbir Singh
University of Southern California
Medical Imaging Science Group
4676 Admiralty Way #932
Marina Del Rey, CA 90025

John Small
National Bureau of Standards
Gas and Particle Science Div.
Washington, DC 20234

Julian H. Sparrow
National Bureau of Standards
Bldg. 245 C-216
Washington, DC 20234

Peter Statham
Link Systems Ltd.
Halifax Road
High Wycombe, Bucks,
England HP123SE

Eric Steel
National Bureau of Standards
Gas and Particle Science Div.
Washington, DC 20234

Robert E. Stone, Inc.
EG&G Ortec
100 Midland Rd.
Oak Ridge, TN 37830

William B. Stroube
National Bureau of Standards
Reactor Bldg. Rm B117
Washington, DC 20034

Kenneth R. Thompson
Nuclear Data Inc.
Golf & Meacham Rds.
Schaumburg, IL 60196

F. J. Walter
EGG-ORTEC
Box 623
Oak Ridge, TN 37836

David B. Williams
Lehigh University
Metallurgy Dept.
Bethlehem, PA 18015

Nestor J. Zaluzec
Oak Ridge National Lab.
P. O. Box X
Oak Ridge, TN 37830

NBS-114A (REV. 2-8C)

U.S. DEPT. OF COMM. BIBLIOGRAPHIC DATA SHEET (See instructions)	1. PUBLICATION OR REPORT NO. NBS SP 604	2. Performing Organ. Report No.	3. Publication Date June 1981

4. TITLE AND SUBTITLE

Energy Dispersive X-Ray Spectrometry
Proceedings of a Workshop on Energy Dispersive X-Ray Spectrometry held at the National Bureau of Standards, Gaithersburg, MD, April 23-25, 1979

5. AUTHOR(S)

K.F.J. Heinrich, D.E. Newbury, R.L. Myklebust, and C.E. Fiori

6. PERFORMING ORGANIZATION (If joint or other than NBS, see instructions)

NATIONAL BUREAU OF STANDARDS
DEPARTMENT OF COMMERCE
WASHINGTON, D.C. 20234

7. Contract/Grant No.

8. Type of Report & Period Covered

Final

9. SPONSORING ORGANIZATION NAME AND COMPLETE ADDRESS (Street, City, State, ZIP)

Same as above.

10. SUPPLEMENTARY NOTES

Library of Congress Catalog Card Number: 81-600047

☐ Document describes a computer program; SF-185, FIPS Software Summary, is attached.

11. ABSTRACT (A 200-word or less factual summary of most significant information. If document includes a significant bibliography or literature survey, mention it here)

This book is the formal report of the Workshop on Energy Dispersive X-Ray Spectrometry held at the National Bureau of Standards, April 23-25, 1979. The papers included in these proceedings cover a wide range of topics in the field: (1) Physics of detectors -- Properties of silicon (lithium), germanium (lithium), intrinsic germanium, and mercuric iodide detectors are described and compared. (2) Windowless x-ray detectors -- The application of windowless energy dispersive x-ray detectors to the measurement of soft x-rays below 1 keV is described, including special electronic techniques for processing pulses produced by low energy x-rays. (3) Electronics for energy dispersive x-ray spectrometry -- The signal processing chain is discussed with special emphasis on state-of-the-art multichannel analyzers. (4) Spectral processing and statistics -- Fundamental statistical considerations in spectral processing are described. A variety of curve techniques is discussed, including sequential simplex and least squares fitting with a digital filter. (5) Artifacts in energy dispersive x-ray spectrometry in electron beam instruments -- Artifacts arising from the basic detection and amplification processes and instrument-related artifacts observed in electron beam instruments operating in the range 10-1000 keV are described. (6) Applications -- Applications of energy dispersive x-ray spectrometry are given in quantitative x-ray microanalysis and x-ray fluorescence analysis.

12. KEY WORDS (Six to twelve entries; alphabetical order; capitalize only proper names; and separate key words by semicolons)

Electron probe microanalysis; energy dispersive x-ray spectrometry; germanium (lithium) detector; scanning electron microscopy; silicon (lithium) detector; spectral deconvolution; x-ray analysis; x-ray fluorescence

13. AVAILABILITY

☒ Unlimited

☐ For Official Distribution. Do Not Release to NTIS

☒ Order From Superintendent of Documents, U.S. Government Printing Office, Washington, D.C. 20402.

☐ Order From National Technical Information Service (NTIS), Springfield, VA. 22161

14. NO. OF PRINTED PAGES

441

15. Price

$9.00

USCOMM-DC 6043-P80

☆U.S. GOVERNMENT PRINTING OFFICE: 1981-340-997/1713

NBS TECHNICAL PUBLICATIONS

PERIODICALS

JOURNAL OF RESEARCH—The Journal of Research of the National Bureau of Standards reports NBS research and development in those disciplines of the physical and engineering sciences in which the Bureau is active. These include physics, chemistry, engineering, mathematics, and computer sciences. Papers cover a broad range of subjects, with major emphasis on measurement methodology and the basic technology underlying standardization. Also included from time to time are survey articles on topics closely related to the Bureau's technical and scientific programs. As a special service to subscribers each issue contains complete citations to all recent Bureau publications in both NBS and non-NBS media. Issued six times a year. Annual subscription: domestic $13; foreign $16.25. Single copy, $3 domestic; $3.75 foreign.

NOTE: The Journal was formerly published in two sections: Section A "Physics and Chemistry" and Section B "Mathematical Sciences."

DIMENSIONS/NBS—This monthly magazine is published to inform scientists, engineers, business and industry leaders, teachers, students, and consumers of the latest advances in science and technology, with primary emphasis on work at NBS. The magazine highlights and reviews such issues as energy research, fire protection, building technology, metric conversion, pollution abatement, health and safety, and consumer product performance. In addition, it reports the results of Bureau programs in measurement standards and techniques, properties of matter and materials, engineering standards and services, instrumentation, and automatic data processing. Annual subscription: domestic $11; foreign $13.75.

NONPERIODICALS

Monographs—Major contributions to the technical literature on various subjects related to the Bureau's scientific and technical activities.

Handbooks—Recommended codes of engineering and industrial practice (including safety codes) developed in cooperation with interested industries, professional organizations, and regulatory bodies.

Special Publications—Include proceedings of conferences sponsored by NBS, NBS annual reports, and other special publications appropriate to this grouping such as wall charts, pocket cards, and bibliographies.

Applied Mathematics Series—Mathematical tables, manuals, and studies of special interest to physicists, engineers, chemists, biologists, mathematicians, computer programmers, and others engaged in scientific and technical work.

National Standard Reference Data Series—Provides quantitative data on the physical and chemical properties of materials, compiled from the world's literature and critically evaluated. Developed under a worldwide program coordinated by NBS under the authority of the National Standard Data Act (Public Law 90-396).

NOTE: The principal publication outlet for the foregoing data is the Journal of Physical and Chemical Reference Data (JPCRD) published quarterly for NBS by the American Chemical Society (ACS) and the American Institute of Physics (AIP). Subscriptions, reprints, and supplements available from ACS, 1155 Sixteenth St., NW, Washington, DC 20056.

Building Science Series—Disseminates technical information developed at the Bureau on building materials, components, systems, and whole structures. The series presents research results, test methods, and performance criteria related to the structural and environmental functions and the durability and safety characteristics of building elements and systems.

Technical Notes—Studies or reports which are complete in themselves but restrictive in their treatment of a subject. Analogous to monographs but not so comprehensive in scope or definitive in treatment of the subject area. Often serve as a vehicle for final reports of work performed at NBS under the sponsorship of other government agencies.

Voluntary Product Standards—Developed under procedures published by the Department of Commerce in Part 10, Title 15, of the Code of Federal Regulations. The standards establish nationally recognized requirements for products, and provide all concerned interests with a basis for common understanding of the characteristics of the products. NBS administers this program as a supplement to the activities of the private sector standardizing organizations.

Consumer Information Series—Practical information, based on NBS research and experience, covering areas of interest to the consumer. Easily understandable language and illustrations provide useful background knowledge for shopping in today's technological marketplace.

Order the **above** *NBS publications from: Superintendent of Documents, Government Printing Office, Washington, DC 20402.*

Order the **following** *NBS publications—FIPS and NBSIR's—from the National Technical Information Services, Springfield, VA 22161.*

Federal Information Processing Standards Publications (FIPS PUB)—Publications in this series collectively constitute the Federal Information Processing Standards Register. The Register serves as the official source of information in the Federal Government regarding standards issued by NBS pursuant to the Federal Property and Administrative Services Act of 1949 as amended, Public Law 89-306 (79 Stat. 1127), and as implemented by Executive Order 11717 (38 FR 12315, dated May 11, 1973) and Part 6 of Title 15 CFR (Code of Federal Regulations).

NBS Interagency Reports (NBSIR)—A special series of interim or final reports on work performed by NBS for outside sponsors (both government and non-government). In general, initial distribution is handled by the sponsor; public distribution is by the National Technical Information Services, Springfield, VA 22161, in paper copy or microfiche form.

U.S. DEPARTMENT OF COMMERCE
National Bureau of Standards
Washington, D.C. 20234

OFFICIAL BUSINESS

Penalty for Private Use, $300

POSTAGE AND FEES PAID
U.S. DEPARTMENT OF COMMERCE
COM-215

SPECIAL FOURTH-CLASS RATE
BOOK